

6

CRDC-SP-85007

AD-A159 094

**PROCEEDINGS OF THE
CHEMICAL RESEARCH AND DEVELOPMENT
CENTER'S 1984 SCIENTIFIC CONFERENCE
ON OBSCURATION AND AEROSOL
RESEARCH**

**Edited by Ronald H. Kohl
Deborah Stroud**

**RONALD H. KOHL & ASSOCIATES
Tullahoma, Tennessee 37388**

DTIC FILE COPY

**DTIC
ELECTE
S AUG 29 1985 D**

June 1985

U.S. Army Armament, Munitions & Chemical Command
Aberdeen Proving Ground, Maryland 21010-5423

This document has been approved
for public release and sale; its
distribution is unlimited.

85 8 26 063

UNCLASSIFIED

SECURITY CLASSIFICATION OF THIS PAGE

AD-A159094

REPORT DOCUMENTATION PAGE

1a. REPORT SECURITY CLASSIFICATION UNCLASSIFIED			1b. RESTRICTIVE MARKINGS		
2a. SECURITY CLASSIFICATION AUTHORITY			3. DISTRIBUTION/AVAILABILITY OF REPORT Approved for public release; distribution unlimited.		
2b. DECLASSIFICATION/DOWNGRADING SCHEDULE					
4. PERFORMING ORGANIZATION REPORT NUMBER(S) CRDC-SP-85007			5. MONITORING ORGANIZATION REPORT NUMBER(S)		
6a. NAME OF PERFORMING ORGANIZATION Ronald H. Kohl & Associates		6b. OFFICE SYMBOL (if applicable)	7a. NAME OF MONITORING ORGANIZATION		
6c. ADDRESS (City, State, and ZIP Code) Cook Road, P.O. Box 1298 Tullahoma, TN 37388			7b. ADDRESS (City, State, and ZIP Code)		
8a. NAME OF FUNDING/SPONSORING ORGANIZATION CRDC		8b. OFFICE SYMBOL (if applicable) SMCCR-RSP-B	9. PROCUREMENT INSTRUMENT IDENTIFICATION NUMBER		
8c. ADDRESS (City, State, and ZIP Code) Aberdeen Proving Ground, MD 21010-5423			10. SOURCE OF FUNDING NUMBERS		
			PROGRAM ELEMENT NO.	PROJECT NO.	TASK NO.
				1A161102A	71A
11. TITLE (Include Security Classification) PROCEEDINGS OF THE CHEMICAL RESEARCH AND DEVELOPMENT CENTER'S SCIENTIFIC CONFERENCE ON OBSCURATION AND AEROSOL RESEARCH					
12. PERSONAL AUTHOR(S) Kohl, Ronald H., and Stroud, Deborah, Editors					
13a. TYPE OF REPORT Special Publication		13b. TIME COVERED FROM 84 01 TO 84 12		14. DATE OF REPORT (Year, Month, Day) 1985 June	
15. PAGE COUNT 555					
16. SUPPLEMENTARY NOTATION COR: Edward W. Stuebing, Ph.D., SMCCR-RSP-B, (301) 671-3089					
17. COSATI CODES			18. SUBJECT TERMS (Continue on reverse if necessary and identify by block number)		
FIELD	GROUP	SUB-GROUP			
15	02				
			Obscurants Aerosols Extinction Smoke		
			Obscuration Aerosol properties Scattering Light		
			Aerosol Absorption Transmission Sizing		
19. ABSTRACT (Continue on reverse if necessary and identify by block number) Fifty papers on current or recent research are included under the headings of Physical and Chemical Properties of Aerosols; Aerosol Characterization Methods; and Optical Properties of Aerosols. <i>Obscurants and obscuration; Aerosol properties; Light scattering; Transmission; Sizing</i>					
20. DISTRIBUTION/AVAILABILITY OF ABSTRACT <input checked="" type="checkbox"/> UNCLASSIFIED/UNLIMITED <input type="checkbox"/> SAME AS RPT. <input type="checkbox"/> DTIC USERS			21. ABSTRACT SECURITY CLASSIFICATION UNCLASSIFIED		
22a. NAME OF RESPONSIBLE INDIVIDUAL BRENDA C. ECKSTEIN			22b. TELEPHONE (Include Area Code) (301) 671-2914		22c. OFFICE SYMBOL SMCCR-SPS-IR

DD FORM 1473, 84 MAR

83 APR edition may be used until exhausted.
All other editions are obsolete.

SECURITY CLASSIFICATION OF THIS PAGE

UNCLASSIFIED

18. Subject Terms

Electromagnetic scattering;
 Millimeter wave radiation;
 Submillimeter wave radiation;
 Infrared and
 Visible radiation;
 Electromagnetic waves
 Spherical particles;
 Mie scattering;
 Rayleigh scattering;
 Raman scattering;
 Concentration sampling;
 Particle dynamics;
 Plumes;
 Diffusive mixing;
 Aerosol growth;
 Nucleation;
 Smoke generation and
 Aerosol generation;
 Photoionization;
 Conductivity;
 Chemical characterization;
 Phosphorus smoke;
 Fluorescence;
 Aerosol clusters;
 Spheres
 Cylinders
 Rough particles
 Irregular particles and
 Nonspherical particles;
 Particle aggregates and
 Particle chains;
 Infrared emission
 Cooperative scattering;
 Dependent scattering and
 Multiple scattering;
 Radiative transfer;
 Coagulation;
 Condensation;
 Liquid drops;
 Drop growth;
 Fog oil smoke and
 Diesel oil smoke;
 Particle mechanics
 Atmospheric optics and
 Atmospheric dispersion;
 Cloud dynamics;
 Scavenging;
 Aerosol collectors
 Aerosol elimination
 Aerosol characterization
 Particle sizing
 Hygroscopic smokes;
 Particle size distribution and
 Particle orientation distribution,

Optical constants and
 Optical properties
 Anomalous diffraction;
 Attenuated total reflection;
 Reflection spectroscopy;
 ATR
 Far-infrared
 Refractive index;
 Index of refraction
 Inversion
 Inversion techniques;
 Gypsum;
 Natural minerals;
 Minerals
 Metal;
 Metallic particles;
 Powdered minerals;
 Complex refractive index
 Effective media
 High energy laser
 Particles
 Aerosol particles
 SERS
 Surface Enhanced Raman Scattering
 Dielectric particles
 Conducting particles
 Cylindrical particles
 Fibers
 Conducting fibers
 Gas-aerosol reactions
 Transport phenomena
 Aerosol measurement
 Spheroids
 Laser pulses
 Optical pulses
 Pulse propagation
 Clouds
 Laser
 Radiation transport
 Fourier analysis
 Plume mechanics

PREFACE

The 1984 Chemical Research and Development Center Scientific Conference on Obscuration and Aerosol Research was held 25-29 June, 1984, at the Edgewood Area of Aberdeen Proving Ground, Maryland. The Conference is held annually, the last full week in June, under the direction of Dr. Edward W. Stuebing, Research Area Coordinator, Aerosol Science, from whom it receives its unique and productive character.

The Conference is an informal forum for scientific exchange and stimulation amongst investigators in the wide variety of disciplines required for aerosol research and a description of an obscuring aerosol and its effects. The participants develop some familiarity with the Army aerosol and obscuration-science research programs and also become personally acquainted with the other investigators and their research interests and capabilities. Each attendee is invited to present any aspect of a topic of interest and may make last minute changes or alterations in his presentation as the flow of ideas in the Conference develops.

While all participants in the Conference are invited to submit written papers for the Proceedings of the Conference, each investigator who is funded by the Army Research Program is requested to provide one or more written papers which document specifically the progress made in his funded effort in the previous year and which indicate future directions. Also, the papers for the Proceedings are collected in the Fall to allow time for the fresh ideas which arise at the Conference to be incorporated. Therefore, while the papers in these proceedings tend to closely correspond to what was presented at the Conference, there is not an exact correspondence.

The reader will find the items relating to the Conference itself--photographs, the list of attendees and the agenda--in the appendixes following the papers and the indexes pertaining to them.

The use of trade names in these proceedings does not constitute an official endorsement or approval of the use of such commercial hardware or software. These proceedings may not be cited for purposes of advertisement.

Reproduction of this document in whole or in part is prohibited except with permission of the Commander, Chemical Research and Development Center, ATTN: DRSMC-CLJ-IR, Aberdeen Proving Ground, Maryland 21010-5423. However, the Defense Technical Information Center and the National Technical Information Service are authorized to reproduce the document for US Government purposes.

This report has been approved for release to the public.

Classification for	
DTIC	<input checked="" type="checkbox"/>
DA&I	<input type="checkbox"/>
DDP	<input type="checkbox"/>
Approved	<input type="checkbox"/>
Classification	



A-1

CONTENTS*

	Page
I. PHYSICAL AND CHEMICAL PROPERTIES OF AEROSOLS	9
A. <u>Particle Formation, Evolution and Composition</u>	
GENERATION OF MONODISPERSE NONSPHERICAL AEROSOL PARTICLES	
K. H. Leong	11
GAS-TO-PARTICLE CONVERSION: THE ROLE OF PRE-EXISTING DIMERS IN THE FORMATION OF CLUSTERS DURING SUPERSONIC EXPANSION	
R. G. Keesee and A. W. Castleman, Jr.	13
AEROSOL PLUME MECHANICS AND PARTICLE GROWTH PROCESSES	
J. R. Brock, T. H. Tsang, and S. G. Kim	23
B. <u>Plume Mechanics</u>	
AEROSOL PLUME MECHANICS AND PARTICLE GROWTH PROCESSES	
J. R. Brock, T. H. Tsang, and S. G. Kim	23
TURBULENT MIXING IN CLOUDS	
J. Latham	37
CHARACTERISTICS OF OBSERVED CONCENTRATION FLUCTUATIONS DURING SMOKE WEEK III	
Steven Hanna and Jonathan Pleim	43
WIND TUNNEL SIMULATION OF DIFFUSION IN A CONVECTIVE BOUNDARY LAYER	
M. Poreh and J. E. Cermak	49
CRITERIA FOR WIND-TUNNEL SIMULATION OF PARTICLE PLUMES IN THE ATMOSPHERIC SURFACE LAYER	
M. Poreh and J. E. Cermak	53
C. <u>Particle Dynamics: Orientation Effects, Concentration Sampling, and Size/Shape Analysis</u>	
THE ORIENTATION DISTRIBUTION FUNCTION OF NONSPHERICAL AEROSOL PARTICLES IN A GENERAL SHEAR FLOW: THE TURBULENT CASE	
Isaiah Gallily and E. M. Krushkal	57
UNIPOLAR CHARGING FOR ULTRAFINE AEROSOLS: THEORY, EXPERIMENT AND SIGNIFICANCE FOR SIZE DISTRIBUTION	
S. W. Davison, S. Hwang, J. Wang, and J. W. Gentry	69
D. <u>Aerosol Elimination</u>	
RESULTS OF PAST AND CURRENT INVESTIGATION OF THE SMOKE PARTICLE SCAVENGING BY NONSPHERICAL COLLECTORS	
J. Podzimek and J. Martin	73
THE COLLISION OF NONSPHERICAL AEROSOL PARTICLES WITH WATER DROPS	
K. H. Leong	85
II. AEROSOL CHARACTERIZATION METHODS	87
(other than Aerodynamic Methods - see IC)	
A. <u>Particle Shape Descriptions and the Value of Effective Size Parameters</u>	
ANALOGS TO THE SHAPE FACTOR OBSERVED IN OPTICAL CALCULATIONS	
Pamela E. Geller and Peter W. Barber	89
(Presented by Edward W. Stuebing--1983 Conference)	

*See also page 517 for the indexes of the authors and the organizations of the authors.

II. AEROSOL CHARACTERIZATION METHODS (continued)

A. Particle Shape Descriptions and the Value of Effective Size Parameters (continued)

CHARACTERIZATION OF SMALL NONSPHERICAL METALLIC PARTICLES W. Scheunemann	101
APPLICATIONS OF CONDITON NUMBERS IN PARTICLE SIZE ANALYSIS AND LINEAR REGRESSION C. R. Kaplan, P. Y. Yu, F. F. Farzanah, J. Hong and J. W. Gentry	109

B. Optical Inversion Methods for Size Distribution (Including Optical Particle Size Analyzers)

USE OF STRUCTURAL RESONANCES IN FLUORESCENCE EMISSION FOR SIZING SPHERES RESTING ON SUBSTRATES R. E. Benner, S. C. Hill, C. K. Rushforth and P. R. Conwell	113
MULTICHANNEL NEPHELOMETER DESIGN A. R. Tokuda, G. M. Hess, R. R. Majoch, S. R. Beck, C. D. Capps and N. E. Carroll	119
PROGRESS OF INVERSION TECHNIQUE EVALUATION J. R. Bottiger	129
AEROSOL SIZE DISTRIBUTION FROM SIMULATED NEPHELOMETRIC DATA W. A. Pearce	141

C. Optical Constants of Liquids and Powders

THE OPTICAL CONSTANTS OF SELECTED MATERIALS IN THE INFRARED, VISIBLE, AND ULTRAVIOLET SPECTRAL REGIONS Marvin R. Querry	145
THE OPTICAL CONSTANTS OF SMOKE MATERIALS IN THE SUBMILLIMETER AND MILLIMETER Larry L. Long, Mark A. Ordal, Robert J. Bell and Ralph W. Alexander, Jr.	167
METALS AND GRAPHITE: PREDICTING OPTICAL PROPERTIES IN THE SUBmmλ AND mmλ RANGES M. A. Ordal, L. L. Long, R. A. Paul, R. W. Alexander, Jr. and R. J. Bell	179
FAR-INFRARED EXTINCTION PROPERTIES OF METAL POWDERS V. P. Tomasevii and K. D. Moeller	207

III. OPTICAL PROPERTIES OF AEROSOLS 215

A. Infrared Emission from Aerosols

INVESTIGATION OF THE REACTION BETWEEN SINGLE AEROSOL ACID DROPLETS AND AMMONIA GAS Glenn O. Rubel and James W. Gentry	217
IR EMISSIVE CLOUD STUDY P. Ase and A. Snelson	223

B. Interaction of Radiation and Spherical (Including Layered) Particles

ON POSSIBLE EXPERIMENTAL APPLICATION OF SOME PROPERTIES OF THE FIRST EXPANSION COEFFICIENTS OF THE PHASE FUNCTION A. Coletti	225
RADIATION TORQUE ON A SPHERE ILLUMINATED WITH CIRCULARLY-POLARIZED LIGHT AND THE ANGULAR MOMENTUM OF THE SCATTERED RADIATION P. L. Marston and J. H. Crichton	233
TRANSMITTED-WAVE AND RAINBOW-ENHANCED GLORIES OF DIELECTRIC SPHERES* P. L. Marston and D. S. Langley	239

III. OPTICAL PROPERTIES OF AEROSOLS (continued)

B. Interaction of Radiation and Spherical (Including Layered) Particles (continued)

INFRARED SPECTROSCOPY OF SINGLE AEROSOL PARTICLES	
S. Arnold and A. B. Pluchino	241
RAMAN SPECTROSCOPY OF SINGLE OPTICALLY LEVITATED DROPLETS	
T. R. Lettieri, R. E. Preston and M. I. Bell	255

C. Workshop: Nonlinear Phenomena

AEROSOL INTERACTIONS WITH INTENSE LIGHT BEAMS	
R. L. Armstrong	259
PROBLEMS IN HEL - AEROSOL INTERACTIONS	
Melvin Lax	273

D. Interaction of Radiation and Nonspherical Particles (Including Aggregates)
With or Without Cooperative Effects

REAL-TIME MEASUREMENT OF PARTICULATE MASS CONCENTRATION BY AIRBORNE SPECTROPHONES - A FEASIBILITY STUDY	
K. Tennal, J. D. Wilson and M. K. Mazumder	281
SPECTROSCOPY OF MOLECULAR CLUSTERS AND SMALL PARTICLES IN SOLID ARGON MATRICES	
Donald R. Huffman	291
ABSORPTION AND SCATTERING BY SMALL PARTICLES; STRUCTURE OF THE INTERNAL AND NEAR FIELDS	
H. Weil and T. B. A. Senior	295
A NEW ITERATIVE EXTENDED BOUNDARY CONDITION METHOD FOR CALCULATING SCATTERING AND ABSORPTION BY ELONGATED OBJECTS	
Magdy F. Iskander	297
COMPLETE MUELLER MATRIX CALCULATIONS FOR LIGHT SCATTERING FROM DIELECTRIC CUBES OF DIMENSIONS OF THE ORDER OF A WAVELENGTH	
Chia-Ren Hu, George W. Kattawar and Mark E. Parkin	307
EXTINCTION BY ROUGH PARTICLES	
R. T. Wang	315
ANGULAR SCATTERING BY ROUGH PARTICLES	
R. T. Wang	327
SCATTERING AND DEPOLARIZATION BY CONDUCTING CYLINDERS WITH VERY ROUGH SURFACES	
Ezekiel Bahar and Mary Ann Fitzwater	365
ANGULAR SCATTERING DISTRIBUTIONS BY LONG COPPER AND BRASS CYLINDERS - EXPERIMENT AND THEORY	
A. Cohen, L. D. Cohen, R. Haracz, V. Tomaselli, J. Colosi and K. D. Moeller . .	373
RECENT RESULTS IN THE SCATTERING AND ABSORPTION BY ELONGATED CONDUCTIVE FIBERS	
N. E. Pedersen, J. C. Pedersen and P. C. Waterman	385
DIPOLE-DIPOLE SCATTERING INTERACTION AND ITS RELATION TO SEPARATION IN COATINGS AND CLOUDS	
D. L. Dye, C. D. Capps, C. Gulacsik, D. H. Holze and John W. Bond	431
DOUBLE SCATTERING FROM CYLINDERS AND SPHEROIDS	
Richard D. Haracz, Leonard D. Cohen and Ariel Cohen	441
ELASTIC AND INELASTIC SCATTERING OF COLLOIDAL PARTICLES	
Milton Kerker	449
ABSORPTION AND SCATTERING BY AGGREGATED AEROSOL PARTICLES	
J. R. Aronson, A. G. Emslie, I. Simon and E. M. Smith	455

III. OPTICAL PROPERTIES OF AEROSOLS (continued)

E. Propagation/Multiple Scattering in Aerosol Media and Radiative Transfer

PROGRESS IN RESEARCH ON WAVE PROPAGATION AND SCATTERING IN DISCRETE RANDOM MEDIA USING MULTIPLE SCATTERING THEORY V. K. Varadan and V. V. Varadan	469
RADIATIVE TRANSFER BY CLOUDS OF CONDUCTIVE FIBERS Peter C. Waterman, Jeanne C. Pedersen and Norman E. Pedersen	477
IMAGING THROUGH A MULTIPLE SCATTERING MEDIUM A. Zardecki, S. A. W. Gerstl and J. F. Embury	491
TRANSPORT METHODS FOR ESTIMATING SINGLE-SCATTERING COEFFICIENTS FROM REMOTE OR IN SITU MULTIPLY-SCATTERED RADIANCE MEASUREMENTS N. J. McCormick	495
ASSESSMENT OF AEROSOL EXTINCTION TO BACKSCATTER RATIO MEASUREMENTS MADE AT 694.3nm IN TUCSON, ARIZONA J. A. Reagan, M. V. Apte, A. Ben-David and B. M. Herman	505
INDEXES FOR PAPERS IN THESE PROCEEDINGS	517
A. Index of Authors	519
B. Index of Authors' Organizations	521
APPENDIXES	523
A. Photographs of Conference Attendees	525
B. List of Conference Attendees	531
C. Conference Agenda	545

I. PHYSICAL AND CHEMICAL PROPERTIES OF AEROSOLS

GENERATION OF MONODISPERSE NONSPHERICAL AEROSOL PARTICLES

K. H. Leong
University of Illinois at U-C
Urbana, IL 61801

ABSTRACT

This work is partly an extension and a reevaluation of a previous study on the morphology of aerosol particles generated from the evaporation of solution drops (J. Aerosol Sci., (1981), 12, 417-435). The results of the previous and later work are used to demonstrate the feasibility of using a vibrating orifice aerosol generator for the controlled generation of monodisperse aerosol particles that are uniformly nonspherical. Crystal habit and solubility effects are discussed in relation to the two primary controlling parameters: the nature of the chemical compound used as the solute and the evaporation rate. Single crystals, prolate spheroids, spheroids, cenospheres and shells have been generated. Further work to define the range of particle shapes possible is in progress.

GAS-TO-PARTICLE CONVERSION: THE ROLE OF PRE-EXISTING DIMERS IN
THE FORMATION OF CLUSTERS DURING SUPERSONIC EXPANSION

R. G. Keesee and A. W. Castleman, Jr.
Department of Chemistry
The Pennsylvania State University
University Park, PA 16802

ABSTRACT

A complete rendition of this contribution is to appear in a paper by J. J. Breen, K. Kilgore, K. Stephan, R. Hofmann-Sievert, B. D. Kay, R. G. Keesee, T. D. Märk, and A. W. Castleman, Jr., "The Use of Similarity Profiles in Studying Cluster Formation in Molecular Beams: Evidence for the Role of Preexisting Dimers," Chem. Phys., in press. Studies of the influence of source temperatures and pressures on the distributions of water, ammonia, and sulfur dioxide clusters are reported. The experiments reveal that nearly identical cluster distributions occur in cases where the pressure of dimer is maintained constant according to a simple equation involving stagnation temperature and pressure. In similar experiments covering the same range of pressures and temperatures, widely differing cluster distributions are obtained under conditions where the dimer concentration is not fixed. Our results suggest that large clusters proceed largely from pre-existing dimers, and that very few new ones are created early enough in the expansion to effect cluster growth. The gas-phase heat of dimerization of sulfur dioxide is determined to be 4.3 ± 0.3 kcal/mole.

INTRODUCTION

At the present time there is widespread interest in the formation and properties of small aggregates of molecules (1,2). These systems constitute a form of matter having properties between those of an isolated gas-phase molecule and the bulk condensed state. Study of their formation and properties is an attractive method of following the continuous course of change of matter from the gaseous to the condensed phase, elucidating nucleation and solvation phenomena, and shedding light on certain problems in the field of surface science (2,3).

In addition to these aspects of cluster properties, there is a strong interest in their formation processes where fundamental questions arise concerning the initial stages of nucleation and growth. More specifically, the interest is in the initial collision partners and the rate limiting step in the clustering reaction scheme. Cluster growth is thought to proceed initially via a three-body association reaction. In this scheme, two particles collide and form an activated complex until a third body removes the excess energy and stabilizes the complex via another collision. Recently, considerable attention has been given to the role of the dimer in cluster growth. Andres et al. (4) have used a multiple expansion cluster source to obtain condensation

accommodation coefficients for water clusters up to the trimer. Their results indicate that the formation of the larger clusters from the dimer is considerably more facile than the formation of the dimer from the monomer. In another experiment Ellenbroek et al. (5) found that when a fraction of the hydrogen fluoride dimers in a cluster beam are vibrationally dissociated with the output of a hydrogen fluoride laser, many of the larger clusters disappeared. These findings suggest that the initial amount of dimers may have a strong influence on the amount and size distribution of large clusters. In accord with these ideas we set out to examine homogeneous cluster distributions over a varied set of stagnation conditions to examine the role of pre-existing dimers on the cluster distributions observed in an adiabatic expansion.

This paper reports the results of studies of the influence of source temperature and pressure on the distribution of clusters formed in a molecular beam. Determination of the factors governing the similarity profiles of cluster distributions has led to additional insight into the mechanisms responsible for the early stage of cluster formation and growth.

EXPERIMENTAL

Although these experiments have been performed over a lengthy time period in which the apparatus has undergone some changes, the main elements have remained the same. The details are described elsewhere (6-8). Briefly, it consists of a supersonic nozzle, the nozzle exhaust chamber, two differential pumping chambers, and a detection chamber housing a quadrupole mass spectrometer. The nozzle exhaust chamber is separated from the differential pumping chamber by a conical skimmer (Beam Dynamics Model II) having either a 0.5 mm or a 1.0 mm diameter aperture. Typical operating pressures are 1×10^{-4} torr in the exhaust chamber, 1×10^{-6} and 1×10^{-7} torr in the differential pumping chambers, and 2×10^{-9} torr in the detection chamber. Mass analysis is accomplished with an electron impact mass spectrometer (Granville Phillips Spectrascan 750). Data are acquired using a multichannel scaling technique in which the data was stored and displayed with a multichannel analyzer (Ino-Tech model no. 5300).

The stagnation chamber is constructed from glass tubing and a roundbottom flask; the total volume is approximately one liter; heating is performed resistively. The temperature in the chamber is monitored with two Chromel/Alumel thermocouples and an electronic zero point reference (Omega Electronics). One thermocouple is placed at the rear of the stagnation chamber and the other is placed near the tip of the nozzle. Temperatures are maintained constant within a range of one degree Celsius. The stagnation pressure is monitored with either a Bourdon-type gauge (Matheson model no. 63-5601) or a Baratron capacitance manometer (model no. 310-CH). In either case the stagnation pressure is maintained constant to within ten torr.

Ammonia and sulfur dioxide are anhydrous grade and obtained from local suppliers. Both are used without further purification. Water is obtained from the buildings deionized water system. Various sized nozzles were used in the experiments ranging from 100 to 300 μ m in diameter. These were convergent glass tubes that incorporated an annular heating/cooling jacket around the entire source assembly. The details are given in Reference 9.

During the course of experiments on cluster distributions, we noted that the distributions are often quite similar under widely differing source conditions, but in other cases quite different with only some relatively minor changes in source conditions (9,10). The present study was undertaken to establish whether dimers might be the primary species initiating cluster formation in the experiments and, more importantly, whether fixing the dimer concentration might lead to identical cluster distributions.

The basis for investigating the importance of dimers is as follows:

$$2A = A_2 \quad (1)$$

An equilibrium constant can be written and related to the standard enthalpy and entropy change of dimerization, ΔH° and ΔS° , respectively. Assuming that the fugacity of a species is approximated by its partial pressure,

$$K = \frac{P_{A_2}}{P_A^2} = \exp[-(\Delta H^\circ - T\Delta S^\circ)/RT] \quad (2)$$

Here, P° is the standard state pressure taken to be one atmosphere. In experiments in which the dimer pressure was maintained constant, but both nozzle and source temperature were varied, thermodynamic properties of the dimer system could be utilized to ascertain appropriate conditions for maintaining the same dimer partial pressure, P_{A_2} ,

$$\frac{P_{A_2}}{P_{A_2}'} = \frac{P_A^2}{P_A'^2} \exp\left[-\frac{\Delta H^\circ}{R} \left(\frac{1}{T_c} - \frac{1}{T_o'}\right)\right] \quad (3)$$

where P_A refers to the monomer pressure, T_o the stagnation temperature, and the prime designates a different source condition. For the dimer partial pressure (P_{A_2}) to remain fixed as the stagnation conditions are changed from (P_A, T_o) to (P_A', T_o') the relationship

$$\ln \left[\frac{P_A}{P_A'} \right] = \frac{1}{2} \frac{\Delta H^\circ}{R} \left[\frac{1}{T_o} - \frac{1}{T_o'} \right], \quad (4)$$

must be satisfied.

TEMPERATURE DEPENDENCE OF CLUSTER DISTRIBUTIONS: WATER AND AMMONIA SYSTEMS

By changing the temperature of the nozzle, it is possible to strongly influence the distribution of clusters observed. In an attempt to determine the role played by the concentration of dimers existing in the pre-expanded gas in determining the final observed cluster distribution, the cluster distributions were measured for a variety of different stagnation conditions. The only constraint imposed upon the stagnation conditions (T_0, P_0) was that the equilibrium partial pressure of the dimer remain fixed as the stagnation conditions were varied.

The value of interest is the relative intensity change with temperature and pressure of the observed ionized cluster distributions. An important fact to note is that in the present studies, the degree of fragmentation of the neutral clusters upon ionization is immaterial since the ionized cluster distribution is used only to monitor shifts in the distribution of the precursor neutral clusters. In the case of water and ammonia, the observed ions are the protonated species $H^+(H_2O)_n$ and $H^+(NH_3)_n$.

Figure 1 displays the resultant cluster distributions measured for the expansion of neat water vapor through a 100 μ m diameter nozzle at various stagnation conditions. The various stagnation conditions (P_{H_2O}, T_0) satisfy Equation (4) when using the theoretically predicted (11) value for ΔH° (-6 kcal/mole). The cluster distributions for various stagnation conditions are essentially indistinguishable, as is clearly displayed in the figure. Figure 2 displays the resultant cluster distributions when the stagnation conditions are arbitrary. The difference between the two distributions in Figure 2 is readily discernible.

An analogous study of ammonia cluster distributions was made using the literature value (12) for the dimerization enthalpy ($\Delta H^\circ = -4.5$ kcal/mole). Figure 3 displays the resultant cluster distributions for the expansion of neat ammonia vapor through a 100 μ m diameter nozzle. The various stagnation conditions have a constant $(NH_3)_2$ partial pressure behind the nozzle according to Equation (4). In these experiments with ammonia the temperature was varied over a range of -25°C to 10°C while the pressure was varied from 480 torr to 760 torr. Yet, the cluster distributions are virtually identical.

Again, when the stagnation conditions are randomly changed, the resultant cluster distribution displays noticeable differences. The results support the hypothesis that pre-existing dimers from the stagnation chamber control the development of the cluster distribution during expansion, at least for the range of conditions examined in the present work.

CLUSTERS OF SO₂ AND THE ENTHALPY OF DIMERIZATION

In the case of sulfur dioxide the present authors know of no reliable value for the heat of dimerization. In view of the success of reproducing cluster distributions for water and ammonia expansions under varying stagnation conditions by controlling the partial pressure of pre-existing dimers, the procedure was reversed for sulfur dioxide. First, an expansion was conducted at 25°C and 500 torr as a reference. Next, a series of expansions were then made at 65°C with the stagnation pressures adjusted at values corresponding (via Equation (4)) to heats of dimerization ranging from 3 to 6 kcal/mole. For sulfur dioxide the main series is (SO₂)_n⁺ but a SO⁺(SO₂)_n series is also observed. The distributions obtained with stagnation pressures corresponding to 4 kcal/mole resulted in fairly good agreement with the reference distribution. As a further test, the stagnation conditions were changed to 45°C and 85°C with the corresponding pressures 620 torr and 880 torr. Again, the distribution profiles matched well with the reference profile and at 85°C we were able to bracket the heat of dimerization between 4 and 4.5 kcal/mole as is readily seen from a comparison of tabulated, measured intensities relative to the reference case, as depicted in Table I. Thus, the enthalpy change for dimerization of sulfur dioxide is determined to be -4.3 ± 0.3 kcal/mole.

Finally, argon was tested in a similar manner to the sulfur dioxide. The result was that the heat of dimerization of argon is too small to be employed by our method. The expected value is about 0.3 kcal/mole (13) and limitations of the apparatus prevent investigation over the wide range of stagnation conditions required to determine such a small heat of dimerization.

DISCUSSION AND CONCLUSION

Clusters formed in an expanding free jet must grow by association kinetics; further growth steps require substantial cooling by collision with a third-body in the expanding jet. The growth is inhibited if the clusters become vibrationally hot through energy release in successive addition steps, or by spontaneous internal reorganization of cluster structures giving rise to additional hydrogen bonds within the complex. Therefore, clusters can decompose by unimolecular decay processes if further cooling collisions do not take place during the time domain for unimolecular decomposition. Consequently, the formation of new dimers is an inherently slow, rate determining step.

The results of the present study demonstrate that identical cluster distributions can be obtained in supersonically expanding jets under widely different expansion conditions when the absolute quantity of dimers was maintained fixed while the nozzle temperature and expansion pressure were substantially varied over a range of values.

The advantage of the present method in studying beams is several fold. First, through the investigation of similarity profiles, the influence of cluster fragmentation is obviated within the assumption that it is not appreciably affected by source temperature. Only the response of the distribution to changing source parameters is considered and there is no necessity of determining absolute ratios between cluster species and particularly between monomer and dimer which may be subject to considerable influence due to fragmentation problems. Furthermore, obtaining similar cluster distributions overcomes the problem of ascertaining what fraction of the measured dimer is attributable to that pre-existing in the source and what portion is due to the formation of new dimers during the course of the expansion.

ACKNOWLEDGMENTS

This research was sponsored by the U.S. Army Research Office under Grant No. DAAG29-82-K-0160 (NH_3 and H_2O studies) and the U.S. National Science Foundation under Grant No. ATM-82-04010 (SO_2 studies). Some of the experimental work was undertaken when the authors were associated with the Department of Chemistry and the Cooperative Institute for Research in Environmental Sciences at the University of Colorado.

REFERENCES

1. Ber. Bunsenges. Phys. Chem. 88, No. 3, March, 1984.
2. T. D. Mark and A. W. Castleman, Jr., "Experimental Studies of Cluster Ions," in Advances in Atomic Molecular Physics, Vol. 20 (D. R. Bates and B. Bederson, Eds.) Academic Press, New York, in press.
3. A. W. Castleman, Jr., in Electronic and Atomic Collisions (J. Eichler, I. V. Hertel, and N. Stolterfoht, Eds.) Elsevier Science Publishers, pp. 579-590 (1984).
4. J. J. Kolstad, R. P. Andres, and J. M. Calo, Proceedings, 186th Annual Meeting of the American Chemical Society, Washington, DC, (1983).
5. T. Ellenbroek, J. Toennies, M. Wilde and J. Wanner, J. Chem. Phys. 75, 3414 (1981).
6. B. D. Kay and A. W. Castleman, Jr., J. Chem. Phys. 78, 4297 (1983).
7. R. Sievert, I. Cader, J. Van Doren, and A. W. Castleman, Jr., "Mass Spectral and Electric Deflection Study of Acetic Acid Clusters," J. Phys. Chem., in press.
8. R. Sievert and A. W. Castleman, Jr., J. Phys. Chem., 88, 3329 (1984).
9. B. D. Kay, T. G. Lindeman and A. W. Castleman, Jr., Rev. Sci. Instrum. 53, 473 (1982).
10. V. Hermann, B. D. Kay, and A. W. Castleman, Jr., Chem. Phys. 72, 185 (1982); B. D. Kay, V. Hermann, and A. W. Castleman, Jr., Chem. Phys. Lett. 80, 469 (1981).
11. J. Del Bene and J. Pople, J. Chem. Phys. 52, 4858 (1970).
12. J. Lowder, J. Quant. Spectrosc. Radiat. Transfer 10, 1085 (1970).
13. J. A. Baker, R. O. Watts, S. K. Lee, T. P. Schafer, and Y. T. Lee, J. Chem. Phys. 61, 308 (1974).

TABLE I
COMPARISON OF NORMALIZED CLUSTER INTENSITIES AS A
FUNCTION OF ASSUMED HEAT OF DIMERIZATION

N	500 Torr (a) 25°C	820 Torr 3.5 kcal/mole 85°C	880 Torr 4.0 kcal/mole 85°C	940 Torr 4.5 kcal/mole 85°C	910 Torr 6 kcal/mole 65°C
2	0.17	0.13	0.12	0.11	0.08
3	0.41	0.40	0.37	0.32	0.24
4	0.66	0.68	0.66	0.60	0.50
5	0.84	0.38	0.85	0.81	0.71
6	0.93	0.99	0.95	0.96	0.85
7	0.93	0.96	0.94	0.98	0.94
8	1	1	1	1	1
9	0.93	0.87	0.91	0.95	0.95
10	0.81	0.74	0.78	0.81	0.8
11	0.73	0.64	0.71	0.75	0.81

^aReference Case

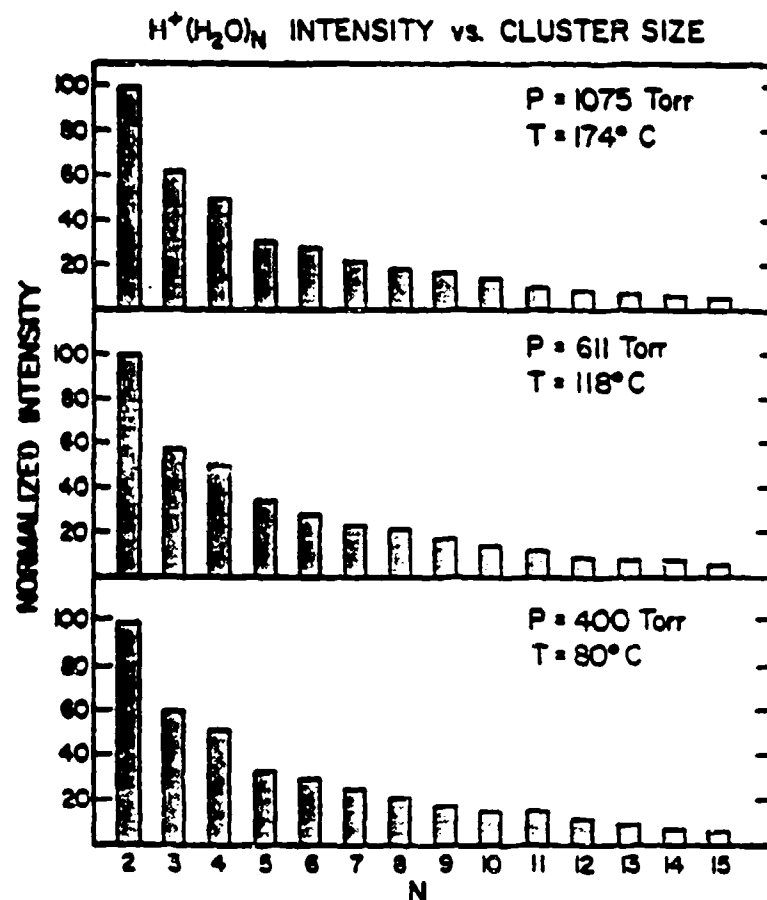


FIGURE 1. LINEAR PLOT OF $H^+(H_2O)_N$ CLUSTER INTENSITY VERSUS CLUSTER SIZE FOR VARIOUS STAGNATION CONDITIONS. Each distribution has the same pre-expansion partial pressure of $(H_2O)_2$.

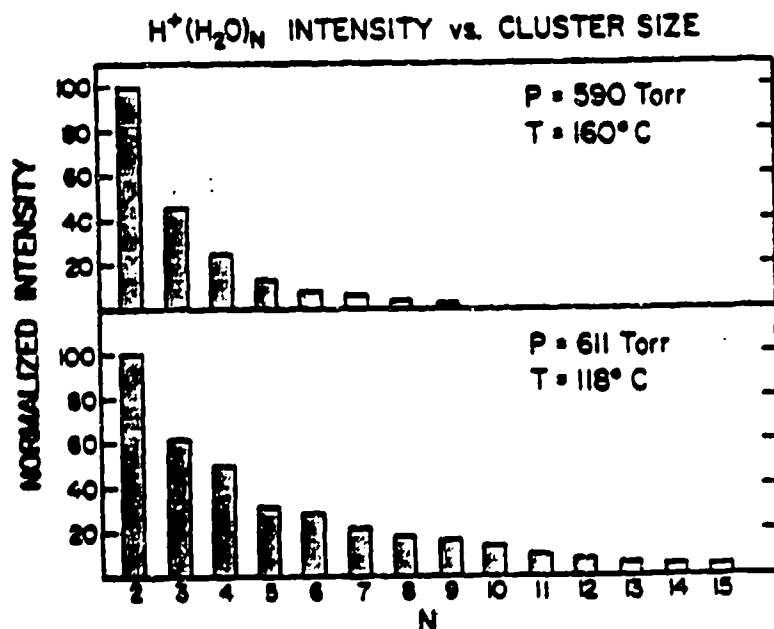


FIGURE 2. LINEAR PLOT OF $H^+(H_2O)_N$ CLUSTER INTENSITY VERSUS CLUSTER SIZE FOR STAGNATION CONDITIONS HAVING DIFFERENT PRE-EXPANSION PARTIAL PRESSURES OF $(H_2O)_2$.

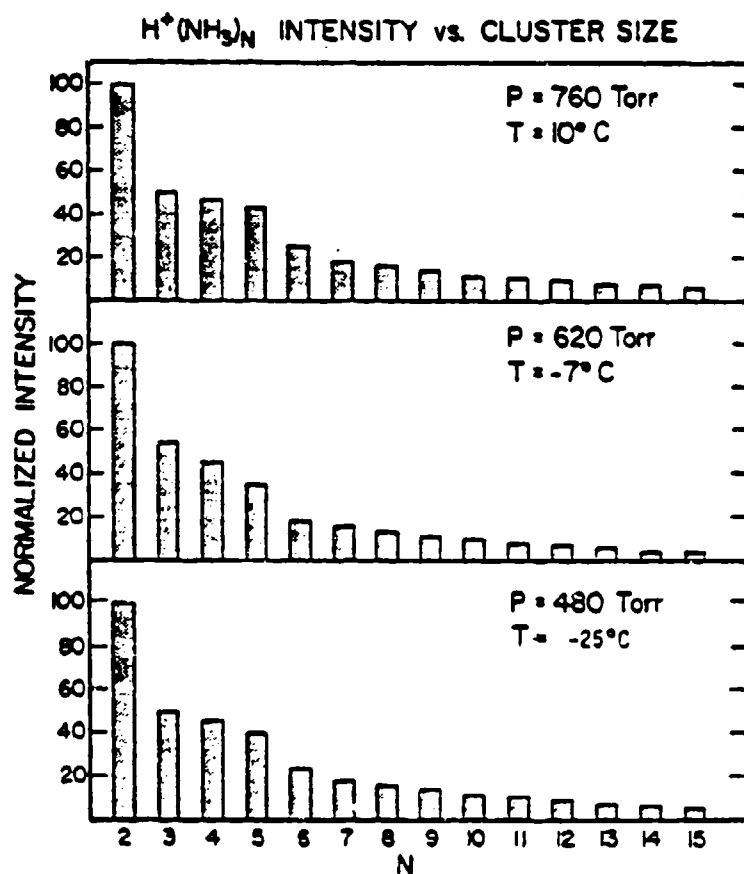


Figure 3

PLOT OF $H^+(NH_3)_N$ CLUSTER INTENSITY VERSUS CLUSTER SIZE
FOR VARIOUS STAGNATION CONDITIONS WITH FIXED PARTIAL
PRESSURE OF $(NH_3)_2$.

BLANK

AEROSOL PLUME MECHANICS AND PARTICLE GROWTH PROCESSES

J. R. Brock, T. H. Tsang, and S. G. Kim
Chemical Engineering Department
University of Texas
Austin, Texas 78712

ABSTRACT

Work under Contract DAAK11-83-K-0006 for the past year is outlined. Six areas of research under the project title, "Aerosol Plume Mechanics and Particle Growth Processes", are listed. (1) Development of aerosol plume dispersion models which in a K-theory model incorporate the processes of dispersion, advection, dry deposition, gravitational settling, coagulation, and condensation/evaporation. (2) Theoretical investigation of particle formation and growth by nucleation, condensation and coagulation. (3) Experimental investigations of growth of multi-component oil aerosols in a laminar coaxial jet. (4) Generation and growth of ferromagnetic and other solid aerosols. (5) Non-linear laser interaction with aerosol particles. (6) Particle deposition, sorption and removal processes. Summaries of work in these areas are given. Some of this work has been presented, published and submitted for publication as follows:

J. R. Brock, "High energy laser interactions with aerosols," High Energy Laser Applications Workshop, New Mexico State University, Las Cruces, N.M., Nov. 11, 1984.

J. R. Brock, "Ostwald ripening and other particle growth processes," Mechanical Engineering Lecture Series, University of Minnesota, Minneapolis, May, 1984.

J. R. Brock, "Kinetic theory and aerosol transport processes," (5 lectures), Visiting lecture series, University of Minnesota, Minneapolis, May, 1984.

J. R. Brock, 1984, Chemical Research and Development Center, Conference on Obscuration and Aerosol Research, June, 1984.

J. R. Brock and J. L. Durham, "Aqueous aerosol as a reactant in the atmosphere," in J. Calvert, Ed., SO₂, NO and NO₂ Oxidation Mechanisms: Atmospheric Considerations, Butterworth, Boston, 1984.

T. H. Tsang and J. R. Brock, "Dispersion of a plume of volatile aerosol," Aerosol Science and Technology, 2 429-36 (1983).

T. H. Tsang and J. R. Brock, "On Ostwald ripening," Aerosol Science and Technology, 4 350 (1984).

T. H. Tsang and J. R. Brock, "Dynamics of Ostwald ripening with coalescence," Physical Review Letters 53 (1984).

J. R. Brock and P. J. Kuhn, "Modifications of oil condensation aerosol growth by low concentrations of unsaturated aliphatic acids," Submitted for publication.

J. R. Brock, Patent Disclosure, "Additive for Control of Particle Size in Oil Smokes," August 1984.

INTRODUCTION

Work under this contract is intended to add to the technological base of the U.S. Army's programs in e.m. radiation obscuration, aerosol technology and chemical detection, identification and warning.

The efficiency of an aerosol obscurant for electromagnetic radiation depends on many factors including particle size, shape, composition and concentration. For an obscurant in the atmosphere, particle size, shape, composition, and concentration are determined by the processes of particle generation and growth as well as the advection, dispersion and other processes of atmospheric motion. While some qualitative features of these various processes are recognized, our knowledge is incomplete. Improvements in aerosol obscurant technology must depend in part on development of the basic knowledge of the various processes cited above.

Most aerosol obscurants are generated by the condensation of atomic or molecular species initiated by a nucleation process. The description of this process remains today as one of the unsolved classic problems of physics. Subsequent to their formation by nucleation, the stable particles grow by coagulation and condensation/evaporation processes. For liquid particles of a single chemical species which coalesce on collision, these processes for restricted homogeneous systems can be described quantitatively. However, even in this limited case, this has only recently been done. For particles that do not coalesce on collision, no general theory is available. Such particles will form larger particles with complex morphology - chains, branched structures, random aggregates, etc. - whose description in the context of a dynamic model has not yet been achieved. When the aerosol is formed from a mixture of chemical species, the problems cited above for single component aerosols are compounded. The study of the evolution of aerosol mixtures is only in its initial stages.

When aerosol obscurants are formed in the atmosphere, the formation and growth processes discussed above will occur in a turbulent environment. First these processes take place in turbulence produced by the obscurant generation device. Then, atmospheric turbulence takes over, and the subsequent evolution occurs in this environment. The description of turbulence also remains as one of the unsolved classical problems of physics. While qualitative descriptions of aerosol evolution in a turbulent environment are available in special cases, no general quantitative description is currently available. Only empirical descriptions of limited validity can be found in the literature. The evolution of an aerosol in an atmospheric plume is a complex process whose average characteristics have only recently been studied quantitatively.

The technology for chemical identification, detection and warning must take into account the interactions between vapor and the aerosol phase. This is an area that is currently poorly understood.

Summarized below are a few examples of work underway through contract DAAK11-83-K-0006. The references listed in the abstract should be consulted for details of some of the work done this past year.

Previous work we have carried out on models incorporating the aerosol processes of coagulation, gravitational sedimentation and dry deposition has been described earlier (e.g. 1, 2, 3). We recently completed a study of the dispersion of a plume of volatile aerosol. We have studied the evolution of the particle distribution function $n(m, x, z, t)$ in a cross wind line source. $n(m, x, z, t) dm$ is the number of particles having masses in the range m, dm at downwind position x at height z at time t . The evolution equation is

$$\begin{aligned} \frac{\partial n(m, x, z, t)}{\partial t} + U(z) \left[\frac{\partial n(m, x, z, t)}{\partial x} \right] + \frac{\partial}{\partial m} [\Psi(m, s) n(m, x, z, t)] \\ = \frac{\partial}{\partial z} K(z) \left[\frac{\partial n(m, x, z, t)}{\partial z} \right] + G_z(m) \left[\frac{\partial n(m, x, z, t)}{\partial z} \right]. \end{aligned} \quad (1)$$

This equation is coupled to the conservation equation for the vapor, which we give in terms of the saturation ratio s :

$$\frac{\partial s(x, z, t)}{\partial z} + U(z) \left[\frac{\partial s(x, z, t)}{\partial x} \right] = \frac{\partial}{\partial z} K(z) \left[\frac{\partial s(x, z, t)}{\partial z} \right] - \frac{1}{c_v} \int_0^\infty \Psi(m, s) n(m, x, z, t) dm. \quad (2)$$

Equations (1) and (2) are subject to the following initial and boundary conditions:

$$n(m, x, z, 0) = 0, \quad (3)$$

$$s(x, z, 0) = 0, \quad (4)$$

$$n(m, 0, h, t) = [Q_0/U(h)] \delta(z-h)f(m), \quad (5)$$

$$s(0, h, t) = 1.0, \quad (6)$$

$$\frac{\partial n(m, x, H, t)}{\partial z} = \frac{\partial s(x, H, t)}{\partial z} = 0, \quad (7)$$

$$nV_d(m) = K \partial n / \partial z, \quad z = 0 \quad (8)$$

$$\partial s / \partial z = 0, \quad z = 0$$

$U(z)$ is the x component of the mean fluid velocity, and $K(z)$ is the vertical eddy diffusivity.

$G_z(m)$ is the gravitational settling speed for a particle of mass m . Q_0 is the source strength, h its height, and $f(m)$ the source size distribution. H is the mixing height. $V_d(m)$ is the deposition velocity of a particle with mass m .

$\Psi(m, s)$ is the condensation/evaporation growth law for a particle. We use the following approximate expression, due to Fuchs and Sutugin (1971):

$$\psi(m,s) = 4\pi(3/4\pi\rho_p)^{1/3} D_{gj}m^{1/3}c_v(s-e^{Ke}) \left(1 + \frac{1.33Kn+0.71}{1+Kn}\right)^{-1} \quad (9)$$

where the diffusion coefficient D_{gj} of vapor j in host gas is related to the mean molecular speed \bar{v}_j and the mean free path L_j by $D_{gj} = 1/2 \bar{v}_j L_j$. In Eq. (9), ρ_p is the particle density; Kn the Knudsen number, $Kn = 2L_j/D_p$; and D_p is the particle diameter. The saturation ratio $s = c/c_v$, where c is the vapor mass concentration and c_v is the vapor mass concentration corresponding to the bulk liquid vapor pressure at plume temperature T . Ke is the Kelvin number, $Ke = 4\gamma v/D_p \kappa T$. γ is the surface tension, v the particle's molecular volume, and κT the thermal energy.

Some of the important observables of $n(m)$ are the total particle number concentration N ,

$$N = \int_0^\infty n(m)dm;$$

the particle mass concentration M ,

$$M = \int_0^\infty mn(m)dm;$$

and the total extinction coefficient σ_{ext} , obtained from the normalized extinction efficiency Q_{ext} (Kerker, 1969):

$$\sigma_{ext} = \left(\frac{4}{4\pi\rho_p}\right)^{2/3} \int_0^\infty Q_{ext}m^{2/3}n(m)dm.$$

The numerical solution of the coupled integro-partial differential Eqs. (1) and (2) presents a challenging problem. The simultaneous solution by an implicit numerical scheme using a matrix technique for 10^4 - 10^5 unknowns is no trivial task. In this work the method of fractional steps is used in the simulation. Advection, diffusion, and evaporation are included as follows:

1. Solve the advection and diffusion equation J_{max} times, where J_{max} is the number of size classes.
2. Solve the evaporation equation by LFEM at each grid point.
3. Solve the advection and diffusion equation for s .
4. Calculate the integral term in Eq. (2), which is a source term for vapor due to evaporation, and update the saturation ratio at that grid point.

If the saturation ratio of the vapor does not change with position - that is, is constant - procedures 3 and 4 are not necessary. The method of fractional steps just outlined decouples Eqs. (1) and (2). The explicit nature of procedure 4 does not pose a problem, because the source term is counterbalanced by the dilution effect of advection and diffusion.

We have demonstrated that dispersion of a plume of volatile aerosol can be simulated numerically by the methods outlined. For the special case where an analytical solution is possible, it has been shown that the numerical solution converges to the analytical solution with a reduction in step size; consequently the error in numerical simulation can be reduced to any desired level. In these comparisons, the validity of the method of fractional steps has been proven with the attendant advantage over fully implicit schemes. From these and other studies it has been demonstrated that the finite-element method using linear basis functions and natural boundary conditions yields accurate numerical solutions for the evaporation process.

With the methods described in part here, many interesting problems in aerosol dynamics can now be studied. We plan to present elsewhere simulations of dispersion of plumes in which both coagulation and various condensation/evaporation processes occur. It would also be of interest to extend these procedures to other problems such as the rapid condensation/evaporation processes in nonisothermal plumes, a problem of some importance.

PARTICLE GROWTH PROCESSES

Ostwald Ripening

Subsequent to their appearance by homogeneous nucleation from a monomer, particles grow by coagulation and condensation/evaporation processes. Such growth by condensation/evaporation has been termed "Ostwald ripening." We have carried out numerical investigations of this process and have noted specific limitations inherent in previous work by others on this problem.

In Ostwald ripening by condensation/evaporation, the evolution equation for the particle size distribution, $n(x,t)$, in an isothermal, uniform system is

$$\frac{\partial n(x,t)}{\partial t} = - \frac{\partial}{\partial x} [\psi(x,t)n(x,t)], \quad (1)$$

where

$$\psi(x,t) = A(x)[s - \exp(K/x^{1/3})], \quad (2)$$

$n(x,t)$ is the number of particles with mass x per unit volume at time t ; ψ is the growth rate of a particle (mass per unit time). Equations (1) and (2) are appropriate for describing the condensation/evaporation process for dilute monomer vapor in inert host gas. In (2) s is the supersaturation ratio; $K/x^{1/3}$ is the Kelvin number, where $K = (4\pi d/3)^{1/3} 2\sigma\gamma/\kappa T$, with σ the surface tension, γ the molecular volume, κT the thermal energy, and d the mass density of a droplet.

The form of $A(x)$ depends on the growth law. For continuum growth:

$$A_c(x) = 2\pi D_p D C_v = \alpha_c x^{1/3}. \quad (3)$$

For kinetic (free molecule) growth:

$$A_k(x) = \frac{1}{4} \pi D_p^2 \left(\frac{8\kappa T}{\pi m_1} \right)^{1/2} C_v = \alpha_k x^{2/3}. \quad (4)$$

Here, m_1 is the monomer molecular mass and κT the thermal energy.

Equation (1) is coupled to the conservation equation for monomer:

$$C_v \frac{ds}{dt} = - \int_{x^*}^{\infty} \psi(x, t) n(x, t) dx - x^* \psi(x^*, t) n(x^*, t), \quad (5)$$

x^* is the mass of the smallest particle that obeys the growth law, Eq. (2).

Two important moments of $n(x, t)$ are the total particle number concentration, M_0 , and mass concentration, M_1 . From (1) and (5):

$$\frac{dM_0}{dt} = \psi(x^*, t) n(x^*, t). \quad (6)$$

$$\frac{d}{dt} (C_v s + M_1) = 0. \quad (7)$$

Equation (7) reflects the conservation of total mass concentration.

Equations (1) and (5) constitute a nonlinear integrodifferential equation for $n(x, t)$. The asymptotic properties of (1) and (5) with the linearization:

$$\exp(K/x^{1/3}) \approx 1 + K/x^{1/3} \quad (8)$$

and $x^* = 0$, were apparently first investigated correctly by Lifschitz and Slyozov, 1958 (LS); subsequent investigations have not modified the LS results. Asymptotic solutions are obtained in terms of the similarity variables:

$$\tau = 3 \ln (D_p / D_{pc}(t)),$$

$$\rho = D_p / D_{pc},$$

τ is implicitly related to t through the dependence, $D_{pc}(t)$. D_{pc} is the critical particle diameter separating the regions of evaporation and condensation. From (2):

$$D_{pc} = 4\sigma\gamma / \kappa T \ln s \quad (9)$$

or, with the linear approximation, Eq. (8):

$$D_{pc} = \sigma\gamma / \kappa T (s-1).$$

The distribution is transformed with the assumption that asymptotically ($t \rightarrow \infty$):

$$n(x, t) = (2/\pi d) M_0(\tau) P(\rho) / D_{pc} D_p^2. \quad (10)$$

For the continuum growth law: $A(x) \sim x^{1/3}$, and the LS result is

$$P(\rho) = \frac{3^3 e}{2^{5/3}} \exp[-1/(1-2\rho/3)]/(\rho+3)^{7/3}(3/2-\rho)^{11/3} \quad (11)$$

and $M_0 \sim 1/t$, valid for the linearization, Eq. (8).

For kinetic (free molecule) growth: $A(x) \sim x^{2/3}$, and it is easy to show that

$$P(\rho) = 24\rho \exp[-3/(2-\rho)]/(2-\rho)^5 \quad (12)$$

and $M_0(t) \sim t^{-3/2}$, valid for the linearization, Eq. (8).

From numerical studies of the condensation/evaporation problem with vapor conservation, we conclude the following:

1. Starting with some arbitrary initial distribution, for long times, an asymptotic limit distribution is approached which agrees, for the linearized Kelvin term, with the analytical similarity solutions for continuum and kinetic (free molecule) growth laws. At this asymptotic limit, details of the initial distributions are completely "forgotten."
2. The time evolution, starting with some arbitrary initial distribution, involves two epochs. In the first, the total number concentration remains sensibly constant. In the second, particles begin to be lost from the distribution and the rate of decrease of total particle concentration approaches that predicted by the asymptotic similarity theory.
3. The time necessary to achieve the asymptotic similarity solutions for continuum and kinetic (free molecule) growth laws increases with increasing dispersion in initial particle size distribution.
4. For long times, the differences in the distributions resulting from use of nonlinear and linear Kelvin terms (Eqs. (2) and (8)) in the growth law are confined to a boundary region near x^* , outside of which the distributions are very nearly identical.
5. As is implicit in the similarity theory development, no unique asymptotic limit distribution occurs in the transition region of Knudsen numbers. This is borne out by our numerical simulations using transition region growth laws.
6. For conditions where coagulation may be neglected, it does not appear to be necessary to include competitive effects in describing aerosol growth by condensation/evaporation.

Ostwald Ripening with Coalescence

Numerous studies have been concerned with the asymptotic stages of growth by condensation/evaporation of droplets or particles following their appearance by a homogeneous nucleation process. Comparatively less attention has been given the associated problem of growth when both condensa-

tion/evaporation and coalescence occur. For aerosols we have carried out the first quantitative study of the Ostwald ripening problem with a realistic coalescence process.

We have investigated the isothermal spatially homogeneous growth of particles suspended in supersaturated monomer vapor and inert host gas. The process is described by the evolution equation for the singlet density function $n(x,t)$:

$$\frac{\partial n(x,t)}{\partial t} + \frac{\partial}{\partial x} [\psi(x,s)n(x,t)] = \int_{x^*}^{x/2} b(x-x',x')n(x-x',t)n(x',t)dx' - n(x,t) \int_{x^*}^{\infty} b(x',x)n(x',t)dx' \quad (1)$$

where $n(x,t)dx$ is the number of particles having masses in the range x, dx at time, t . $\psi(x,s)$ is the growth law for a particle by the condensation/evaporation process and $b(x',x)$ is the coalescence rate coefficient for two particles of masses x' and x . x^* is the mass of the smallest particle in the population and s is the supersaturation ratio of monomer vapor. We do not consider here competitive growth effects, as the theory for this is lacking when coalescence is significant.

Equation (1) is coupled to the mass conservation equation for monomer vapor:

$$C_V \frac{ds}{dt} = - \int_{x^*}^{\infty} \psi(x,s)n(x,t)dx - x^* \psi(x^*,s)n(x^*,t) \quad (2)$$

where C_V is the equilibrium bulk vapor concentrations.

Equations (1) and (2) obey the mass conservation:

$$\frac{d}{dt} (C_V s + M_1) = 0$$

where $M_1 = \int_{x^*}^{\infty} xn(x,t)dx$ is the mass concentration of particles. An important additional moment of $n(x,t)$ is the total number concentration, $N(t) = \int_{x^*}^{\infty} n(x,t)dx$. It follows from Equation (1) that:

$$\frac{dN}{dt} = \psi(x^*,s)n(x^*,t) - \int_{x^*}^{\infty} \int_{x^*}^{\infty} b(x',x)n(x',t)n(x,t)dx'dx'.$$

For continuum condensation/evaporation:

$$\psi(x,s) = 4\pi R D C_V (s - \exp(K/R))$$

where $x = (4\pi/3)R^3 d$, D is the binary diffusion coefficient of monomer in host gas, K is the Kelvin coefficient for the dependence of vapor pressure on droplet curvature, and d is the mass density of a particle with radius R . The rate coefficient for coalescence is that appropriate to the continuum Brownian process:

$$b(x',x) = 2kT/3\mu (x^{1/3} + x'^{1/3}) \left(\frac{1}{x^{1/3}} + \frac{1}{x'^{1/3}} \right)$$

where kT is the thermal energy and μ is the viscosity coefficient of the host gas.

Equation (1) may be put into nondimensional form through the substitutions: $p = x/\bar{x}_0$, $\tau = 4\pi D C_V (3/4\pi \bar{x}_0^2)^{1/3} t$, $\phi = \bar{x}_0 n(x,t)/N_0$. \bar{x}_0 is the initial mean particle mass and N_0 the initial number

concentration of particles. In these variables, Equation (1) becomes:

$$\frac{\partial \phi(\rho, \tau)}{\partial \tau} + \frac{\partial}{\partial \rho} [\rho^{1/3} (s - \exp(K'/\rho^{1/3})) \phi(\rho, \tau)] = \alpha \int_{\rho^*}^{\rho/2} b_1(\rho - \rho', \rho') (\rho - \rho', \tau) d\rho' - \phi(\rho, \tau) \int_{\rho^*}^{\infty} b_1(\rho', \rho) \phi(\rho', \tau) d\rho' \quad (3)$$

where

$$\alpha = kTN_0 \bar{x}_0^{2/3} / 3\pi\mu D C_V (3/4\pi d)^{1/3}.$$

The coefficient α is a measure of the relative rates of coalescence to condensation/evaporation. In Equation (3), for $\alpha \rightarrow \infty$, the coalescence process becomes dominant and for $\alpha \rightarrow 0$, only the condensation/evaporation process remains with results previously described.

A question addressed by others using scaling arguments is which mechanism - condensation/evaporation or coalescence - will be dominant for intermediate values of α . The conclusion from these analyses is that asymptotically coalescence will dominate at higher particle mass concentrations - that is for large values of α . We show here that this is not the case and that apparently coalescence can only be dominant asymptotically for the growth laws studied for vanishingly small rates of the condensation/evaporation process. This is illustrated by presenting a result from numerical solution of Equations (1) and (2) for the stated growth laws. Parameters used yield: $\alpha = 0.31$, $\tau = 5.3 \times 10^3 t$, $s(t=0) = 10$, $K/\bar{R}_0 = 1.0$.

For this system, condensation/evaporation and coalescence are competitive processes and it is not obvious which is dominant. Since, separately, condensation/evaporation and coalescence both give the result, $N(t) \sim t^{-1}$, for the continuum diffusive cases, scaling arguments are insufficient to establish which of the two mechanisms is dominant asymptotically.

Figure 1 shows the contribution to the total rate of change of N , dN/dt , by each of the two processes - condensation/evaporation and coalescence. The continuous curve is that for the ratio of coalescence rate of change of N to the total rate and the dashed curve that for the condensation/evaporation processes according to Equation (1). Clearly, the contribution of coalescence to the change of N decreases with time while that for condensation/evaporation increases. Therefore, previous conjectures on the dominance of either of the two processes appear to be incorrect for these continuum diffusive growth processes.

GROWTH OF AEROSOL IN LAMINAR COAXIAL JET

Our studies of aerosol growth in a laminar coaxial jet have been described in previous CSL Proceedings and in publications in the scientific literature. These may be consulted for descriptions of the experimental system.

In our studies of growth of multicomponent oil aerosols (including oils such as dioctyl phthalate, dihexylphthalate, dibutyl phthalate and squalane) we have found that in binary oil mixtures the total particle number concentration decreases slightly (up to 80% by volume) and then rapidly decreases (at greater than 80% by volume) as the proportion of the more volatile component increases. Also, the number and volume mean diameters increase as the proportion of the more volatile component increases. The variance of the distribution decreases as the proportion of the more volatile component increases. In all cases, increasing the oil vapor concentration in the jet increases the number and volume mean diameters and decreases the total particle number concentration and variance of the distribution.

A patent disclosure and a paper for publication have been submitted concerning large increases in apparent nucleation rates produced by addition to oil vapor of small amounts ($\leq 1\%$ by volume) of classes of organic acids. We have demonstrated that this effect is strongly dependent on temperature. Above a certain critical temperature, the additive causes a very rapid increase (by an order of magnitude over a $\sim 10^\circ\text{C}$ interval) in total particle number concentration and a decrease in mean particle diameter of the oil aerosol.

We have also carried out the first measurements of variation of composition with particle size in a binary aerosol. We find a relatively large variation of composition with particle size, the smaller particles in the aerosol containing a relatively large concentration of the less volatile component. This phenomenon is now being studied theoretically as the final step toward publication.

GENERATION OF FERROMAGNETIC CHAIN AEROSOLS

We have carried out studies of the generation and growth of ferromagnetic chain aerosols using two different experimental systems. In one, condensation of iron vapor is carried out in inert gas. Gas flow rate, gas pressure and furnace temperatures are varied. Results from these studies have been reported in previous CSL Proceedings. In the other experimental system ferromagnetic chain aerosols are generated in a stopped flow reactor in the aqueous and other phases by the reaction of borohydride ion with dissolved cations, Fe^{++} , Co^{++} , Ni^{++} for example.

In the liquid phase process, we have studied the effect of variation of reaction conditions on primary particle size. For production of iron particles, the variation of mean primary particle size with reaction temperature is shown by Figure 2. Over a $\sim 40^\circ\text{C}$ change of temperature, the primary particle size varies by a factor of 3 from $\sim 300 \text{ \AA}$ to $\sim 900 \text{ \AA}$. This reflects the relationship between the temperature dependence of the reaction rate coefficient for Fe^{++} reduction by borohydride and the nucleation rate. The effect of variation of Fe^{++} concentration on primary

particle size is shown in Figure 3. Over a narrow range of Fe^{++} concentration, $\sim 0.02 - 0.04$ M, the mean primary particle size changes from $\sim 1300 \text{ \AA}$ to $\sim 400 \text{ \AA}$, and above and below this concentration range, changes very little with concentration.

We have investigated the variation of primary particle size with particle composition for binary particles of Fe + Co and Fe + Mn. Above $\sim 60\%$ Fe, for both binary systems, the mean primary particle size increases by a large factor from $\sim 80 \text{ \AA}$ to 560 \AA for the 100% iron particles. This behavior is in fact analogous to that found for binary oil aerosols. The large change in particle size reflects the change in nucleation rate with variation of composition. We have developed a model to explain these results.

ACKNOWLEDGMENT

Work reported here was performed under Contract DAAK11-83-K-0006 from Chemical Research & Development Center, U. S. Army. The advice and assistance of Dr. Edward W. Stuebing and Mr. Glenn O. Rubel of the Chemical Research & Development Center are gratefully acknowledged.

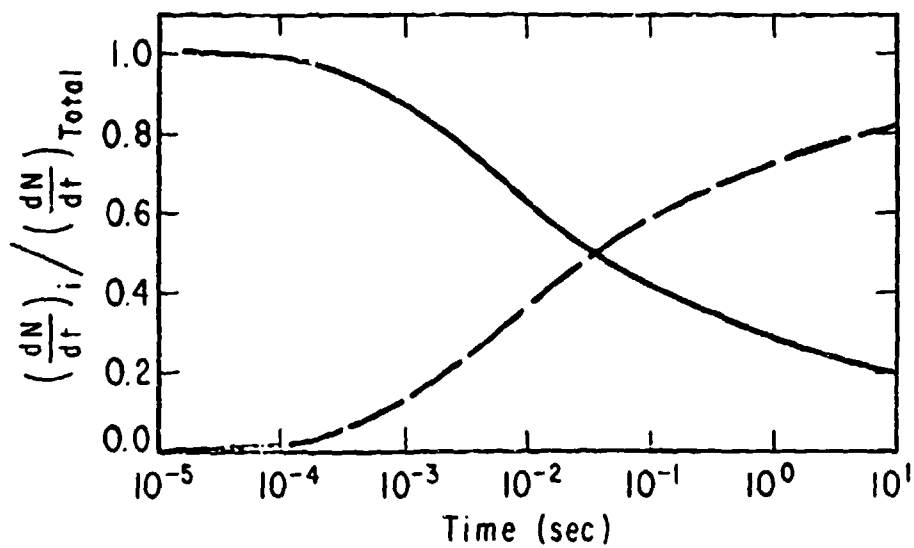


Figure 1. Contribution to the total rate of change of particle number concentration, $(\frac{dN}{dt})_{\text{total}}$, by condensation/evaporation (dashed curve) and coalescence (solid curve). Asymptotically, for values of parameters used in numerical simulation the contribution of coalescence apparently approaches zero.

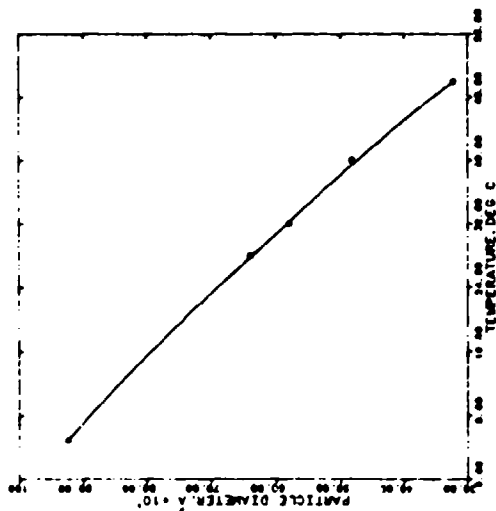


Figure 2. Variation of mean diameter of primary particles with reaction temperature for aqueous phase reaction with 0.1 M Fe^{++} and 0.1 M BH_4^- .

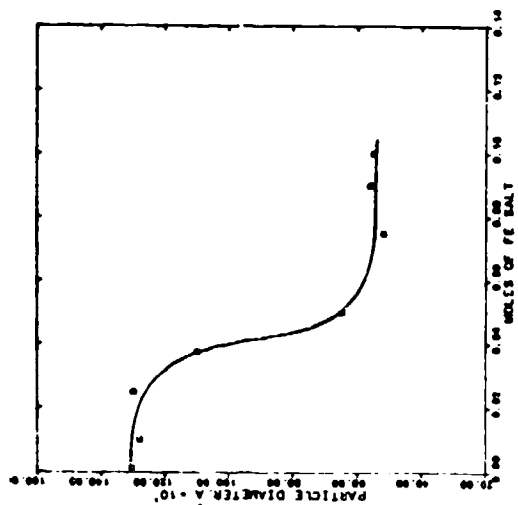


Figure 3. Variation of mean diameter of primary particles for aqueous phase reaction with Fe^{++} concentration at 0.1 M BH_4^- .

BLANK

TURBULENT MIXING IN CLOUDS

J Latham
Physics Department, UMIST
Manchester M60 1QD, England

ABSTRACT

Turbulent mixing of cloudy and cloud-free air may play an important role in determining the overall dynamical and microphysical behavior of warm clouds. We present a model of turbulent mixing based on laboratory and theoretical studies of chemically reacting shear layers, extended to include the effects of buoyancy instabilities and droplet sedimentation. It is found to be consistent with recent observations of microphysical variability in natural clouds.

1. INTRODUCTION

The ideas and investigations described herein are abstracted from a more detailed paper by Baker, Breidenthal, Choulaton and Latham (1982, J Atmos Sci, 41, 299-304).

Entrainment of environmental air into clouds and subsequent turbulent mixing of clear and cloudy air are important to overall cloud dynamics and possibly microphysical development in water clouds. In the past, mixing has been parameterized in several ways, usually in terms of a prescribed or calculated mixing time or mixing velocity, but the actual physical processes producing the mixing have received little or no attention.

One of the oldest and most popular approaches to the study of turbulent mixing is via the concept of gradient diffusion, for which turbulent motions must be small in scale compared to the distance across which the concentration of the diffusing quantity changes significantly. Gradient diffusion describes an average over many realizations of mixing events and cannot give an accurate description of processes (such as phase change) which are nonlinear in the concentrations of the fluids being mixed. In a recent paper, Broadwell and Breidenthal (1982) proposed instead a simple new model for turbulent mixing in the shear layer, with predictions which are in reasonable accord with laboratory experiment. For a full account of this model by Baker et al, and its application to mixing processes in clouds, the reader is referred to these two papers.

2. SPECIFIC MIXING PROCESSES IN CLOUDS

In this brief section, we identify illustrative mixing situations which occur in natural clouds, and estimate values of the parameters which govern the mixing.

We discuss first the Kelvin-Helmholtz instability leading to entrainment at the top of layer clouds. This case is directly analogous to mixing in the laboratory shear layer, except that here one of the fluids is considerably more turbulent than the other. If ΔU is the difference in horizontal wind velocity across the shear layer and L its thickness, then $\tau_L = L/\Delta U$. Measurements in stratocumulus (Brost et al, 1982; Caughey et al, 1982) show: $\Delta U \sim 4-8 \text{ m s}^{-1}$, $L \sim 15 \text{ m}$, so $\tau_L \sim 2-4 \text{ s}$. The ratio of cloudy to clear air in the mixing region is of the order of unity. The cloudy air is heavier than the air above cloudtop, so that buoyancy effects impede rather than accelerate mixing in this first step. The process will not appear diffusion-like but will occur within discrete vortices bounded by the shear-layer.

This very small-scale cloudtop mixing is coupled with large-scale convective motions in the form of up- and down-drafts, which are thought to behave basically like thermals. We next focus on scales for mixing between these thermals and their surroundings, and consider entrainment of cloudy air into downdrafts and mixing of entrained parcels into cloudy updrafts. Laboratory experiments on jets (Broadwell and Breidenthal, 1982; Broadwell, 1982) show that the composition of the jet at any cross-section is quite uniform, but that engulfment distorts the instantaneous "shape" of the jet on scales comparable with L , the radius of the jet, or thermal. Thus, $\tau_L = L/W$, where W is the relative velocity of the thermal and the background. These vertical velocities vary between 0.5 and 10 m s^{-1} in cumulus (Austin et al, 1982; Boatman, 1981); so for $L \sim 100 \text{ m}$, $\tau_L \sim 10-200 \text{ s}$. The ratio of newly entrained to mixed plume fluid is less than one. Thus, we expect to see uniform regions bounded by sharp edges and characterized by microphysical and dynamical parameters distinctly different from those in the air being engulfed, which is consistent with the cumulus observations discussed earlier. Buoyancy effects may be important in this case.

Convective instability causes cloud scale mixing in times short compared with the adiabatic cascade time. During the mixing process tongues of fluid of roughly cloud scale are broken down into local patches, which continue to break down until the Kolmogorov scale is reached. If one such patch finds itself in a region of fairly homogeneous turbulence in which the energetic eddies are small, then the mixing process there will be similar to diffusion, as found by Baker and Latham (1982). On the other hand, in cases in which geometry imposes a global scale, such as in the shear layer or thermal, the mixing cannot resemble diffusion, as noted above.

3. THE INFLUENCE OF MIXING ON CLOUD DROPLET SPECTRA

In this section we review evidence for spectral variability resulting from mixing processes in natural clouds, examine the effects of the Broadwell-Breidenthal mixing mechanism, buoyancy-induced mixing and sedimentation upon droplet spectra, and endeavor to draw together these arguments in an overall assessment of spectral change resulting from the mixing of cloudy and droplet-free air.

Fine scale measurements in cumulus (Austin et al, 1982; Rodi, 1981), stratocumulus (Caughey et al, 1982) and cap clouds (Baker et al, 1982) show that often the liquid water in a penetration at constant pressure can be classified either as "uniform" or as "highly variable", with few measurements falling between. In the first type of observation, the variability is very low; typically low enough to be attributable to random sampling errors. The average value of the liquid water can be approximately equal to or substantially below that expected if cloud growth had occurred without entrainment of outside air. In the second class of observations, usually those made under conditions in which direct entrainment effects are thought to be important, the variability is much greater and vorticity higher than in the first class, and the values of the liquid water fluctuate between almost zero and a value characteristic of adjacent, uniform regions. The transition between uniform and adjacent highly variable regions is usually quite abrupt. The picture is not consistent with one in which entrained air diffused smoothly throughout a given level.

An important finding in the variable regions is that the measured droplet spectral shape remains quite constant in spite of the large variation in total drop number. The constancy of shape is most evident for small drops and low turbulence levels.

The foregoing features of the droplet spectrum - which have not been explained in terms of specific mixing mechanisms - are consistent, qualitatively, with the Broadwell-Breidenthal description of mixing. In the absence of significant effects due to buoyancy-induced mixing and sedimentation, it is clear that at all times during the mixing process, i.e. during the breakdown of the inhomogeneity from scale L to λ_K , a measuring instrument with resolution, large compared to the Kolmogorov scale will "see" an average spectrum in the mixing region of the same shape as that in the original cloudy air but simply diluted by unresolved filaments of cloudfree air. Recent measurements using a laser holography system (Conway et al, 1982) show that in

cap clouds, significant structure exists in droplet spectra on scales down to 1cm, and slide measurements by Warner of small-scale structure in cumulus appear to show that structure exists on scales above 1m. These small-scale structures would not be revealed by any standard particle measuring system such as those in general use in cloud physics experiments. Thus, whether or not the clear air is saturated, the droplet spectrum measured by typical devices during the first part of the mixing process may be very similar to that in the adjacent high liquid water content regions. The number of droplets, however, will be diminished in the ratio of cloudy-to-total air averaged over by the measuring apparatus. When the Kolmogorov scale is reached, all the droplets in the region of scale L experience the same environment. If this is undersaturated, there will be uniform evaporation. This will produce a region of scale L in which the (fairly uniform) spectrum is shifted to lower sizes than would be found if mixing had not occurred. The foregoing presents a physical mechanism to explain observations of spectral preservation in situations of fluctuating liquid water content, which gave rise to the concept of inhomogeneous mixing advanced by Baker et al (1980). If the environmental air is saturated the results of the present model are consistent with those of the dilution-only picture of Telford and Chai (1980). Some evidence for this mechanism is found in Montana cumulus where liquid water variability is primarily due to variability in droplet number at the smallest scales measured (2m) but is also due to spectral shift at larger scales (Austin et al, 1982).

If the largest eddies responsible for mixing of two parcels are small, both with respect to the scale of the parcels being mixed and to the resolution of the measuring instruments used, then the measured gradients of conserved quantities near the mixing region will appear diffusion-like. Baker and Latham (1982) have shown that under these circumstances, droplet spectral variability can also be adequately reproduced by a diffusion model of the mixing. However, diffusion is not in general a satisfactory representation of the turbulent motions bringing the fluids into contact.

The foregoing discussion has revealed considerable support for the Broadwell-Breidenthal mixing model in explaining the observed spectral shapes and variability in clouds. In the absence of buoyancy-induced mixing and sedimentation, it predicts that an individual mixing event between volumes V_d and V_c of dry and cloudy air will result, at the Kolmogorov time, in a homogeneous volume $V_d + V_c$. Let $R = V_d S \rho_s / (V \rho_1)$; S is the undersaturation, ρ_s the saturation vapor density of the droplet-free

air and ρ_l the liquid-water density of the cloudy air. If, crudely, $R < 1$, there will be a finite amount of liquid water in the mixed volume and the droplet spectrum will have shifted to smaller sizes, according to the classical droplet growth equation. If, on the other hand, $R > 1$, which corresponds to a vapor deficit exceeding the water content of U_c , the final result is a homogeneous region of undersaturated air containing no droplets. Since mixing events can occur with a range of values of R , the overall result of the Broadwell-Breidenthal model will be a distribution of homogeneous regions of various sizes, liquid-water-contents and undersaturations.

For a consideration of the influence of sedimentation and buoyancy-induced mixing upon this picture, the reader is referred to the arguments of Baker et al.

4. CONCLUSIONS

A simple model of turbulent mixing in the presence of buoyancy instabilities and sedimentation has been proposed to explain observed dynamic and microphysical variability in warm clouds. Rough estimates of droplet spectral variability caused by mixing indicate that sedimentation and buoyancy effects may be as important as shear-induced effects under a range of realistic conditions.

The results predicted will not be fully consistent with existing treatment [(e.g. classical mixing, Warner (1969); inhomogeneous evaporation; Baker et al (1980); dilution only, Telford and Chai (1980)]. The model suggests specific numerical laboratory and field tests, now underway, to evaluate the significance of the contributing processes.

While this note has largely addressed the microphysical consequences of the model, the macrophysical implications may have more significance. The model suggests that the mixing process is initiated by global engulfment of discrete parcels of fluid. The ultimate result of the process is production of identifiable entities of more or less homogeneously mixed fluid.

One would expect to find results closest to those of the simple Broadwell-Breidenthal picture close to the top of shallow layer clouds in which the entrainment instability criterion is not satisfied, and so the contributions from both buoyancy-induced mixing and droplet sedimentation ($\bar{r} \approx 5\mu\text{m}$) will be small. Under these conditions a picture close to that of the extreme inhomogeneous kind would be found on very small scales. However, as the averaging scale is increased, an increasing proportion of the liquid water changes would be due to changes in spectral shape.

At the top of deep convective clouds in which the cloudtop instability criterion is satisfied, buoyancy-induced mixing and the sedimentation of large drops will both be important, and a picture closer to extreme inhomogeneous evaporation is to be expected on all scales. The connection between global structure and entrainment is strong.

REFERENCES

- Austin R, M B Baker and J Jensen 1982 Entrainment, mixing and spectral evolution in CCOPE clouds. Proc Conf. Cloud Physics, Chicago, Amer Meteorol Soc,
- Baker M B and J Latham 1982 A diffusion model of the turbulent mixing of dry and cloudy air. Quart J Roy Meteor Soc, 108, 871-898
- Baker M B, R G Corbin and J Latham 1980 The influence of entrainment on the evolution of cloud droplet spectra: I A model in inhomogeneous mixing. *ibid*, 106, 581-598
- Baker M B et al, 1982 Field studies of the effect of entrainment upon the structure of clouds at Great Dun Fell. *ibid*, 108, 899-916
- Boatman J 1981 An observational study of the rate of cloudtop entrainment in cumulus clouds. PhD dissertation, Univ. Wyoming
- Broadwell J E 1982 A model on turbulent diffusion flames and nitric oxide generation. Part I. TRW Document No 38515-6001-UT-00
- Broadwell J E and R E Breidenthal 1982 A simple model of mixing and chemical reaction in a turbulent shear layer. J Fluid Mech, 125, 397-410
- Brost R A, J C Wyngaard and D H Lenschow, 1982 Marine stratocumulus layers. J Atmos Sci, 39, 800-817
- Caughey S J, B A Crease and W T Roach 1982 A field study of nocturnal stratocumulus II. Turbulent structures and entrainment. Quart J Roy Meteor Soc, 108, 125-144
- Conway B J, S J Caughey, A N Bentley and S D Turton 1982 Ground based and airborne holography of ice and water clouds. Atmos Environ, 16, 1193-1208
- Rodi A 1981 Study of the fine scale structure of cumulus clouds. PhD dissertation, Univ Wyoming
- Telford J W and S K Chai 1980 A new aspect of condensation theory. Pure Appl Geophys, 118, 720-741
- Warner J W 1969 Time variation of updraught and water content in small cumulus clouds. J Atmos Sci, 26, 1049-1059

**CHARACTERISTICS OF OBSERVED CONCENTRATION FLUCTUATIONS
DURING SMOKE WEEK III**

by
Steven Hanna and Jonathan Plein
Environmental Research and Technology, Inc.
696 Virginia Road, Concord, MA 01742

ABSTRACT

This paper concerns an analysis of concentration fluctuations observed during Smoke Week III. Parts of this analysis have been published as follows:

Hanna, S.R., 1984a. Concentration Fluctuations in a Smoke Plume. Atmos. Environ., **18**, 1091-1106.

Hanna, S.R., 1984b. The Exponential Probability Density Function and Concentration Fluctuations in Smoke Plumes. To be published in Bound. Lay. Meteorol.

Hanna, S.R., 1984c. Observed and Modeled Concentration Fluctuations in a Small Smoke Plume. Proceedings of Fourth Joint Conference on Applications of Air Pollution Meteorology. Am. Meteorol. Soc., 126-131.

Further characteristics of observed concentration fluctuations are presented in this paper, including measures of the probability distributions of the instantaneous plume width, the plume centroid, the maximum concentration, and the cross-wind integrated concentrations.

1. INTRODUCTION

The U.S. Army is interested in concentration fluctuations in smoke plumes primarily because of their effects on visibility weapons systems, and remote sensing devices during smoke screening operations. In previous published reports (Hanna 1984a, 1984b, 1984c) general models and data sets concerning concentration fluctuations were reviewed and a new model developed. The new analytical model was shown to simulate observations in U.S. Army experiments quite well. In this paper the U.S. Army data are further analyzed in order to present specific statistical results that would be useful to researchers studying the response characteristics of remote sensing devices.

The U.S. Army tested several types of munitions and sampling devices during the Smoke Week III experiment at Eglin Air Force Base, Florida. We selected data from two trials in which fog oil was released continuously over a period of about five minutes at a height of 2 m (Sutherland et al. 1981). The atmosphere was slightly unstable during both trials. One-second average concentrations were observed on two lines of aerosol photometers at distances of 70 m and 100 m from the source in Trial 2 and 30 m and 60 m from the source in Trial 4. We emphasize the far line of monitors, since it has 33 aerosol photometers with 9 m spacing. Because the source operates for only about 300 sec in these experiments, we consider data only from the time marking the first significant impact ($C > 15$) anywhere on the line to the time marking the last impact. We use a threshold of C equal to 3 to calculate the

intermittency, I , which is defined as the fraction of non-zero concentration observations, since spurious values of C equal to 1 or 2 seem to represent "noise." More details on the experiments are given by Hanna (1984b, 1984c).

Figure 1 is an example of a time series of concentration observations from the data set studied in this program. The observed concentration fluctuations are due to both meandering and in-plume turbulence. Meandering is defined as the swaying back and forth of the entire plume, leading to relatively long periods of either high concentrations or zero concentrations at a given monitor. The in-plume turbulence causes large short-term variations in concentration within the plume (e.g., at times ranging from 70s to 140s in Figure 1).

A measure of concentration fluctuations is the standard deviation σ_c . In the smoke stack data the ratio of the standard deviation to the mean, σ_c/\bar{C} , was about 1.3 on the average plume axis and about 5 on the plume edges. The intermittency, I , was about 0.6 on the average plume axis and about 0.1 on the plume edges. The following simple model was shown by Hanna (1984b, 1984c) to satisfactorily fit these data:

$$I = 0.60 \exp(-y^2/2\sigma_y^2) \quad (1)$$

$$\sigma_c/\bar{C} = (3.33 \exp(y^2/2\sigma_y^2) - 1)^{1/2} \quad (2)$$

where y is lateral distance from the average plume axis and σ_y is the standard deviation of the lateral distribution of the average plume concentration. The variation of σ_c^2 with averaging time, T , was shown to be well-simulated by the formula:

$$\frac{\sigma_c^2(T)}{\sigma_c^2(0)} = 2 \frac{T_I}{T} \left(1 - \frac{T_I}{T} (1 - \exp(-\frac{T}{T_I}))\right) \quad (3)$$

where T_I is the integral time scale.

2. FURTHER RESULTS

In addition to the results summarized above which were previously reported, further calculations have been made using these concentration data. For example, the variability of the instantaneous cross-wind concentration distribution is shown in Figure 2. This figure summarizes all the cross-wind instantaneous distributions in Trial 4 by normalizing all concentrations by the maximum concentration at a particular second and normalizing the cross-wind distance by the instantaneous σ_{yI} . There are over 200 individual distributions included in this figure, with the mean and plus and minus the standard deviation of all the observations at each lateral distance shown. The calculated skewness and

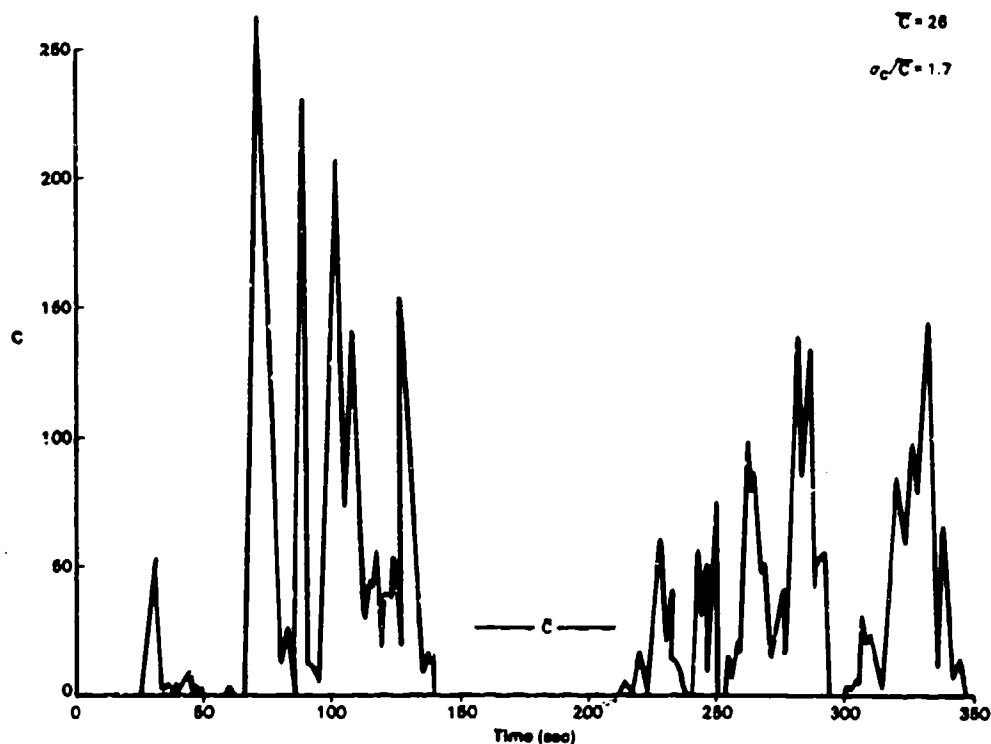


FIGURE 1. TIME SERIES OF CONCENTRATION FOR A MONITOR NEAR THE MEAN PLUME CENTER IN TRIAL 2.

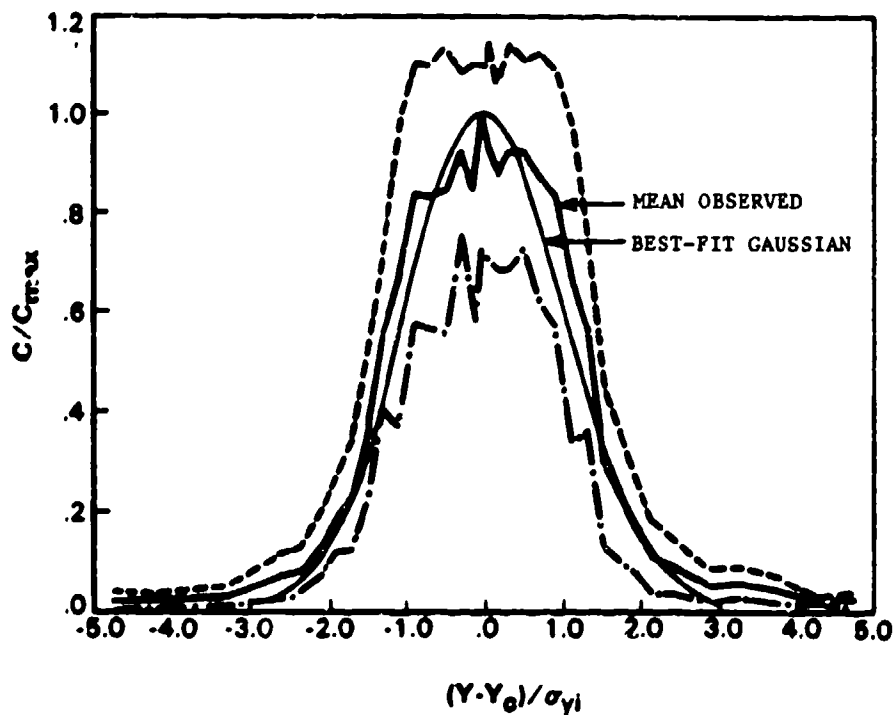


FIGURE 2. SUMMARY OF CROSS-WIND INSTANTANEOUS CONCENTRATION DISTRIBUTIONS IN TRIAL 4. The mean and plus and minus one standard deviation of all observations at each lateral distance are shown. A best-fit normal curve is also plotted.

kurtosis are 0.12 and 5.3, respectively. The major difference between the observed distribution and a normal distribution (also shown on the figure) is the large number of observed cases at the tails or edges, as reflected by the large kurtosis (for a normal distribution, the kurtosis is 3.0).

A summary of a variety of plume statistics is given in Table 1. The data in the first line (cross-wind integrated concentration or CWI Conc.) remove the effect of lateral meandering and deal solely with the vertical component of the turbulence. The value of σ_c/\bar{C} (CWI Conc.) for this component is 0.55 for Trial 2 and 0.48 for Trial 4. This ratio would be expected to decrease at distances farther from the source. The last column in the table gives the integral time scale, T_I , which is defined here as the time lag at which the autocorrelogram drops to 0.37 (for an exponential autocorrelogram, $\exp(-t/T_I)$ equals 0.37 when t/T_I equals one, where t is the time lag). For these two experiments, T_I equals about 7s.

TABLE 1. SUMMARY OF STATISTICAL ANALYSIS OF SMOKE WEEK III
TRIAL 2 AND TRIAL 4 DATA

		Mean	Standard Deviation	Skewness	Kurtosis	Integral Time Scale (s)
CWI Conc.	Trial 2	161	89	.4	2.7	7.0
	Trial 4	212	101	.6	3.2	7.5
Y-centroid (y_c , m)	Trial 2	-	26.8	-1.8	7.8	42
	Trial 4	-	22.5	-2.6	16.5	32
σ_{yI} (m)	Trial 2	9.7	5.1	.9	3.6	17
	Trial 4	5.8	2.1	.5	3.0	7
Width (W_I , m)	Trial 2	45.9	19.5	.3	2.0	20
	Trial 4	31.5	10.7	1.3	6.5	5.5
C_{max}	Trial 2	77	48	1.1	4.6	4.5
	Trial 4	128	61	0.5	3.3	4.5

The next row in Table 1 deals with the variability of the instantaneous plume centroid position, y_c , which is dominated by lateral meandering. Note that the integral time scale here is about 30 to 40s, or a factor of 5 to 6 above the integral time scale for the vertical component or CWI Conc. When meandering is present at all time scales, as it usually is in the atmosphere, the calculated T_I becomes a function of the sampling time, which is about 300s for these experiments. If the sampling time doubled, the calculated T_I for the plume centroid positions would also double. The skewness and kurtosis of the centroid positions suggest that the distribution is non-Gaussian with a relatively large number of observed centroid positions at the tails of the distribution.

The next two entries in the table are the standard deviation σ_{yI} and the total width, W_I , of the lateral distribution of material in the instantaneous plume. The ratio of W_I to σ_{yI} averages 5.0, in agreement with the findings of the Nuclear Regulatory Commission for atmospheric wind direction data (Markee 1963). The variability of individual measurements of σ_{yI} is fairly high, since the ratio of the standard deviation of σ_{yI} to the mean σ_{yI} is about 0.5. The integral time scale for σ_{yI} variations is closer to that for CWI Conc. variations than that for y_c variations, since the fluctuations in instantaneous plume size are due to turbulent eddies much smaller than the eddies responsible for the meandering.

Statistics for the maximum concentration C_{max} in the instantaneous plume are given in the last row in Table 1. Because the maximum concentration is most strongly influenced by smaller eddies, the integral time scale for these data is relatively small (4.5s). The ratio of the standard deviation of C_{max} to the mean of C_{max} is about 0.5, in agreement with similar ratios for CWI Conc. and σ_{yI} .

3. FUTURE EXPERIMENTS

The information given above is only an example of the types of calculations that can be made with the U.S. Army Smoke Week experiments. Depending on the interests of the researcher, many other characteristics of the concentration fluctuations could be similarly parameterized. However, there are improvements in the data that could be made in future experiments:

- e The source strength should be maintained as constant as possible.
- e Arcs of monitors should be located at distances of about 20, 200 and 2000 m.
- e Fast response measurements of concentrations in discrete particle size ranges should be made.
- e Lidar cross-sections of the plume concentration distribution would be of interest.

ACKNOWLEDGEMENT

This research was sponsored by the Army Research Office under contract number DAAG29-83-C-0005, with Dr. Walter Bach as technical contract monitor.

REFERENCES

- Hanna, S.R., 1984a. Concentration Fluctuations in a Smoke Plume. Atmos. Environ., 18, 1091-1106.
- Hanna, S.R., 1984b. The Exponential PDF and Concentration Fluctuations in Smoke Plumes. To appear in Bound. Lay. Meteorol.
- Hanna, S.R., 1984c. Observed and Modeled Concentration Fluctuations in a Small Smoke Plume. Proceedings of Fourth Joint Conference on Applications of Air Pollution Meteorology, Am. Meteorol. Soc., 128-131.

Markee, E.H., 1963. On the Relationships of Range to Standard Deviation of Wind Fluctuations.

No. Wea. Rev., 91, 83-87.

Sutherland, R.A., D.W. Hooch and R.B. Gomez, 1981. An Objective Summary of U.S. Army Electro-Optical Modeling and Field Testing in an Obscuring Environment. Report No. ASL-TR-0096 from U.S. Army Atmospheric Sciences Laboratory, White Sands Missile Range, NM 88002.

WIND TUNNEL SIMULATION OF DIFFUSION IN A CONVECTIVE BOUNDARY LAYER

M. Poreh and J. E. Cermak
Colorado State University
Fort Collins, CO 80523

ABSTRACT

This paper describes simulation of diffusion from ground level and elevated sources within a convective boundary layer. The work has been presented and published as follows:

M. Poreh and J. E. Cermak, Wind Tunnel Simulation of Diffusion in a Convective Boundary Layer, 29th OHOLO Biological Conference, Zichron Ya'Acov, Israel, 25-28 March 1984. Proceedings will be published in Boundary Layer Meteorology (1984).

J. E. Cermak, P. K. Shrivastava and M. Poreh, Wind-Tunnel Research on the Mechanics of Plumes in the Atmospheric Surface Layer. Fluid Dynamics and Diffusion Laboratory, Department of Civil Engineering, Colorado State University, Fort Collins, Colorado 80523, Report CER83-84JEC,PKS-MP12, Chapter 5, December 1983.

DESCRIPTION OF WIND TUNNEL SIMULATION

When the wind speed is very weak and the temperature of the ground is higher than that of the air, the upward flux of heat becomes one of the important physical parameters which determines the turbulent structure of the unstable boundary layer near the ground and the mechanics of transport processes within this layer. Usually such an unstable layer is capped by an inversion at height h above the ground, which acts as a lid for upward fluxes and pollutants. Such a capped unstable layer is also termed a convective boundary layer (CBL). The CBL is composed of several layers: the surface layer, where the wind shear plays a dominant role; the free convection layer, extending to approximately $0.1 h$, where the shear is no longer important but the height z is a significant parameter; the mixed layer, where turbulent structure is independent of both height and shear; and the entrainment interfacial layer.

The characteristic velocity scale of the CBL is usually defined as $w^* = (hg \overline{w'\theta'}/\theta)^{1/3}$, where $\rho C_p \overline{w'\theta'}$ is the heat flux and θ an average potential temperature. The Monin-Obukhov length L , which characterizes the thickness of the surface layer is $L = -(v^*)^3 \theta / (g \overline{w'\theta'})$, where $v^* = (\tau_0 / \rho)^{1/2}$ is the shear velocity. Previous studies of diffusion in the CBL are based on physical simulations in a water tank with no mean velocity and shear [Deardorff and Willis, 1975] and numerical simulations [Deardorff, 1970, 1972; Lamb, 1979]. The present simulations were done in the Meteorological Wind-Tunnel (MWT) at Colorado State University. The CBL was created by heating a 12.3 m section of the 27 m long wind-tunnel floor to approximately 150°C . Two floor configurations were used: a smooth floor and a rough floor. The characteristics of the simulated layers were:

	Smooth Floor	Rough Floor
Mean Velocity \bar{U} (m/sec)	1.9	1.7
Shear Velocity V^* (m/sec)	0.085	0.115
Convective Velocity w^* (m/sec)	0.25	0.28
CBL Height h (m)	0.75	0.90
h/L	11	6

A neutrally buoyant hydrocarbon tracer was released at three source heights $z^s = 0, 10$, and 20 cm above the floor. Concentrations downstream were measured by gas chromatography.

EXPERIMENTAL RESULTS

The velocity and temperature measurements revealed that the wind-tunnel flow displayed the major characteristics of full-scale convective boundary layers [Lamb, 1981], although some effects of the upstream rough wind-tunnel floor were recognized for the smooth floor configuration, and the inversion above h was not very strong.

Concentration profiles at 6 stations downstream of the sources revealed the unique features of diffusion in a CBL. Figure 1 shows selected dimensionless concentration profiles at the plume centerline $C(x,z,0)Uh^2/Q$, where Q is the discharge rate of the source. The dimensionless distance denoted in these figures by X is defined as $X = xw^*/(Uh)$. One sees that at $X > 0.5$ the maximum concentration is no longer at ground level. Comparison of the maximum ground-level concentration distributions in Figure 2 shows that at certain distances from the sources elevated sources give higher ground-level concentrations than ground-level sources of the same strength. These phenomena, discovered first by Deardorff et al., cannot be predicted by gradient-type or Gaussian models. Measurements of lateral diffusion, presented in Figure 3 for the smooth floor configuration, show that contrary to observations in neutral boundary layers, the initial cross-wind diffusion in the CBL is larger for ground-level sources than for elevated sources. Similar results were obtained for the rough floor configuration although h/L was smaller. The measurements for the ground-level source appear to be in agreement with the Prairie Grass measurements reported by Barad.

Measurements in this work were limited to $X = O(1)$. It is planned to extend the measurements to larger values of X and to increase the stability of the inversion above the CBL layer to obtain a better simulation of the diffusion in mixed layers.

REFERENCES

- Antonia, R. A. and Luxton, R. E. 1971. The Response of a Turbulent Boundary Layer to a Step Change in Surface Roughness, J. Fl. Mech. 48, p. 721.
- Barad, M. L. (ed.) 1952. Project Prairie Grass -- A Field Program in Diffusion, Geophysical Research Paper 59, Geophysical Directorate, Bedford, Mass.
- Caughey, S. J. 1981. In Nieuwstadt and van Dop (1982).
- Cermak, J. E. 1981. Wind Tunnel Design for Modelling of Atmospheric Boundary Layer, J. of Eng. Mech. Div., ASCE 107, No. EM3, 623-642.
- Cermak, J. E., Shrivastava, P. K., and Poreh, M. 1983. Wind-Tunnel Research on the Mechanics of Plumes in the Atmospheric Surface Layer. Fluid Dynamics and Diffusion Laboratory, Department of Civil Engineering, Colorado State University, Fort Collins, Colorado 80523, Report CER83-84JEC, PKS-MP12, Chapter 5.
- Deardorff, J. W. 1970. Preliminary Results from Numerical Integration of the Unstable Boundary Layer, J. Atm. Sci. 27, 1205-1211.
- Deardorff, J. W. 1972. Numerical Investigation of Neutral and Unstable Planetary Boundary Layers, J. Atm. Sci. 29, 91-115.
- Deardorff, J. W. and Willis, G. E. 1975. A Parameterization of Diffusion into the Mixed Layer, J. Appl. Meteor. 14, 1451-1458.
- Lamb, R. G. 1979. A Numerical Simulation of Dispersion from an Elevated Point Source in the Convective Planetary Boundary Layer, Atm. Environ. 12, 1297-1304.
- Lamb, R. G. 1979. The Effects of Release Height on Material Dispersion in the Convective Planetary Boundary Layer, Preprint vol. AMS Fourth Symposium on Turbulence, Diffusion and Air Pollution, Reno, Nevada.
- Lamb, R. G. 1981. Diffusion in the CBL. in Nieuwstadt and van Dop (1982).
- Nieuwstadt, F. T. M. and van Dop, H. 1982. Editors, Atmospheric Turbulence and Air Pollution Modeling - A course held in The Hague, September 1981. D. Reidel Publishing Co., Boston, Massachusetts, U.S.A.
- Poreh, M., and Cermak, J. E. 1984. Wind Tunnel Simulation of Diffusion in a Convective Boundary Layer, 29th OHIO Biological Conference, Zichson Ya'Acov, Israel, 25-28 March 1984. Proceedings will be published in Boundary Layer Meteorology (1984).

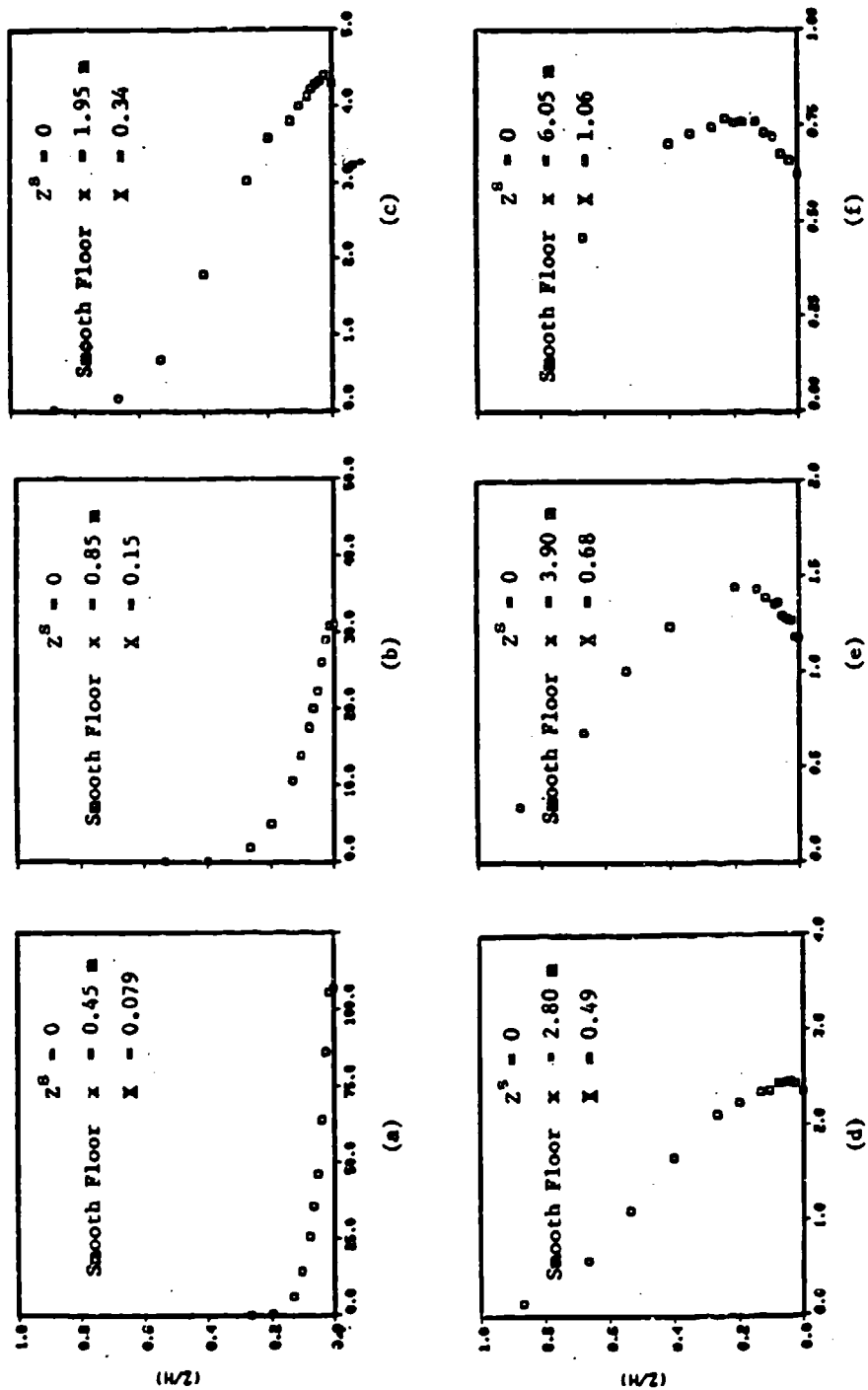


Figure 1. Selected dimensionless concentration profiles $C(x,0,z)$ $U h^2 / Q$, for smooth floor $z^S = 0$.

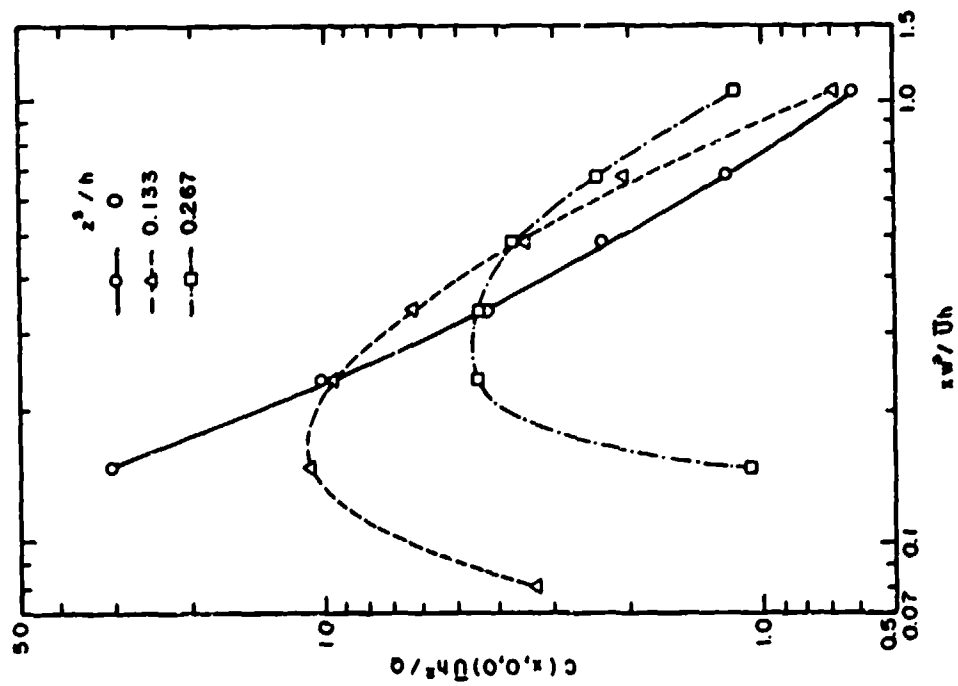


Figure 2. Dimensionless maximum ground-level concentrations smooth floor.

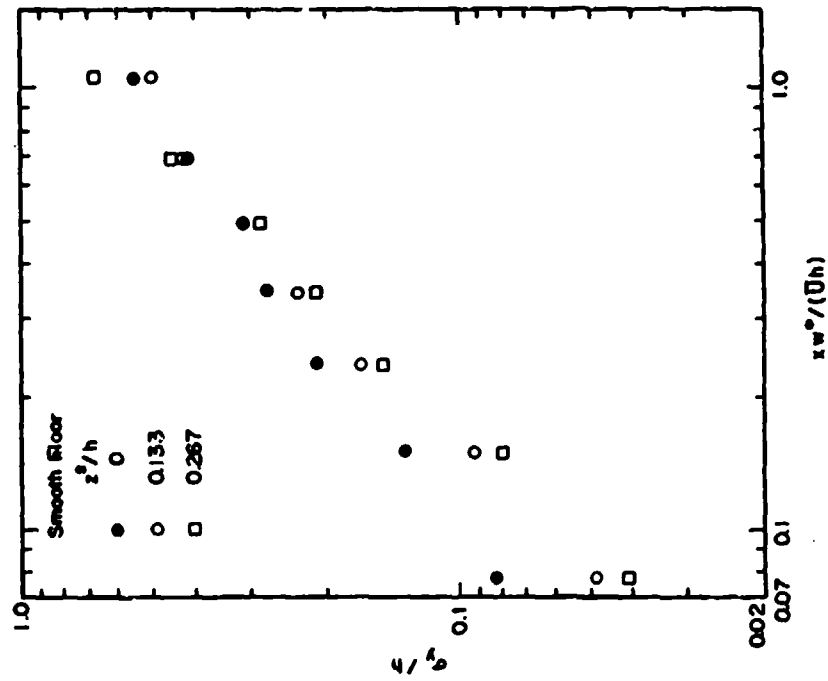


Figure 3. Cross-wind spread, smooth floor.

CRITERIA FOR WIND-TUNNEL SIMULATION OF PARTICLE PLUMES IN THE ATMOSPHERIC SURFACE LAYER

M. Poreh and J. E. Cermak
Colorado State University
Fort Collins, CO 80523

ABSTRACT

This paper discusses requirements and constraints related to wind-tunnel simulation of different classes of particle plumes. The work has been published in Appendix A of the following report:

J. E. Cermak, P. K. Shrivastava and M. Poreh. Wind Tunnel Research on the Mechanics of Plumes in the Atmospheric Surface Layer, Fluid Dynamics and Diffusion Laboratory, Dept. of Civil Engineering, Colorado State University, Fort Collins, CO 80523, Report CER83-84JEC-PKS-MP/12, December 1983.

CLASSIFICATION OF PARTICLE PLUMES

The analysis focuses on steady, stable particle plumes (PP) from elevated sources. Two parameters affect the behavior of such plumes:

- The relative velocity $r = V_g/U$ where V_g is the fall velocity of the individual particle, and U is a reference mean wind velocity at the height of the source.
- The relative (negative) buoyancy of the initial air-particle source. The buoyancy for steady state sources is determined by the buoyancy flux. Heavier-than-air particles will cause negative buoyancy but when mixed with hot air or other gases, positive buoyancy can result.

Based on the relative significance of these factors, four classes of PP have been recognized, see Figure 1,

- PRP - Passive Reference Plumes
- BP - Buoyant Plumes
- HPP - Heavy Particle Plumes
- HPP/BP - Heavy Particle Plumes diffusing together with a Buoyant Plume.

The PRP is the limiting case for both small relative fall velocities and negligible buoyancy effects. The diffusion of the PRP is identical to that of inert neutral tracers. It has been shown in previous investigations (Cermak, 1981) that the dispersion of PRP can be simulated in meteorological wind tunnels. Detailed criteria for such simulations are given in the above reference.

When the concentration of particles in the PP is increased the plume might be exposed to negative buoyancy effects, although the relative fall velocity of the particles might be relatively small. Such plumes are classified as Buoyant Plumes (BP) with either positive or negative buoyancy. Simulation of BP in a wind tunnel is possible by matching the dimensionless buoyancy flux of the plume in the model and the atmosphere.

When buoyancy effects are negligible but the relative fall velocity of individual particles is not small, each particle will experience a gravity force which will enhance a mean downward motion and an early deposit on the ground. No interaction between particles is expected in this case and the motion of the particles is not expected to modify the air flow. Such plumes are classified as Heavy Particle Plumes (HPP). Clearly, only monodispersed HPP need to be investigated in wind tunnels.

When only a small fraction of a polydispersed PP has a non-negligible relative fall velocity, that fraction will disperse as a HPP whereas the rest of the particles will be dispersed as a PRP. However, when the plume is exposed to buoyancy effects, the entire velocity field and the dispersion of the individual heavy particles will be affected. This case is referred to as a HPP/BP combination.

Approximate limits for the different classes defined above were calculated. The effect of the fall velocity can be usually neglected when $r = V_g/U < 0.4 \sigma_z/x$, where σ_z is the standard deviation of the diffusion plume and x is the distance from the source. The ratio σ_z/x is a mild function of x . Based on its value at $x = 1000$ m one finds that PP with $r < 0.015$ will diffuse in adiabatic atmosphere boundary layers as PRP. The corresponding value of r for stable flow is 0.01 or smaller. Particle plumes in unstable flows will behave as PRP at larger values of r .

The effect of buoyancy is expected to be recognized when the plume descent or rise, ΔH , will be larger than $0.4 \sigma_z$. Given the buoyancy flux of the plume, $F = \Delta \rho g Q / \rho_p$ where $\Delta \rho$ is the relative specific density of the BP and Q is the discharge, it is estimated that effect of buoyancy in neutral flows becomes significant when $F / (U^3 x) > 0.4 \times 10^{-6}$. The limits of the various types of plumes for neutral flows are shown schematically in Fig. 1.

WIND-TUNNEL SIMULATION OF HPP

In addition to the general requirements for simulation of the atmospheric surface layer (Cermak, 1981) it is essential to maintain for simulation of HPP the same relative fall velocity V_f/U in the model and the atmosphere. It is also required, for an exact simulation of the particle motion in the turbulent flow, that the value of $U^2/g\ell$, where ℓ is the scale of the turbulent eddies, be the same in the model and atmosphere. This additional requirement implies that the velocity scales in the model must be proportional to the square root of the length scale; $\lambda_U = \lambda_L^{1/2}$.

In addition, it is required to maintain a sufficiently large Reynolds number in the model and thus only large models with relatively large mean velocities can be used. It has been shown, however, that when $U^2/g\ell < 0.15$ the particle motion will be practically independent of their inertia and will very closely follow the turbulent fluid motion. In such cases it is not essential to maintain the same ratio of $U^2/g\ell$ in the model and atmosphere. The size of the energy-containing eddies at a height h above the ground is of the order of h and the effect of eddies smaller than $0.1h$ on the average diffusion of a steady plume can be neglected. This implies that the requirement $\lambda_U = \lambda_L^{1/2}$ can be relaxed and replaced by $U^2/g\ell < 0.015$ (Equation 9 in the full report). Another requirement which follows from the work of Smith (1961) is that $U_f/U < 0.15$ (Eq. 11).

The above constraints were used to calculate the permissible ranges for simulation of HPP in wind tunnels, as shown for example in Fig. 2 for the case of an elevated source at $h = 60$ m in a neutral boundary layer.

It is planned to simulate the diffusion of HPP in the meteorological wind tunnel at Colorado State University. On the basis of the above criteria, a model scale of approximately 1:500 will be used. The modeling will be limited to relative fall velocities of $V_f/U = 0.07$.

REFERENCES

- Briggs, G. W. 1969. Plume Rise, U.S. Atomic Energy Commission, Division of Technical Information.
- Cermak, J. E. 1981. Wind Tunnel Design for Physical Modelling of Atmospheric Boundary Layers, J. of the Engineering Mech. Division, ASCE, 107, pp. 623-642.
- Csanady, G. T. 1963. Diffusion of Heavy Particles with Atmosphere, J. of Atmospheric Sciences, 20, 201.
- Pasquill, F. 1974. Atmospheric Diffusion, 2nd Edition. John Wiley and Sons, New York.
- Poreh, M. and A. Kacherginsky. 1981. Simulation of Plume Rise in Small Wind-Tunnel Models, J. of Wind Engineering and Industrial Aerodynamics, 7, pp. 1-14.
- Smith, F. B. The Turbulent Spread of a Falling Cluster, in Atmospheric Diffusion and Air Pollution, Edited by F. N. Frenkiel and P. H. Sheppard, Advances in Geophysics, 6, Academic Press.
- Snyder, S. H. 1981. Guideline for Fluid Modeling of Atmospheric Diffusion. U.S. Environmental Protection Agency, Research Triangle Park, NC, APA-600/8-81-009.
- Stewart, R. E. 1967. Atmospheric Diffusion of Particulate Matter Released from an Elevated Continuous Source. Presented at the 60th Annual Meeting APCA, Cleveland, OH, 1967. Florida Eng. and Ind. Exp. Station Tech. Rept. 388.

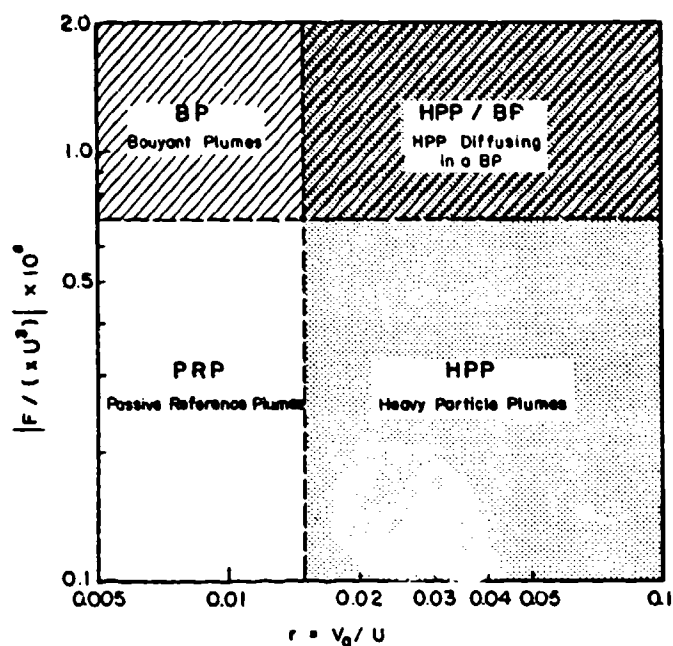


Figure 1. Classification of Particle Plumes for Neutrally Stratified ASL

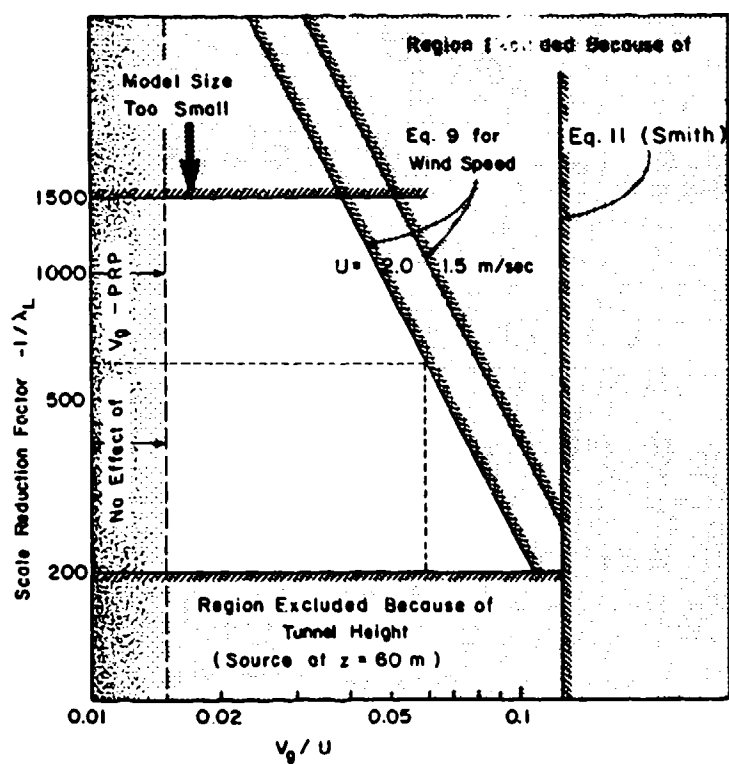


Figure 2. Constraints for Wind Tunnel Simulation of a HP Source Height 60 m, Neutral ASL. (Example: $U = 1.5$ m/sec, $V_g/U = 0.06$, $200 < \lambda_L \leq 600$)

The Orientation Distribution Function of Nonspherical
Aerosol Particles in a General Shear Flow: The Turbulent Case

Isaiah Gallily and E.M. Krushkal

Department of Atmospheric Sciences,

The Hebrew University of Jerusalem, Jerusalem, Israel

Previous Publications: Krushkal, E.M. and Gallily, I., "On the
Orientation Distribution Function of Nonspherical Aerosol
Particles in a General Shear Flow. I. The Laminar Case" J. Colloid
Interface Sci. 99, 141 (1984), and in the Proceedings of the 1983
CSL Conference on Obscuration and Aerosol Research.

ABSTRACT

The models

Having performed a study on the orientation density function (o.d.f.) of small, spheroidal aerosol particles in a general field of an arbitrary strength, (1,2) it became possible to treat the orientation problem in a turbulent medium. To this end, two interconnected physical models were applied. In the first, "The Realizations Model," it was assumed that the turbulent particle field constituted an ensemble of an infinite number of realizations, j , each one of which is characterized by one set of the o.d.f., $F^{(j)}(x, t)$, values. The latter was taken in that model to essentially coincide with the previously found solution of the Fokker-Planck equation (1,2) in the field of the realization

$$\frac{\partial F^{(j)}}{\partial t} + \nabla \cdot [\omega(W_{1k}^{(j)}, R)F - \alpha_e^{-1(j)} \nabla F^{(j)}] \quad [1]$$

where ω is the rotational velocity of the particles and $\alpha_e^{(j)}$ is their rotational Peclet number defined by $W_0 / \Gamma D_e$, W_0 being a typical component of the (fluid) gradient tensor, ΓD_e an effective rotational diffusion coefficient and R the particle aspect ratio; $W_{1k}^{(j)}$ is a gradient component

$\partial u_1 / \partial x_k$ (u_1 - a component of the fluid velocity). The use of the solution is based on the estimate that, even for the highest (Kolmogoroff) frequency component of u_1 , the rotational Reynolds number for the studied particles is small enough to render their motion (quasi) stationary.



In the second, "The Micro-turbulence Model," a relation between the so-called turbulent rotational diffusion coefficient r_{D_t} of the particles and the physical characteristics of the fluid field was supplied. This coefficient and the Brownian rotational diffusion one, r_{D_B} , compose the effective diffusion coefficient r_{D_e}

$$r_{D_e} = r_{D_t} + r_{D_B} . \quad [2]$$

Expressing the stochastic quantities of the system as $F = \bar{F} + F'$, $\omega_1 = \bar{\omega}_1 + \omega'_1$, $W_{1k} = \bar{W}_{1k} + W'_{1k}$ and $u_1 = \bar{u}_1 + u'_1$, it could be shown that the realizations average of F , $F(\bar{W}_{1k}^{(j)}, r_{D_B}, R)$ for a space-time point is actually $F(\bar{W}_{1k}, r_{D_e}, R)$ for that point and that

$$\overline{\omega'_1 F'} = -r_{D_t} \nabla \bar{F} . \quad [3]$$

The particles considered were taken to be much smaller than the Kolmogoroff scale; so, the turbulent rotational diffusion coefficient itself, r_{D_t} , was assumed, in the second model, to depend on the randomizing action of the turbulent pressure fluctuations at the particles' surface which arise from the (Kolmogoroff) micro-turbulence.

From dimensional analysis it was obtained that

$$r_{D_t} = (\epsilon/\nu)^{1/2} \quad [4]$$

where ϵ , the turbulent dissipation energy, is given for an homogeneous steady field by (3)

$$\epsilon = \nu \sum_{i,k} \overline{W'_{ik}{}^2} . \quad [5]$$

Applications

As the turbulent gradient tensor W'_{ik} is not completely known in many fluid systems, it was necessary in the present study either to supplement the missing data by the results of numerical simulations or (reasonable) guesses or both. In cases of interest, there was conducted a parametric investigation in which the effect of structure changes in the gradient tensor on the o.d.f. was tested.

The numerical simulations of the turbulent field were carried out according to the method of Wang and Frost (4) where $u_1' = u_1'(t)$ is found. In this method, however, only the three components W_{11}' ($i = 1, 2, 3$) could be acquired due to the applicability of the relationship known as the Taylor hypothesis, viz.

$$\frac{\partial u_1'}{\partial t} = -u_1' \frac{\partial u_1'}{\partial x_1} \quad [6]$$

to those components alone.

The rest of the gradient components were extracted either from the experimental findings of Klebanoff (5) for the studied situations of a turbulent flow over a flat surface as in the atmospheric boundary layer or from those of Wignansky and Fiedler (6) for the studied situation of a free round turbulent jet, or from parametric checks as mentioned above. The experimentally acquired gradient components are given in the form of $\Delta W_{1k}' = (\overline{W_{1k}^2})^{1/2}$ and so were taken the rest of the components. The (turbulent) fluid was assumed to be incompressible, viz. $W_{11}' = 0$, and it was set that

$$\Delta W_{22}' = \Delta W_{33}' = -1/2 \Delta W_{11}' \quad [7]$$

or with reversed signs.

Obviously, since in addition to the average value of F , \bar{F} , or its maximal value F_m , some measure of the spread of the o.d.f. values is desired, a procedure was adopted in which this (F) function was calculated for the following three realization fields:

$$(1) \quad W_{1k}^{(1)} = \bar{W}_{1k}', \quad [8a]$$

$$(2) \quad W_{1k}^{(2)} = \bar{W}_{1k}' - \Delta W_{1k}', \quad [8b]$$

and

$$(3) \quad W_{1k}^{(3)} = \bar{W}_{1k}' + \Delta W_{1k}'. \quad [8c]$$

Finally, to account for any uncertainties in the turbulent field data, the (determining) effective Peclet number was parameterized by a numerical factor α_0 to be

$$\alpha_e = \alpha_0 \frac{W_0}{r_{De}} \quad [9]$$

where $W_0 = \bar{W}_0 + W_0'$, $W_0' = [(\Delta W'_{ik})_0]$ being a typical turbulent component.

Results

Two physical situations were studied:

1. The near-ground atmospheric boundary layer, in which only

$$\bar{u}_1(z) = \frac{u^*}{k_0} \ln \left(1 + \frac{z}{z_0} \right) \quad [10]$$

and

$$\bar{W}_{13} = \frac{\delta \bar{u}_1}{\delta z} = \frac{u^*}{k_0(z+z_0)} \quad [11]$$

essentially exist, z being the elevation above ground, \bar{u}_1 the mean horizontal velocity, u^* the friction velocity, k_0 von Karman Constant and z_0 the roughness height.

2. The turbulent round free jet, for which the Schlichting's solution for the average velocity components (7) was used. In this solution, the (molecular) kinematic viscosity ν is replaced by a virtual (turbulent) kinematic viscosity ϵ_0 given in the equation

$$\epsilon_0 = 0.161 J'^{1/2} \quad [12]$$

where $J' (=J/\rho) = 1.59 b_{1/2} \bar{u}_0$, J' is the kinematic momentum of the jet, $b_{1/2}$ is its half-width and \bar{u}_0 is the average fluid velocity along its axis ($b_{1/2} = cx_1$ in which c is 0.63 to 0.79, as experimentally found).

In the boundary layer situation, both the case of a "weak turbulence", where $W_0' = \bar{W}_0$, and a "strong turbulence", where $W_0' > \bar{W}_0$, were investigated.

For the first case, numerical simulations were employed while for the second one Klebanoff's experimental data (5) supplemented by simulations was applied. Also, in the latter case, the version

$$\overline{W'_{32}^2} = \overline{W'_{23}^2} = \overline{W'_{13}^2} \quad [13a]$$

or

$$\overline{W'_{32}^2} = \overline{W'_{23}^2} = \overline{W'_{11}^2} \quad [13b]$$

was taken. The calculations in both cases were carried out with $\nu = 0.15 \text{ cm}^2/\text{sec.}$, δ (thickness of the atmospheric boundary layer) $= 10^3 \text{ m}$, $z_0 = 0.1 \text{ m}$, $k_0 = 0.4$, $\Gamma_{D_0} = 1 \text{ sec}^{-1}$, and ϵ deduced from Eq. [5]. The calculation time for \bar{F} was greater than the relaxation time of the particles, and $\Delta\theta = \Delta\phi = \pi/12$ or $\pi/24$.

In the turbulent jet situation, the ratio between the various values of $\overline{W'_{ik}^2}$ was obtained (6) through

$$c_2 \overline{W'_{i1}^2} = \overline{W'_{k1}^2} \quad (i, k = 1, 2, 3; i \neq k) \quad [14]$$

where $c_2 = 1 + \exp(-200r^2)$, r being the radial distance within the jet.

For both situations, the absolute values of $\Delta W'_{ik}$ were deduced by normalization according to Eq. [5]. Values of \bar{F} , and F_m , together with the deviations of F for fields (2)&(3)(above), were calculated as a function of height above ground (and hence ϵ) in the boundary layer situation, the aspect ratio of the particles, R ($R > 1$ for fibers and $R < 1$ for platelets), and the parameterization factor a_p . However, only the following typical figures are presented here:

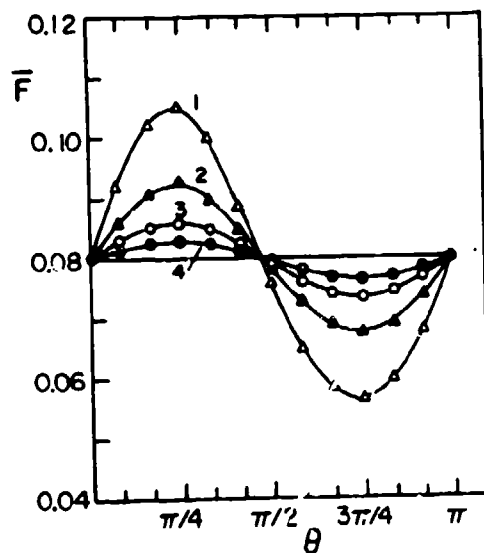


Figure 1. The average o.d.f., \bar{F} , vs. θ for the atmospheric boundary layer, "weak turbulence". With $z = 2.5$ to 20m (1) 2.5m , (2) 5m , (3) 10m , (4) 20m ,

$R = 10$, $\phi = \pi/2$,

$\alpha_0 = 1$, $\bar{W}_{13} (= \bar{W}_0)$ according to Eq. [11], $W_0' = \Delta W_{13}'$.

Solid lines are simulation results (254 realizations, usually); points are values calculated from the \bar{W}_{ik} field.

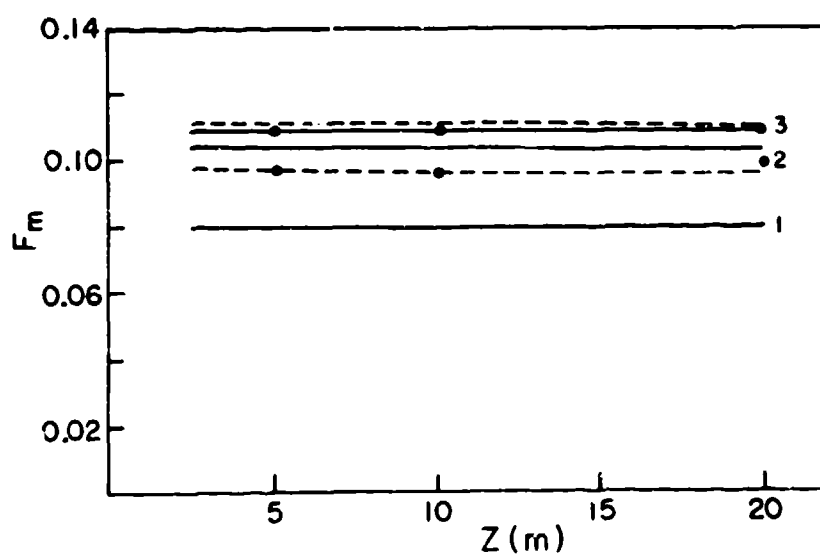


Figure 2. The maximal o.d.f., P_m , vs. height for the atmospheric boundary layer, "strong turbulence". $R = 50$; ϵ decreases with height according to Ball (8). (1) $W_{ik}^{(1)}$, (2) $W_{ik}^{(2)}$, (3) $W_{ik}^{(3)}$; dashed lines are cases where terms of Eq. [7] are taken with opposite signs; points relate to combination of Eq. [13b]. (Line 1 essentially coincides with the random distribution one.)

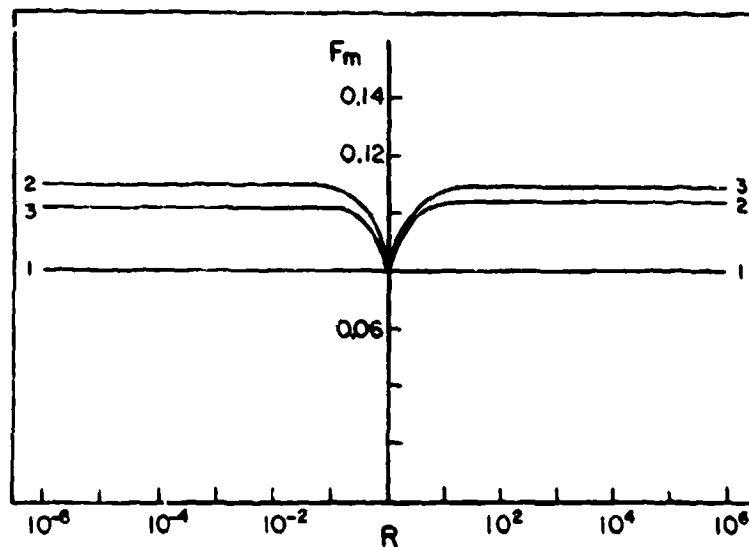


Figure 3. The maximal o.d.f., F_m , vs. particle aspect ratio R for the atmospheric boundary layer, "strong turbulence".

$$z = 5m, \epsilon = 230 \text{ cm}^2/\text{sec}^{-3}$$

$$(1) W_{1k}^{(1)}, (2) W_{1k}^{(2)}, (3) W_{1k}^{(3)}$$

(Line 1 essentially coincides with the random distribution one.)

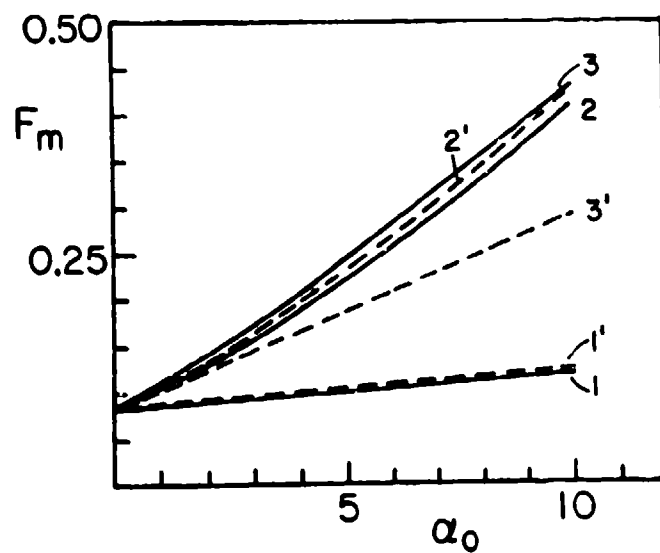


Figure 4. The maximal o.d.f. F_m vs. the parameter α_0 for the atmospheric boundary layer; "strong turbulence".

$R = 50$ ———; $R = 0.02$ - - - -; $z = 2.5m$; $\epsilon = 5 \text{ cm}^2/\text{sec}^3$.

(1) $W_{1k}^{(1)}$, (2) $W_{1k}^{(2)}$, (3) $W_{1k}^{(3)}$

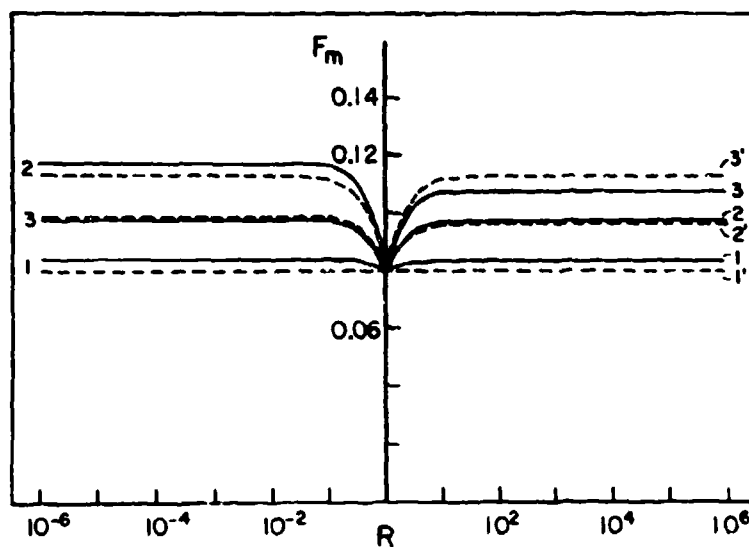


Figure 5. The maximal o.d.f., F_m , vs. particle aspect ratio R for a free turbulent jet.

location: $x_1 = 2$, $x_2 = x_3 = 0.05$ (see ref. 1),

$$\bar{W}_0 = 5 \text{ sec}^{-1}, \quad \epsilon = 250 \text{ cm}^2/\text{sec}^3$$

$(1), (1') : w_{1k}^{(1)}; (2), (2') : w_{1k}^{(2)}; (3), (3') : w_{1k}^{(3)}$ for $Q^{(1)}, (2'), (3')$ terms of Eq. [7] are taken with opposite signs.

(Line 1 essentially coincides with the random distribution one.)

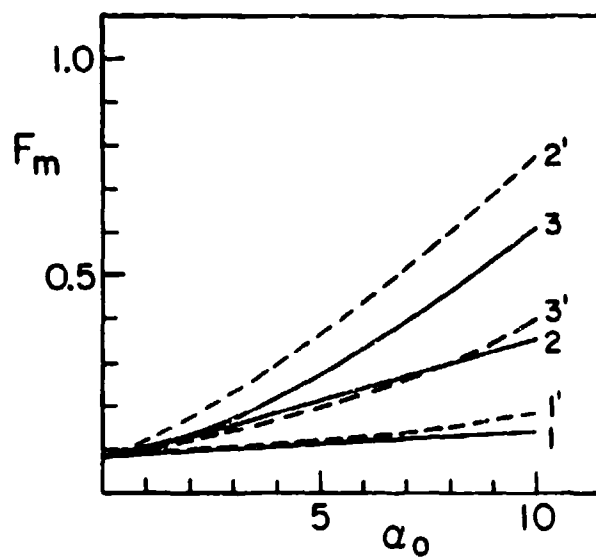


Figure 6. The maximal o.d.f., F_m vs. the parameter α_0 for a free turbulent jet.

$$\overline{W}_0 = 5 \text{ sec}^{-1} \quad x_1=2, \quad x_2=x_3=0.05 \text{ (see ref.1)}$$

$$c = 125 \text{ cm}^2/\text{sec}^3, \quad R = 50 \text{ ————}, \quad R = 2 \text{ - - - -}$$

Conclusions

Atmosphere boundary layer (up to 20 m height) :

1. The average o.d.f. in a weak turbulent field shows structured (preferred) orientation.
2. The maximal (and average) o.d.f. in a strong, commonly occurring, turbulent field of the average realisation $W_{ik}^{(1)}$ essentially coincide with the random distribution while the spread of the values of the function between fields $w_{ik}^{(2)}$ and $w_{ik}^{(3)}$ is quite significant. This spread of values may have practical connotations.
3. The values of F_m and its deviations increase with the parameter α_0 as expected.

Free turbulent jet :

Conclusions 2 and 3 of the former situation apply here too.

References

1. E.M. Krushkal and Isaiash Gallily, J. Colloid Interface Sci. 99, 141 (1984).
2. Isaiash Gallily and E.M. Krushkal, Proceedings of the 1983 CSL Conference on Obscuration and Aerosol Research.
3. Hinze, J.O., "Turbulence, " McGraw-Hill, Inc. (1975).
4. Wang, S.T., and Froet, W., NASA CR 3309 (1980).
5. Klebanoff, P.A., NACA TN 3178 (1954).
6. Wignansky, I., and Fiedler, H., J. Fluid Mech. 38, 577 (1969).
7. Schlichting, H., "Boundary Layer Theory" McGraw-Hill Inc. (1968) pp. 220, 699.
8. Ball, F.K., J. Meteorol., 18, 553 (1961).

Unipolar Charging for Ultrafine Aerosols:
Theory, Experiment and Significance for Size Distribution

S. W. Davison
Engineering Department, University of Maryland Baltimore County
Catonsville, Maryland 21228

S. Hwang, J. Wang, J. W. Gentry
Chemical and Nuclear Engineering Department
University of Maryland
College Park, Maryland 20740

Abstract

This paper discusses the theoretical bases of models for diffusion charging of ultrafine particles and applies several models to predicting unipolar charge levels. The model predictions are compared to new experimental data. The comparison requires calculation of the extent of particle loss in the unipolar charger due to electrostatic precipitation. This work has been submitted for publication as follows:

S. W. Davison and J. W. Gentry. Fundamental Hypotheses on the Charging of Ultrafine Particles by Diffusion of Ions. Submitted to Particulate Science and Technology August, 1983.

S. W. Davison, S. Y. Hwang, J. Wang and J. W. Gentry. Unipolar Charging of Ultrafine Particles by Diffusion of Ions: Theory and Experiment. Submitted to Langmuir July, 1984. Accepted October, 1984.

The next objectives of this work will be the application of the models and experimental techniques to fibrous particles.

Introduction

The electrical aerosol analyzer (EAA) imparts a unipolar charge to aerosol particles by means of a corona discharge and prevents the more electrically mobile particles from the stream as it passes between charged metal plates (this part of the device is called the mobility analyzer). Particles entering the EAA and those emerging from the mobility analyzer can be counted. By changing the electric field strength in the mobility analyzer a mobility distribution of the aerosol stream can be obtained, and if the charge distribution on the aerosol is known the mobility distribution can be inverted to a size distribution. Up to the present time users of this device have relied upon calibration curves distributed with it rather than direct knowledge of the charge distribution. The ability to compute unipolar charge levels as a function of time could improve the flexibility of the device by allowing use of ion concentration-residence time products (Nt) other than those tabulated and also by allowing corrections to be made for the effects of different ambient conditions (ion species effects).

When a monodisperse aerosol is needed for experimentation it is frequently extracted from a polydisperse source by a differential mobility analyzer (DMA) which selects particles with mobilities between narrow limits. In this device the aerosol is given a bipolar equilibrium charge and the assumption is usually made that the number of multiply charged particles is negligible. If it is necessary to select particles smaller than the mean size from the distribution, however, this assumption may not be valid. Therefore it is necessary to know the equilibrium bipolar charge distribution for small particles. This distribution is difficult to measure directly. Measurements of unipolar attachment rates will help to calculate it.

To calculate unipolar charge levels it is necessary to obtain transient solutions of a system of differential equations. Among the parameters of the system are the ion attachment coefficients. Calculation of these coefficients requires the adoption of some model of the mechanism of aerosol charging. Several such models have been formulated. Four are used here (Fuchs, 1963; Gentry,

1972; Hoppel, 1977; Laframboise and Chang, 1977). The derivations of these theories are discussed in detail elsewhere (Davison and Gentry, 1983). Simulations of aerosol charging in accordance with these theories were used to identify parameter regions of interest. Some of the simulations are presented with the experimental data.

Experimental Apparatus and Procedure

Experiments were carried out to measure the unipolar charge level of a monodisperse aerosol as a function of size and Nt value. A schematic of the apparatus appears as Figure 1. The aerosol was generated by vaporization and recondensation of silver and a monodisperse stream was extracted by an electrical aerosol classifier (EAC). The monodisperse aerosol was neutralized and passed through a corona discharge at various different Nt values. The charge distribution of the aerosol was measured using an EAA, a condensation nucleus counter (CNC), and an electrometer.

The results of the experiments were then compared to the predictions of the theories. The model solutions previously discussed gave the charge distributions (according to the various theories) coming out of the charger. In order to compare these values with the experimental data it was necessary to simulate the operation of the EAA to take into account the particle loss due to electrostatic precipitation of particles in the charger. Both the simulations and experiments indicated that this particle loss is substantial and that failure to allow for it leads to significant error in interpretation of EAA data.

Early in the experimental program it became evident that significant numbers of particles were being lost in the EAA through mechanisms other than precipitation in the mobility analyzer. The charger is depicted in Figure 2. It consists of a fine tungsten wire held at a potential of no more than 6 KV from ground. The wire is surrounded by a metal cylinder which is partly solid (sections 1 and 3) and consists partly of a metal screen (section 2). This inner cylinder is held at a potential of about 0.2 KV. Surrounding the inner cylinder is another, larger cylinder which is grounded. The aerosol passes in laminar flow between these two cylinders. It is charged by the ions emitted by the tungsten wire which penetrate the screen and move under the influence of the electric field toward the outer cylinder.

In section 1 of the charger the aerosol is assumed to be uncharged and, therefore, unaffected by the field. In section 2 the aerosol is undergoing charging and the path of the charged particles will be affected by the field. In section 3 it is assumed that there are no ions and, therefore, no charging occurs. There is, however, an electric field so that migration and precipitation of the aerosol particles will occur.

Results

Comparison of experimental with model predictions can be made with respect to the fraction of uncharged particles and the ratio of the total number of elementary charges leaving the unipolar charger to the number of particles entering. The charge distribution of the aerosol leaving the charger can also be calculated, and has been presented elsewhere (Davison et al., 1984).

Figure 3 shows typical results for the fraction of uncharged particles as a function of Nt . As expected, as this product approaches zero the uncharged fraction approaches unity. Simulated results using the four models are shown by the curves. The experimental data and the model curves lie on straight lines on the semilog plot. For the 32 nm data the slope for the experimental data is -2.5 cc / ion-sec. This lies between the Hoppel value of -2.3 and the Gentry value of -3.5 . The Gentry model was observed to predict a lower fraction of uncharged particles for all particle sizes between 18 and 42 nm. The Laframboise and Chang model predicts a slope of -0.61 and a much higher fraction of uncharged particles. The most important result is that the three models which include the image term are qualitatively consistent with the experimental data.

The charge/number ratio can be obtained by measuring the charge with the Faraday cage and the number density with the CNC. Data for ten charging rates (expressed as Nt product) are plotted for the 32 nm case in Figure 4. The maxima observed in the curves occur as a result of loss of the more heavily charged particles in the charger. If the particle loss in the charger had been neglected in the model calculations these curves would have been monotonically increasing; Figure 4 clearly indicates the importance of particle loss. The qualitative agreement between the experimental results and those theories including the image effect is good. Generally the measurements fall between the predictions of the Fuchs and Gentry theories.

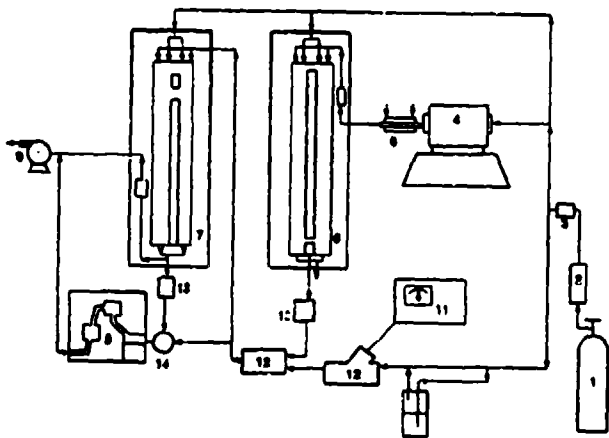
Conclusions

The importance of accounting for particle loss in the charger was indicated by both experiment and simulation. This loss occurs primarily as a result of the electrostatic precipitation of charged particles caused by the field produced by the corona discharge. In order to simulate this it is necessary to model the aerosol's parabolic flow profile and the charger field.

Of the four models used those of Fuchs, Gentry and Hoppel gave results that were qualitatively consistent with the data. The theory of Laframboise and Chang did not, perhaps due to the fact that this theory does not include the effects of the image potential.

References

- S. W. Davison and J. W. Gentry. Fundamental Hypotheses on the Charging of Ultrafine Particles by Diffusion of Ions. Pacific Region Meeting of the Fine Particle Society. August 1 - 5, 1983. Honolulu, Hawaii.
- N. Fuchs. On the Stationary Charge Distribution on Aerosol Particles in a Bipolar Ionic Atmosphere. *Geofisica Pura e Applicada*. V. 56, 1963 pg. 185.
- J. W. Gentry. Charging of Aerosol by Unipolar Diffusion of Ions. *Aerosol Science*. V. 3, 1972 pg. 63.
- W. Hoppel. Ion-Aerosol Attachment Coefficients and the Diffusional Charging of Aerosols. In *Electrical Processes in Atmospheres*, Proc. of the Fifth Int. Conf. on Atmospheric Electricity. Dr. Dietrich Steinkopf Verlag, Darmstadt, FRG, 1977
- J. Laframboise and J. Chang. Theory of Charge Deposition on Charged Aerosol Particles of Arbitrary Shape. *J. Aerosol Sci.* V. 8, 1977 pg. 331



- | | |
|----------------|--------------------|
| 1 Gas Cylinder | 8 TSI 3020 CNC |
| 2 Dryer | 9 Vacuum Pump |
| 3 Filter | 10 Humidifier |
| 4 Generator | 11 Hygrometer |
| 5 Condenser | 12 Mixing Chamber |
| 6 TSI 3071 B/ | 13 Neutralizer |
| 7 TSI 3020 / | 14 Three Way Valve |

FIGURE 1 EXPERIMENTAL APPARATUS

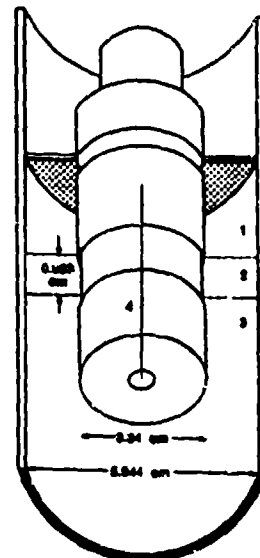


FIGURE 2 BIPOLAR CHARGER

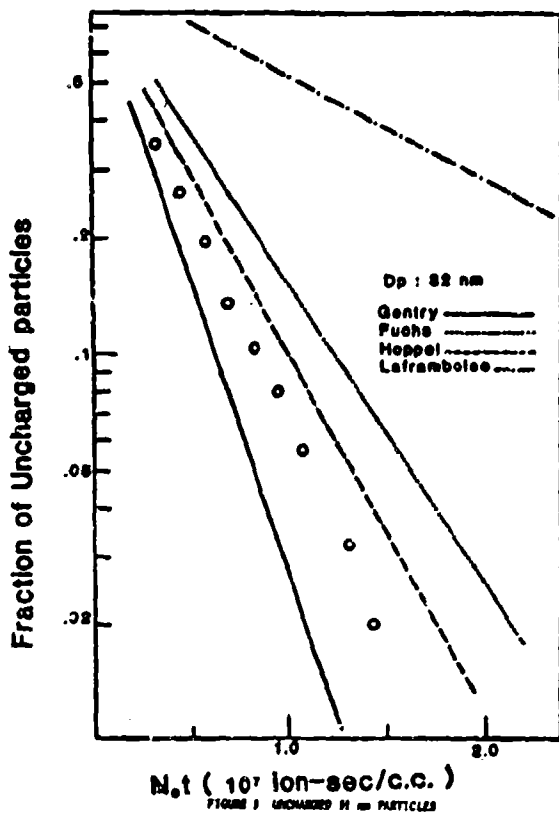


FIGURE 3 UNCHARGED 0.2 nm PARTICLES

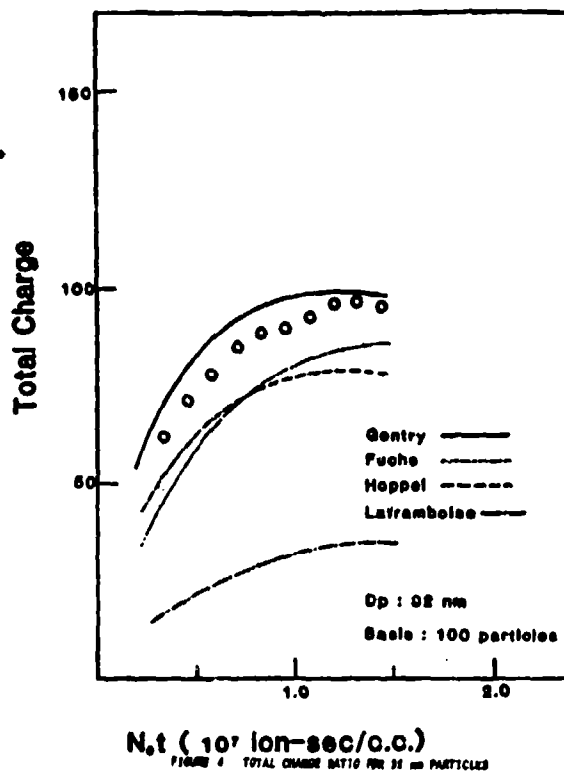


FIGURE 4 TOTAL CHARGE RATIO FOR 0.2 nm PARTICLES

RESULTS OF PAST AND CURRENT INVESTIGATION OF THE
SMOKE PARTICLE SCAVENGING BY NONSPHERICAL COLLECTORS

J. Podzimek and J. Martin
Graduate Center for Cloud Physics Research
University of Missouri-Rolla

ABSTRACT

This contribution summarizes the main results of theoretical and experimental studies of smoke particle scavenging performed since 1981 under the U.S. Army Grants DAAK-11-81-C-0075 and DAAK-11-83-K-0007 and outlines the task of the future research.

PAST STUDIES

The premise at the beginning of the research program was that a planar collector has a higher scavenging efficiency than a sphere (drop) in the range of scavenger sizes between 0.1 and 1.0 cm and smoke particle diameters from 0.1 to 10 μm . Higher scavenging efficiencies of disk type collectors in comparison with spheres of the same diameter have been found during experiments with smoke particle deposition in a laboratory wind tunnel (Podzimek, 1983). These results were supported also by theoretical studies (Martin and Podzimek, 1982) which considered the deposition of smoke particles of radius $0.001 < r < 10 \mu\text{m}$ on a thin oblate spheroid under the influence of Brownian diffusion, phoretic, electrostatic and inertial forces. In the range of collector Reynolds numbers, $Re_c > 4.0$, the calculated collision efficiency, E , of an oblate spheroid was one order of magnitude larger than that of a sphere ($E = 10^{-3}$). This difference increased with increasing Re_c (for $4.0 < Re_c < 50.0$).

Preliminary measurements also indicated that the number of smoke particles deposited on the reverse side of a disk is comparable with that on the obverse side. The particle size and number distribution is different on each specific side. On the obverse side it reminds one of the pattern predicted by the theory (Podzimek and Martin, 1982), however, the total number of deposited particles is almost one order of magnitude lower than that calculated from the model (Podzimek, 1981, 1983). The main discrepancy between the model and measurement was found on the reverse side of the disk and close to the rim.

Another hypothesis established at the initiation of the program was the

potential effect of the mode of motion of a symmetrical or unsymmetrical collector on the smoke particle deposition. Mean aerodynamic characteristics (C_D , V_z , Re_z , etc.) have been deduced from time-lapse camera pictures and the frequency or wave length of the oscillatory motion of the models determined (Podzimek, 1983). The maximal frequencies observed for a falling paper disks with $r < 1.0$ cm were used for simulation of the scavenger oscillatory motion in a wind tunnel. In mean the smoke particle deposition on oscillating disks was higher than on quiescent disks (23% higher for frequencies 10 to 60 Hz and amplitudes $\pm 10^\circ$). The particle deposition on the reverse side was considerably higher (Fig. 1) than that of a quiescent disk ($N_p/N_B = 0.745$ for 60 Hz and $Re = 80$). The experimental facilities have been described in previous reports (Podzimek, 1981, 1983).

Considerable attention has been paid to the influence of an electric charge on the smoke particle deposition. Disks of different material (metal, plastic material, glass) permanently connected with the electrode collected more smoke particles (passing through a charge neutralizer). The collection efficiencies for particles with radii around $0.3 \mu m$ were approximately one order of magnitude higher than those observed on uncharged disks (Fig. 2) for $0.1 < Re < 50$ (Podzimek and Martin, 1984). Extremely high deposits were found along the disk's rim, where spherical smoke particles of $TiCl_4$ formed peculiar chain-like aggregates (Podzimek, 1983). Experiments performed with an instantaneously charged conductive or dielectric model showed that the significant charge effect lasts only for about 30 seconds at a smoke particle concentration of $3,000$ to $5,000 \text{ cm}^{-3}$. A preliminary explanation of this fast decrease of collector charges was found by assuming a collector charge neutralization by oppositely charged smoke particles. An uncertainty still exists about the charge equilibrium (or charge distribution) of smoke particles passing through the filter and charge neutralizer (Kr-85) before reaching the test section of the wind tunnel. The assumed symmetrical, Boltzmann-like, charge distribution on particles seems to not be supported by the current measurements. Usually a considerable difference was found between the number of particles deposited on collectors bearing electric charge of the same magnitude, but opposite sign.

CURRENT INVESTIGATIONS

The experiments in 1984 concentrated mainly on smoke particle deposition on cylinders, grid type models and fibers. One hoped that in the case of a broad size spectrum of smoke particles one could enhance, by using the grid type scavengers, both

the diffusional deposition on a large surface and inertial deposition at high Stokes numbers. Major importance was assigned to the effect of direct particle and collector charging and to the particle charging through induction in an electrostatic field (up to several kV cm^{-1}) because of the negligible effect of phoretic forces acting on particles in the "Greenfield gap" size domain.

Collection efficiencies of uncharged metallic and plastic cylinders at $3.4 < \text{Re} < 44.0$ (measured at airflow velocity of 1.0 m s^{-1}) were below 0.1% ($E < 0.001$). Electrically charged cylinders (0.5 kV to 8.0 kV between the collector and tunnel wall at 6.5 cm) showed collection efficiencies for TiCl_4 smoke particles (with mean radii of $0.25 \text{ }\mu\text{m}$) between 0.36 and 5.60%. The pattern of deposited particles strongly reminded one of the figures depicting the interaction of inertial and electrical forces acting on an aerosol particle: greater large particle deposition on the cylinder's front face and high deposition of small particles ($r < 0.35 \text{ }\mu\text{m}$) on the back side at $5.0 < \text{Re} < 25.0$ and a potential difference of several kV (Podzimek, 1983). There is, however, a large scatter of measured data (collection efficiency) in the dependence on charge and Re (Fig.3).

Deposition of smoke particles on grid type models was investigated with uncoated electron-microscope grids (mesh 50 and 300, 0.3 cm in diameter) because of their well-defined shape. The deposition on the front surface of an uncharged grid is characterized by a low deposition of smoke particles with diameters smaller than $0.7 \text{ }\mu\text{m}$ and a relatively high deposition of particles larger than $1.0 \text{ }\mu\text{m}$ due to inertial forces. The total collection efficiency for all smoke particle sizes featured by the distribution curve in Fig. 4 of an uncharged grid is higher ($E = 0.0175$) than that of a thin solid disk of the same diameter ($E = 0.0105$). The charge effect (electrode permanently connected with the scavenger-collector) is depicted in Fig. 5. The effect is very significant for potential difference greater than 1.0 kV per 6.5 cm and has a maximum around 5.0 kV at which the total collection efficiency of a disk can surpass 10% ($E > 0.1$). The total collection efficiency is defined as a total number of smoke particulates of a specific size deposited on both sides of a collector divided by the number of particulates passing through the main cross section of the scavenger (including the effect of interception) at the same time. Fig. 5 shows clearly the charge effect on the deposition of very small particulates ($d < 0.7 \text{ }\mu\text{m}$) which is significant at low charges (1.0 kV) and air velocities of 0.25 m s^{-1} . At a potential difference of 5.0 kV there is a maximum in

the collection efficiency curves for particles with diameters smaller than $1.4 \mu\text{m}$ (measured only for 1.0 m s^{-1} curve). In accordance with the theory there is an insignificant effect of the electric charge on particles with diameters larger than $1.4 \mu\text{m}$ due to the prevailing effect of inertial forces especially at the flow velocity of 1.0 m s^{-1} .

In Fig. 6 a very interesting comparison is made of collection efficiencies of the front face of a solid disk and an electron microscopical grid of the same diameter. The curves drawn for 1.0 kV and 5.0 kV show clearly that the grids are more effective collectors (scavengers) for small particle sizes ($d < 0.7 \mu\text{m}$) than solid disks if only the deposition on the front surface is considered. The disk is clearly more effective for particulates with diameters larger than $1.4 \mu\text{m}$ due to the effect of inertial forces. The comparison of the total collection efficiencies (of the front and back faces) of a disk and a grid (mesh 300) is made in Fig. 7. Irrespective of the large scatter of data the grid is a more effective scavenger than a disk of 0.3 cm in diameter for the uncharged and charged particles (0.5 to 8.0 kV per 6.5 cm).

The fiber material selected for experiments was a "dust magnet" filter from which fibers with individual diameters between 20 and $50 \mu\text{m}$ were selected and stretched in a metallic ring exposed to the aerosol flow in a wind tunnel at velocities ranging from 0.25 to 1.50 m s^{-1} . The deposition on uncharged and charged individual fibers having the properties of "electret" fibers are currently completed by the experiments with two or more hydrodynamically interacting fibers.

In Figs. 8 and 9 the number of particulates of a specific size are represented in percent of the total number of particulates of all sizes deposited on the fiber of approximately 0.003 cm in diameter at the aerosol flow velocity of 0.25 and 1.00 m s^{-1} . The percentage of deposited smoke particulates of a specific size seems not to be influenced much by the electric charge and airflow velocity (with the exception of one point for 0.0 kV and particle diameter of $0.5 \mu\text{m}$). Deposition of smoke particles on charged fibers is plotted in Fig. 10 which shows clearly how with increasing fiber charge the total collection efficiency of a fiber is increasing up to 15.5% ($E = 0.15$) for the air velocity of 0.25 m s^{-1} and electric charge corresponding to 5.0 kV per 6.5 cm. The increase in collection efficiency is almost linearly proportional to the charge. Bearing in mind the total length of a fiber net scavenger, one can estimate the potential significant effect of the fiber scavenger on the clearing of

smoke cloud. For the removal of small particulates ($d < 0.7 \mu\text{m}$) the lower settling velocity (which can be adjusted by selecting the fiber net frame of different weight) should be preferred.

CONCLUSION AND FUTURE RESEARCH

Very useful characteristics of the falling symmetrical and unsymmetrical scavengers have been obtained. These parameters can be applied while modeling the clearing of a smoke cloud and estimating the complex effect of a falling particle zone. In addition to the current research, another set of experiments with clearing of TiCl_4 smoke clouds in a cylindrical tank--described in previous reports--will be performed. The main goal of these investigations is to use the most promising scavengers found in the past and current experiments and to confront the visibility measurement with a simple model describing the action of a population of scavengers dropped in a smoke cloud.

The study of the smoke aerosol removal by inertial and diffusional deposition on oscillating models led to the conclusion that the increase of smoke particle ($0.1 < r < 2.0 \mu\text{m}$) deposition on oscillating paper disks will not override 30% of the total number of particles deposited on stationary disks ($E = 0.01$). In general, the oscillatory motion will enhance the deposition of small smoke particles on the reverse side of a model.

Because of the insignificant effect of phoretic forces around the artificial scavengers, the electrical forces seem to be the most important for smoke particle deposition in the Greenfield gap. The models permanently charged can increase their collection efficiency by one order or magnitude ($E = 0.1$). There is a strong indication that field charging--currently studied--will also considerably increase the collection of smoke particles. The electric charge on scavengers, however, is quickly neutralized by the deposition of charged smoke particles at high concentration. Another possibility to increase the smoke particle removal in the Greenfield gap is to enhance their deposition on fast-evaporating secondary droplets of composite structure (liquid-solid, liquid-liquid) and use subsequent removal of large particles ($r > 2.0 \mu\text{m}$) by nonspherical scavengers. This mechanism will be studied in the future and will be the subject of an application for patent protection.

Among the scavengers tested, the grid and fiber ("dust magnet") type collectors seems to be the most efficient. They are very efficient in the domain of small

particle ($r < 0.35 \mu\text{m}$) removal at low scavenger fall velocities ($v = 0.25 \text{ m s}^{-1}$). Currently the enhancement of their collection efficiency by a suitable electric charge is being investigated. Permanently charged grids and fibers often showed collection efficiencies higher than 15% ($E = 0.15$).

ACKNOWLEDGEMENT

This investigation has been supported by the U.S. Army Research Office under the grant DAAK-11-83-C-0007. The authors are indebted to Mr. V. Wojnar, A. Keshavarz and G. Stowell, who assisted in the laboratory measurements, and to Mrs. V. Maples who ably prepared the text for printing.

REFERENCES

- Martin, J.J., and J. Podzimek, 1982: Scavenging of Smoke Particles by Planar Collectors, Proc. of the 1982 Scient. Conf. on Obscuration and Aerosol Res., Aberdeen, June; R.H. Kohl and Assoc., Tullahoma, Tenn.
- Martin, J.J., K.P. Wang, and H.R. Pruppacher, 1980: A Theoretical Determination of the Efficiency with Which Aerosol Particles are Collected by Simple Ice Crystal Plates, J. Atmos. Sci. 36, 1628-1638.
- Podzimek, J., 1981: Clearing of Military Smoke Cloud with Scavenging Technique, Final Report DAAG 29-79-C-0073, UMR, June.
- Podzimek, J., 1983: Investigation of a Technique Clearing/Modifying a Military Smoke Cloud, Final Report DAAK-11-81-C-0075, UMR, September.
- Podzimek, J., and J.J. Martin, 1984: Deposition of Particulates on Charged Planar Scavengers, Preprint Vol. VII International Conf. on Atmos. Electricity, Albany, NY, June, AMS, Boston, 57-62.

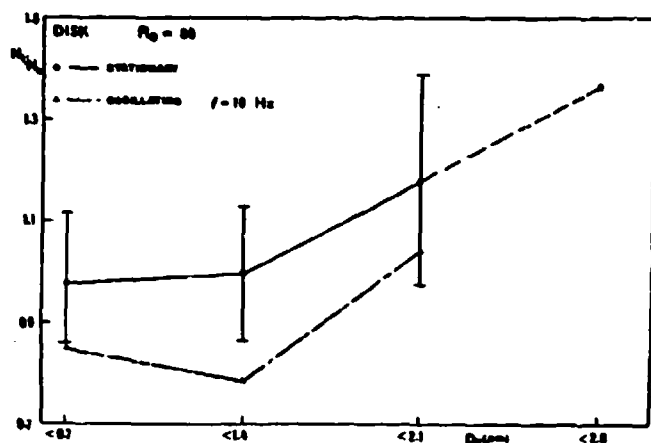
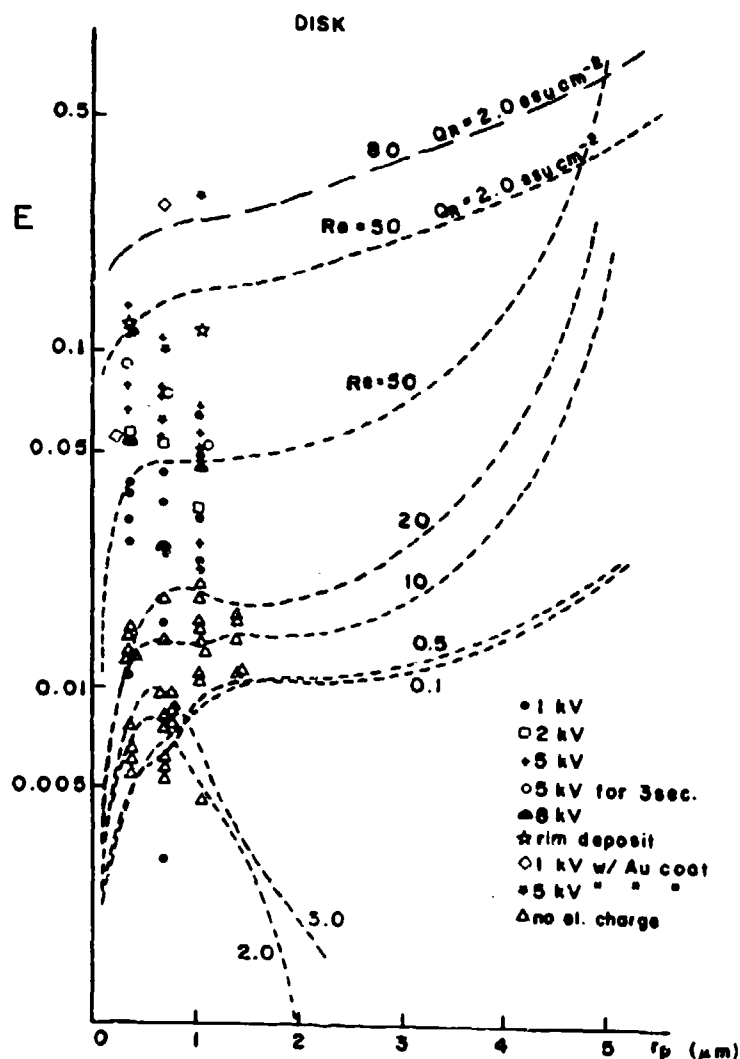


FIGURE 1. RATIO OF DEPOSITED SMOKE PARTICLES ON THE FRONT AND BACK SIDE OF A STATIONARY AND OSCILLATING GLASS DISK ($R=0.33$ cm) AS A FUNCTION OF PARTICLE SIZE. Mean values were calculated from 11 individual measurements for stationary disks and from 5 measurements for disks oscillating at a frequency 10 Hz. Bars indicate the maximal scatter of individual measurements for stationary disks.

FIGURE 2. MEASURED AND CALCULATED (DASHED LINES) COLLECTION EFFICIENCIES OF A DISK AT $0.1 < Re < 80$. Particle deposition was calculated in accordance with the model described by Martin et al. (1980) and by Martin and Podzimek (1982). Electric charge effect was calculated for $Re = 50$ and 80 under the assumption that Coulomb forces with inertial and phoretic forces were effective.



BRASS CYLINDERS

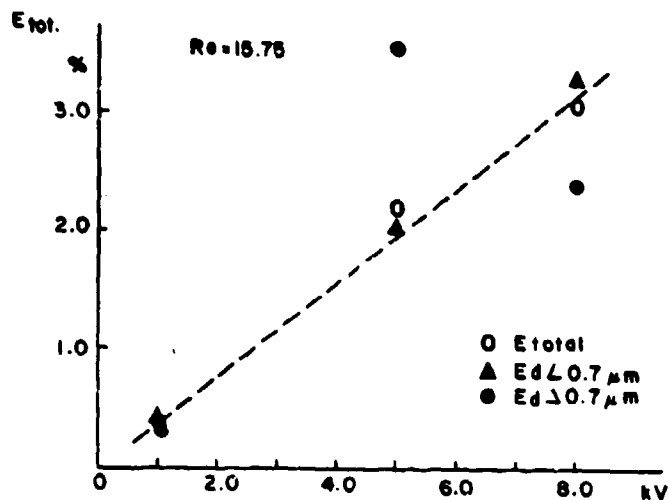


FIGURE 3. TOTAL COLLECTION EFFICIENCIES (IN %) OF BRASS CYLINDERS measured for different Re , particle size and collector electrostatic charge.

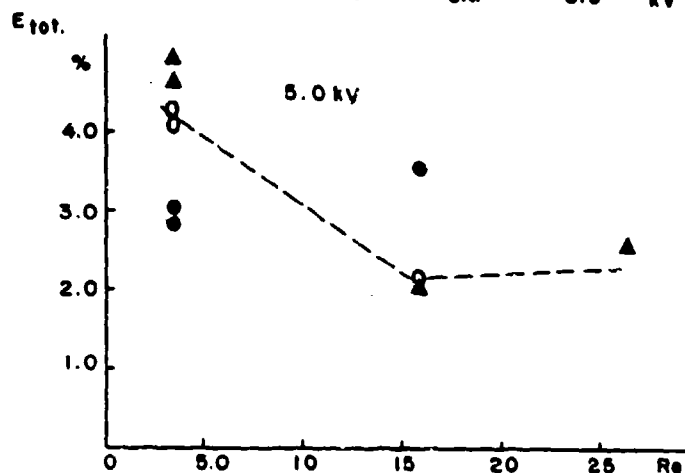
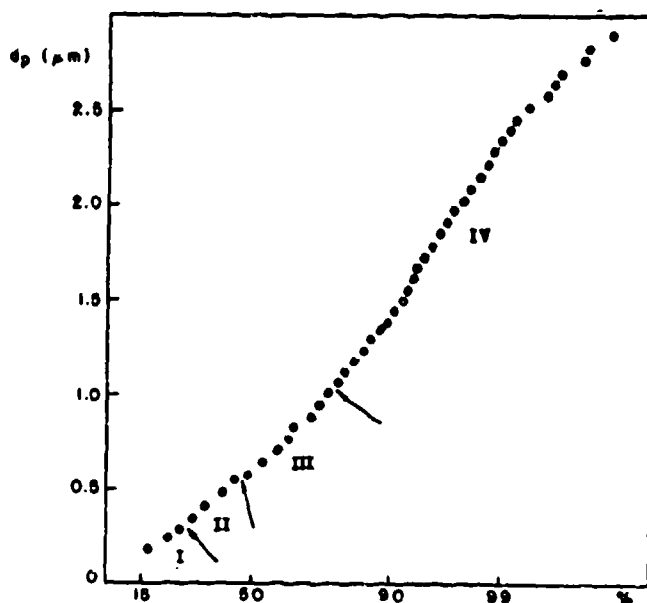


FIGURE 4. CUMULATIVE SIZE DISTRIBUTION OF $TiCl_4$ SMOKE PARTICULATES generated by the reaction of $TiCl_4$ and H_2O .



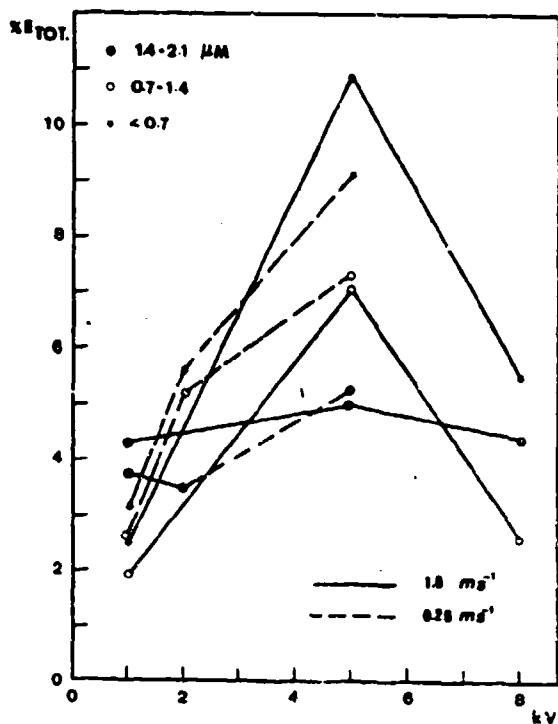
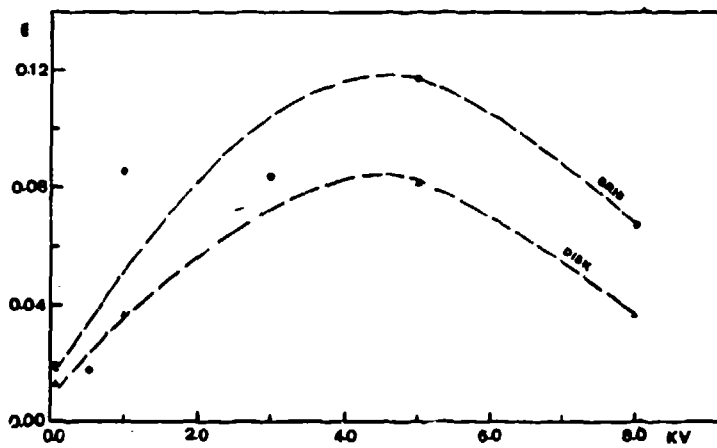


FIGURE 5. COLLECTION EFFICIENCIES OF GRID TYPE (MESH 300) SCAVENGERS FOR DIFFERENT SMOKE PARTICLE SIZE, ELECTROSTATIC CHARGE AND TWO AIRFLOW VELOCITIES (1.0 m s^{-1} - full line; 0.25 m s^{-1} - dashed line). The points are mean values of 2 to 5 individual measurements.

FIGURE 6. COMPARISON OF THE COLLECTION EFFICIENCIES (IN %) ON THE FRONT SIDES OF A DISK AND A GRID in dependence of smoke particle size and electric charge. Each point is a mean value of 3 individual measurements.



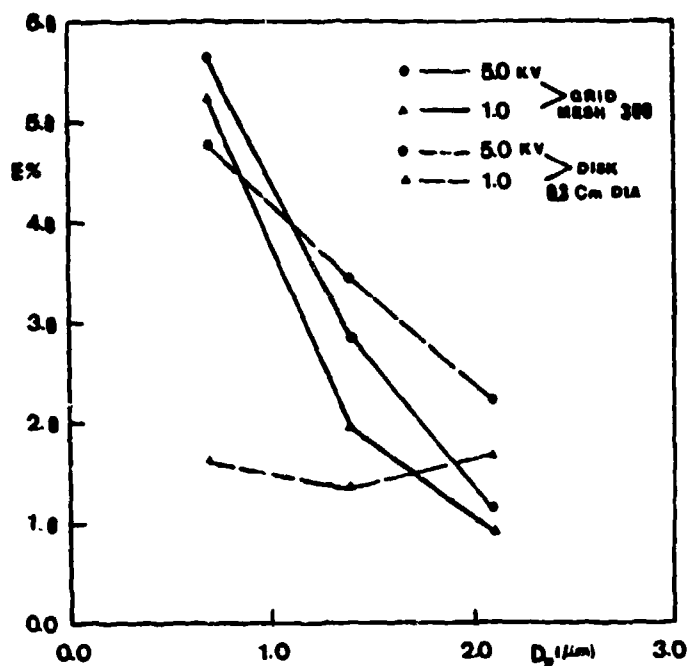
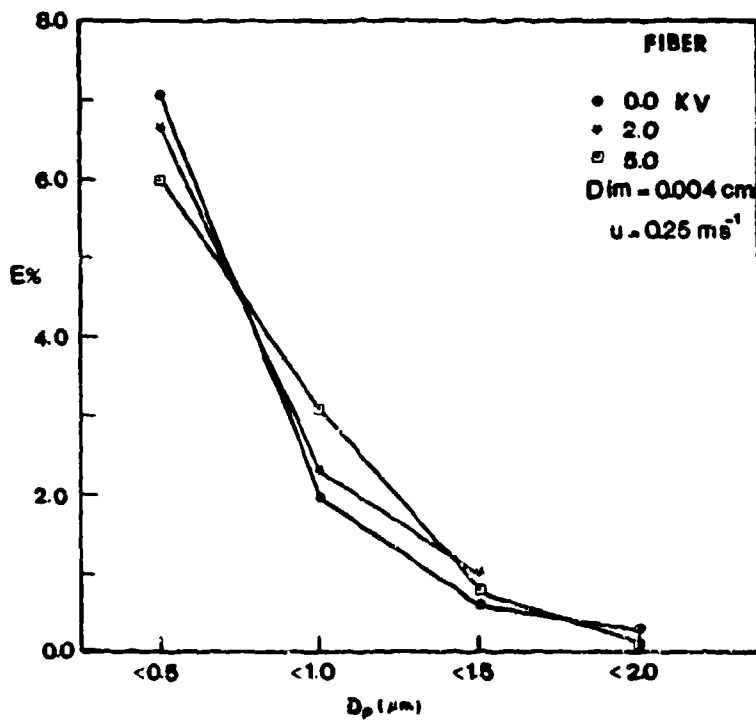


FIGURE 7. COMPARISON OF TOTAL COLLECTION EFFICIENCIES, E , FOR A GRID AND A DISK at different electric charge on the collector of 0.3 cm diameter.

FIGURE 8. TOTAL NUMBER, N , (IN %) OF PARTICLES DEPOSITED ON A "DUST MAGNET" FIBER ($d = 0.003$ cm) which is uncharged or charged. Airflow velocity was 0.25 m s^{-1} .



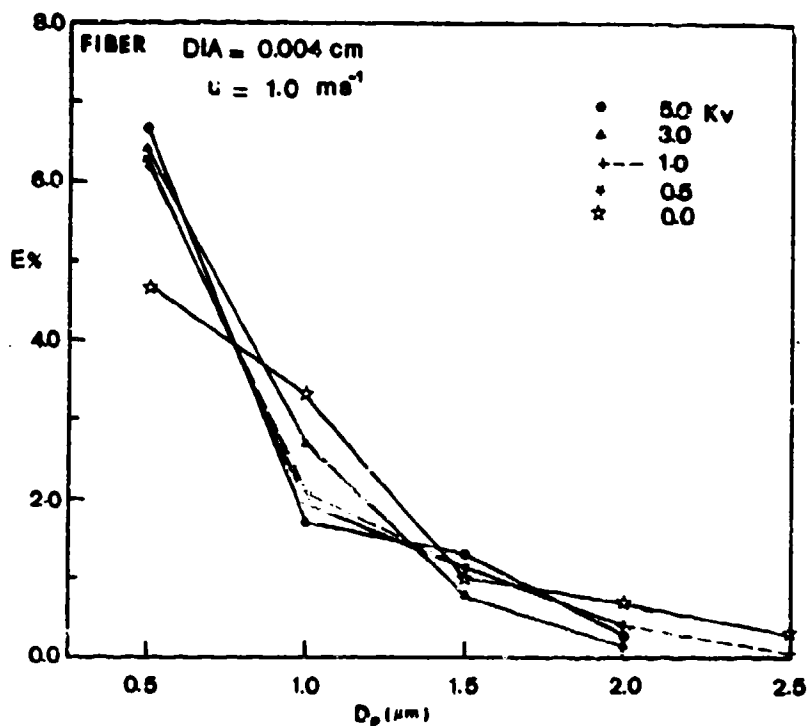
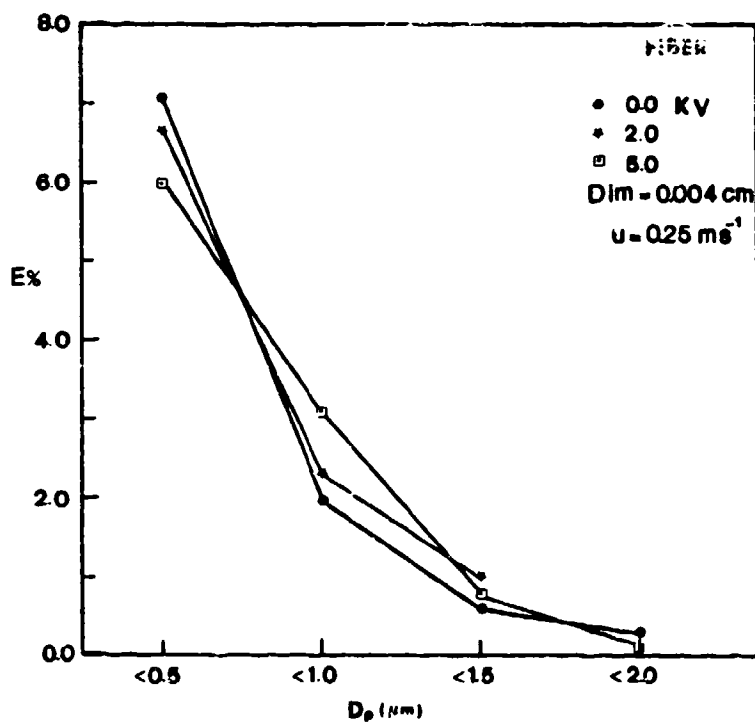


FIGURE 9. TOTAL NUMBER, N , (IN %) OF PARTICLES DEPOSITED ON A "DUST MAGNET" FIBER ($d = 0.003 \text{ cm}$) which is uncharged or charged. Airflow velocity was 1.0 m s^{-1} .

FIGURE 10. COMPARISON OF COLLECTION EFFICIENCIES, E , FOR "DUST MAGNET" FIBER ($d = 0.003 \text{ cm}$) at different electrostatic charges and at the air-flow of 0.25 m s^{-1} and 1.0 m s^{-1} .



BLANK

THE COLLISION OF NONSPHERICAL AEROSOL PARTICLES
WITH WATER DROPS

K. H. Leong
University of Illinois at U-C
Urbana, IL 61801

ABSTRACT

This theoretical study estimates the effects of nonspherical particle rotation in shear flow and the particle shape dependency of the thermophoretic force in the computation of collision efficiencies of small evaporating water droplets. The collision efficiencies obtained for nonspherical aerosol particles with a 30 μ m radius drop showed a strong dependence on the axis ratio of the particles. The results indicate that the orientation effects of the shear flow will tend to decrease the thermophoretic force on the particle towards the drop surface and the gravity effect that decreases collision efficiency. These effects can lead to large relative changes in the collision efficiency, lowering the efficiencies in the size regime where phoresis dominates and increasing the efficiencies in the regime where gravity dominates.

A significantly lower thermophoresis towards a drop surface for nonspherical particles can have significant impacts on the scavenging efficiencies of cloud droplets by reversing the direction of phoresis. It has been shown that thermophoresis dominates over diffusiophoresis for spherical particles with relatively low thermal conductivity. However, for the case of a nonspherical particle near an evaporating drop, the decrease in thermophoresis because of the orientation effects may prevent particle capture whereas enhancement may result during drop growth. The decrease of the gravity effect will also have a significant effect in that the so-called Greenfield gap in particle scavenging by cloud droplets may be substantially reduced because of the higher collection efficiencies of nonspherical particles in that size regime.

A detailed discussion of the results have been submitted to Aerosol Science and Technology for publication.

BLANK

II. AEROSOL CHARACTERIZATION METHODS
(Other than Aerodynamic Methods - See IC)

ANALOGS TO THE SHAPE FACTOR OBSERVED IN
OPTICAL CALCULATIONS

PAMELA E. GELLER
UNIVERSITY OF UTAH

PETER W. BARBER
CLARKSON COLLEGE

PRESENTED BY

EDWARD W. STUEBING
CHEMICAL SYSTEMS LABORATORY

(A presentation at the 1983 Conference
which is included in these Proceedings
by request).

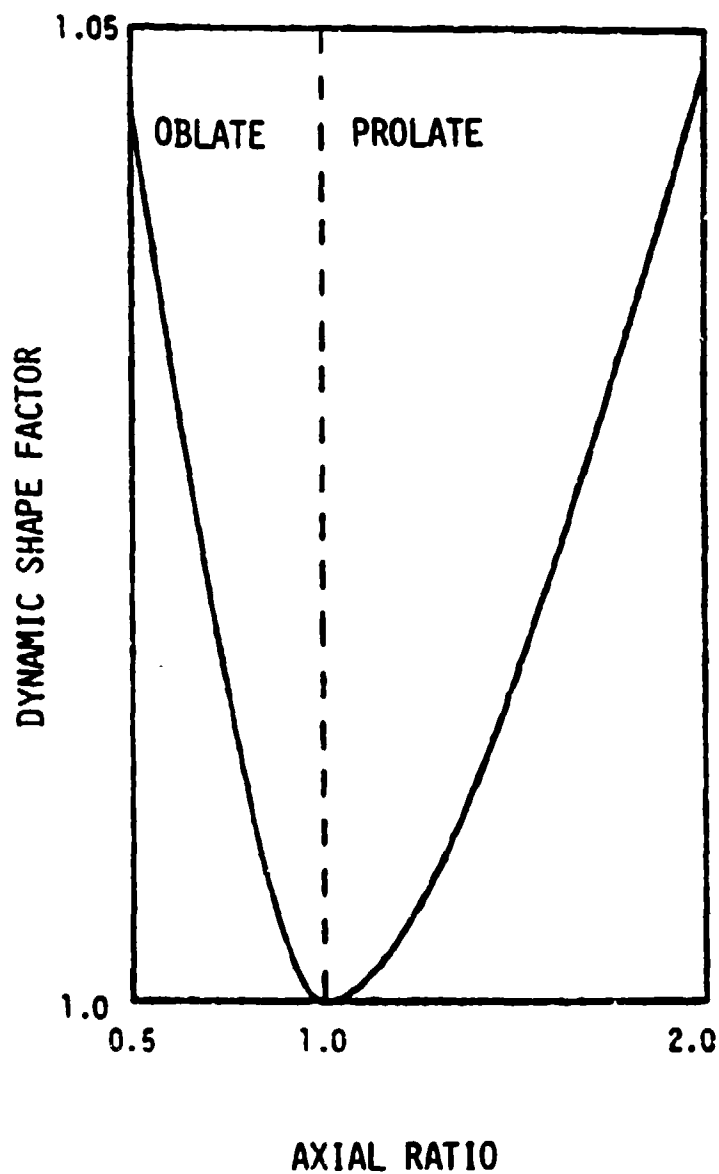


Figure 1 - The dynamic shape factor (d.s.f.) as a function of the axial ratio for spheroidal particles. The d.s.f. for an arbitrary particle is referenced to a equal volume sphere. We seek a similar representation for the optical scattering features.

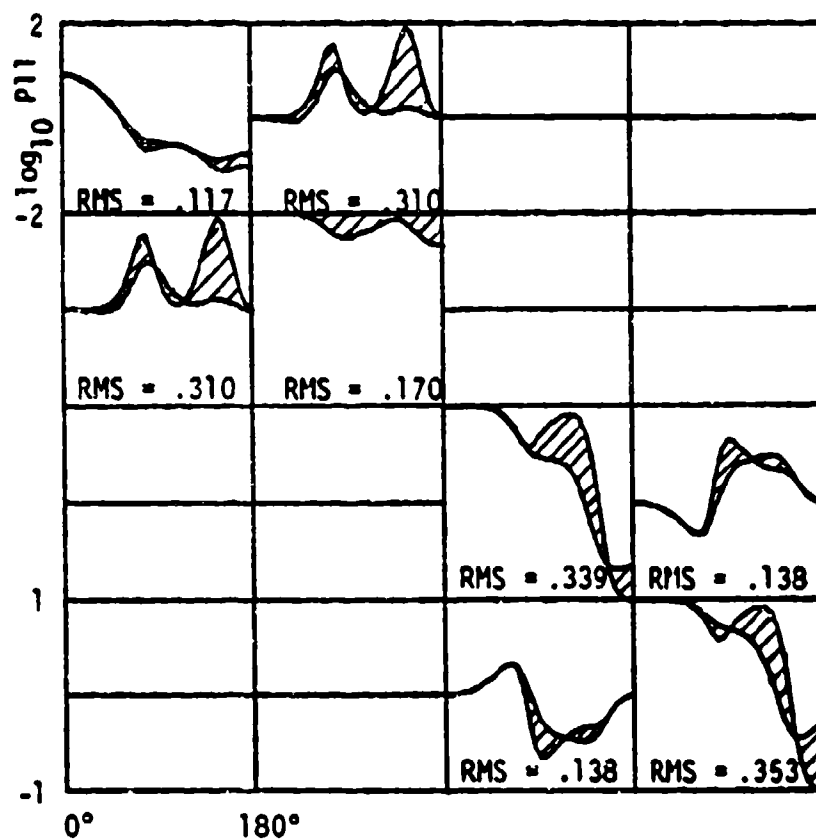


Figure 2 - One approach to the parameterization problem is to reduce the scattering information contained in the Mueller Matrix to a set of numbers.
Example:

- (1) Calculate the eight nonzero elements of the matrix for a randomly oriented spheroid.
- (2) Calculate the matrix for an equal volume sphere.
- (3) Calculate the root-mean-square (r.m.s.) difference between the eight matrix elements.

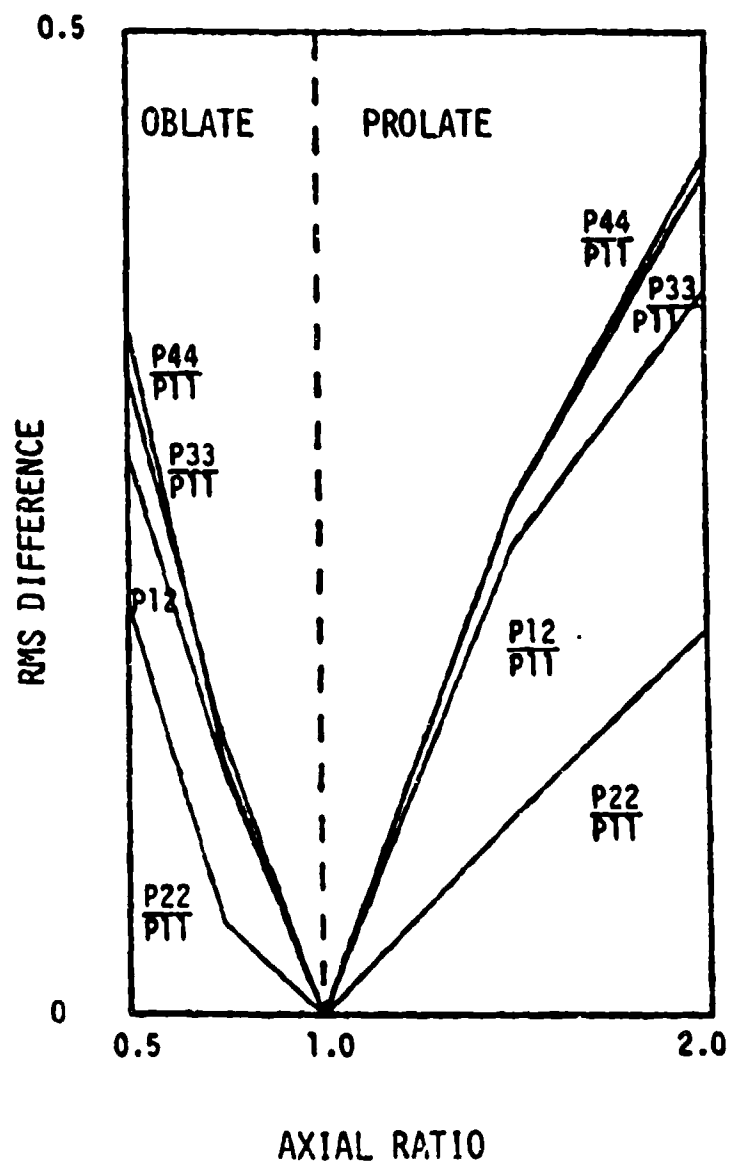


Figure 3 - A plot of the r.m.s. differences of four of the matrix elements as a function of the axial ratio. Note the similarity to the dynamic shape factor representation.

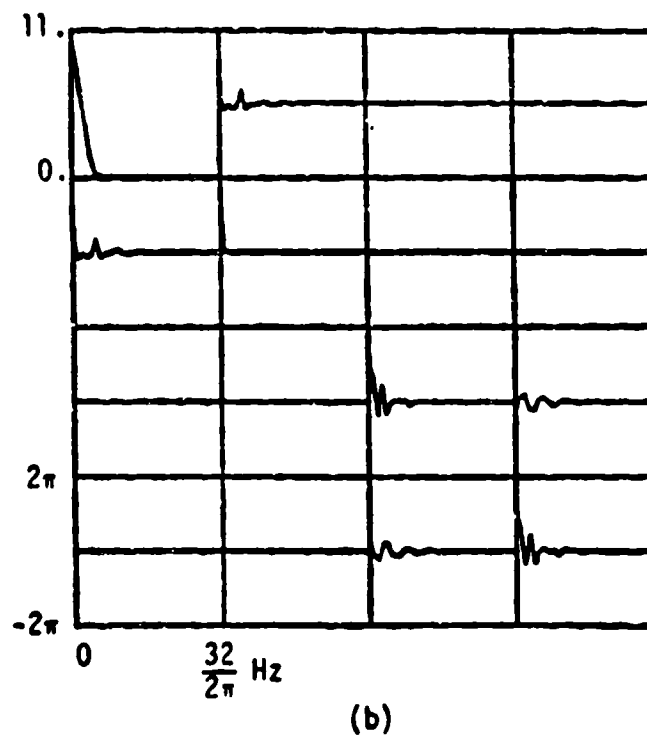
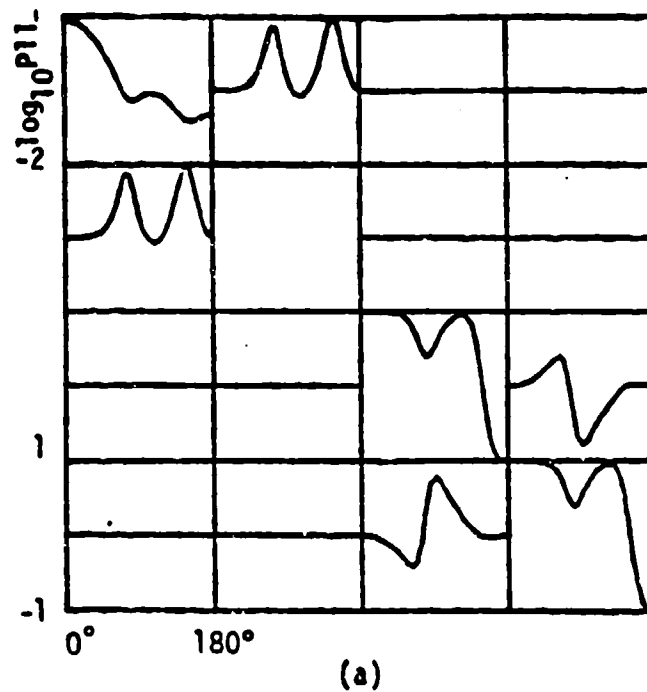


Figure 4 - Auxiliary optical scattering information can be obtained by Fourier analyzing the angular variation of the matrix elements. Fig. (a) is the Mueller Matrix and Fig. (b) shows the spectral features of each element. Note that for the small size parameter illustrated here, only low-frequency spectra result.

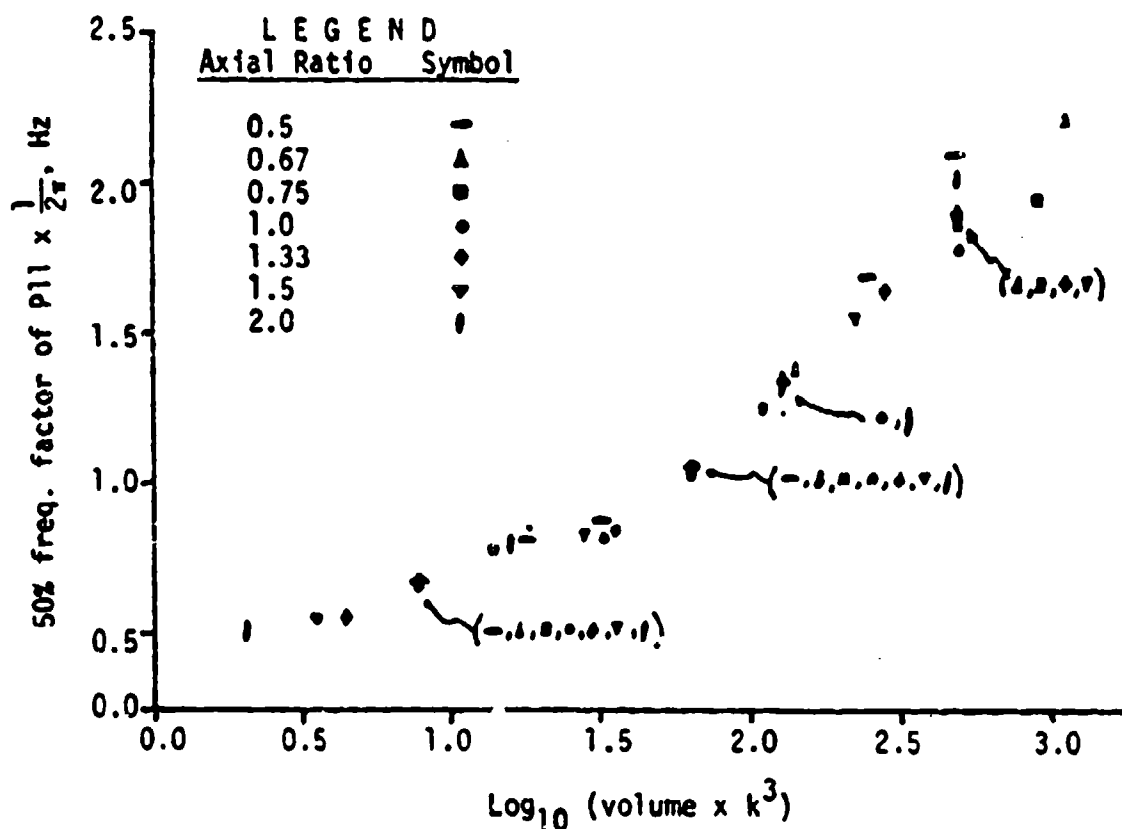


Figure 5 - We have quantified the spectral content of the P_{11} element by calculating the frequency at which half of the energy is contained in lower frequencies and half is contained in higher frequencies.

The 50% frequency factor has been calculated for spheroids of different size and shape. (For reference - the size parameter of a sphere corresponding to $\log_{10}(V \times k^3) = 3.0$, the right hand end of the horizontal scale, is 6.2.) We note that for these small particles, the 50% frequency factor is almost independent of particle shape.

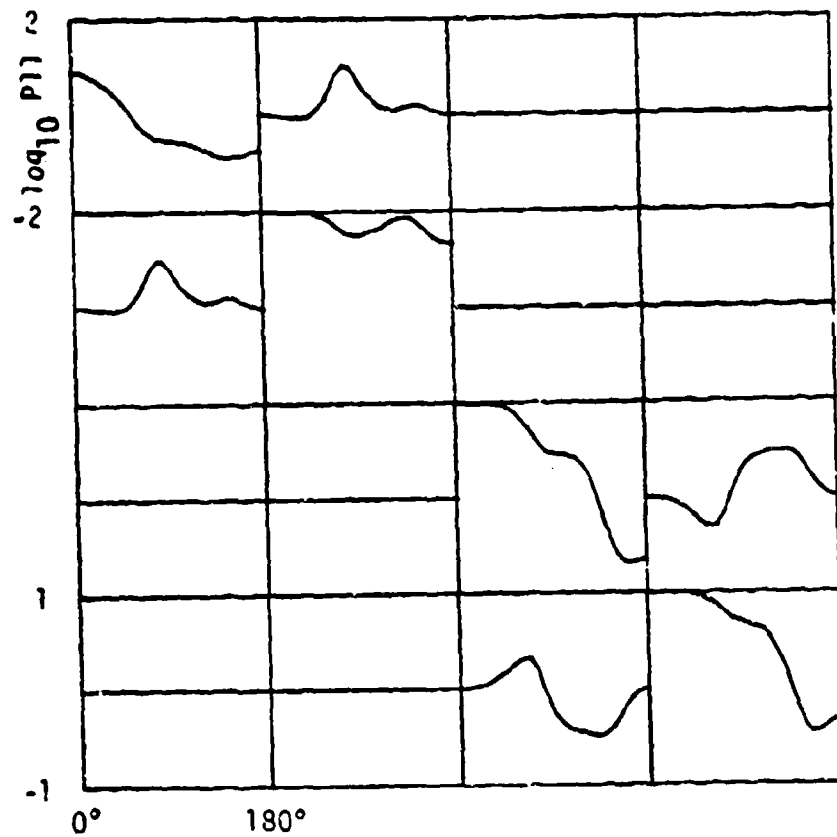


Figure 6 - An inversion example. Assume that we know the index of refraction and that the particle is a spheroid with axial ratio between 0.5 and 2.0.

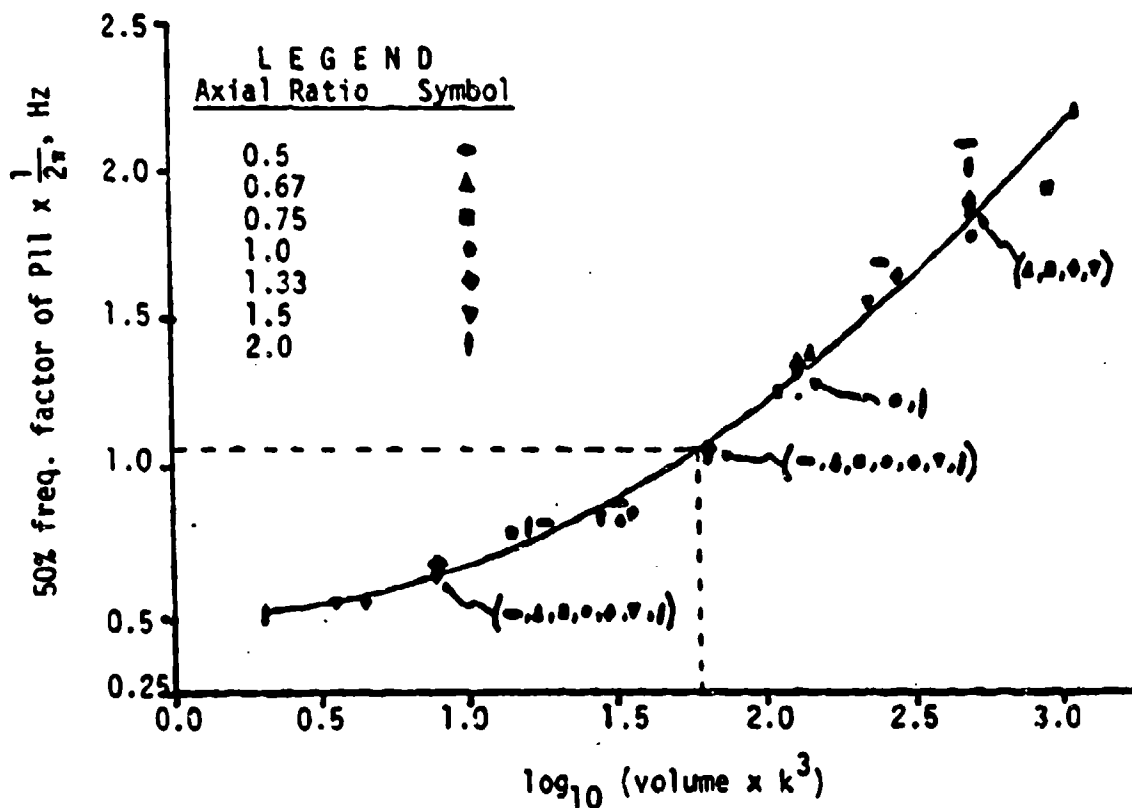


Figure 7 - Use the Fast Fourier Transform (FFT) on the P_{11} element and find the 50% frequency factor. Read $V \times k^3$ from the curve = 61.5. This gives the volume of the unknown spheroid. From this we can calculate the size parameter of the equal-volume sphere (= 2.45).

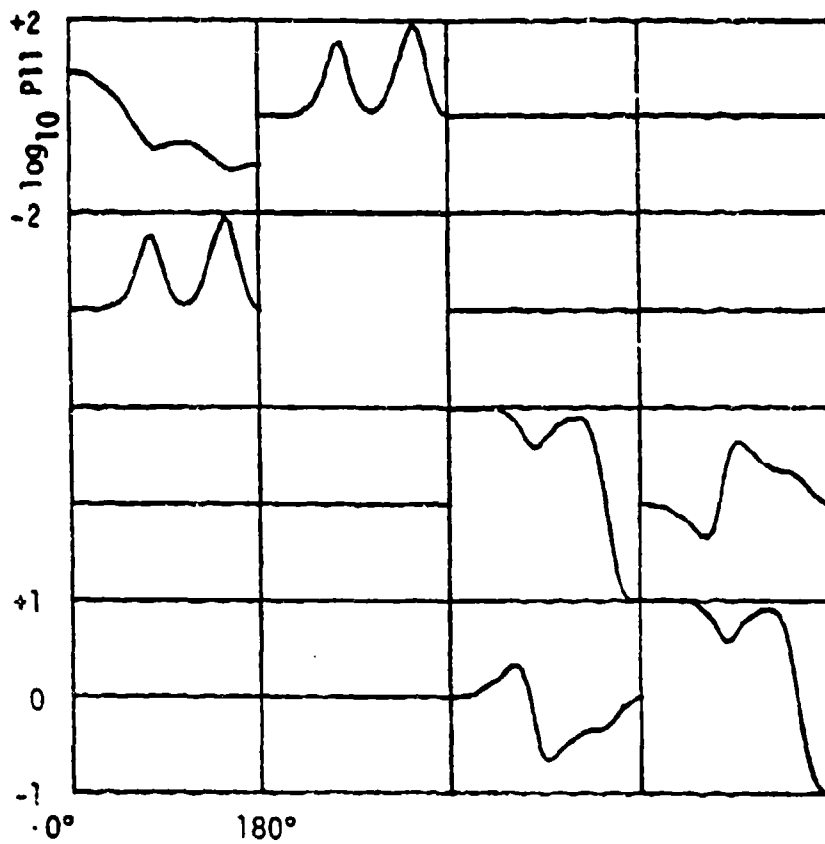


Figure 8 - The Mueller Matrix for a sphere (size parameter = 2.45) which was the same volume as the unknown spheroid.

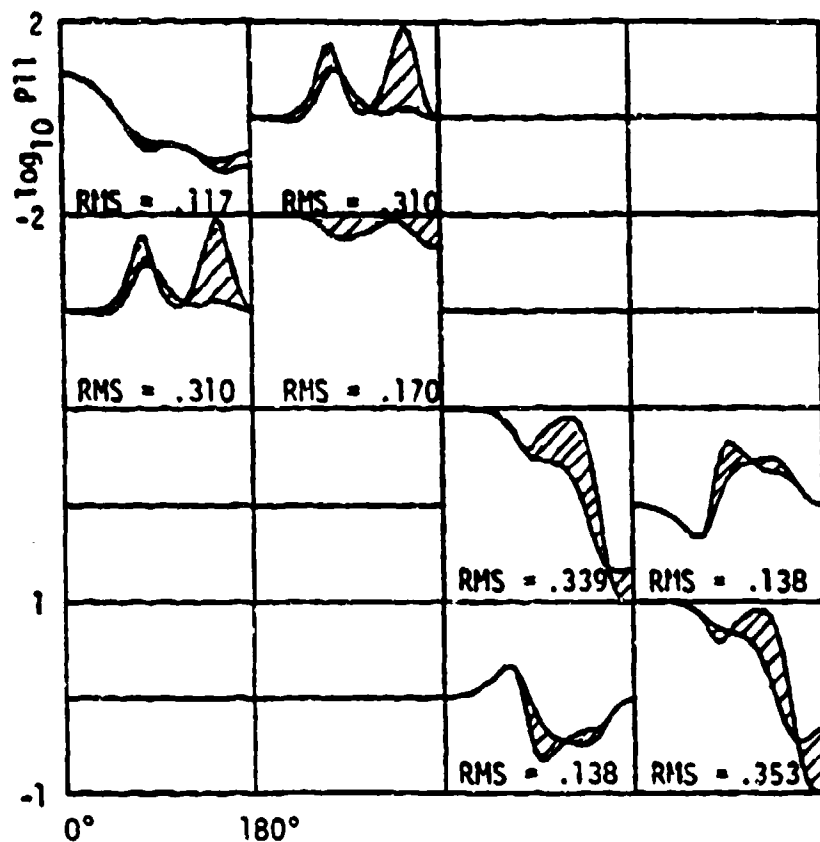


Figure 9 - Calculate the r.m.s. difference between the Mueller Matrix of the unknown spheroid and that of the equal volume sphere.

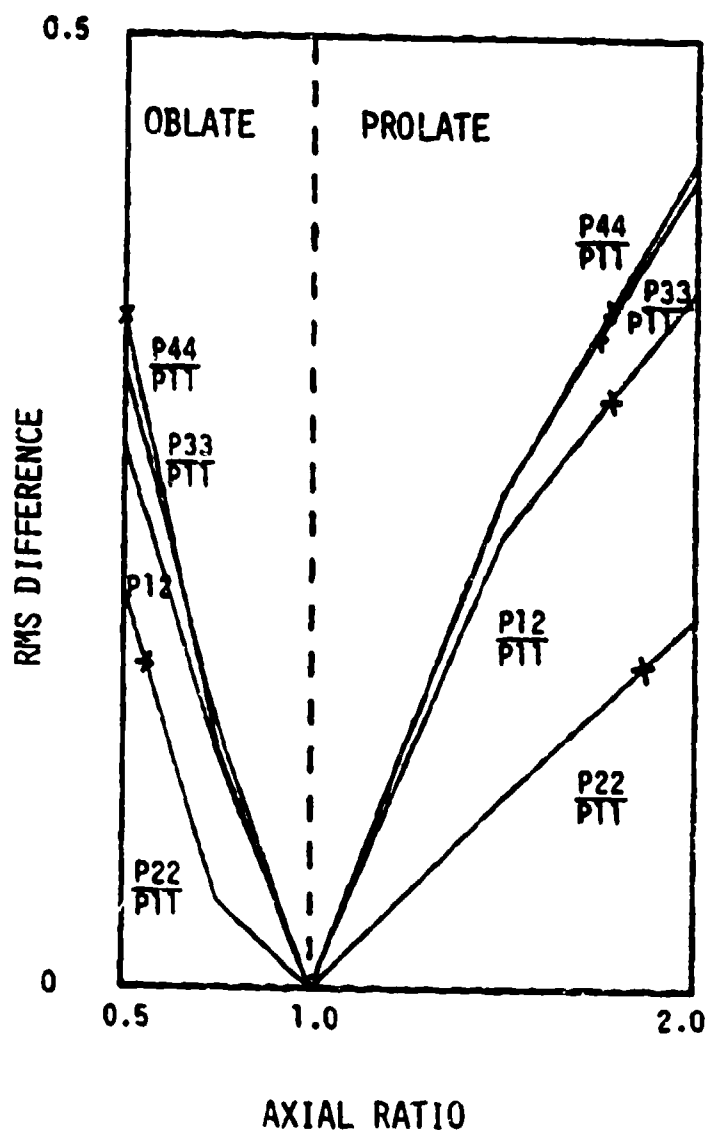


Figure 10 - Mark the r.m.s. values on a plot of r.m.s. difference as a function of axial ratio which has been calculated for spheroids with the volume of interest. The only results that fit on the plot indicate that the unknown spheroid is prolate with an axial ratio of 1.85 (actual is 1.75). The actual Vk^3 is 65.45.

Conclusion

We have described one approach to parameterizing the scattering features of a particle. It has two advantages: (1) It uses all of the information contained in the Mueller Matrix, and (2) the representation is similar to that which is used to describe particle shape. The method needs to be tested with actual measured data.

CHARACTERIZATION OF SMALL NONSPHERICAL
METALLIC PARTICLES

W. SCHEUNEMANN
Bundesinstitut für chemisch-technische Untersuchungen
beim
Bundesamt für Wehrtechnik und Beschaffung (BICT)
D 5357 Swisttal-Heimerzheim
FRG

ABSTRACT

This paper covers experimental details of testing and evaluation of various metallic pigments (metal flakes). Applied are different methods to measure the major axes of the particles as well as their thickness, i.e. scanning electron microscopy and specific watercoverage. These methods are compared with results obtained by cascade impactors.

INTRODUCTION

Simple optical considerations in the domain of geometric optics as well as model calculations on the basis of RALEIGH-GANS scattering theory for small ellipsoidal particles, have shown the great influence of shape effects on the optical behavior of small particles (Refs. 1, 2, 3). The results of these calculations indicate that, especially, thin metallic particles should exhibit broad band spectral characteristics. Chamber measurements have proven this fact. Therefore, greater effort has been placed on the characterization of this type of particles.

EXPERIMENTAL

The size characterization of spherical particles having well known physical parameters such as optical constants, specific gravity, etc. is in itself not a simple measuring procedure. On the contrary, it is one of the most difficult problems in modern aerosol research. Difficulties may arise from many factors, e.g., lack of accepted aerosol standards for calibration purposes, limited dynamic ranges of aerosol classifiers for particle size and number density, sampling problems due to aerosol transport problems, etc. These difficulties, obviously, increase when dealing with irregularly shaped particles. In addition, it was the criterion for this work that only simple and easily performed techniques were sought. The following types of measurement techniques have been applied: Determination of the specific water coverage S (m^2/g) and specific bulk gravity of the particles ρ (g/cm^3) allow the determination of the mean particle thickness D (μm). Information on the great axes of the platelets has been obtained by scanning electron microscopy (SEM) and further statistical analysis. The samples for SEM analysis have been collected on adhesive targets by gravimetric settling of the aerosolized particles during the actual optical measuring process. Normally, per trial, about 15 different SEM photographs, each containing about 30 particles with appro-



appropriate magnification, are generated. The contours of the particles are digitized using a pencil follower, and fed into a computer. For each particle, an equivalent diameter of a circle having the same aspect area as the particle under investigation is computed. A software package has been developed for statistical analysis of these equivalent diameters. Computed are, for example, the moments μ_i ($i = 1, 2, 3, 4$) of the size distribution as well as the geometric mean diameter D_g and the geometric standard deviation σ_g . From these moments a variety of different characteristic diameters may be computed as shown in Table 1. For further definitions see Ref. 4.

As a prototype for aerodynamic measurements, cascade impactors have been used for particle size determination also. Although the implied theory calls for spherical particles, this type of aerosol classifier is still useful, especially, in characterizing dense aerosols.

Both types of particle classification have the advantage of characterizing the aerosol rather than the material as delivered. Aerosol yield factors, on the order of 0.4 or smaller, indicate that particle sizes determined on material as received may be different from those characterizing the aerosol.

RESULTS

Table 2 contains the aerodynamic particle size data for two metallic aerosols IR-M1 and IR-M2 as an example. Listed are the mass median diameters D_{MM}^K (μm), the geometric standard deviations σ_g , and the corresponding particle masses M_{DMM}^K (g) assuming spherical particles.

Table 3 summarizes the data from statistical analysis of SEM photographs for the materials IR-M1 and IR-M2.

Table 4 contains the data for the specific coverage of water S and the deduced average thickness D of the particles.

Figures 1 and 2 are plots of the SEM data in cumulative form. Figure 1 is the cumulative number distribution of aerosol IR-M1 having to a SEM count median diameter $D_{NM} = 2.2 \mu m$. Assuming, for the particles, disks of thickness D as determined by the specific-water-coverage method, this number distribution may be converted into a cumulative mass distribution, which is plotted in Figure 2. For further comparison the cascade impactor data are given in Figure 3. When assuming spheres, the mass median diameter for material IR-M1 becomes $D_{MM}^K = 0.98 \mu m$. In the disk model this parameter becomes $\hat{D}_{MM}^K = 2.64 \mu m$.

Applying this procedure to similar materials IR-M2, IR-B1 and IR-B2, all having nearly the

same density and thickness as material IR-M1, the impactor data may be related to the SEM data as shown in figure 4. This graph indicates that the aerodynamic diameters determined by the cascade impactor are strongly dependent on the particle shape. The impaction efficiency of disk-type materials is much greater than the impaction efficiency of spheres having the same mass.

Table 5 summarizes all discussed particle data for material IR-M1. The SEM analysis leads to a ranking of the diameters, which is expected for a "log-normal-distribution", namely,

$$D_{NM} < D_g < D_1 < D_2 < D_{MM} < D_{32}$$

whereas in the discussed case the impactor leads to

$$\hat{D}_{MM}^K < D_1 .$$

SUMMARY AND CONCLUSIONS

Statistical analysis of SEM photographs and cascade impactors have been used for particle analysis of dense aerosols consisting of strongly aspherical particles. Although these techniques are non-real time measurement techniques, they seem to be useful tools in characterizing metal flakes. In future experiments these techniques will be compared with optical particle size analyzers.

REFERENCES

1. Scheunemann, W., "Testing of Screening Smokes at BICT", Proceedings of the Smoke/Obscurants Symposium VII, Adelphi, MD 20783, April 1983.
2. Lebedeva, V.N., Distler, G.I., Opt. Spektrosk. 23, 968 (1967), (Opt. Spectrosc. 23, 527 (1967)).
3. Embury, J., "Absorption by Small Regular Non-Spherical Particles in the Raleigh Region", Proceedings of the International Workshop on Light Scattering by Irregularly Shaped Particles, University at Albany, June 1979.
4. Dennis, R., Editor, "Handbook on Aerosols", NTIS Publication TID-26608, January 1976.

TABLE 1. DEFINITIONS

Characteristic Particle Diameters

$D_1 = \mu_1 = \bar{D}$	Arithmetic Mean
$D_2 = \mu_2^{1/2}$	Area Mean
$D_3 = \mu_3^{1/3}$	Volume Mean
$D_{32} = \mu_3 / \mu_2$	Volume / Area Mean
$D_{43} = \mu_4 / \mu_3$	Mass Mean
$D_g = \exp(\sum f_i \ln D_i)$	Geometric Mean
$\sigma_g = \exp(\sum f_i (D_i / D_g)^2)$	Geom. Stand. Dev.

TABLE 2. MASS MEDIAN DIAMETERS D_{MM}^K , GEOMETRIC STANDARD DEVIATIONS σ_g , AND CORRESPONDING PARTICLE MASSES M_{DMM}^K .

	D_{MM}^K (μm)	σ_g	M_{DMM}^K (g)
IR-M1	0.98	1.69	$3.42 \cdot 10^{-12}$
IR-M2	1.29	1.68	$8.00 \cdot 10^{-12}$

TABLE 3. RESULTS FROM STATISTICAL ANALYSIS OF SEM PHOTOGRAPHS FOR MATERIALS IR-M1 and IR-M2.

	IR-M1	IR-M2
μ_1 (μm)	3.06	4.56
μ_2 (μm^2)	13.51	31.77
μ_3 (μm^3)	76.66	299.03
μ_4 (μm^4)	519.89	3520.18
D_G (μm)	2.44	3.50
σ_g	1.74	1.92

TABLE 4. SPECIFIC COVERAGE OF WATER S , AND MEAN PARTICLE THICKNESS D .

	S (m^2/g)	D (μm)
IR-M1	1.60	0.09
IR-M2	1.14	0.12

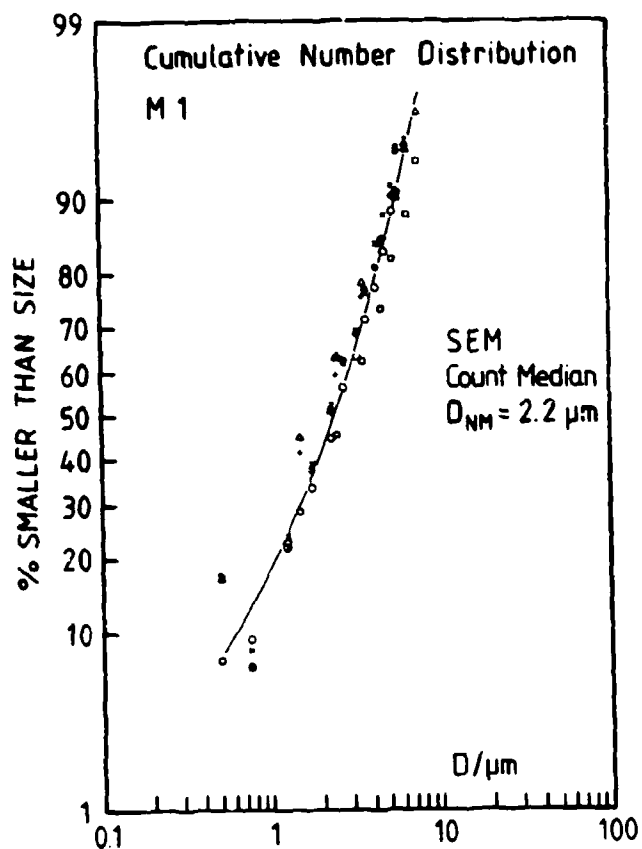


FIGURE 1. SEM CUMULATIVE NUMBER DISTRIBUTION for material IR-M1.

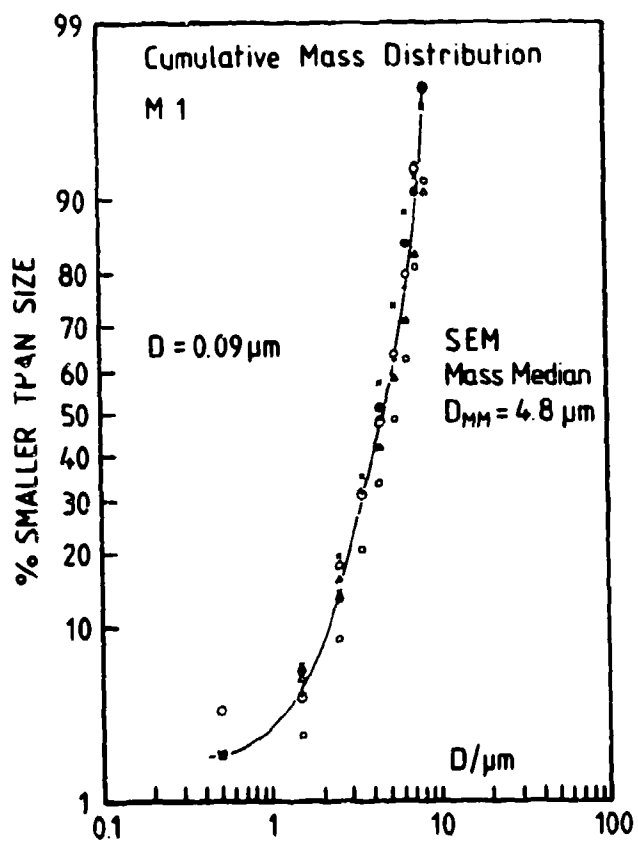


FIGURE 2. SEM CUMULATIVE MASS DISTRIBUTION for material IR-M1.

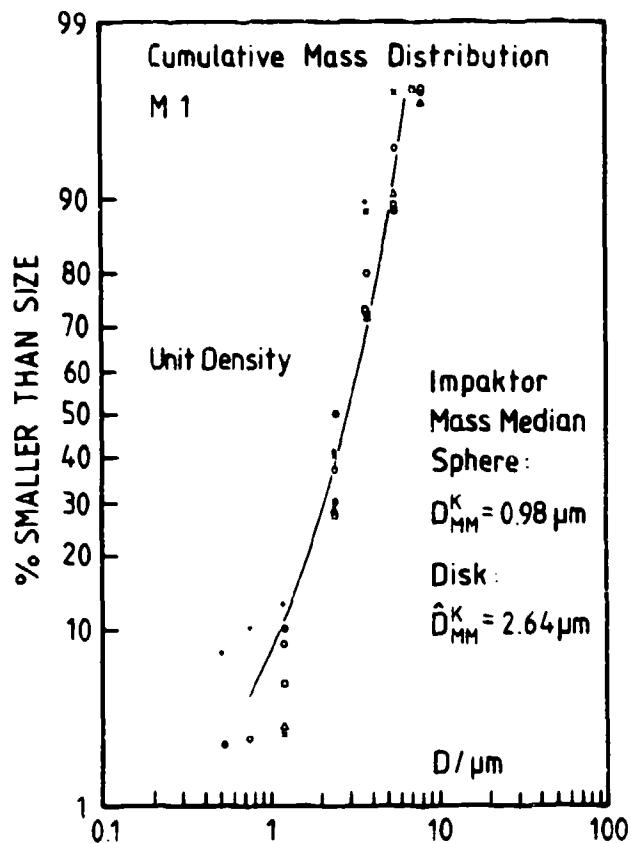


FIGURE 3. CASCADE IMPACTOR CUMULATIVE MASS DISTRIBUTION for material IR-M1.

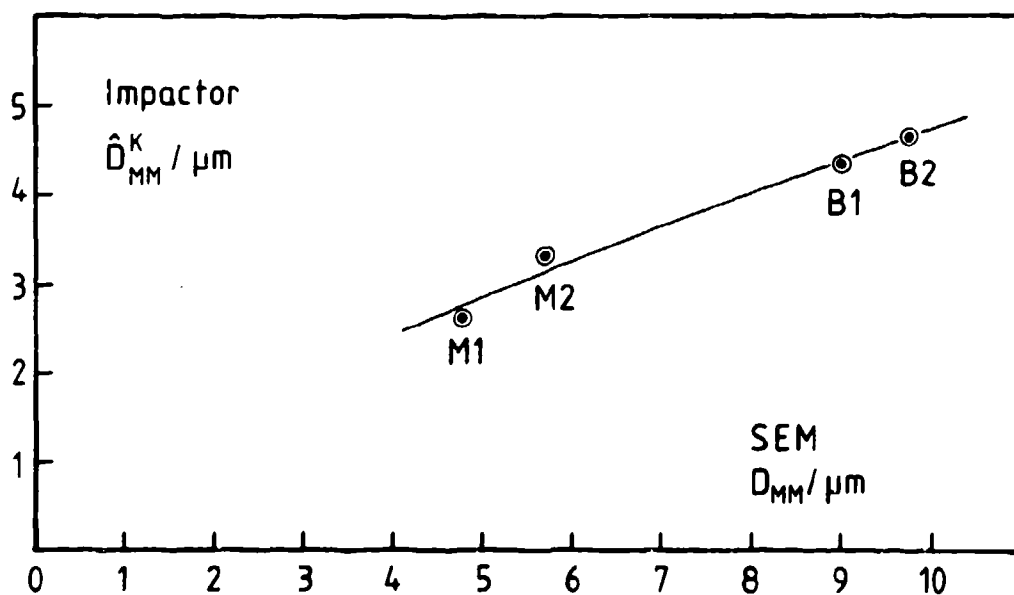


FIGURE 4. COMPARISON OF MASS MEDIAN DIAMETERS. Cascade impactor mass median diameters are plotted versus SEM mass median diameters for different materials.

APPLICATIONS OF CONDITION NUMBERS IN PARTICLE SIZE ANALYSIS AND LINEAR REGRESSION

C. R. Kaplan, P. Y. Yu, F. F. Farzanah, J. Hong
and J. W. Gentry
Department of Chemical Engineering
University of Maryland
College Park, Maryland 20742

INTRODUCTION

The objective of this paper is to show that mathematical parameters designed as condition numbers can be generalized to provide a guide for preliminary experimental design and to provide explanations for observed experimental phenomena.

Three cases were used to illustrate the above.

1. Condition numbers were used to provide criteria for the selection of indicator elements in identifying pollutant sources from trace element analysis,

2. Condition numbers were used to provide a means of comparing different classifiers and evaluating inversion algorithms in determining the size distribution of aerosols,

3. Condition numbers were used to suggest an appropriate form for the development of semi-empirical correlations.

CONDITION NUMBERS

Condition numbers provide quantitative criteria for determining how well conditioned a set of linear, algebraic equations is. For a badly conditioned set of equations a small perturbation in the forcing function implies a large change in the solutions. Specifically for the equations:

$$A_{ik} X_k = B_i \quad (1)$$

The relative change in the norms of the solution vector are bounded by the product of the relative norm of the forcing function and the condition number

$$\frac{|\Delta X|_p}{|X|_p} < C_p \frac{|\Delta B|_p}{|B|_p} \quad (2)$$

Although the condition numbers differ slightly depending on the particular norm used, one can establish that condition numbers for two different norms p and p' are related by the inequality

$$a_1 C_{p'} \leq C_p \leq a_2 C_{p'} \quad (3)$$

where α_1 and α_2 are constant $\sim 1/3$ and 3 respectively.

In summary one can calculate a condition number for any norm and be assured that the condition number for any other norm would show the same qualitative behavior.

CASE-I (Indicator Elements)

Recent work in identifying the relative strengths of generic sources (i.e. oil-fired combustion, automobiles, etc.) has been based on the solution of the algebraic equations:

$$[A^T A]_{ij} S_j = [A^T B]_i \quad (4)$$

where A is a matrix whose elements are the elemental strengths for different generic sources, S are the magnitudes of the sources, and B are the elemental composition in the measured ambient samples. The number of elements as determined by neutron activation exceeds the number of sources, so that in general the sources are determined from least squares regression. Recently Gordon and co-workers suggested that a pre-selection of 6-8 indicator elements gave better (more stable) estimates of the generic source strengths.

We were able to show that the condition numbers for a properly chosen sub-class of elements were substantially less than for all elements. Furthermore, choosing elements so that the condition number is minimized results in choosing the same group of elements found by trial and error to yield the most stable estimates of the sources. Furthermore, the number of sources that could be obtained with reasonable values for the condition number were consistent with practice. In summary, selecting sources and indicator elements based on the criterion of minimum condition number suggested the same procedures as currently used.

CASE-II

We examined the inversion algorithms to determine particle size distributions from penetration or efficiency measurements by computing the condition numbers. These condition numbers were based on the algebraic equations

$$\sum_{j=1}^N Ef(Z_i, D_j) F_j = \overline{Ef}_i \quad (5)$$

where F_j is the frequency of particles in size class j, \overline{Ef}_i is the measured efficiency at condition Z_i , and $Ef(Z_i, D_j)$ are the theoretical efficiencies. We found that:

1. The condition numbers were strongly dependent on the type of classifier (Table 1). This limited the number of size classes that could be obtained from experimental

TABLE I. CONDITION NUMBERS FOR CLASSIFIERS

	C_1	C_2	C_∞
Inertial Impactor	1.2	1.2	1.2
Elutriator	$2.3 \cdot 10^2$	$1.5 \cdot 10^2$	$1.9 \cdot 10^2$
Diffusion Battery	$3.4 \cdot 10^4$	$2.0 \cdot 10^4$	$2.8 \cdot 10^4$
Cyclone	$2.3 \cdot 10^2$	$1.6 \cdot 10^2$	$2.0 \cdot 10^2$

TABLE II. NUMBER OF COLLOCATION POINTS OR PARAMETERS
OBTAINABLE FROM PENETRATION MEASUREMENTS

Diffusion Battery	< 5
Elutriator	7-13
Impactor	Not Restricted (> 13)

measurements.

2. Lower condition numbers were obtained when the frequencies were analyzed as discrete sizes rather than cumulative distributions.

3. The condition numbers were altered when the operating conditions of the experiments was varied. These results are consistent with previously reported measurements and suggest apriori criteria for experimental design. More promising is the fact that the condition number can be reduced by selecting the operating conditions of experiments differently.

CASE-III

We have found that the condition number can be used as an apriori check on the function forms for empirical correlations. For example, the heat of vaporization (H_v) of a compound is frequently expressed as a power series in temperature i.e.

$$H_v = A_0 + A_1T + A_2T^2 + A_3T^3 + \dots + A_n T^n \quad (6)$$

Computing the condition numbers for a set of linear equations derived from equation (6), one finds that there is a jump of several orders of magnitude between $n = 3$ and $n = 4$. The conclusion one should draw is that no more than three terms (assuming the power series) should be used for fitting the experimental measurements.

CONCLUSION

The condition numbers are simple, quantitative measurements of how well-conditioned a set of linear, algebraic equations are. We have found that they provide explanations for current practice in the selection of indicator elements, in inversion of diffusion battery measurements, and in empirical correlations. More important they suggest criteria for evaluating inversion algorithms and experiment design.

LITERATURE REFERENCES

1. Farzanah, F.; Kaplan, C.; Yu, P.; Hong, J.; Gentry, J.; "Condition Numbers as Criteria for Evaluation of Atmospheric Aerosols", Appearing in Environmental Science & Technology, 18 (1985).
2. Y, P.Y., Gentry, J.W., "A Critical Comparison of Three Size Distribution Analysis Methods": J. Aerosol Sci., 15, 407-411 (1984).

USE OF STRUCTURAL RESONANCES IN FLUORESCENCE EMISSION
FOR SIZING SPHERES RESTING ON SUBSTRATES

R. E. Benner, S. C. Hill, C. K. Rushforth
Department of Electrical Engineering
University of Utah
Salt Lake City, Utah 84112

and

P. R. Conwell
Department of Physics
University of Utah
Salt Lake City, Utah 84112

ABSTRACT

This paper describes a technique for sizing dielectric spheres resting on substrates based on their measured fluorescence spectra. The experimental methods, sizing algorithm, and typical results are presented. This work has been presented, published, and submitted for publication as follows:

R. E. Benner, S. C. Hill, C. K. Rushforth, and P. R. Conwell, "Use of Structural Resonances in Fluorescence Emission for Sizing Spheres Resting on Substrates," 1984 CRDC Conference on Obscuration and Aerosol Research, June 1984.

S. C. Hill, R. E. Benner, C. K. Rushforth, and P. R. Conwell, "Structural Resonances Observed in the Fluorescence Emission from Small Spheres on Substrates," Appl. Opt. 23 (1984) 1680.

P. R. Conwell, C. K. Rushforth, R. E. Benner, and S. C. Hill, "An Efficient Automated Algorithm for the Sizing of Dielectric Microspheres Using the Resonance Spectrum," to be published in J. Opt. Soc. Am. A, December, 1984.

The sizing algorithm described in this paper is currently being extended to include the possibility of multiple orders of resonance being present in the observed resonance spectra.

INTRODUCTION

The existence of resonances in the elastic scattering efficiency for small dielectric spheres as a function of wavelength in the visible portion of the spectrum has been well established [1-6]. Analogous resonances are also observed in the fluorescence and Raman emission from small spheres [7,8]. By analyzing the features of resonance spectra, an accurate indication of particle size and relative refractive index can be obtained. For example, we have recently reported an automated algorithm for extracting sphere size from resonance data in which only first order resonances are observed [9]. This algorithm is based only on the wavelength positions of the resonances and requires that the relative refractive index of the sphere as a function of wavelength be known exactly. In other work, both size and refractive index were determined by analyzing lineshape features of resonance data [10]. Although the resonance locations predicted by elastic scattering theory are known to correspond to those measured in fluorescence and Raman emission [7,8], a detailed theory for predicting lineshape features in fluorescence emission is not yet available. Such a theory would need to account for position-dependent optical gain within the particle. Models for the fluorescence and spontaneous Raman

emission of small spheres [11] and for the stimulated emission of small spheres under conditions of constant gain [12] have been presented.

In previous work involving the use of structural resonances for sizing small particles, the particles have been suspended in homogeneous media such as air or water. Studies in homogeneous surroundings are appropriate for applications such as aerosol sizing and cell sorting based on fluorescence emission or for the chemical identification of aerosols by Raman scattering. For some applications, however, it is desirable to deposit particulates on a substrate prior to analysis. For example, the collection of aerosols on filters prior to analysis is often necessary to obtain a statistically valid sample. In addition, particulate samples for Raman microprobe analysis are often deposited on substrates to facilitate heat conduction [13]. Our recent work has addressed the question of whether or not our sizing algorithm [9] which is based on the elastic scattering by spheres in homogeneous surroundings can be adapted to the sizing of spheres resting on substrates based on their inelastic (fluorescence or Raman) emission. We have found that the wavelength positions, at which the resonances of a polystyrene sphere having a diameter in the range between approximately 4 and 10 micrometers occur, do not appear to be significantly affected by deposition on a dielectric substrate. However, in some cases, the resonant peaks from spheres on dielectric substrates appear to be slightly broadened and attenuated compared to the corresponding peaks when similar spheres are examined in homogeneous surroundings. In addition, in the spectra of spheres resting on silver surfaces, the amplitudes of transverse magnetic modes are decreased [14].

EXPERIMENTAL

Fluorescence data from dye-impregnated, polystyrene spheres deposited on substrates were obtained using conventional Raman microprobe instrumentation. Radiation from an argon laser operating at 514.5 nm was focused by the objective (40X) of a Zeiss optical microscope onto a single sphere deposited on a polished silicon wafer. Verification that only a single sphere was being illuminated was accomplished by viewing the scattering volume through the microscope eyepieces. The inelastic emission from the sphere was collected with the same 40X objective and imaged through a series of beam splitters onto the entrance slit of a scanning triple monochromator. A GAs photomultiplier and photon counting electronics were used for detection. Figure 1 (a) displays the fluorescence intensity measured as a function of wavelength from a dye-impregnated polystyrene sphere having a nominal diameter of 5.08 micrometers with a standard deviation of 3%. Excellent correspondence between the resonance locations in the measured fluorescence spectrum and those in the calculated elastic scattering efficiency for a polystyrene sphere with a diameter of 5.1802 micrometers was obtained. It should, however, be noted

that the experimental fluorescence linewidths are substantially broader than those predicted by the elastic scattering theory. In addition, both first and second order resonances were observed in the fluorescence emission. In order to achieve such good agreement between the experimental and calculated spectra, it was necessary to account for the dispersion in the refractive index of polystyrene over the wavelength range of the experiment. The sphere diameter of 5.1802 micrometers, which is well within the standard deviation of our lot of spheres, was determined by the sizing algorithm described below.

SIZING ALGORITHM

The sphere sizing algorithm used in this study has been described in detail elsewhere [9,15]. A key feature of the algorithm is that it is based on peak locations only and does not require an analysis of lineshape features. Thus, it can be applied to fluorescence as well as other types of spectroscopic data. The algorithm does, however, currently require that the relative refractive index of the sphere be known exactly as a function of wavelength. Our initial algorithm [9] was limited to cases in which only first order resonances were observed, but this restriction has been eliminated in the current algorithm [15]. Both algorithms employ a peak detection routine that determines the resonant frequencies which are present in experimentally measured spectra. The measured resonance locations are then compared with entries from a library of stored resonance locations to determine the most likely radius of the particle. The details of the resonance location matching routines depend upon whether one or more orders of resonance are present in the experimental data. Nevertheless, both algorithms are computationally efficient and could be automated for nearly real-time analysis of sphere size using a microprocessor.

CONCLUSION

Structural resonances have been observed in the fluorescence emission from microspheres deposited on substrates. It is significant that the substrates do not appear to affect the peak locations of the resonances of the spheres. Thus, the sizing algorithm we have developed for sizing spheres in homogeneous surroundings can also be applied to sizing spheres collected on filters or other surfaces. A major advantage of our experimental approach of using a Raman microprobe configuration in conjunction with spheres on substrates is that the particle remains fixed in space and can be examined for extended periods to improve spectroscopic signal-to-noise ratios. It should also be possible to study the scattering from clusters of multiple particles.

We thank the National Science Foundation for partial support of this work under grant CPE-8116087.

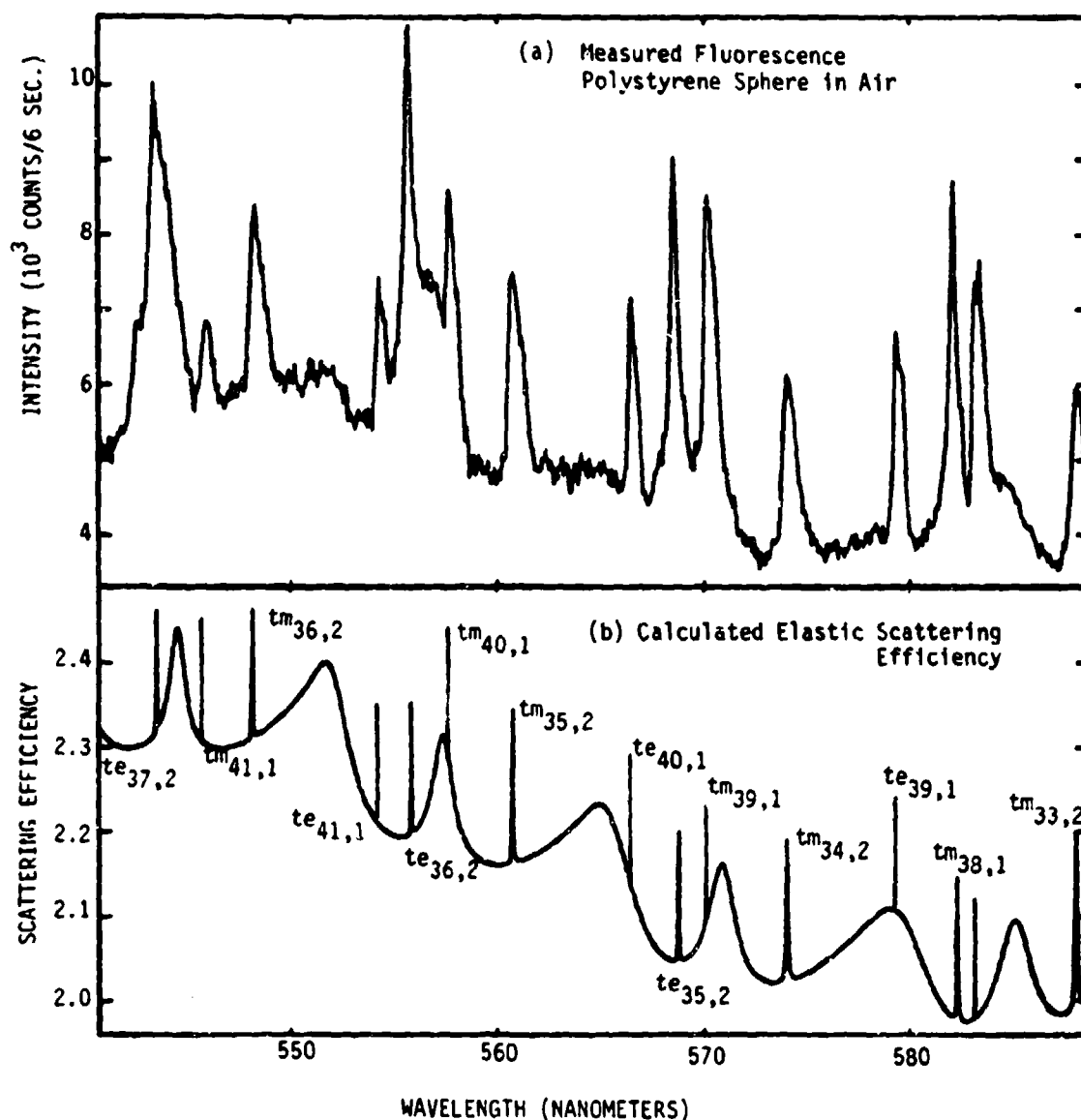


FIGURE 1. MEASURED FLUORESCENCE EMISSION (a) AND CALCULATED SCATTERING EFFICIENCY (b) FOR A DYE-IMPREGNATED POLYSTYRENE SPHERE WITH A CALCULATED DIAMETER OF 5.1802 MICROMETERS. The subscripts on the transverse electric (te) and transverse magnetic (tm) resonances refer to the mode number and order number. The sharp first order resonances in the scattering efficiency have been represented by lines of arbitrary height having a width greater than the linewidth of the actual resonance. The unlabeled broad peaks in the calculated scattering efficiency arise from third order resonances.

REFERENCES

1. P. Chylek, "Partial-Wave Resonances and the Ripple Structure in the Mie Normalized Cross Section," J. Opt. Soc. Am. 66 (1976) 285.
2. P. Chylek, J. T. Kiehl, M. K. W. Ko, "Optical Levitation and Partial-Wave Resonances," Phys. Rev. A 18 (1978) 2229.
3. G. J. Rosasco and H. S. Bennett, "Internal Field Resonance Structure: Implications for Optical Absorption and Scattering by Microspheric Particles," J. Opt. Soc. Am. 68 (1978) 1242.
4. P. Chylek, J. T. Kiehl, and M. K. W. Ko, "Narrow Resonance Structure in the Mie Scattering Characteristics," Appl. Opt. 17 (1978) 3019.
5. P. W. Barber, J. F. Owen, and R. K. Chang, "Resonant scattering for Characterization of Axisymmetric Objects," IEEE Trans. Ant. Prop. AP-30 (1982) 168.
6. P. R. Conwell, P. W. Barber, and C. K. Rushforth, "Resonant Spectra of Dielectric Spheres," J. Opt. Soc. Am. 1 (1984) 62.
7. R. E. Benner, P. W. Barber, J. F. Owen, and R. K. Chang, "Observation of Structure Resonances in the Fluorescence Spectra from Microspheres," Phys. Rev. Lett. 82 (1980) 475.
8. J. F. Owen, P. W. Barber, and R. K. Chang, "Morphology Dependent Raman Spectra from Microparticles," in Microbeam Analysis 1982, K. F. J. Heinrich, Ed. (San Francisco Press, 1982) 255.
9. P. R. Conwell, C. K. Rushforth, R. E. Benner, and S. C. Hill, "An Efficient Automated Algorithm for the Sizing of Dielectric Microspheres Using the Resonance Spectrum," to be published in J. Opt. Soc. Am. A, December, 1984.
10. P. Chylek, V. Ramaswamy, A. Ashkin, and J. M. Dziedzic, "Simultaneous Determination of Refractive Index and Size of Spherical Dielectric Particles from Light Scattering Data," Appl. Opt. 22 (1983) 2302.
11. H. Chew, P. J. McNulty, and M. Kerker, "Model for Raman and Fluorescent Scattering by Molecules Embedded in Small Particles," Phys. Rev. A 13 (1976) 396.
12. H. Chew, M. Sculley, M. Kerker, P. J. McNulty, and D. D. Cooke, "Raman and Fluorescent Scattering by Molecules Embedded in Small Particles: Results for Coherent Optical Processes," J. Opt. Soc. Am. 68 (1979) 1686.
13. M. Delhaye, P. Dhameincourt, and F. Wallert, "Analysis of Particulates by Raman Microprobe," Toxicol. Environ. Chem. Rev. 3 (1979) 73.
14. S. C. Hill, R. E. Benner, C. K. Rushforth, and P. R. Conwell, "Structural Resonances Observed in the Fluorescence Emission from Small Spheres on Substrates," Appl. Opt. 23 (1984) 1680.
15. S. C. Hill, C. K. Rushforth, R. E. Benner, and P. R. Conwell, "Sizing Dielectric Microspheres by Aligning Measured and Computed Resonance Locations: An Algorithm for Multiple Resonance Orders," to be submitted to Appl. Opt.

BLANK

MULTICHANNEL NEPHELOMETER DESIGN

A. R. Tokuda, G. M. Hess, T. R. Majoch, S. R. Beck, C. D. Capps, and N. E. Carroll
Boeing Aerospace Company
P.O. Box 3999, Seattle, WA 98124

ABSTRACT

This paper is an interim report on work in progress toward designing and developing a multichannel nephelometer, which accesses, measures, and records the far-field scattering pattern of a single aerosol particle illuminated by a CW laser. Future work will include the integration of systems, an extensive test program, and delivery and demonstration of the device to CRDC.

INTRODUCTION

The Boeing Aerospace Company is developing and building a multichannel nephelometer capable of measuring and recording the far-field light-scattering pattern generated by the interaction of individual particles of an aerosol with a laser beam. Since calibrating the light-scattering pattern for even the most simple nonspherical particle (e.g., an ellipsoid) is difficult at best, a method of building an empirical data base relating scattering patterns to particle physical characteristics for various aerosol types is required. This relationship may possibly be inverted so that the light-scattering pattern, including polarization information, will be useful in characterizing the optical properties of the particles for purposes such as identification of remote aerosols or evaluation as obscurants. This instrument will also be useful in comparing actual light-scattering measurements to theoretical scattering models that are being developed.

The multichannel nephelometer unit includes an aerosol system, scattering chamber, and data acquisition system. Figure 1 shows a conceptual drawing of the multichannel nephelometer. The mounting table is 3 by 6 ft and is mounted on casters with retractable support pads. The overall height is 8 ft. Aerosol diluters, which draw the sample from a source, are mounted on rollout slides for ease of operation in their overhead location. The rack holding these diluters can be dismounted, which will allow the system to clear the top of doorways. The laser is mounted under the table, allowing the entire system to maintain mechanical and optical alignment once initial setup is completed. The chamber unit is thus basically self-contained, requiring only power, aerosol source, and data output connections. Depending on their configuration, it is possible that additional small aerosol sources could be mounted directly to the diluters to perform other operations such as calibration.

The front-end electronics are attached directly to the photomultiplier tube detectors on the sphere. The remainder of the data acquisition system consists of a computer, monitor, keyboard, A/D converter, printer, and power supplies attached by a cable bundle to the front-end electronics.

Figure 2 illustrates the relationship between system-level requirements and allocated system requirements. The system goals shown in the center block determine the design requirements of the three systems. In addition,

each system has individual design objectives shown in the outer blocks. Other system-level requirements, shown in the ovals, result in design compromises between only two systems. The design process consists of optimizing this interactive network of requirements. These systems are described in detail in the sections that follow and are briefly summarized below.

AEROSOL SAMPLING SYSTEM

The aerosol sampling system is designed to sample aerosols of number densities up to 10^6 particles/cc, dilute as required (with minimal size biasing) to produce a flowing stream of single aerosol particles, and entrain that flow in a laminar clean air sheath directed through the laser beam. The particles traverse the laser beam, one at a time, at a nominal rate of 10 particles/sec, and are expected to rotate less than 3.6° during their transit through the laser beam.

Dilution is accomplished by two ATEC 303-LF diluters, which achieve the desired aerosol concentration by successively drawing off samples of the aerosol through capillary tubes and mixing them with clean air (see figure 3). The diluters are stacked vertically to minimize the bias of larger particle sizes and allow cascading.

Localization and confinement of the diluted stream through the laser beam sampling volume is provided by sheath air and purge air flows working in conjunction (figure 4). The sheath air laminar flow jet surrounding the diluted aerosol sample is added in a specially designed block that serves to localize the particles and minimize contamination to the light-scattering chamber and optics. A purge air flow is added to the chamber and is regulated so as to reinforce the integrity of the sheath air jet across the gap where the scattering event occurs.

All the aerosol particles are trapped on filters prior to exhausting the air. The entire sampling train is constructed to allow easy disassembly for routine cleaning and inspection (figure 5).

LIGHT-SCATTERING CHAMBER

The light-scattering system includes a visible argon-ion laser, a 10.4-in-diameter scattering chamber, and 108 photodetectors. The 1.5-mm-diameter CW laser beam is to be shielded by an optically sealed entrainment system that complies with TB MED279, "Control of Hazards to Health From Laser Radiation." A 14-in access space is provided in front of the scattering chamber.

The scattered light resulting from the intersection of the 0.3- to 10-micron particles with the laser beam is received by individual and arrayed photodetectors surrounding the intersection point. The detectors are arranged in an unsymmetric fashion along great circles of the spherical chamber and lie in three planes spaced by 45° (see figure 6). Detection begins at 90° from forward scatter and extends to within 110° of the backscatter.

The arrayed detectors, situated from 90° to 210° off the forward scatter direction where additional resolution is required, use Hamamatsu R1770 photomultiplier tubes selected for their response, geometry, and spacing attributes (see figure 7). As reflected light was not considered a problem for the array units in the near-forward direction, a simple optical design was developed, consisting of a rotatable polarizer and an aperture plate in front of eight rectangular photomultiplier tubes. Each detector element subtends 1.5° .

The individual detectors use Hamamatsu R647 photomultiplier tubes, selected because of their cylindrical geometry and response characteristics (see figure 8). They are mounted in black plastic molded assemblies which contain a removable sheet-type dichroic linear polarizer preceded by a lens and pinhole system that strictly limits their field of view, thus minimizing the "noise" factor from reflections within the chamber. Their unsymmetric spacing also prevents specular reflections off optics in the near-forward scattering directions from reaching detectors in the near-backscatter direction. Each individual detector subtends 6° .

The response levels from the detectors allow intensity measurement accuracies of the scattered light to $\pm 10\%$ in the 0° to 90° region and $\pm 30\%$ in the 90° to 110° and 140° to 180° regions. These accuracies are based on the "worst case" of a 0.3-micron particle with albedo not less than 0.5.

The scattering chamber itself consists of two near-hemispheric shells bolted to a mounted plate housing the sampling system. Its walls are anodized black to decrease surface reflections. The chamber is designed for easy access and disassembly. Numerous O-rings seal the system both mechanically and optically.

DATA ACQUISITION SYSTEM

The data acquisition system reads the detector responses to each scattering event, digitizes that information, and stores the results on computer memory for subsequent analysis (figure 9). The front-end electronics package filters the signal from the photomultiplier tubes using a bandwidth selected (as determined by the pulse width of the scattered light) to reduce the system's sensitivity to molecular scattering and signal noise. Further signal processing on detected scattering waveforms is performed to allow dynamic rejection of data from particles moving slower and faster than the "design" velocity. The signal is then amplified, logarithmically compressed into a standard voltage range, stored by a track/hold amplifier, and digitized for input to the computer. The computer stores the intensity measurements of 119 of these signal channels at a nominal rate of 10 particles/sec. Data sufficient to characterize six aerosols (six Mueller matrices) can be held on a mass storage disk. The data to characterize each aerosol may be transferred to three floppy diskettes for long-term storage. In addition to the basic data acquisition circuitry and main computer, the data processing equipment includes a graphics terminal, a graphics printer, and the auxiliary floppy diskette drive used for long-term storage.

SYSTEM INTEGRATION AND TESTING

The operational and functional characteristics of the multichannel nephelometer will be demonstrated in a test program designed to exercise the system over its full range of capabilities and to define the limits of these capabilities. After the hardware and software of the systems are integrated and tested individually and in different combinations to confirm operation as designed, the three systems will be combined and tested to ensure compliance with the required performance levels.

ACKNOWLEDGEMENT

This work was supported by the U.S. Army Chemical Research Development Center, Aberdeen Proving Ground, Maryland, under contract DAAK11-83-C-0089.

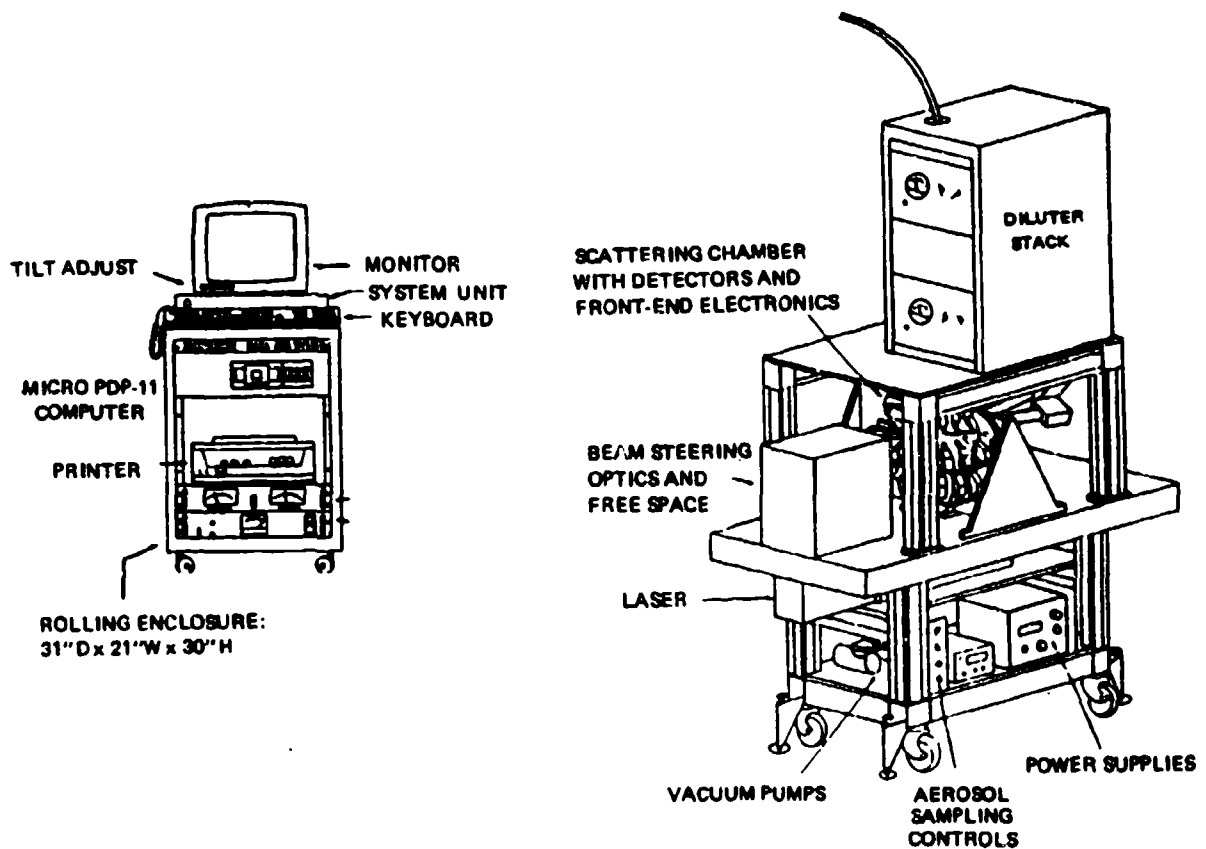


FIGURE 1. MULTICHANNEL NEPHELOMETER

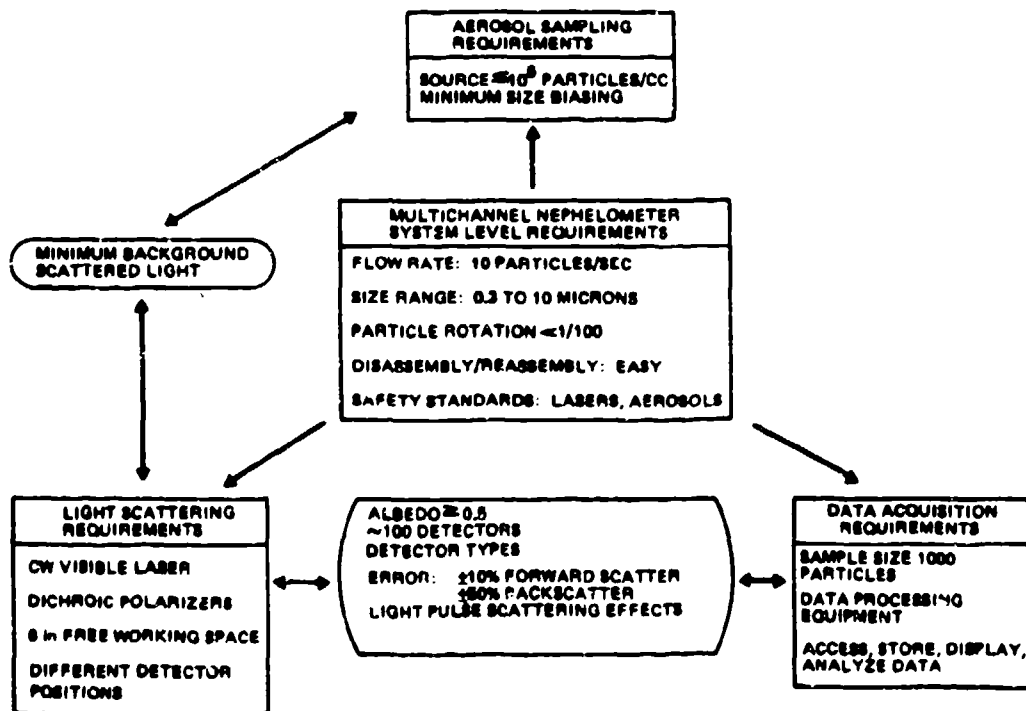


FIGURE 2. MULTICHANNEL NEPHELOMETER DESIGN REQUIREMENTS

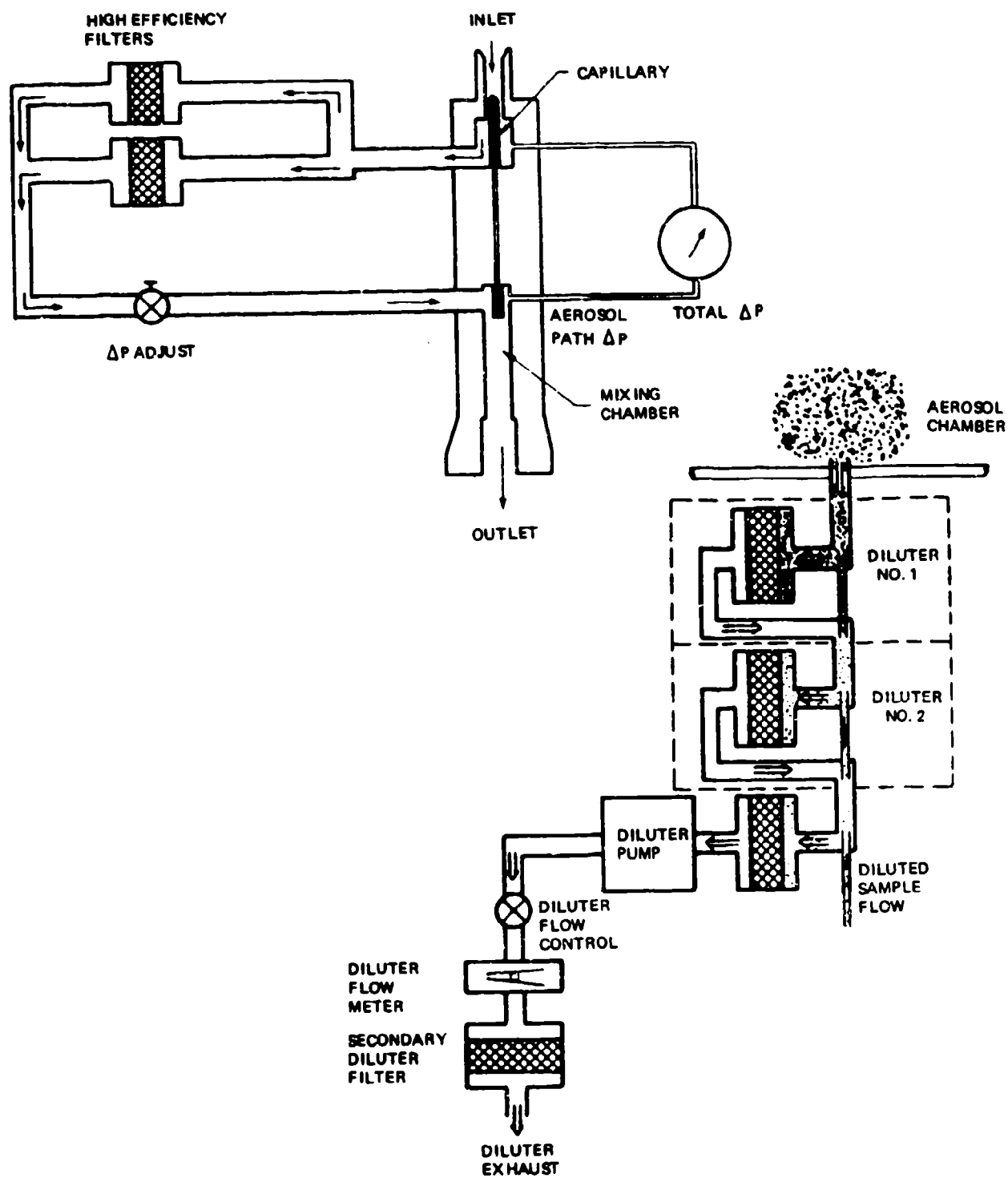


FIGURE 3. DILUTER SCHEMATIC

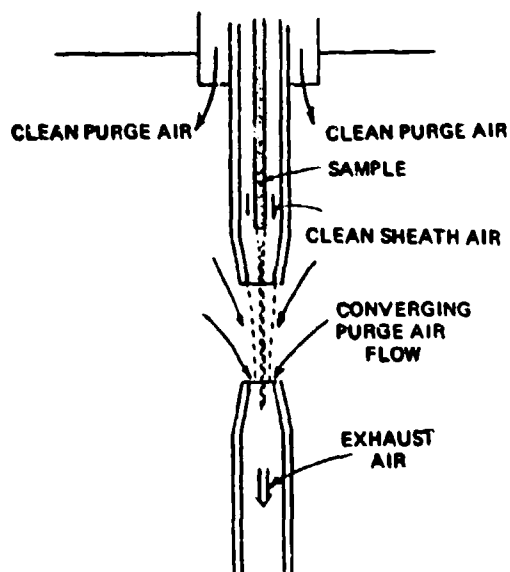


FIGURE 4. AEROSOL JET SYSTEM

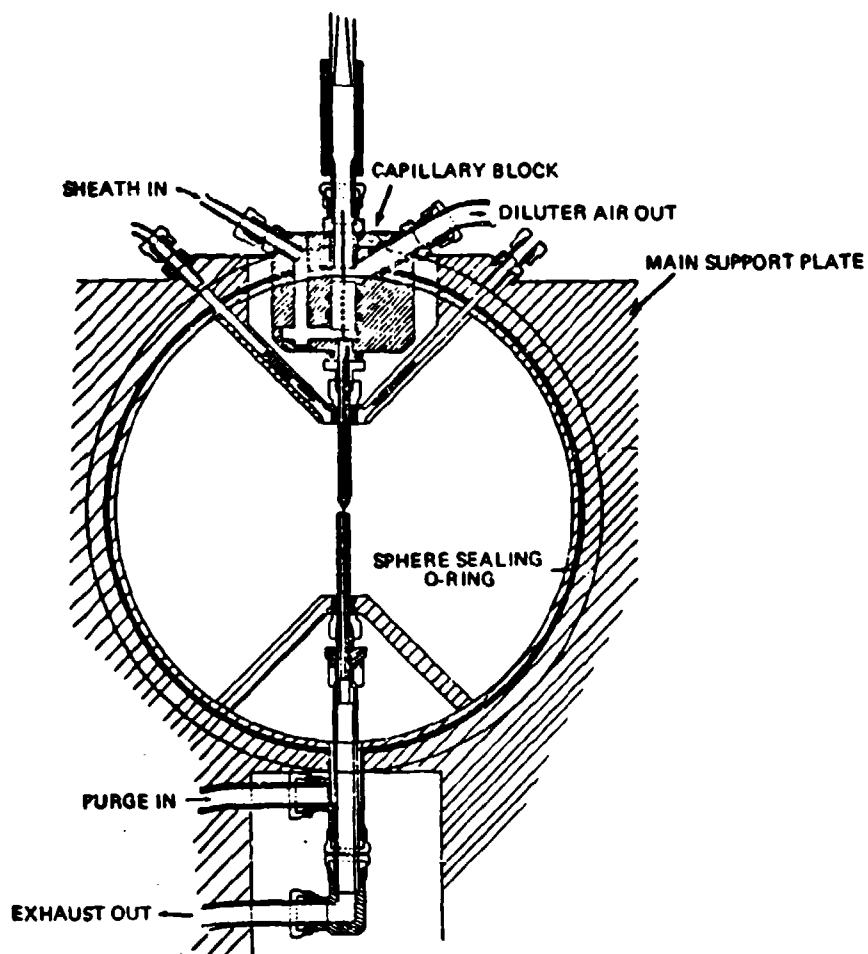


FIGURE 5. AEROSOL SAMPLING SYSTEM CONCEPT

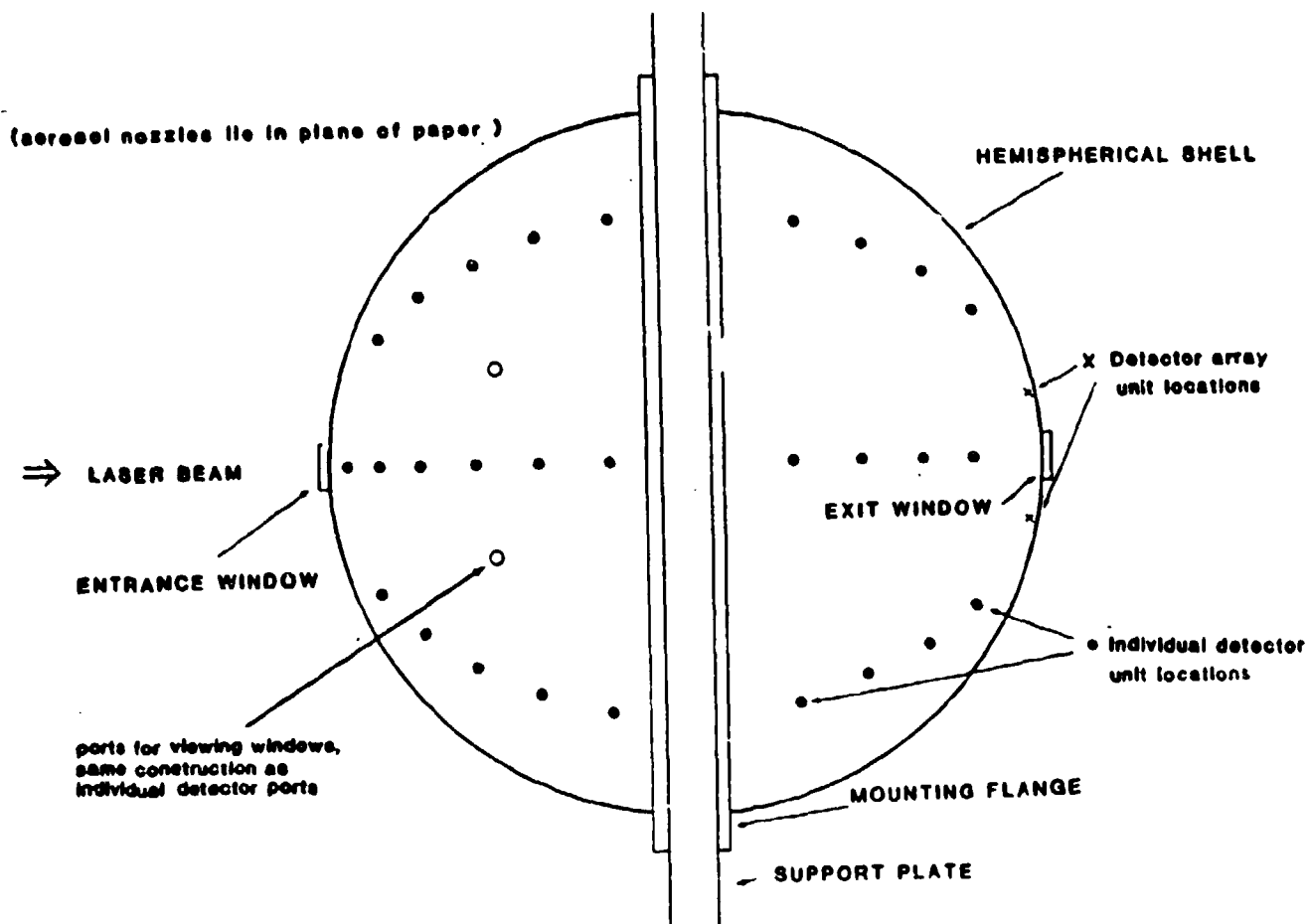


FIGURE 6. LIGHT-SCATTERING CHAMBER

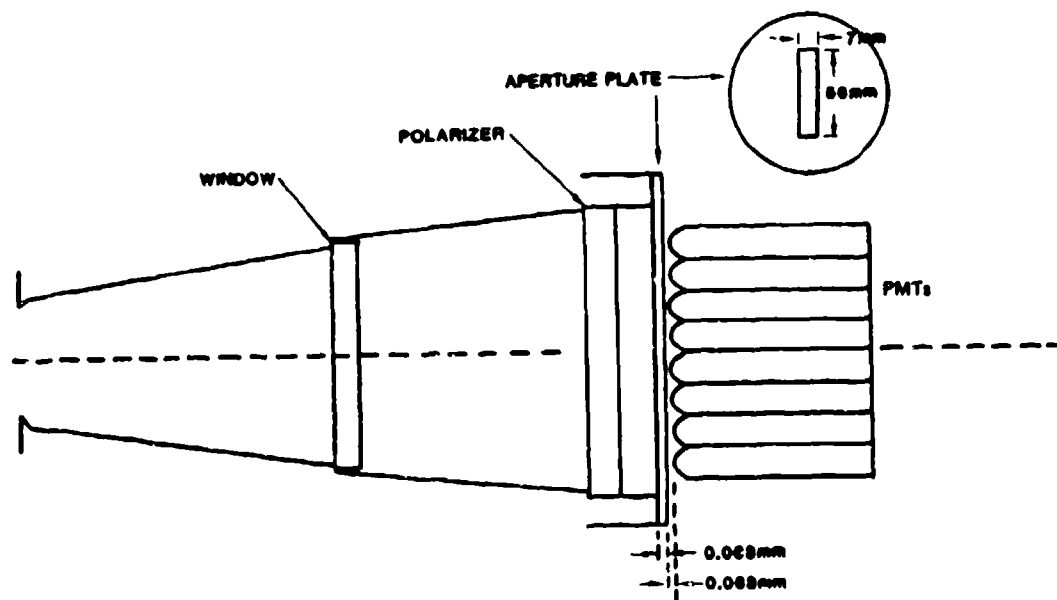
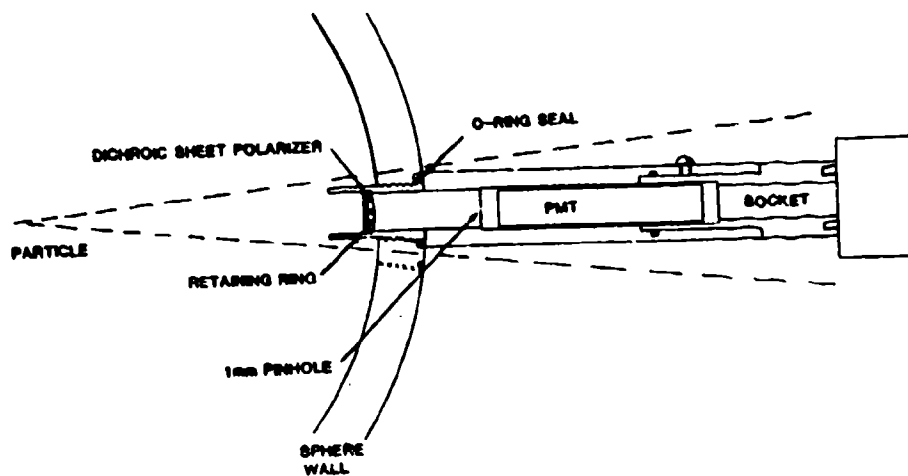


FIGURE 7. DETECTOR ARRAY UNIT



OPTICAL ELEMENT: SYMMETRIC CONVEX LENS

FIGURE 8. INDIVIDUAL DETECTOR UNIT

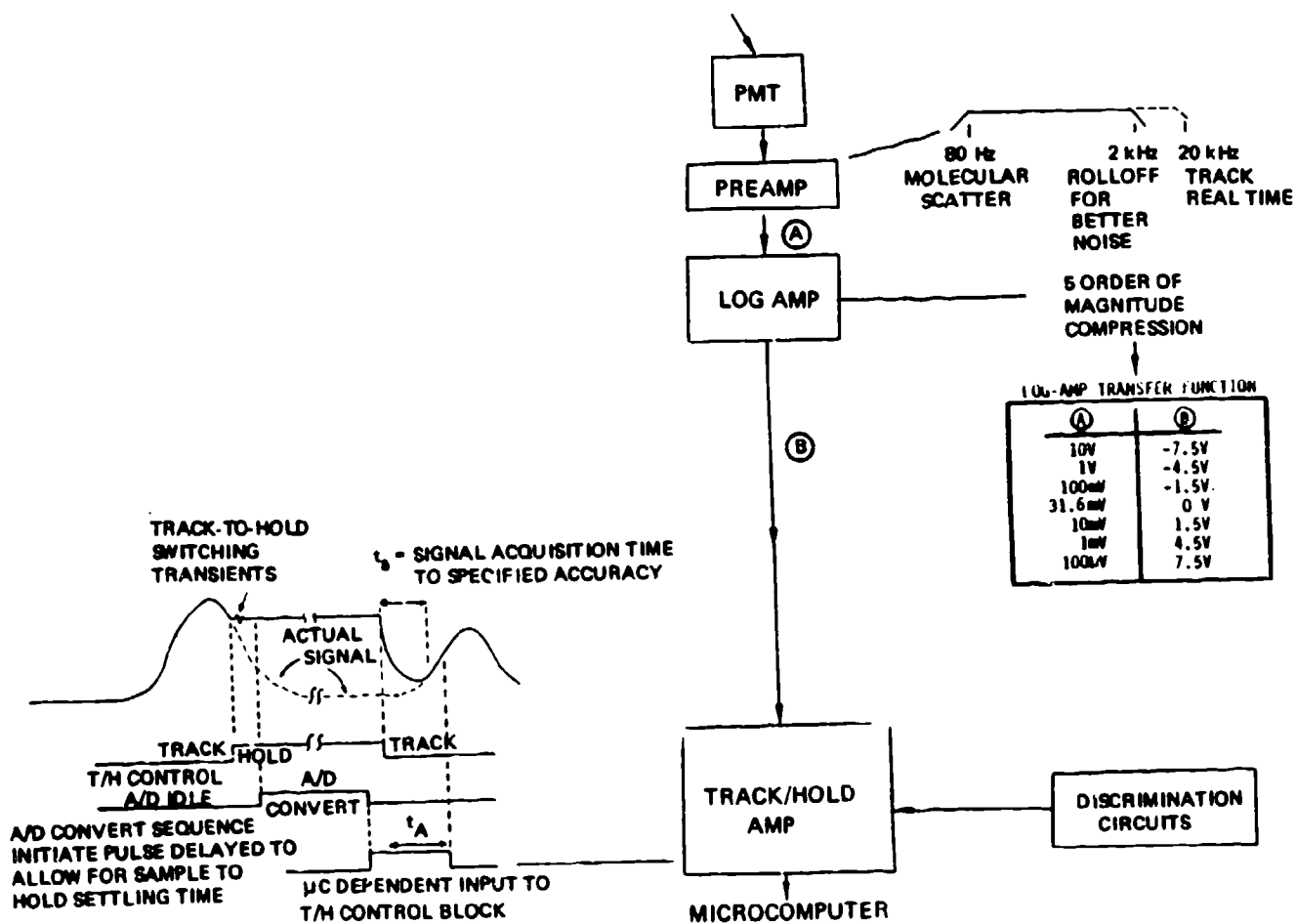


FIGURE 9. DATA ACQUISITION SYSTEM

BLANK

PROGRESS OF INVERSION TECHNIQUE EVALUATION

J. R. Bottiger
Chemical Research and Development Center
Aberdeen Proving Ground, MD 21010-5423

ABSTRACT

Light scattering data corresponding to four trial particle size distribution functions has been generated and used (by others) as the basis for inversions. We report here on the nature of the synthetic scattering data and make some observations on the adequacy of the returned solutions.

1. INTRODUCTION

For the purpose of following dynamic processes in conventional evaporation/condensation obscurants such as phosphorus smokes and diesel oil, the Army aerosol research program would benefit greatly from a method of particle size distribution determination based on inversion of light scattering data. Such methods would be non-intrusive and potentially very rapid - at least in the acquisition of data. Numerous inversion techniques have already been developed for other areas of study, particularly in the field of meteorological remote sensing. However, our application, dealing with distributions of truly spherical particles, provides a nearly ideal test bed for evaluating the relative merits of inversion techniques since the needed kernel functions are exact and readily calculated by the Mie theory. Accordingly we have undertaken a study to answer such questions as 1) what measurements should be included in the data set upon which an inversion is to be performed; 2) which mathematical technique should be employed; 3) what is the consequence of experimental errors in the light scattering measurements; and 4) what a priori knowledge (or assumptions) about the distribution is required or desirable and what is the effect of incomplete or incorrect assumptions.

Particle size distribution functions (PSDF's) are made up at CRDC, with the assumption that the particles are all homogeneous spheres with the same known real refractive index and at concentrations low enough so that only single scattering need be considered. Scattering data, representing potential measurements, are calculated for the trial distribution systems and perturbed with known levels of random error to simulate experimental uncertainties. This scattering data, along with controlled amounts of a priori knowledge of the systems (usually none) is then given to the participants in the study whose job is to invert the data and recover the original trial PSDF's, each researcher selecting whichever data he desires from the simulated measurements and employing his own inversion technique. Those performing inversions

during the past year were William Curry and Earl Kiech at AEDC (constrained eigenfunction expansion and nonlinear regression), Benjamin Rerman and John Reagan at University of Arizona (constrained linear inversion), and William Pearce and Robert Thomas at EG&G (B-spline).

In this paper we will discuss the nature of the four trial PSDF's and associated data generated, and make some general observations about the inverted solutions. Details of the inversion calculations and the resulting specific solutions may be found in the papers written by the above inverters and included in this Proceedings.

2. TRIAL DISTRIBUTION FUNCTIONS

The four PSDF's examined during the past year, and labeled G through J, are all log-normals of some order of a sum of two log-normals, and may be described by the general equation

$$F(r) = R r^{l_1} e^{-\frac{(\ln r/\bar{r}_1)^2}{2\sigma_1^2}} + r^{l_2} e^{-\frac{(\ln r/\bar{r}_2)^2}{2\sigma_2^2}}.$$

Table I lists the appropriate parameters for each trial distribution, as well as the low and high radii cutoff values outside of which $F(r) = 0$.

TABLE I. TRIAL DISTRIBUTION PARAMETERS

Dist	R	\bar{r}_1	σ_1	l_1	\bar{r}_2	σ_2	l_2	r_{lo}	r_{hi}
G	0.0	n/a	n/a	n/a	1.92	.35	0.0	.672	7.786
H	1.0	1.3	0.2	0.0	2.4	.15	0.0	.713	4.373
I	3.0	1.1	0.2	-1.0	2.1	.20	-1.0	.604	4.674
J	0.0	n/a	n/a	n/a	1.6	.25	-1.0	.756	4.349

The number-normalized distribution function, $N(r)$, is proportional to the PSDF, $F(r)$, with a proportionality constant such that $\int_r N(r) dr = 1$. In Figure 1

are plotted the number-normalized distribution functions for trials G through J. Figure 2 displays the corresponding mass-normalized distribution functions. $M(r)$ is proportional to $r^3 F(r)$ and normalized such that $\int_r M(r) dr = 1$. This second representation is somewhat more directly meaningful to those accustomed to thinking in terms of mass extinction coefficients, and in many cases more accurately weights the distribution with respect to the particles' relative contribution to the total scattering.

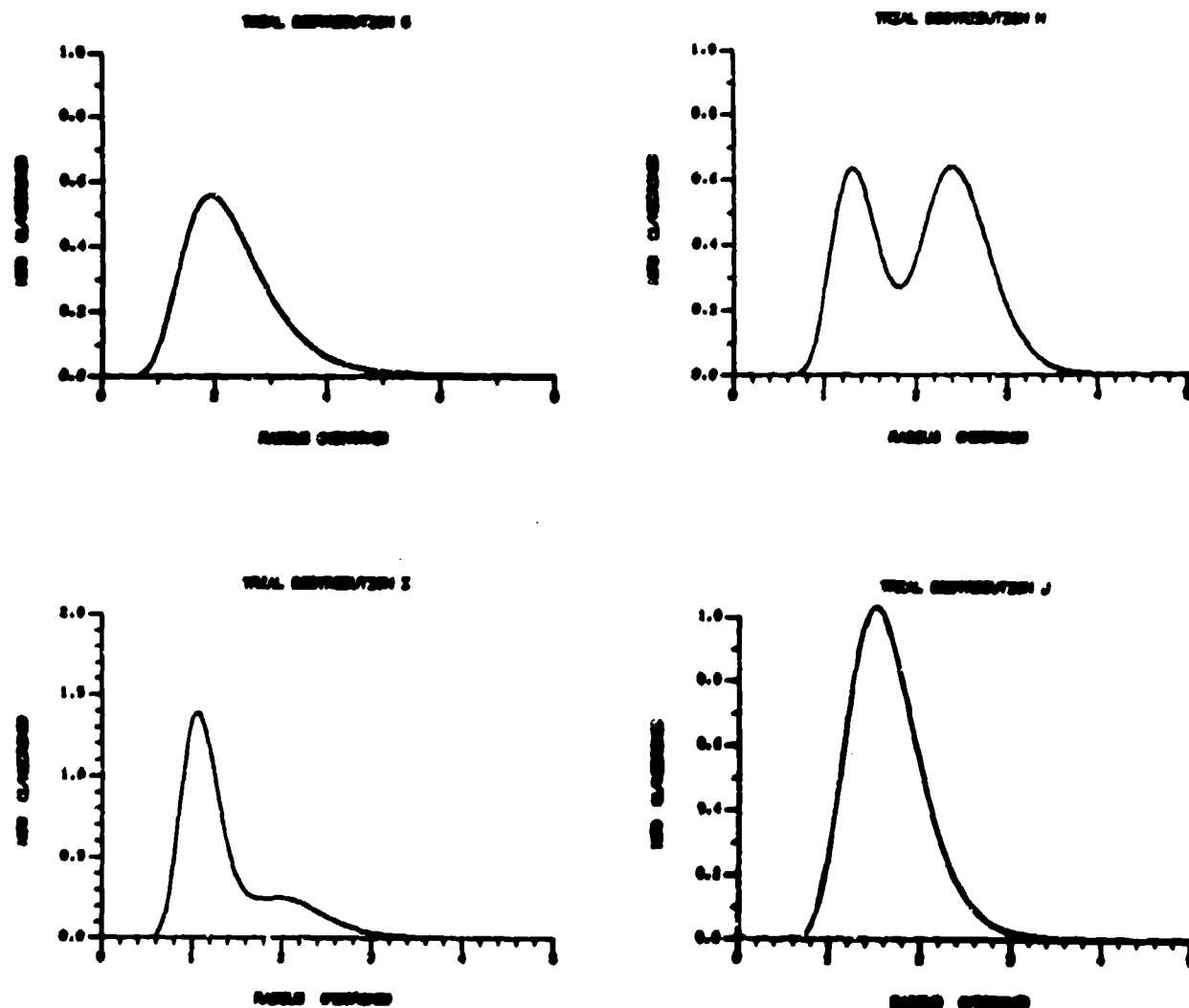


FIGURE 1. NUMBER NORMALIZED TRIAL DISTRIBUTIONS

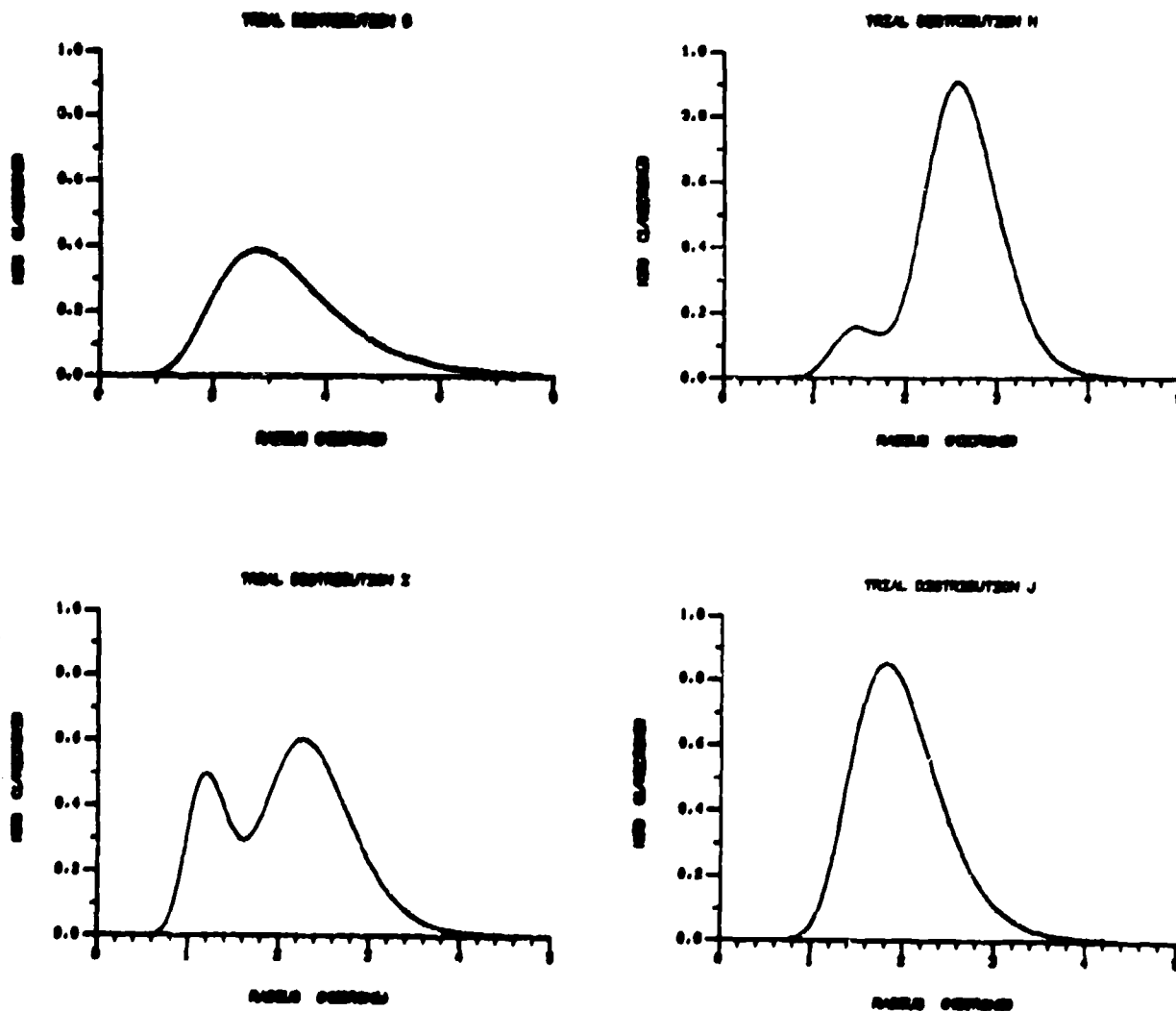


FIGURE 2. MASS NORMALIZED TRIAL DISTRIBUTIONS

3. SCATTERING DATA

Calculations were done on the CRDC Univac 1100/60 using a modified version of a program developed at WSMR, called PCAUS2. The heart of the program, a subroutine called MIXOS, was unaltered. From its output list for each radius interval we can form $i_1(\theta)$ and $i_2(\theta)$, the intensity functions, and $\delta(\theta)$, the phase difference between the corresponding complex amplitude functions. These were used to construct

the various scattering functions described below. Calculations were performed for each of 15 incident wavelengths. Table II lists the wavelengths (in vacuum), and the refractive indices assumed for the medium and the particles. These parameters were valid for all the trial distributions, and each inverter was given this information from the beginning.

TABLE II. REFRACTIVE INDICES

Number	Wavelength in vacuum	Real refractive index (sphere)	Real refractive index (medium)
1	.300	1.6948	1.349
2	.357	1.6485	1.343
3	.697	1.5839	1.337
4	1.038	1.5739	1.327
5	1.374	1.5706	1.321
6	2.023	1.5682	1.305
7	2.727	1.5674	1.170
8	3.580	1.5669	1.383
9	3.873	1.5668	1.359
10	4.828	1.5666	1.330
11	5.125	1.5666	1.321
12	5.403	1.5666	1.305
13	6.560	1.5665	1.336
14	8.000	1.5664	1.291
15	10.600	1.5664	1.179

In Table III are listed the 14 angular scattering functions which were calculated at each wavelength for scattering angles from 0° to 180° in 5° increments. Here $k = 2\pi/\lambda$ and $f(r_i)$ is the value of the particle size distribution function at the i th radius, with normalization such that $\sum_i f(r_i) = 1$. In every case the range of radii over which $P(r)$ was non-zero was divided into 1000 equal size intervals for the summations.

The first four angular scattering functions represent planned experimental nephelometer measurements. In each case the light is incident plane polarized at 45° to the scattering plane. A polarizer in front of the detector is oriented with its transmission axis either parallel to the scattering plane (MR00), or perpendicular to it (MR90), or at 45° to it (MR45). In the fourth case the analyzing polarizer is at 0° , as in MR00, but is preceded by a quarter wave plate with its fast axis at 45° with respect to the scattering plane (MRL4). The numbers calculated are the measured

TABLE III. ANGULAR SCATTERING FUNCTIONS

<u>Name</u>	<u>Expression</u>
MR00	$1/k^2 \sum f(r_i) i_2(r_i, \theta)$
MR90	$1/k^2 \sum f(r_i) i_1(r_i, \theta)$
MR45	$1/k^2 \{ \sum f(r_i) (i_2(r_i, \theta) + i_1(r_i, \theta)) + \sum f(r_i) i_3(r_i, \theta) \cos \delta(r_i, \theta) \}$
MRL4	$1/k^2 \{ \sum f(r_i) (i_2(r_i, \theta) + i_1(r_i, \theta)) - \sum f(r_i) i_3(r_i, \theta) \sin \delta(r_i, \theta) \}$
COM1	$1/k^2 i_4 \{ \sum f(r_i) i_2(r_i, \theta) + \sum f(r_i) i_1(r_i, \theta) \}$
COM2	$1/k^2 \sum f(r_i) i_3(r_i, \theta) \cos \delta(r_i, \theta)$
COM3	$1/k^2 \sum f(r_i) i_3(r_i, \theta) \sin \delta(r_i, \theta)$
S12	$2(MR00 - MR90) / COM1$
S33	$COM2 / COM1$
S43	$COM3 / COM1$
UNPL	$1 - SS$
PLFX1	$(SS - S12) / 2$
PLFX2	$(SS + S12) / 2$
DELPL	$ATAN2(S43, S33) \ 180/\pi$

$$\text{where } SS = \sqrt{S12^2 + S33^2 + S43^2}$$

ratios of the scattered intensity to the incident intensity - except for a constant factor which has been dropped and depends on the distance from the common volume to the detector and on the total number of spheres within the common volume. Only ratio type measurements are contemplated; the concentration is not assumed known (except that it be below the multiple scattering threshold) nor is it required as part of the solution. It is further assumed that all the scattering spheres are confined to a very small region within the common volume so the variation in common volume size with scattering angle may be ignored for now.

From these four basic measurements one could form various combinations, including the next three angular scattering functions. $COM1 = \frac{1}{2} (MR00 + MR90)$ is the phase function. $COM2 = MR45 - COM1$ and $COM3 = COM1 - MRL4$ depend only on i_3 ($= \sqrt{i_1 i_2}$)

and on either the cosine or sine of δ .

Seven additional angular scattering functions were calculated for each trial distribution although these were not made available to the inversion teams. They include three normalized Mueller matrix elements S_{12} , S_{33} , S_{43} , and four functions defined in the following way. Let, as before, the incident light be plane polarized at 45° to the scattering plane. The light scattered in any direction can be thought of as the (incoherent) sum of a 100% unpolarized beam and a 100% polarized beam; the polarized fraction of the scattered beam can be further regarded as the (coherent) sum of a component polarized parallel to the scattering plane and a component polarized perpendicular to the plane, with some phase angle between them. UNPL is the fraction of the total scattered intensity which is unpolarized, PLPX1 and PLPX2 the fractions plane polarized perpendicular and parallel to the scattering plane respectively, and DELPL the phase angle between them. Table III indicates how these last seven quantities may be calculated from the first seven.

In addition to the angular scattering functions, the backscatter, extinction, scattering, and absorption cross sections were calculated as part of the program for each incident wavelength. However, in all the cases studied so far, only real refractive indices were considered, so $\sigma_e = \sigma_s$ and $\sigma_a = 0$.

Once the exact data were calculated, stored, and printed out as described above, a perturbation was introduced to simulate random experimental error. A set of random numbers was generated, normally distributed about 1.0 with a preselected standard deviation (.04 for the trial distributions reported on here). From this set a different error factor was multiplied with each data point from the four angular scattering functions MROO through MRL4, as well as each of the cross sections. Data points for the remaining ten angular scattering functions were recomputed based on the perturbed values of the first four functions, although owing to the nature of the combinations, this led in some cases to relative errors far in excess of the 4% level intended. These perturbed values comprised the set of synthetic data available to the inversion teams.

4. RESULTS

From the nearly 4000 data points available for each trial distribution, the inversion teams were free to choose any subset they felt was efficient for their inversion method. The smallest set selected was the backscatter cross sections, only

15 points per distribution. The fidelity with which the inverted solutions represented the original distributions varied from team to team and somewhat less so from trial to trial, ranging from vague to indistinguishable from the original. Since examples of the inversion results will appear separately in this Proceedings under papers by Herman, Curry, and Pearce, they will not be reproduced here. However, we shall select one result as typical to illustrate the way in which the inversions are being analyzed and to indicate some of the problems generally encountered with inversions.

Figure 3 shows the inverted solution to distribution C as calculated by Herman with the constrained-linear-inversion method and using as input data the 15 backscatter cross sections.

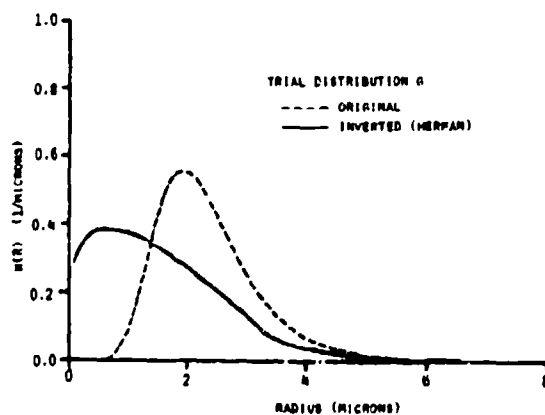


FIGURE 3. INVERTED SOLUTION TO DISTRIBUTION C

While other representations of the same data (for example, mass normalization) can show a better overall fit, it is clear that the inverted solution does not agree with the original distribution in several respects. One way to judge this inverted solution is to recompute all the scattering data based on the inverted solution as the distribution function, and compare that scattering data with the data calculated from the original distribution (all without the random error perturbation). Unless there is an error in the inversion calculation we should expect agreement in the two cases over that subset of scattering data which was used as input to the inversion; the more interesting question is whether there exists other subsets of scattering data whose

values differ markedly depending upon which distribution function is used (the original one or the inverted one) for the forward calculation.

The present example was inverted on the basis of backscatter cross sections. By supplementing the original set of wavelengths and refractive indices with 185 new points, smoothly incorporating the original 15, we can form an apparently continuous plot of backscatter cross sections vs wavelength. The two such plots formed -- one based on the original distribution G , the other on Herman's inverted solution for G -- were virtually identical on the entire wavelength range examined, except for a constant factor. The backscatter calculated with Herman's inverted solutions was lower than with the original, as would be expected from his relative preponderance of smaller particles, but it was uniformly lower so the shapes of the backscatter curves were the same. Since only relative intensity measurements are contemplated, such a difference can have no significance. In Figure 4 is plotted with a solid line, the backscatter cross section calculated using Herman's inverted solution, and on it (corrected for the constant factor mentioned above) the 15 backscatter cross sections given belonging to the original distribution. As one can see, both distributions are equivalent with respect to backscatter.

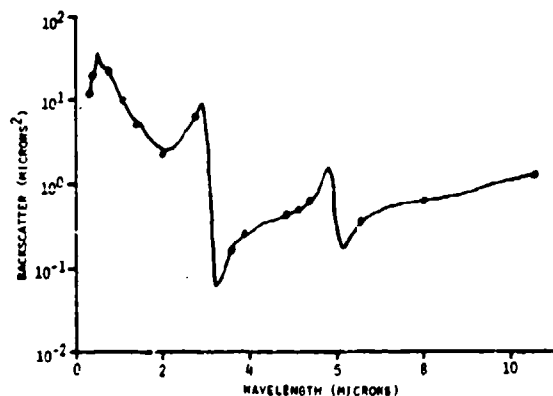


FIGURE 4. BACKSCATTER CROSS SECTIONS. Solid line derived from Herman's inverted solution, circles represent original data points.

To check how well Herman's solution does with respect to other scattering data, one can imagine doing the forward calculations based on Herman's solution and making a graph of each scattering function vs scattering angle, one for each wavelength, and comparing them to corresponding graphs based on the original distribution. However, given the product of 14 scattering functions, 15 wavelengths, and (this time) four trial distributions done by four inversion methods, such a project quickly gets out of hand. Instead, a single number is calculated to represent the degree of discrepancy between two corresponding graphs. The graphs are not actually plotted but they readily can be later if something looks interesting. These average error factors are tabulated for all combinations of scattering functions and incident wavelengths. The exact definition of the average error factor varies among the different scattering functions, depending upon whether a uniform correction factor is permitted (as was the case in the backscatter comparison above) whether the scattering function values are bounded, whether they can pass through zero, etc. When a distribution function is compared with itself, the average error factors are, as expected, all zero; when two unrelated distributions are compared, say C with I, the factors are (mostly) all large, on the order 0.2 ~ 2.0. The error factors generated when comparing the original distribution C with Herman's inverted solution C are given in Table IV.

Recalling that the scattering data supplied to the inverters had a random error level of 4% to start with, average error factors in the vicinity of .04 or less are expected and of no particular interest. That eliminates most of the table. The relatively high error factors at the shortest two or three wavelengths are also of no consequence; they arise because of the jagged nature of the graphs plotted from Herman's solution at these wavelengths which in turn is due to the relatively large radii bins over which Herman's inverted solution was defined. The occasional large average error factor in the DELPL column is due to an easily rectified quirk in the computer program which sees, for example, DELPL (phase shift) values of 178° and -179° as differing by 357° , when physically they differ only by 3° . That leaves only COM3 and MR45, at longer wavelengths, as possible candidates for further investigation. In particular, none of the polarization scattering functions (SI2 through DELPL) appear to be of value.

These average error factor tables were produced for Herman's solutions to the other three trial distributions, and for Curry's constrained eigenfunction expansion solutions, with similar results. That is, inverted solutions, though differing from

TABLE IV. AVERAGE ERROR FACTORS

WAVELENGTH	MR00	MR90	MR45	MRL4	COM1	COM2	COM3
01	.096	.071	.089	.103	.069	.054	1.068
02	.090	.069	.084	.066	.059	.066	.858
03	.062	.066	.050	.068	.055	.029	.229
04	.052	.036	.033	.043	.032	.038	.122
05	.025	.027	.020	.026	.018	.028	.149
06	.040	.032	.034	.039	.024	.018	.091
07	.025	.023	.033	.021	.021	.026	.065
08	.040	.030	.075	.024	.025	.050	.087
09	.042	.033	.081	.025	.024	.049	.085
10	.032	.029	.095	.027	.026	.057	.092
11	.029	.033	.099	.027	.028	.059	.099
12	.031	.031	.104	.030	.028	.057	.102
13	.037	.043	.122	.039	.041	.073	.132
14	.047	.056	.156	.045	.050	.076	.138
15	.048	.056	.197	.043	.045	.072	.143

WAVELENGTH	S12	S33	S43	UNPL	PLFX1	PLFX2	DELPL
01	.046	.060	.057	.028	.067	.046	.278
02	.058	.041	.042	.033	.082	.048	.380
03	.032	.025	.031	.020	.035	.033	.110
04	.027	.017	.024	.012	.032	.029	.108
05	.016	.015	.019	.010	.016	.025	.090
06	.016	.014	.015	.014	.017	.019	.134
07	.014	.014	.008	.012	.014	.022	.030
08	.013	.008	.012	.012	.021	.011	.331
09	.016	.010	.008	.014	.023	.014	.177
10	.010	.010	.012	.013	.022	.010	.017
11	.010	.012	.013	.013	.021	.012	.020
12	.009	.012	.016	.014	.020	.015	.019
13	.008	.010	.016	.009	.011	.013	.019
14	.012	.010	.014	.010	.013	.015	.023
15	.019	.021	.013	.017	.029	.023	.030

the original distributions, were consistent not only with the data points used to derive them but with virtually all the other light scattering data that might have been used, possibly excepting MR45 or COM3. The inverted solutions of the Curry/Kiech nonlinear regression method and Pearce's B-spline method have not yet been examined in this way, though their solutions are so close to the original distributions that it's unlikely anything could be learned.

Apparently we can not devise a practical (perhaps not even an impractical) procedure based solely on light scattering measurements which insures convergence to the correct solution. These results emphasize the necessity for having an inversion

scheme that permits the incorporation of the maximum amount of a priori (i.e., non-light-scattering) information that may be available. Even then the best that may be said of a solution is that it is consistent with all the known information about the scattering system.

AEROSOL SIZE DISTRIBUTION FROM
SIMULATED NEPHELOMETRIC DATA

W. A. Pearce
EG&G Washington Analytical Services Center, Inc.
6801 Kenilworth Avenue
Riverdale, Maryland 20737

ABSTRACT

This paper addresses the latest in a series of objective tests of the B-spline technique for inferring aerosol size distributions from scattering matrix data. While a paper fully describing the method is in preparation, several aspects of the technique are presented in:

W. A. Pearce, "A Benchmark Evaluation of an Aerosol Size Distribution Inversion Technique", EG&G/WASC Applied Sciences Dept. Report TR-W22-001/84 July, 1984.

W. A. Pearce, "B-Spline Representations for Aerosol Size Distribution Inversion", Proceedings of the 1982 CSL Conference on Obscuration and Aerosol Research, R. H. Kohl, ed. (1983).

W. A. Pearce, "Aerosol Size Distribution from Scattering Matrix Data", EG&G/WASC Applied Systems Dept. Report 00781.

W. A. Pearce, "Inference of Scatterer Size Distribution from Single Scattering Matrix Data" in Light Scattering by Irregularly Shaped Particles, D. W. Schuerman, ed., Plenum Press, New York 1979.

Test inversions will be performed on experimental data sets when they become available. Expected extensions of the effort include investigations of non-linear constraints and of the information content of optimal and sub-optimal data sets.

INTRODUCTION

We have performed a set of benchmark tests of the B-spline size distribution inference technique. The (simulated) data for the tests were provided by J. Bottiger (CSL) who released to us only the data as it would be available from nephelometric measurements. The underlying size distributions were unknown to us when the inversions were performed.

Given a set of data \tilde{X}_1 , we solve the (overdetermined) set of equations:

$$X_k = \sum_i W_{ki} \tilde{X}_1 = \sum_{ij} W_{ki} \tilde{S}_{ij} \eta_j = \sum_j S_{kj} \eta_j \quad (1)$$

where W is a weight matrix ($W_{ki} = \delta_{ki}/\epsilon \tilde{X}_1$, ϵ is a fixed percentage data error). The η_j 's are the parameters of expansion of the size distribution $n(r)$ in terms of B-splines ($B(r)$):

$$n(r) = \sum_j B_j(r) \eta_j, \quad (2)$$

and the effective kernel is

$$\tilde{S}_{ij} = \int \hat{S}_1(r) B_j(r) dr. \quad (3)$$

S is a monodisperse Mie scattering matrix element appropriate to the measurement. To solve (1), we use a singular value decomposition of S to obtain its pseudo-inverse:

$$S^+ = V \Gamma^+ U^T \quad (4)$$

Here, V is a matrix whose elements are eigenvectors of $S^T S$; the columns of U are eigenvectors of SS^T ; and Γ^+ is diagonal with elements given by the inverse of the square root of the positive definite eigenvalues of $S^T S$.

Often, the unconstrained full solution contains unphysical oscillations with possible negative regions. We have implemented an adjunct iterative procedure which partially damps this unwanted behavior. An estimate of the solution vector is iteratively updated using

$$\eta_{NEW} = \eta_{OLD} + \Delta\eta \quad (5)$$

Using $\delta = V[1/(\sigma_1 + \alpha)] U^T [X - S\eta]$, $\Delta\eta$ is given by

$$\Delta\eta = \begin{cases} \delta & \text{if } (\eta_{OLD} + \delta) > 0 \\ 0 & \text{otherwise} \end{cases} \quad (6)$$

DATA

The test data consisted of values of matrix elements at angles 0 (5) 180 degrees together with extinction, scattering, absorption, and backscattering cross sections at each of 15 wavelengths (from 300 nm to 10600 nm). These data were provided for each of the four test distributions (G,H,I, and J). We elected to use only a minimal subset consisting of the matrix element $MR00$ defined as

$$MR00 = (1/k^2) \sum_{i=1}^N n(r_i) i_2(r_i, \theta); \quad k = 2\pi/\lambda \quad (7)$$

at each of the 37 angles and at two wavelengths (690 and 3400 nm). The data, as presented to us, incorporated 4% random additive errors.

RESULTS

The rms errors of the solution fits to the data and the knot structure of the fitting B-splines are shown in Table 1.

TABLE I. SOLUTION SUMMARY

Size Distribution	RMS Relative Data Residual Error (%)		No. Knots	Spacing	Diameter Range (10^{-6}m)
	Solution	Iterative Solution			
G	3.2	6.4	20	linear	.5 - 16.0
H	3.6	11.0	20	linear	.5 - 10.0
I	3.8	7.2	20	linear	.5 - 10.0
J	4.18	N.A.	10	exponential	1.5 - 7.5

The inversion results are presented in Figure 1 and are compared with the underlying "true" distributions (which have recently been revealed).

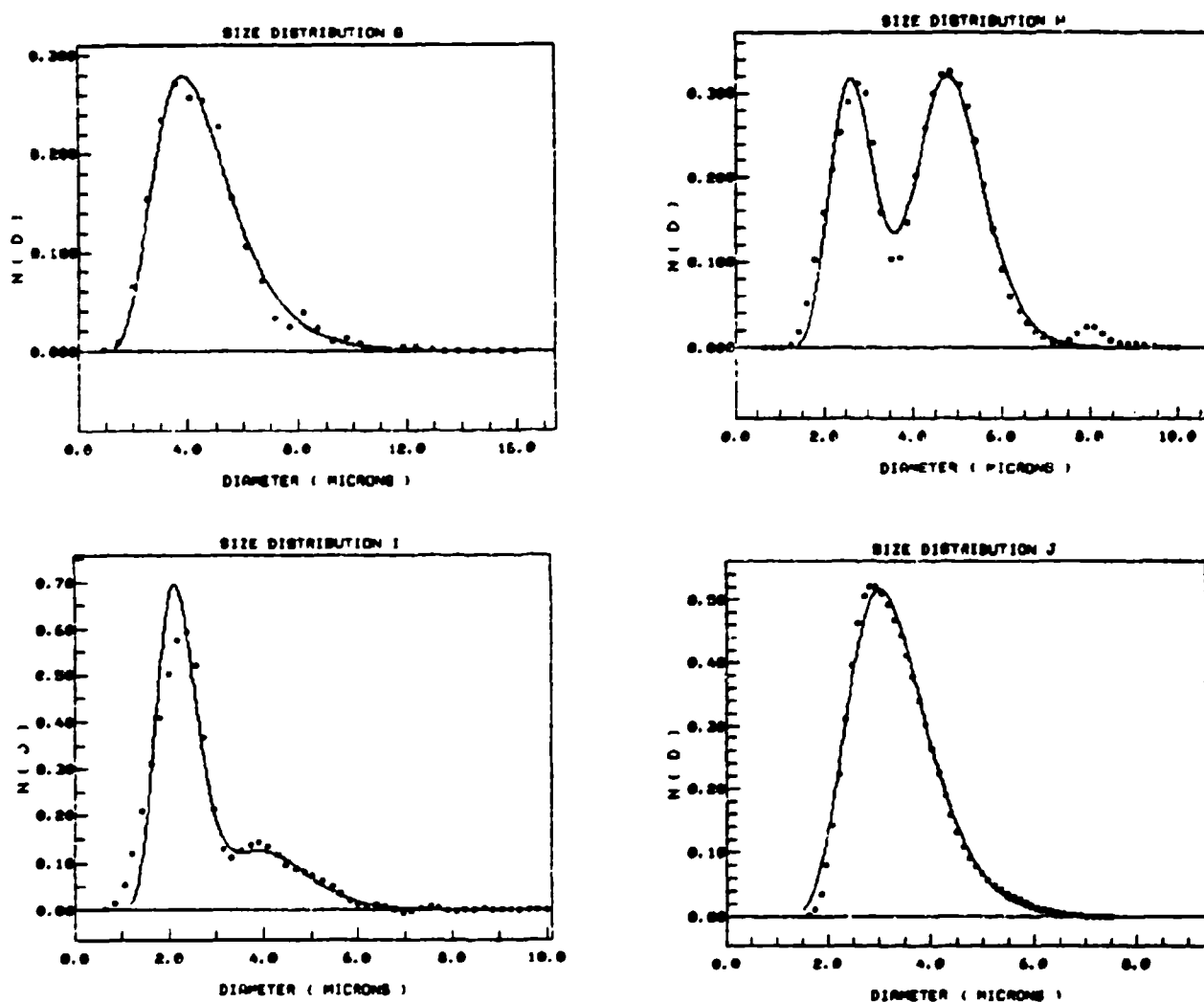


FIGURE 1. INFERRED AND TRUE DISTRIBUTIONS. True size distributions (lines) compared with inferred (points) for tests G (iterated solution), H (iterated solution), I (direct solution), and J (direct solution).

Our technique will be tested using experimental data when they become available. Meanwhile, we will continue to investigate means for constraining solutions to physically meaningful domains and examine the relative information content of particular subsets of data.

The Optical Constants of Selected Materials
in the Infrared, Visible, and Ultraviolet
Spectral Regions

Marvin R. Querry
Physics Department
University of Missouri - Kansas City
Kansas City, Missouri 64110

RECENT PUBLICATIONS

1. M.R. Querry, "Optical Properties of Compressed Powders," Proceedings of the 1983 CSL Conference on Obscuration and Aerosol Research, J. Farmer and R.H. Kohl, eds., p. 147-158.
2. M.R. Querry, "Optical Constants," Final Technical Report, Contract DAAK-11-82-C-0069, 31 May 1984, pp. 407.

ABSTRACT

Optical Constants of 23 samples were determined throughout the 200-50,000 cm^{-1} wave-number region of the infrared, near infrared, visible, and ultraviolet. The materials were graphites, copper, brass, aluminum, aluminum oxide, TCNQ salts, iron, iron oxides, zinc oxide, intercalated graphite, and pyrolytic graphite.

I. Introduction

We prepared samples from 21 different materials, measured 23 different reflectance spectra for those materials, used Kramers-Kronig methods to compute spectral values of the complex refractive index $n+ik$ from each of the 23 reflectance spectra, and presented¹ the measurements and results of the computations in graphical and tabular form. All data were delivered on computer cards to the technical monitor, Mr. Merrill Milham, CRDC. Those data are now available for use in Mie scattering codes to compute radiant transport through and radiant backscatter by aerosol clouds that are composed of these 21 materials.

The 23 samples were

1. Sapphire ($\alpha\text{-Al}_2\text{O}_3$) E//C (uniaxial crystal)
2. Sapphire ($\alpha\text{-Al}_2\text{O}_3$) E+C (uniaxial crystal)
3. Oxidized Aluminum Mirror
4. Iron (polycrystalline)
5. Hematite ($\alpha\text{Fe}_2\text{O}_3$) E//C (uniaxial crystal)
6. Hematite ($\alpha\text{Fe}_2\text{O}_3$) E+C (uniaxial crystal)
7. Magnetite (Fe_3O_4) (isotropic crystal)
8. Cuprous Oxide (Cu_2O powder, pellet)

9. Zinc Oxide (ZnO powder, pellet)
10. Copper Ingot
11. Brass Ingot (90%Cu/10%Zn)
12. Brass Ingot (85%Cu/15%Zn)
13. Brass Ingot (70%Cu/30%Zn)
14. Dixon KS-2 Graphite (powder, pellet)
15. Dixon HPN-2 Graphite (powder, pellet)
16. Dixon 200-10 Graphite (powder, pellet)
17. Asbury Micro 260 Graphite (powder, pellet)
18. Dixon 1102 Intercalated Graphite (powder, pellet)
19. Asbury 3222 Intercalated Graphite (powder, pellet)
20. Pyrolytic Graphite
21. TTF/TCNQ (powder, pellet)
22. Cu/TCNQ (CRDC pellet)
23. Li/TCNQ (powder, pellet)

In this paper we present measurements of the reflectance spectrum and the optical constants of iron. These data are presented in graphical and tabular form. The presentation here for iron is similar in format to that for all 23 samples. Readers interested in data for the other 22 samples are referred to Reference (1).

II. THE IRON SAMPLE

The iron sample was 1.2 cm dia. by 1 cm long, polycrystalline, and was Assar puratronic grade obtained from Johnson Matthey, Inc., P.O. Box 1087, Seabrook, NH 03874. The purity was 99.9985% and the specific gravity 7.87. The 1.2 cm dia. end face of the rod was mechanically polished with 6 μ m diamond paste, 0.3 μ m α -Al₂O₃, and 0.05 μ m α -Al₂O₃. A mirror surface was obtained and remained bright and untarnished for several months after the polish was applied. Reflectance spectra of the iron sample were obtained in dry air immediately after polishing.

III. REFLECTANCE AND OPTICAL CONSTANTS

A near normal incidence reflectance spectrum for the polished iron sample was obtained throughout the 180-50,000 cm⁻¹ wave-number region (55.55-0.2 μ m).

In the infrared region, 180-4,000 cm⁻¹ (55.5-2.5 μ m), the reflectance spectrum was obtained by use of a Perkin-Elmer 580 spectrophotometer and specular reflectance accessory. The infrared spectrum was measured relative to that of a first surface aluminum mirror. Multiplication of the relative

reflectance spectrum by the reflectance of the aluminum mirror provided the absolute reflectance spectrum of the iron sample.

In the UV-Vis-MIR region, $4,000-50,000 \text{ cm}^{-1}$ ($2.5-0.2 \mu\text{m}$), the reflectance spectrum was obtained by use of a Cary Varian 2300 spectrophotometer and a V-W reflectance accessory that provided measurements of the absolute reflectance.

The reflectance spectrum was analyzed by use of Kramers-Kronig methods to obtain spectral values of the complex refractive indices $n+ik$; i.e. the so called optical constants.

The measured reflectance spectrum of iron is presented in Figs. 1-2, where comparisons are made with reflectance of iron as previously determined by Weaver *et. al.*, Bolotin *et. al.* and Johnson and Christy. Spectral values of n and k are presented in Figs. 3-6 where similar comparisons are made with values presented by other investigators.

The first derivative of the infrared reflectance spectrum is presented in Fig. 7. We have not determined the physical sources of the structure in the first derivative spectrum. Possible sources are electronic transitions and/or surface contamination by oxides or adsorbed species.

Tabulation of the reflectance and $n+ik$ are also presented in the following pages. In the Table the columns from left to right provide wave number (cm^{-1}), WN; wavelength (μm), WL; n , k ; uncertainty in n and k , (DN and DK); and the reflectance R . The relatively large values of DN and DK in the infrared are characteristic of small errors in measurements of R producing large DN and DK when the Fresnel reflectance equations are used to determine $n+ik$ for highly reflecting materials.

IV. REFERENCES

1. M.R. Querry, "Optical Constants," Final Technical Report, Contract DAAK-11-82-C-0069, 31 May 1984, p. 407.
2. J.H. Weaver, E. Colavita, D.W. Lynch, and R. Rosei, "Low-energy interband absorption in bcc Fe and hcp Co," Phys. Rev. B 19, 3,850-3,856 (1979).
3. G.A. Bolotin, M.M. Kirillova, and V.M. Mayevskii, Phys. Met. Metallurg. 27, 224-234 (1969).
4. P.B. Johnson and R.W. Christy, "Optical Constants of Transition Metals: Ti, V, Cr, Mn, Fe, Co, Ni, and Pd," Phys. Rev. B 9, 5,056-5,070 (1974).

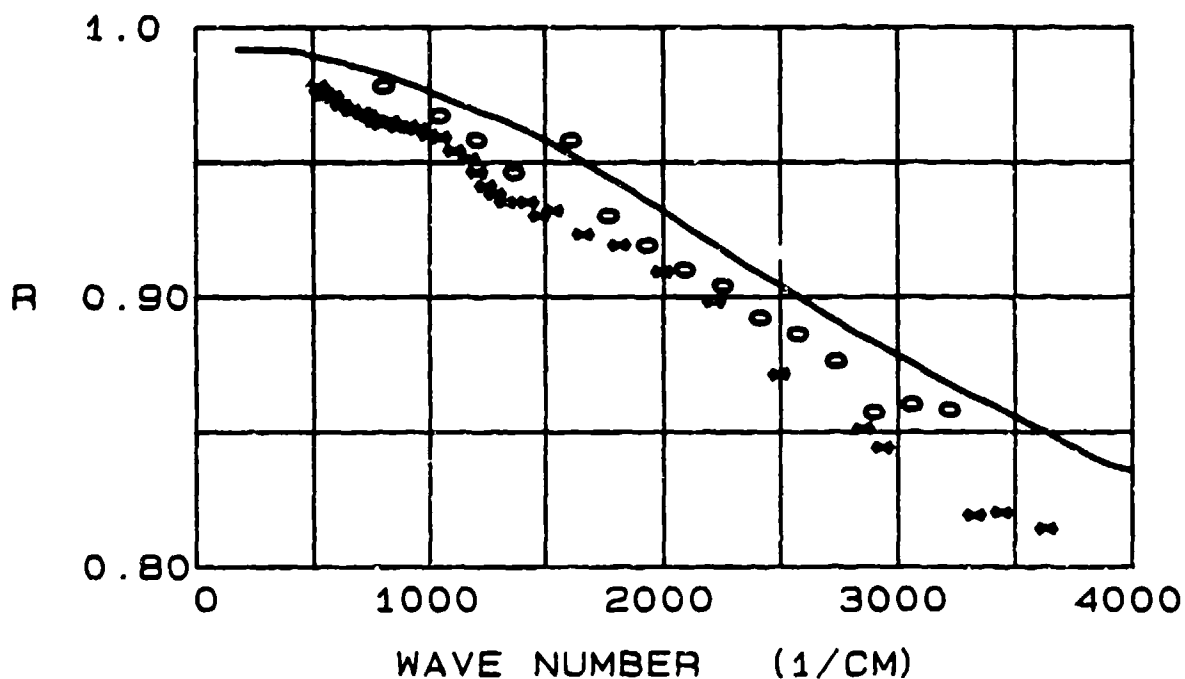


FIGURE 1. INFRARED REFLECTANCE OF IRON. The infrared reflectance of iron is shown in the 180-4,000 cm^{-1} wave-number region: the continuous curve denotes our measurements; O, Weaver *et. al.*; and *, Bolotin *et. al.*

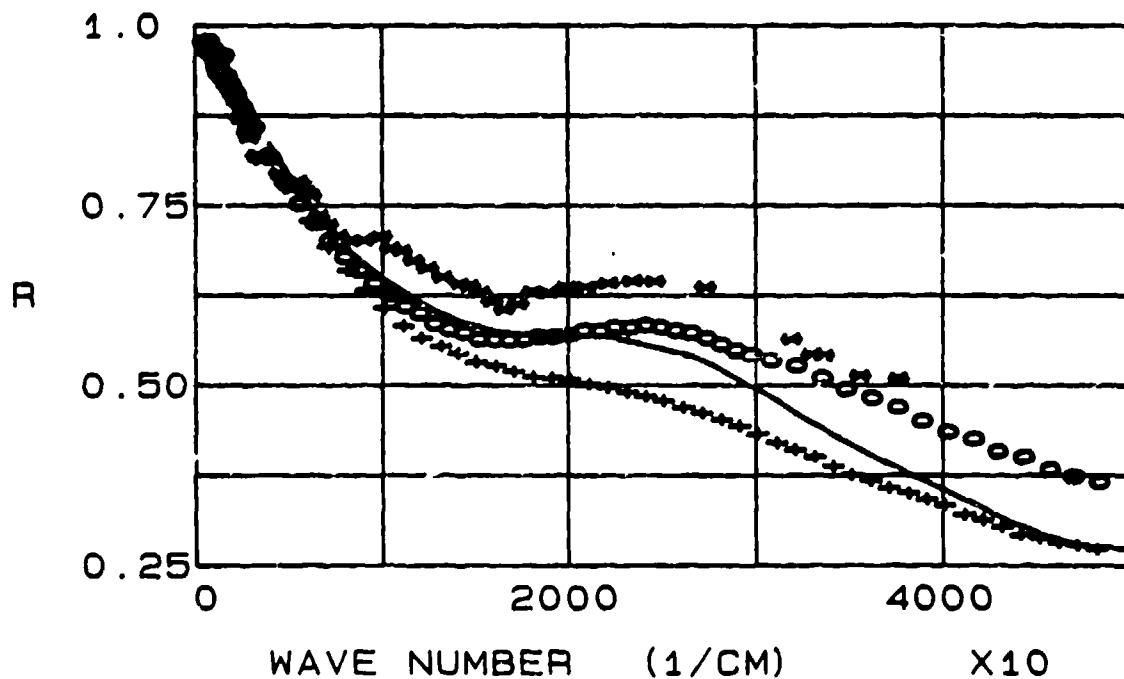


FIGURE 2. NIR-VIS-UV REFLECTANCE OF IRON. Our measurements of the NIR-Vis-UV reflectance of iron in the 4,000-50,000 cm^{-1} wave-number region are denoted by the continuous curve. The other symbols denote measurements by Weaver *et. al.*, O; Bolotin *et. al.*, *; and Johnson and Christy, +.

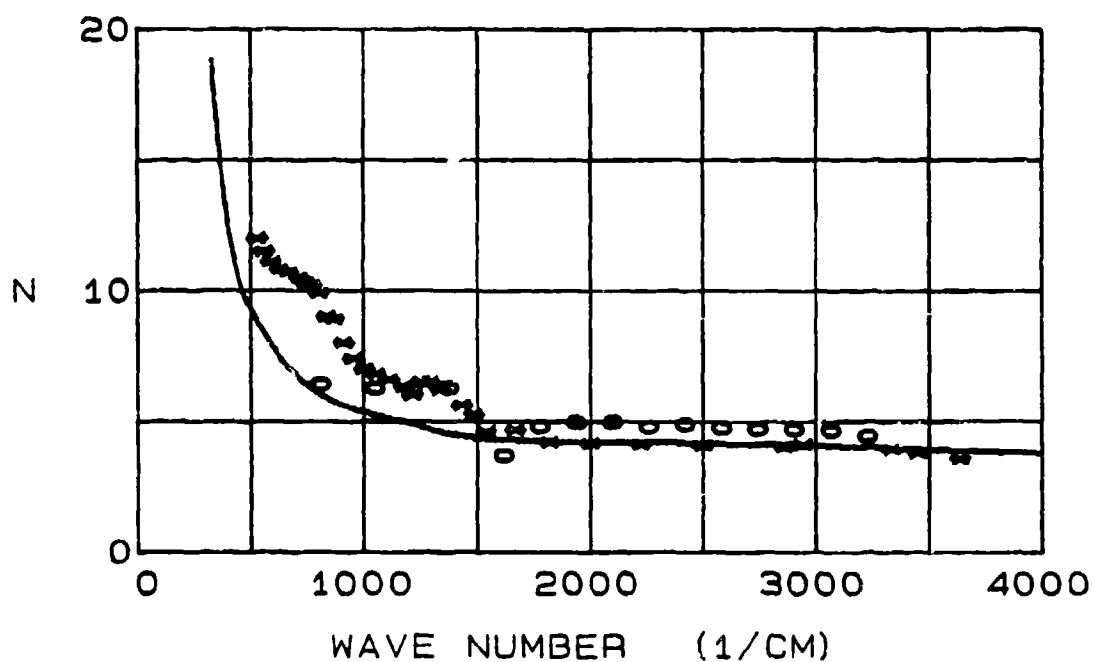
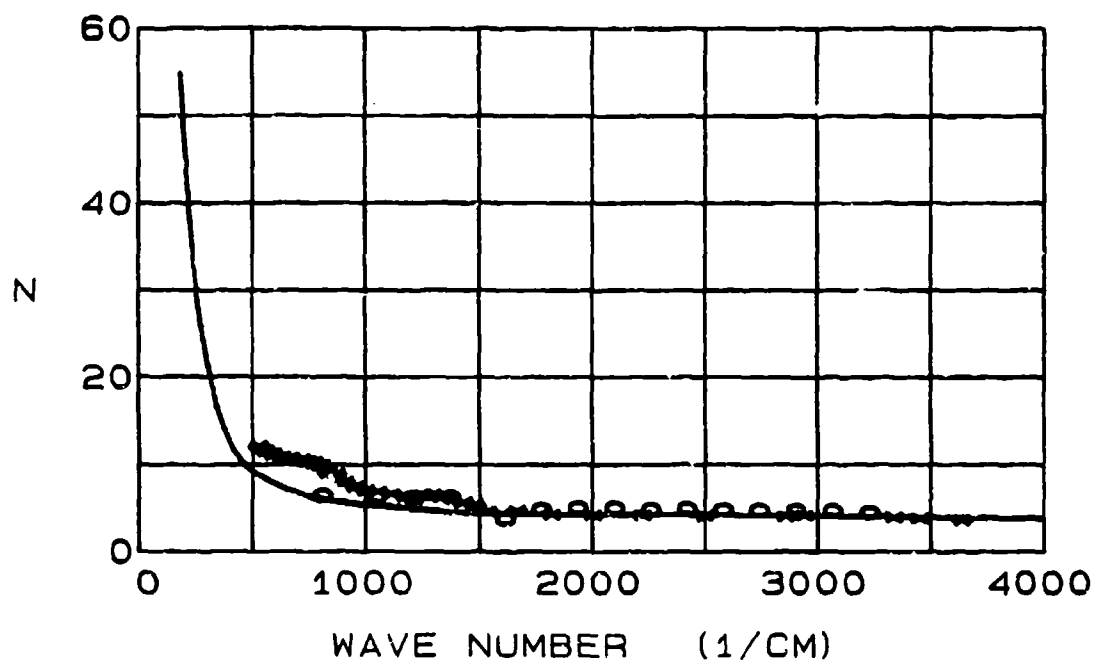


FIGURE 3. REAL PART OF IRON'S INFRARED REFRACTIVE INDEX. The continuous curve denotes n as determined from our investigations. Values of n determined by others are: Weaver *et. al.*, \circ ; and Bolotin *et. al.*, $*$. The top graph shows n throughout the 180-4,000 cm^{-1} wave-number region. The bottom graph shows an expanded ordinate for better comparison of our values of n with those of Weaver *et. al.* and Bolotin *et. al.*

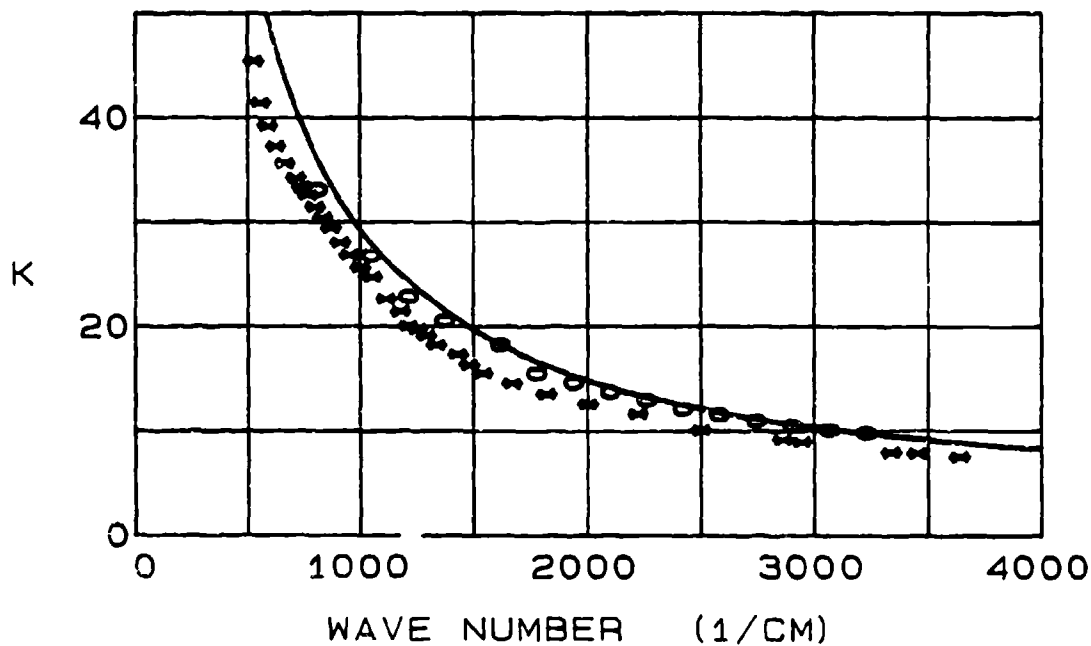
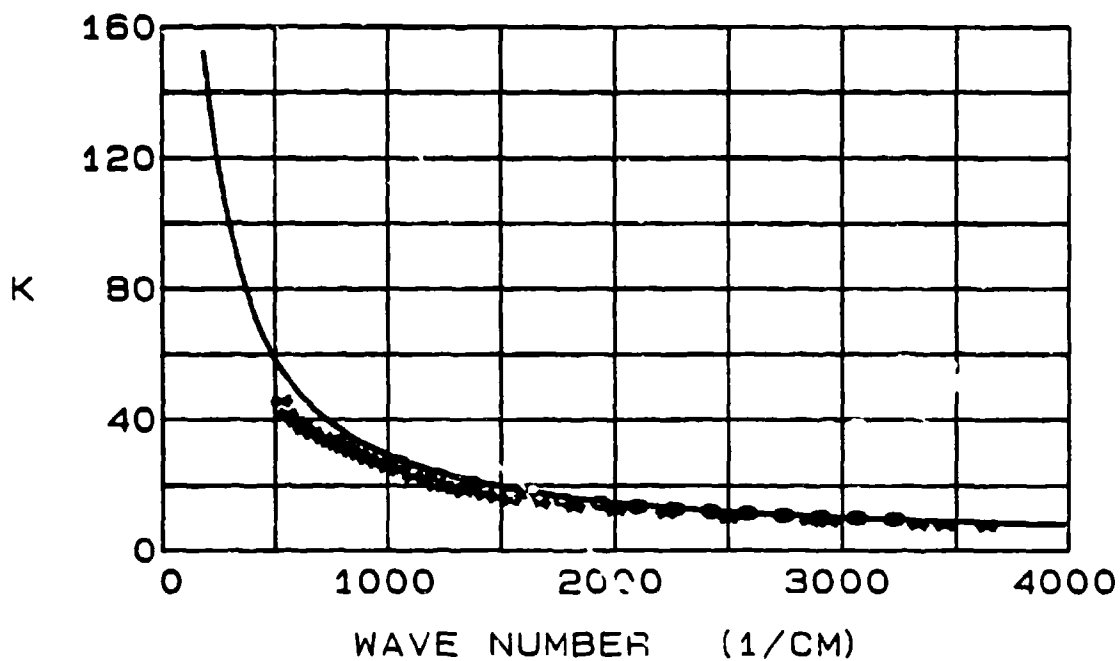


FIGURE 4. IMAGINARY PART OF THE IRON'S INFRARED REFRACTIVE INDEX. The continuous curve denotes k as determined from our investigations. Values of k determined by others are: Weaver *et. al.*, \circ ; and Bolotin *et. al.*, \ast . The top graph shows k throughout the $180\text{--}4,000\text{ cm}^{-1}$ wave-number region. The bottom graph shows k on an expanded ordinate for better comparison of our values of k with those of Weaver *et. al.* and Bolotin *et. al.*

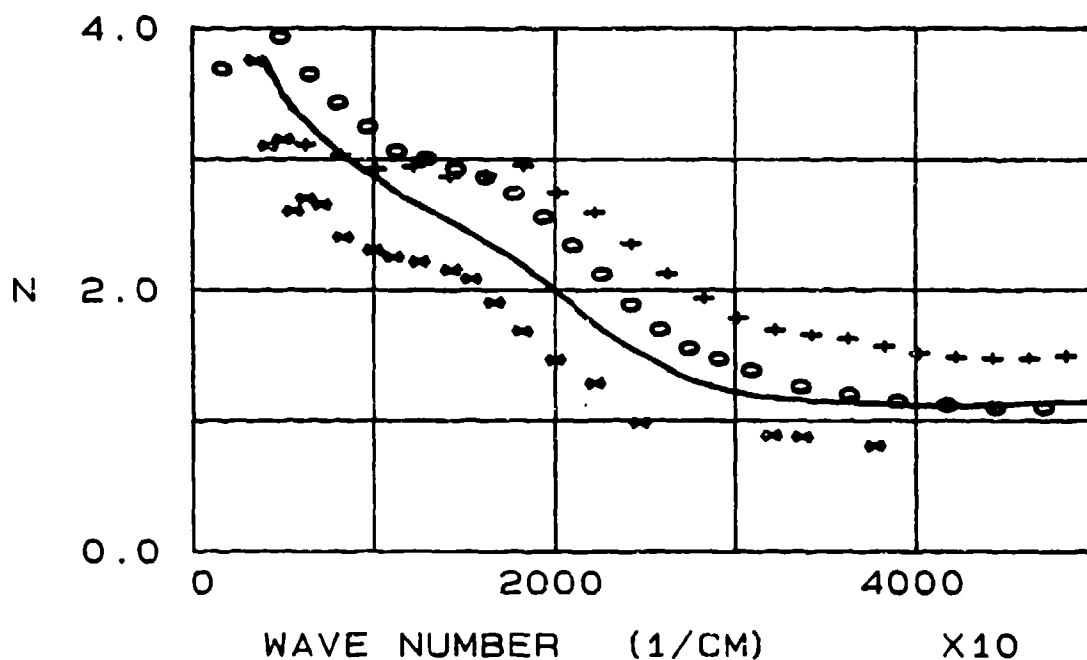


FIGURE 5. REAL PART OF IRON'S NIR-VIS-UV REFRACTIVE INDEX. The continuous curve denotes n as determined from our investigations. Values of n determined by others are: Weaver *et. al.*, O; Bolotin *et. al.*, \bullet ; and Johnson and Christy, +.

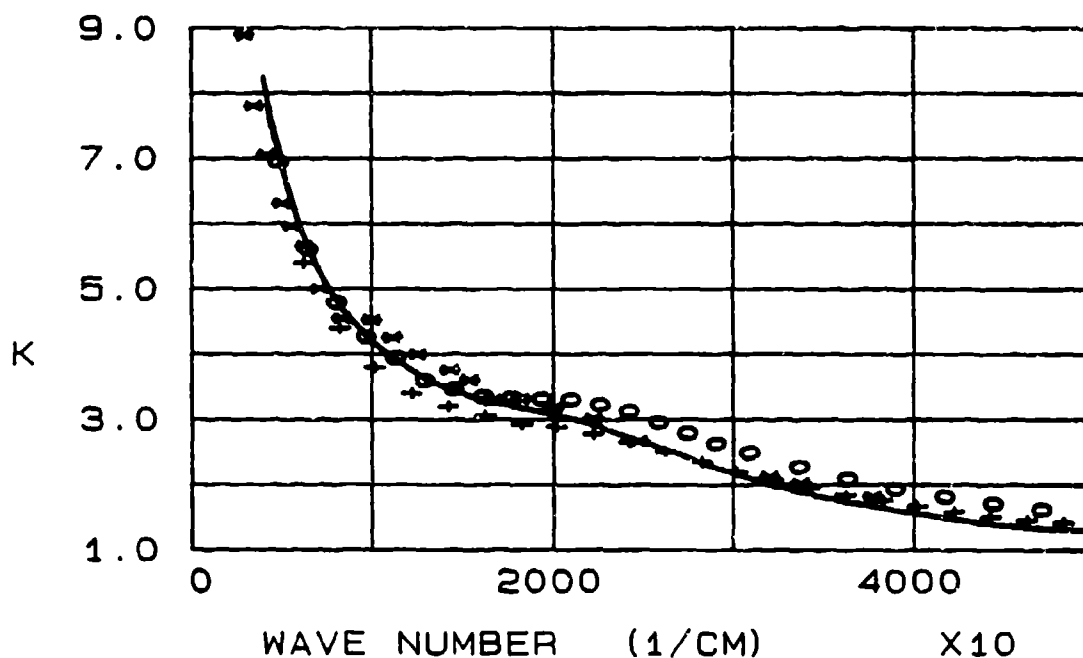


FIGURE 6. IMAGINARY PART OF IRON'S NIR-VIS-UV REFRACTIVE INDEX. The continuous curve denotes k as determined from our investigations. Values of k determined by others are: Weaver *et. al.*, O; Bolotin *et. al.*, \bullet ; and Johnson and Christy, +.

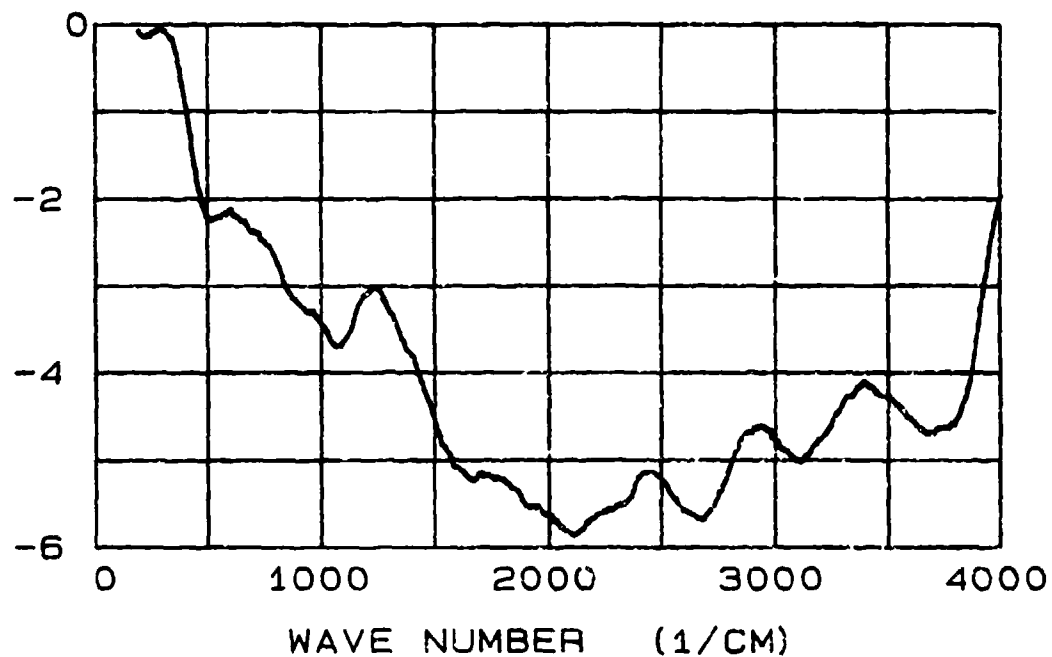


FIGURE 7. FIRST DERIVATIVE OF IRON'S INFRARED REFLECTANCE SPECTRUM. We have not determined the physical sources of the structure in this first derivative spectrum. Possible sources, however, are interband transitions and/or surface contamination by oxides or surface adsorbates.

WN	WL	N	K	DN	DK	R
180.00	55.5556	54.848	152.133	21.240	17.973	0.99170
190.00	52.6316	49.736	145.745	20.038	15.949	0.99170
200.00	50.0000	45.257	139.754	18.655	14.044	0.99170
210.00	47.6190	41.364	134.110	17.359	12.434	0.99169
220.00	45.4545	37.988	128.832	16.160	11.075	0.99167
230.00	43.4783	35.070	123.929	15.063	9.932	0.99163
240.00	41.6667	32.461	119.413	14.077	8.947	0.99161
250.00	40.0000	30.095	115.205	13.180	8.088	0.99160
260.00	38.4615	27.921	111.240	12.354	7.327	0.99160
270.00	37.0370	25.982	107.465	11.584	6.662	0.99159
280.00	35.7143	24.261	103.902	10.873	6.084	0.99157
290.00	34.4828	22.745	100.563	10.222	5.584	0.99153
300.00	33.3333	21.354	97.458	9.632	5.140	0.99151
310.00	32.2581	20.050	94.541	9.093	4.741	0.99151
320.00	31.2500	18.813	91.768	8.592	4.375	0.99152
330.00	30.3030	17.653	89.100	8.121	4.042	0.99153
340.00	29.4118	16.597	86.524	7.677	3.743	0.99154
350.00	28.5714	15.637	84.044	7.259	3.474	0.99153
360.00	27.7778	14.786	81.664	6.867	3.237	0.99151
370.00	27.0270	14.017	79.390	6.502	3.025	0.99147
380.00	26.3158	13.336	77.211	6.160	2.837	0.99141
390.00	25.6410	12.729	75.133	5.842	2.669	0.99133
400.00	25.0000	12.195	73.151	5.545	2.520	0.99123
410.00	24.3902	11.721	71.267	5.270	2.387	0.99111
420.00	23.8095	11.294	69.477	5.015	2.268	0.99098
430.00	23.2558	10.907	67.770	4.778	2.159	0.99084
440.00	22.7273	10.553	66.135	4.555	2.060	0.99069
450.00	22.2222	10.249	64.565	4.346	1.971	0.99052
460.00	21.7391	9.991	63.067	4.152	1.893	0.99031
470.00	21.2766	9.779	61.651	3.972	1.823	0.99008
480.00	20.8333	9.589	60.320	3.806	1.760	0.98984
490.00	20.4082	9.413	59.066	3.654	1.702	0.98960
500.00	20.0000	9.238	57.878	3.512	1.648	0.98937
510.00	19.6078	9.066	56.742	3.379	1.595	0.98915
520.00	19.2308	8.901	55.652	3.254	1.546	0.98893
530.00	18.8679	8.749	54.608	3.136	1.500	0.98870
540.00	18.5185	8.604	53.611	3.026	1.456	0.98847
550.00	18.1818	8.459	52.659	2.922	1.415	0.98826
560.00	17.8571	8.310	51.742	2.824	1.375	0.98805
570.00	17.5439	8.167	50.854	2.731	1.336	0.98784
580.00	17.2414	8.026	49.996	2.642	1.300	0.98764
590.00	16.9492	7.894	49.168	2.558	1.265	0.98743
600.00	16.6667	7.758	48.367	2.478	1.231	0.98724
610.00	16.3934	7.624	47.586	2.401	1.198	0.98704
620.00	16.1290	7.495	46.822	2.327	1.166	0.98684
630.00	15.8730	7.379	46.076	2.256	1.137	0.98663
640.00	15.6250	7.275	45.357	2.188	1.109	0.98652
650.00	15.3846	7.182	44.654	2.123	1.084	0.98615
660.00	15.1515	7.095	43.981	2.062	1.059	0.98590
670.00	14.9254	7.011	43.332	2.004	1.036	0.98565

IRON ROD

PAGE 2

WN	WL	N	K	DN	DK	R
680.00	14.7059	6.931	42.706	1.948	1.014	0.98540
690.00	14.4928	6.851	42.102	1.896	0.993	0.98516
700.00	14.2857	6.770	41.516	1.845	0.972	0.98492
710.00	14.0845	6.689	40.946	1.797	0.952	0.98468
720.00	13.8889	6.609	40.389	1.750	0.932	0.98445
730.00	13.6986	6.530	39.847	1.705	0.913	0.98422
740.00	13.5135	6.453	39.316	1.662	0.895	0.98398
750.00	13.3333	6.379	38.797	1.620	0.877	0.98374
760.00	13.1579	6.308	38.289	1.560	0.860	0.98350
770.00	12.9870	6.243	37.793	1.541	0.844	0.98324
780.00	12.8205	6.181	37.309	1.503	0.828	0.98298
790.00	12.6582	6.122	36.839	1.467	0.813	0.98272
800.00	12.5000	6.063	36.380	1.432	0.799	0.98246
810.00	12.3457	6.005	35.930	1.399	0.784	0.98219
820.00	12.1951	5.951	35.486	1.366	0.771	0.98191
830.00	12.0482	5.907	35.050	1.334	0.758	0.98161
840.00	11.9048	5.867	34.629	1.304	0.746	0.98129
850.00	11.7647	5.832	34.222	1.275	0.734	0.98097
860.00	11.6279	5.796	33.827	1.247	0.723	0.98065
870.00	11.4943	5.760	33.441	1.221	0.712	0.98033
880.00	11.3636	5.726	33.065	1.195	0.702	0.98001
890.00	11.2360	5.693	32.699	1.170	0.692	0.97969
900.00	11.1111	5.662	32.342	1.146	0.682	0.97934
910.00	10.9890	5.630	31.994	1.123	0.672	0.97904
920.00	10.8696	5.600	31.654	1.101	0.663	0.97871
930.00	10.7527	5.569	31.323	1.079	0.654	0.97839
940.00	10.6383	5.539	30.999	1.058	0.645	0.97807
950.00	10.5263	5.507	30.682	1.038	0.636	0.97775
960.00	10.4167	5.475	30.371	1.018	0.628	0.97743
970.00	10.3093	5.444	30.064	0.999	0.619	0.97711
980.00	10.2041	5.415	29.762	0.980	0.611	0.97678
990.00	10.1010	5.387	29.466	0.962	0.603	0.97644
1000.00	10.0000	5.362	29.175	0.945	0.595	0.97610
1010.00	9.9010	5.339	28.891	0.927	0.588	0.97574
1020.00	9.8039	5.318	28.613	0.911	0.581	0.97538
1030.00	9.7087	5.298	28.342	0.895	0.574	0.97502
1040.00	9.6154	5.279	28.078	0.880	0.567	0.97466
1050.00	9.5238	5.259	27.820	0.865	0.561	0.97429
1060.00	9.4340	5.239	27.566	0.850	0.555	0.97393
1070.00	9.3458	5.221	27.317	0.836	0.548	0.97356
1080.00	9.2593	5.205	27.075	0.822	0.542	0.97319
1090.00	9.1743	5.188	26.838	0.809	0.536	0.97282
1100.00	9.0909	5.171	26.608	0.796	0.531	0.97245
1110.00	9.0090	5.155	26.382	0.784	0.525	0.97208
1120.00	8.9286	5.138	26.161	0.772	0.520	0.97172
1130.00	8.8496	5.122	25.946	0.760	0.514	0.97136
1140.00	8.7719	5.104	25.738	0.749	0.509	0.97101
1150.00	8.6957	5.084	25.534	0.738	0.504	0.97067
1160.00	8.6207	5.061	25.334	0.728	0.499	0.97036
1170.00	8.5470	5.036	25.136	0.717	0.494	0.97005

WN	WL	N	K	DN	DK	R
1180.00	8.4746	5.009	24.941	0.707	0.488	0.96975
1190.00	8.4034	4.982	24.746	0.697	0.483	0.96945
1200.00	8.3333	4.955	24.554	0.687	0.478	0.96915
1210.00	8.2645	4.928	24.365	0.677	0.473	0.96885
1220.00	8.1967	4.901	24.177	0.668	0.467	0.96855
1230.00	8.1301	4.873	23.992	0.658	0.462	0.96826
1240.00	8.0645	4.844	23.809	0.649	0.457	0.96797
1250.00	8.0000	4.814	23.626	0.640	0.452	0.96768
1260.00	7.9365	4.786	23.442	0.631	0.448	0.96737
1270.00	7.8740	4.761	23.259	0.622	0.443	0.96704
1280.00	7.8125	4.739	23.080	0.613	0.438	0.96670
1290.00	7.7519	4.718	22.904	0.605	0.434	0.96635
1300.00	7.6923	4.698	22.733	0.597	0.429	0.96601
1310.00	7.6336	4.676	22.565	0.589	0.425	0.96567
1320.00	7.5758	4.652	22.399	0.581	0.421	0.96535
1330.00	7.5188	4.628	22.233	0.573	0.417	0.96502
1340.00	7.4627	4.606	22.067	0.565	0.412	0.96468
1350.00	7.4074	4.587	21.901	0.558	0.408	0.96431
1360.00	7.3529	4.569	21.739	0.550	0.404	0.96394
1370.00	7.2993	4.552	21.580	0.543	0.401	0.96356
1380.00	7.2464	4.534	21.423	0.536	0.397	0.96319
1390.00	7.1942	4.517	21.269	0.529	0.393	0.96281
1400.00	7.1429	4.500	21.115	0.522	0.389	0.96243
1410.00	7.0922	4.484	20.963	0.515	0.386	0.96204
1420.00	7.0423	4.469	20.813	0.509	0.382	0.96164
1430.00	6.9930	4.455	20.664	0.502	0.379	0.96123
1440.00	6.9444	4.442	20.518	0.496	0.375	0.96082
1450.00	6.8966	4.430	20.375	0.490	0.372	0.96040
1460.00	6.8493	4.417	20.233	0.484	0.369	0.95998
1470.00	6.8027	4.405	20.092	0.478	0.366	0.95956
1480.00	6.7568	4.393	19.952	0.472	0.363	0.95912
1490.00	6.7114	4.383	19.814	0.466	0.359	0.95867
1500.00	6.6667	4.374	19.678	0.461	0.356	0.95822
1510.00	6.6225	4.366	19.544	0.455	0.354	0.95776
1520.00	6.5789	4.358	19.412	0.450	0.351	0.95729
1530.00	6.5359	4.351	19.281	0.445	0.348	0.95681
1540.00	6.4935	4.344	19.153	0.439	0.345	0.95633
1550.00	6.4516	4.338	19.025	0.434	0.342	0.95584
1560.00	6.4103	4.334	18.899	0.429	0.340	0.95533
1570.00	6.3694	4.331	18.776	0.425	0.337	0.95482
1580.00	6.3291	4.327	18.656	0.420	0.335	0.95431
1590.00	6.2893	4.324	18.538	0.415	0.332	0.95379
1600.00	6.2500	4.321	18.422	0.411	0.330	0.95328
1610.00	6.2112	4.319	18.307	0.407	0.328	0.95277
1620.00	6.1728	4.316	18.195	0.402	0.325	0.95226
1630.00	6.1350	4.313	18.085	0.398	0.323	0.95175
1640.00	6.0976	4.309	17.976	0.394	0.321	0.95125
1650.00	6.0606	4.305	17.868	0.390	0.318	0.95074
1660.00	6.0241	4.301	17.761	0.386	0.316	0.95023
1670.00	5.9880	4.299	17.655	0.382	0.314	0.94971

IRON ROD

PAGE 4

WN	WL	N	E	DN	DK	R
1680.00	5.9524	4.296	17.551	0.378	0.312	0.94919
1690.00	5.9172	4.294	17.449	0.375	0.310	0.94867
1700.00	5.8824	4.291	17.348	0.371	0.308	0.94815
1710.00	5.8480	4.288	17.248	0.367	0.306	0.94763
1720.00	5.8140	4.286	17.149	0.364	0.304	0.94709
1730.00	5.7803	4.285	17.052	0.360	0.302	0.94656
1740.00	5.7471	4.284	16.957	0.357	0.300	0.94602
1750.00	5.7143	4.283	16.865	0.354	0.298	0.94549
1760.00	5.6818	4.280	16.774	0.351	0.296	0.94498
1770.00	5.6497	4.276	16.684	0.347	0.294	0.94449
1780.00	5.6180	4.271	16.594	0.344	0.292	0.94399
1790.00	5.5866	4.266	16.504	0.341	0.290	0.94350
1800.00	5.5556	4.261	16.414	0.338	0.288	0.94297
1810.00	5.5249	4.258	16.325	0.335	0.286	0.94246
1820.00	5.4945	4.255	16.236	0.332	0.285	0.94192
1830.00	5.4645	4.254	16.149	0.329	0.283	0.94137
1840.00	5.4348	4.252	16.064	0.326	0.281	0.94083
1850.00	5.4054	4.249	15.980	0.323	0.279	0.94030
1860.00	5.3763	4.247	15.896	0.320	0.278	0.93976
1870.00	5.3476	4.244	15.814	0.318	0.276	0.93922
1880.00	5.3191	4.242	15.731	0.315	0.274	0.93867
1890.00	5.2910	4.240	15.650	0.312	0.273	0.93812
1900.00	5.2632	4.239	15.570	0.310	0.271	0.93756
1910.00	5.2356	4.238	15.492	0.307	0.269	0.93701
1920.00	5.2083	4.237	15.414	0.305	0.268	0.93645
1930.00	5.1813	4.235	15.338	0.302	0.266	0.93590
1940.00	5.1546	4.234	15.262	0.300	0.265	0.93535
1950.00	5.1282	4.232	15.187	0.297	0.263	0.93480
1960.00	5.1020	4.230	15.113	0.295	0.262	0.93425
1970.00	5.0761	4.229	15.039	0.293	0.260	0.93369
1980.00	5.0505	4.227	14.966	0.290	0.259	0.93313
1990.00	5.0251	4.226	14.894	0.288	0.257	0.93257
2000.00	5.0000	4.225	14.823	0.286	0.256	0.93201
2010.00	4.9751	4.224	14.752	0.284	0.254	0.93144
2020.00	4.9505	4.222	14.682	0.282	0.253	0.93088
2030.00	4.9261	4.221	14.613	0.279	0.252	0.93031
2040.00	4.9020	4.221	14.544	0.277	0.250	0.92973
2050.00	4.8780	4.221	14.476	0.275	0.249	0.92915
2060.00	4.8544	4.221	14.409	0.273	0.247	0.92857
2070.00	4.8309	4.221	14.343	0.271	0.246	0.92798
2080.00	4.8077	4.221	14.278	0.269	0.245	0.92740
2090.00	4.7847	4.221	14.213	0.267	0.244	0.92682
2100.00	4.7619	4.221	14.150	0.265	0.242	0.92624
2110.00	4.7393	4.221	14.087	0.264	0.241	0.92566
2120.00	4.7170	4.221	14.025	0.262	0.240	0.92508
2130.00	4.6948	4.221	13.964	0.260	0.238	0.92450
2140.00	4.6729	4.221	13.903	0.258	0.237	0.92392
2150.00	4.6512	4.222	13.843	0.256	0.236	0.92333
2160.00	4.6296	4.222	13.784	0.255	0.235	0.92275
2170.00	4.6083	4.223	13.726	0.253	0.234	0.92217

WN	WL	N	K	DN	DK	R
2180.00	4.5872	4.224	13.669	0.251	0.233	0.92159
2190.00	4.5662	4.224	13.613	0.250	0.231	0.92102
2200.00	4.5455	4.224	13.557	0.248	0.230	0.92046
2210.00	4.5249	4.224	13.503	0.247	0.229	0.91990
2220.00	4.5045	4.223	13.449	0.245	0.228	0.91934
2230.00	4.4843	4.221	13.395	0.244	0.227	0.91882
2240.00	4.4643	4.219	13.341	0.242	0.226	0.91828
2250.00	4.4444	4.217	13.288	0.240	0.225	0.91773
2260.00	4.4248	4.216	13.234	0.239	0.224	0.91717
2270.00	4.4053	4.216	13.181	0.237	0.223	0.91660
2280.00	4.3860	4.215	13.129	0.236	0.222	0.91603
2290.00	4.3668	4.215	13.077	0.235	0.221	0.91547
2300.00	4.3478	4.214	13.026	0.233	0.219	0.91491
2310.00	4.3290	4.214	12.977	0.232	0.218	0.91435
2320.00	4.3103	4.213	12.927	0.230	0.217	0.91380
2330.00	4.2918	4.212	12.878	0.229	0.216	0.91325
2340.00	4.2735	4.211	12.830	0.228	0.215	0.91270
2350.00	4.2553	4.210	12.782	0.226	0.214	0.91215
2360.00	4.2373	4.209	12.734	0.225	0.213	0.91161
2370.00	4.2194	4.208	12.688	0.224	0.213	0.91107
2380.00	4.2017	4.207	12.642	0.223	0.212	0.91054
2390.00	4.1841	4.205	12.597	0.221	0.211	0.91002
2400.00	4.1667	4.203	12.552	0.220	0.210	0.90951
2410.00	4.1494	4.200	12.507	0.219	0.209	0.90899
2420.00	4.1322	4.197	12.462	0.218	0.208	0.90848
2430.00	4.1152	4.195	12.418	0.216	0.207	0.90797
2440.00	4.0984	4.192	12.374	0.215	0.206	0.90746
2450.00	4.0816	4.189	12.330	0.214	0.205	0.90695
2460.00	4.0650	4.185	12.287	0.213	0.204	0.90645
2470.00	4.0486	4.181	12.243	0.212	0.203	0.90595
2480.00	4.0323	4.178	12.200	0.211	0.202	0.90544
2490.00	4.0161	4.174	12.156	0.209	0.201	0.90493
2500.00	4.0000	4.171	12.111	0.208	0.200	0.90439
2510.00	3.9841	4.168	12.068	0.207	0.199	0.90385
2520.00	3.9683	4.166	12.024	0.206	0.198	0.90330
2530.00	3.9526	4.164	11.982	0.205	0.198	0.90276
2540.00	3.9370	4.162	11.940	0.204	0.197	0.90222
2550.00	3.9216	4.159	11.898	0.203	0.196	0.90168
2560.00	3.9063	4.157	11.857	0.202	0.195	0.90114
2570.00	3.8911	4.155	11.815	0.201	0.194	0.90060
2580.00	3.8760	4.153	11.774	0.200	0.193	0.90005
2590.00	3.8610	4.151	11.733	0.198	0.192	0.89950
2600.00	3.8462	4.149	11.692	0.197	0.192	0.89894
2610.00	3.8314	4.148	11.652	0.196	0.191	0.89838
2620.00	3.8168	4.147	11.612	0.195	0.190	0.89781
2630.00	3.8023	4.146	11.572	0.194	0.189	0.89724
2640.00	3.7879	4.145	11.533	0.193	0.188	0.89667
2650.00	3.7736	4.145	11.495	0.192	0.187	0.89611
2660.00	3.7594	4.144	11.457	0.192	0.187	0.89555
2670.00	3.7453	4.143	11.420	0.191	0.186	0.89499

WN	WL	N	K	DN	DK	R
2680.00	3.7313	4.142	11.382	0.190	0.185	0.89443
2690.00	3.7175	4.142	11.345	0.189	0.184	0.89387
2700.00	3.7037	4.142	11.309	0.188	0.184	0.89331
2710.00	3.6900	4.141	11.272	0.187	0.183	0.89274
2720.00	3.6765	4.141	11.237	0.186	0.182	0.89218
2730.00	3.6630	4.141	11.201	0.185	0.181	0.89162
2740.00	3.6496	4.142	11.167	0.184	0.181	0.89106
2750.00	3.6364	4.142	11.134	0.184	0.180	0.89052
2760.00	3.6232	4.141	11.101	0.183	0.179	0.88999
2770.00	3.6101	4.141	11.068	0.182	0.179	0.88947
2780.00	3.5971	4.140	11.036	0.181	0.178	0.88896
2790.00	3.5842	4.139	11.004	0.180	0.177	0.88845
2800.00	3.5714	4.137	10.973	0.180	0.177	0.88795
2810.00	3.5587	4.135	10.941	0.179	0.176	0.88745
2820.00	3.5461	4.134	10.910	0.178	0.175	0.88695
2830.00	3.5336	4.132	10.879	0.177	0.175	0.88646
2840.00	3.5211	4.131	10.849	0.177	0.174	0.88597
2850.00	3.5088	4.128	10.819	0.176	0.174	0.88551
2860.00	3.4965	4.125	10.789	0.175	0.173	0.88504
2870.00	3.4843	4.122	10.759	0.174	0.172	0.88458
2880.00	3.4722	4.119	10.729	0.174	0.172	0.88412
2890.00	3.4602	4.116	10.699	0.173	0.171	0.88366
2900.00	3.4483	4.113	10.670	0.172	0.170	0.88319
2910.00	3.4364	4.109	10.640	0.172	0.170	0.88273
2920.00	3.4247	4.106	10.610	0.171	0.169	0.88227
2930.00	3.4130	4.102	10.581	0.170	0.168	0.88180
2940.00	3.4014	4.099	10.551	0.169	0.168	0.88133
2950.00	3.3898	4.096	10.522	0.169	0.167	0.88086
2960.00	3.3784	4.092	10.492	0.168	0.167	0.88039
2970.00	3.3670	4.089	10.463	0.167	0.166	0.87992
2980.00	3.3557	4.086	10.435	0.167	0.165	0.87945
2990.00	3.3445	4.082	10.406	0.166	0.165	0.87898
3000.00	3.3333	4.079	10.377	0.165	0.164	0.87852
3010.00	3.3223	4.075	10.349	0.165	0.163	0.87805
3020.00	3.3113	4.071	10.320	0.164	0.163	0.87758
3030.00	3.3003	4.068	10.291	0.163	0.162	0.87709
3040.00	3.2895	4.065	10.262	0.163	0.162	0.87660
3050.00	3.2787	4.062	10.233	0.162	0.161	0.87610
3060.00	3.2680	4.059	10.205	0.161	0.160	0.87560
3070.00	3.2573	4.057	10.177	0.161	0.160	0.87510
3080.00	3.2468	4.054	10.149	0.160	0.159	0.87459
3090.00	3.2362	4.052	10.121	0.159	0.159	0.87409
3100.00	3.2258	4.051	10.094	0.159	0.158	0.87358
3110.00	3.2154	4.048	10.067	0.158	0.157	0.87309
3120.00	3.2051	4.046	10.040	0.158	0.157	0.87259
3130.00	3.1949	4.044	10.014	0.157	0.156	0.87211
3140.00	3.1847	4.042	9.988	0.156	0.156	0.87162
3150.00	3.1746	4.040	9.962	0.156	0.155	0.87113
3160.00	3.1646	4.038	9.936	0.155	0.155	0.87064
3170.00	3.1546	4.036	9.910	0.155	0.154	0.87015

WN	WL	N	K	DN	DK	R
3180.00	3.1447	4.034	9.885	0.154	0.154	0.86966
3190.00	3.1348	4.033	9.860	0.153	0.153	0.86917
3200.00	3.1250	4.031	9.836	0.153	0.153	0.86871
3210.00	3.1153	4.028	9.812	0.152	0.152	0.86823
3220.00	3.1056	4.026	9.789	0.152	0.152	0.86780
3230.00	3.0960	4.023	9.765	0.151	0.151	0.86735
3240.00	3.0864	4.020	9.741	0.151	0.151	0.86689
3250.00	3.0769	4.018	9.717	0.150	0.150	0.86643
3260.00	3.0675	4.015	9.693	0.150	0.150	0.86597
3270.00	3.0581	4.013	9.670	0.149	0.149	0.86551
3280.00	3.0488	4.011	9.647	0.149	0.149	0.86505
3290.00	3.0395	4.008	9.624	0.148	0.148	0.86461
3300.00	3.0303	4.006	9.602	0.148	0.148	0.86417
3310.00	3.0211	4.003	9.580	0.147	0.147	0.86374
3320.00	3.0120	4.000	9.558	0.147	0.147	0.86332
3330.00	3.0030	3.996	9.536	0.146	0.146	0.86291
3340.00	2.9940	3.993	9.514	0.146	0.146	0.86250
3350.00	2.9851	3.989	9.493	0.145	0.145	0.86209
3360.00	2.9762	3.985	9.471	0.145	0.145	0.86168
3370.00	2.9674	3.981	9.448	0.144	0.144	0.86126
3380.00	2.9586	3.977	9.426	0.144	0.144	0.86084
3390.00	2.9499	3.973	9.405	0.143	0.143	0.86042
3400.00	2.9412	3.970	9.383	0.143	0.143	0.86001
3410.00	2.9326	3.965	9.362	0.142	0.143	0.85959
3420.00	2.9240	3.961	9.340	0.142	0.142	0.85918
3430.00	2.9155	3.958	9.318	0.141	0.142	0.85875
3440.00	2.9070	3.954	9.296	0.141	0.141	0.85832
3450.00	2.8986	3.950	9.275	0.140	0.141	0.85791
3460.00	2.8902	3.946	9.254	0.140	0.140	0.85749
3470.00	2.8818	3.942	9.232	0.140	0.140	0.85708
3480.00	2.8736	3.938	9.211	0.139	0.139	0.85665
3490.00	2.8653	3.934	9.189	0.139	0.139	0.85622
3500.00	2.8571	3.930	9.167	0.138	0.138	0.85578
3510.00	2.8490	3.926	9.146	0.138	0.138	0.85534
3520.00	2.8409	3.923	9.125	0.137	0.137	0.85491
3530.00	2.8329	3.919	9.104	0.137	0.137	0.85447
3540.00	2.8249	3.916	9.083	0.136	0.137	0.85404
3550.00	2.8169	3.912	9.062	0.136	0.136	0.85360
3560.00	2.8090	3.908	9.041	0.135	0.136	0.85317
3570.00	2.8011	3.904	9.020	0.135	0.135	0.85273
3580.00	2.7933	3.901	8.999	0.135	0.135	0.85229
3590.00	2.7855	3.897	8.978	0.134	0.134	0.85184
3600.00	2.7778	3.894	8.957	0.134	0.134	0.85138
3610.00	2.7701	3.891	8.936	0.133	0.133	0.85092
3620.00	2.7624	3.888	8.915	0.133	0.133	0.85046
3630.00	2.7548	3.885	8.895	0.132	0.133	0.84999
3640.00	2.7473	3.882	8.874	0.132	0.132	0.84953
3650.00	2.7397	3.880	8.854	0.131	0.132	0.84906
3660.00	2.7322	3.877	8.834	0.131	0.131	0.84859
3670.00	2.7248	3.875	8.814	0.131	0.131	0.84812

WN	WL	N	K	DN	DK	R
3680.00	2.7174	3.873	8.794	0.130	0.130	0.84765
3690.00	2.7100	3.870	8.774	0.130	0.130	0.84718
3700.00	2.7027	3.868	8.754	0.129	0.130	0.84671
3710.00	2.6954	3.866	8.735	0.129	0.129	0.84624
3720.00	2.6882	3.865	8.716	0.129	0.129	0.84577
3730.00	2.6810	3.863	8.697	0.128	0.128	0.84531
3740.00	2.6738	3.861	8.679	0.128	0.128	0.84485
3750.00	2.6667	3.859	8.660	0.127	0.128	0.84440
3760.00	2.6596	3.857	8.642	0.127	0.127	0.84395
3770.00	2.6525	3.855	8.624	0.127	0.127	0.84350
3780.00	2.6455	3.853	8.606	0.126	0.127	0.84305
3790.00	2.6385	3.851	8.588	0.126	0.126	0.84260
3800.00	2.6316	3.850	8.570	0.126	0.126	0.84215
3810.00	2.6247	3.848	8.553	0.125	0.125	0.84170
3820.00	2.6178	3.846	8.535	0.125	0.125	0.84125
3830.00	2.6110	3.845	8.518	0.125	0.125	0.84080
3840.00	2.6042	3.844	8.502	0.124	0.124	0.84036
3850.00	2.5974	3.843	8.485	0.124	0.124	0.83992
3860.00	2.5907	3.842	8.468	0.124	0.124	0.83951
3870.00	2.5840	3.840	8.455	0.123	0.123	0.83911
3880.00	2.5773	3.839	8.440	0.123	0.123	0.83872
3890.00	2.5707	3.837	8.426	0.123	0.123	0.83836
3900.00	2.5641	3.835	8.412	0.122	0.123	0.83801
3910.00	2.5575	3.832	8.398	0.122	0.122	0.83769
3920.00	2.5510	3.829	8.385	0.122	0.122	0.83739
3930.00	2.5445	3.825	8.372	0.122	0.122	0.83710
3940.00	2.5381	3.821	8.358	0.121	0.121	0.83682
3950.00	2.5316	3.816	8.346	0.121	0.121	0.83656
3960.00	2.5253	3.811	8.333	0.121	0.121	0.83632
3970.00	2.5189	3.805	8.320	0.121	0.121	0.83611
3980.00	2.5126	3.797	8.307	0.120	0.120	0.83592
3990.00	2.5063	3.789	8.294	0.120	0.120	0.83575
4016.06	2.4900	3.763	8.247	0.119	0.119	0.83503
4032.26	2.4800	3.752	8.216	0.118	0.118	0.83438
4048.58	2.4700	3.744	8.183	0.118	0.118	0.83361
4065.04	2.4600	3.741	8.149	0.117	0.117	0.83263
4081.63	2.4500	3.741	8.120	0.116	0.116	0.83177
4098.36	2.4400	3.738	8.095	0.116	0.116	0.83106
4115.23	2.4300	3.730	8.071	0.115	0.115	0.83053
4132.23	2.4200	3.723	8.042	0.115	0.115	0.82979
4149.38	2.4100	3.720	8.014	0.114	0.114	0.82900
4166.67	2.4000	3.715	7.991	0.114	0.114	0.82840
4184.10	2.3900	3.705	7.966	0.113	0.113	0.82789
4201.68	2.3800	3.696	7.936	0.113	0.113	0.82717
4219.41	2.3700	3.691	7.903	0.112	0.112	0.82622
4237.29	2.3600	3.689	7.877	0.112	0.111	0.82545
4255.32	2.3500	3.680	7.849	0.111	0.111	0.82478
4273.50	2.3400	3.674	7.820	0.111	0.110	0.82398
4291.85	2.3300	3.671	7.790	0.110	0.110	0.82309
4310.35	2.3200	3.665	7.763	0.109	0.109	0.82231

WN	WL	N	K	DN	DK	R
4329.00	2.3100	3.662	7.732	0.109	0.108	0.82135
4347.83	2.3000	3.660	7.705	0.108	0.108	0.82052
4366.81	2.2900	3.656	7.677	0.108	0.107	0.81965
4385.96	2.2800	3.654	7.652	0.107	0.107	0.81885
4405.29	2.2700	3.647	7.626	0.107	0.106	0.81816
4424.78	2.2600	3.644	7.599	0.106	0.106	0.81729
4444.44	2.2500	3.640	7.573	0.106	0.105	0.81651
4464.29	2.2400	3.632	7.548	0.105	0.105	0.81583
4484.30	2.2300	3.626	7.519	0.105	0.104	0.81498
4504.50	2.2200	3.624	7.491	0.104	0.104	0.81404
4524.89	2.2100	3.621	7.466	0.104	0.103	0.81321
4545.45	2.2000	3.616	7.440	0.103	0.102	0.81245
4566.21	2.1900	3.611	7.415	0.103	0.102	0.81166
4587.16	2.1800	3.606	7.390	0.102	0.101	0.81090
4608.29	2.1700	3.598	7.366	0.102	0.101	0.81023
4629.63	2.1600	3.589	7.338	0.101	0.100	0.80947
4651.16	2.1500	3.583	7.309	0.101	0.100	0.80855
4672.90	2.1400	3.578	7.281	0.100	0.099	0.80766
4694.84	2.1300	3.572	7.254	0.100	0.099	0.80679
4716.98	2.1200	3.569	7.227	0.099	0.098	0.80586
4739.34	2.1100	3.563	7.199	0.099	0.097	0.80498
4761.90	2.1000	3.559	7.175	0.098	0.097	0.80417
4784.69	2.0900	3.550	7.151	0.098	0.097	0.80348
4807.69	2.0800	3.542	7.120	0.097	0.096	0.80252
4830.92	2.0700	3.538	7.094	0.097	0.096	0.80158
4854.37	2.0600	3.531	7.068	0.096	0.095	0.80080
4878.05	2.0500	3.522	7.042	0.096	0.094	0.80003
4901.96	2.0400	3.512	7.012	0.095	0.094	0.79913
4926.11	2.0300	3.507	6.981	0.095	0.093	0.79802
4950.50	2.0200	3.500	6.956	0.094	0.093	0.79721
4975.12	2.0100	3.483	6.927	0.094	0.092	0.79656
5000.00	2.0000	3.483	6.879	0.093	0.091	0.79456
5025.13	1.9900	3.494	6.855	0.093	0.091	0.79321
5050.50	1.9800	3.487	6.831	0.092	0.090	0.79238
5076.14	1.9700	3.484	6.806	0.092	0.090	0.79144
5102.04	1.9600	3.478	6.782	0.091	0.089	0.79057
5128.20	1.9500	3.470	6.755	0.091	0.089	0.78969
5154.64	1.9400	3.463	6.728	0.090	0.088	0.78872
5181.35	1.9300	3.456	6.699	0.090	0.088	0.78769
5208.33	1.9200	3.449	6.667	0.089	0.087	0.78649
5235.60	1.9100	3.450	6.636	0.089	0.086	0.78508
5263.16	1.9000	3.447	6.612	0.088	0.086	0.78410
5291.00	1.8900	3.442	6.586	0.088	0.085	0.78307
5319.15	1.8800	3.438	6.561	0.087	0.085	0.78207
5347.59	1.8700	3.431	6.534	0.087	0.084	0.78106
5376.34	1.8600	3.428	6.511	0.087	0.084	0.78012
5405.40	1.8500	3.414	6.486	0.086	0.084	0.77939
5434.78	1.8400	3.406	6.454	0.086	0.083	0.77810
5464.48	1.8300	3.402	6.424	0.085	0.082	0.77690
5494.50	1.8200	3.397	6.396	0.085	0.082	0.77575

WN	WL	N	K	DN	DK	R
5524.86	1.8100	3.392	6.370	0.084	0.081	0.77465
5535.56	1.8000	3.382	6.342	0.084	0.081	0.77366
5586.59	1.7900	3.376	6.311	0.083	0.080	0.77236
5617.98	1.7800	3.370	6.281	0.083	0.080	0.77104
5649.72	1.7700	3.367	6.251	0.082	0.079	0.76972
5681.82	1.7600	3.363	6.224	0.082	0.078	0.76850
5714.29	1.7500	3.356	6.196	0.081	0.078	0.76733
5747.13	1.7400	3.351	6.167	0.081	0.077	0.76601
5780.35	1.7300	3.347	6.136	0.080	0.077	0.76462
5813.95	1.7200	3.343	6.109	0.080	0.076	0.76333
5847.95	1.7100	3.338	6.080	0.079	0.076	0.76202
5882.35	1.7000	3.335	6.052	0.079	0.075	0.76066
5917.16	1.6900	3.329	6.027	0.078	0.075	0.75951
5952.38	1.6800	3.326	5.996	0.078	0.074	0.75799
5988.02	1.6700	3.323	5.970	0.077	0.074	0.75675
6024.10	1.6600	3.318	5.941	0.077	0.073	0.75533
6060.61	1.6500	3.315	5.915	0.077	0.073	0.75400
6097.56	1.6400	3.311	5.889	0.076	0.072	0.75279
6134.97	1.6300	3.307	5.863	0.076	0.072	0.75147
6172.84	1.6200	3.301	5.837	0.075	0.071	0.75022
6211.18	1.6100	3.296	5.809	0.075	0.071	0.74885
6250.00	1.6000	3.294	5.784	0.074	0.070	0.74751
6289.31	1.5900	3.286	5.759	0.074	0.070	0.74638
6329.11	1.5800	3.281	5.733	0.074	0.069	0.74505
6369.43	1.5700	3.275	5.707	0.073	0.069	0.74378
6410.26	1.5600	3.270	5.683	0.073	0.069	0.74261
6451.61	1.5500	3.260	5.657	0.072	0.068	0.74146
6493.51	1.5400	3.253	5.627	0.072	0.067	0.73992
6535.95	1.5300	3.251	5.600	0.071	0.067	0.73840
6578.93	1.5200	3.242	5.578	0.071	0.066	0.73738
6622.52	1.5100	3.234	5.549	0.071	0.066	0.73598
6666.67	1.5000	3.229	5.522	0.070	0.065	0.73448
6711.41	1.4900	3.221	5.496	0.070	0.065	0.73317
6756.76	1.4800	3.212	5.469	0.069	0.064	0.73185
6802.72	1.4700	3.205	5.438	0.069	0.064	0.73021
6849.31	1.4600	3.201	5.410	0.069	0.063	0.72860
6896.55	1.4500	3.194	5.385	0.068	0.063	0.72728
6944.44	1.4400	3.186	5.355	0.068	0.062	0.72568
6993.01	1.4300	3.181	5.327	0.067	0.062	0.72405
7042.25	1.4200	3.176	5.300	0.067	0.061	0.72248
7092.20	1.4100	3.170	5.273	0.066	0.061	0.72096
7142.86	1.4000	3.162	5.246	0.066	0.060	0.71947
7194.25	1.3900	3.156	5.217	0.065	0.060	0.71780
7246.38	1.3800	3.151	5.188	0.065	0.059	0.71603
7299.27	1.3700	3.148	5.159	0.065	0.058	0.71424
7352.94	1.3600	3.145	5.133	0.064	0.058	0.71255
7407.41	1.3500	3.141	5.109	0.064	0.058	0.71111
7462.69	1.3400	3.135	5.086	0.063	0.057	0.70972
7518.80	1.3300	3.125	5.061	0.063	0.057	0.70839
7575.76	1.3200	3.118	5.034	0.063	0.056	0.70674

WN	WL	N	K	DN	DK	R
7633.59	1.3100	3.114	5.008	0.062	0.056	0.70512
7692.31	1.3000	3.105	4.985	0.062	0.055	0.70377
7751.94	1.2900	3.096	4.957	0.061	0.055	0.70212
7812.50	1.2800	3.091	4.931	0.061	0.054	0.70042
7874.02	1.2700	3.083	4.908	0.061	0.054	0.69906
7936.51	1.2600	3.071	4.880	0.060	0.053	0.69751
8000.00	1.2500	3.064	4.852	0.060	0.053	0.69571
8064.52	1.2400	3.056	4.827	0.060	0.053	0.69418
8130.08	1.2300	3.046	4.800	0.059	0.052	0.69247
8196.72	1.2200	3.036	4.773	0.059	0.052	0.69089
8264.46	1.2100	3.018	4.743	0.058	0.051	0.68926
8333.33	1.2000	3.022	4.699	0.058	0.050	0.68573
8403.36	1.1900	3.028	4.681	0.057	0.050	0.68413
8474.58	1.1800	3.016	4.656	0.057	0.049	0.68261
8547.01	1.1700	3.009	4.632	0.057	0.049	0.68102
8620.69	1.1600	3.002	4.605	0.056	0.049	0.67914
8695.65	1.1500	2.996	4.581	0.056	0.048	0.67740
8771.93	1.1400	2.987	4.556	0.055	0.048	0.67574
8849.56	1.1300	2.980	4.530	0.055	0.047	0.67392
8928.57	1.1200	2.972	4.503	0.055	0.047	0.67206
9009.01	1.1100	2.965	4.479	0.054	0.046	0.67030
9090.91	1.1000	2.957	4.454	0.054	0.046	0.66857
9174.31	1.0900	2.948	4.431	0.054	0.046	0.66697
9259.26	1.0800	2.937	4.405	0.053	0.045	0.66517
9345.79	1.0700	2.927	4.377	0.053	0.045	0.66326
9433.96	1.0600	2.918	4.350	0.053	0.044	0.66122
9523.81	1.0500	2.910	4.325	0.052	0.044	0.65941
9615.38	1.0400	2.899	4.299	0.052	0.043	0.65759
9708.74	1.0300	2.891	4.270	0.051	0.043	0.65534
9803.92	1.0200	2.883	4.243	0.051	0.042	0.65325
9900.99	1.0100	2.877	4.216	0.051	0.042	0.65108
10000.00	1.0000	2.868	4.192	0.050	0.042	0.64924
10101.01	0.9900	2.863	4.164	0.050	0.041	0.64689
10204.08	0.9800	2.857	4.145	0.050	0.041	0.64535
10309.28	0.9700	2.845	4.122	0.049	0.040	0.64376
10416.67	0.9600	2.836	4.099	0.049	0.040	0.64198
10526.32	0.9500	2.821	4.075	0.049	0.040	0.64029
10638.30	0.9400	2.812	4.047	0.048	0.039	0.63797
10752.69	0.9300	2.802	4.026	0.048	0.039	0.63633
10869.56	0.9200	2.790	4.001	0.048	0.039	0.63448
10989.01	0.9100	2.777	3.976	0.047	0.038	0.63256
11111.11	0.9000	2.766	3.948	0.047	0.038	0.63027
11235.95	0.8900	2.757	3.926	0.047	0.037	0.62848
11363.64	0.8800	2.742	3.903	0.046	0.037	0.62679
11494.25	0.8700	2.729	3.879	0.046	0.037	0.62491
11627.91	0.8600	2.713	3.852	0.046	0.036	0.62286
11764.71	0.8500	2.700	3.822	0.045	0.036	0.62037
11904.76	0.8400	2.689	3.795	0.045	0.035	0.61793
12048.19	0.8300	2.678	3.769	0.044	0.035	0.61577
12195.12	0.8200	2.666	3.741	0.044	0.035	0.61331

WN	WL	N	K	DN	DK	R
12345.68	0.8100	2.657	3.714	0.044	0.034	0.61076
12500.00	0.8000	2.649	3.693	0.043	0.034	0.60887
12658.23	0.7900	2.633	3.669	0.043	0.033	0.60691
12820.51	0.7800	2.623	3.642	0.043	0.033	0.60447
12987.01	0.7700	2.611	3.619	0.042	0.033	0.60245
13157.89	0.7600	2.597	3.595	0.042	0.032	0.60040
13333.33	0.7500	2.587	3.569	0.042	0.032	0.59793
13513.51	0.7400	2.577	3.549	0.041	0.032	0.59603
13698.63	0.7300	2.564	3.527	0.041	0.031	0.59412
13988.89	0.7200	2.549	3.507	0.041	0.031	0.59243
14084.51	0.7100	2.533	3.485	0.041	0.031	0.59069
14285.71	0.7000	2.519	3.463	0.040	0.031	0.58875
14492.75	0.6900	2.503	3.443	0.040	0.030	0.58707
14705.88	0.6800	2.486	3.423	0.040	0.030	0.58542
14925.37	0.6700	2.468	3.404	0.040	0.030	0.58397
15151.51	0.6600	2.448	3.383	0.039	0.030	0.58240
15384.62	0.6500	2.427	3.361	0.039	0.029	0.58082
15625.00	0.6400	2.408	3.336	0.039	0.029	0.57860
15873.02	0.6300	2.391	3.317	0.038	0.029	0.57700
16129.03	0.6200	2.370	3.297	0.038	0.029	0.57561
16393.44	0.6100	2.350	3.277	0.038	0.028	0.57414
16666.67	0.6000	2.328	3.259	0.038	0.028	0.57288
16949.15	0.5900	2.305	3.241	0.038	0.028	0.57183
17241.38	0.5800	2.281	3.223	0.037	0.028	0.57087
17543.86	0.5700	2.252	3.210	0.037	0.028	0.57070
17857.14	0.5600	2.219	3.190	0.037	0.028	0.57001
18181.82	0.5500	2.189	3.171	0.037	0.028	0.56916
18518.52	0.5400	2.156	3.153	0.036	0.028	0.56881
18867.92	0.5300	2.119	3.134	0.036	0.028	0.56861
19230.77	0.5200	2.080	3.113	0.036	0.028	0.56829
19607.84	0.5100	2.039	3.091	0.035	0.028	0.56811
20000.00	0.5000	1.996	3.067	0.035	0.027	0.56784
20408.16	0.4900	1.952	3.043	0.035	0.027	0.56770
20833.33	0.4800	1.903	3.019	0.034	0.027	0.56830
21276.60	0.4700	1.846	2.989	0.034	0.027	0.56874
21739.13	0.4600	1.790	2.949	0.033	0.027	0.56778
22222.22	0.4500	1.736	2.906	0.032	0.027	0.56639
22727.27	0.4400	1.682	2.858	0.032	0.026	0.56423
23255.81	0.4300	1.631	2.806	0.031	0.026	0.56133
23809.52	0.4200	1.583	2.753	0.030	0.026	0.55781
24390.24	0.4100	1.538	2.698	0.029	0.025	0.55387
25000.00	0.4000	1.492	2.644	0.029	0.025	0.55020
25641.03	0.3900	1.442	2.588	0.028	0.024	0.54675
26315.79	0.3800	1.390	2.526	0.027	0.024	0.54254
27027.03	0.3700	1.339	2.454	0.026	0.023	0.53633
27777.78	0.3600	1.296	2.375	0.025	0.022	0.52742
28571.43	0.3500	1.262	2.295	0.024	0.022	0.51622
29411.76	0.3400	1.234	2.217	0.023	0.021	0.50416
30303.03	0.3300	1.207	2.141	0.023	0.020	0.49200
31250.00	0.3200	1.179	2.061	0.022	0.019	0.47834

IRON ROD

PAGE 13

WN	WL	N	K	. DN	DK	R
32258.06	0.3100	1.164	1.976	0.021	0.018	0.46049
33333.33	0.3000	1.155	1.902	0.020	0.017	0.44356
34482.76	0.2900	1.142	1.829	0.020	0.016	0.42701
35714.29	0.2800	1.134	1.757	0.019	0.016	0.40899
37037.04	0.2700	1.127	1.690	0.019	0.015	0.39204
38461.54	0.2600	1.117	1.621	0.018	0.014	0.37444
40000.00	0.2500	1.109	1.553	0.017	0.013	0.35602
41666.67	0.2400	1.104	1.480	0.017	0.012	0.33546
43478.26	0.2300	1.110	1.408	0.016	0.011	0.31287
45454.55	0.2200	1.125	1.347	0.016	0.010	0.29188
47619.05	0.2100	1.141	1.305	0.015	0.010	0.27659

BLANK

THE OPTICAL CONSTANTS OF SMOKE MATERIALS IN THE
SUBMILLIMETER AND MILLIMETER

Larry L. Long, Mark A. Ordal, Robert J. Bell, and
Ralph W. Alexander, Jr.
Physics Department, University of Missouri-Rolla
Rolla, Mo 65401

RECENT PUBLICATIONS:

1. M.A. Ordal, L.L. Long, R.J. Bell, S.E. Bell, R.R. Bell, R.W. Alexander, Jr., and C.A. Ward, Appl. Opt. 22, 1099 (1983).
2. M.A. Ordal, L.L. Long, R.J. Bell, and R.W. Alexander, Jr., 'Optical Properties of Minerals at Millimeter and Submillimeter Wavelengths,' Proceedings of the 1983 CSL Conference on Obscuration and Aerosol Research, J. Farmer and R.H. Kohl, eds., p. 159.
3. R.E. Paul, M.A. Ordal, L.L. Long, R.W. Alexander, Jr., and R.J. Bell, 'Optical Properties of Metals in the Submillimeter and Millimeter Wavelengths,' Proceedings of the 1983 CSL Conference on Obscuration and Aerosol Research, J. Farmer and R.H. Kohl, eds., p 161.

ABSTRACT

Optical constants of a number of naturally occurring minerals in the submillimeter and millimeter wavelength range were determined from the reflectance spectra of pressed powder samples. The effect of the loss of the water of hydration and of surface roughness was studied for two minerals.

I. INTRODUCTION

We begin by pointing out a very important feature of this work. We obtained optical constants by means of Kramers-Kronig transformation of reflectance data using data from this laboratory and the laboratory of Dr. Marvin Querry of the Optical Science Laboratory of the Physics Department, University of Missouri-Kansas City. This means that a very large spectral range is available, which is critically important for accurate results from the Kramers-Kronig transformation. In the case of the natural minerals, having data sets from both laboratories is especially crucial because the reflectance spectra have many features in the region where the two data sets overlap. So-called wing corrections are difficult to make satisfactorily using only one or the other of the two data sets.

The reflectance of a number of natural minerals was measured in the 20-400 cm^{-1} spectral range. This data was combined with that supplied by Dr. Querry (when available) to obtain optical constants for the spectral range from 20 to 4000 cm^{-1} by use of the Kramers-Kronig transformation. Our work, along with that of Querry suggests that gypsum made anhydrous (e.g., by exposure to vacuum) would make a good standard sample for pressed pellet powder studies undertaken by various laboratories.

The optical constants obtained in this project are important for the calculation of atmospheric transmission in the presence of aerosols derived from soils. Recently, Milham has compared the observed transmission in a chamber with the calculated transmission using measured optical constants and current scattering theory.¹ Reasonable agreement was obtained.

We acknowledge the support and cooperation of Dr. Marvin Querry of the University of Missouri-Kansas City. Dr. Querry supplied us with his infrared and visible data on a number of samples prior to publication and provided us with most of his sample materials. We emphasize that having data from both his and our spectral range greatly improved the accuracy of the Kramers-Kronig analysis necessary to obtain the optical constants from the reflectance data. Availability of his samples allowed comparison of the data from both laboratories in the region of spectral overlap. All frequencies in this report are in wavenumbers. Previous work on additional minerals was reported at this conference last year.² For these minerals we now have data available from Querry so we present the optical constants based upon the reflectance from 20 to 4000 cm^{-1} .

II. NATURAL MINERALS

This section begins with some definitions. Optical constants were measured, and are presented in two forms. They may be expressed as a complex index of refraction, $n_0 = n + ik$, or as a complex dielectric constant, $\epsilon = \epsilon_1 + i\epsilon_2$. The ways of expressing the optical constants are related by

$$\epsilon_1^2 = n^2 - k^2$$

and

$$\epsilon_2^2 = 2nk.$$

Table 1 lists the natural minerals whose optical constants were measured as part of this project. Most of them are not available as single crystals. This is particularly true for clay minerals, which, of course, are major constituents of many soils. Because most of these minerals are available only as powders, measurement techniques appropriate to powders had to be used.

Samples were prepared by pressing the powder sample with no binder or matrix into a pellet using relatively high pressure. For many minerals, this results in a pellet with a mirror-like or near mirror-like finish at visible wavelengths. Such surfaces are more than sufficiently smooth for infrared and submillimeter reflectance measurements. Dr. Marvin Querry was the first to fully develop this method and show that it gave good results.³ Because of the excellent results obtained by Querry using pressed pellets, we adopted this method for most of our measurements upon the naturally occurring minerals.

Before discussing the measurements, it is necessary to discuss some of the drawbacks of the pressed pellet technique. A major problem results from the anisotropy of most of the minerals studied. When a pressed pellet is made, the orientation of the crystallites making up the sample is

random or, as we shall see later, partially oriented. This means that the measured reflectance from the pressed pellet is an average of some kind over all the possible orientations of the crystal axes. This drawback is suffered by all methods which use powdered samples, but must be accepted for materials for which single crystals are unavailable. It may be less of a drawback than first appears because any scattering calculation of an aerosol transmission must average over particle orientation and the average obtained from the pressed pellet measurements is probably as good as any. In any case, regions of strong absorption are clearly identified.

Another drawback of the pressed pellet is not all materials are sufficiently soft to make pellets which stick together. For the minerals of this study, pellets could be made from all of them. However, the surface finish varied. Softer materials made pellets with smoother surfaces.

Our conclusion is in agreement with that of Querry, that of the available techniques, the pressed pellet reflectance method is the best for those materials from which pellets can be pressed.

TABLE I. NATURAL MINERALS STUDIED

Sample	Spectral Range*	Comments
Limonite	20-4000 cm^{-1}	Naturally occurring powder
Illite	20-4000 cm^{-1}	Naturally occurring powder
Hematite	70-400 cm^{-1}	Limonite made anhydrous by heating
Gypsum	20-4000 cm^{-1}	Naturally occurring powder
Gypsum	20-400 cm^{-1}	Made anhydrous by exposure to vacuum
Montmorillonite	20-4000 cm^{-1}	Naturally occurring powder
Kaolin	20-4000 cm^{-1}	Naturally occurring powder
Gypsum	70-400 cm^{-1}	Surface roughened by 1 micrometer grit
Gypsum	70-400 cm^{-1}	Surface roughened by 3 micrometer grit
Gypsum	70-400 cm^{-1}	Surface roughened by 8 micrometer grit
Gypsum	70-400 cm^{-1}	Surface roughened by #600 grit
Gypsum	70-400 cm^{-1}	Surface roughened by #400 grit
Montmorillonite	70-400 cm^{-1}	Surface roughened by 1 micrometer grit
Montmorillonite	70-400 cm^{-1}	Surface roughened by 3 micrometer grit
Montmorillonite	70-400 cm^{-1}	Surface roughened by 8 micrometer grit
Montmorillonite	70-400 cm^{-1}	Surface roughened by #600 grit
Montmorillonite	70-400 cm^{-1}	Surface roughened by #800 grit

* Includes reflectance data of Dr. Marvin Querry, Optical Science Laboratory, Physics Department, University of Missouri-Kansas City, when available, for 400 cm^{-1} to 4000 cm^{-1} .

Before pressing into pellets, powders were ground as finely as possible with a mortar and pestle. This powder was then pressed with a commercial infrared pellet die to make one-half inch diameter pellets. Forces on the die ram ranged up to 25 thousand pounds. This process usually produced pellets with a good surface finish and a density ranging from 75 to 90 percent of the bulk density. Evidence is discussed below that a surface layer exists on the pellet which has a density

considerably higher than the average density of the pellet. This means that the reflection measurements are made on a surface layer having a density near the bulk value.

The reflection measurements were made with a commercial RIIC FS-720 Fourier transform spectrometer. A laboratory-built reflection attachment was used to obtain reflection spectra of several samples without the need to break the instrument vacuum when changing samples. A gold or aluminum mirror was used as the reference. In the 20-400 cm^{-1} region, no correction needs to be made for the reflectivity of these reference mirrors.

The spectrometer was controlled by an IBM PC which acquired the interferogram and then computed the Fourier transform. Several interferograms could be co-added (averaged) if needed to improve the signal to noise ratio. The resulting reflectance spectra were then Kramers-Kronig transformed to obtain ϵ_1 and ϵ_2 , or n and k . When reflectance data from Querry was available it was added on to our data set before the Kramers-Kronig transform was performed.

LIMONITE

Limonite is harder than some materials, but pellets with good surface finish could be pressed. The measured reflectance spectrum is shown in Fig. 1. The resulting index of refraction is plotted in Fig. 2.

In addition to the powder sample, a solid piece of limonite was ground and polished. The reflectance of this sample is shown in Fig. 3. Note there are some differences between the powder sample and the rock sample. This is probably due to partial orientation of the crystallites in the rock during its formation.

ILLITE

Illite is yet another naturally occurring clay type material. The reflectance of a pressed pellet is shown in Fig. 4 and the index of refraction is shown in Fig. 5.

HEMATITE

Hematite is the anhydrous form of limonite. Our samples were produced by heating the light orange limonite until it turned dark red. Pellets were pressed from this red powder. The measured reflectance is shown as Fig. 6. As no infrared data were available, only the region from 20 to 400 cm^{-1} is shown for the index of refraction in Fig. 7. The appreciable changes in the spectra seen upon loss of the water of hydration in the change from limonite to hematite are discussed below.

III. SURFACE ROUGHNESS

The effect of surface roughness was studied to make sure that the surfaces of the pressed pellets were sufficiently smooth to not influence the reflectance measurements. That this is indeed

true can be seen from Fig. 8. Plotted there is the reflectance as a function of wavenumber for pellets of montmorillonite 'polished' with abrasive papers of various grit sizes from 1 micrometer to #400 grit. There are at least two important observations to be made. Note that roughening with 1 micrometer grit and 8 micrometer grit lead to identical spectra. We interpret this as meaning roughness at the level of 8 micrometers does not influence the IR measured reflectance. Second, the fact that polishing with 1 micrometer grit reduces the reflectance of the pellet as pressed indicates that the polishing operation is removing a thin layer of density greater than the average density of the pellet. It is this evidence that convinces us that the measured reflectance (and hence the derived optical constants) corresponds more closely to material of nearly the density of single crystals than the measured average density of the pellets would indicate.

The effects of surface roughness upon reflectance has been studied in the near infrared and visible by a number of workers. For example, see the paper by H. R. Bennett and J. O. Porteus⁴. Their analysis suggests that the reflectance should depend upon the wavelength, λ , and the RMS surface roughness, s , in the form:

$$R = R_0 \exp [-(As/\lambda)^2] \quad \text{Eq. (1)}$$

where R_0 is the reflectance of the smooth surface. Figure 9 shows a fit to the montmorillonite reflectance data for surfaces polished with 8 micrometer, #600 and #400 grits. The fit with Eq.(1) is shown where s is chosen to give a good fit and is considerably smaller than the grit size. The significance of this fit should not be over emphasized because the model is being pushed rather hard to use it for our wavelength region and roughness. If the data is plotted as a function of wavenumber, instead of wavelength, a linear fit as a function of wavenumber works quite well, as shown in Fig. 10. The significance of this is not obvious.

A gypsum pellet was also polished with several grit sizes, this time starting with the coarse #400 grit and then with successively finer grits. Gypsum was chosen because it has several strong absorptions between 100-400 cm^{-1} . The results are shown in Fig. 11. Once again the results suggest the removal of a thin surface layer of density higher than the average for the pellet.

IV. LOSS OF WATER HYDRATION

GYPSUM

Figure 12 shows the measured reflectance of a pressed pellet of gypsum powder. As discussed above, this spectrum was combined with the spectrum supplied by Querry for 400-4000 cm^{-1} and the Kramers-Kronig transformation used to obtain n and k plotted in Fig. 13. This, of course, is an average over the various orientations of the gypsum crystallites at the pellet surface. Gypsum is

available as a single crystal and Querry has made comparisons between the spectra of a single crystal and the powder sample in the infrared in his talk at the CSL Conference on Aerosols and Obscurants in 1983³.

ANEHYDROUS GYPSUM

Naturally occurring gypsum contains waters of hydration. Heating gypsum or exposing it to vacuum causes the loss of this water. The resulting anhydrous gypsum is called anhydrite. We studied the effect of this loss of water upon the optical constants. The pellet sample was prepared from gypsum as described in the previous section. It was then exposed to vacuum for a number of days which produced a surface anhydrite layer which retained most of the surface finish quality of the original gypsum pellet. The reflectance of this pellet is shown as Fig. 14. Data from Querry were not available for this sample so the optical constants obtained by Kramers-Kronig transform of our reflectance spectrum from 20 to 400 cm^{-1} . The real and imaginary parts of the dielectric function are shown in Fig. 14. Note the considerable differences between the spectra of the hydrated and anhydrous gypsum. The ease with which gypsum loses its water of hydration suggests that an aerosol formed in a low humidity atmosphere would probably consist of a mixture of hydrated gypsum particles and particles of gypsum that had lost various amounts of water.

When limonite loses its water of hydration, it becomes hematite. The spectra of these two materials have already been discussed above.

IV. COMMENTS ON KRAMERS-KRONIG ANALYSIS

One of the difficulties with the Kramers-Kronig analysis is the need for data over a large frequency range. Typically one needs to make a 'wing correction' to fill in the regions of the spectrum where one has no measurements available. A number of methods have been developed for making wing corrections, but all such approximations have difficulty if strong absorptions exist in the spectral region where measurements have not been made. As a result, any wing correction is doubtful at best unless some information is known about the resonance. The best method is to use near-infrared data made available by Dr. Querry of U.M.K.C.. Figure 16 presents the optical constants n and k for gypsum in the 0 - 400 cm^{-1} spectral range in three forms first U.M.R., second U.M.K.C. and finally the combined set. The main differences are located at the edge of the data sets. Notice that the effect of the U.M.R. data is to basically extend the U.M.K.C. data set and improve the resolution below 400 cm^{-1} .

This example indicates how important it is to have data over a very wide frequency range such as that covered by the combination of the University of Missouri-Rolla and University of

V. KAOLIN AND MONTMORILLONITE

At last year's CSL conference, Querry³ and we² reported the optical constants of kaolin and montmorillonite, but at that time we did not have the Kramers-Kronig analysis available for the combined data sets. We have now done this. Kaolin is a soft material which presses into pellets with a good surface finish. The index of refraction of Kaolin from 20 to 4000 cm^{-1} obtained from the Kramers-Kronig analysis of the combined Rolla and Kansas City reflectance data is shown in Fig. 17. Chemically pure Kaolin was also measured but showed no significant differences from the naturally occurring material. X-ray diffraction and x-ray fluorescence indicated the naturally occurring material was 90% kaolinite, 5% muscovite, and 5% quartz.

The index of refraction of a pressed pellet of montmorillonite is shown in Fig. 18. X-ray diffraction and x-ray fluorescence measurements indicated the following composition for this naturally occurring material: montmorillonite 80%, quartz 20%.

VI. FUTURE WORK

Currently we are measuring pressed pellets of a number of additional minerals. Measurements will also be extended to longer wavelengths using a liquid-helium cooled detector. This work will continue to be done in cooperation with Dr. Querry so that advantages of the extremely wide spectral range will be available.

VII. SUMMARY

Optical constants have been measured for a number of naturally occurring minerals. The effect of loss of the water of hydration has been studied. The effects of surface roughness upon reflectance measurements has been determined and found to be negligible in our spectral region. The importance of having measurements over as wide a spectral range as possible is emphasized. This work is being prepared for publication in the near future.

VIII. REFERENCES

1. M.E. Milham and David H. Anderson, 'Extinction by explosively dispersed soil particles,' *Appl. Opt.* **22**, 3672 (1983).
2. M.A. Ordal, L.L. Long, R.J. Bell and R.W. Alexander, Jr., 'Optical properties of Minerals at Millimeter and submillimeter wavelengths,' Proceedings of the 1983 CSL Scientific Conference on Obscuration and Aerosol Research, J. Farmer and R.E. Kohl, eds., p 159.
3. M.E. Querry, 'Optical properties of compressed powders,' Proceedings of the 1983 CSL Scientific Conference on Obscuration and Aerosol Research, J. Farmer and R.E. Kohl, eds, p. 147.
4. H.E. Bennett and J.O. Porteus, 'Relation between surface roughness and specular reflectance at normal incidence,' *J. Opt. Soc. Am.* **51**, 10 (1965).

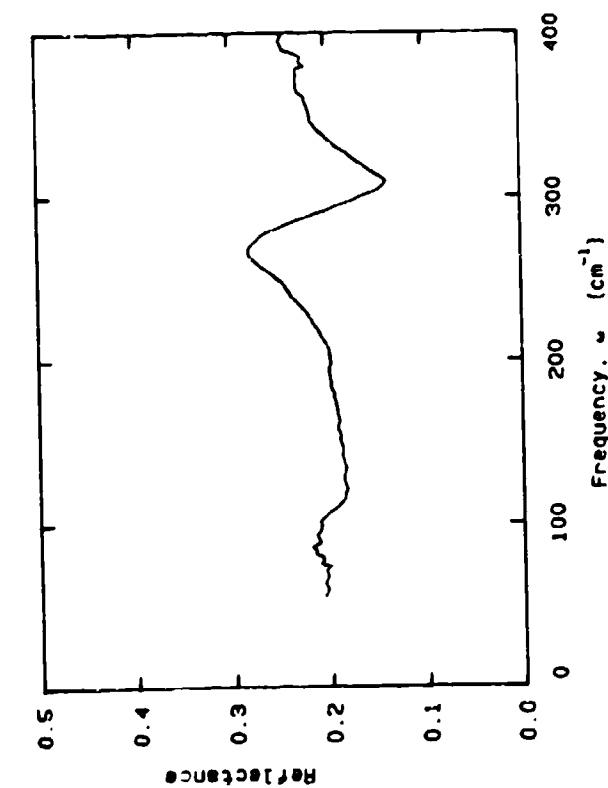


FIGURE 1. REFLECTANCE OF PRESSED LIMONITE POWDER.

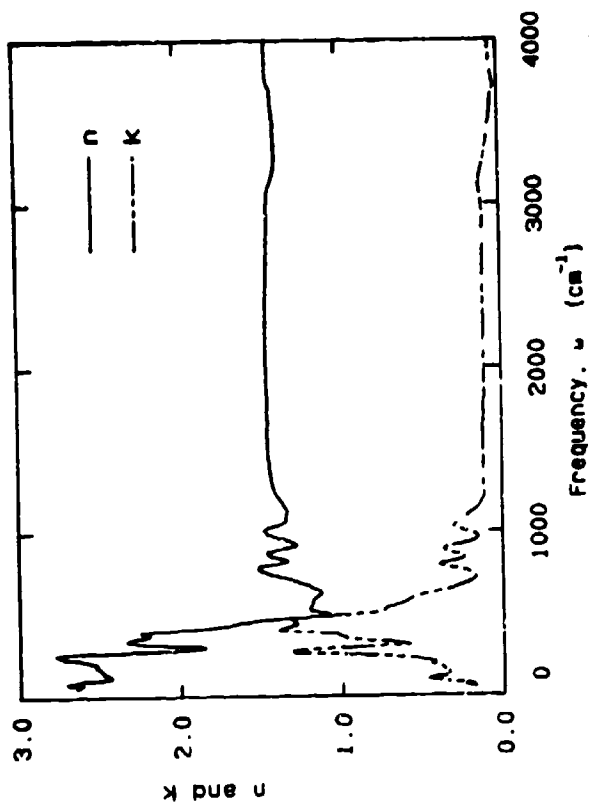


FIGURE 2. n AND k OF PRESSED LIMONITE POWDER.

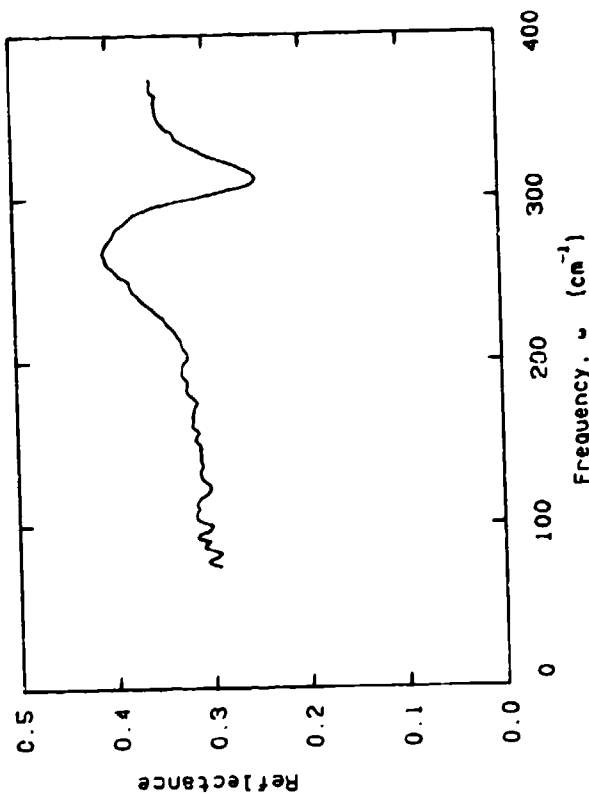


FIGURE 3. REFLECTANCE OF LIMONITE ROCK SAMPLE.

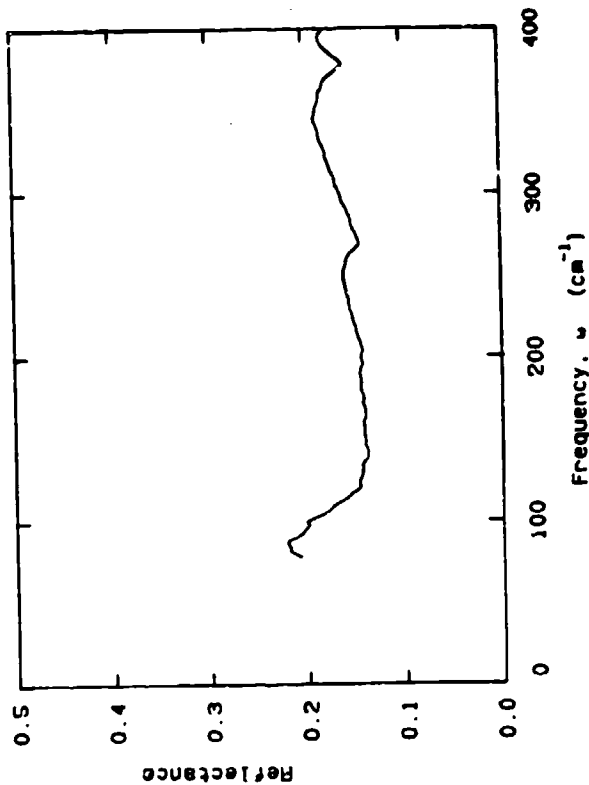


FIGURE 4. REFLECTANCE OF PRESSED ILLITE POWDER.

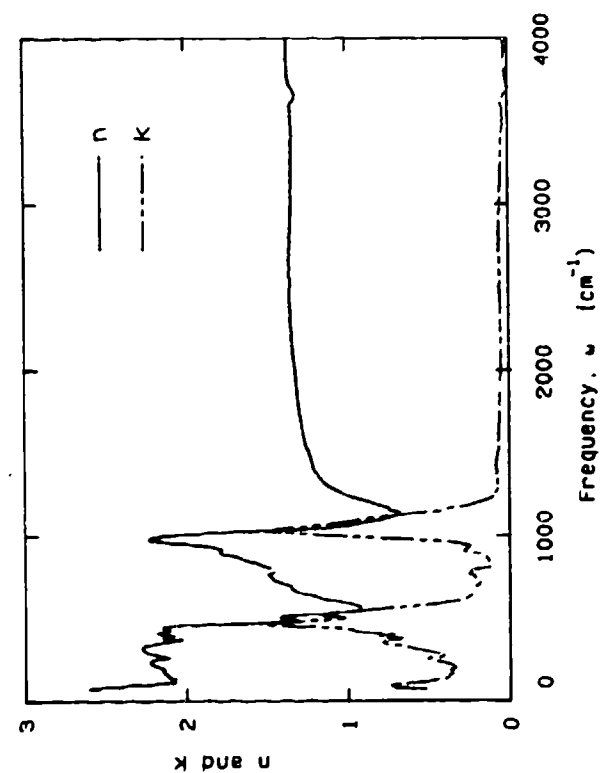


FIGURE 5. n AND k OF PRESSED ILLITE POWDER.

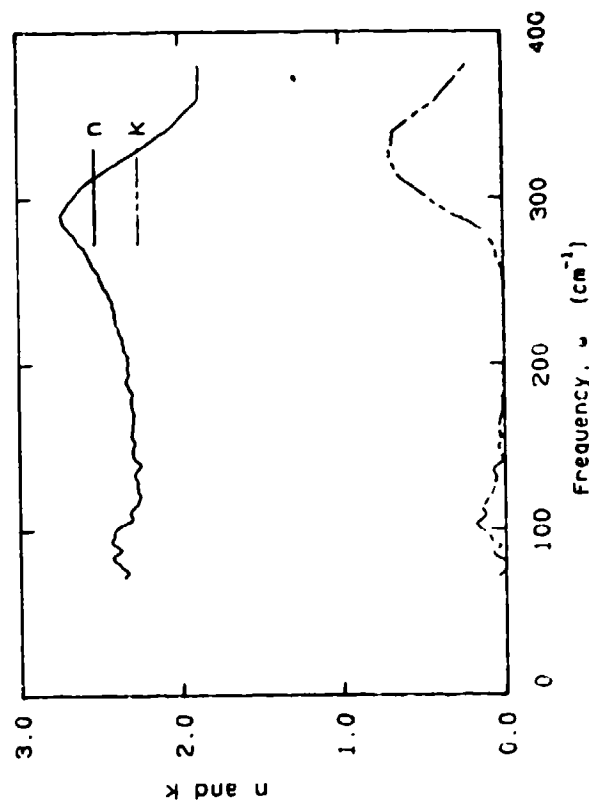


FIGURE 7. n AND k OF PRESSED HEMATITE POWDER.

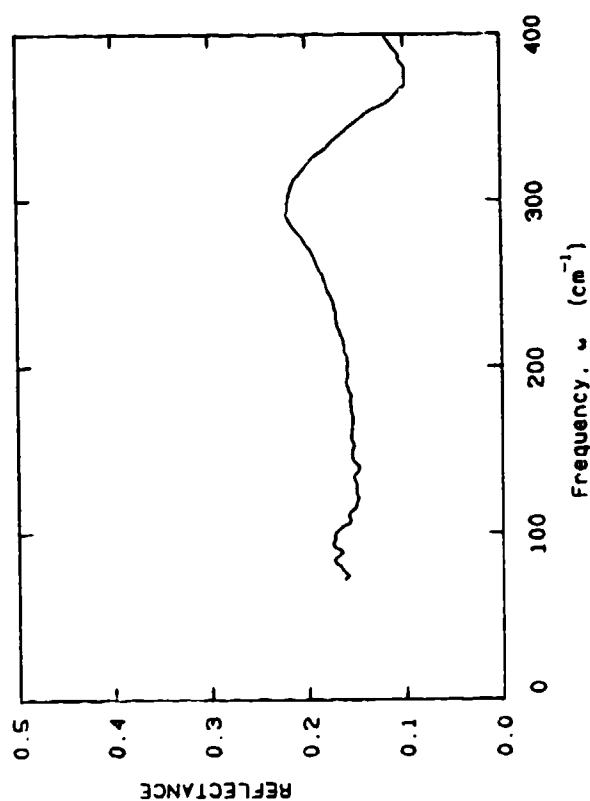


FIGURE 6. REFLECTANCE OF PRESSED HEMATITE POWDER.

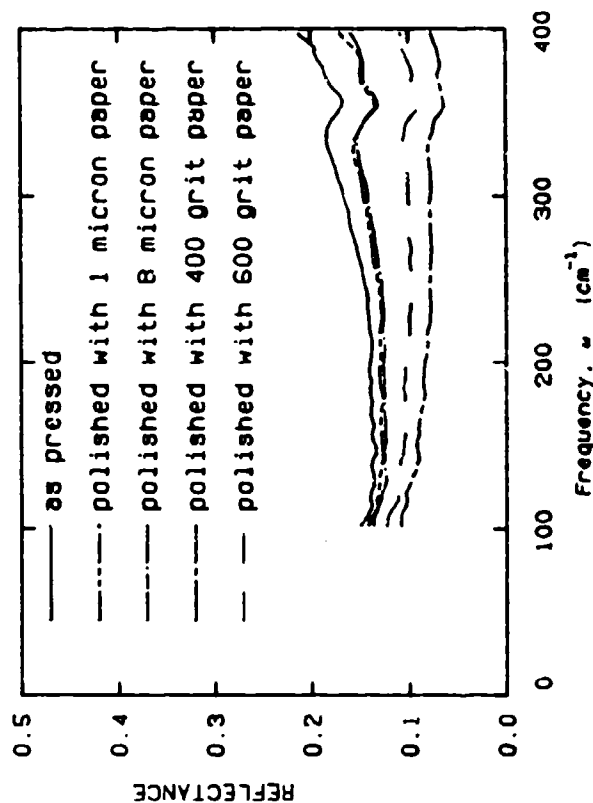


FIGURE 8. REFLECTANCE OF ROUGHENED MONOCRILLONITE.

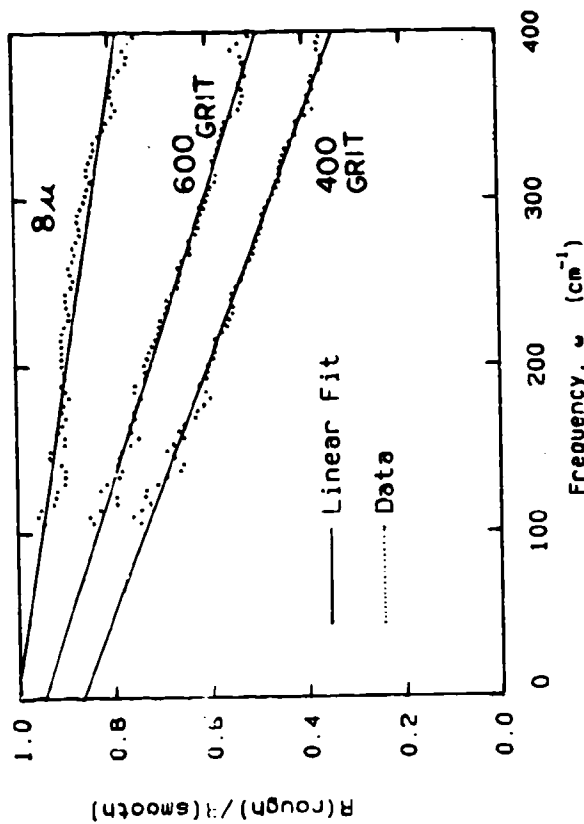


FIGURE 10. STRAIGHT LINE FIT OF R VS WAVELENGTH FOR REFLECTANCE SHOWN IN FIG. 8.

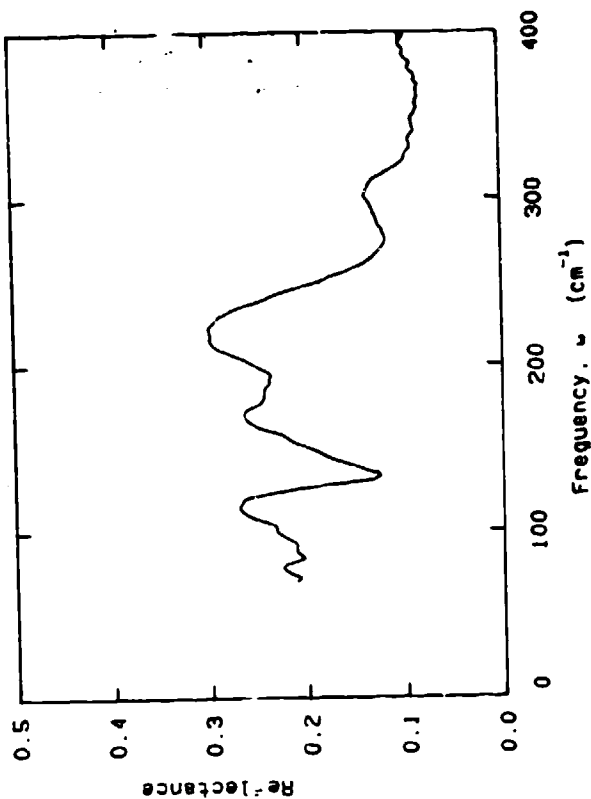


FIGURE 12. REFLECTANCE OF PRESSED GYPSUM POWDER.

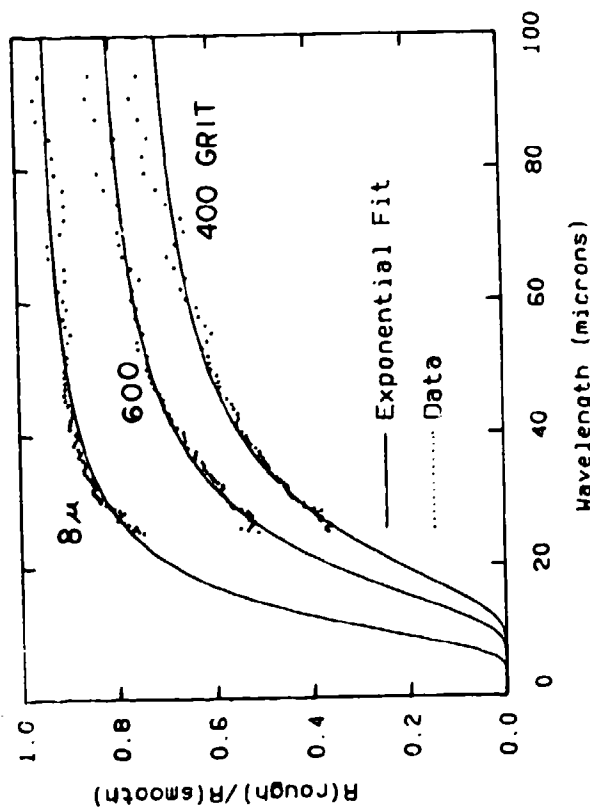


FIGURE 9. EQ. (1) FITTED TO REFLECTANCE OF FIG. 8.

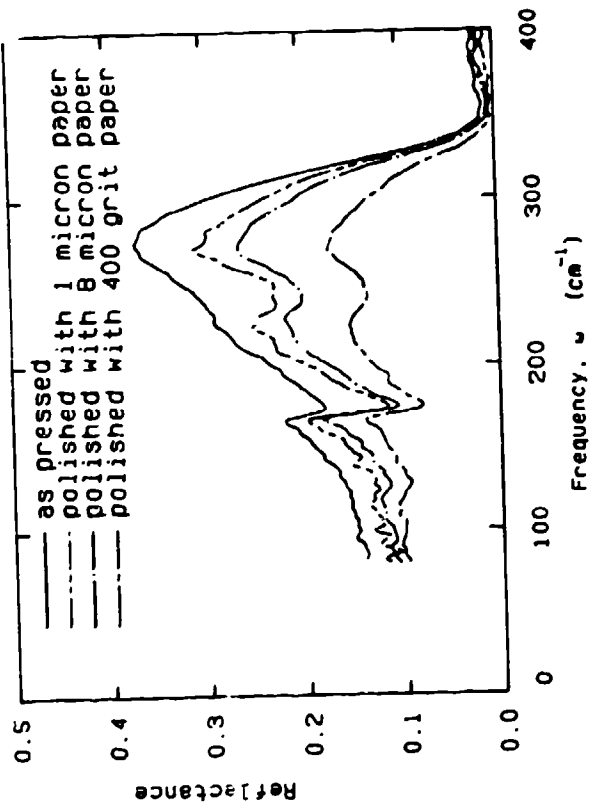


FIGURE 11. REFLECTANCE OF ROUGHENED GYPSUM.

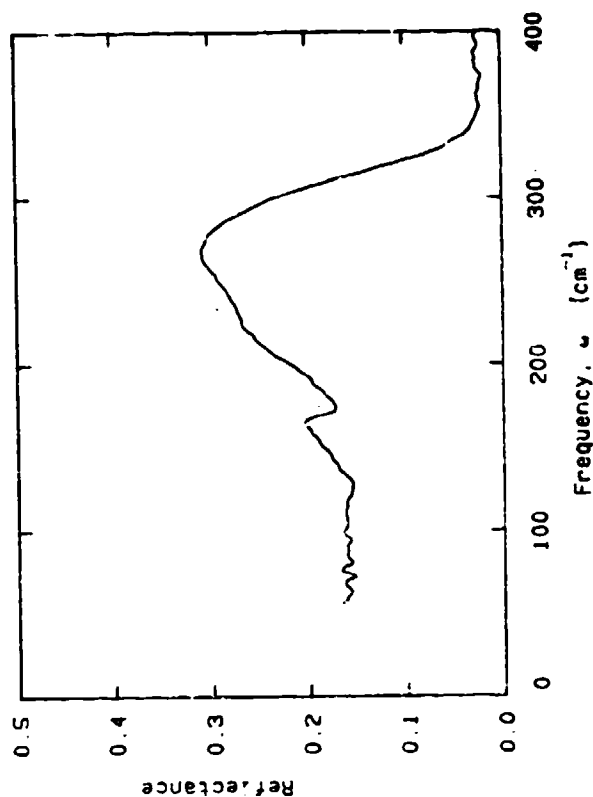


FIGURE 14. REFLECTANCE OF ANHYDROUS GYPSUM POWDER.

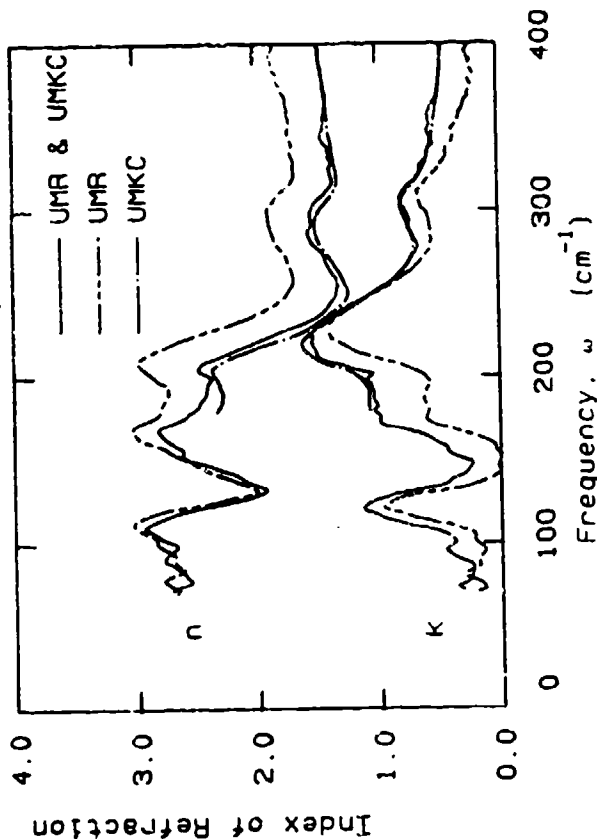


FIGURE 16. n AND k OF PRESSED GYPSUM POWDER. See text for details of the three data sets used.

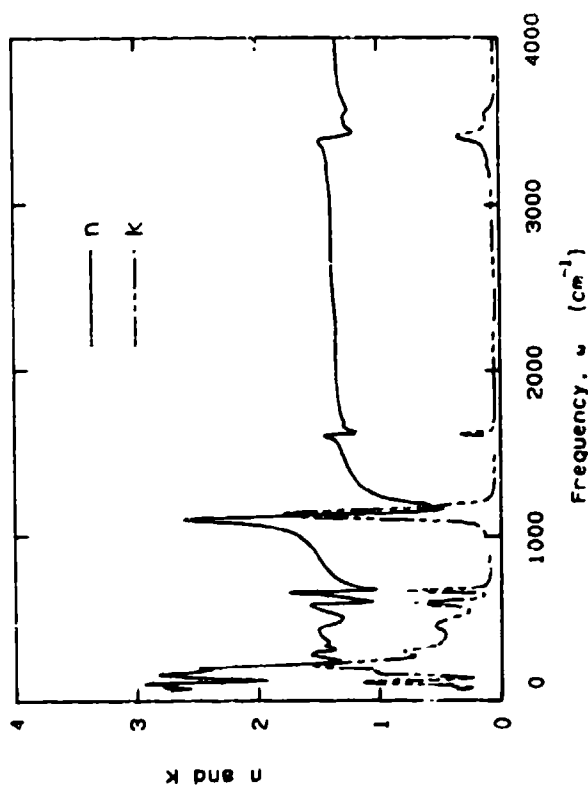


FIGURE 13. n AND k OF PRESSED GYPSUM POWDER.

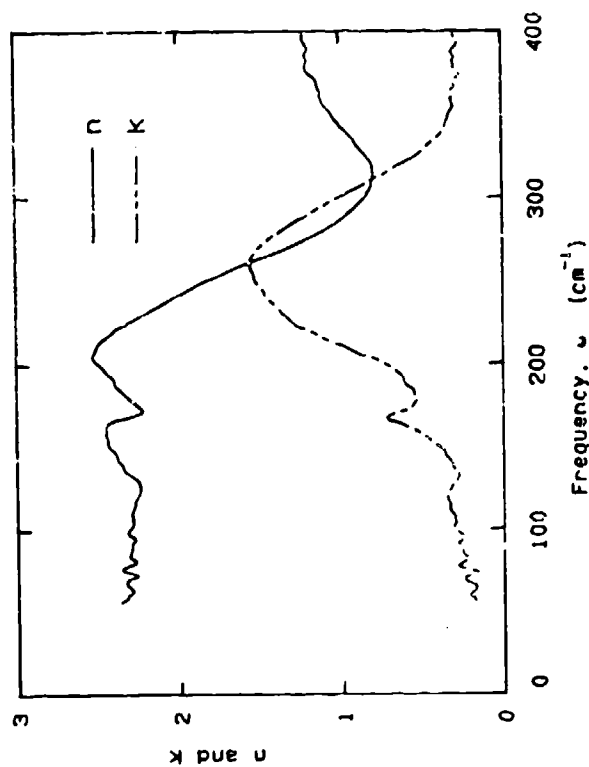


FIGURE 15. n AND k OF ANHYDROUS GYPSUM POWDER.

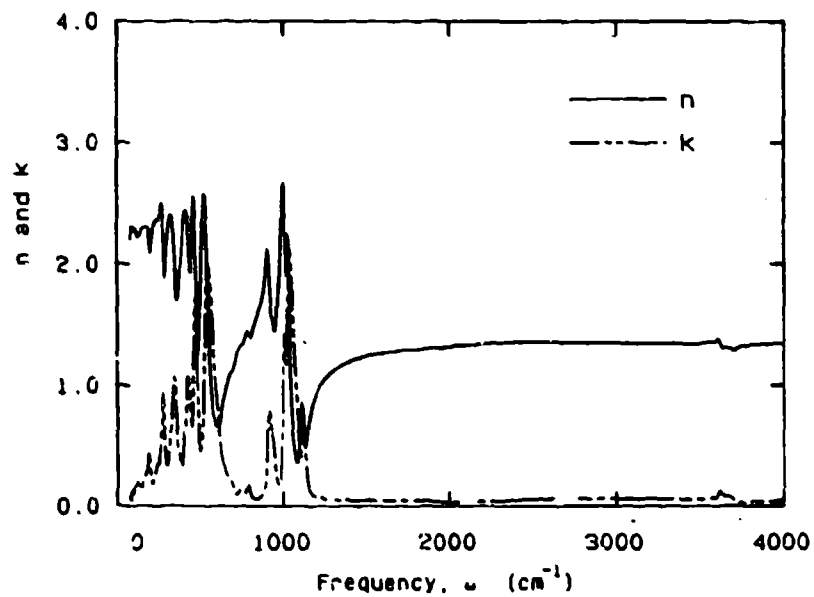


FIGURE 17. n AND k FOR PRESSED KAOLINITE

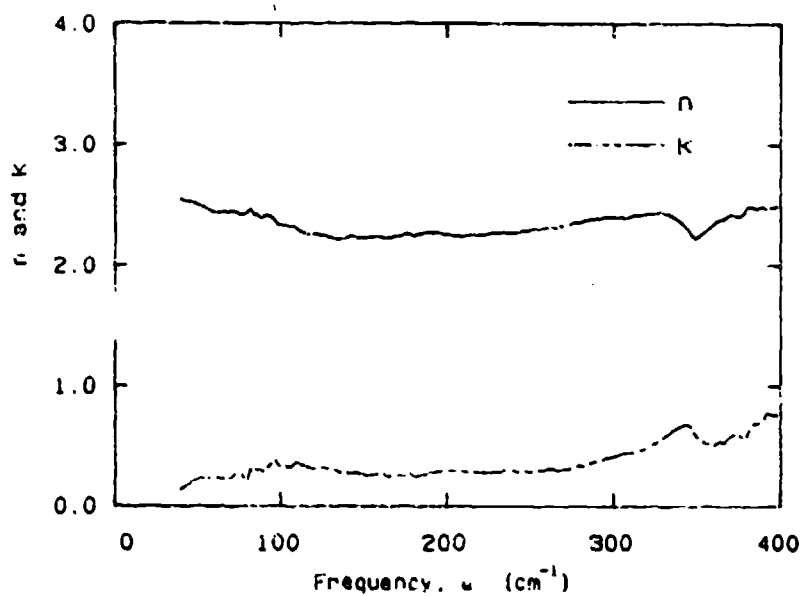


FIGURE 18. n AND k FOR PRESSED MONTMORILLONITE

Metals and Graphite: Predicting Optical Properties in the

Submm and mm Ranges*

M. A. Ordal, L. L. Long, R. A. Paul, R. W. Alexander, Jr., and

Robert J. Bell

Physics Department, University of Missouri-Rolla

Rolla, MO 65401

RECENT PUBLICATIONS:

1. M. A. Ordal, L. L. Long, R. J. Bell, S. E. Bell, R. R. Bell, R. W. Alexander, Jr., and C. A. Ward, Appl. Opt. **22**, 1099 (1983).
2. M. A. Ordal, L. L. Long, R. J. Bell, and R. W. Alexander, Jr., 'Optical Properties of Minerals at Millimeter and Submillimeter Wavelengths'; Proceedings of the 1983 CIL Conference on Obscuration and Aerosol Research, J. Farmer and R. H. Kohl, eds. p. 159.
3. R. E. Paul, M. A. Ordal, L. L. Long, R. W. Alexander, Jr., and R. J. Bell, 'Optical Properties of Metals in the Submillimeter and Millimeter Wavelengths'; Proceedings of the 1983 CIL Conference on Obscuration and Aerosol Research, J. Farmer and R. H. Kohl, eds., p. 161.

ABSTRACT

Optical constants in the FIR, submm, and mm have been studied for graphite and fifteen metals: Al, Cr, Co, Cu, Au, Fe, Mo, Pb, Ni, Pd, Pt, Ag, Ti, V, and W. Special attention has been paid to Fe and graphite. The optical properties of Fe are well described by the free electron Drude model with the scattering frequency $\omega_\tau = 147 \text{ cm}^{-1}$, and the plasma frequency $\omega_p = 3.29 \times 10^4 \text{ cm}^{-1}$. These values yield the optical resistivity $\rho_{\text{opt}} = 8.15 \times 10^{-6} \text{ } \Omega \text{ cm}$. The optical properties of a pressed pellet of graphite are dominated in these spectral ranges by an overdamped harmonic oscillator and virtually no free carriers $N < 10^{19} \text{ cm}^{-3}$. The resonance frequency, ω_{10} , for this overdamped oscillator is about 99.5 cm^{-1} with a damping frequency $\Gamma = 705 \text{ cm}^{-1}$, a high frequency dielectric constant $\epsilon_\infty = 49.8$ and an oscillator strength $S_0 = 3.04 \times 10^3$. A new technique using the first derivatives with respect to frequency, ω , of either $-\epsilon_1$ or ϵ_2 has been introduced for the dielectric function $\epsilon_0 = \epsilon_1 + i\epsilon_2$. In this technique if only $-\epsilon_1$ vs. ω is known experimentally (or only ϵ_2 vs. ω is known), one can obtain both Drude model parameters ω_τ and ω_p in both cases at all frequencies for which the Drude model applies.

I. Introduction

We were asked to measure the optical constants of Fe and graphite in the submm and mm ranges. In order to design experiments, to interpret and predict results, and to understand the optical properties, we had to include other metals in our general studies. New data interpolation techniques had to be developed to smooth experimental data for further analysis. In the case of graphite, lattice effects in the form of an overdamped harmonic oscillator are introduced.

The optical properties of Fe found in the open literature vary considerably.^{1,2} In the submm and mm ranges, the reflectance of metals is generally over 99 percent making simple reflectance or transmission experiments extremely difficult. This has forced us to reconsider known, more elaborate, experimental techniques and to design new experimental approaches. Above about 10^3 wavenumbers band effects become important for most metals.²

Graphite has lower reflectances at these frequencies and so direct reflectance measurements have been made. However, the measured optical properties have forced the introduction of phonon or lattice effects³ which dominate in the submm range and in a good part of the mm range.

To use updated experimental studies, we utilize the visible, IR, and FIR iron data of Querry⁴ and our submm and mm data for graphite. We believe earlier Fe data¹ should be replaced with the results of Querry's recent experiments.

For free electron dominated metals⁵⁻⁷ ϵ_1 is negative whenever $\omega < \omega_p$, as is the case for all metals studied so far at the low frequencies. For lattice dominated materials⁸ such as graphite one finds $\epsilon_1 > 0$ in the submm and at least in most of the mm range. In the wavenumber range $\omega \leq 2 \text{ cm}^{-1}$, free electron effects may again dominate yielding overall negative ϵ_1 's for graphite.

In this article all frequencies are in wavenumbers, and all resistivities are in Ohm cm. Everything else is in cgs units.

12. Utilization of IR Literature

The basic equations needed for the analysis of the open literature data begin with the general definitions

$$\epsilon_0 = \epsilon_1 + i\epsilon_2 = n_0^2 = (n+ik)^2 = (n^2 - k^2) + i(2nk) \quad (1)$$

where ϵ_0 is the complex dielectric function, and n_0 is the complex index of refraction.

For the free electron model⁵⁻⁷ with an added damped harmonic oscillator⁸ included, the dielectric functions become

$$\epsilon_1 = \epsilon_\infty - \frac{\omega_p^2 / \omega_\tau^2}{1 + \left[\frac{\omega}{\omega_\tau}\right]^2} + \frac{(\delta\epsilon)(1 - \omega^2/\omega_{TO}^2)}{\left[1 - \omega^2/\omega_{TO}^2\right]^2 + \left[\Gamma^2 \omega^2/\omega_{TO}^4\right]} \quad (2)$$

and

$$\epsilon_2 = \frac{\omega_p^2 / (\omega_\tau \omega)}{1 + \left[\frac{\omega}{\omega_\tau}\right]^2} + \frac{(\delta\epsilon)(\omega/\omega_{TO}^2)}{\left[1 - \omega^2/\omega_{TO}^2\right]^2 + \left[\Gamma^2 \omega^2/\omega_{TO}^4\right]} \quad (3)$$

where ω_τ is the free electron scattering frequency, ω_p is the free electron plasma frequency, $(\delta\epsilon) = (\epsilon_0 - \epsilon_\infty)$, ϵ_0 is the low frequency dielectric function, ϵ_∞ is the high frequency dielectric constant, Γ is the damping frequency for the damped oscillator, and ω_{TO} is the transverse optical frequency or resonant frequency.

At frequencies such that the Drude model is valid, one may obtain both ω_τ and ω_p at a given frequency ω from¹

$$\omega_\tau = \frac{\omega \epsilon_2}{1 - \epsilon_1} \quad (4)$$

and

$$\omega_p^2 = (1 - \epsilon_1)(\omega_\tau^2 + \omega^2). \quad (5)$$

At low frequencies it is well known that

$$\epsilon_2 = \frac{\omega_p^2}{\omega \omega_\tau} = \frac{60}{\omega \rho_{opt}} \text{ (Ohm cm)} \quad (6)$$

As an example, we used Query's Fe data⁴ and applied Eqs. (4) and (5) to obtain ω_{τ} and ω_p . With $\omega_{\tau} = 147 \text{ cm}^{-1}$ and $\omega_p = 3.29 \times 10^4 \text{ cm}^{-1}$ for Fe, we extrapolated $-\epsilon_1$ and ϵ_2 into the submm and mm ranges as can be seen in Fig. 1. Query's reflection data, Fig. 2 was analyzed using the Kramers-Kronig relations^{9,10} to yield either n and k vs. ω as shown in Fig. 3 or $-\epsilon_1$ and ϵ_2 as shown in Fig. 1. Using Eq. (6) we obtained $\rho_{\text{opt}} = 8.15 \times 10^{-6} \text{ Ohm cm}$.

For another example from the open literature, we show a similar set of data for Au in Fig. 4. The reflectance data had been analyzed by others to obtain $-\epsilon_1$ and ϵ_2 vs. ω in the literature.¹ We fit the data using Eqs. (4) and (5). One sees that both materials have high frequency band problems², but as ω decreases they behave like free electron dominated metals. For the Au, we obtained $\omega_{\tau} = 215 \text{ cm}^{-1}$, $\omega_p = 7.28 \times 10^4 \text{ cm}^{-1}$ and $\rho_{\text{opt}} = 2.43 \times 10^{-6} \text{ Ohm cm}$.

We have studied many metals to obtain a feel for the Drude model parameters ω_{τ} , ω_p and ρ_{opt} . We have done the analyses as we did for Fe and have obtained the results for 15 metals given in Table 1. For comparison ρ_{opt} and ρ_{dc} are given for each metal along with ω_{τ} and ω_p . Experience has taught us that the Drude model does well at low frequencies - even better than generally thought. The trend is that new more precise optical data come closer to the predictions of the model based on ρ_{dc} in Eq. (6) than previously found. On occasion it seems that some values of ρ_{dc} should be remeasured.

Figures 5a and 5b show the values of ρ_{opt} and ρ_{dc} (given in Table 1) plotted against one another. All of the good conductors follow the Drude model quite well as can be seen in Fig. 5a. However, only a few of the higher resistivity metals exhibit good agreement with the Drude model. It could be that both better IR and/or resistivity measurements should be made.

In studying the optical properties of metals one needs to know which bulk and skin effects are dominant in given frequency and temperature ranges. Is the metal obeying the rules for the classical, relaxation, transmission, anomalous skin effect, or anomalous reflection regions?⁵⁻⁷ To grapple with the problem one prepares ω_{τ} vs. ω plots (called Casimir-Wooten diagrams) for each metal.^{7,12} The boundaries between the regions for Fe at room temperature are shown in Fig. 6. We used $\omega_{\tau} = 147 \text{ cm}^{-1}$, $\omega_p = 3.29 \times 10^4 \text{ cm}^{-1}$ and the parameter $X = 14.4 \text{ cm}^{-1}$ from

$$X = \left[\frac{V_F}{2\pi c} \right] \omega_p = \left[\frac{3 \pi^3}{80 c^2 m} \right]^{1/3} \omega_p^{5/3} = 4.249 \times 10^{-7} \omega_p^{5/3} \quad (7)$$

where V_F is the Fermi velocity.¹³ Query's Fe Drude-like data is represented by the solid horizontal bar at $\omega = 147 \text{ cm}^{-1}$. The dashed line is also his data but is in a non-Drude-like regime at $\omega \geq 800 \text{ cm}^{-1}$ due to band effects.² The squiggles⁷ in each region illustrate a multiply scattered electron's path as it scatters from the surface and other targets (such as phonons, other electrons, defects, etc.) in a high frequency radiation field. The metal surface (represented by the vertical solid line) has photons

incident from the left. The vertical dashed line is at the skin depth from the surface. Of course, the scattering is a function of both the scattering frequency ω_c and the frequency of the radiation. A good reference is Wooten's book⁷, but one notes his ω is in radians per second i.e., $\omega = 2\pi\nu$ (with ν in Hz) and his τ is in seconds. That is, Wooten's τ and our ω_c are related by the expression $\tau = 1/(2\pi\omega_c)$, where ω_c is in wavenumbers and $c = 3 \times 10^{10}$ cm/sec.

III. Slopes and the Drude Model

In the submm and mm ranges, one is dealing with a two parameter (ω_c and ω_p) theory.⁵⁻⁷ Often an experiment will yield ϵ_2 and not $-\epsilon_1$ or vice versa. If the data follows the Drude model, the slopes of ϵ_2 vs. ω (or $-\epsilon_1$ vs. ω) can be used with ϵ_2 (or $-\epsilon_1$) to obtain both ω_c and ω_p and thus $-\epsilon_1$ (or ϵ_2).

Taking derivatives yields the exact Drude model results if one only knows ϵ_2 and wants ϵ_1 :

$$D = -\omega \frac{d(\ln(\epsilon_2))}{d\omega} \quad (8)$$

which gives the exact results (at all Drude valid frequencies) of:

$$\omega_c = \omega \left[\frac{(3-D)}{(D-1)} \right]^{1/2} \quad (9)$$

and

$$\omega_p = [\epsilon_2 \omega_c \omega (1 + \omega^2/\omega_c^2)]^{1/2} \quad (10)$$

Note that there are simple integral limits (1,2,3) on D:

$$\begin{aligned} \omega^2 \ll \omega_c^2 &\rightarrow D=1 \\ \omega = \omega_c &\rightarrow D=2 \\ \omega^2 \gg \omega_c^2 &\rightarrow D=3 \end{aligned} \quad (11)$$

If one only has ϵ_1 he can obtain ϵ_2 using these exact equations from the Drude model:

$$E = -\omega \frac{d[\ln(1 - \epsilon_1)]}{d\omega} \quad (12)$$

which gives the exact results (at all Drude valid frequencies) of

$$\omega_c = \omega [(2-E)/E]^{1/2} \quad (13)$$

and

$$\omega_p = [(1-s_1)\omega_c^2 [1+\omega^2/\omega_c^2]]^{1/2} \quad (14)$$

with integer (0, 1, 2) limits on E:

$$\begin{aligned} \omega << \omega_c &\rightarrow E=0 \\ \omega = \omega_c &\rightarrow E=1 \\ \omega >> \omega_c &\rightarrow E=2 \end{aligned} \quad (15)$$

The magnitude of D or E indicates whether or not the s_1 or s_2 data is above or below the crossover frequency for $-s_1$ equal s_2 found at $\omega = \omega_c$ i.e., the boundary between the classical and relaxation regimes. If D and E as calculated are outside their ranges of $1 \leq D \leq 3$ or $0 \leq E \leq 2$, the metal is not Drude-like at that frequency. In fact, the ranges on D and E can sometimes be used to check whether or not a metal is Drude-like at some frequency. If the metal is Drude-like, one can ascertain at a given ω whether $\omega_c < \omega$ or $\omega_c \geq \omega$. That is, the metal is in the classic region ($\omega < \omega_c$) if $1 \leq D \leq 2$ and $0 \leq E \leq 1$ or it is in the relaxation region ($\omega > \omega_c$) if $2 \leq D \leq 3$ and $1 \leq E \leq 2$. If the sample is not Drude-like the computed D and E's can fall outside of their ranges of 1 to 3 for D and 0 to 2 for E. For calculations of other sorts it is interesting to note that

$$D = E + 1 \quad (16)$$

at all Drude-like frequencies. In practice we often smooth¹⁴ the data before taking derivatives, and we keep the frequency intervals small.

In Table 2 to illustrate the slope method, using Fe as an example, we evaluated the $-s_1$ vs ω data to obtain the ω_c 's and ω_p 's in the first two columns. Likewise, solely with s_2 vs ω data, we obtained the results in the last two columns. These numbers are to be compared to $\omega_c = 147 \text{ cm}^{-1}$ and $\omega_p = 3.29 \times 10^4 \text{ cm}^{-1}$ found with the fitting of the complete IR data^{1,14,15} using Eqs. (4) and (5). For determining ω_c the slope method using $-s_1$ yields the best values. The best results for ω_p would come from averaging the values found in both slope methods.

In Table 3 for fifteen samples^{15,16} we compare ω_c 's obtained by the slope method used on s_2 vs ω data, Eqs. (9) and (10), with those found by the fitting method (Table 1).^{1,2,15}

IV. Using Surface Electromagnetic Waves to Obtain ρ_{SEW}

If one measures in cm the $1/e$ intensity propagation distance, L_x , of surface electromagnetic waves¹⁷⁻²⁰ (SEW) for frequencies below about 10^3 wavenumbers, he can obtain the SEW resistivities, ρ_{SEW} in Ω cm from

$$\rho_{SEW} = \frac{30}{\pi L_x \omega^2} \quad (17)$$

The propagation distances near 10^3 cm^{-1} are of the order of 1 cm for good conductors and of 2 to 5 mm for poorer conductors such as transition metals.²⁰⁻²² As ω is lowered the propagation distances increase¹⁷ and as ω approaches 100 cm^{-1} , one may have the best way to obtain low frequency resistivities. Since Eq. (17) holds from 10^3 cm^{-1} to ω_c ¹⁷, one is not concerned where $\omega = \omega_c$ and with other approximations.

In Table 4 the results of analyzing SEW propagation distances for many metals to obtain ρ_{SEW} are presented. These results are compared with ρ_{opt} from fitting IR data and ρ_{dc} from handbooks.¹¹ The agreements are not particularly good, but we feel better values of L_x can be measured on more fully characterized metal samples.

V. Not Using Thermal Methods

Studies of about 20 metals have shown that thermal data, such as electronic heat capacities, etc., are of limited value to estimate the optical constants of metals at submm and mm. Using electronic heat capacity coefficients,¹³ Hall coefficients, R_H and ρ_{dc} 's facilitate easy calculations of the optical constants. However, the results compare well with the IR based measurements only for the good conductors. The complicated Fermi surfaces of many metals ruined many attempts to find a reliable method of obtaining an average Hall coefficient. If anyone is further interested, he may find R_H values in Hurd's, Chien and Westgate's, and Kittel's books^{23,24,13} and γ values from Visser and Falicov.²⁵

VI. Graphite Dominated By A Resonance

We have measured the reflectance of a Dixon 200-10 graphite²⁵ pressed pellet from 400 to 3.2 cm^{-1} . From the visible range to 180 cm^{-1} Query has made reflectance measurements on the same sample and our joint results are plotted in Fig. 7. The dashed line is obtained by a Drude model fit to the data calculated from mainly handbook¹¹ information: $\rho_{dc} = 1.375 \times 10^{-3} \Omega \text{ cm}$, $\rho = 1.80 \text{ gm/cm}$ (measured by us), the lowest valence, $V = 2$ and $M = 12.01 \text{ gm/mole}$. These parameters yield $\omega_c = 3.71 \times 10^5 \text{ cm}^{-1}$ and $\omega_p = 1.27 \times 10^5 \text{ cm}^{-1}$ from the well known relations

$$\omega_c^2 = \frac{\omega_p^2 \rho_{dc} (\Omega \text{ cm})}{60} \quad (18)$$

and

$$\omega_p^2 = \frac{Ne^2}{\pi c^2 m} = \frac{e^2 VLP}{\pi c^2 MM} \quad (19)$$

where L is Avogadro's number. These Drude reflectance predictions look fine until one uses Eq. (19) to learn that $N = 1.8 \times 10^{23}$ free carriers per cm^3 is estimated. Such a high concentration of free carriers does not agree, even remotely, with $N = 2 \times 10^{19} \text{ cm}^{-3}$ measured by Woolf, et al²⁷ or as related by Spain.²⁸ Furthermore, using these parameters one obtains $\epsilon_1 = +0.9$ which is a very small, positive constant over the whole submm and mm λ ranges. These last comments arise from having $\omega_c > \omega_p$ which in itself is quite unusual.

On the other hand, if one uses a Kramers-Kronig analysis^{9,10} of these reflectance data he obtains ϵ_1 and ϵ_2 as presented in Fig. 8. This data is reminiscent of an overdamped harmonic oscillator as given for lattice or phonons effects in Eqs. (2) and (3) and not of large free carrier concentrations. The best eyeball fits to these data come from $\omega_\infty = 49.8$, $\delta\epsilon = 3.04 \times 10^3$, $\omega_{TO} = 99.5 \text{ cm}^{-1}$, and $\Gamma = 705 \text{ cm}^{-1}$. (A good fit requires the three significant figures, but the original reflectance data does not warrant such accuracy.) Using our papers^{3,29} on electron-phonon interactions and both bulk³ and surface effects²⁹, we place an upper limit on N of about 10^{19} cm^{-3} which is about what Woolf, et al.²⁷ found in their data. (See their paper for 10 cm long and 35 μm diameter graphite fibers produced from benzene compounds.)

In Fig. 9 the ϵ_1 and ϵ_2 data of Fig. 8 is re-introduced to show that the Drude model can be very misleading if not examined in different aspects as we have done. In Fig. 9, one sees that the high frequency values of ϵ_2 are very well estimated by the Drude model, so-much-so, that the Drude model does better than the overdamped oscillator model of Fig. 8. However, at low frequencies the Drude model

obviously does not predict the peak in ϵ_2 . The most telling defects of the Drude-handbook predictions are the ϵ_1 values. Since the experimental data show $\epsilon_{1,\text{exp}} \gg \epsilon_{1,\text{Drude}}$ and that there is a large dip near 300 cm^{-1} which is not in the free carrier model, one has to abandon any model which is dominated by free carriers for graphite in the submm and in at least most of the mm range. In this view one might conjecture that band effects are important in graphite for $\omega > 400 \text{ cm}^{-1}$ and that could account for the disagreements between the oscillator model calculations of ϵ_2 and the experimental data for ϵ_2 at the higher frequencies. These observations obviously reject a purely free-carrier dominated model for graphite in the submm and mm ranges.

As one makes more measurements in the lower mm and cm ranges, it is likely that free carrier effects will appear in electron-phonon interactions.³ These interactions can produce dips in the reflectances both above and below ω_{TO} .

For completeness, in Fig. 10 the values of n and k vs ω are given from the Kramers-Kronig analysis of the reflectance of the Dixon 200-10 graphite sample shown in Fig. 7.

VII. Future Work

We need to take more low frequency data for Fe and graphite. We have developed our techniques involving ordinary FTS³⁰, non-resonant cavities, plane parallel waveguides, high incidence angle reflection, solid state mm sources³¹ with isolators, and an asymmetric Fourier transform spectrometer.³⁰ These techniques will enable us to extend our present results. There are several types of graphite yet to be studied- submm and mm data are needed- and we plan to use LHe temperature detectors to enormously increase our sensitivity in almost all of the experiments. We want to continue developing new measurement and data analysis techniques.

VIII. Summary

We have sorted the ϵ_1 and ϵ_2 data for Fe and conclude that $\omega_c = 147 \text{ cm}^{-1}$, $\omega_p = 3.29 \times 10^4 \text{ cm}^{-1}$, and $\rho_{\text{opt}} = 8.15 \times 10^{-6} \text{ } \Omega \text{ cm}$ within the Drude model framework. Graphite behaves more like an overdamped harmonic oscillator with very few free carriers with oscillator values of $\epsilon_\infty = 49.8$, $\delta\epsilon = 3.04 \times 10^3$, $\omega_{\text{TO}} = 99.5 \text{ cm}^{-1}$, and $\Gamma = 705 \text{ cm}^{-1}$. The combined electron-phonon effects³ await more mmλ and cmλ studies. Many metals obey the Drude model, even more than sometimes expected. It is recommended that dc measurements of the resistivity of each sample be made whenever possible.

We have gone beyond the requests for Fe and graphite data and have determined values of ω_c , ω_p and ρ_{opt} for fifteen metals. These results are in Table 1.^{1,2,4,15}

New data analysis techniques have been developed by us using the slopes of dielectric function vs ω data to obtain ω_c and ω_p when only ϵ_1 is known and not ϵ_2 (and vice versa). We studied SEW and thermal techniques to obtain optical constants and conclude that there is promise in the SEW technique but not the thermal approaches for most metals.

We have several papers at the writing stage to be presented to refereed journals.

Acknowledgements

This work was partially supported by grant No. DAAK-11-82-C-0052 and Dr. Querry's grant No. DAAK-11-82-C-00069. We wish to thank Dr. M. R. Querry for productive interaction and early mutual data sharing and theoretical discussions. Also, Drs. J. L. Peacher and W. F. Parks gave generous assistance. We are thankful to Dr. Ian Spain who provided stimulating input concerning the low free carrier concentrations in graphite.

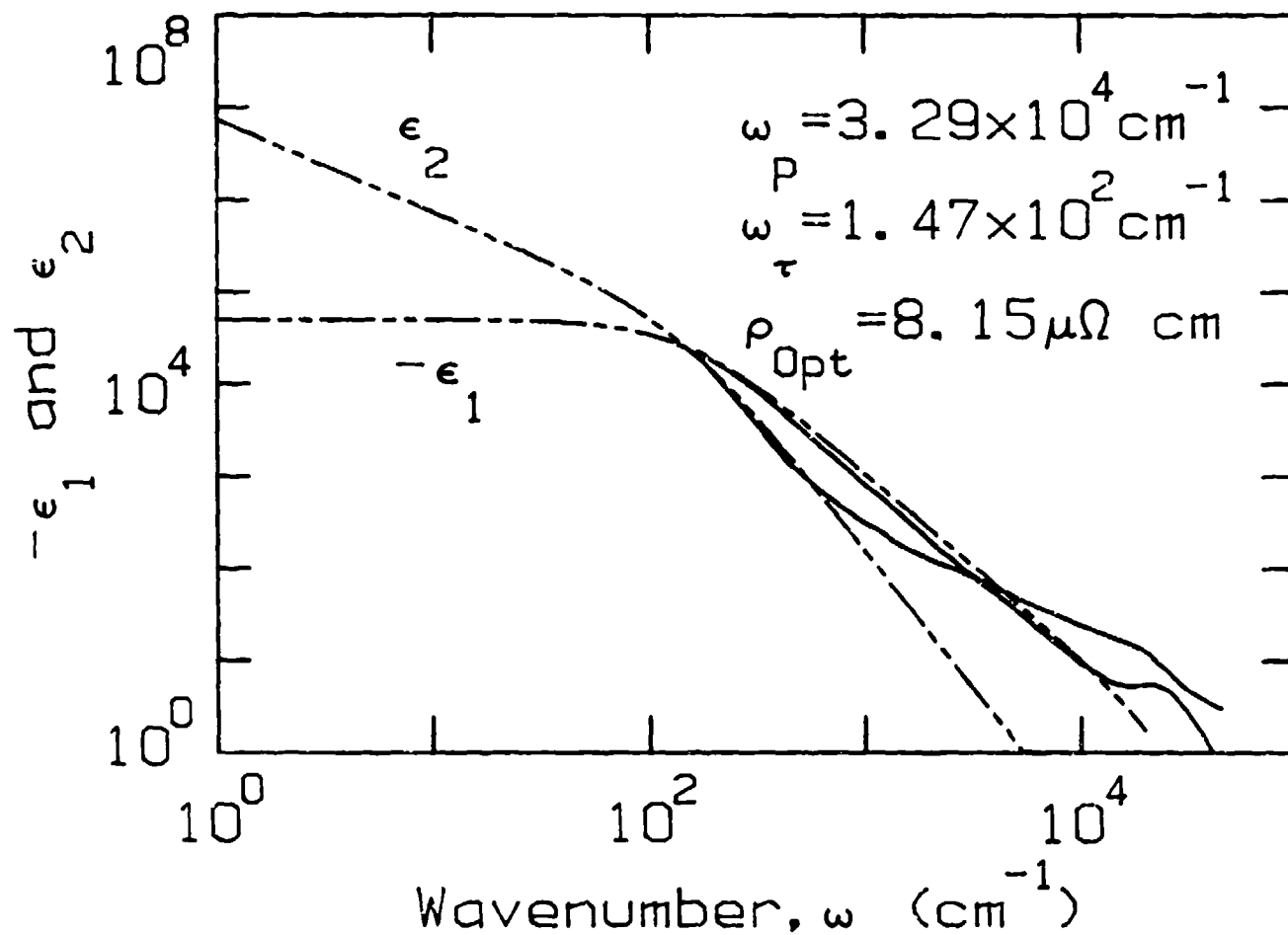


Fig. 1. Kramers Kronig results ($-\epsilon_1$ and ϵ_2) for Fe. Heavy lines are Querrey's data⁴ transformed and the lighter lines are our IR fit to the data^{1,14} with $\omega_\tau = 147 \text{ cm}^{-1}$ and $\omega_p = 3.29 \times 10^4 \text{ cm}^{-1}$ implying $\rho_{\text{opt}} = 8.15 \times 10^{-6} \Omega \text{ cm}$.

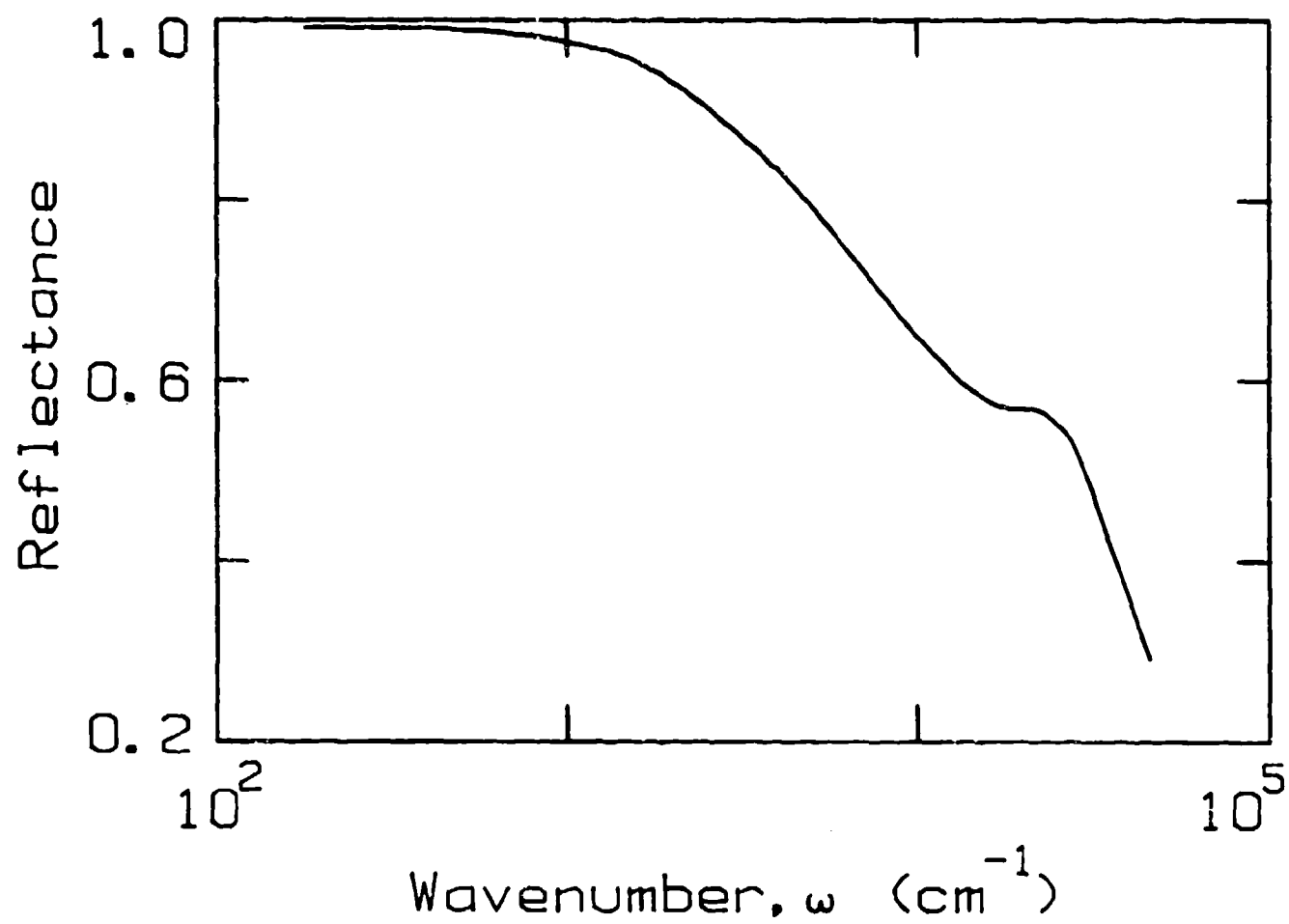


Fig. 2. Reflectance vs wavenumber of Fe as determined by Query.⁴

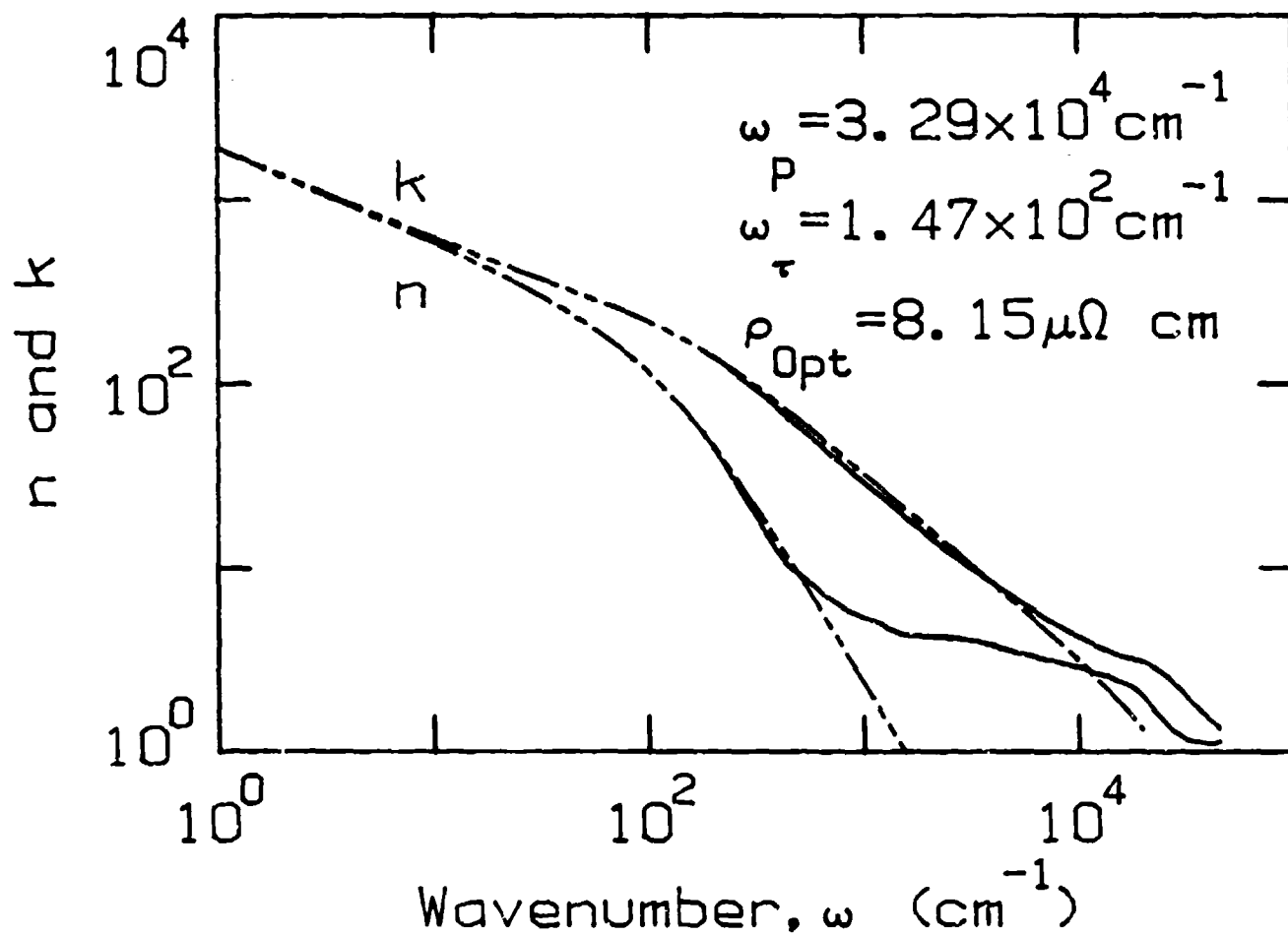


Fig. 3. Values of n and k for Iron corresponding to the $-a_1$ and a_2 curves in Figure 1.^{1,4}

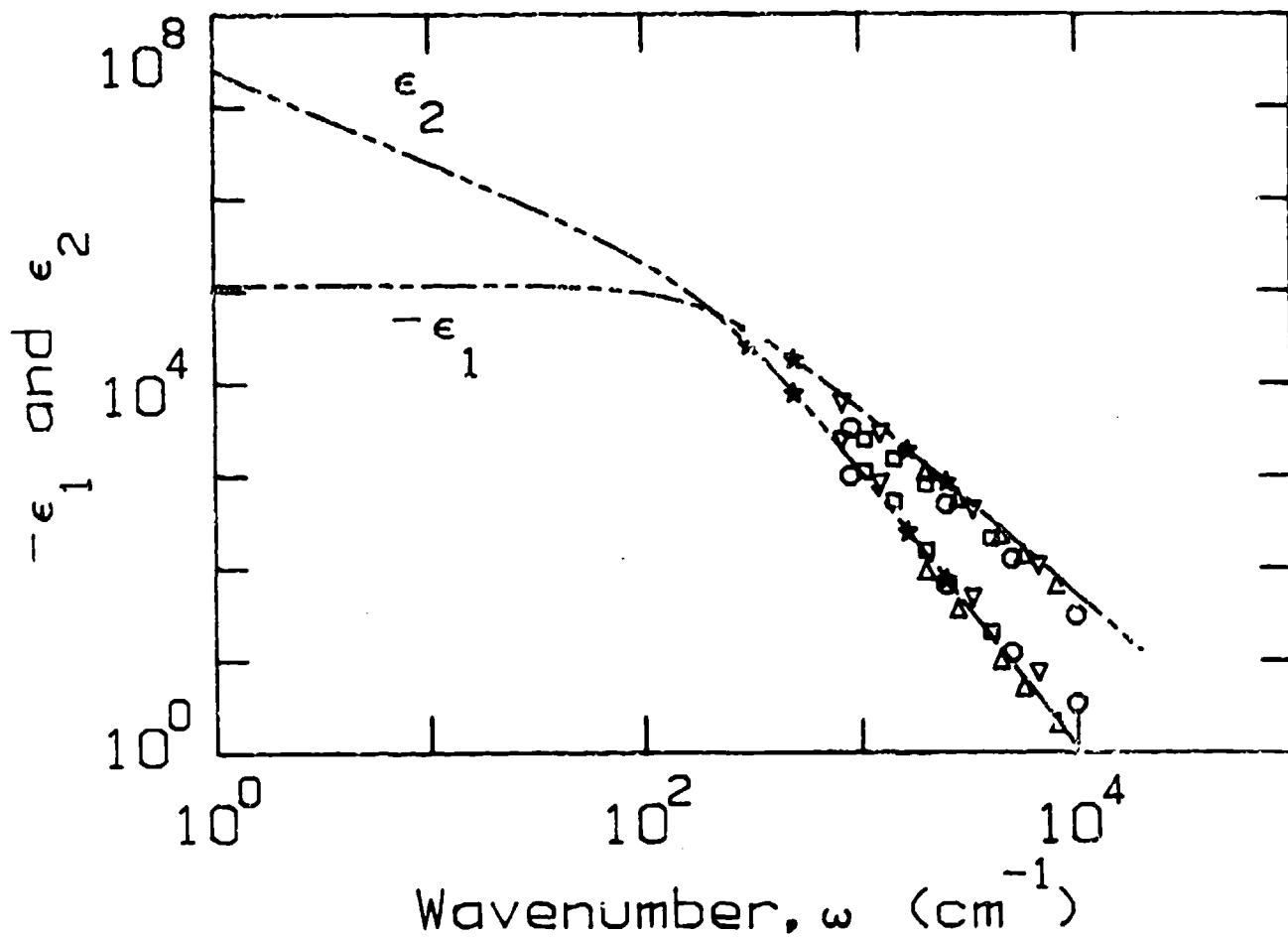


Fig. 4. Dielectric Function ($-\epsilon_1$ and ϵ_2) for Au.¹ The dashed line is the Drude theory with $\omega_p = 7.28 \times 10^4$ cm^{-1} , and $\omega_r = 215$ cm^{-1} (and $\rho_{\text{opt}} = 2.49 \times 10^{-6}$ $\Omega \text{ cm}$). The data was summarized in Refs. 1 and 2.

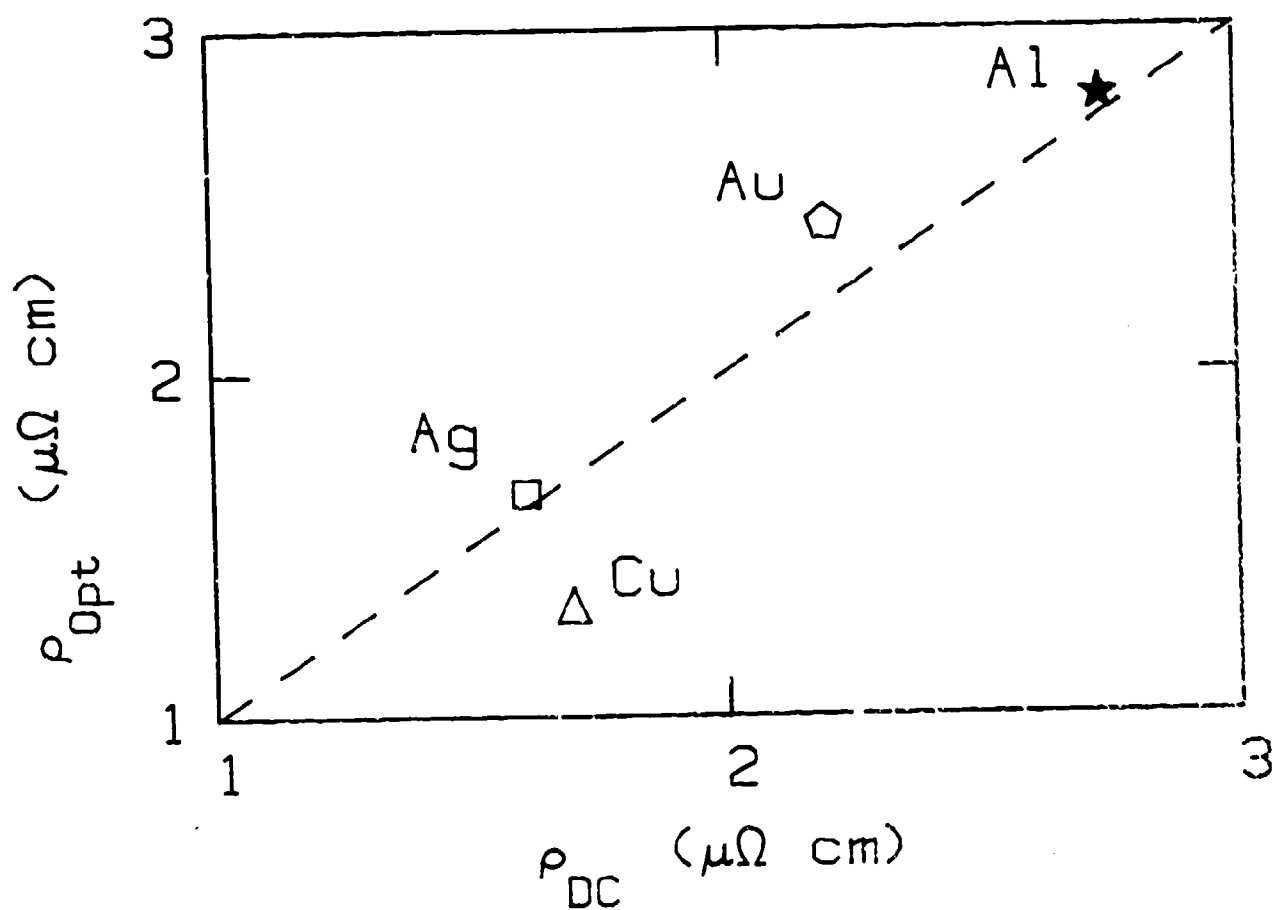


Fig. 3. a. ρ_{opt} vs ρ_{dc} for good conductors (Al, Cu, Au, Ag).

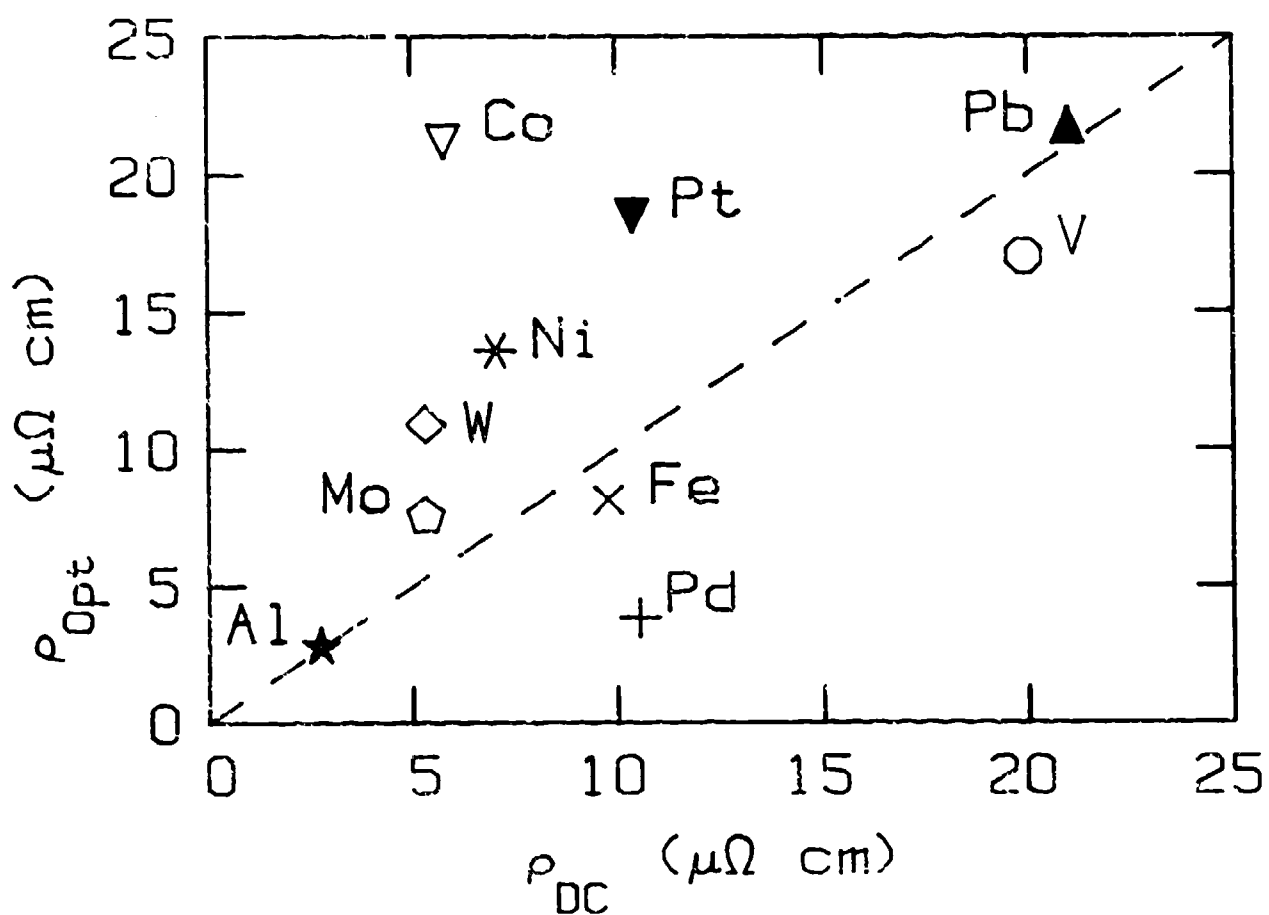


Fig. 5. b. ρ_{opt} vs ρ_{DC} for Al, Co, Fe, Pb, Mo, Ni, Pd, Pt, V, W.

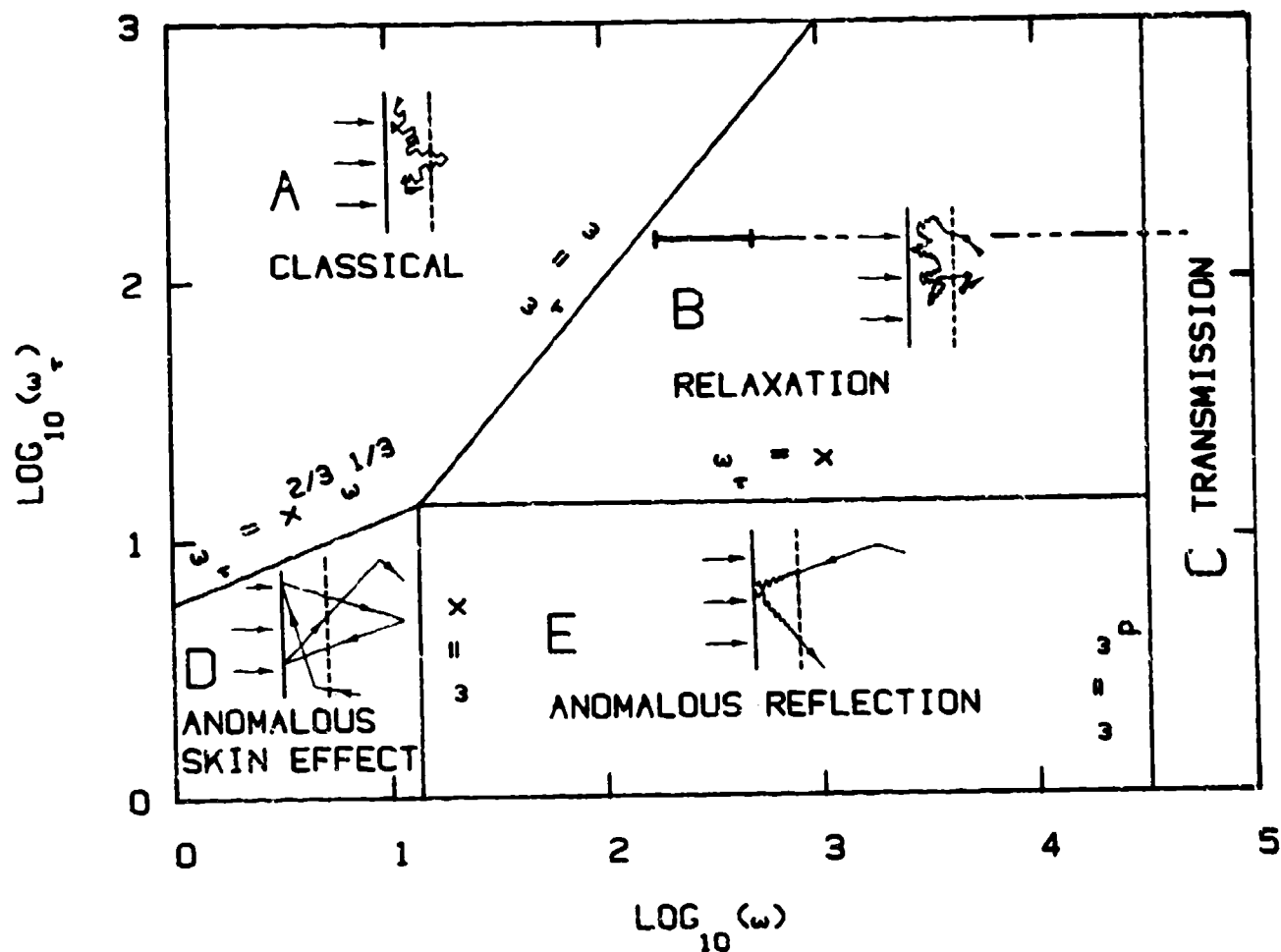


Fig. 6. 'Casimir¹²-Wooten⁷ Diagram' or $\omega\tau$ vs ω chart for Fe. $\omega_c = 147 \text{ cm}^{-1}$, $\omega_p = 3.29 \times 10^4 \text{ cm}^{-1}$, and $\chi = 14.4 \text{ cm}^{-1}$.

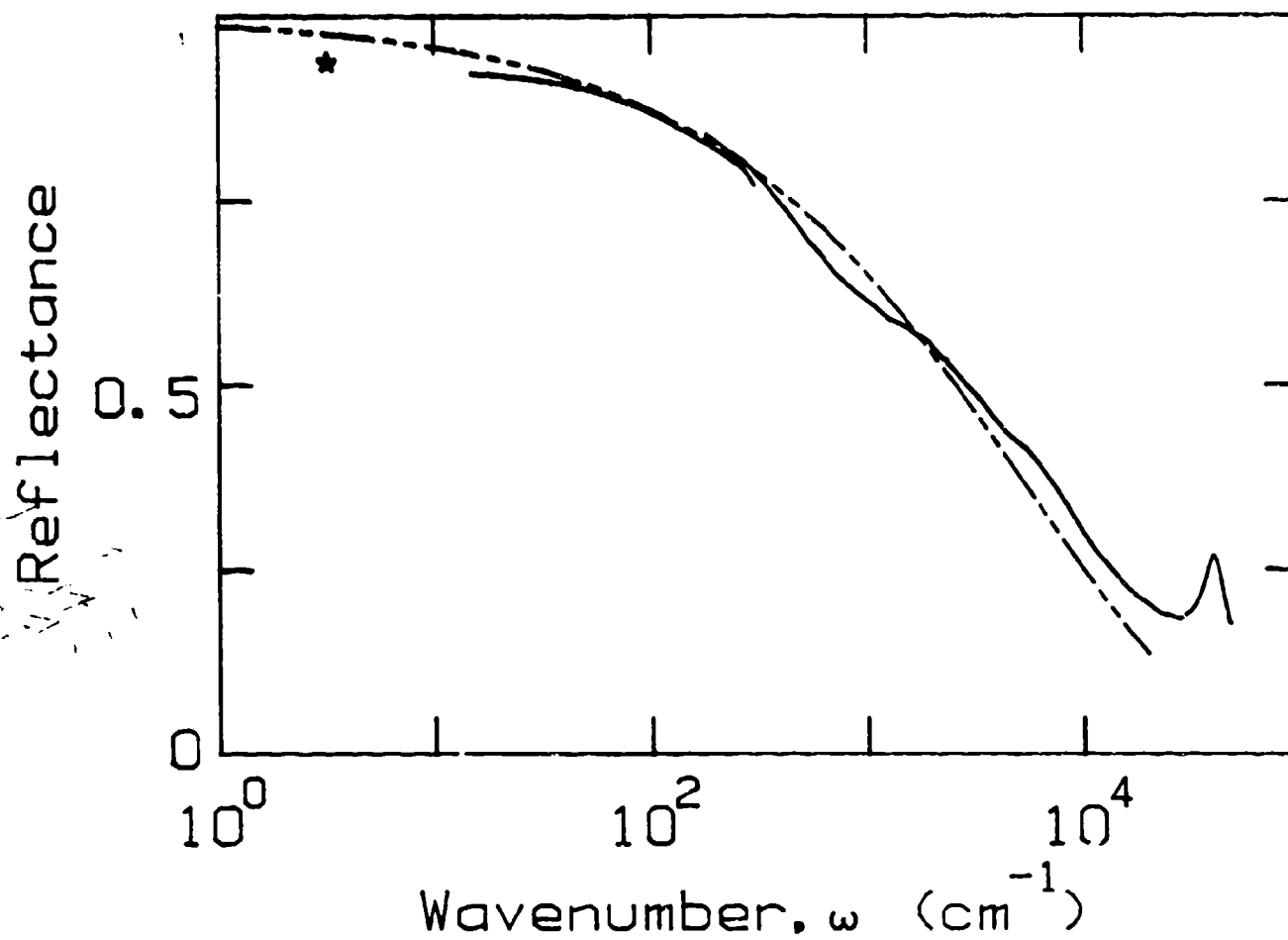


Fig. 7. Reflectance vs ω for Dixon 200-10 graphite. The high frequency data is from Query⁴ and the low frequency solid line and star are ours. Using handbook¹¹ parameters yielding $\omega_p = 1.27 \times 10^5 \text{ cm}^{-1}$ and $\omega_v = 3.7 \times 10^3 \text{ cm}^{-1}$, the dashed line was computed. Beware of this fit to the data—see Fig. 8.

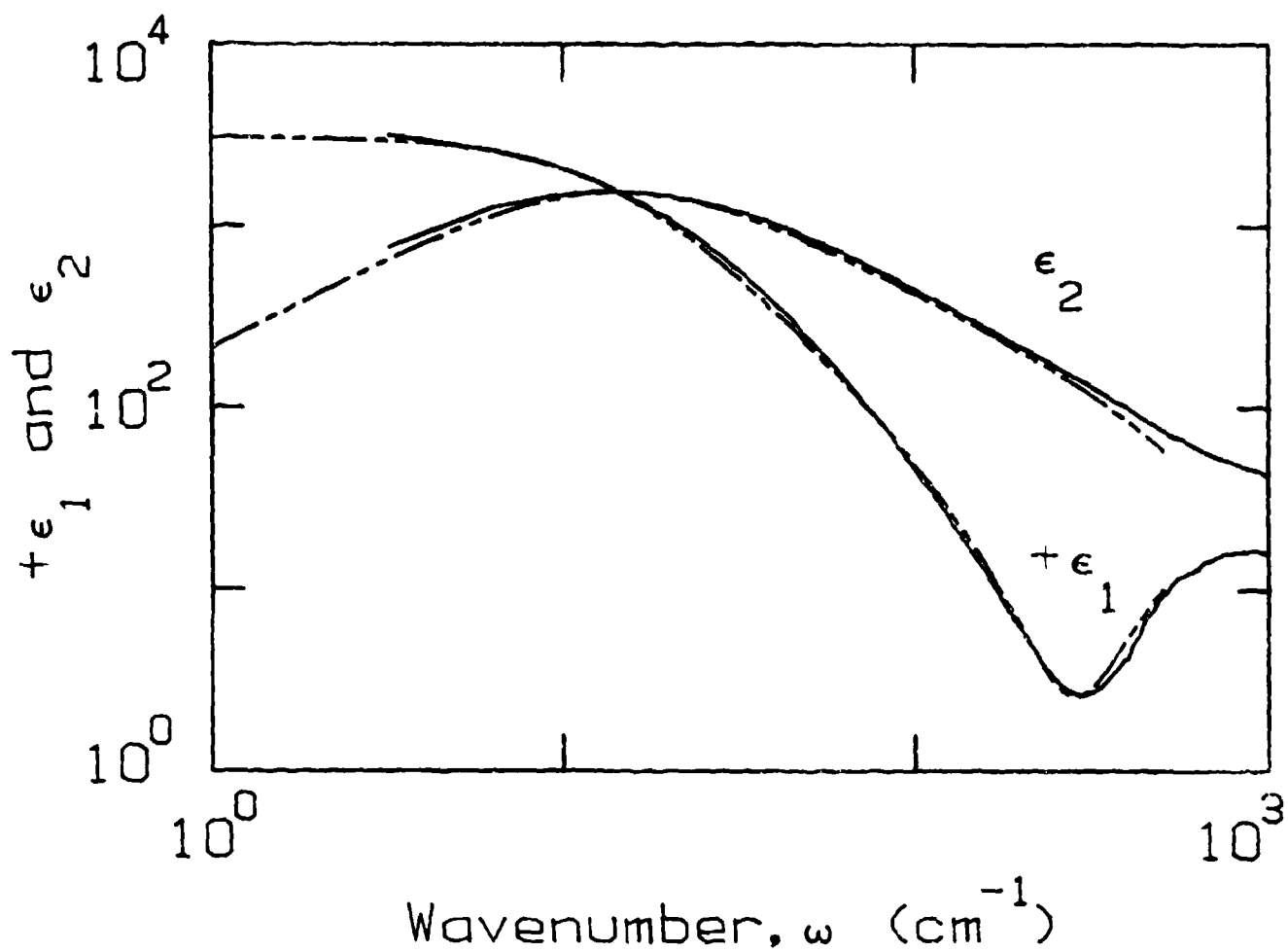


Fig. 8. $+\epsilon_1$ and ϵ_2 from a KK analysis of the reflectance data in Fig. 7. The dashed line is the eyeball fit to the data using an overdamped harmonic oscillator model in Eqs. (2) and (3) with no free carrier contribution.

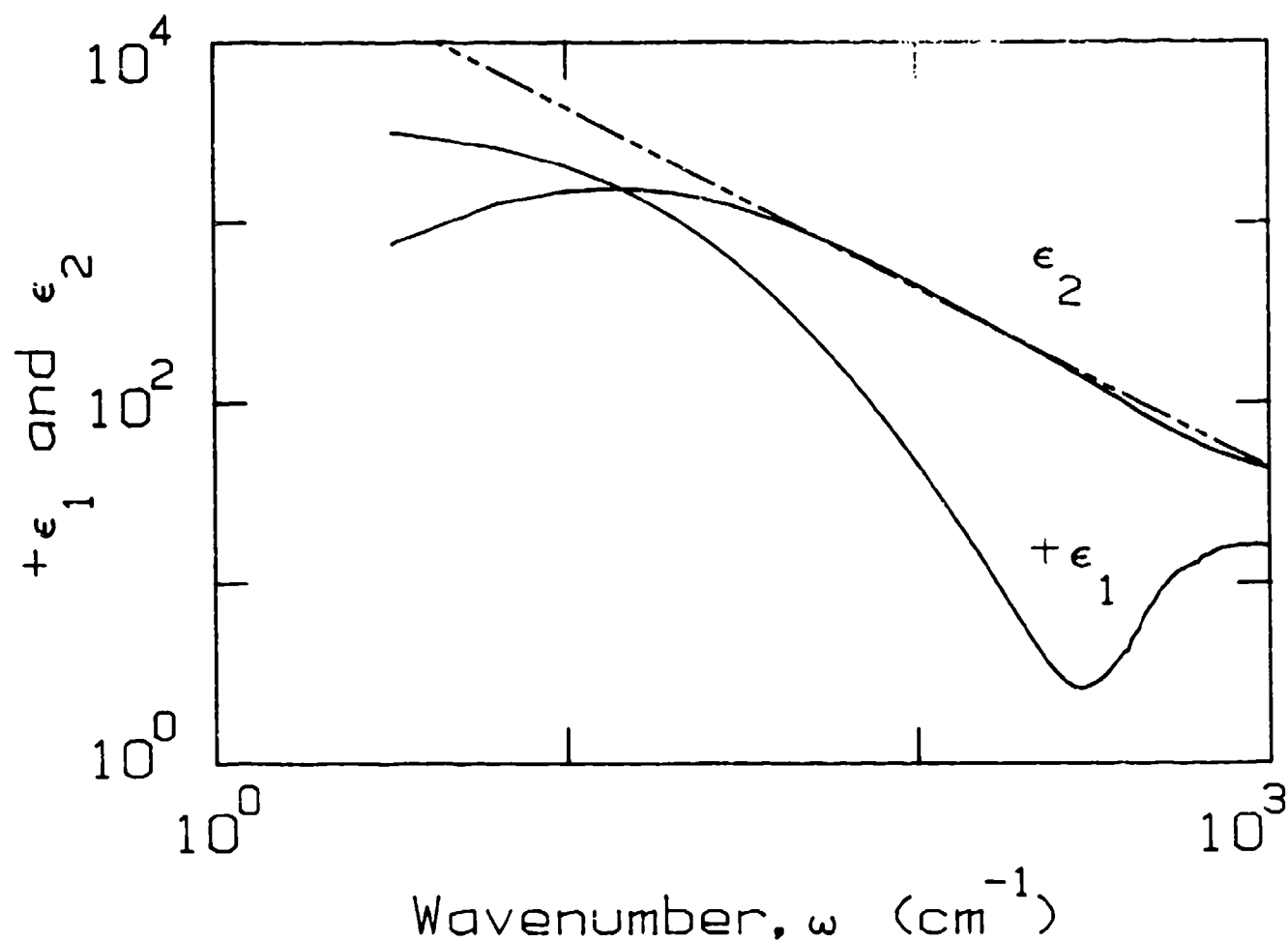


Fig. 9. ϵ_1 and ϵ_2 vs ω for the Dixon 200-10 graphite sample. The smooth curves were obtained from the KX analysis of the reflectance vs ω data. The dashed line assumes the handbook based computations of $\omega_c = 3.71 \times 10^5 \text{ cm}^{-1}$ and $\omega_p = 1.27 \times 10^5 \text{ cm}^{-1}$. This graph shows the good, fortuitous fit to the ϵ_2 data for this graphite sample. The extremely poor, non-existent fit to the ϵ_1 data (the constant, computational curve is off the graph at the bottom) is obvious.

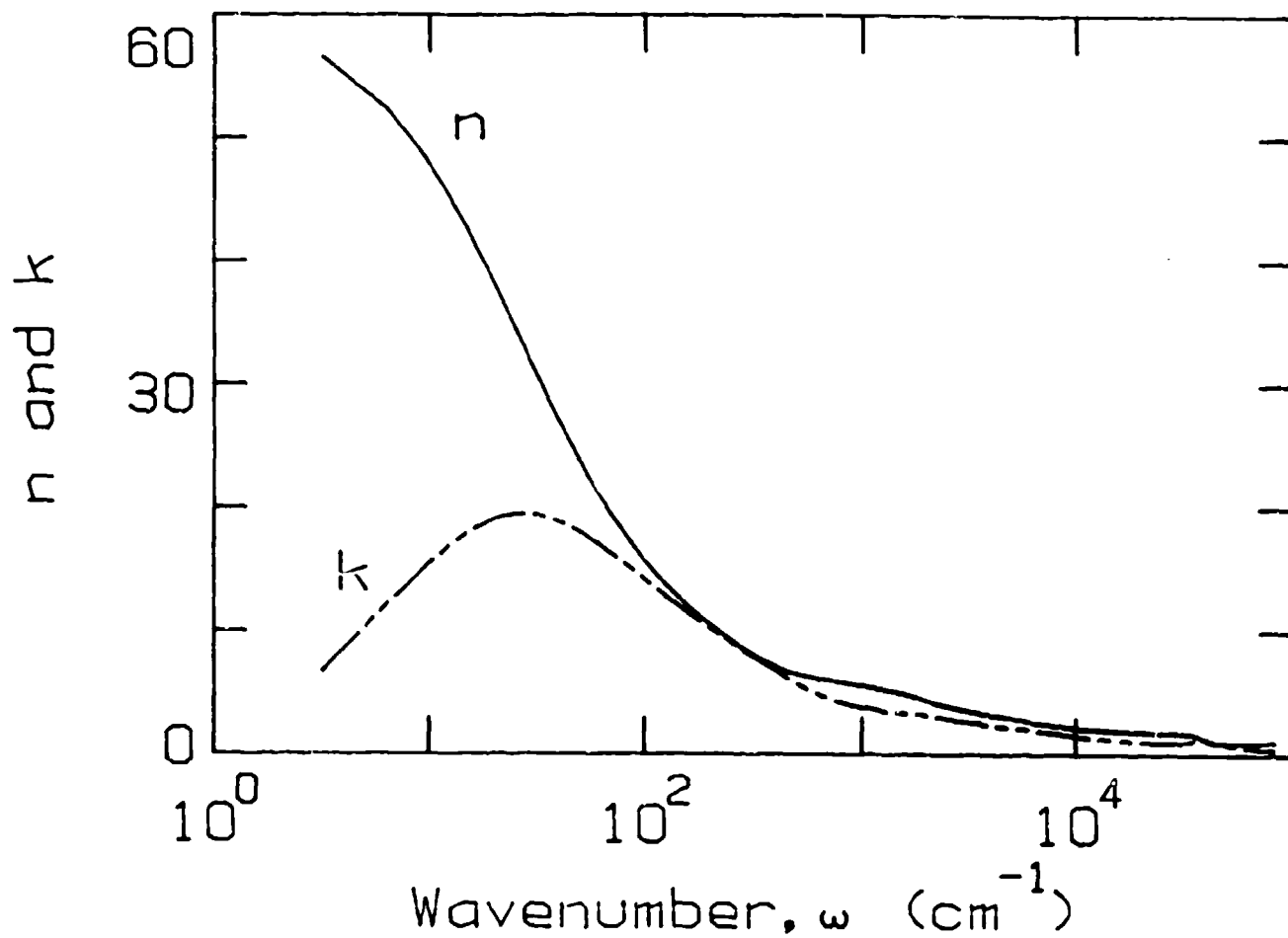


Fig. 10. n and k vs ω for the Dixon 200-10 graphite sample. The curves come from a KK analysis of the reflectance data in Fig. 7.

Table 1. Summary of IR Fit Results

Metal	$10^{-2}\omega_T$ (cm^{-1})	$10^{-4}\omega_p$ (cm^{-1})	ρ_{optical} ($\mu\Omega\text{-cm}$)	ρ_{dc}^a ($\mu\Omega\text{-cm}$)
Al	6.61	11.9	2.80	2.74
Cr	5.59	3.07	35.6	12.9
Co	3.78	3.26	21.3	5.80
Cu	0.68	5.58	1.32	1.70
Au	2.15	7.28	2.43	2.20
Fe	1.47	3.29	8.15	9.8
Pb	13.9	6.20	21.7	21.0
Mo	4.61	6.05	7.56	5.33
Ni	3.51	3.94	13.6	7.04
Pd	1.24	4.40	3.84	10.55
Sn	5.22	4.10	18.6	10.42
Ag	1.45	7.27	1.65	1.61
Ti	3.62	2.03	55.6	43.1
V	4.89	4.16	17.0	19.9
W	4.67	5.17	10.9	5.33

^a(At 22 degrees C) taken from pages 9-39 and 9-40 of the AIP Handbook, 3rd ed., McGraw-Hill (1972).

Table 2. Use of the slope method to find ω_T and ω_p
for Fe (all quantities shown are in cm^{-1}).

Wavenumber	$10^{-2}\omega_T$ (from $-\epsilon_1$ slope)	$10^{-4}\omega_p$	$10^{-2}\omega_T$ (from ϵ_2 slope)	$10^{-4}\omega_p$
185	1.35	3.20	0.915	3.66
190	1.31	3.16	0.917	3.66
195	1.29	3.15	0.896	3.68
200	1.28	3.14	0.886	3.70
205	1.25	3.12	0.890	3.69
210	1.22	3.10	0.907	3.67
215	1.21	3.09	0.899	3.68
220	1.18	3.06	0.925	3.64
225	1.18	3.08	0.933	3.63
230	1.16	3.06	0.944	3.62
235	1.18	3.07	0.956	3.60
240	1.13	3.05	0.962	3.59
245	1.17	3.07	0.975	3.57
250	1.17	3.07	0.971	3.58
255	1.15	3.06	0.981	3.57
260	1.13	3.05	0.977	3.57
265	1.11	3.04	0.970	3.58
270	1.16	3.06	0.955	3.60
275	1.16	3.06	0.939	3.63
280	1.11	3.04	0.902	3.69

Table 3. Summary of ω_T and ω_p values obtained from the IR Fit and Slope methods.

Metal	$10^{-2}\omega_T$ (cm^{-1})	$10^{-4}\omega_p$ (cm^{-1})	Method
Al	6.61	11.9	IR Fit
Al	6.45	13.5	Slope
Cr	5.59	3.07	IR Fit
Cr	3.20	3.26	Slope
Co	3.78	3.26	IR Fit
Co	3.95	2.42	Slope
Cu	0.68	5.58	IR Fit
Cu	0.56	5.44	Slope
Au	2.15	7.28	IR Fit
Au	2.03	7.97	Slope
Fe	1.47	3.29	IR Fit
Fe	1.07	3.36	Slope
Pb	13.9	6.20	IR Fit
Pb	18.5	6.27	Slope
Mo	4.61	6.05	IR Fit
Mo	6.23	3.96	Slope
Ni	3.51	3.94	IR Fit
Ni	3.12	3.20	Slope
Pt	5.22	4.10	IR Fit
Pt	6.51	3.61	Slope
Ag	1.45	7.27	IR Fit
Ag	1.43	7.58	Slope
Ti	3.82	2.03	IR Fit
Ti	6.41	1.80	Slope
V	4.89	4.16	IR Fit
V	4.97	4.29	Slope
W	4.87	5.17	IR Fit
W	8.15	4.01	Slope

Table IV. Comparison of handbook resistivities with resistivities calculated from the SEW, and IR Fit results.

Metal	Wavenumber (cm^{-1})	Propagation Length (cm)	Resistivity ($\mu\Omega$ cm)		
			ρ_{sew}^a	ρ_{opt}^b	ρ_{dc}^c
Al	1080	0.75	11	2.8	2.7
Al	1080	1.1	7.4	2.8	2.7
Al	945	0.65	15	2.8	2.7
Al	945	1.25	8.6	2.8	2.7
Cr	945	0.1	110	36	13
Cr	945	0.075	140	36	13
Cu	1080	0.92	8.9	1.3	1.7
Cu	1080	1.85	4.4	1.3	1.7
Cu	1000	2.6	3.7	1.3	1.7
Cu	945	1.6	6.7	1.3	1.7
Cu	945	0.74	14	1.3	1.7
Cu	945	1.25	8.6	1.3	1.7
Cu	945	2.4	4.5	1.3	1.7
Au	1080	1.25	6.6	2.4	2.2
Au	945	0.3	36	2.4	2.2
Au	945	1.72	6.2	2.4	2.2
Au	945	0.5	21	2.4	2.2
Fe	945	0.12	89	8.2	9.8
In	945	0.24	45	... ^d	8.8

Table IV (continued). Comparison of handbook resistivities
with resistivities calculated from the
SEW, and IR Fit results.

Metal	Wavenumber (cm^{-1})	Propagation Length (cm)	Resistivity ($\mu\Omega \text{ cm}$)		
			ρ_{sew}^a	ρ_{opt}^b	ρ_{dc}^c
Mo	1080	0.58	14	7.6	5.3
Mo	945	0.78	14	7.6	5.3
Ni	1000	0.35	27	14	7.0
Pd	1000	0.23	42	3.8	11
Pt	1000	0.37	26	19	10
Ag	1080	1.5	5.5	1.7	1.6
Ag	945	2.0	5.4	1.7	1.6
Ag	945	0.5	21	1.7	1.6
Ti	1000	0.13	71	55	43
W	1000	0.41	25	11	5.7
SS304	945	0.16	57	1.2 ^d	72

^afrom Table IV in reference [15].

^bValues of ρ_{opt} taken from Table I in reference [15].

^c(at 22 degrees C) taken from pages 9-39 and 9-40 of
the AIP Handbook, 3rd ed., McGraw-Hill (1972).

^dNot listed in Table I of reference [15].

IX. References

* This work was partially supported by U.S. Army grant DAAK 11-82-C-0052.

1. M. A. Ordal, L. L. Long, R. J. Bell, S. E. Bell, R. R. Bell, R. W. Alexander, Jr., and C. A. Ward, *Appl. Opt.* **22**, 1099 (1983).
2. J. H. Weaver, C. Krafka, D. W. Lynch, and E. E. Koch, 'Part 1: The Transition Metals'; 'Part 2: Noble Metals, Aluminum, Scandium, Yttrium, the Lanthanides, and the Actinides'; in Physics Data, Optical Properties of Metals (Fachinformationszentrum 7514 Eggenstein-Leopoldshafen 2, Karlsruhe, Federal Republic of Germany, 1981).
3. T. J. McMahon and R. J. Bell, *Phys. Rev.* **182**, 526 (1969).
4. M. R. Querry, to be published in the 1984 CRDC conference proceedings.
5. P. Drude, Theory of Optics (Longmans, Green, NY, 1922 and Dover, NY, 1968).
6. B. Donovan, Elementary Theory of Metals, Vol. 2 of the International Encyclopedia of Physical Chemistry and Chemical Physics, Ed. M. Blackman (Pergamon Press, Oxford, 1967).
7. F. Wooten, Optical Properties of Solids (Academic Press, NY, 1972).
8. John M. Stone, Radiation and Optics (McGraw-Hill Book Company, NY, 1963), p. 377.
9. G. Andermann, A. Caron, and D. A. Dows, *J. Opt. Soc. Am.*, **55**, 1210 (1965).
10. P. N. Schatz, S. Maeda, and K. Koz'ma, *J. of Chem. Phys.* **38**, 2658 (1963).
11. J. Babiakin and J. Robert Anderson, AIP Handbook, p. 9-38 (McGraw-Hill Book Co., NY, 1972).
12. H. B. G. Casimir and J. Ubbink, *Philips Technical Review*, **28**, 366 (1967).
13. C. Kittel, Introduction to Solid State Physics (J. Wiley and Sons, NY, 1971), 4th Ed. p. 246ff.
14. J. Pachner, Handbook of Numerical Analysis Applications (McGraw-Hill Book Co., NY, 1984), pages 2.19-20 and P.79.
15. M. A. Ordal, L. L. Long, R. Paul, R. W. Alexander, Jr., and R. J. Bell, to be published.
16. R. J. Bell, M. A. Ordal, R. W. Alexander, R. A. Paul, and J. L. Peacher, to be published.
17. C. A. Ward, R. J. Bell, R. W. Alexander, G. S. Kovener, and I. Tyler, *Appl. Opt.* **13**, 2378 (1974).
18. R. J. Bell, R. W. Alexander, Jr., W. F. Parks, and G. Kovener, *Opt. Commun.* **8**, 147 (1973).
19. R. W. Alexander and R. J. Bell, *J. Non-Crys. Sol.* **19**, 93 (1975).

20. G. N. Zhishin, M. A. Moskalova, E. V. Shomina, and V. A. Yakovlev in Surface Polaritons. Electromagnetic Waves at Surfaces and Interfaces, Eds. V. M. Agranovich and D. L. Mills (North Holland Publishing Co., Amsterdam, 1982) p. 93ff.
21. D. L. Begley, D. A. Bryan, R. W. Alexander, Jr., R. J. Bell, and C. A. Goben, *Surf. Sci.* **60**, 99 (1976).
22. D. A. Bryan, D. L. Begley, K. Bhasin, R. W. Alexander, R. J. Bell, and R. Gerson, *Surf. Sci.* **57**, 53 (1976).
23. C. Hurd, Hall Effects in Metals and Alloys (National Research Council of Canada, Ottawa, 1972).
24. The Hall Effect and Its Applications, Ed. C. L. Chien and C. R. Westgate (Plenum Press, NY, 1980).
25. P. B. Visser and L. M. Falicov, *Phys. Stat. Sol. (b)* **54**, 9 (1972). A review article.
26. The Joseph Dixon Crucible, Co., Jersey City, NJ, 07303.
27. L. D. Woolf, J. Chin, Y. R. Lin-Liu, and H. Ikezi, *Phys. Rev. B* **30**, 861 (15 July, 1984).
28. Ian Spain, private communication.
29. W. E. Anderson, R. W. Alexander, Jr., and R. J. Bell, *Phys. Rev. Letters*, **27**, 1057 (1971).
30. R. J. Bell (with R. W. Alexander), Introductory Fourier Transform Spectroscopy (Academic Press, NY, 1972).
31. Hughes Dynamics Division, 3100 West Lomita Blvd., Torrance, CA, 90509. Telephone (213)-534-2121.

FAR-INFRARED EXTINCTION PROPERTIES OF METAL POWDERS

V. P. Tomaselli
K. D. Moeller
Fairleigh Dickinson University
Physics Research Laboratory
Hackensack, N.J. 07601

ABSTRACT

We describe the results of extinction measurements made on dispersed metal powders. These results are a continuation of previously reported studies. Data for copper spheres and bronze flakes are presented and compared. The wavelength range covered in these measurements is from 10 to 125 micrometers.

DISCUSSION

The extinction coefficient for metal powders dispersed in a transparent polyethylene matrix has been determined using transmission measurements.* Data obtained from three instruments are used to characterize the powders: a grating spectrophotometer for the infrared region, a Fourier transform spectrometer for the far-infrared region, and a CO₂ laser-based photometer system operating at 10.6 micrometers. The laser-based apparatus was incorporated to study sample discs having high concentrations of powder, and thus low transmittance.

The objectives sought in this series of measurements is to investigate the effect of (a) wavelength, (b) particle size and shape, (c) particle concentration, and (d) powder composition on the measured optical properties.

* For a discussion of the sample preparation technique and experimental method, see "Infrared Study of Metal Powder Extinction Properties", V. P. Tomaselli and K. D. Moeller, Proc. 1982 CSL Conference on Obscuration and Aerosol Research, p.153

In Table I, we list the physical characteristics of the metal powders under consideration for this series of experiments. All powders were obtained from commercial sources and were used without any subsequent modification or treatment. As can be seen from Table I, powders with a reasonable range of physical characteristics are available commercially. However, the fabrication of controlled, "custom-made" particles should be considered as the next step in this project.

TABLE I
Physical Properties of Metal Powders Studied

<u>Type</u>	<u>Name</u>	<u>Shape</u>	<u>Size</u>	<u>Apparent Density</u>
Copper	200-U	Flake	$\sim 44 \mu$	0.5 g/cc
	R-9427	Flake	$\sim 44 \mu$	1.41
	R-9428	Flake	$\sim 30 \mu$	0.52
	Leico	Spheres	1-5 μ	
Bronze	Pale Gold Flake		3-5 μ	(90% Cu/10% Zn)

Measurement error and reproducibility effects continue to be a significant part of this project. Figure 1 presents some typical results of errors introduced by data scatter in transmittance measurements (upper plot) and fluctuation in data resulting from repeated trials on the same series of samples (lower plot). These results were obtained for a bronze powder at a concentration of 1% by weight, but similar behavior was observed for other powders as well.

In Figures 2 and 3, we show the wavelength-dependence of the absorption coefficient for a bronze powder and a series of copper powders, respectively. The Pale Gold 1400 graph includes data at four concentrations ranging from 0.1% to 1.0%. The quantity plotted on the vertical axis, $\alpha(\lambda)/f_w$ is a weight fraction normalized absorption coefficient expressed in units of 1000 cm^{-1} . Here f_w is the weight fraction of metal powder dispersed in the transparent matrix. Figure 2 shows that the absorption decreases with increasing wavelength for all values of f_w , that good agreement between the values obtained from the three methods is quite good, and that the weight-normalized absorption coefficient is essentially independent of concentration. The data point labelled "CO₂" represents a value obtained from the laser photometer method.

In Figure 3, data for four different copper powders is presented. All powders are in the form of flakes, but they differ in their average particle size and apparent density. Density differences here are attributed to the variation in the thickness of the flake. The data in Figure 3 shows that the weight normalized absorption coefficient is independent of wavelength in the region investigated, and has a lower numerical value than does the bronze flake powder.

In Figure 4, we have plotted the absorption coefficient against metal powder concentration, for two wavelengths. There does not appear to be any significant concentration dependence for this data. A listing of experimental data for copper powders is presented in Table II.

The decreasing absorption from 10μ to 120μ in Pale Gold particles suggests that we are observing the tail of the resonance behavior. According to elementary dipole theory, the resonance should be about two times the average particle size. The nearly flat shape of the copper flake curves does not support this viewpoint. We have undertaken to examine the behavior of spherical particles in more detail, and other participants in the Smoke Program are investigating cubes. For the next step in this project, we will

study "custom-made" particles having exact dimensions and arranged in unclustered arrays in a known dielectric environment. The size of these particles will be chosen to produce an expected resonance in the center of the spectral region to be studied.

TABLE II
Some Experimental Results for Copper Powders

<u>Name</u>	<u>Size</u>	<u>Shape</u>	<u>f_w</u>	<u>$\alpha(\lambda)/f_w \times 10^{-3}, \text{cm}^{-1}$</u>		
				<u>10.0μ</u>	<u>33.3μ</u>	<u>100μ</u>
Leico	1-5 μ	Sphere	.01	1	1	1
			.02	1	1	1
200-U ~ 44 μ		Flake	.01	6.7	7.4	7.2
			.02	5.9	6.5	---
R-9427 ~ 44 μ		Flake	.001	0	1	1
			.01	1	1	1
R-9428 ~ 30 μ		Flake	.001	3.3	6.3	8.5
			.01	4.8	5.1	5.8
R-9429 ~ 10 μ		Flake	.001	4.7	7.7	7.3
			.01	6.5	6.6	2.8

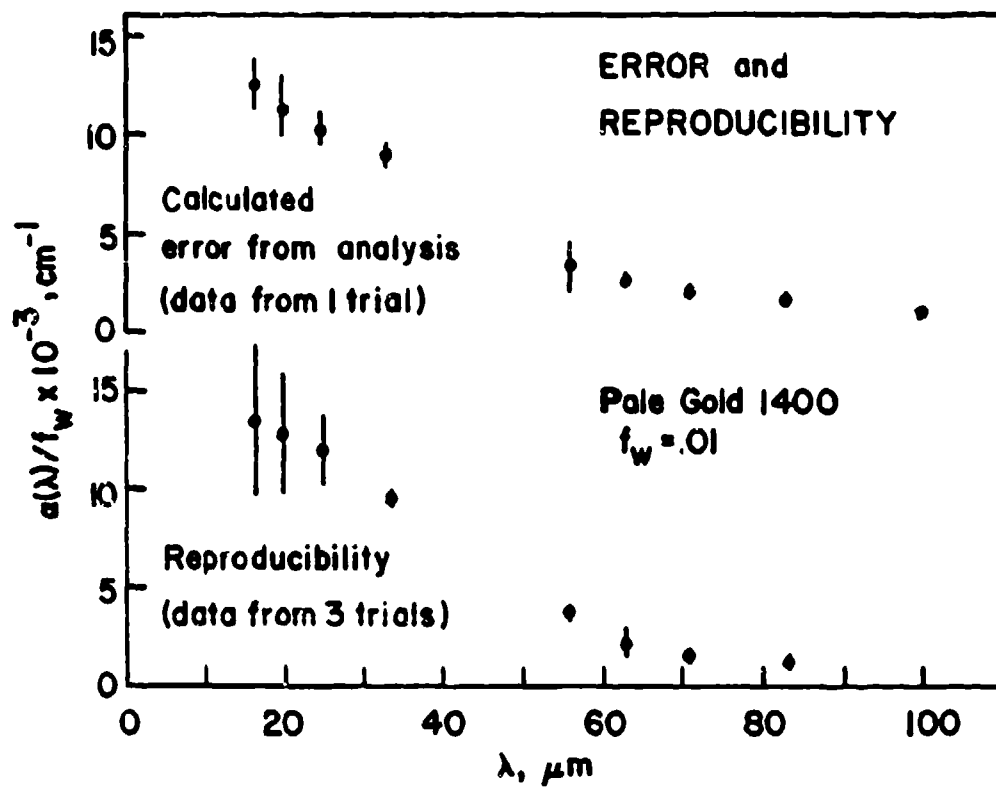


Figure 1 - Example of error and reproducibility in measured absorption data.

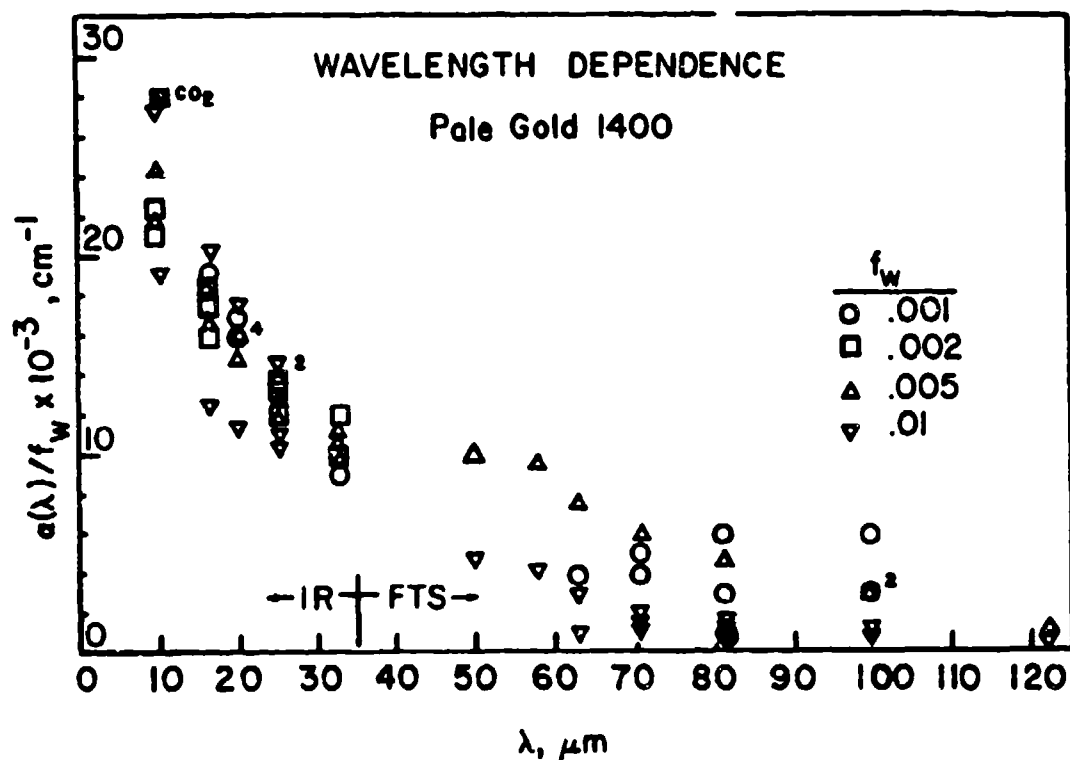


Figure 2 - Wavelength dependence of the weight normalized absorption coefficient of a bronze powder. The powder particles are in the form of flakes. The parameter f_w is the weight fraction of metal powder suspended in the host medium. Small numbers adjacent to data points represent repeated values. Pale Gold 1400 is the product name for a bronze powder (90% copper, 10% zinc) supplied by Atlantic Powder Metals (Elizabeth, NJ).

WAVELENGTH DEPENDENCE

Copper Flake Powders, $f_w = .01$

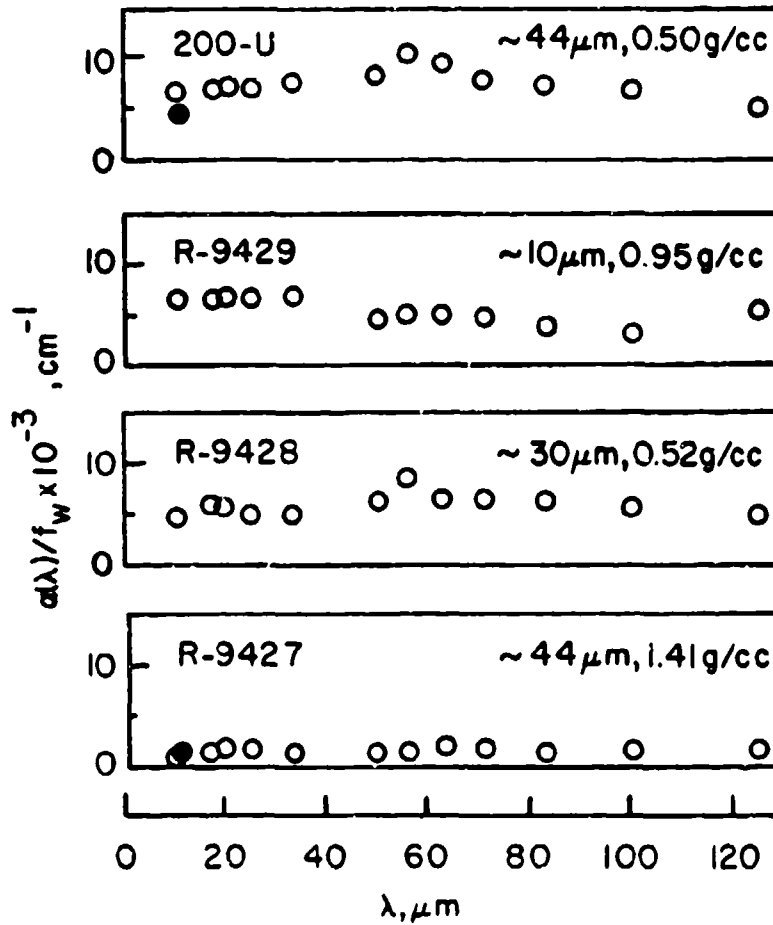


Figure 3 - Wavelength dependence of the weight normalized absorption coefficient of copper powders.

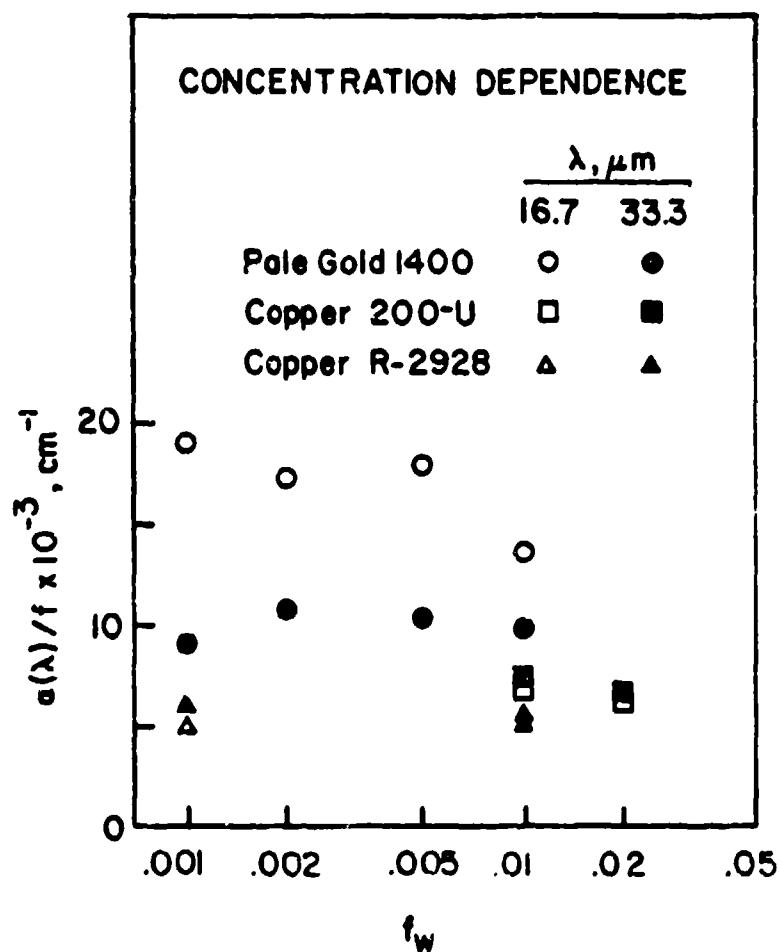


Figure 4 - Concentration dependence of weight - normalized absorption coefficient.

III. OPTICAL PROPERTIES OF AEROSOLS

Investigation of the Reaction between Single Aerosol
Acid Droplets and Ammonia Gas

Glenn O. Rubel
US Army Armament, Munitions and Chemical Command
Chemical Research and Development Center
Aberdeen Proving Ground, Maryland 21010

James W. Gentry
Department of Chemical Engineering
University of Maryland
College Park, MD 20783

ABSTRACT

This paper concerns the measurement of the reaction dynamics between single acid droplets and ammonia gas. This work has been submitted for publication as follows:

G. Rubel and J. Gentry, "Investigation of the Reaction between Single Aerosol Acid Droplets and Ammonia Gas", in press, J. Aerosol Science, 1984.

Future research will be directed at measuring the reaction dynamics in the presence of monolayers.

INTRODUCTION

One of the earlier investigations of the reaction between acid droplets and ammonia gas was conducted by Robbins and Cadle (1958), hereafter referred to as RC. Determining the aerosol ammonium ion concentration as a function of downstream distance in an aerosol flow reactor, the extent of reaction of the aerosol was determined as a function of particle size for discrete times. The extent of reaction, for a fixed time, increased with decreasing particle size and the initial reaction rate was governed by a second order surface phase reaction. However, surface phase reaction models, with constant velocity constants, could not predict the entire reaction history of the aerosol. In general the experimental reaction rate was significantly smaller than that predicted by a surface phase reaction model which employed the aforementioned velocity constant. Changing the aerosol carrier gas from pure nitrogen to a mixture of helium and nitrogen, RC detected no measurable difference in the aerosol reaction rate. Since the ammonia gas phase diffusion coefficient was measurably disparate for the two carrier gases, it was concluded the rate controlling process observed by RC during the later stages of reaction was not gas phase diffusion but internal particle diffusion.

Also using an aerosol flow reactor, Huntzicker, Cary and Ling (1980), hereafter referred to as HCL, studied the reaction between H_2SO_4 droplets and NH_3 gas for relative humidities between 8 and 80%. The experiments were similar to those of RC in that the particle size range of interest varied from approximately 0.3 to 1.0 micrometers in diameter. However, the NH_3 gas partial pressure employed by HCL was approximately 0.1 dyne/cm^2 , roughly two orders of magnitude lower than the pressures used by RC. Furthermore, as opposed to the conclusion of RC, HCL proposed that the reaction dynamics were controlled by gas phase diffusion and internal particle diffusion. HCL found no evidence of surface phase reaction.

From mass transport considerations the reaction coefficient, the fraction of molecules striking a surface which react, was found to increase with particle size, varying from 0.3 to 0.7 for particle diameters varying from 0.3 to 1.2 micrometers.

It is the intent of this study to investigate the reaction dynamics between acid aerosol droplets and ammonia gas. Understanding the role that surface phase reaction, gas phase diffusion and internal particle diffusion play in the aerosol reaction dynamics will be of central importance. A new experimental method is employed to study the aerosol-reaction dynamics continuously; continuous monitoring permits the identification of transition points in the reaction history which are associated with catastrophic events such as particle crystallization. Such detailed information is difficult to discern from discrete time analyses characteristic of aerosol flow reactors.

EXPERIMENTAL SYSTEM

The measurement of the reaction dynamics of single acid droplets in the presence of NH_3 gas is based on the principle of electrodynamic balance within a continuously mixed chamber (Rubel and Gentry, 1984). A charged droplet is stabilized at the null point of an alternating electric field which is established by impressing an alternating voltage across a hyperboloidal electrode. Changes in droplet mass are determined by changes in the direct current voltage required to balance the droplet at the focal point of a 35mm objective. In the present study, the extent of reaction, which defines the relative amount of reacted and unreacted acid, is determined from the increasing weight-balancing voltage.

RESULTS

Figure 1 depicts the reaction dynamics measured in the electrodynamic chamber for phosphoric acid droplets with diameters 42, 50, 65, and 72 micrometers, at an external NH_3 partial pressure of 400 dynes/ cm^2 . In all cases, for the first second of reaction, a rapid increase in the extent of reaction occurs. The maximum extent of reaction achieved during the initial growth phase is relatively insensitive to particle size. Following the initial growth phase, a slower growth phase dominates and the maximum extent of reaction achieved during the latter growth phase increases with increasing particle size. Specifically for particle diameters 50, 65, and 72 micrometers, the maximum extent of reaction is 22%, 34%, and 57% respectively. Remarkably for the 42 micrometer droplet, the second growth phase is completely inhibited and subsequent internal particle diffusion does not occur.

At some characteristic time, a sharp transition in the reaction dynamics occurs and the particle reaction rate slows once more. Supported by visual observations that particle crystallization occurs just after the onset of this slower rate process, it is asserted that gas-phase diffusion-controlled particle-reaction dynamics are terminated once particle crystallization occurs. The sharp transition in the reaction dynamics is consistent with a catastrophic event such as particle crystallization.

The effect of the external NH_3 partial pressure on the reaction dynamics is shown in Figure 2. The maximum extent of reaction achieved during the second reaction phase decreases with increasing external NH_3 partial pressure.

Figure 2 shows the comparison between experiment and theory when the total reaction dynamics is modeled as an initial surface-phase reaction and a secondary gas-phase diffusion-controlled process. The value of the second-order velocity constant k is set equal to $1.0 \times 10^5 \text{ cm}^4 \text{ mole}^{-1} \text{ sec}^{-1}$ in agreement with the findings of RC for the $\text{H}_2\text{SO}_4/\text{NH}_3$ system. As is evident from Figure 2, the maximum extent of reaction achieved during the gas-phase diffusion-controlled process decreases with increasing NH_3 partial pressure. At $P_A^g(\infty) = 1000 \text{ dynes/cm}^2$ the gas-phase diffusion-controlled process is short lived and it is expected with increasing NH_3 pressure the gas-phase diffusion will completely vanish. The total reaction dynamics for these conditions appear as an initial surface phase reaction followed by an internal particle diffusion controlled process, as was observed by RC. As the NH_3 partial pressure is reduced, the gas-phase diffusion-controlled process becomes more prominent as was evidenced by HCL.

REFERENCES

- Huntzinger, J. J., Cary, R. A., and Ling, C., *Env. Sci. and Tech.* 14, 819 (1980).
Robbins, R. C. and Cadle, R. D., *J. Physical Chemistry*, 62, 469 (1958).
Rubel, G. O. and Gentry, J. W., *Particulate Science and Technology* (In press).

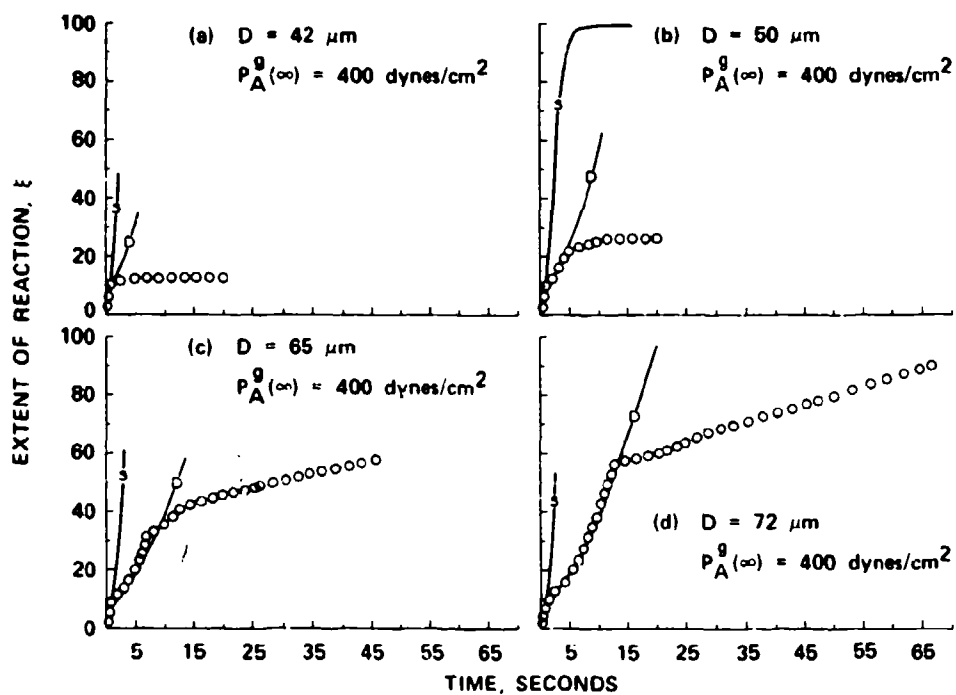


FIGURE 1. REACTION DYNAMICS AS A FUNCTION OF PARTICLE SIZE. With increasing particle size the gas phase diffusion (D) is accentuated and particle crystallization is delayed.

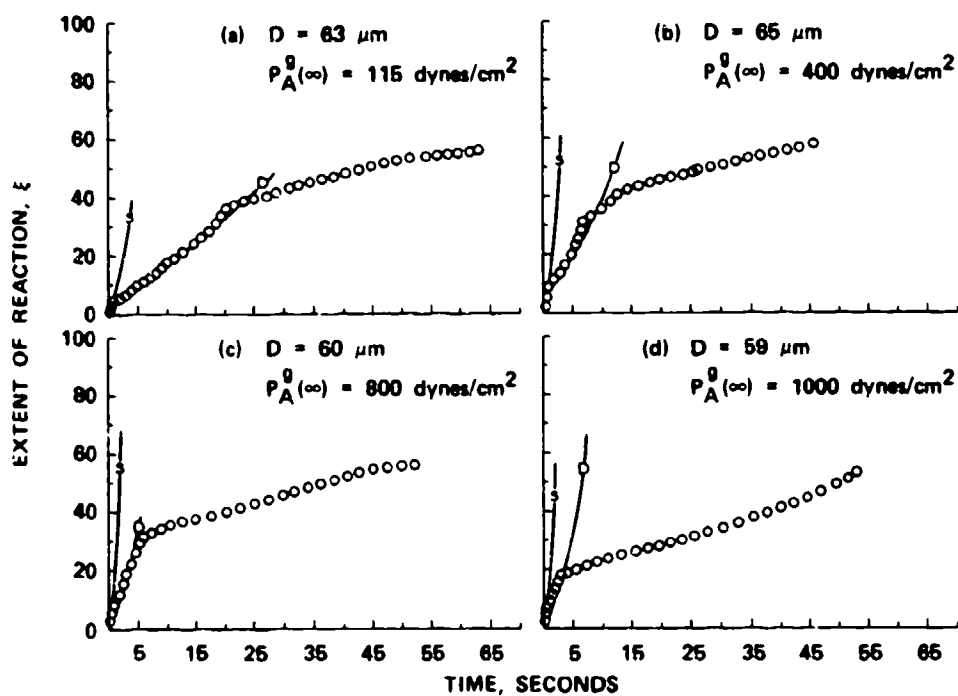


FIGURE 2. REACTION DYNAMICS AS A FUNCTION OF NH_3 GAS PRESSURE. Increasing gas pressure diminishes the duration of the gas phase diffusion process (D) and accelerates particle crystallization.

BLANK

IR EMISSIVE CLOUD STUDY

P. Ase and A. Snelson
IIT Research Institute
Chicago, IL 60616

ABSTRACT

The production of an infrared emitting aerosol requires an exothermic chemical or physical reaction to occur in a cloud of suspended material. The effectiveness of such a system depends on the chemical composition, size, shape and phase of the particles involved, the chemical and physical processes responsible for heat generation and the dissemination technique employed. During the last year, experimental work has continued to investigate some of the above facets of the IR emissive cloud problem. The results of these studies will be presented in a Technical Report to be submitted in October, 1984.

The above study was supported by the Chemical Systems Laboratory, Aberdeen Proving Ground, through the U. S. Army Missile Command, Red Stone Arsenal under Contract No. DLA900-80-C-2853.

Other documentation of this work may be found in:

P. Ase, R. Remaly and A. Snelson, "IR Emissive Cloud Study", Proceedings of the 1983 CSL Conference on Obscuration and Aerosol Research p. 185.

P. Ase, R. Remaly and A. Snelson, "IR Emissive Cloud Study", Tactical Weapon Guidance and Control Information Analysis Center, Final Report No. GACIAC SOAR-83-05, June, 1983.

Future work is expected to be directed at investigation of a new infrared aerosol.

BLANK

ON POSSIBLE EXPERIMENTAL APPLICATION OF SOME PROPERTIES
OF THE FIRST EXPANSION COEFFICIENTS
OF THE PHASE FUNCTION

A. Coletti
School of Geophysical Sciences
Georgia Institute of Technology
Atlanta, Georgia 30332

ABSTRACT

The possibility of applying semi-empirical models based on the formulas of geometric optics to the light scattered by non-spherical particles has been investigated with laboratory experiments. They demonstrated some properties of the asymmetry parameter that are applicable in determining the internal homogeneity of monodisperse aerosols. A complete description of the results is given in:

A. Coletti, 1984: Light Scattering by Nonspherical Particles: A Laboratory Study, *Aerosol. Sci. and Tech.*, 3, 39-52.

In the case of aerosol polydispersions, Grams, (1981), Pollack and Cuzzi (1980) and Ackerman et al. (1981) suggested that anomalously low values of asymmetry parameter can be found in nature as an effect of nonsphericity of the particles. Consequently, a study on the radiative properties of the stratospheric cloud of El Chichón was initiated and results were reported in:

A. Coletti, D.J. Hofmann and J.M. Rosen, 1984: Radiative Properties of the Stratospheric Cloud of the Eruption of El Chichón at Visible Wavelength: A Comparison Between Balloon-borne Horizon Photography and Optical Counters (Submitted to *Jour. of Atmos. Sci.*)

Specific aspects of these subjects have also been discussed during presentations at the 1984 CRDC conference on Obscuration and Aerosol Research (poster session) and at the International Radiation Symposium, Perugia (Italy), 21-29 August 1984.

One of the problems commonly encountered analyzing experimental data of light scattering is related to the fact that it is practically inconvenient to take measurements for directions close to the direction of the illuminating beam (0 and 180°); therefore, data interpolations are sometimes necessary in the forward and backward directions in order to complete the data set.

In this paper some preliminary results of numerical calculations will be discussed. These calculations were performed in an attempt to establish general criteria to apply to interpolations of light scattering data for backward directions. At this stage, the analysis has been carried out on spherical particles.

INTRODUCTION

In the case of spherical particles the geometric optics approximation gives results comparable with the Mie theory for values of the size parameter x ($=2\pi r/\lambda$) of the order of 100 or 1000. In the case of nonspherical particles, there are many features in the angular light scattering diagram (phase function) that practically disappear when averaged over the total number of possible orientations of the particle in space. Therefore, in some of these cases semi-empirical approximations, based on formulas of geometric optics, have been suggested and applied even for very low values of size parameters of the equivalent volume sphere. Since semi-empirical approximations sometimes fail to properly describe the backward scattering (Coletti, 1984), it is interesting to investigate how the oscillations characteristic of the functions describing the light scattering by spherical particles, merge into the smoother domain where the formulas of the geometric optics are valid.

Mathematically, the angular characteristics of light scattering can be described by any convenient set of orthogonal polynomials. In particular, van de Hulst (1980) in Fig. 10.5 shows how Legendre polynomial coefficients up to the 35th order have a common characteristic behavior as function of size parameter. For increasing size parameters, higher orders of polynomial coefficients start to become relevant and, after reaching a maximum, they start oscillating with decreasing amplitudes. In the case of non-polarized light, the first two coefficients are proportional to scattering coefficient and asymmetry parameter, respectively. In what follows, the meaning of these two coefficients will be discussed in respect to the polarization of the light.

DEFINITIONS

Light rays crossing a large light-absorbing particle are strongly attenuated so that only the rays reflected from the surface and those diffracted need to be taken into account. Under these circumstances, the scattering and extinction coefficients (indicated with Q_{sca} and Q_{ext} , respectively) can be approximated by formulas of the kind (see Irvine, 1965; van de Hulst, 1957; Kerker, 1969):

$$Q_{ext} = 2 \quad (1)$$

$$Q_{sca} = 1 + w' = 1 + \frac{1}{2} (w_1' + w_2') \quad (2)$$

and the asymmetry parameter by:

$$\langle \cos \theta \rangle = (1 + w'g') / (1 + w') \quad (3)$$

where

$$w' = \frac{1}{2} (w_1 + w_2) \quad (4)$$

and

$$g' = \frac{1}{2w'} \int_0^1 (2\sigma - 1)(|r_1|^2 + |r_2|^2) d\sigma = \frac{1}{2} (g_1 + g_2) \quad (5)$$

where r_1 and r_2 are Fresnel reflectances (M. Born and E. Wolf, 1969, Sec. 13.4), $\sigma = \cos 2\tau$, and τ is the complement of the angle of incidence of a ray on the particle surface. Here, we redefine the quantities w_1' and g_1' ($i = 1, 2$ for the two orthogonal planes of linear polarization) in a slightly different way. Starting from the phase function $P_i(\theta)$, we can define the integral quantities:

$$g_i = \frac{1}{2} \int_{-1}^1 P_i(\theta) \cos \theta d(\cos \theta) \quad (6)$$

$$w_i = \frac{1}{2} Q_{sca} \int_{-1}^1 P_i(\theta) d(\cos \theta) \quad (7)$$

In analogy with the preceding case results,

$$\langle \cos \theta \rangle = \frac{1}{2} (g_1 + g_2) \quad (8)$$

$$Q_{\text{sca}} = \frac{1}{2} (w_1 + w_2) \quad (9)$$

Since the quantities g_1 , g_2 , and w_1 , w_2 are related one to the other, through the asymmetry parameter $\langle \cos \theta \rangle$ and the scattering coefficient Q_{sca} , we found it convenient to plot the ratios:

$$R_g = g_1 / \langle \cos \theta \rangle \quad (10)$$

and

$$R_w = w_1 / Q_{\text{sca}} \quad (11)$$

RESULTS

Let us start considering the scattering coefficient and the asymmetry parameter shown in Figs. 1a and 1b for particles having the same real part of the index of refraction ($n = 1.6$) and three different values of the imaginary part ($k = 0, 0.05, 0.5$).

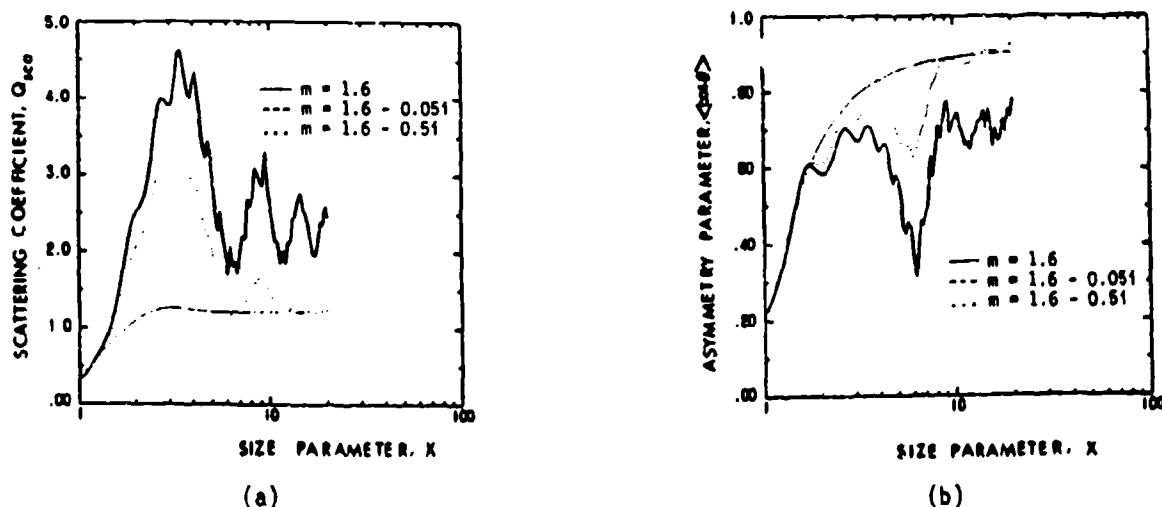


FIGURE 1. SCATTERING COEFFICIENT (a), AND ASYMMETRY PARAMETER (b).

The previously defined scattering ratio R_w and asymmetry ratio R_g are shown in Figs 2 and 3 as a function of size.

For values of size parameter smaller than 1.5 the ratios are practically constant and equal to the asymptotic value they assume in the case of Rayleigh scattering. While the asymptotic value of R_w can be easily computed analytically, the value of $R_g = 1.18$ has to be computed as a limit for

decreasing x , because both numerator and denominator of R_g identically vanish in the Rayleigh scattering.

In Figure 2, for size parameter equal to 1, the value of R_w is just slightly higher for non-light-absorbing particles than for absorbing particles. This is due to the relatively low value of polarization at 90° exhibited by light absorbing particles. For size parameters between 1 and 2, R_w decreases. In fact, as indicated in Fig. 4a, the angle of maximum polarization is moved toward the backward direction decreasing the difference between the values of the two scattering integrals.

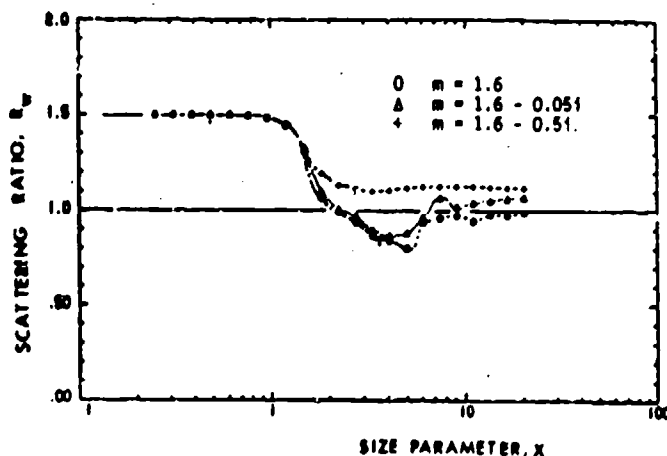


FIGURE 2. SCATTERING RATIO. The ratio between the scattering integrals for parallel polarization and unpolarized light as defined in Eq. (11).

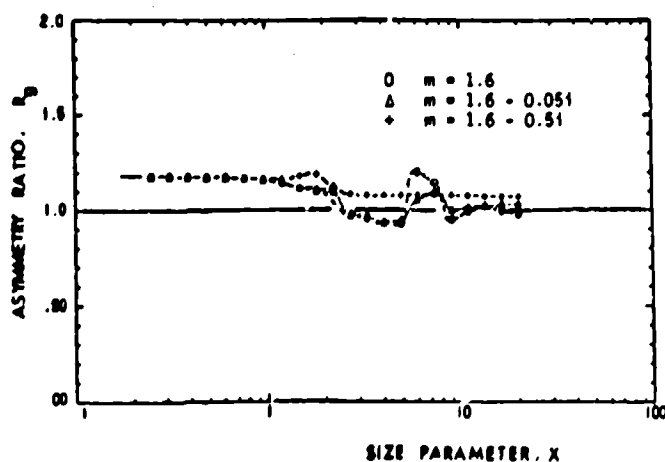


FIGURE 3. ASYMMETRY RATIO. The ratio between the integrals of asymmetry for light polarized and unpolarized, as defined in Eq. (10).

Light absorbing particles at size parameter 1.6 have features in the polarized phase functions that are characteristic of larger values of size. In fact, Fig. 4b shows a scattering lobe forming at angles around 140° in $P_2(\theta)$. The evolution of the lobe with x along with a simultaneous decrease in the forward scattering causes the value of R_w for light-absorbing particles to be greater for size parameter 1.6 and above. In fact, the absolute value of the complex refractive index is higher for light-absorbing particles, having the same real part of refractive index of non light-absorbing particles. Therefore, the light rays crossing the light absorbing particles undergo longer optical pathlength.

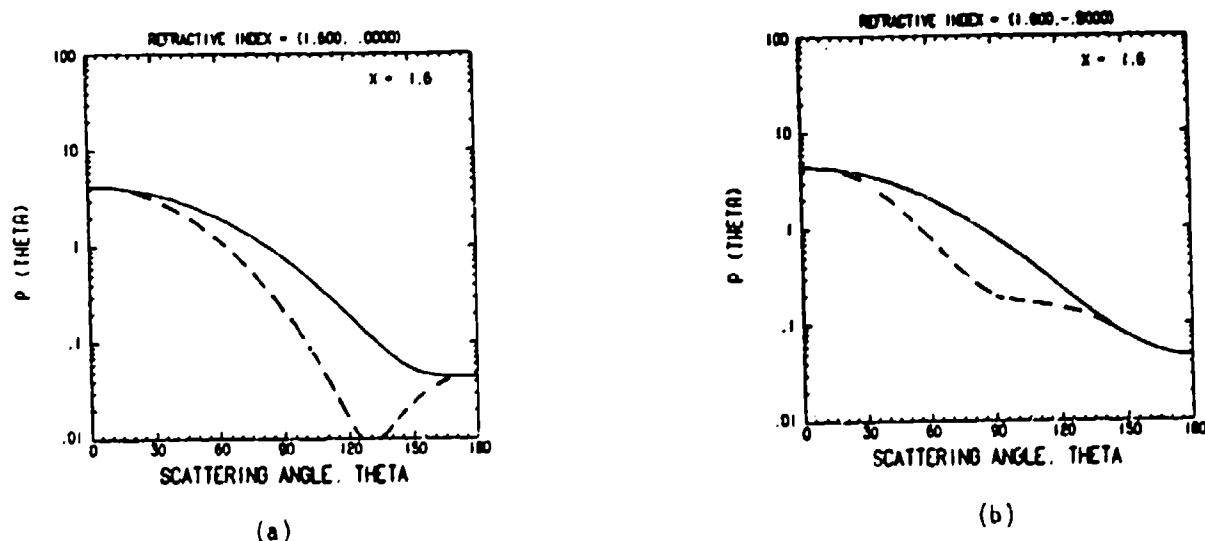
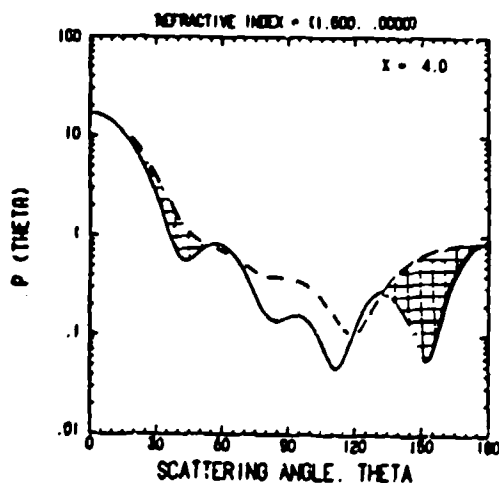
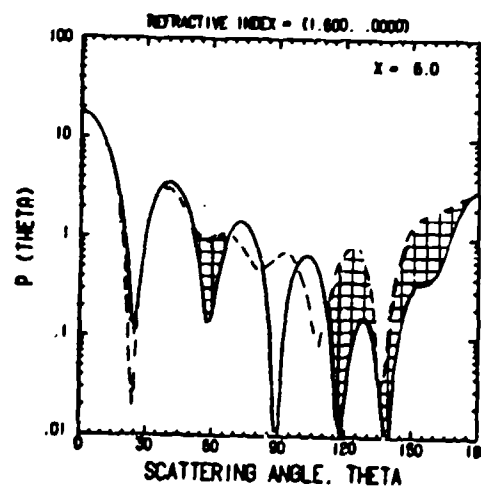


FIGURE 4. POLARIZED PHASE FUNCTIONS. Particles of size parameter $x = 1.6$. Solid curve is $P_1(\theta)$; dashed curve is $P_2(\theta)$. (a) Non-light absorbing. (b) Light-absorbing with $k = 0.5$.

The ratio R_w for refractive index $m = 1.6-10.5$ reaches 1.12 for $x = 7$; simultaneously, the scattering efficiency Q_{sca} in Fig. 1a loses its ripple. The ratio R_g of Fig. 3 for the less absorbing particles has a pronounced broad peak for x around 7 when, correspondingly, the scattering efficiency and the asymmetry parameter have the first main minimum. The reason for this is easily found in the polarized phase functions for values of sizes inside and outside the peak. Figure 5a shows the phase functions $P_1(\theta)$ and $P_2(\theta)$ for non-light-absorbing particles of size parameter 4 and Fig. 5b for size parameter 6. In the figures, the shaded area marks the region contributing the most to the values of ratio R_g . For size parameter 6, the shaded area in the backward scattering has relatively higher importance than in the case of $x = 4$. In fact, at size parameter 6, refracted and diffracted rays undergo negative interference, decreasing the importance of the forward scattering. As further proof, it is possible to observe that the positive peak in the R_g plot (Fig. 3) diminishes as the imaginary part of the refractive index attenuates the refracted rays. For increasing imaginary part of the refractive index, both ratios become



(a)



(b)

FIGURE 5. POLARIZED PHASE FUNCTIONS. Non light-absorbing particles. (a) Size parameter $x = 4$. (b) Size parameter $x = 6$.

less sensitive to the size parameter and the asymptotic value given by the geometric optics for large absorbing spheres is approached for x between 10 and 30. This asymptotic value depends slightly on the complex refractive index entering in the Fresnel formulas (on this topic see also the cases discussed by Prishivalko, 1963).

Experiments performed in the laboratory suggested that in the case of particles of irregular shape and complex refractive index close to $1.5-0.1i$, this asymptotic value can be reached for size parameters as little as 7 (Coletti, unpublished data).

CONCLUSIONS

The discussion presented and the examples reported demonstrate the information content of the integral quantities w_1 and g_1 introduced in Eqs. (6), (7), (10), and (11). While some of these quantities may have modest physical meanings, their use in the applications may be convenient. Experimentally, R_w and R_g present numerous advantages as ratios of polarization measurements which are insensitive to multiplying factors in the instrumental calibration and are relatively immune to noise and experimental errors.

During extensive optical measurements of angular scattering, these or analogous quantities may be profitably used for real-time monitoring of experiments, or for generating a "quick look" at large data sets.

The next step of this research will be that of repeating an analogous discussion for the orders of Legendre polynomials that enter more directly in the backward scattering.

REFERENCES

- Born, M. and E. Wolf, Principles of Optics, Pergamon Press, Oxford, 1965.
- Coletti, A., Aerosol Sci. and Tech., 3, 39-52, 1984.
- Grams, G.W., Geophys. Res. Lett., 8, 13-14, 1981.
- Irvine, W. M., J. Opt. Soc. Am., 55, 16-21, 1965.
- Kerker, M., The Scattering of Light and Other Electromagnetic Radiation, Academic Press, NY, 1969.
- Pollack, J.B. and J.N. Cuzzi, J. Atmos. Sci., 37, 868-881, 1980.
- Prishivalko, A.P., Opt. Spectry. (U.S.S.R.), English Translation, 14, 139-141, 1963.
- van de Hulst, H.C., Light Scattering by Small Particles, Wiley, New York, 1957.
- van de Hulst, H.C., Multiple Light Scattering, Academic Press, New York, 1980.

RADIATION TORQUE ON A SPHERE ILLUMINATED WITH CIRCULARLY-POLARIZED
LIGHT AND THE ANGULAR MOMENTUM OF THE SCATTERED RADIATION

P. L. Marston⁺
Department of Physics, Washington State University
Pullman, Washington 99164

and

J. R. Crichton
School of Natural and Mathematical Sciences, Seattle Pacific University
Seattle, Washington 98119

ABSTRACT

This paper concerns the calculation of the radiation torque on spheres and the conceptual understanding of the angular momentum transport of scattered electromagnetic fields. Related work which has been published includes:

1. P. L. Marston and J. R. Crichton, "Radiation Torque on a Sphere Illuminated with Circularly Polarized Light," *Journal of the Optical Society of America* **B1**, 528-529 (1984).
2. P. L. Marston and J. R. Crichton, "Radiation Torque on a Sphere Caused by a Circularly-Polarized Electromagnetic Wave," *Physical Review* **A30**, 2508-2516 (1984).

In the present paper the principal results of these calculations are summarized together with a novel explanation of the rate at which angular momentum is radiated by the scattered field. This angular momentum is decomposed into its "orbital" and "spin" parts. This decomposition explains why the torque should vanish on a nonabsorbing isotropic dielectric sphere.

RADIATION TORQUE ON A SPHERE

We recently calculated the torque on an isotropic sphere illuminated by a circularly polarized plane wave.^{1,2} The formulation of the other fundamental cross sections by Mie (1908) and Debye (1909) for homogeneous isotropic spheres give the well-known efficiency factors for scattering, absorption, extinction, and radiation pressure usually designated by Q_{sc} , Q_{abs} , Q_{ext} , and Q_{pr} respectively.

Consider a homogeneous isotropic sphere of radius a illuminated in vacua by a z-directed wave of positive helicity (i.e. the z-projection of the photon-spin is positive). We refer to this wave as being left-circularly polarized. The incident wave's fields may be written² $E_0 \text{Re}[\vec{E}_1 \exp(-i\omega t)]$ and $E_0 \text{Re}[\vec{B}_1 \exp(-i\omega t)]$ where $\vec{E}_1 = (\hat{x} + i\hat{y}) \exp(ikz)$ and $\vec{B}_1 = -i\vec{E}_1$; \vec{E}_2 and \vec{B}_2 designate similarly dimensionless scattered fields. The origin O of the coordinate system (Fig. 1) coincides with the center of the sphere. It is also the center about which the radiation torque is specified. The radiation torque $\vec{\tau}$ is equal to the average rate which field angular momentum is transported into the sphere. For the steady-state problem under consideration, this equals the flux of angular

⁺P. L. Marston was supported in part by an Alfred P. Sloan Fellowship and by the Office of Naval Research.

momentum through a concentric spherical surface of radius $r > a$. A conservation theorem relates this flux to the time-averaged Maxwell stress dyad $\langle \vec{T} \rangle$ of the total (incident + scattered) fields via the surface integral²

$$\vec{\Gamma} = - \int d\vec{S} \cdot \langle \vec{T} \rangle \times \vec{r} . \quad (1)$$

The symmetry of the problem under consideration gives $\Gamma_x = \Gamma_y = 0$ while²

$$\Gamma_z = I_L \pi a^2 Q_T / \omega \quad (2)$$

where $I_L = E_0^2 c / 4\pi$ is the incident irradiance and Q_T is the torque efficiency factor. The integral in Eq. (1) may be partitioned giving²

$$Q_T = Q_{11} + Q_{12} + Q_{21} + Q_{22} , \quad (3)$$

$$Q_{ij} = -k(2\pi a^2)^{-1} G_{ij} , \quad (4)$$

$$G_{ij} = r^2 \text{Re} \int [\vec{E}_i \cdot \vec{E}_j^* (\vec{E}_j^* \times \vec{r} \cdot \hat{z}) + \vec{E}_j \cdot \vec{E}_i^* (\vec{E}_i^* \times \vec{r} \cdot \hat{z})] d\Omega , \quad (5)$$

and the integration is over a solid angle of 4π sr. Equation (3) partitions Q_T into terms involving incident fields (Q_{11}), scattered fields (Q_{22}), and mixed terms ($Q_{12} + Q_{21}$). Evaluation of the Q_{ij} is facilitated with the modern formulation of vector spherical harmonics and associated theorems.² The expansion coefficients of the \vec{E}_2 and \vec{B}_2 follow from the usual boundary conditions at the radius a used in Mie theory.

It is not difficult to show that $Q_{11} = 0$; the remaining Q_{ij} may be evaluated in the $kr \rightarrow \infty$ limit. Occasionally tedious algebra reduces them to usual Mie-theoretic efficiency factors:

$$Q_{22} = -Q_{sc} , \quad Q_{12} = Q_{ext} \quad (6a,b)$$

and $Q_{21} = 0$. Evidently the torque efficiency factor is

$$Q_T = Q_{ext} - Q_{sc} = Q_{abs} \quad (7)$$

so that Q_T vanishes for a lossless dielectric sphere.

The analysis leading to Eqs. (2) and (7) has been extended to include spheres with radial gradients of the refractive index and elliptically polarized plane-wave illumination.² We need not consider these results here or in the discussion which follows.

Central to the prediction that the torque vanishes for a lossless dielectric sphere is the intermediate result, Eq. (6a), which requires the flux of the z-component of the angular momentum radiated by the scattered field (considered alone) be proportional to the total scattered power. This requirement may at first appear to be in conflict with the following physical argument. Consider the radial flux density of angular momentum at a distant observer ($r \gg ka^2$ from the sphere's center) where the scattered field \vec{E}_2, \vec{B}_2 has the local appearance of an elliptically polarized plane wave. These fields may be locally approximated as due to superposition of left and right hand plane waves having irradiances of I_+ and I_- , respectively. According to this argument the radial flux of the radial-component of the angular momentum is proportional to $(I_+ - I_-)$ while the radial flux of the z-component of the angular momentum should be proportional to $(I_+ - I_-) \cos\theta$ where θ is the scattering angle as defined in Fig. 1. Since the illumination is circularly polarized the flux densities must be independent of the azimuthal angle ϕ . A detailed calculation of the rate of spin angular momentum radiated by the flux of photons into all directions gives the following result

$$\frac{d\vec{J}_{\text{spin}}}{dt} = 2 \frac{I_L \pi a^2}{\omega} Q_{\text{spin}}, \quad (8)$$

$$Q_{\text{spin}} = \frac{r^2}{I_L \pi a^2} \int (I_+ - I_-) \cos\theta \, d\Omega, \quad (9)$$

where the integration is over a solid angle of 4π sr. The reason for the spin designation on this flux (and on the efficiency factor Q_{spin}) will be evident from a subsequent discussion.

The left and right handed irradiances I_+ and I_- may be computed using the expressions for the dimensionless scattered fields \vec{E}_2 and \vec{B}_2 . Expressions for the far-zone scattered fields appropriate for circularly-polarized illumination may be alternately obtained using conventional Mie theory and a linear transformation like the one described on page 189 of Ref. 3 (supplemental list of Reference, below). Either approach gives the following proportionalities

$$I_{\pm} \propto I_L |S_{\pm}^{\pm}|^2, \quad (10)$$

where $S_{\pm} = S_1 \pm S_2$ in which S_1 and S_2 are Mie scattering amplitudes in the usual notation (see e.g. Ref. 3). Evaluation of the required proportionality constants and a tedious evaluation of the integral in Eq. (9) yields the following "spin" efficiency factor

$$Q_{\text{spin}} = \frac{2}{(ka)^2} \sum_{n=1}^{\infty} \frac{(2n+1)}{n(n+1)} \{ |a_n|^2 + |b_n|^2 \} + \frac{2n(n+2)}{n+1} \operatorname{Re}[a_{n+1} b_n^* + a_n b_{n+1}^*] \quad (11)$$

where a_n and b_n are the "scattering coefficients" of Mie theory in the usual notation.^{2,3} (The coefficients a_n and b_n are proportional to the strengths of oscillating electric and magnetic multipoles, respectively, which give rise to the scattered fields.²) We have numerically evaluated Eq. (11) for representative lossless and lossy spheres and find that $0 < Q_{\text{spin}} < Q_{\text{sc}}$. Since $Q_{\text{spin}} \neq Q_{\text{sc}}$, it is evident that Eq. (8) does not give all of the angular momentum flux of the scattered field. Indeed, if one assumes that the flux to be entirely specified by Q_{spin} , it would be expected that $Q_T = Q_{\text{ext}} - Q_{\text{spin}}$ which does not vanish for a lossless dielectric sphere!

To resolve the apparent conflict, it is necessary to identify radiated angular momentum not included in Eq. (8) which was included in our exact evaluation of Q_{22} . The local angular momentum density of the scattered field is proportional to²

$$\vec{j}_2 = \operatorname{Re}[\vec{r} \times (\vec{E}_2 \times \vec{B}_2)] , \quad (12)$$

where \vec{E}_2 and \vec{B}_2 are normalized scattered fields as in Eq. (5) and the normalization used is such that²

$$Q_{22} = - \frac{kr^2}{2\pi a^2} \int \hat{z} \cdot \vec{j}_2 d\Omega , \quad (13)$$

in the limit $kr \rightarrow \infty$ and the integration is over a solid angle of 4π sr. The relevant component of \vec{j}_2 may be split into the following terms

$$\hat{z} \cdot \vec{j}_2 = \hat{z} \cdot \vec{j}_{\text{spin}} + \hat{z} \cdot \vec{j}_{\text{orbital}} + \hat{z} \cdot \vec{j}_{\text{surface}} , \quad (14)$$

$$\hat{z} \cdot \vec{j}_{\text{spin}} = \frac{-1}{k} \operatorname{Re}[i \hat{z} \cdot (\vec{E}_2^* \times \vec{E}_2)] , \quad (15)$$

$$\hat{z} \cdot \vec{j}_{\text{orbital}} = \frac{1}{k} \operatorname{Re}(\vec{E}_2^* \cdot \vec{L}_z \vec{E}_2) , \quad (16)$$

$$\hat{z} \cdot \vec{j}_{\text{surface}} = \frac{1}{k} \operatorname{Re}[i \nabla \cdot [\vec{E}_2^* (\vec{r} \times \vec{E}_2) \cdot \hat{z}]] , \quad (17)$$

where use has been made of conditions $\nabla \cdot \vec{E}_2 = 0$, $\nabla \cdot \vec{B}_2 = 0$ and the requirement that the physical fields are solutions of Maxwell's equations having a harmonic time dependence. In Eq. (16), L_z denotes operator $\hat{z} \cdot \vec{L}$ in which $\vec{L} = -i(\vec{r} \times \nabla)$ is an infinitesimal rotation operator.⁴ Hence the identification of right side of Eq. (16) with the orbital angular momentum of the field. The angular momentum associated with the right side of Eq. (15) lacks a lever arm and hence it may be attributed to the intrinsic spin of the field. The decomposition of field angular momentum given by Eqs. (14)-(17) is similar to that discussed by Humblet⁵ and others^{4,6} except we choose to write it in a gauge-invariant form.

In our original evaluation of Q_{22} , the integral in Eq. (13) was evaluated directly using a multipole expansion of \vec{E}_2 and \vec{B}_2 . This procedure gave Eq. (6a). We now summarize the results of using Eq. (14) in the evaluation of this integral. These are as follows:

$$\int \hat{z} \cdot \vec{j}_{\text{surface}} d\Omega = 0, \quad (18)$$

$$\frac{kr^2}{2\pi a^2} \int \hat{z} \cdot \vec{j}_{\text{spin}} d\Omega = Q_{\text{spin}}, \quad (19)$$

$$\frac{kr^2}{2\pi a^2} \int \hat{z} \cdot \vec{j}_{\text{orbital}} d\Omega = Q_{\text{sc}} - Q_{\text{spin}}, \quad (20)$$

where Q_{spin} is defined as in Eqs. (9) and (11). Inspection of Eqs. (13), (14), (18), (19), and (20) confirms that $Q_{22} = -Q_{\text{sc}}$.

DISCUSSION

The physical result of this analysis is that Eq. (8) correctly describes the spin contribution to the radiated angular momentum but it fails to include the orbital part described by Eq. (20). The result that the field possesses an orbital angular momentum is consistent with decompositions applied to other radiation problems.⁴⁻⁷ Our analysis affirms our previous prediction^{1,2} that the torque should vanish for a lossless isotropic dielectric sphere illuminated by a plane wave.

Consider the application of this analysis to "Rayleigh scattering" from a small sphere for which the only nonvanishing scattering coefficient may be taken to be a_1 . Then the scattering efficiency reduces to³ $Q_{\text{sc}} \approx 6|a_1|^2/(ka)^2$ so that Eq. (11) gives $Q_{\text{spin}} \approx Q_{\text{sc}}/2$. Hence the radiated z-component of the angular momentum is partitioned equally between orbital and spin parts. Equation (7) requires that the scatterer not be lossless if there is to be a torque. From the perspective of

classical physics, losses give rise to a phase shift between the induced dipole moment and the rotating E-field of the incident wave. This phase shift is essential if there is to be a radiation torque.

ACKNOWLEDGMENTS

We are grateful to B. T. Unger and to X. Shen for checking the algebra leading to Eq. (11). This research was supported in part by the Office of Naval Research and by an Alfred P. Sloan Fellowship held by one of us (P.L.M.). We are grateful to the Army Research Office for making possible our participation in the 1984 CRDC Conference.

SUPPLEMENTAL REFERENCES

3. C. F. Bohren and D. R. Huffman, Absorption and Scattering of Light by Small Particles (Wiley, 1983).
4. E. J. Konopinski, Electromagnetic Fields and Relativistic Particles (McGraw-Hill, 1981).
5. J. Humblot, "Sur le moment d'impulsion d'une onde electromagnetique," *Physica* 10, 585-603 (1943).
6. A. Messiah, Quantum Mechanics Vol. II (Wiley, 1963) p. 1051 (problem 7).
7. C. G. Darwin, "Notes on the theory of radiation," *Proc. Roy. Soc. A* 136, 36-51 (1932).

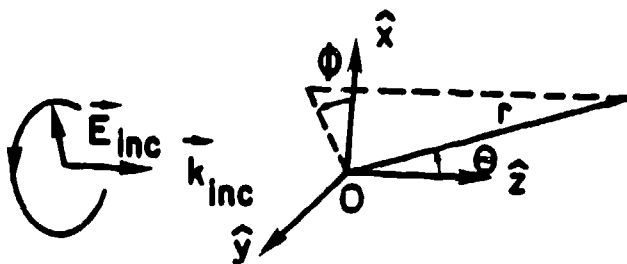


FIGURE 1. COORDINATE SYSTEM.

P. L. Marston and D. S. Langley**

Department of Physics
Washington State University
Pullman, WA 99164

ABSTRACT

This paper reviews research on enhanced backscattering and polarization phenomena due to the axial and rainbow focusing of rays having non-zero impact parameters. The emphasis is on glory waves associated with rays transmitted through the sphere in contrast to the well known case in which parts of the glory ray travel circumferentially on the sphere's surface. For this class of "transmitted-wave" glories, we have developed novel models of (i) the focal parameters of the virtual ring-like source of glory waves; (ii) the angle-dependent phase and amplitude properties of these waves in near-backward directions, and (iii) polarization phenomena for incident linear and circularly-polarized illumination. Some of the research is discussed in the following publications:

1. D. S. Langley and P. L. Marston, "Glory in the Optical Backscattering from Air Bubbles," *Physical Review Letters* 47, 913-916 (1981).
2. P. L. Marston, D. S. Langley, and D. L. Kingsbury, "Light Scattering by Bubbles in Liquids: Mie Theory, Physical-Optics Approximations, and Experiments," *Applied Scientific Research* 38, 373-383 (1982).
3. P. L. Marston and D. S. Langley, "Glory in Backscattering: Mie and Model Predictions for Bubbles and Conditions on Refractive Index in Drops," *Journal of the Optical Society of America* 72, 456-459 (1982).
4. P. L. Marston, "Light Scattering by Bubbles in Liquids: Comments and Applications of Results to Circularly Polarized Incident Light," *Applied Scientific Research* 40, 3-5 (1983).
5. P. L. Marston, "Uniform Mie-theoretic Analysis of Polarized and Cross-Polarized Optical Glories," *Journal of the Optical Society of America* 73, 1816-1818 (1983).
6. P. L. Marston and D. S. Langley, "Glory- and Rainbow-Enhanced Acoustic Backscattering from Fluid Spheres: Models for Diffracted Axial Focusing," *Journal of the Acoustical Society of America* 73, 1464-1475 (1983).
7. P. L. Marston, K. L. Williams, and T. J. B. Hanson, "Observation of the Acoustic Glory: High-Frequency Backscattering from an Elastic Sphere," *Journal of the Acoustical Society of America* 74, 605-618 (1983).
8. K. L. Williams and P. L. Marston, "Mixed-mode acoustical glory scattering from a large elastic sphere: Model and experimental verification," *Journal of the Acoustical Society of America* 76, 1555-1563 (1984).
9. P. L. Marston and D. S. Langley, "Strong backscattering and cross polarisation from bubbles and glass spheres in water," *Proceedings of the Society of Photo-Optical Instrumentation Engineers* 489, 130-141 (1984).

The last item listed includes a review of most of the earlier optical research. The emphasis of this research has been on bubbles or drop-like scatterers for which the relative refractive index is < 1.18 . The focal-parameters derived and the approximations for the amplitude and phases of the glory waves may be trivially generalized to other drop-like scatterers. For example, when the relative

*Research supported in part by the Office of Naval Research and in part by an Alfred P. Sloan Fellowship held by P. L. M.

**Present address: Department of Physics, Whitman College, Walla Walla, WA 99362.

refractive index is between $2^{1/2}$ and 2, there will be a strong glory wave due to the transmitted wave having two chords (and a single reflection). Previous calculations of the focal parameters and the existence conditions for transmitted-wave glories are critiqued in items 3 and 6. Items 6-8 are concerned with the acoustical analog of glory scattering. These are listed since they give the most complete derivations of focal parameters and angle-dependent phase shifts and they describe both the far-field₄ (distance to the observation point $r \gg ka$) and the less restrictive Fresnel region ($r \gg ka$).

Infrared Spectroscopy of Single Aerosol Particles

S. Arnold
Dept. of Physics
Polytechnic Institute of New York
Brooklyn, New York 11201

A.B. Pluchino
Infrared Space Optics Section, Chemistry and Physics Laboratory
Aerospace Corp.
P.O.Box 92957, Los Angeles, California 90009

This paper describes a means for obtaining the infrared absorption spectrum of a single aerosol particle by photothermal modulation of visible scattered light near a structure resonance (Structure Resonance Modulation Spectroscopy). This work was presented, published and submitted for publication as follows.

1. A.B. Pluchino and S. Arnold, "IR Spectrum of a Single Aerosol Particle by Photothermal Detuning Spectroscopy", Presented at Chemical Systems Laboratory Scientific Conference on Obscuration and Aerosol Research, Aberdeen Proving Ground, Maryland, June 1982.
2. S. Arnold and A.B. Pluchino, "IR Spectrum of a Single Aerosol Particle by Photothermal Modulation of Structure Resonances", Appl. Opt. 21, 4199(1982).
3. S. Arnold and A.B. Pluchino, "IR Absorption of a Single Aerosol Particle by Photothermal Modulation of Structure Resonances", Maryland Meeting of the American Association for Aerosol Research, April, 1983; Aerosol Sci. and Tech. 2, 194(1983).
4. S. Arnold and A.B. Pluchino, "Molecular Spectroscopy of a Single Aerosol Particle", San Francisco Meeting of the American Physical Society, Bull. Am. Phys. Soc. 28, 1345(1983).
5. S. Arnold, M. Neuman and A.B. Pluchino, "Molecular Spectroscopy of a Single Aerosol Particle", Opt. Lett. 9, 4(1984).
6. S. Arnold, and A.B. Pluchino, "Infrared Spectroscopy of Single Micron-Sized Particles", 1984 CRDC Conference on Obscuration and Aerosol Research, Aberdeen Proving Ground, Maryland, June, 1984.
7. S. Arnold, E.K. Murphy, and G. Sageev, "Aerosol Particle Molecular Spectroscopy", Submitted to the Journal of Applied Optics, August, 1984.

INTRODUCTION

This paper is concerned with a means for measuring the spectrum of Q_s on a single aerosol particle in the IR. There are a number of reasons for wanting to make such a measurement. Our motivation originally arose in connection with modeling photophoresis. The force in this case was shown to be proportional to

Q_a as well as an anisotropy factor which describes the distribution of the internal field sources.^{1,2} Consequently the only way to isolate the anisotropy factor experimentally was to measure both the photophoretic force and Q_a . Unfortunately at the time no means existed for measuring Q_a on an isolated particle. Since the spectrum of Q_a would also provide fairly complete information concerning both the emissivity of the particle as well as local effects which control aerosol obscuration, we attempted to formulate the first such spectroscopy. In what follows we will show that the spectrum of Q_a may now be determined experimentally. In addition since the absorption of IR is sensed by photothermal evaporation from the particle, our measurements allow us to follow the associated mass transport processes.

Measurement Principle

This new method is called Structure Resonance Modulation Spectroscopy (SRMS).³ SRMS is in a sense an amplification scheme, where a small amount of absorbed IR causes a large change in visible scattered light. When infrared radiation is absorbed by a small solution drop in equilibrium with water vapor, the droplet evaporates slightly; it shrinks in size. The evaporation is caused by an increase in vapor pressure at the surface of the drop as its temperature increases. The new smaller size is stable as long as the radiation is continuous. The mechanism for this phenomena may be understood, for an ideal solution, in terms of Raoult's Law. Simply stated, the vapor pressure of the water at the surface of such a solution is the vapor pressure of pure water times the mole fraction of water in solution. When a drop is heated the vapor pressure increases, a flux of vapor is emitted into the external medium, and the drop shrinks. Since this shrinkage causes a decrease in the mole fraction of water in the particle, the vapor pressure at the surface of the drop begins to fall. Eventually the particle reaches a vapor pressure equal to the external environment and the particle stabilizes in size. For the weak intensity produced by a monochromatized incandescent IR source ($\sim 10\text{cm}^{-1}$ bandwidth), the size change of a particle 5 μ in diameter may be smaller than 1 Å. However this size change is easily detected by measuring a corresponding change in elastically scattered visible light. To do this the

narrow band radiation from a tunable dye laser is positioned at the low wavelength side of a structure resonance of the particle. This resonance, detected through visible scattered light⁴, is a natural electromagnetic mode of the particle.⁵ It can be shown¹ that a fractional change in particle radius $\delta a/a$ leads to precisely the same change in resonant wavelength $\delta \lambda_r/\lambda_r$. Thus a given resonance is shifted to shorter wavelength as the particle shrinks. If the incident radiation is positioned at the short wavelength side of a resonance, a reduction in particle size will lead to an increase in scattered light. As one can see from the calculated backscattering spectrum of a water droplet in Fig.1, a 3Å change in particle radius (out of 24,980Å) leads to more than a 25% change in visible scattered light at 5346.5Å. The transfer parameter describing the scattered light change is $\beta = (a/S)(\partial S/\partial a)$. The value of β at 5346.5Å in Fig.1 is -2500. This means a 1% increase in scattered light would reveal a 0.1Å decrease in radius!

Experimental Setup

The particle is electrically suspended in air within a sealed chamber by the use of a quadrupole trap. The sample particle is prepared by injecting a dilute solution droplet of $(\text{NH}_4)_2\text{SO}_4$ from an impulse jet placed above the chamber. A saturated KCl solution placed in the chamber provides a stable water-vapor background. A typical sample was 5 to 10 microns in diameter. The dye laser beam was introduced from below as shown in Fig.2.

A typical spectrum of light scattered at 90° is shown by the lower curve in Fig.3. The upper curve shows the effect of introducing steady, unfiltered radiation from a Nernst Glower. The shift of the resonances to shorter wavelengths is due to evaporative shrinkage. The dynamics of this process is recorded in Fig.4. The upper curve shows the scattered light fluctuation corresponding to a chopped IR source. The visible laser was positioned half way up on the low wavelength side of a narrow structure resonance. We see that the time variation of the scattered light is triangular in comparison with the square wave modulation of the incident IR. The phase boundary relaxation process

giving rise to this behavior will be discussed in the next section.

By filtering the IR source with an optical wedge monochromator we obtain the IR Structure Resonance Modulation Spectrum through phase sensitive detection at 20Hz. Fig.5 shows the IR SRMS spectrum near the prominent vibrational resonance of the SO_4^{2-} ion at 9.1μ . Since the water fraction is known from the external vapor pressure through thermodynamics, one can compare the line shape in Fig.5 with predictions of Mie theory based on measurements of complex refractive index.⁶ In fact the solid line through the data in Fig.5 is such a calculation. We see that the SRMS spectrum is proportional to Q_s . In addition the signal at a given wavelength is found to be proportional to both the incident IR intensity and the transfer function β . So our empirical result is that the first harmonic of the scattered light fluctuation, δS , is given by

$$\delta S(\lambda_2)/S = F\beta(\lambda_2)Q_s(\lambda_1)I_1(\lambda_1) \quad (1)$$

where λ_1 and λ_2 are the IR and visible wavelengths.

I_1 is the first harmonic of the IR intensity, and S is the average visible scattered light intensity. In what follows we will develop a simple physical model to rationalize Eq.1 and design a critical experiment for testing this model.

Physical Model

The equations describing the detailed coupling between a heated drop and the associated hydrodynamic modes of external gas and vapor are in general nonlinear. Due to this inherent nonlinearity, we lean on experimental evidence in developing a model for the interaction of such a drop with weak radiation. The first apparent fact is that the phase-boundary relaxation process is much slower than the characteristic time for the temperature and vapor fields to come to steady state. From Fig.4 we see that the phase boundary relaxation time is slower than 1/40 sec. However, the characteristic time for steady state of the vapor field is $\beta_v^{-1} = a^2/3D$, which would be on the order of 10^{-7} sec for the particle in Fig.4. The corresponding time for the

temperature field is on the same order. Consequently both fields will be assumed always to be in steady state. In addition since the temperature increase over ambient is less than one hundredth of a degree Kelvin, the Grashof number will be much less than one, and hydrodynamic influences on external heat and mass transport may be safely neglected.⁷ The particle size is controlled by its mass. Within our diffusive model the time rate of change of the particle mass dm/dt is

$$dm/dt = \int D \nabla C \cdot \hat{n} dA. \quad (2)$$

In order to perform the integration in Eq.2 we make the additional assumption of spherical symmetry. This assumption is justified since the thermal relaxation time within the particle is short compared with the relaxation time observed in Fig.4. Thus the vapor density outside the particle will fall off like $1/r$ and the time rate of change of the particle radius (with particle mass density ρ_p assumed constant) is

$$da/dt = -D \delta C_s / (\rho_p a). \quad (3)$$

where δC_s is the vapor density at the particle surface minus that at infinity. We see that as the surface vapor density increases the particle radius will shrink. To model the effects of size and temperature on the surface vapor density we combine Raoult's Law (including an appropriate van't Hoff factor) with the Clausius-Clapeyron equation. The temperature increase is related to the light absorption through an equation of energy conservation. The optical power absorbed is dissipated through thermal conduction into the ambient gas and in providing the latent heat of vaporization of surface molecules. All of these effects are included in Eqn.3 and the resulting equation is expanded to first order in size change, $\epsilon(t)$. A simple differential equation for the time rate of change of ϵ evolves,

$$d\epsilon/dt = -aI(t) - \gamma\epsilon, \quad (4)$$

where I is the incident intensity and a and γ are constants which depend on the physical makeup of particle, vapor and ambient gas,

$$\alpha = (Z/(LZ+1)) \cdot (Q_g/4\rho_p) \quad (5a)$$

and

$$\gamma = \beta_v (1C_p/\rho_p \alpha^2 f_w) X_w (1-X_w)/(LZ+1) \quad (5b)$$

with $Z = (DC_p/K_g T)(1-i(1-X_w)) \cdot ((LM/RT)-1)$.

In Eqns.5, X_w , f_w are the mole fraction and weight fraction of water in the droplet, L is the latent heat for water at the surface, i is the van't Hoff factor of the solute, C_p and M are the mass density and molecular weight of pure water and, K_g and T are the thermal conductivity and temperature of the ambient gas.

We see from Eqn.5 that the time for the phase boundary to relax is considerably slower than the time for the vapor field to reach steady state, β_v^{-1} . Since the ratio of the density of water vapor to the density of liquid water, C_p/ρ_p , near room temperature is 10^{-5} one immediately can see the large effect which evaporation has on the relative magnitudes of γ and β_v . The other contributions to γ in Eqn.5 further this distinction.

Test of Physical Model

We have tested the above model for SRMS by direct measurements of the phase boundary relaxation rate. The experiment involved pulsing the IR radiation while measuring the transient scattered light. For the weak radiation levels used in our spectroscopy ($<20\text{mW/cm}^2$) we find the relaxation measurements agree with our model within the measurement uncertainty ($\sim 15\%$).

Discussion

The proportionality of the SRMS signal with Q_g and the incident IR intensity (Eqn.1) is rationalized through Eqn.4. The agreement between this equation and pulsed experiments is good, and thereby enables us to determine the proportionality factor F in Eqn.1.

For a periodically modulated IR source, at angular frequency ω the factor F in Eqn.1 will depend on ω . If we suppose a harmonic excitation $I = I_0 \exp(j\omega t)$, the corresponding size fluctuation may be evaluated from Eqn.4. Using this response function and Eqn.1, F is found

to be

$$F = Z / (4\pi \rho_p (\omega^2 + \gamma^2)^{1/2} (LZ + 1)) \quad (6)$$

From Eqn.6 one sees the large effect of the modulation frequency, ω , on the function F , and therefore on the scattered light fluctuation. For large particles containing a large mole fraction of water, γ may be less than 1 sec^{-1} , and one must go to extremely slow modulations (linear frequency $< (2\pi)^{-1} \text{ Hz}$), in order to optimize the signal. Since $1/f$ type noise sources make signal retrievable difficult in this region, higher frequencies are desirable. Fortunately for aerosol size particles near deliquescence, larger and therefore more manageable values of γ are obtained.

Conclusion

We see from the foregoing that the SRMS technique provides the only means at present for measuring the absorption spectrum of a single isolated particle. The modulation is adequately described by a steady-state model for vapor and temperature transport. Our assumptions are specific in applying to the case of low intensity and low Knudsen Number.

Future

Our work in the future will encompass three areas. First, we will extend our work on SRMS to the region of large Knudsen number where the effects of gas mean free path are expected to make the phase boundary relaxation process sensitive to water sticking.⁸ Second, we will begin to look at the SRMS IR spectrum of the supersaturated phase. Surprisingly little work has been done on this phase although it is known that a significant fraction of aerosol particles in the atmosphere are supersaturated. Finally, we will begin to investigate the SRMS spectrum from adsorbates on solid spherical particles, in order to gain an understanding for the manner in which molecular adsorbates effect the photophysical interaction.

References

1. S. Arnold and M. Lewittes, J. Appl. Phys., 53, 5314(1982).
2. A.B. Pluchino, Appl. Opt., 22, 103(1983).
3. S. Arnold, M. Neuman, and A.B. Pluchino, Opt. Lett., 9, 4(1984).
4. A. Ashkin and J.M. Dziedzic, Appl. Opt., 20, 1803(1981)
5. P. Chylek, J.T. Kiehl, and M.K.W. Ko, Phys. Rev. A, 18, 2229(1978).
6. E.E. Remsberg, Appl. Opt., 12, 1389(1973).
7. L.D. Landau, and E.M. Lifshitz, Fluid Dynamics (Pergamon Press, London 1959)
8. P.E. Wagner: In Aerosol Microphysics II; chap. 5, "Aerosol Growth by Condensation", edited by W.H. Marlow, (Springer-Verlag, Berlin, 1982).

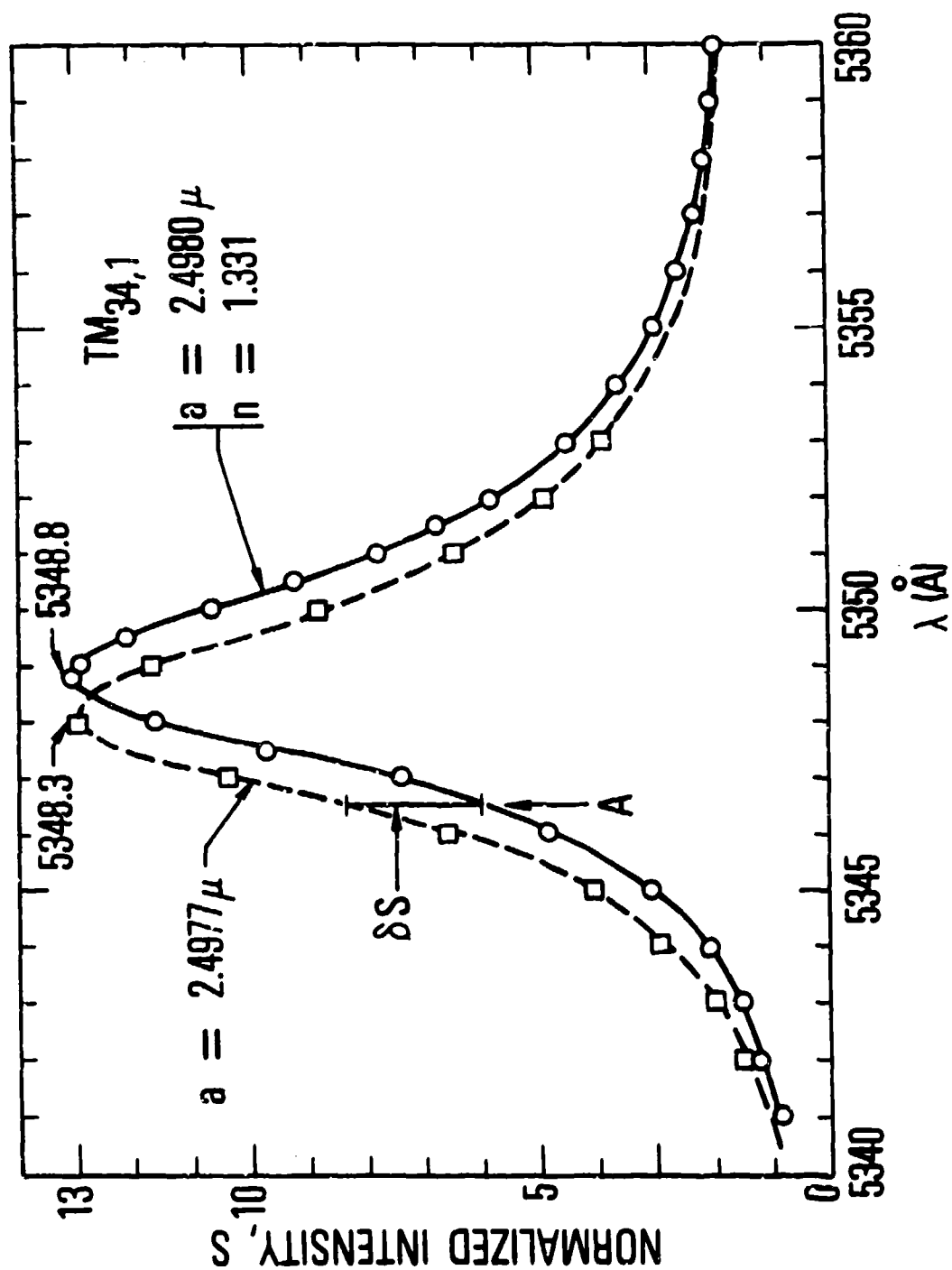


Fig.1. Backscattering spectrum for the $TM_{34,1}$ resonance of a 4.9960- micron droplet of water.

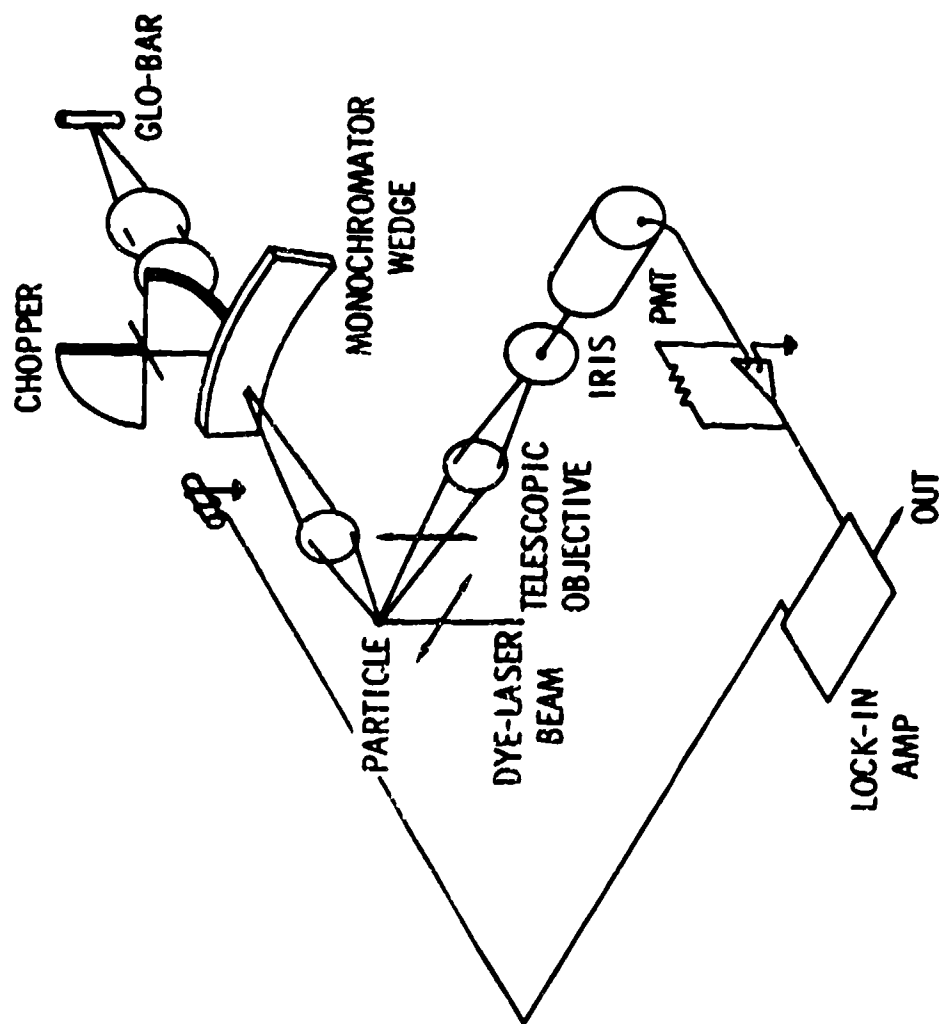


Fig.2 Schematic diagram of the measurement system in SMS.

ⓐ +

+

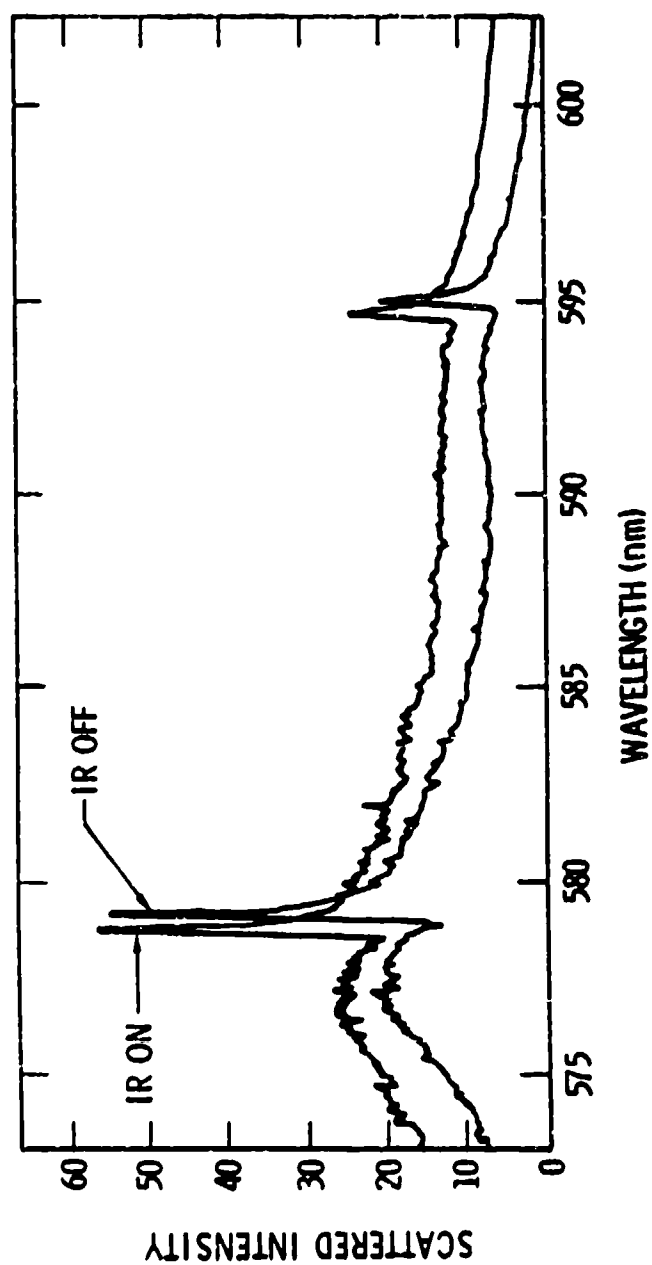


Fig.3 The scattered-light excitation spectrum for a particle of $(\text{NH}_4)_2\text{SO}_4$ 2.7 microns in radius. The upper excitation spectrum was taken for the same particle irradiated with broadband IR (1100 K) having an intensity of 240 mW/cm^2

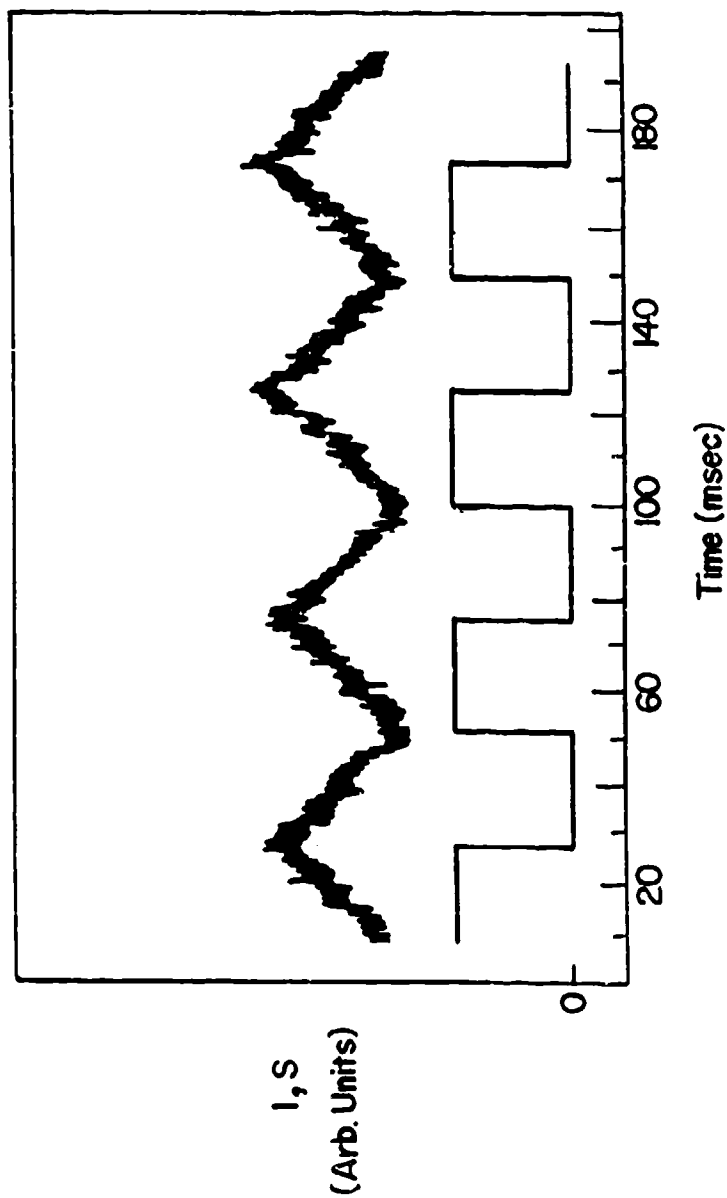


Fig. 4 An oscillogram of both the scattered light modulation (above) and incident IR intensity (below) for an $(\text{III}_4)_2\text{SO}_4$ particle, 5 microns in diameter. The frequency of the visible incident light was positioned on the low wavelength side of a structure resonance.

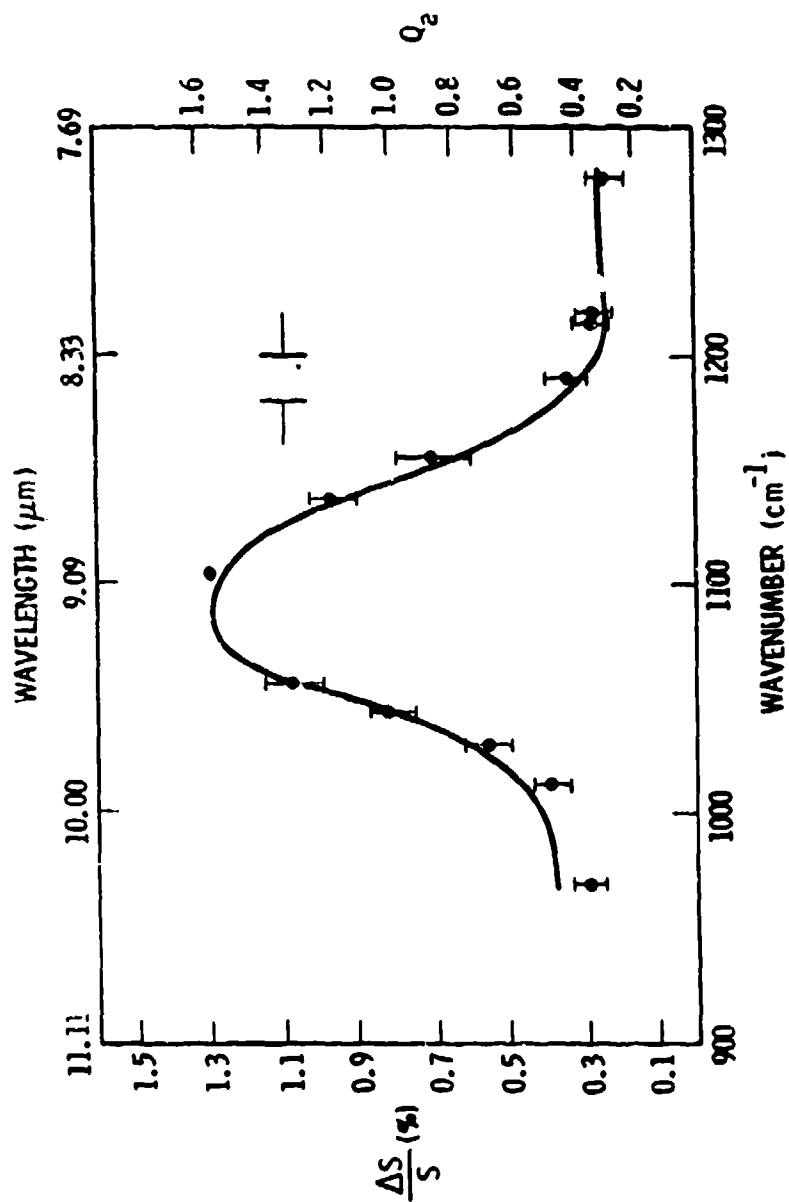


Fig.5 The SRMS spectrum of the $(\text{NH}_4)_2\text{SO}_4$ solution droplet whose scattered-light excitation spectrum is shown in Fig.2. This spectrum is compared in line shape to a calculation of Q_d for 39% concentration.

BLANK

RAMAN SPECTROSCOPY OF SINGLE OPTICALLY LEVITATED DROPLETS

T. R. Lettieri, R. E. Preston, and M. I. Bell
National Bureau of Standards
Gaithersburg, MD 20899

ABSTRACT

Spontaneous Raman scattering has been observed from single aerosol droplets optically levitated by an argon ion laser beam. All of the Raman bands of bulk liquid silicone oil and dioctyl phthalate were present in spectra taken of droplets of the same liquids. This suggests that chemical characterization of individual droplets may be possible without the undesirable effects of a supporting substrate. The droplet spectra also contained unexplained, size-dependent sharp features superimposed on the Raman peaks. The new technique may have applications in chemical characterization studies of evaporating multicomponent droplets, droplets in chemically reacting flows, and other transient processes involving single liquid droplets.

Raman spectroscopy has been shown to be a valuable technique for the chemical characterization of single micrometer-sized aerosol particles and liquid droplets resting on supporting substrates [1]. Often, however, the presence of the substrate causes unwanted effects, such as background Raman scattering or luminescence, optical coupling to the substrate, and droplet shape distortion, which can distort the spectra and complicate their interpretation. Therefore, the spectra obtained from single suspended droplets should be more directly comparable to those obtained from bulk samples and to the predictions of theoretical models for Raman scattering from microscopic spheres [2]. Of the several methods for particle suspension, optical levitation by laser radiation pressure [3] is particularly useful in Raman spectroscopy since the same beam which suspends the particle can also act as the Raman excitation source.

This paper reports an investigation into the application of optical levitation techniques to the micro-Raman spectroscopy of single aerosol droplets. In particular, spectra were taken of both silicone oil and dioctyl phthalate (DOP) droplets ranging in diameter from 10 to 35 μm .

The experimental apparatus consisted of a 0.75-m double monochromator with holographic gratings, a CW argon ion laser, an optical cell in which the droplets levitated, collection and focusing lenses, a cooled photomultiplier tube, photon counting electronics, and a minicomputer for data acquisition and experimental control. About 500 mW of laser power were used to levitate a droplet, the diameter of which was determined from the fringe spacing at 90 degrees [4].

In Fig. 1 are shown spontaneous Raman spectra of DOP for the bulk liquid (Fig. 1a) and for a single droplet of nominal 25 μm diameter (Fig. 1b). Comparison of the two spectra indicates that all of the Raman peaks of the bulk liquid spectrum are also present in the droplet spectrum. Additionally, characteristic group frequencies, such as the aromatic and the paraffinic C-H stretches, are clearly distinguishable in the droplet spectrum and occur at the same frequencies as in the bulk liquid. These results suggest that the combination of optical levitation and Raman spectroscopy may permit chemical characterization studies on single microdroplets, although no experiments with multicomponent droplets were conducted in the present investigation. Future work will focus on the time-resolved characterization of evaporating, two-component droplets having known starting concentrations.

In addition to the bulk liquid Raman peaks, the spectrum in Fig. 1b also contains sharp, reproducible features

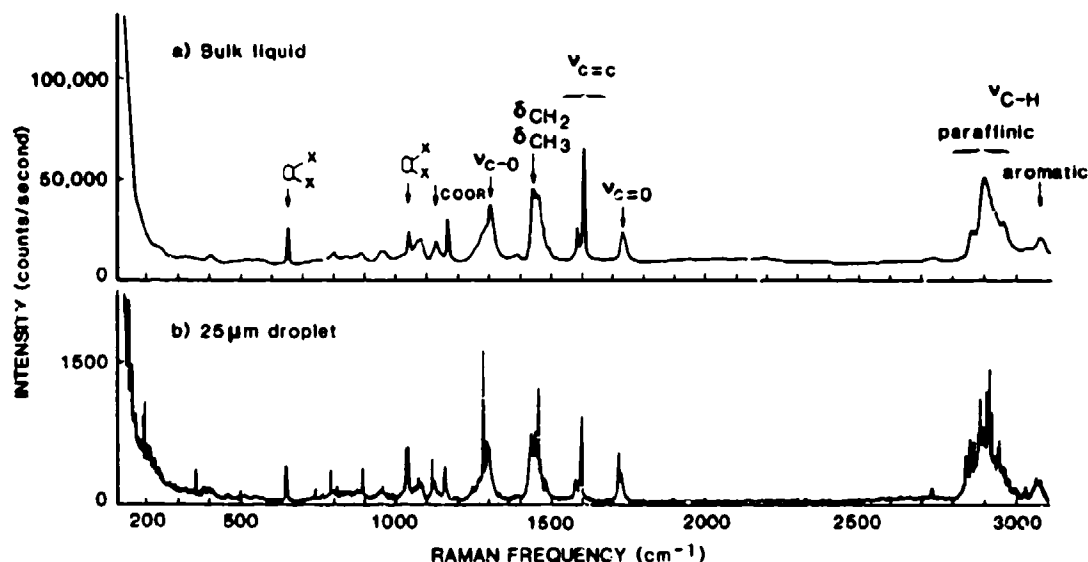


FIGURE 1. RAMAN SPECTRA OF DIOCTYL PHTHALATE. (a) bulk liquid; (b) a single 25- μm droplet. Peak assignments are from Reference 7.

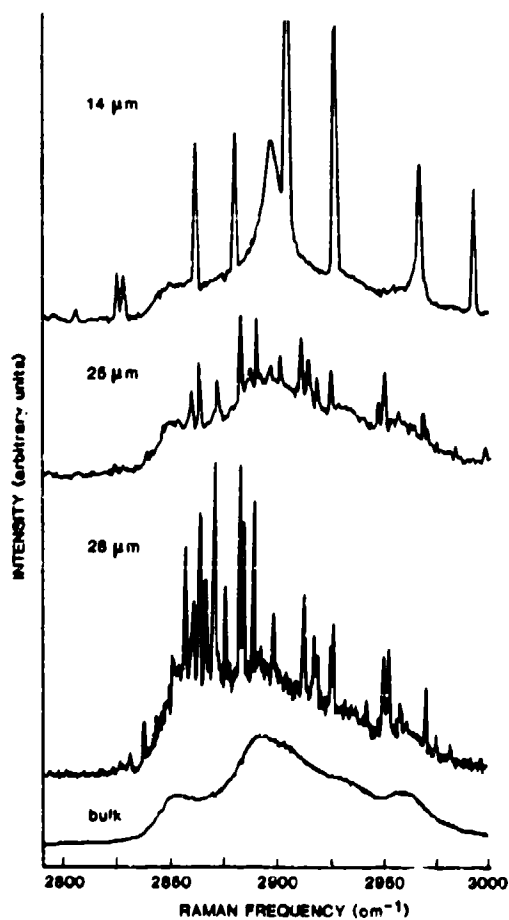


FIGURE 2. C-H STRETCHING MODES OF DIOCTYL PHTHALATE. Raman spectra of droplets of three different sizes and bulk liquid.

superimposed on these peaks. Although previous studies of fluorescent light emission from microspheres have shown size-parameter-dependent resonances which relate to the electromagnetic modes of the microsphere [6], there is evidence that the sharp Raman features in the present study are not related to these resonances [6]. However, they too depend on droplet size, as indicated by Fig. 2, which contains Raman spectra across the C-H stretch region for three different DOP droplets of various sizes. It is noted from the figure that the sharp features become narrower, more closely spaced in frequency, and vary in amplitude as the droplet size increases. Further investigation into the origin of these sharp features is underway [6].

These preliminary experiments with single-component droplets are a first step in a series of experiments involving the chemical characterization of individual aerosol droplets. Possible areas of investigation include compositional studies of multicomponent droplets, time-resolved studies of droplet evaporation and surface adsorption, and surface reactions on a droplet in a chemically reacting flow.

The experiments reported here were conducted in the Raman Spectroscopy Facility of the Center for Materials Science, National Bureau of Standards.

REFERENCES

- [1] See for example: G. J. Rosasco in "Advances in Infrared and Raman Spectroscopy", R. J. H. Clark and R. E. Hester, Eds. (Heyden, London, 1980), 7, p. 223; E. S. Etz, Scanning Electron Microscopy 1979/I, p. 67 (1979); P. Dhamelincourt, F. Wallart, M. Leclercq, A. T. N'Guyen, and D. O. Landon, Anal. Chem. 51, p. 414A (1979).
- [2] G. J. Rosasco and H. S. Bennett, J. Opt. Soc. Am. 68, p. 1242 (1978); P. J. McNulty, H. W. Chew, and M. Kerker in "Aerosol Microphysics I", W. H. Marlow, Ed. (Springer-Verlag, Berlin, 1980), p. 89.
- [3] A. Ashkin and J. M. Dziedzic, Appl. Phys. Lett. 19, p. 283 (1971).
- [4] T. R. Lettieri, W. D. Jenkins, and D. A. Swyt, Appl. Opt. 20, 2799 (1981).
- [5] R. K. Chang, J. F. Owen, P. W. Barber, B. J. Messinger, and R. E. Benner, J. Raman Spectrosc. 10, 178 (1981); R. E. Benner, P. W. Barber, J. F. Owen, and R. K. Chang, Phys. Rev. Lett. 44, 476 (1980); S. C. Hill, R. E. Benner, C. K. Rushforth, and P. R. Conwell, Appl. Opt. 23, 1680 (1984); H. M. Tzeng, K. F. Wall, M. B. Long, and R. K. Chang, Opt. Lett. 9, 273 (1984).
- [6] T. R. Lettieri and R. E. Preston (to be published).
- [7] R. A. Nyquist and R. O. Kagel in "Infrared and Raman Spectroscopy", E. G. Brame and J. G. Grasselli, Eds. (Marcel Dekker, New York, 1977), Part B, p. 441.

AEROSOL INTERACTIONS WITH INTENSE LIGHT BEAMS

R. L. Armstrong
Physics Department, Applied Laser Optics Group
New Mexico State University
Las Cruces, NM 88003

ABSTRACT

The irradiation of absorbing aerosols by intense light beams is investigated. This analysis is aided by the introduction of certain characteristic interaction times which identify, after a given irradiation time, the dominant aerosol-beam interactions. The results of this study include a description of steady-state vaporization, the approach to steady-state conditions, and an approximate treatment of aerosol-enhanced breakdown.

This work has been published as follows:

R. L. Armstrong, "Aerosol Heating and Vaporization by Pulsed Light Beams", U.S. Army Research Office Battelle-Columbus Laboratories Report for Contract DAAG29-81-D-0100, August, 1982.

R. L. Armstrong, "Interactions of Aerosols with Intense Light Beams: Steady-state Vaporization and Shock-wave Formation," U.S. Army Research Office Battelle-Columbus Laboratories Report for Contract DAAG29-81-D-0100, May, 1983.

R. L. Armstrong, "Interactions of Aerosols with Intense Light Beams: Absorption, Vaporization and Enhanced Breakdown Effects," U.S. Army Research Office Battelle-Columbus Laboratories Report for Contract DAAG29-81-D-0100, September, 1983.

R. L. Armstrong, "Aerosol Heating and Vaporization by Pulsed Light Beams," Appl. Opt. 23, 148 (1984).

R. L. Armstrong, "Propagation Effects on Pulsed Light Beams in Absorbing Media," Appl. Opt. 23, 156 (1984).

R. L. Armstrong, "Aerosol Interactions with Intense Light Beams," 1984 CRDC Conference on Obscuration and Aerosol Research, June, 1984.

R. L. Armstrong, "Interactions of Absorbing Aerosols with Intense Light Beams," J. Appl. Phys. 56, 2142 (1984).

Absorbing aerosols irradiated by intense light beams may rapidly reach elevated temperatures, exhibit correspondingly high vaporization rates, and serve as the source of shock wave disturbances both within the aerosols and in the surrounding vapor. The increased free electron collision frequency in the hot, dense vapor adjacent to the aerosols may also result in a dramatic reduction (3-4 orders of magnitude) in the clean-air breakdown threshold. The study of these phenomena is aided by the identification of certain characteristic interaction times which provide, after a given irradiation time, a measure of the dominant aerosol-beam interactions. The existence of these characteristic times is especially significant in the case of pulsed beams since aerosol-beam interactions occurring on a time scale long compared to the pulse length will make only a negligible contribution to the behavior of the irradiated aerosols.

If the beam intensity is low, approximate analytical expressions may be obtained for the aerosol temperature, mass flux and radius as a function of time(1). These expressions have been used to calculate the response of water droplets to pulsed light beams. Figures 1 and 2 illustrate the results of these calculations for selected droplets. Figure 1 shows the increase in temperature of small droplets when they are irradiated by a rectangular pulse of 10μ radiation. 5 μ sec in duration, with an intensity of 10^5 W/cm^2 . The smaller droplets reach a steady-state temperature in a time $< 5\mu$ sec whereas the temperature of the largest droplet continues to rise throughout the pulse. The larger droplets are also seen to return to ambient temperature at a slower rate after the passage of the pulse. Figure 2 illustrates the change in the droplet radius with time for selected droplets irradiated by a steady beam of 10μ radiation with an intensity of 10^5 W/cm^2 . The curves in Fig. 2 have been computed under the assumption that the droplet temperature remains fixed at its initial steady-state value. Recent detailed numerical calculations(2,3), however, reveal that the steady-state droplet temperature generally decreases after prolonged heating so that the curves given in Fig. 2 then represent excessive estimates of droplet decay.

The above analysis of aerosol heating and vaporization is valid in the limit of small mass flux. This will always be the case for sufficiently weak incident beams. As the beam intensity increases, however, both the aerosol temperature and mass flux rise, and the above analysis no longer applies. A great deal of information about the

behavior of absorbing aerosols irradiated by beams of arbitrary intensity may be obtained from the analysis of steady-state vaporization(4). Corresponding to an extremely wide range of incident intensities, typically $10^4 \leq I \leq 10^{11}$ W/cm² for many aerosols, a steady-state, developed vaporization regime (DVR) is established in the aerosol, characterized by a constant temperature and mass flux. The time needed to establish the DVR, which is inversely proportional to the beam intensity, spans the corresponding range $10^{-10} \leq t_D \leq 10^{-3}$ sec. The steady-state, DVR temperature, surprisingly, varies by a factor of only about 3 over this range of intensities and times.

The establishment of a DVR in an irradiated aerosol requires that a balance be maintained between vaporization and radiant absorption. The effect of thermal conductivity in this model is simply to define the heated volume of the aerosol after a given irradiation time. In this discussion, the establishment of DVR conditions in spherical aerosol droplets is investigated. Spherically symmetric heating of the droplets is assumed. However, a distinction is made between optically thick and optically thin droplets according to whether the droplet radius $a > \delta$ or $a < \delta$ ($\delta = \kappa^{-1}$), where κ is the bulk absorption coefficient. In the case of optically thick droplets, 4 characteristic interaction times may be defined. The shortest of these, the acoustic time (τ_a), provides an estimate for the onset of vaporization after the arrival of the pulse. The remaining three are thermal diffusion times, and provide estimates of the times, after the arrival of the pulse, when conductive heating of the remainder of the droplet begins (τ_δ), when the droplet has become uniformly heated by conduction (τ_σ), and after which conductive heat losses into the surrounding medium must be taken into account (τ_c). It is generally true that the inequalities $\tau_a \ll \tau_\delta \ll \tau_\sigma \ll \tau_c$ hold so that a time line may be established delineating the dominant aerosol-beam interactions after a given irradiation time. For the case of optically thin droplets, we must set $\tau_\delta = \tau_\sigma$ with a corresponding simplification in the time line.

Figures 3 and 4 illustrate the establishment of DVR conditions in an optically thick 10 μ quartz droplet. Figure 3 plots the incident intensity as a function of the time needed to reach DVR conditions. Figure 4 is an analogous plot of DVR temperature as a function of DVR time. For this droplet, the characteristic times are $\tau_a = 2.0 \times 10^{-10}$ sec, $\tau_\delta = 2.3 \times 10^{-7}$ sec, $\tau_\sigma = 2.3 \times 10^{-5}$ sec, and $\tau_c = 2.3 \times 10^{-3}$ sec. Figure 3 reveals that an intensity of about 2.4×10^{10} W/cm² is needed to "spontaneously" (within the acoustic

time, τ_a) vaporize the δ -zone while an intensity of about $7.7 \times 10^3 \text{ W/cm}^2$ will establish a DVR in the time τ_c . The steady-state, DVR temperature is seen from Fig. 4 to vary by only a factor of about 3 over this range of intensities. Steady-state conditions also exist for times $> \tau_c$ with the distinction that conductive coupling to the surrounding medium must now be accounted for. Steady-state droplet behavior in the presence of this external conductive coupling has been discussed earlier in this paper for the case of weak beams (1,2,3) (see Fig. 2). A perturbation analysis is also available(4) to probe the establishment of steady-state conditions for times $\geq \tau_c$.

The establishment of a DVR at a constant temperature and mass flux requires that a balance be maintained between vaporization and radiant absorption. For times $< \tau_a$, however, vaporization is absent in the present model (it is certainly suppressed at these early times) so that the δ -zone may reach a temperature at $t = \tau_a$ that is higher than the DVR temperature corresponding to that intensity. In this case, the δ -zone temperature will subsequently drop to the steady-state, DVR value. An estimate of this temperature overshoot phenomenon is given in Fig. 5 for a 10μ quartz drop. Figure 5 reveals that the phenomenon persists for intensities $> 5 \times 10^9 \text{ W/cm}^2$ in our model. We note, however, that hydrodynamic effects, neglected in the present model, should be included in a complete analysis of aerosol-beam interactions of these high beam intensities.

The dominant aerosol-beam interactions, which lead to the identification of the characteristic times discussed above, may be further exploited to develop an approximate analysis of the time development of irradiated aerosols from ambient to DVR conditions. Figure 6 shows the time development of an irradiated 10μ quartz droplet for several representative beam intensities. It is interesting to note that little spontaneous (within the time τ_a) heating of the δ -zone occurs for intensities $< 10^8 \text{ W/cm}^2$. The assumption, used in the present model, of the sudden onset of vaporization at τ_a will, therefore, not introduce a significant error for beam intensities $< 10^8 \text{ W/cm}^2$.

The vaporization model discussed in the preceding paragraphs may be used to estimate the aerosol-induced breakdown threshold using a model of this phenomenon developed elsewhere(5). Figure 7 shows the results of this calculation for carbon spheres together with available experimental data on carbon(6). In this experiment, carbon particles were irradiated by 200 n sec pulses of 10.6μ laser light and the observed breakdown threshold plotted against particle diameter (μ). The model

calculation was restricted to spheres with diameter $>1\mu$ to ensure the optical thickness of the aerosols. There is general agreement between the results of the model calculation and the experimental data points but discrepancies exist that are in excess of the experimental error bars. The approximate treatment of electron loss mechanisms in the cited breakdown model(5) might be the source of a portion of the observed discrepancy. It should also be noted that the formation time for the plasma, as calculated using the present model, is less than the DVR time for particle diameters $<50\mu$, becoming slightly longer than the DVR time for larger particle diameters. An improved model for aerosol-enhanced breakdown should, therefore, include a dynamical analysis of the irradiated aerosol from ambient to DVR conditions such as is sketched, in approximate form, in Fig. 6.

The results of this modeling study suggest several areas where a more general treatment of aerosol-beam interactions is needed. First, the simplifications introduced into the modeling analysis by the introduction of the characteristic interaction times suggests that the identification of such times for other aerosol geometries and heating scenarios merits attention. Second, the assumption of spherically symmetric aerosol heating becomes increasingly invalid for large, optically thick aerosols with the appearance of "hot spots" on the entrance and exit faces(7). It should be noted, however, that the spherical heating assumption will have only a minimal influence on the time development of aerosols irradiated by sufficiently weak beams where the DVR time $>\tau_0$. This follows since, for times $>\tau_0$, the aerosol temperature becomes substantially uniform as a result of internal thermal conductivity effects. For more intense beams, where the DVR time $<\tau_0$, the spherical heating assumption may become invalid. Even in the regime of higher beam intensities, an extension of the characteristic time analysis to include an approximate treatment of non-uniform aerosol heating may prove valuable(4). Finally, hydrodynamic effects, both within the heated aerosol and in the surrounding vapor should be investigated. They will become increasingly important at higher beam intensities and may be expected to modify the aerosol heating, vaporization and subsequent plasma formation scenarios sketched here.

References

1. R. L. Armstrong, Appl. Opt. 23, 148 (1984).
2. G. Sageev and J. H. Seinfeld, to be published in Appl. Opt.
3. A. Zardecki and R. L. Armstrong, to be submitted.
4. R. L. Armstrong, J. Appl. Phys. 56, 2142 (1984)
5. D. C. Smith, J. Appl. Phys. 48, 2217 (1977).
6. D. E. Lencioni, Appl. Phys. Lett. 23, 12 (1973).
7. P. W. Dusel, M. Kerker and D. D. Cooke, J. Opt. Soc. Am. 69, 55 (1979).

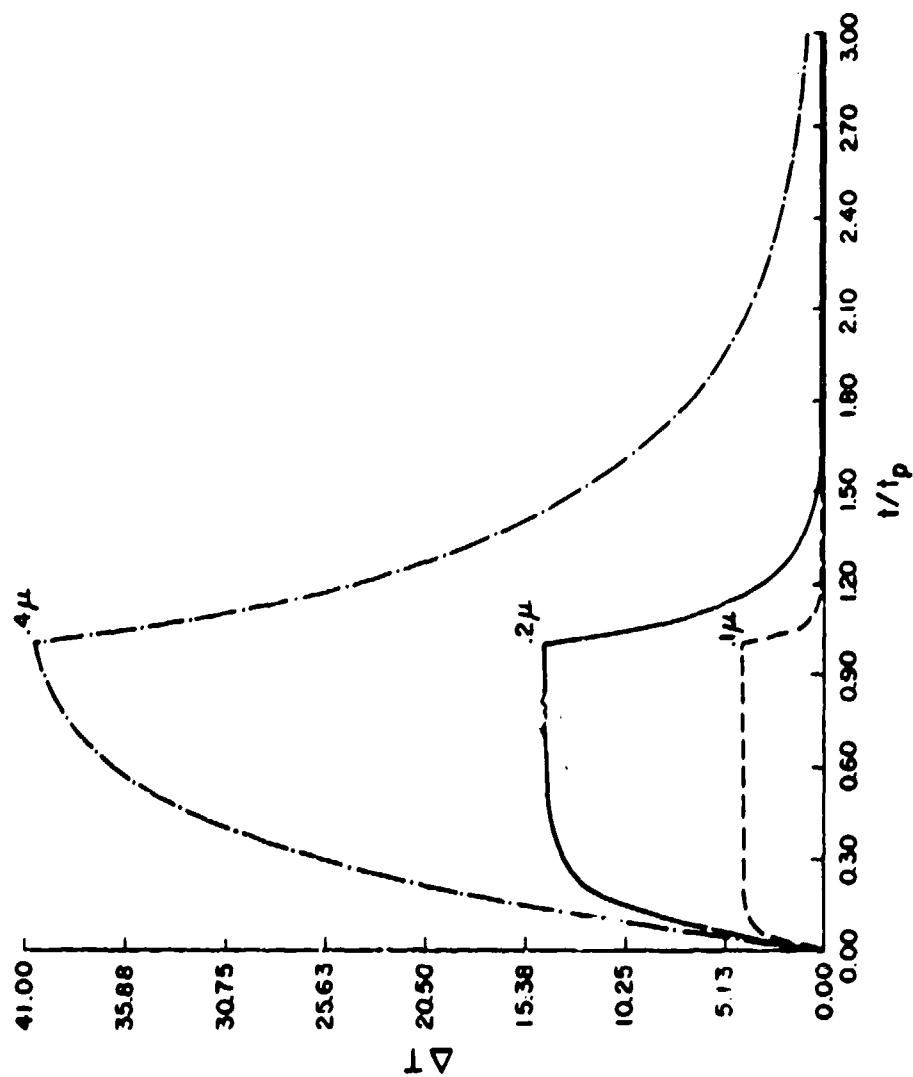


Fig. 1. Droplet temperature rise $\Delta T(K)$ versus time (t/t_p) for $t_p = 5 \mu\text{sec}$,
 $I = 10^5 \text{W/cm}^2$, $\sigma = 0.1, 0.2, 0.4 \mu$.

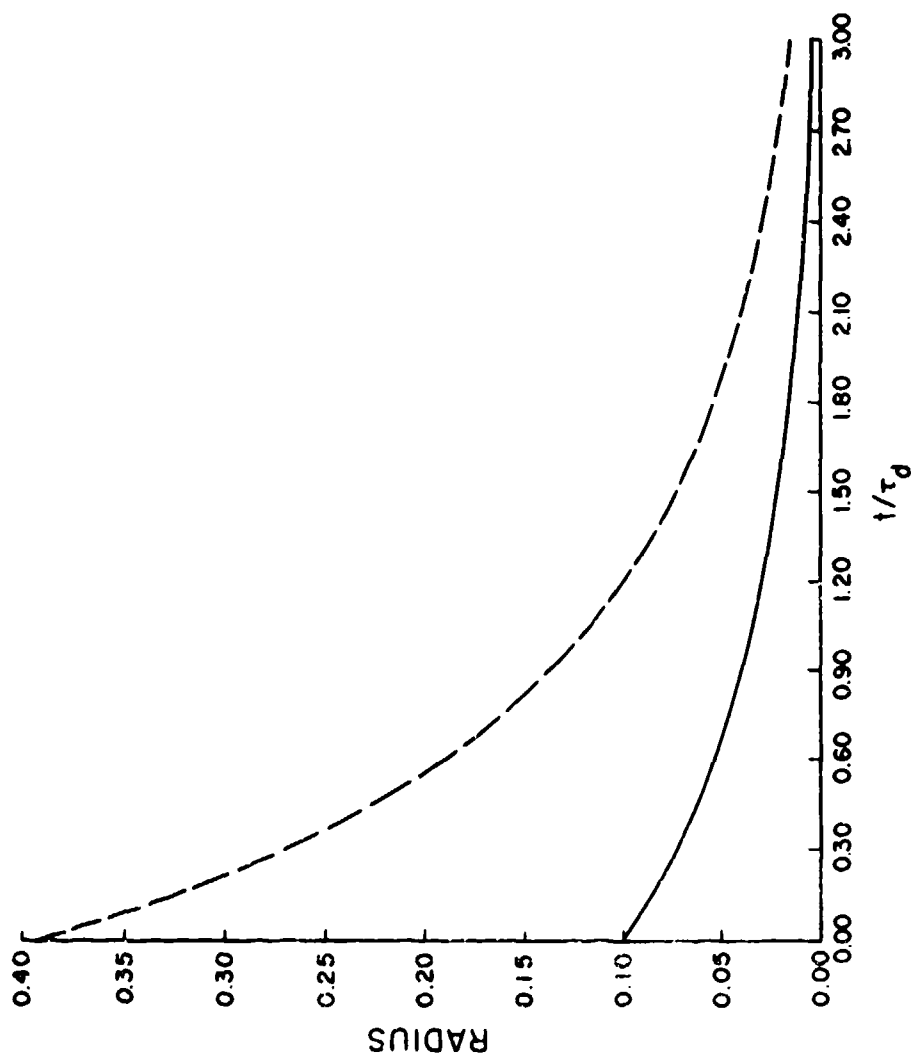


Fig. 2. Steady state droplet decay versus time (t/τ_d) for $\tau_d = 96.4 \mu\text{sec}$, $I = 10^5 \text{W/cm}^2$, $\sigma = 0.1, 0.4 \mu$.

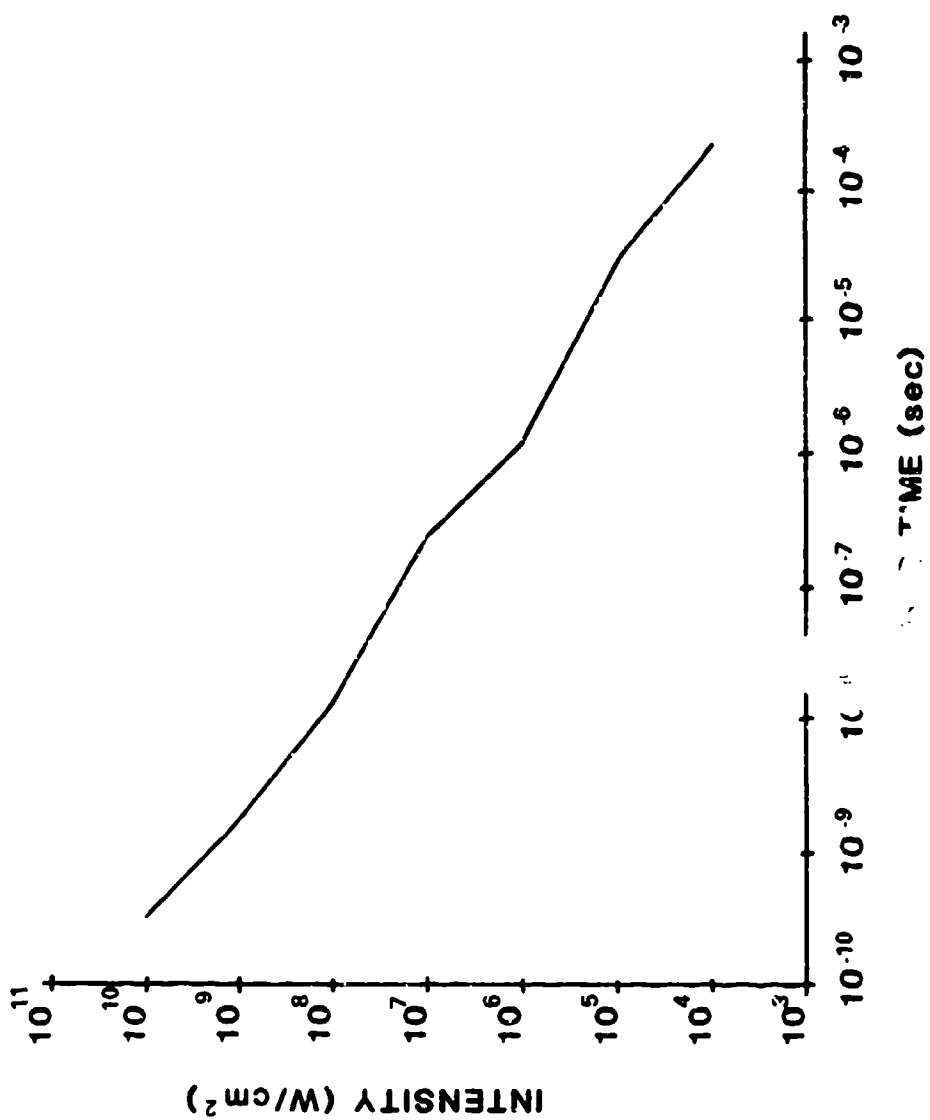


Fig. 3. Intensity versus time for the 10 μ quartz droplet.

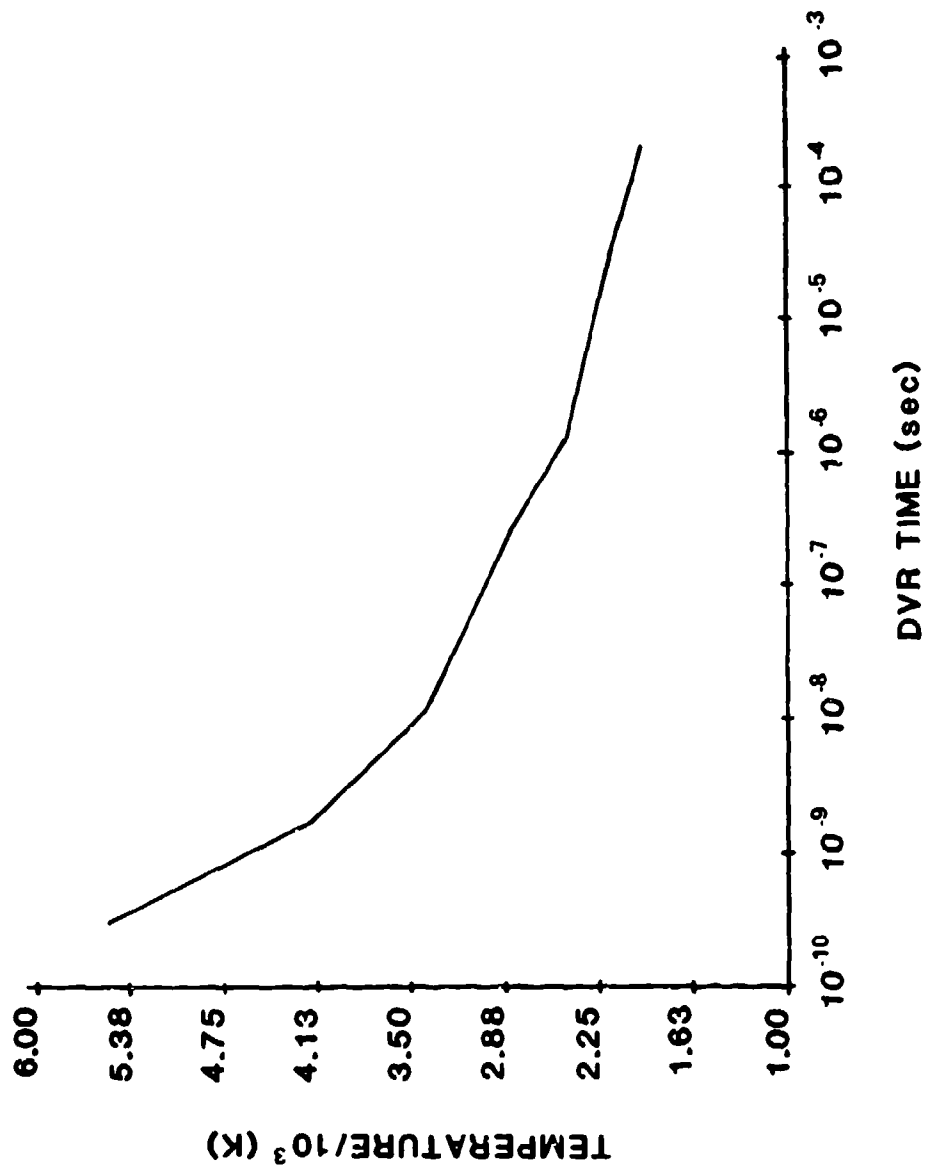


Fig. 4. DVR temperature versus DVR time for 10 μ quartz droplet.

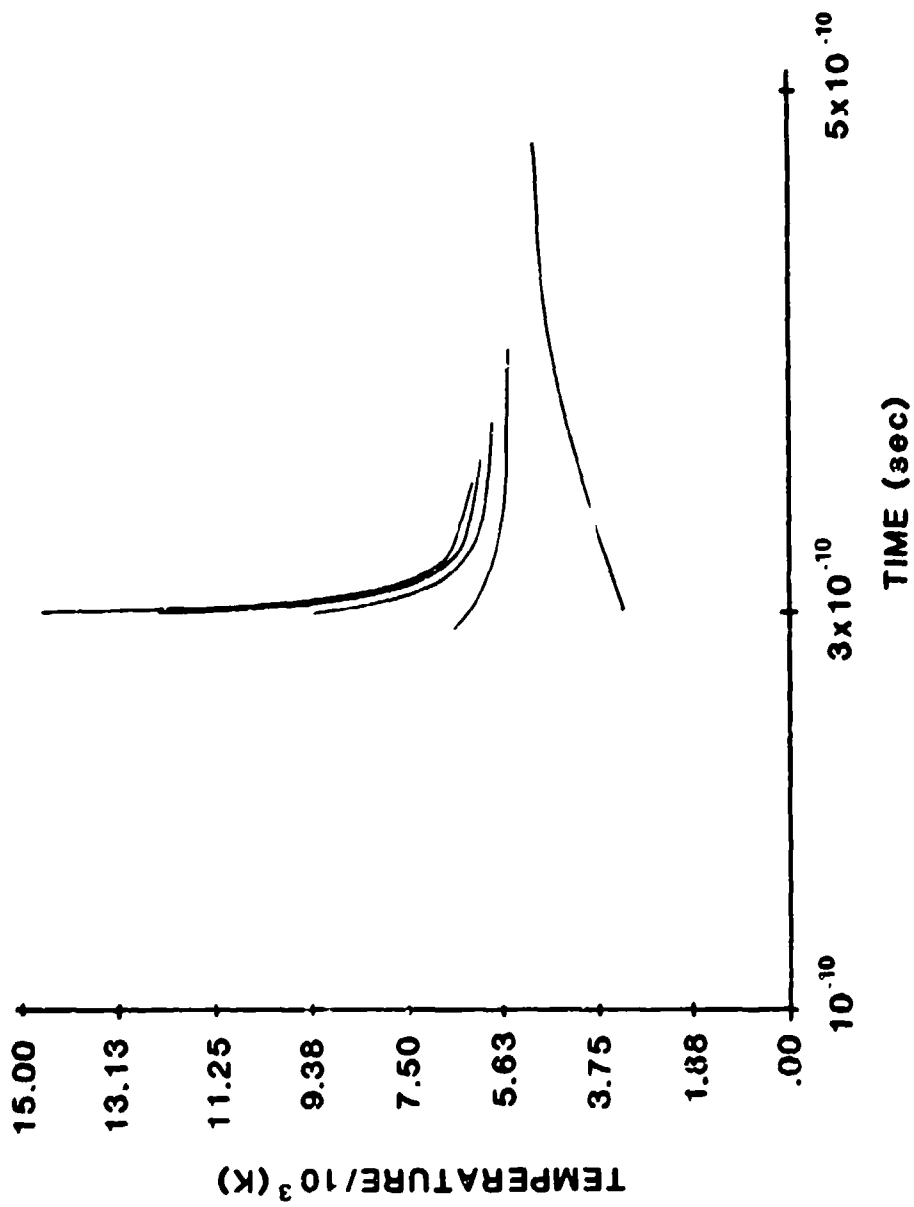


Fig. 5. Temperature overshoot for 10μ quartz droplet: from top, curves are for $I = 2.36 \times 10^{10}$, 2.0×10^{10} , 1.5×10^{10} , 1.0×10^{10} , 5.0×10^9 (W/cm^2).

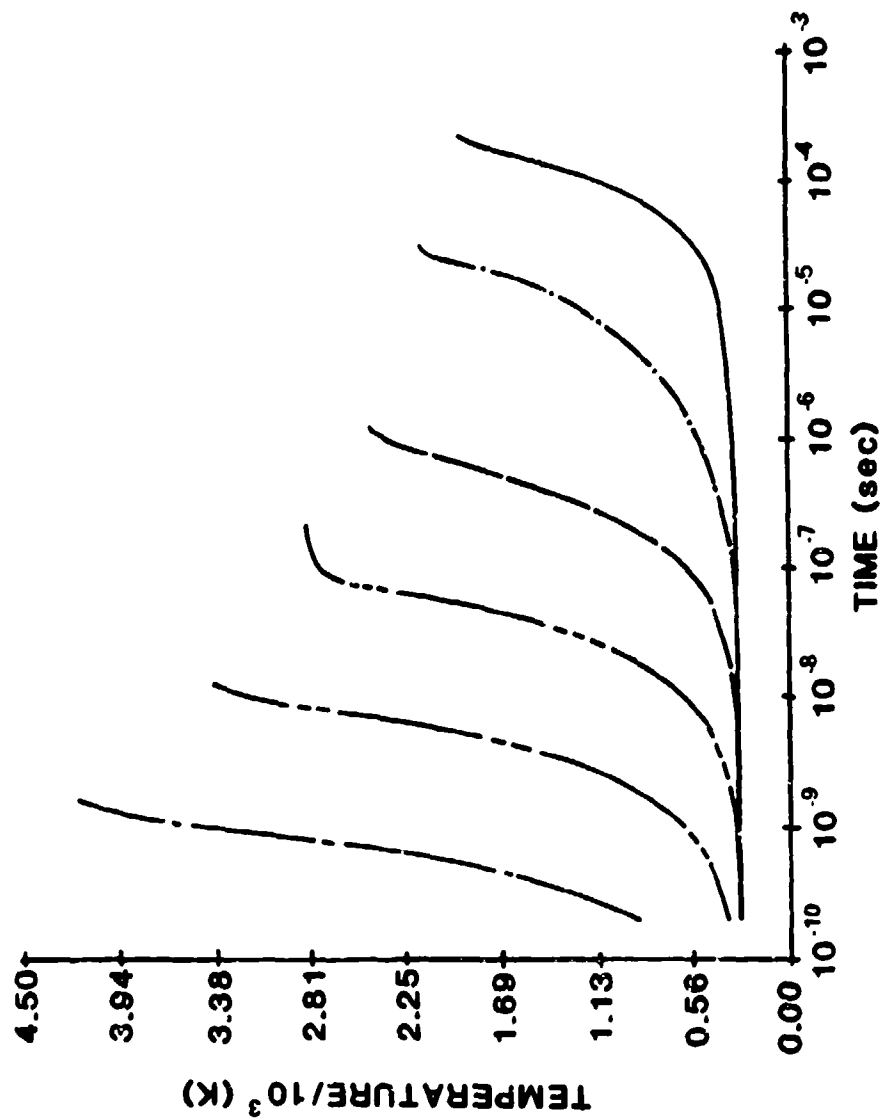


Fig. 6. Temperature rise of 10 μ quartz droplet from ambient to DVR conditions: from right, curves are for $I = 10^4, 10^5, 10^6, 10^7, 10^8, 10^9$ (W/cm²).

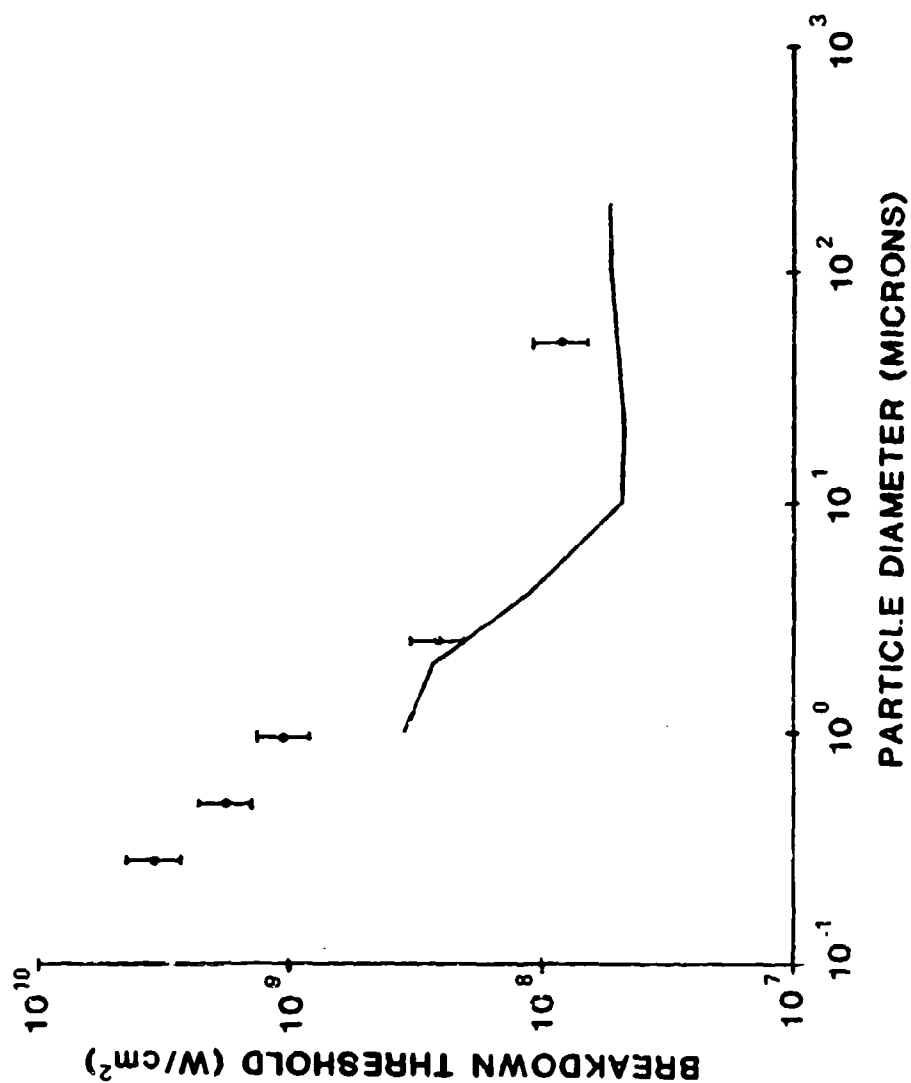


Fig. 7. Breakdown threshold (W/cm^2) versus diameter (μ) for carbon spheres irradiated by 200 n sec pulses of 10.6 μ laser light: solid line, theoretical curve; unconnected points, experimental data.

BLANK

PROBLEMS IN HEL - AEROSOL INTERACTIONS

Melvin Lax

Physics Department of the City College
and the Graduate Center* of the City University of New York,
New York, N.Y. 10031

ABSTRACT

This paper reviews the problems concerned with absorption of a high energy laser beam in an aerosol, and its coupling to hydrodynamic motion. The electromagnetic formulation draws on work appearing in the 1983 Chemical Systems Laboratories Conference on Obscuration and Aerosol Research under the title "*New Theoretical Approach to Scattering from Thin Fibers.*"

1. INTRODUCTION

As indicated in previous talks in this session by Cipolla and Morse, R. Armstrong, J. R. Brock, J. B. Pendleton and R. G. Pinnick, and R. K. Chang et. al., the problem of nonlinear interaction of a high energy laser beam with an aerosol is a difficult problem. Progress can be made by a number of drastic assumptions - such as uniform absorption of laser energy, or by brute force code that will work for large droplets only on a supercomputer.

I would like, at least, to outline the nature of the problems to be solved and discuss some symmetry aspects of the solution. I believe in the divide and conquer method: divide the problem into two parts - one of which is easy. Solve the easy problem, and then iterate the procedure on the hard part. Unfortunately, as I shall show, the first step is not possible - but after that the procedure may work.

The first step is to give separate consideration to small drops (compared to the wave-length) and to large drops. Each of these cases, however, is hard, and progress can only be made by a further subdivision.

*Work at City College supported in part by the Army Research Office, and the Chemical Research and Development Center.

A. SMALL DROPS

Small drops are easy, because the absorption is approximately uniform. The electromagnetic part of the problem has a quasi-electrostatic solution of a form known to Rayleigh. However, it may happen (depending on the altitude) that the collision mean free path in the vapor surrounding the drop is now comparable to the drop size. In this case, the vapor can not be treated using hydrodynamics, but one must employ transport theory instead, without using a diffusion approximation. One may, however, be able to make a diffusion-type approximation provided that one introduces the concept of an extrapolation length as introduced in neutron transport theory¹ and applied to spherical geometries by Marshak and others.² Of course, the neutron procedure is not adequate, since one must take explicit account of factors such as the latent heat of vaporization and the possibility of explosive vaporization. In this case, the electromagnetic problem is trivial, but the transport problem is not.

For short times, and high powers, however, a shock will develop, and it should be possible at these times to neglect the reaction of the atmosphere on the drop.

B. LARGE DROPS

For large drops, transport theory is unnecessary; hydrodynamics with mass and energy transport are adequate, but the electromagnetic problem is difficult - the absorption can be highly non-uniform since the spherical drop can act as a lens with focussing properties that will produce highly non-uniform fields, hence a highly non-uniform absorption. Since vaporization is sensitive to the maximum temperature reached, not the average energy absorbed, a highly non-symmetric hydrodynamic response can occur. Moreover, this hydrodynamic response, with possible development of a shock wave will modify the electromagnetic response by modifying the index of refraction.

I would now like to consider symmetry aspects of the electromagnetic solution. In particular, I will assume that because of energy absorption and the resulting droplet motion, the dielectric response (which is proportional to the local density) possesses cylindrical symmetry - with its axis along the direction of propagation of the incident beam. Will the electromagnetic absorption be such as to maintain this cylindrical symmetry? Like all good questions, the answer to this is yes and no

¹B. Davison and J. B. Sykes, *Neutron Transport Theory*, Oxford Univ. Press (1957).

²R. E. Marshak, *Phys. Rev.* 71, 943 (1947).

2. ELECTROMAGNETIC FORMULATION

An exact integral formulation for a scatterer described by a complex index of refraction n

$$\mathbf{E}(\mathbf{r}) = \mathbf{E}^{\text{inc}}(\mathbf{r}) + k^2 \mathbf{P} + \nabla (\nabla \cdot \mathbf{P}(\mathbf{r})) \quad (2.1)$$

$$\mathbf{P}(\mathbf{r}) = \int \frac{\exp(ikR)}{4\pi R} [n^2(\mathbf{r}') - 1] \mathbf{E}(\mathbf{r}') d\mathbf{r}'. \quad (2.2)$$

where

$$R^2 = |\mathbf{r} - \mathbf{r}'|^2 = (z - z')^2 + \rho^2 + \rho'^2 - 2\rho\rho' \cos(\phi - \phi'). \quad (2.3)$$

and $k = \omega/c$.

Symmetry about an axis can be exploited by making the expansions

$$\mathbf{E}(z, \rho, \phi) = \sum_{m=-\infty}^{\infty} \mathbf{E}_m(z, \rho) \exp(im\phi) \quad (2.4)$$

$$\mathbf{P}(z, \rho, \phi) = \sum_{m=-\infty}^{\infty} \mathbf{F}_m(z, \rho) \exp(im\phi) \quad (2.5)$$

where

$$\mathbf{F}_m(z, \rho) = \frac{1}{2} \int G_m(z - z', \rho, \rho') [n^2(z', \rho') - 1] \mathbf{E}_m(z', \rho') \rho' d\rho' dz', \quad (2.6)$$

and

$$G_m(z - z', \rho, \rho') = \frac{1}{2\pi} \int_{-\pi}^{\pi} d\phi \frac{\exp(ikR)}{R} e^{im\phi}, \quad (2.7)$$

This results in a set of equations for the triplet E_m^z , E_{m+1}^+ and E_{m-1}^- where

$$E^+ = E_x + i E_y; \quad E^- = E_x - i E_y, \quad (2.8)$$

are components of circular polarization:

$$\begin{aligned} E_m^z = E_m^{\text{inc } z} + \left(k^2 + \frac{\partial^2}{\partial z^2} \right) F_m^z + \frac{1}{2} \left[\frac{\partial}{\partial \rho} - \frac{m-1}{\rho} \right] \frac{\partial}{\partial z} F_{m-1}^- \\ + \frac{1}{2} \left[\frac{\partial}{\partial \rho} + \frac{m+1}{\rho} \right] \frac{\partial}{\partial z} F_{m+1}^+ \end{aligned} \quad (2.9)$$

$$E_{m+1}^+ = E_{m+1}^{\text{inc}+} + \left[k^2 + \frac{1}{2} \left(\nabla_\rho^2 - \frac{(m+1)^2}{\rho^2} \right) \right] F_{m+1}^+ + \left[\frac{\partial}{\partial \rho} - \frac{m}{\rho} \right] \frac{\partial}{\partial z} F_m^+ - \frac{1}{2} \left[\frac{\partial}{\partial \rho} - \frac{m}{\rho} \right] \left[\frac{\partial}{\partial \rho} - \frac{m-1}{\rho} \right] F_{m-1}^+ \quad (2.10)$$

$$E_{m-1}^- = E_{m-1}^{\text{inc}-} + \left[k^2 + \left(\nabla_\rho^2 - \frac{(m-1)^2}{\rho^2} \right) \right] F_{m-1}^- + \left[\frac{\partial}{\partial \rho} + \frac{m}{\rho} \right] \frac{\partial}{\partial z} F_m^- + \frac{1}{2} \left[\frac{\partial}{\partial \rho} + \frac{m}{\rho} \right] \left[\frac{\partial}{\partial \rho} + \frac{m+1}{\rho} \right] F_{m+1}^- \quad (2.11)$$

where

$$\nabla_\rho^2 = \frac{1}{\rho} \frac{\partial}{\partial \rho} \left[\rho \frac{\partial}{\partial \rho} \right] \quad (2.12)$$

Equation (2.11) can be omitted in the future, since it can be replaced by the simpler statement

$$E_m^- = \pm E_m^+ \quad (2.13)$$

with the upper sign, the important case for thin scatterers, used below.

3. CROSS-SECTIONS

The absorption cross-section can readily be shown to take the form:

$$\sigma_{\text{abs}} = k \operatorname{Im} \int (n^2 - 1) \frac{|E|^2}{|E^{\text{inc}}|^2} d\tau \quad (3.1)$$

Equation (3.1) can be given the interpretation that the attenuation constant is

$$\alpha = k \operatorname{Im} n^2 \quad (3.2)$$

It must be remembered, however, that the squared index of refraction, or at least $n^2 - 1$, is proportional to the local density, and the latter is to be determined by solving the hydrodynamic equations self-consistently with the field. Whereas the total scattering cross-section into polarization e can be written:

$$\sigma_{sc} = \frac{k^4}{4\pi} \int |e \cdot g(\theta, \phi)|^2 \frac{d\Omega}{4\pi} \quad (3.3)$$

where the scattering amplitude g is defined by

$$g(\theta, \phi) = \int \exp[-ik \cdot n \tau] [n^2(r) - 1] E(r) d\tau \quad (3.4)$$

Complete results can be obtained by inserting the expression Eq. (2.4) for $E(r)$.

4. SPATIAL DEPENDENCE OF ABSORBED ENERGY

If a sphere is illuminated by a beam propagating in the z -direction, will the absorbed energy possess azimuthal symmetry about the z -axis? Let us assume that $n^2(r)$ possesses this cylindrical symmetry before illumination. If the answer to the above question is yes, then this symmetry will be maintained in the nonlinear case.

Although the integral equation Eq. (2.1)-(2.3) can be attacked directly, via numerical techniques, it is advantageous to exploit the rotational symmetry by exploiting the Fourier expansion in the azimuthal angle of Eqs. (2.4) and (2.5).

For the case of on-axis illumination the incident field has the form

$$E_m^{inc} = e \exp(ikz \cos \theta_0) J_m(k \rho \sin \theta_0) \quad (4.1)$$

with $\theta_0 = 0$. Thus

$$E_m^{inc} = e \exp(ikz) \delta(m, 0) \quad (4.2)$$

vanishes for $m \neq 0$. Moreover, the polarization vector e is perpendicular to the z direction, so that

$$E_0^{incz} = 0 \quad (4.3)$$

The only surviving incident fields are E_0^+ and E_0^- . The first gives rise to the triplet

$$\begin{aligned} E_0^+(\rho, z) &= e_+ \exp(ikz) + \left[k^2 + \frac{1}{r} \nabla_\rho^2 \right] F_0^+ + \left[\frac{\partial}{\partial \rho} + \frac{1}{\rho} \right] \frac{\partial}{\partial z} F_{-1}^+ + \frac{1}{r} \left[\frac{\partial}{\partial \rho} + \frac{1}{\rho} \right] \left[\frac{\partial}{\partial \rho} + \frac{2}{\rho} \right] F_{-2}^+ \\ E_{-1}^+(\rho, z) &= 0 + \left[k^2 + \frac{\partial^2}{\partial z^2} \right] F_{-1}^+ + \frac{1}{r} \left[\frac{\partial}{\partial \rho} + \frac{2}{\rho} \right] \frac{\partial}{\partial z} F_{-2}^+ + \frac{1}{r} \frac{\partial}{\partial \rho} \frac{\partial}{\partial z} F_0^+ \\ E_{-2}^+(\rho, z) &= 0 + \left[k^2 + \left[\nabla_\rho^2 - \frac{4}{\rho^2} \right] \right] F_{-2}^+ + \left[\frac{\partial}{\partial \rho} - \frac{1}{\rho} \right] \frac{\partial}{\partial z} F_{-1}^+ + \frac{1}{r} \left[\frac{\partial}{\partial \rho} - \frac{1}{\rho} \right] \frac{\partial}{\partial \rho} F_0^+ \end{aligned} \quad (4.4)$$

The second gives rise to the dual triplet

$$\begin{aligned}
E_0^-(\rho, z) &= e_- \exp(ikz) + \left(k^2 + \nabla_\rho^2\right) F_0^- + \left(\frac{\partial}{\partial \rho} + \frac{1}{\rho}\right) \frac{\partial}{\partial z} F_1^+ + \frac{1}{z} \left(\frac{\partial}{\partial \rho} + \frac{1}{\rho}\right) \left(\frac{\partial}{\partial \rho} + \frac{2}{\rho}\right) F_2^+ \\
E_1^-(\rho, z) &= 0 + \left(k^2 + \frac{\partial^2}{\partial z^2}\right) F_1^+ + \frac{1}{z} \left(\frac{\partial}{\partial \rho} + \frac{1}{\rho}\right) \frac{\partial}{\partial z} F_0^- + \frac{1}{z} \left(\frac{\partial}{\partial \rho} + \frac{2}{\rho}\right) \frac{\partial}{\partial z} F_2^+ \\
E_2^-(\rho, z) &= 0 + \left[k^2 + \frac{1}{z} \left(\nabla_\rho^2 - \frac{4}{\rho^2}\right)\right] F_2^+ + \left(\frac{\partial}{\partial \rho} - \frac{1}{\rho}\right) \frac{\partial}{\partial z} F_1^+ + \frac{1}{z} \left(\frac{\partial}{\partial \rho} - \frac{1}{\rho}\right) \frac{\partial}{\partial z} F_0^- \quad (4.5)
\end{aligned}$$

For right (or left) circular polarization only the first (second) triplet survives. For linear polarizations, the second set of amplitudes is equal to the first set (except possibly for sign). Thus, only one set of three coupled equations need be solved.

Although the combination of

$$E_0^+(\rho, z) + E_{-1}^-(\rho, z)e^{-i\phi} + E_{-2}^-(\rho, z)e^{-2i\phi}, \quad (4.6)$$

appears to display an angular dependence to $|E|^2$ we have to remember that these three components are vectorially orthogonal to each other:

$$E = E_0^+(\rho, z) \frac{1}{z} (\hat{x} + i\hat{y}) + E_{-1}^-(\rho, z) e^{-i\phi} \hat{z} + E_{-2}^-(\rho, z) e^{-2i\phi} \frac{1}{z} (\hat{x} - i\hat{y}) \quad (4.7)$$

where \hat{x} , \hat{y} , and \hat{z} are the three cartesian unit vectors, so that

$$|E|^2 = \frac{1}{z^2} |E_0^+(\rho, z)|^2 + |E_{-1}^-(\rho, z)|^2 + \frac{1}{z^2} |E_{-2}^-(\rho, z)|^2, \quad (4.8)$$

is indeed independent of ϕ . The above result is quoted for the case of right circular polarization.

More generally

$$\begin{aligned}
E = E_0^+ \frac{1}{z} (\hat{x} + i\hat{y}) + E_0^- \frac{1}{z} (\hat{x} - i\hat{y}) + E_{-2}^- \frac{1}{z} (\hat{x} - i\hat{y}) e^{-2i\phi} + E_2^+ \frac{1}{z} (\hat{x} + i\hat{y}) e^{2i\phi} \\
+ E_{-1}^- \hat{z} e^{-i\phi} + E_1^+ \hat{z} e^{i\phi} \quad (4.9)
\end{aligned}$$

If the incident field is polarized in the \hat{x} direction

$$E_{-m}^-(\rho, z) = E_m^+(\rho, z); \quad E_{-m}^-(\rho, z) = E_m^-(\rho, z), \quad (4.10)$$

then

$$E = \left[E_0^+ + E_2^+ e^{2i\phi}\right] \frac{1}{z} (\hat{x} + i\hat{y}) + \left[E_0^+ + E_{-2}^- e^{-2i\phi}\right] \frac{1}{z} (\hat{x} - i\hat{y}) + E_{-1}^- 2\hat{z} \cos\phi, \quad (4.11)$$

and

$$|E|^2 = \frac{1}{2} |E_0^+ + E_0^- e^{2i\phi}|^2 + \frac{1}{2} |E_0^+ + E_0^- e^{-2i\phi}|^2 + |E_{-1}^+|^2 4\cos^2\phi, \quad (4.12)$$

is ϕ dependent in this case of plane polarization.

5. SUMMARY

We see that for circularly polarized radiation (and for geometrical optics - a result not proven here), the absorption will retain cylindrical symmetry. Although this will not be true in general, it seems useful to force this assumption on our problem since it reduces any calculations from three spatial dimensions to two dimensions. Computation time could be reduced by orders of magnitude. This reduction is absolutely necessary, even on a supercomputer, when one couples in the hydrodynamics, and treats the problem in a time-dependent way.

A treatment of the full problem should be coupled with an experimental investigation of the spatial distribution of the absorption energy, and the associated hydrodynamic response. A CO_2 laser could be used to irradiate a large drop (more than 10 microns in size) and an optical laser beam, and/or time dependent spectroscopy could be used to probe the response.

BLANK

Real-Time Measurement of Particulate Mass Concentration by Airborne Spectrophones - A Feasibility Study

K. Tennal, J. D. Wilson and M. K. Mazumder
University of Arkansas Graduate Institute of Technology
P. O. Box 3017
Little Rock, Arkansas 72203

ABSTRACT

One commercially available non-resonant spectrophone (Rurleigh PAS-100) and two laboratory made spectrophones - one operating in a Helmholtz resonant mode, and the other operating in a longitudinally resonant mode - were evaluated for their sensitivity in measuring particulate mass concentration of aerosols in real time. A major focus of this study was to determine the response of the spectrophone to vibration and acoustic noise sources related to measurements made on board an aircraft or other moving vehicle, and to develop methods for minimizing these noise contributions. To compensate the noise contribution arising from vibration, an accelerometer or a second microphone was used so that its signal generated by vibrations was of opposite polarity to that of the spectrophone. The two signals were added for automatic compensation. In this manner, the effect of vibration could be reduced by approximately 40 dB. Acoustic isolation was found effective against broadband noise with a sound power level of up to 100 dB. Both the Rurleigh spectrophone and the Helmholtz resonant spectrophone suffered from window noise. The longitudinally resonant spectrophone did not have optical windows. It provided the greatest sensitivity of $3.0 \times 10^{-7} \text{ m}^{-1}$ with one watt of chopped laser power. While actual in-flight data are needed for an evaluation of the spectrophone for aerosol measurements with respect to sensitivity and immunity from external noises and interference from gaseous absorbers, it was found that a longitudinally resonant photoacoustic cell with an appropriate nulling system and acoustic insulation may provide the desired sensitivity and signal-to-noise ratio for rapid measurement of mass concentration of aerosol particles.

The continuing work will include testing the resonant spectrophones for automatic compensation when they are subjected to both noise sources of vibration and sound, investigating the use of spectrophones for making real-time in-situ mass concentration measurements on various aerosols, and making in-flight evaluation.

INTRODUCTION

While photoacoustic methods are applicable to real-time mass concentration measurements under certain conditions, a major problem arises in using these methods for airborne measurements since microphones used in photoacoustic cells are sensitive to the vibration and acoustic noise which are generally encountered onboard aircraft. In the frequency range of 75 to 1000 Hertz, the airframe of a

jet transport plane can typically reach vibration accelerations²¹ of 10 g, where g is the acceleration due to gravity. Measurements made by Langley Research Center²² aboard a CV-990 aircraft show peak vibrations of the floor rail within a one Hertz bandwidth at frequencies in this range to be 0.17 g under conditions of normal smooth flight. Acoustic noise can reach levels in excess of 100 dB. Real time measurements of particulate mass concentrations of aerosols are often desired for studying atmospheric dispersions and obscurations. Measurements of light absorption by atmospheric aerosols have been carried out in three ways:

1) airborne devices have been used to determine the radiative flux divergence in layers of the atmosphere which, on subtracting the calculated gaseous component, yields the aerosol absorption component.³⁻⁶ Careful instrumentation is necessary and long term averaging is required due to inhomogeneities in the surface albedo.

2) absorption analysis of filter-collected aerosol particle samples has been carried out.⁷⁻⁹ There is, however, the possibility that the sample will be modified by collection especially in the case of liquid or liquid-coated particles.

3) absorption coefficients have been inferred from the scattering properties of the aerosol.^{10,11} This requires detailed information on the scattering properties to carry out the required Mie calculations.

These methods, while providing good estimates, are based upon indirect means of calculating the light absorption by particles. Photoacoustic techniques¹²⁻²⁰ offer a method of measuring absorption of light by aerosol particles directly. Absorption sensitivities as low as 10^{-8} m^{-1} have been reported using photoacoustic cells.¹² The instrument provides temporal and spatial resolution suitable for atmospheric measurement. The technique has been applied to the study of liquids, gases and solids. Several researchers have used photoacoustics for the study of aerosol absorption in both laboratory and field environments. Diesel exhaust^{13,15}, acetylene smoke¹⁶, NaCl, NiCl₂, cigarette smoke¹⁷, silica dust¹⁸, and ambient aerosols^{19,20} have been studied using photoacoustic techniques. Roessler¹⁵ has shown that either opacity measurements or photoacoustically measured absorption can be used to measure the mass concentration of the particulate component of exhaust from an automotive diesel engine with an uncertainty of about 20 percent.

When light energy is absorbed by a particle, molecules of the particle are excited to higher potential energy states. In general, this absorbed energy results in heating of the particle with subsequent transfer of the heat to the surrounding gas. If the sample aerosol is contained in a closed cell, this heating of the gas results in an increase in the pressure within the cell. If the light source is intensity modulated or chopped, then pressure variations will occur in the cell at the modulation frequency. These pressure variations can be detected with a microphone. The cell with

windows and microphone is called either a photoacoustic cell or a spectrophone.

When the light source is only weakly attenuated in the spectrophone, the microphone signal S is given by

$$S = RBA_a M_c W, \quad (1)$$

where W is the time averaged power of the light source, A_a is the specific absorption with units of inverse length per unit mass concentration, M_c is the sample mass concentration, R is the responsivity of the spectrophone which depends on the cell geometry and the microphone sensitivity, and B is the fraction of the absorbed optical energy that is converted into translational energy of the gas molecules. For fixed physical and chemical make up of the particles and a fixed light source A_a is a constant. Hence, S is proportional to the mass concentration of particulates in the aerosol.

EXPERIMENTS

Three spectrophones were tested for their sensitivity in making light absorption measurements: 1) a Burleigh Instruments, Inc., PAS-100 non-resonant spectrophone, 2) a laboratory-built Helmholtz-resonant spectrophone and, 3) a laboratory-built longitudinally-resonant spectrophone. The Burleigh spectrophone was tested for vibration and sound sensitivity and methods for isolation from these noise sources were incorporated into the system. Light absorption measurements on aerosols were made using the Burleigh and longitudinally resonant spectrophones.

The Burleigh spectrophone had an optical pathlength of 9 cm along a cylindrical gas cell of 8 mm diameter. It was constructed of type 316 stainless steel. Brewster's windows made of calcium fluoride were mounted at the ends. A microphone was mounted in the wall at the bottom center of the main cylinder and a single valve was mounted near one end.

The main cylinder was modified for our experiments by adding a second valve near the opposite end from the original valve and by mounting a second microphone (Knowels model 1759) diametrically opposed to the original microphone. This microphone could be replaced by a plate-mounted accelerometer (Endevco model 22200). The first of these modifications allowed gases to flow through the cell, thus permitting continuous measurement. The second modification was part of a vibration nulling system.

The experimental arrangement used to test the Burleigh spectrophone is shown in Figure 1. A Rofin optical chopper was used to modulate the beam from an argon-ion laser operating at 488 nm. An E G & G model 125A lock-in amplifier was used to detect the photoacoustic signal generated in dilute NO_2 . Gas from a tank of premixed NO_2 in air at 10 ppm was mixed with N_2 . Flow rates and, hence, NO_2 concentration were varied by controlling the upstream pressure to the capillary tubing. Saltzman's

reagent²¹ was used to measure the NO_2 concentration of the gas flowing through the spectrophone. Flow rates of one to three cm^3/s were used during photoacoustic measurements.

A Bruel and Kjaer PM vibration exciter type 4809 was used to subject the Burleigh spectrophone to both sinusoidal and broadband vibrations. The signal from either the Knowles microphone or the accelerometer was added to that of the spectrophone to reduce the spectrophone's response to vibration noise.

The response of the spectrophone to external acoustic noise was examined by placing the spectrophone in a chamber and subjecting it to sound power levels of up to 108 dB. The chamber was a box made of plywood 1.9 cm thick. It was 1.2 m high, 1.5 m long, and 1.4 m deep. Several dispersive elements were placed in the corners to reduce the possibility of specific resonances. Two speakers 30 cm in diameter were placed in the chamber and driven by sinusoidal signals or by broadband noise. For acoustic isolation a box made of 3.2 mm thick aluminum and lined with 4.5 cm thick cellular foam was placed over the spectrophone. The response of the spectrophone to acoustic noise was measured with and without the isolation box while the spectrophone was sitting on vibration isolators on the bottom of the chamber. A GENRAD 1988 precision integrating sound level meter and analyzer were used to measure the sound power level in the chamber. A Hewlett Packard spectrum analyzer model 186A was used to measure the responses of the spectrophone and the sound level meter to frequencies of sound between 0 and 2000 Hertz and to broadband noise.

The Helmholtz resonant spectrophone is shown in Figure 2. It consisted of two identical absorption chambers 12.7 cm long and 1.27 cm in diameter joined at their longitudinal midpoints by a connecting tube 8 cm long and 0.46 cm in inner diameter. The material was type 316 stainless steel. Brewster's angle windows were mounted on the ends of the absorption chambers. The resonant frequency was measured to be 242 Hz and the resonance gain was 16.

At resonance the pressures in the two absorption chambers were 180 degrees out of phase with each other. It was therefore possible to use both halves of the chopped laser beam, thus increasing the photoacoustic signal. The optical system for this is shown in Figure 2. The chopper had eight blades and was made from a plexiglas disk 0.95 cm thick and 10 cm in diameter. The laser beam was displaced rather than blocked by the blades so that it could be directed alternately through the two absorption chambers.

The third spectrophone tested was a double-open-ended tube operated in its first longitudinally resonant mode. A type 316 stainless steel tube 20 cm long and with an inner diameter of 0.46 cm was used. A Radio Shack 270-092A electret condenser microphone was glued over a 3.2 mm hole in the wall at the center. The first longitudinal resonance was at 814 Hz and the resonance gain was 16. This tube was housed inside a 5 cm i.d. by 90 cm long tube for acoustic isolation from laboratory noises. Sample

flow rates of $10 - 15 \text{ cm}^3/\text{s}$ were used. Figure 3 shows the experimental arrangement for making measurements of light absorption by aerosols using this spectrophone.

Measurements of the absorption of 488 nm laser light by cigarette smoke were made simultaneously with measurements of the particle size distribution and the approximate number concentration of particles using a single particle aerodynamic relaxation time (SPART) analyzer.²² The aerosol chamber was a cube one meter on an edge. It contained an internal mixing fan and an exhaust blower for flushing out aerosols. The sample flow rates for the spectrophone and the SPART were both set to around $10 \text{ cm}^3/\text{s}$. A cigarette was allowed to burn in the chamber until the count rate meter on the front panel of the SPART reached about 200/s (about 10-15 seconds). The spectrophone signal was recorded while the particle count rate gradually dropped. This procedure was repeated using $0.9 \mu\text{m}$ NaCl generated with a DeVilbiss ultrasonic nebulizer model 358 and $1.09 \mu\text{m}$ polystyrene latex spheres (PLS) aerosols generated with a Bard-Parker pneumatic nebulizer.

RESULTS AND DISCUSSIONS

Table I shows the responsivities and sensitivities of the three spectrophones. The average power of the chopped laser beam was assumed to be one watt in each case.

Table I

	<u>Sensitivity (m^{-1})</u>	<u>Responsivity</u>
Rurleigh	6.5×10^{-6}	$0.077 \text{ V/m}^{-1} \cdot \text{W}$ (100 Hz)
Helmholtz	2.5×10^{-6}	$0.26 \text{ V/m}^{-1} \cdot \text{W}$ (242 Hz)
Longitudinal	3×10^{-7}	$0.32 \text{ V/m}^{-1} \cdot \text{W}$ (814 Hz)

The sensitivities reported here are for a one second time constant on the lock-in amplifier and for a signal-to-noise ratio of one. The noise levels were measured under ambient laboratory conditions with no absorber in the spectrophone. Figure 4 shows an absorption measurement made on 25 to 30 pph NO_2 in N_2 flowing at a rate of $10 \text{ cm}^3/\text{sec}$ through the longitudinally resonant spectrophone. The noise level of the spectrophone output with a continuous flow was about three times that with no flow. The average laser power was 250 mW and the time constant on the lock-in amplifier was one second.

The Rurleigh spectrophone was found to have a response to sinusoidal vibrations of 1.3 mV/g where g is the acceleration due to gravity. Figure 5 illustrates the degree of vibration isolation achieved with the nulling circuitry. Broadband vibration was applied with an rms acceleration of $0.02 \text{ g}/(\text{Hz})^{1/2}$ at 400 Hz. Section (a) of the trace (Fig. 5) shows the lock-in amplifier output for the situation where the signal from the Knowles microphone was added to the signal from the spectrophone. Section

(b) of the trace was made with the Knowles microphone disconnected. The noise was reduced by nearly 40 dB with the summing circuit. Section (c) of the trace was the background noise level with no vibration. These results were obtained with the spectrophone valves closed, with N_2 in the spectrophone and with 250 mW of chopped laser power passing through it. Similar vibration noise reduction was achieved with the accelerometer.

Figure 6 shows an absorption measurement for 7.6 ppm NO_2 in air while nulling vibrations with the Knowles microphone circuit. The gas was flowing through the spectrophone at $1.1 \text{ cm}^3/\text{s}$. The nulling improved the signal to noise ratio by 20 dB. The noise was not reduced as much as with the valves closed probably due to acoustic noise entering the spectrophone through the flow tubes. Bandpass filters were used in the nulling circuits since the lock-in amplifier did not eliminate odd harmonics of the detection frequency. At these higher frequencies, the relative phase shifts in the nulling circuit were different than the phase shift for the fundamental and hence compensation was not effective over the entire spectrum.

Mechanical isolation against vibration was tested using a two inch thick cellular foam pad placed between the spectrophone's baseplate and the vibration exciter. This arrangement provided 30 dB isolation from sinusoidal vibrations at 100 Hz and 60 dB at frequencies above 400 Hz.

Using broadband acoustic noise with a sound power level of 108 dB the spectrophone noise increased a maximum of $6 \text{ dB}/(\text{Hz})^{1/2}$ in the 50 to 2000 Hz frequency range. When the speakers were driven with a single frequency sinusoidal source such that the sound power level at the spectrophone was 100 dB, the spectrophone response was 18 dB above its background. The acoustic isolation box reduced this response by 10 - 15 dB for frequencies between 500 and 1000 Hz but did not reduce the response for frequencies below 300 Hz.

Figure 7 shows the experimental data on the number concentration of cigarette smoke particles measured by the SPART analyzer plotted against the photoacoustic signal from the longitudinally resonant spectrophone. A count rate of 10 particles/s on the SPART analyzer corresponded to a concentration of $200 \text{ particles}/\text{cm}^3$. Figure 8 shows the spectrophone signal for filtered air, room air, and dilute cigarette smoke. The chopped laser power at the spectrophone was about 200 mW and the lock-in amplifier was set for a 0.1 second time constant. The signal with filtered air was probably due primarily to absorption in the windows or cell walls, however, the possibility of a background gaseous absorber was not eliminated.

The background noise level of less than 100 nV and the absorption signal for cigarette smoke of about three μV per $100 \text{ particles}/\text{cm}^3$ indicates a detection limit of about three particles/ cm^3 . The particle concentration at which the spectrophone signal begins to saturate was not determined.

The photoacoustic signal from NaCl particles was found to be humidity dependent and was nearly

three orders of magnitude less than for cigarette smoke for an equal particle concentration. The photoacoustic signal from PLS particles was two orders of magnitude less than for cigarette smoke.

The longitudinally resonant spectrophone was the simplest, least expensive and most sensitive of the three spectrophones tested and since it was windowless, contamination problems were minor. The photoacoustic signals generated by light absorption in the windows of the Rurlough and Helmholtz resonant spectrophones were found to vary due to contamination of the windows. These variations were at levels significantly greater than the background noise and, hence, decreased the sensitivity of the two systems with respect to that shown in Table I. Continuous flow and window purging with clean air would be necessary to allow them to be used with aerosols.

Isolation of a non-resonant spectrophone from the vibration and acoustic noise present on an airplane appeared to be quite feasible. An estimated 40 dB reduction in vibration could be obtained with commercial mechanical vibration isolators.¹ The electronic nulling circuitry used here supplied an additional 35 dB. The rms vibration level measured² on board the CV-990 aircraft of $0.17 \text{ g}/(\text{Hz})^{1/2}$ and the spectrophone response of 1.3 mV/g give an expected rms noise due to vibration of $0.2 \text{ mV}/(\text{Hz})^{1/2}$. Reducing this by 75 dB yields a vibration noise of $35 \text{ nV}/(\text{Hz})^{1/2}$. The noise level of the spectrophone was $500 \text{ nV}/(\text{Hz})^{1/2}$ at 100 Hz and was inversely proportional to the detection frequency.

Acoustic isolation from high level broadband noise appears to be easily achieved. If high level single frequency sources exist on an airplane, it should be possible to simply use a chopping frequency several Hz away from them.

ACKNOWLEDGEMENT

The work was supported in part by the National Aeronautics and Space Administration under contract number NAG 2-147. The authors wish to thank B. Regent for his suggestions and comments, D. Jackson for technical assistance, D. Watson and D. Belk for their editorial assistance.

REFERENCES

1. Application Selection Guide, Barry Controls Bulletin C6-181, Barry Wright Corp. (1981).
2. Measurements performed aboard a CV-990 aircraft at Langley Research Center by the CV-990 Project group.
3. W. R. Roach, "Some Aircraft Observations of Fluxes of Solar Radiation in the Atmosphere," *Quart. J. R. Met. Soc.*, 87, 346-363 (1966).
4. G. D. Robinson, "Some Determinations of Atmospheric Radiation Measurements of Solar Radiation from Aircraft and at the Surface," *Quart. J. R. Met. Soc.*, 92, 263-269 (1966).
5. K. Ya. Kondratyev, D. R. Vassilyev, V. S. Grishchkin and L. S. Ivlev, "Spectral Radiative Flux Divergence and its Variability in the Troposphere in the 0.4 - 2.4 μ m Region," *Appl. Optics*, 13, 478-486 (1974).

6. F. P. J. Valero, W. J. Y. Gore, L. P. M. Giver, "Radiative Flux Measurements in the Troposphere," *Appl. Optics*, 21, 831-838 (1982).
7. K. Fischer, "Mass Absorption Coefficients of Natural Aerosols in the 0.4 - 2.4 μm Wavelength Interval," *Reit. Phys. Atm.*, 46, 89-100 (1973).
8. R. E. Weiss, A. P. Waggoner, and R. J. Charlson, "Studies of the Optical, Physical and Chemical Properties of Light Absorbing Aerosols," Proceedings of Conference in "Carbonaceous Particles in the Atmosphere," March 20-22, 1978, Berkeley, CA., T. Novakov (Ed.), Lawrence Berkeley Laboratory Report LBL 9037 CONF 7803101, UC 11, June 1979.
9. C. A. Bennett, Jr., R. R. Patty and W. A. McClemmey, "Photoacoustic Detection of Carbonaceous Particles," *Appl. Optics*, 20, 3475-7 (1981).
10. R. Eiden, "Determination of the Complex Index of Refraction of Spherical Aerosol Particles," *Appl. Optics*, 10, 749-754 (1971).
11. G. W. Grams, I. H. Rlifford, D. A. Gillette, and P. B. Russell, "Complex Index of Refraction of Airborne Soil Particles," *J. App. Met.*, 13, 459-471 (1974).
12. C. K. N. Patel and R. J. Kerl, "A New Optoacoustic Cell with Improved Performance," *Appl. Phys. Lett.*, 30, 578-579 (1977).
13. F. R. Faxvog and D. M. Roessler, "Optoacoustic Measurements of Diesel Particulate Emissions," *J. Appl. Phys.*, 50, 7880-2 (1979).
14. A. C. Szkarlat and S. M. Japar, "Light Absorption by Airborne Aerosols: Comparison of Integrating Plate and Spectrophone Techniques," *Appl. Optics*, 20, 1151-5 (1981).
15. D. M. Roessler, "Photoacoustic Insights on Diesel Exhaust Particles," *Appl. Optics*, 23, 1148-55 (1984).
16. D. M. Roessler and F. R. Faxvog, "Optoacoustic Measurement of Optical Absorption in Acetylene Smoke," *J. Opt. Soc. Am.*, 69, 1699-1704 (1980).
17. R. W. Terhune and J. E. Anderson, "Spectrophone Measurements of the Absorption of Visible Light Aerosols in the Atmosphere," *Opt. Lett.*, 1, 70-2 (1977).
18. C. W. Bruce and R. G. Pinnick, "In-situ Measurements of Absorption with a Resonant CW Laser Spectrophone," *Appl. Optics*, 16, 1762-5 (1977).
19. C. W. Bruce, Y. P. Yee, B. D. Hinds, R. J. Brewer, J. Minjores and R. G. Pinnick, "Initial Field Measurements of Atmospheric Absorption at 9 - 11 μm Wavelengths," *J. Appl. Met.*, 19, 997-1004 (1980).
20. J. S. Foot, "Spectrophone Measurements of the Absorption of Solar Radiation by Aerosols," *Quart. J. R. Met. Soc.*, 105, 275-83 (1979).
21. B. E. Saltzman, "Colorimetric Microdetermination of Nitrogen Dioxide in the Atmosphere," *Anal. Chem.*, 92, 12, 1949 - 55 (Dec. 1954).
22. M. K. Mazumder, R. E. Ware, J. D. Wilson, R. G. Renninger, F. C. Hiller, P. C. McLeod, R. M. Raible, and M. K. Testerman, "SPART Analyzer: Its Application to Aerodynamic Size Distribution Measurement," *J. Aerosol Sci.*, 10, 561 (1979).

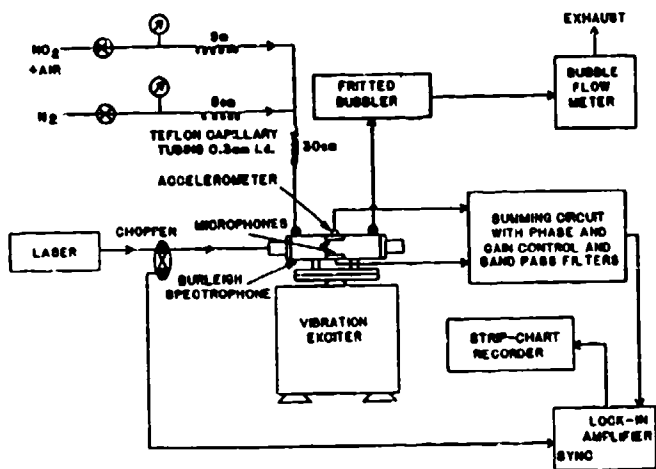


Figure 1. Experimental arrangement for making light absorption measurements and vibration measurements with the Rurleigh Spectrophone.

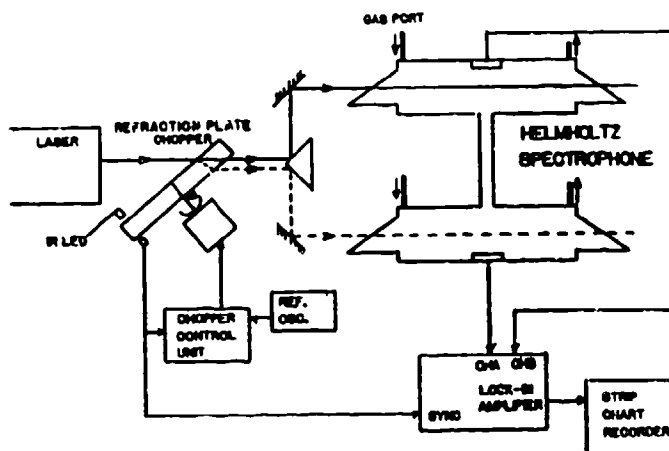


Figure 2. Helmholtz Resonant Spectrophone. The refraction plate chopper allows the spectrophone to be driven by both halves of the chopped laser beam.

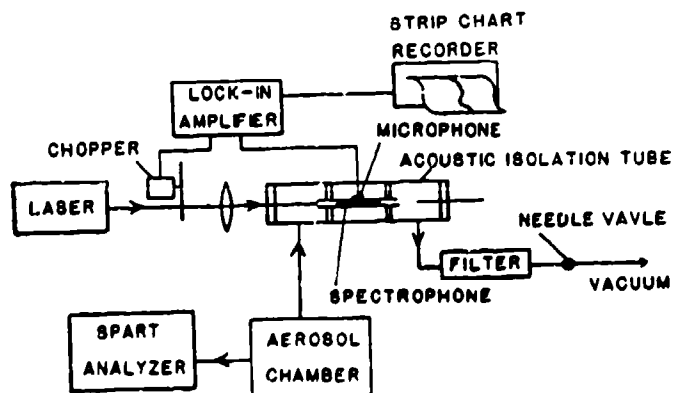


Figure 3. Longitudinally Resonant Spectrophone. Experimental arrangement for making photoacoustic measurements and particle concentration measurements on an aerosol.

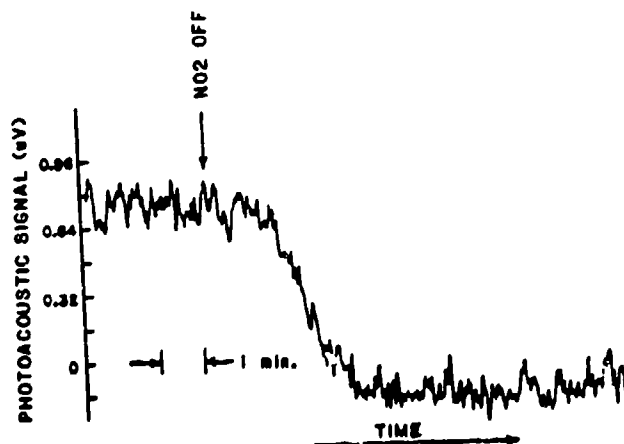


Figure 4. Measurement of Light Absorption by NO_2 in the Longitudinally Resonant Spectrophone. The lock-in amplifier time constant was one second and the gas flow rate was $10 \text{ cm}^3/\text{second}$. The NO_2 concentration was 25 - 30 ppb in N_2 .

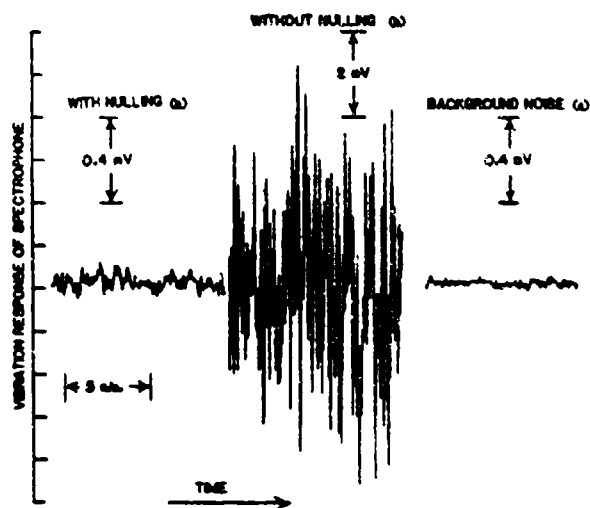


Figure 5. Reduction of the Vibration Response of the Burleigh Spectrophone. During traces (a) and (b) the spectrophone was subjected to broadband vibrations. In (a) the noise of the spectrophone was reduced by subtracting from it the signal from the Knowles microphone.

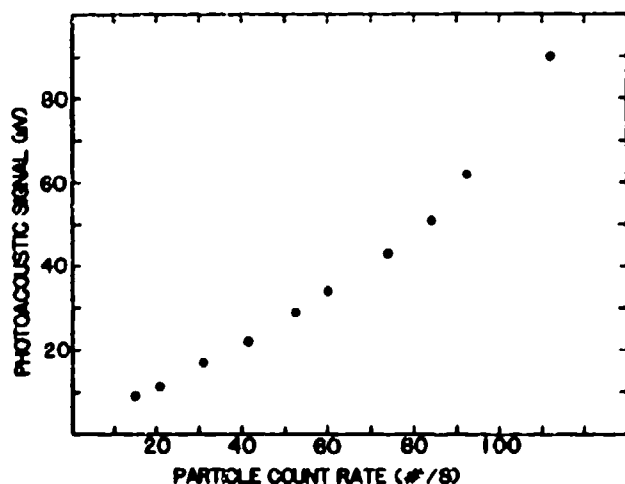


Figure 7. Photoacoustic Signal from Cigarette Smoke Plotted as a Function of Particle Count Rate. A count rate of 10 counts/s on the SPART analyzer is equivalent to a particle number concentration of 200 particles/cm³.

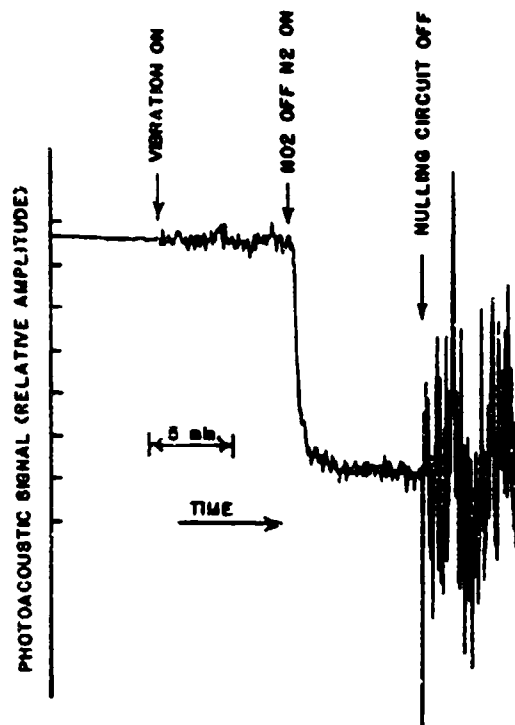


Figure 6. Photoacoustic Measurements under Vibrationally Noisy Conditions. The lock-in amplifier output shows the Burleigh spectrophone response to light absorption by NO₂ when the instrument is subjected to broadband vibrations with and without nulling circuitry.

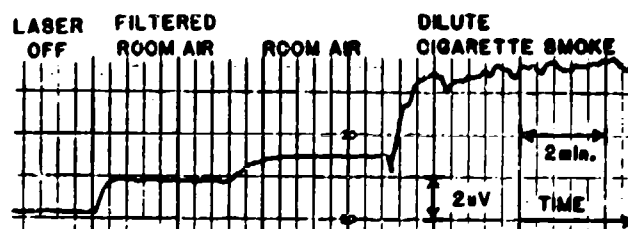


Figure 8. Photoacoustic Measurements of Aerosols using a Longitudinally Resonant Spectrophone.

SPECTROSCOPY OF MOLECULAR CLUSTERS AND SMALL PARTICLES
IN SOLID ARGON MATRICES

Donald R. Huffman
Department of Physics
University of Arizona
Tucson, Arizona 85721

ABSTRACT

We have begun a program to isolate atoms and small molecular clusters in low temperature solid argon matrices for the purpose of doing spectroscopy in the ultraviolet, visible, and infrared regions. The samples of interest are metals and carbon. In the early stages of this work we have profited greatly from collaboration with two research groups in West Germany. Two presentations based on these collaborations were made at the Third International Symposium on Molecular Clusters and Small Particles held in West Berlin, July, 1984. The papers, listed below, are also being published in a special edition of Surface Science.

K. P. Pflibaen and D. R. Huffman, "Electronic and Vibrational Spectra of AgNa Molecular Clusters and Small Particles," Surface Science, 1984.

W. Krätschmer, N. Sorg, and D. R. Huffman, "Spectroscopy of Matrix Isolated Carbon Cluster Molecules Between 200 and 850 nm Wavelength," Surface Science, 1984.

In the present report we present recent results on spectroscopy of molecular clusters of carbon in the visible and ultraviolet. A monochromator for the infrared spectral range is being designed for simultaneous spectroscopy in the uv and ir. By further annealing of matrix isolated molecular clusters we hope to follow spectroscopically the transition from molecular clusters to small solid particles.

INTRODUCTION

In spectral regions where the real part of the complex dielectric function is negative there occur very strong absorption effects in small particles, often called surface plasmons as they occur in the ultraviolet spectra of metallic particles and surface phonons in the infrared spectra of insulating particles. Shape effects including both nonsphericity of individual particles and aggregation of particles have extreme effects in these regions.¹ In experimental studies aimed at understanding these optical effects it has been practically impossible to eliminate particle aggregation for particles in the sub-micrometer size range, since the particles almost invariably aggregate during the production process. In an effort to avoid this problem while producing very small particles (i.e. 50 Å size) we have begun a program to build up small particles from atomic constituents while keeping the clusters immobilized in the medium of a solid rare gas, such as solid argon.

The technique, known as matrix isolation spectroscopy has been used for many

years,²⁻⁴ primarily by chemists studying unstable species such as free radicals. Pioneering work for the purpose of bridging the gap between molecular and small particle, solid state spectroscopies has been done by the Stuttgart group under Dr. T. P. Martin.^{5,6} Considerable progress has already been made in collaboration with the Max-Planck Institutes at Heidelberg and at Stuttgart in West Germany. At Heidelberg our emphasis has been on the visible and ultraviolet spectra of molecular clusters of carbon. At Stuttgart the emphasis has been on alloyed molecular clusters of dissimilar metal atoms, utilizing both ultraviolet spectroscopy for probing electron states and far infrared spectroscopy for probing vibrational states. Some work along both lines is continuing in our laboratory in Tucson. Examples of both the carbon cluster spectroscopy and the alloyed metal spectroscopy were presented at the Third International Symposium on Molecular Clusters and Small Particles held in West Berlin in July, 1984. These papers have been accepted for publication in Surface Science. In this report we present results only for the carbon cluster problem.

EXPERIMENT

As in other typical matrix isolation apparatus, we use a liquid helium-cooled cold finger supporting a transparent sapphire substrate in the beam of the spectrophotometer. With the substrate held at a temperature between 10 and 15 K, argon is allowed to condense onto the substrate to form the matrix. During this deposition carbon vapor, produced by evaporating a pointed carbon rod, is introduced into the argon gas stream to form isolated atoms and small molecular clusters of carbon in the frozen matrix. Later warming of the substrate to 25 - 30 K allows larger clusters and small particles to form by diffusion and coagulation of the carbon atoms.

RESULTS

One example of extinction (absorption + scattering) spectra for carbon vapor trapped in solid argon is shown in the figure. Curves are shown before and after the annealing process. Superimposed on a small extinction rise toward the uv (which we interpret as due to scattering) are numerous absorption bands due to molecular clusters of carbon. Even the small details of these spectra are reproducible. Initially the most prominent feature is the well known C_3 band at 410 nm.⁷ Upon annealing, the C_3 band decreases and other bands increase, which we

interpret as due to the growth of larger molecular clusters. Because of the tendency of carbon molecules to form linear chains, the observed spectra are tentatively thought to be due to carbon chains. Details of the first suggested identifications are given in reference 8. At the present time it is not possible to confidently identify all major bands in the complicated spectra.

FURTHER WORK

Similar matrix isolation apparatus for carbon is being set up on a McPherson vacuum-ultraviolet spectrophotometer to extend this work down to about 120 nm wavelength. This should reveal the supposed C_3 bands in the 170-180 nm region which form an important tie-point for the proper identification of larger clusters. In the design stage is an infrared monochromator system to be adapted to the visible and vacuum-uv apparatus for simultaneous measurements of both infrared and ultraviolet spectra. With such a combination the development of vibrational mode absorption can be followed in synchronism with the development of electronic absorption as the clusters grow.

Finally, it is hoped that the development of molecular absorption bands can be followed as they grow with further annealing into solid state absorptions, such as the well known 220 nm surface plasmon band in small graphite particles.

ACKNOWLEDGEMENT

This work was supported by the Chemical Systems Laboratory, U. S. Army, Aberdeen Proving Ground, Maryland.

REFERENCES

1. C. F. Bohren and Donald R. Huffman, Absorption and Scattering of Light by Small Particles, (Wiley, New York), 1983, chapter 12.
2. B. Meyer, Low Temperature Spectroscopy, (American Elsevier, New York), 1971.
3. H. E. Hallam, Vibrational Spectroscopy of Trapped Species, (Wiley, New York), 1973.
4. M. Moskowitz ed., Crystalline Chemistry, (Wiley, New York), 1976.
5. T. P. Martin, Phys. Rev. B15, 4071 (1977).
6. T. P. Martin, J. Chem. Phys. 67, 5207 (1977).
7. W. Weltner and D. M. McCleod, J. Chem. Phys. 40, 1305 (1964).
8. W. Krätschmer, N. Borg, and Donald R. Huffman, Surface Science (1984) in press.
9. K. W. Chang and W. R. M. Graham, J. Chem. Phys. 77, 4300 (1982).

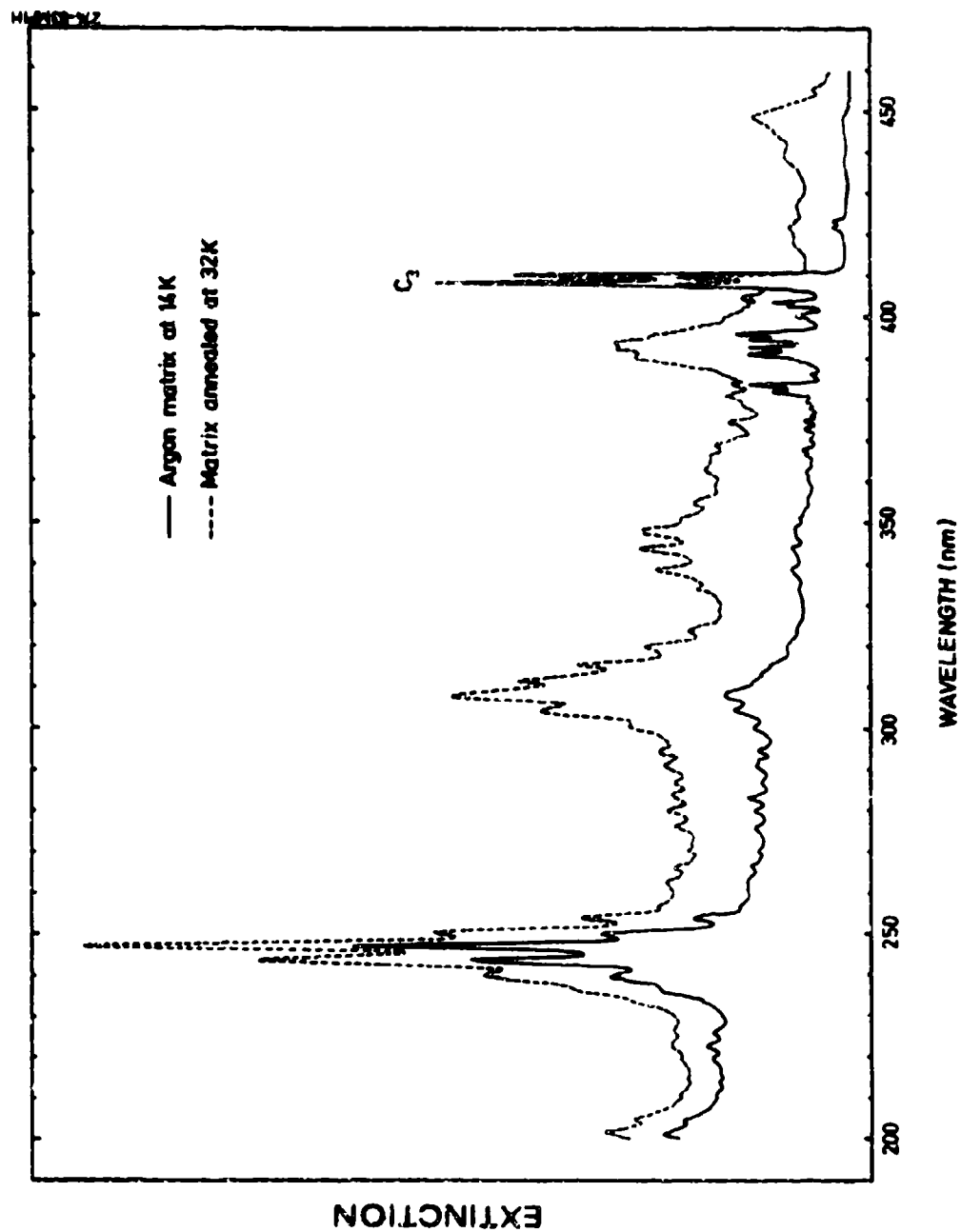


FIGURE 1
EXTINCTION SPECTRA FOR CARBON VAPOR ISOLATED IN SOLID ARGON,
BEFORE AND AFTER ANNEALING THE MATRIX.

ABSORPTION AND SCATTERING BY
SMALL PARTICLES; STRUCTURE OF
THE INTERNAL AND NEAR FIELDS

H. Weil and T.B.A. Senior
Radiation Laboratory
Department of Electrical Engineering and Computer Science
The University of Michigan
Ann Arbor, Michigan 48109

This paper concerns work completed or in progress on computing the electric fields induced by radiation incident on small particles. Emphasis has been on the fields inside and near the particles when the incident radiation is in an absorption band of the bulk material. This work has been presented, published, and submitted for publication as follows.

T.B.A. Senior and H. Weil, "Structure of Polariton Modes," Proceedings of the 1983 CSL Conference on Obscuration Research, submitted Sept. 1983.

H. Weil and T.B.A. Senior, "Structure of Surface Polariton Modes In and Near Small Particles," National Radio Science Meeting (USNC/URSI, IEEE) Boulder, CO; presented Jan. 1984.

H. Weil, T.B.A. Senior and T. M. Willis III, "Internal and Near Fields of Small Particles Irradiated in Spectral Absorption Bands," submitted to Journal of the Optical Society of America, Sept. 1984.

Related work based on the same integral equation and theoretical-numerical techniques is in progress to determine the effects on scattering and absorption of isolated surface irregularities, of surface roughness and of periodic surface microstructure. In all this work rotational symmetry of the particles has been assumed in order to keep the mathematics "relatively" simple.

A completely different integral-equation-based method has been applied to the study of scattering and absorption by thin flakes of arbitrary shape. The entire flake is small compared to the free space wavelength. Here the thickness effects are approximately taken into account by incorporating them into an impedance boundary condition on an equivalent zero-thickness flake. This simplification is what permits the analysis to be applied readily to non-rotationally symmetric shapes. The following two publications have so far resulted and work is still in progress.

T.B.A. Senior and M. Naor, "Low Frequency Scattering by a Resistive Plate," IEEE Trans. AP-32, pp 272-275, March 1984.

T.B.A. Senior and D. A. Ksienski, "Determination of a Vector Potential," Radio Science, 19 pp 603-607, March-April 1984.

The latter paper deals with the fact that the standard, low-frequency scattering theories fail in the case of open surfaces (i.e., two dimensional objects representing a discontinuity in space) and are inconvenient for solid objects. The problem of the open surface was solved and an improved

method of solution for solid objects was also developed. The two methods were presented in the paper by Senior and Ksienski.

All the above work is for Rayleigh particles, all dimensions small compared to λ , the incident wavelength. To study the effects of having one dimension comparable to the wavelength we are investigating the scattering, absorption and internal fields for thin circular disks as the disk radius a varies from $a \ll \lambda$ to $a \sim \lambda$. To do this we have revised and extended a moment method due to C. M. Chu and H. Weil (Applies Optics 19, pp 2066-2071, June 15, 1980). The original Chu-Weil formulation was not accurate when $a \ll \lambda$ mainly because the basis functions were inappropriate in that case; it also did not completely compute the internal fields but only the coefficients for an expansion of the internal fields in terms of the basis functions. A modified and expanded set of basis functions has been introduced and the program rewritten to account for this change and to compute the internal fields. This work is largely completed but the final computing programs are undergoing more testing.

A NEW ITERATIVE EXTENDED BOUNDARY CONDITION METHOD FOR CALCULATING
SCATTERING AND ABSORPTION BY ELONGATED OBJECTS

Magdy F. Iskander
Department of Electrical Engineering
University of Utah
Salt Lake City, Utah 84112

Abstract

The extended boundary condition method (EBCM), which is a popular procedure for solving scattering and absorption by dielectric objects, is based on an integral equation formulation which utilizes spherical expansions to solve for the unknown fields. Such a procedure is known to be limited and inadequate for elongated dielectric objects and particularly those of large complex permittivities. As the shape of the object deviates from that of a sphere, a large number of terms in the vector spherical harmonics expansion of the unknown fields is required, which forces the matrix formulation to include Hankel functions of large arguments and orders and, in turn, results in an ill-conditioned system of equations.

In this paper we describe a new procedure, the iterative extended boundary condition method (IEBCM), for improving the solution stability and extending the frequency range of the EBCM. The new procedure has two main features including:

1. It involves dividing the internal volume of the dielectric object into several overlapping regions and employing separate field expansions in each of these overlapping subregions.
2. It is iterative since it starts with a known solution that approximates the scattering problem.

For high-loss dielectric objects of large aspect ratio, the initial assumption of the surface fields was obtained by approximating the object by a perfectly conducting one of the same size and shape. Numerical results were obtained for frequencies up to seven times the resonance of these objects. Up to 11 overlapping subregions were found necessary to describe the internal fields of these objects.

For low-loss elongated dielectric objects commonly encountered in optical applications, on the other hand, the initial assumption was obtained by approximating the object's geometry, rather than its properties, by a spherical one and using the Mie solution to obtain the approximate surface fields. Also in this case, we carry out the iterative procedure by solving for objects of intermediate geometries between the initial sphere and the elongated object of interest. Thus, while in utilizing the perfect conductor initial assumption, we use the iterative procedure to build in the properties of the object; in the low-loss dielectric object case we preferably iterate to build in the geometry of the elongated object.

We also examined the application of the IEBCM to solve for composite bodies using mixed basis functions. In a capped cylindrical object, the interior volume was first divided into several overlapping spherical subregions and alternatively partitioned into a finite cylindrical subregion and two spherical end caps. Spherical expansions were used in the spherical subregions and a cylindrical expansion was utilized for the cylindrical subregion. The obtained numerical results clearly illustrated the computational advantages in choosing the expansion functions compatible with the geometry of the object.

Numerical results for spheroids of aspect ratios as large as 12:1 are obtained, thus illustrating the feasibility of using the IEBCM for highly elongated objects at frequencies at and beyond the resonance frequency range. The obtained numerical results also illustrated the importance and the computational advantages of using different basis functions such as cylindrical and spherical to solve for very highly elongated objects.

This work has been published and presented as follows:

Journal Articles

M. F. Iskander, A. Lakhtakia, and C. H. Durney, "A new procedure for improving the solution stability and extending the frequency range of the EBCM," IEEE Transactions on Antennas and Propaga-

tion, Vol. AP-31, 1983, pp. 317-324.

M. F. Iskander and A. Lakhtakia, "Extension of the iterative EBCM to calculate scattering by low-loss or lossless elongated dielectric objects," Applied Optics, Vol. 23, 1984, pp. 948-953.

M. F. Iskander, A. Lakhtakia, and C. H. Durney, "A new iterative procedure to solve for scattering and absorption by dielectric objects," Proceedings of the IEEE, Vol. 70, 1982, pp. 1361-1363.

A. Lakhtakia, M. F. Iskander, and C. H. Durney, "An iterative extended boundary condition method for solving the absorption characteristics of lossy dielectric objects of large aspect ratios," IEEE Transactions on Microwave Theory and Techniques, Vol. MTT-31, 1983, pp. 640-647.

A. Lakhtakia and M. F. Iskander, "Theoretical and experimental evaluation of power absorption in elongated objects at and beyond resonance," IEEE Transactions on Electromagnetic Compatibility, Vol. EMC-25, 1983, pp. 448-453.

Conference Presentations

M. F. Iskander, S. C. Olson, and C. H. Durney, "Extension of the iterative EBCM to calculate scattering by low-loss elongated dielectric objects and its hybridization with the geometrical optics approximation," International IEEE/AP-S Symposium and National Radio Science Meeting, Boston, Massachusetts, June 25-29, 1984.

M. F. Iskander, "An iterative extended boundary condition method for calculating scattering and absorption by elongated dielectric objects," invited presentation in the special session on numerical techniques at the URSI Annual Meeting, Boulder, Colorado, January 1984.

M. F. Iskander, S. C. Olson, and C. H. Durney, "Calculation of the average resonance absorption by human and animal models," presented in the Sixth Annual Meeting of the Bioelectromagnetics Society, Atlanta, Georgia, July 15-19, 1984.

M. F. Iskander, "New iterative extended boundary condition method for calculating scattering and absorption by elongated and composite objects," presented at CRDC Scientific Conference on Obscuration and Aerosol Research, June 25-29, Aberdeen Proving Ground, Maryland, 1984.

A. Lakhtakia, M. F. Iskander, and C. H. Durney, "On the use of the iterative EBCM to solve for absorption by composite dielectric objects -- the introduction of mixed basis functions," presented at the International IEEE/AP-S Symposium, Houston, Texas, May 23-26, 1983.

A. Lakhtakia, M. F. Iskander, and C. H. Durney, "Theoretical and experimental evaluation of the average SARs at and beyond resonance," presented at the Fifth Annual Meeting of the Bioelectromagnetics Society, Boulder, Colorado, June 12-16, 1983.

M. F. Iskander, A. Lakhtakia, and C. H. Durney, "Scattering and absorption by dielectric objects," IEEE/AP-S International Symposium, Albuquerque, New Mexico, May 24-28, 1982.

M. F. Iskander, A. Lakhtakia, C. H. Durney, and H. Maasoudi, "Iterative solution to improve the stability and frequency range of the EBCM," Fourth Annual Meeting of the Bioelectromagnetics Society, Los Angeles, California, June 28-July 2, 1982.

Introduction

It is generally known that the extended boundary condition method (EBCM) is a popular procedure to solve for the scattering and absorption of electromagnetic radiation by dielectric objects. Such scattering and absorption problems have many important applications in a variety of fields, including light scattering by particles, fiber optics communication, and in evaluating the hazardous effects associated with electromagnetic radiation. Among the many available techniques for solving the three-dimensional scattering problems, the EBCM has been widely utilized in calculating the scattering and absorption characteristics of axisymmetric dielectric objects. Our group at the University of Utah,

for example, has utilized the EBCM in calculating the power absorption characteristics of spheroidal biological models of humans and animals exposed to plane-wave [1, 2] or near-field radiation [3-7]. In all cases, however, the calculations were limited to the preresonance frequency range simply because of certain numerical instabilities in the EBCM at and beyond the resonance frequency range [3]. This problem becomes pronounced the more the shape of the dielectric object deviates from that of a sphere, such as for a spheroidal model of large a/b ratio. For such cases, a large number of terms in the vector spherical harmonics expansion is required to describe the field variations, which forces the matrix formulation to include Hankel functions of large arguments and orders, and which, in turn, result in an ill-conditioned system of equations. The solution procedure employed earlier to overcome this problem and described in some of our publications [1, 3] was temporary. Although it allowed one to obtain results at relatively high frequencies, it did not solve the basic problem involved, and hence was once again inaccurate as the frequency approached resonance [1-3].

In this paper, we describe a new iterative procedure called "the iterative extended boundary condition method (IEBCM)" for improving the stability and extending the frequency range of the EBCM.

Description of the New Method

The new technique is iterative since it requires an initial estimate of the tangential fields on the object's surface and also utilizes the key process of representing the fields inside the dielectric object by several overlapping subregional expansions. For objects which are characterized by large complex relative permittivities, the initial estimate was obtained by replacing the dielectric object by a perfectly conducting one of the same shape and size and then solving for the current densities on the substitute object [8-10]. This initial estimate is then utilized iteratively to obtain the correct solution for the dielectric object of interest. It is shown that the dielectric properties of the original object are actually gradually built in the solution from the initial assumption through the iterative procedure.

For the case where we approximate the object by a perfectly conducting one, the surface current density of the l th iteration is obtained by solving the following integral equation [8, 9, 10]

$$\begin{aligned}
 & \{ \bar{E}^i(\bar{r}) + \nabla \times \int_s [\hat{n}(\bar{r}') \times \bar{E}_{\text{int}}^{(l-1)}(\bar{r}') \cdot \bar{G}(\bar{k}\bar{r}/\bar{k}\bar{r}')]] d\bar{s}' \\
 & - \nabla \times \nabla \times \int_s \frac{1}{j\omega\epsilon_0} [\hat{n}(\bar{r}') \times \bar{H}_{\text{int}}^{(l-1)}(\bar{r}') \cdot \bar{G}(\bar{k}\bar{r}/\bar{k}\bar{r}')]] d\bar{s}' \} \\
 & = \nabla \times \nabla \times \int_s \frac{1}{j\omega\epsilon_0} [\hat{n}(\bar{r}') \times \Delta \bar{H}_+^{(l)}(\bar{r}') \cdot \bar{G}(\bar{k}\bar{r}/\bar{k}\bar{r}')]] d\bar{s}' \quad (1)
 \end{aligned}$$

where \hat{n} is the unit outward normal to the surface s , $\bar{G}(k\bar{r}/k\bar{r}')$ is the free-space transverse dyadic Green's function, and $k = \omega\sqrt{\mu_0\epsilon_0}$ is the wave number in free space. The internal fields $\bar{E}_{int}^{(-1)}$ and $\bar{H}_{int}^{(-1)}$ are the known fields from the internal problem of the previous iteration. The only unknown in Eq. (1) is the incremental surface current density $\hat{n} \times \Delta\bar{H}_+^{(2)}$ to be calculated as the solution to the external problem. This incremental current, when determined, is added to $\hat{n} \times \bar{H}_+^{(1)}$ from the previous iteration to give a new and refined value of the total surface current $\hat{n} \times \bar{H}_+^{(2)}$.

To extend the application of this technique to low-loss or lossless dielectric objects, the initial assumption was obtained by approximating the geometry of the object. A solution for the original geometry was obtained by iteratively obtaining solutions of objects of intermediate shapes between the initial approximate (substitute) shape and the final geometry of interest. For example, for a highly elongated dielectric object, the initial assumption of the surface fields may be obtained from the Mie solution of a spherical object with the same dielectric properties. The iterative procedure is then utilized to build in gradually the geometry of the elongated object. In other words, while in our previous work the initial assumption was obtained by approximating the object's properties (i.e., permittivity) by perfectly conducting one and the original dielectric properties are built in gradually through the iteration, in the low-loss dielectric objects case, the object's geometry (rather than properties) was approximated to obtain the initial assumption, and the original geometry was built in through the iterations.

The iterative solution for the low-loss or lossless dielectric case utilizes the following equation [11]:

$$\begin{aligned} \bar{E}^i(\bar{r}) + \nabla \times \int_s [\hat{n}(\bar{r}) \times \bar{E}_{int}^{(-1)}(\bar{r}')] \cdot \bar{G}(k\bar{r}/k\bar{r}') ds' \\ - \nabla \times \nabla \times \int_s \frac{1}{j\omega\epsilon_0} [\hat{n}(\bar{r}') \times \bar{H}_{int}^{(-1)}(\bar{r}') \cdot \bar{G}(k\bar{r}/k\bar{r}') ds' \\ = \nabla \times \nabla \times \int_s \frac{1}{j\omega\epsilon_0} [\hat{n}(\bar{r}') \times \Delta\bar{H}_+^{(0)}(\bar{r}')] \cdot \bar{G}(k\bar{r}/k\bar{r}') ds' \\ + \nabla \times \int_s \frac{1}{j\omega\epsilon_0\epsilon_r} [\hat{n}(\bar{r}') \times \nabla' \times \Delta\bar{H}_+^{(0)}(\bar{r}')] \cdot \bar{G}(k\bar{r}/k\bar{r}') ds' \end{aligned} \quad (2)$$

where $\Delta\bar{H}_+^{(0)}$ and $\nabla' \times \Delta\bar{H}_+^{(0)}$ are the incremental magnetic and electric fields to be solved for. $\bar{E}_{int}^{(-1)}$ and $\bar{H}_{int}^{(-1)}$ are known from the solution of the approximate geometry, as indicated earlier. It should be noted that while in the high-loss objects case, we iterated only over the surface electric current density [first term in the right-hand side of Eq. (2) [8] in the low-loss case, we maintained both the

electric and magnetic current density terms in Eq. (2) (i.e., complete integral equation of the EBCM approach), since we effectively iterate between various geometries and solve the complete equation for each geometry. In other words, in extending the IEBCM solution procedure to lossless or low-loss dielectric objects, we obtain the initial assumption of the surface fields $\vec{E}_{\text{int}}^{(-1)}$ and $\vec{H}_{\text{int}}^{(-1)}$ by approximating the object by a spherical one and using the Mie solution to obtain this initial assumption of the fields. By solving Eq. (2) on the surface S of the elongated object, we determine $\Delta \vec{H}_+^{(0)}$, $7' \times \Delta \vec{H}_+^{(0)}$, which when added to the initial guess of the fields $\vec{H}_{\text{int}}^{(-1)}$ and $\vec{E}_{\text{int}}^{(-1)}$ provide a complete solution for the elongated object. Clearly, the closer the shape of the spherical substitute to the nonspherical one, the better the initial guess is, and hence accurate final results are obtained readily after utilizing the assumed fields in Eq. (2). For significant differences between the shapes of the spherical substitute and the actual object of interest, we found it necessary to use objects of intermediate shapes between the initial sphere and the final nonspherical object.

It should be emphasized that there are two important similarities between the IEBCM procedures for both the lossless and high-loss dielectric cases. The first is related to the fact that a point matching procedure was used in both cases to enforce the continuity of the surface field calculated from the approximate initial assumption and the internal fields in the nonspherical object of interest. Since Eqs. (1) and (2) are then used to solve only for incremental fields, fewer terms were used in the vector spherical harmonics expansions, and hence ill-conditioning of the resulting system of equations [2, 3] did not occur.

The other point is related to the key advantage of the IEBCM technique [8], which is due to the division of the internal volume of the dielectric object into several overlapping subregions, in each of which a separate field expansion was used. Thus in determining the internal fields, the approximate initial assumption was matched to several expansions of $\vec{H}_{\text{int}}^{(-1)}$ at the surface of the elongated object [8]. The continuity of the internal fields throughout the object was also assured by enforcing the continuity of these expansions at several points (typically 4-6 points) in the overlapping regions, as shown in Fig. 1. This process thus overcomes the basic problem with the regular EBCM, which is related to utilization of a single spherical expansion to describe the field inside the dielectric object. The surface integrations on the left-hand side of Eq. (2) thus utilize more than one (if needed) spherical expansion of $\vec{E}_{\text{int}}^{(-1)}$ and $\vec{H}_{\text{int}}^{(-1)}$; each is used to calculate the surface fields only over a portion of the surface S.

Numerical Results

Figure 2 shows the average specific absorption rate (W/kg) for the spheroidal object of $a/b = 5.54$, and $a = 0.865$ meters. The range of variation of the complex permittivity values over the fre-

quency range of interest is also indicated on Fig. 2. The figure clearly illustrates the advantage of using the IEBCM over the regular EBCM to extend the calculation to and beyond the resonance frequency of the dielectric object. Table I [11] illustrates the advantage of applying the IEBCM to the highly elongated lossless spheroidal object of $ka = 1.35$ and $\epsilon_r^* = 5 + j0$. From the table, it is clear that the accuracy of the EBCM results started to deteriorate when the aspect ratio of the object exceeded $a/b = 4$. The EBCM results for $a/b > 4$ were, therefore, not reported in Table I. Since the dielectric object used for the calculations in Table I is lossless, the accuracy of the obtained results was judged by comparing the extinction and scattering efficiencies. Many other numerical aspects of the IEBCM, such as the number of overlapping regions, the number of intermediate steps, and the number of iterations as well as the CPU time may be found in our other publications available in the literature [8-10]. Table II compares the IEBCM procedure with the regular EBCM technique. Table III sets the IEBCM in perspective.

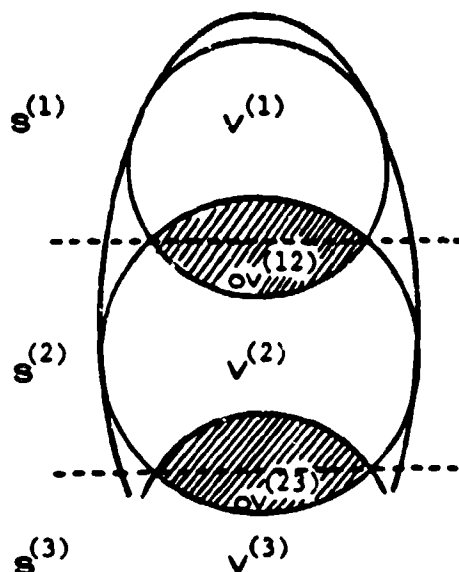
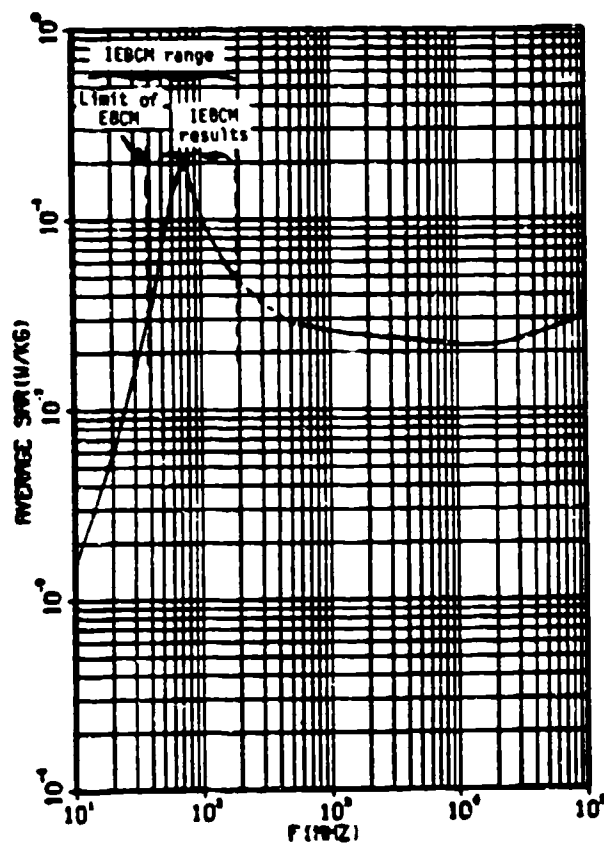


Fig. 1. Schematic illustrating the division of the spheroidal volume V into spherical subvolumes $V^{(i)}$. The i th subvolume is characterized by the surface $S^{(i)}$ and the adjoint overlap regions $OV^{(i,i+1)}$ and $OV^{(i-1,i)}$.



$$a/b = 5.54, \quad a = 0.865 \text{ m}$$

$$\epsilon^* = 65 + j200 \text{ to } 38 + j78$$

(40 MHz) (200 MHz)

Fig. 2. The specific absorption rate (SAR) in (W/kg) in a spheroidal model of $a = 0.865 \text{ m}$ and $a/b = 5.54$. The figure specifically indicated extending the frequency range using the IEBCM.















Table 1. The scattering and extinction efficiencies for a spheroidal dielectric object of $ka = 1.35$ and $\epsilon = 5. + j0$. for spheroidal ratio $x = a/b > 4$, the regular EBCM method did not provide convergent results. The results for $x > 6$ were obtained by using the IEBCM with two spherical expansions in the overlapping subregions.

ka	Spheroidal Ratio $x = a/b$	Extinction Efficiency		Scattering Efficiency	
		EBCM	IEBCM	EBCM	IEBCM
1.35	2:1	0.1449	0.1449	0.1449	0.1449
	3:1	0.210×10^{-1}	0.210×10^{-1}	0.210×10^{-1}	0.210×10^{-1}
	4:1	0.581×10^{-2}	0.579×10^{-2}	0.581×10^{-2}	0.579×10^{-2}
	5:1	N/A	0.2197×10^{-2}	N/A	0.2197×10^{-2}
	6:1	N/A	0.1009×10^{-2}	N/A	0.1009×10^{-2}
	7:1	N/A	0.531×10^{-3}	N/A	0.530×10^{-3}
	8:1	N/A	0.306×10^{-3}	N/A	0.306×10^{-3}
	10:1	N/A	0.1218×10^{-3}	N/A	0.1218×10^{-3}

Table 2. Comparison between the basic features of the regular extended boundary condition method (EBCM) and the new advantages of the new iterative technique (IEBCM).

Comparison between EBCM and IEBCM	
EBCM	IEBCM
<ul style="list-style-type: none"> • Single spherical expansion • Analytical continuity implicitly assumed • One step solution • Application: Limited to small and moderate aspect ratios 	<ul style="list-style-type: none"> • Multiple expansions spherical and mixed • Continuity explicitly enforced • Iterative and requires initial surface fields • Applications: <ul style="list-style-type: none"> + small and moderate aspect + highly elongated objects + objects of large ϵ^* and K_a + composite objects, chains, clusters, etc.

Table 3. The new technique IEBCM in perspective.

	EBCM	IEBCM
• Highly elongated objects		
• Large K_a , and high ϵ^*		
• Composite objects: chains, clusters		
• Small objects		
• Matrix size		
• CPU		
• Simplicity to use		

References

- [1] P. W. Barber, "Scattering and absorption efficiencies for nonspherical dielectrical objects -- biological models," IEEE Transactions on Biomedical Engineering, Vol. BME-25, 1978, pp. 155-159.
- [2] P. W. Barber, "Resonance electromagnetic absorption by nonspherical dielectric objects," IEEE Transactions on Microwave Theory and Techniques, Vol. MTT-25, 1977, pp. 373-381.
- [3] M. F. Iskander, P. W. Barber, C. H. Durney, and H. Massoudi, "Irradiation of prolate spheroidal models of humans in the near field of a short electric dipole," IEEE Transactions on Microwave Theory and Technique, Vol. MTT-28, 1980, pp. 801-807.
- [4] A. Lakhtakia, M. F. Iskander, C. H. Durney, and H. Massoudi, "Irradiation of prolate spheroidal models of humans and animals in the near field of a small loop antenna," Radio Science, Vol. 17 (5S), 1982, pp. 775-845.
- [5] A. Lakhtakia, M. F. Iskander, C. H. Durney, and H. Massoudi, "Near-field absorption in prolate spheroidal models of humans exposed to a small loop antenna of arbitrary orientation," IEEE Transactions on Microwave Theory and Techniques, Vol. MTT-29, 1981, pp. 588-594.
- [6] A. Lakhtakia, M. F. Iskander, C. H. Durney, and H. Massoudi, "Absorption characteristics of prolate spheroidal models exposed to the near fields of electrically small apertures," IEEE Transactions on Biomedical Engineering, Vol. BME-29, 1982, pp. 569-576.
- [7] A. Lakhtakia and M. F. Iskander, "Scattering and absorption characteristics of lossy dielectric objects exposed to the near fields of aperture sources," IEEE Transactions on Antennas and Propagation, Vol. AP-31, 1983, pp. 111-120.
- [8] M. F. Iskander, A. Lakhtakia, and C. H. Durney, "A new procedure for improving the solution stability and extending the frequency range of the EBCM," IEEE Transactions on Antennas and Propagation, Vol. AP-31, 1983, pp. 317-324.
- A. Lakhtakia, M. F. Iskander, and C. H. Durney, "An iterative extended boundary condition method for solving the absorption characteristics of lossy dielectric objects of large aspect ratios," IEEE Transactions on Microwave Theory and Techniques, Vol. MTT-31, 1983, pp. 640-647.
- [10] A. Lakhtakia and M. F. Iskander, "Theoretical and experimental evaluation of power absorption in elongated biological objects at and beyond resonance," IEEE Transactions on Electromagnetics Compatibility, Vol. EMC-25, 1983, pp. 448-453.
- [11] M. F. Iskander and A. Lakhtakia, "Extension of the iterative EBCM to calculate scattering by low-loss or lossless elongated dielectric objects," Applied Optics, Vol. 23, 1984, pp. 948-953.

BLANK

COMPLETE MUELLER MATRIX CALCULATIONS FOR
LIGHT SCATTERING FROM DIELECTRIC CUBES OF
DIMENSIONS OF THE ORDER OF A WAVELENGTH

Chia-Ren Hu, George W. Kattawar and Mark E. Parkin
Department of Physics, Texas A&M University
College Station, Texas 77843

ABSTRACT

A new resolvent kernel technique is used to calculate the complete Mueller matrix for the scattering of an electromagnetic plane wave from a dielectric cube whose dimension is of the order of a wavelength. A brief summary of both the theory and computational method is presented. Certain Mueller matrix elements, as well as cross sections are presented for several cube orientations and compared to the Mie scattering results from an equivalent volume sphere. Preliminary analysis indicates that certain symmetry properties of the scatterer dictate the behavior of the elements for forward and backward scattering as well as the extinction cross section.

THEORY

In this section we briefly describe the theoretical method used in the present calculation. Maxwell's equations for time-harmonic problems may be written as

$$\vec{\nabla} \times \vec{\nabla} \times \vec{E} - k^2 \vec{E} = k^2 (m^2 - 1) \vec{E}, \quad (1)$$

$$\vec{H} = -ik^{-1} \vec{\nabla} \times \vec{E}, \quad (2)$$

where we have assumed $\vec{D} = \epsilon \vec{E}$, $\vec{J} = \sigma \vec{E}$, $\vec{B} = \vec{H}$, $k = \omega/c$, and $m(\vec{r})$ is the local complex index of refraction

$$m^2(\vec{r}) \equiv \epsilon(\vec{r}) + 4\pi i \sigma(\vec{r})/\omega. \quad (3)$$

Using a dyadic Green's function $\vec{G}(\vec{r}, \vec{r}')$ defined by $\vec{\nabla} \times \vec{\nabla} \times \vec{G}(\vec{r}, \vec{r}') - k^2 \vec{G}(\vec{r}, \vec{r}') = \vec{1} \delta^3(\vec{r} - \vec{r}')$, Eq. (1) for scattering problems may be recast as an integral equation:

$$\vec{E}(\vec{r}) = \vec{E}_{inc}(\vec{r}) + k^2 \int \vec{G}(\vec{r}, \vec{r}') \cdot [m^2(\vec{r}') - 1] \vec{E}(\vec{r}') d^3 r', \quad (4)$$

where \vec{E}_{inc} is the incident radiation field. For the present purpose we take $\vec{E}_{inc} = \vec{E}_0 e^{i\vec{k} \cdot \vec{r}}$. The proper dyadic Green's function contains a singular term:

$$\vec{G}(\vec{r}, \vec{r}') = -\frac{\vec{1}}{3k^2} \delta^3(\vec{r}) + \theta(R-\epsilon) \vec{G}_{LS}(\vec{R}). \quad (5)$$

where $\hat{R} = \hat{r} - \hat{r}'$, ϵ is a positive infinitesimal quantity, $\theta(x) = 1$ for $x > 0$ and 0 for $x < 0$, and

$$G_{LS}(\vec{R}) = \left[\frac{1}{k^2} \left(1 - \frac{1}{kR} - \frac{1}{k^2 R^2} \right) - \hat{R} \hat{R} \left(1 - \frac{3}{kR} - \frac{3}{k^2 R^2} \right) \right] \frac{e^{ikR}}{4\pi R} \quad (6)$$

where $\hat{R} = \vec{R}/R$ and $R = |\vec{r} - \vec{r}'|$.

Assuming the scatterer is uniform, then $m(\vec{r}) = m$ inside the volume V of the scatterer and unity outside. We may then rewrite Eq. (4) for \vec{r} inside V as

$$\vec{E}_{eff}(\vec{r}) = \vec{E}_{inc}(\vec{r}) + 4\pi\alpha k^2 \int_V \vec{G}_{LS}(\vec{r} - \vec{r}') \cdot \vec{E}_{eff}(\vec{r}') d^3r' \quad (7)$$

where $\vec{E}_{eff} \equiv [(m^2+2)/3]\vec{E}$, $\alpha \equiv (3/4\pi)(m^2-1)/(m^2+2)$, and the "primed integration" $\int' d^3r'$ over V excludes an infinitesimal sphere (or cube) around $\vec{r}' = \vec{r}$. Once Eq. (7) is solved for \vec{r} inside V , the scattered radiation in the far field region may be obtained via

$$\vec{E}_{SC}(\vec{r}) = -k^2 \frac{e^{ikr}}{r} \hat{r} \times \hat{r} \times \left[\alpha \int_V \vec{E}_{eff}(\vec{r}') e^{-ik\hat{r} \cdot \vec{r}'} d^3r' \right]. \quad (8)$$

When $\vec{E}_{SC}(\vec{r})$ is determined for two mutually perpendicular polarizations of the incident field, one may deduce the amplitude scattering matrix as defined, for example, in Ref. 1, and from which, the complete 4×4 Mueller matrix can be calculated.

The integral equation Eq. (7) can be discretized and converted into a set of simultaneous equations. This set of equations would then have to be solved for each state of polarization of the incident wave, direction of incidence and complex refractive index m . However, instead of solving it this way, it is more convenient to first solve the following equation for a resolvent kernel $\vec{R}(\vec{r}, \vec{r}')$:

$$\vec{R}(\vec{r}, \vec{r}') = 4\pi k^2 \theta(R-\epsilon) \vec{G}_{LS}(\vec{r}, \vec{r}') + 4\pi\alpha k^2 \int_V \vec{G}_{LS}(\vec{r}, \vec{s}) \cdot \vec{R}(\vec{s}, \vec{r}') d^3s, \quad (9)$$

(where the primed, integration implies an infinitesimal exclusion around $(\vec{s} = \vec{r})$ and then obtain the solution of Eq. (7) by one more integration:

$$\vec{E}_{eff}(\vec{r}) = \vec{E}_{inc}(\vec{r}) + \alpha \int_V \vec{R}(\vec{r}, \vec{r}') \cdot \vec{E}_{inc}(\vec{r}') d^3r'. \quad (10)$$

We note that Eq. (9) is independent of the direction of \vec{k} , and the incident polarization. Following the idea of Marouf,² Eq. (9) may be further converted to a matrix Riccati differential equation

$$\frac{d\vec{R}(\vec{r}, \vec{r}')}{d\alpha} = \int_V \vec{R}(\vec{r}, \vec{s}) \cdot \vec{R}(\vec{s}, \vec{r}') d^3s \quad (11)$$

with an initial condition

$$\vec{R}(\vec{r}, \vec{r}')|_{\alpha=0} = 4\pi k^2 \epsilon(R-\epsilon) \vec{G}_{LS}(\vec{r}, \vec{r}') . \quad (12)$$

Therefore, one single integration of Eq. (11) allows us to obtain $\vec{R}(\vec{r}, \vec{r}')$ for a whole physical range of α values, for a given volume of the scatterer (in units of k^{-3}), and k which appears in Eq. (12). In solving Eq. (11), we discretize the volume V and convert the equation to a large number of coupled ordinary differential equations, or equivalently, a matrix differential equation

$$d\vec{R}/d\alpha = \vec{R} \vec{R} . \quad (13)$$

Symbolically Eq. (13) has a solution of the form

$$\vec{R} = (\vec{R}_0^{-1} - \alpha)^{-1} , \quad (14)$$

where \vec{R}_0 is the value of \vec{R} at $\alpha = 0$, and is given by discretizing the right hand side of Eq. (12). Thus any eigenvalue λ of \vec{R}_0 will give rise to a pole in \vec{R} at $\alpha = \lambda^{-1}$. The matrix \vec{R}_0 is, however, not Hermitian and we find all its eigenvalues to lie in the upper half α -plane. Thus all poles of \vec{R} are located in the lower half α -plane, implying that \vec{R} is analytic in the upper half plane. When some eigenvalue, λ_1 , of \vec{R}_0 is close to the real line, the solution of Eq. (13) will run into convergence problems near $\alpha = \lambda_1^{-1}$. We have overcome this difficulty by employing a path integration around the pole in the upper-half α -plane and confirmed that the result is path-independent.

COMPUTATIONAL TECHNIQUES AND RESULTS

In order to solve the Riccati differential equation for the resolvent kernel, we have to discretize the volume integral over the cube. To do this we partition the cube into N subcubes where the field was calculated at the center of each subcube. However to evaluate the dyadic Green's function, six additional points were placed at the center of the faces of each subcube to obtain a good average for the center. Since this is the first time, to our knowledge, that calculations have been performed for the Mueller matrix for cubes, careful testing has to be performed. One of the most significant tests we have performed is the test of analyticity of the resolvent kernel. To do this we

took different paths in the upper half complex plane in going from an initial to a final value. The worst disagreement in the different runs was only one part in 10^4 . We have also established that certain symmetry properties are present in the computational results for both the Mueller matrix elements and the cross sections.

Complete Mueller matrix calculations were performed for a cube whose refractive index was $1.574 - 6 \times 10^{-3}i$ and whose edge-length to wavelength ratio (L/λ) was 0.76967. This particular ratio will yield an equivalent volume sphere whose size parameter $\rho = 2\pi r/\lambda = 3.0$ where r is the radius of the sphere. The cube was subdivided into 125 subcubes which yielded a complex resolvent kernel matrix of order 375. Calculations were performed for three directions of the incident wave vector $\vec{k}(k_x, k_y, k_z)$. The coordinate system is situated at the center of the cube with the axes passing through the centers of three orthogonal faces. The three directions chosen were face-on specified by (1,0,0); edge on (1,1,0) and corner-on (1,1,1). The scattering plane is defined as the plane perpendicular to one component of the incident electric field vector which we label as \vec{E}_\perp , the parallel component as \vec{E}_\parallel . For the calculation presented the orientation of the orthogonal triad \vec{k} , \vec{E}_\perp , \vec{E}_\parallel are such that one of the coordinate axes of the cube is in the plane determined by \vec{k} and \vec{E}_\perp . This configuration will produce right-left symmetry in the scattering plane and, therefore, scattering angles only from 0-180° have to be considered.

In Table I we present results of the various cross sections for the three orientations chosen and also the corresponding ones for an equivalent volume sphere of the same refractive index. What is particularly noteworthy is that for the incident wave polarized perpendicular to the scattering plane, more absorption is generated in the cube than the equivalent volume sphere for all three orientations. In fact, for edge-on incidence (1,1,0) there is -56% more absorption by the cube.

TABLE I

Absorption cross section (σ_a), scattering cross section (σ_s) and extinction cross section (σ_e) in units of λ^2 for three orientations of the cube and corresponding quantities for an equivalent volume sphere. The superscripts \perp and \parallel refer to perpendicular and parallel polarization states respectively.

Incident Direction	CUBE					
	σ_a^\perp	σ_a^\parallel	σ_b^\perp	σ_b^\parallel	σ_T^\perp	σ_T^\parallel
(1,1,0)	0.0544	0.0976	2.006	3.1957	2.0603	3.2933
(1,0,0)	0.0901	0.0901	2.9286	2.9286	3.0187	3.0187
(1,1,1)	0.0632	0.0632	2.3770	2.3770	2.4401	2.4401
SPHERE						
	0.0626	0.0626	2.6382	2.6382	2.7008	2.7008

In Figs. 1a and 1b we show a comparison of P_{11} and P_{12} elements of the reduced Mueller matrix for three directions of incidence and also the equivalent volume sphere. The element P_{11} , oftentimes referred to as the phase function, is shown in Fig. 1a. There are several features to this curve which are interesting. The scattered radiation is rather insensitive to orientation for angles up to about 60° . However beyond this they become quite dissimilar. In particular when the cube is hit edge-on $(1,1,0)$ a secondary maximum appears around 90° . This may be attributable to geometric optics effects where a face can specularly reflect the incoming radiation producing a maxima at 90° . When the cube is hit face-on $(1,0,0)$ a strong maximum appears at 180° since the radiation can be reflected directly backwards from the faces hit by the direct beam.

In Fig. 1b we show the element P_{12} which would give the degree of linear polarization for an unpolarized incident beam. The case for corner-on $(1,1,1)$ incidence more closely resembles the sphere; however, the other two orientations show large disparities. Of particular interest is the fact that the case for edge-on incidence $(1,1,0)$ is nonzero at 0° and 180° . This behavior can be explained by certain symmetry properties. A complete symmetry analysis of all of the elements of the Mueller matrix at 0° and 180° will be presented in a future publication.

In Figs. 2a and 2b we present the elements P_{33} and P_{34} . Again large disparities exist between the various cube orientations and the equivalent volume sphere. It should also be mentioned that we have developed a routine to calculate the Mueller matrix for a cube in random orientation. The results will be presented in a future publication.

In Fig. 3 we show the element P_{22} . What is interesting is that only the case of corner-on $(1,1,1)$ incidence differs from unity. This element will deviate from unity even when the cube is in random orientation. This element is a true indicator of non-sphericity.

ACKNOWLEDGMENT

This research was supported by the U.S. Army Research office under Contract No. DAAG29-83-K-0074.

REFERENCES

1. Bohren, C. F., Huffman, D. R. (1983), "Absorption and Scattering of Light by Small Particles", John Wiley & Sons, New York.
2. Marouf, E. A. (1975), "The Rings of Saturn: Analysis of a Bistatic-Radar Experiment", Technical Report No. 3240-1 Center for Radar Astronomy, Stanford Electronics Laboratories.

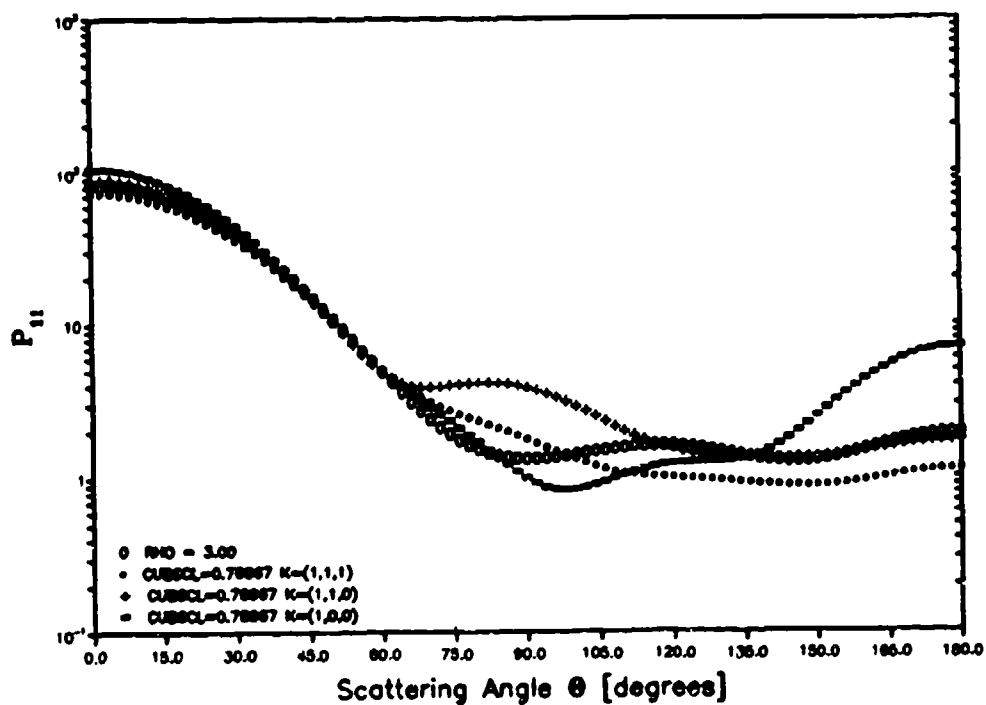


Fig. 1a
Mueller matrix element P_{11} as a function
of scattering angle for three cube orientations
and for an equivalent volume sphere.

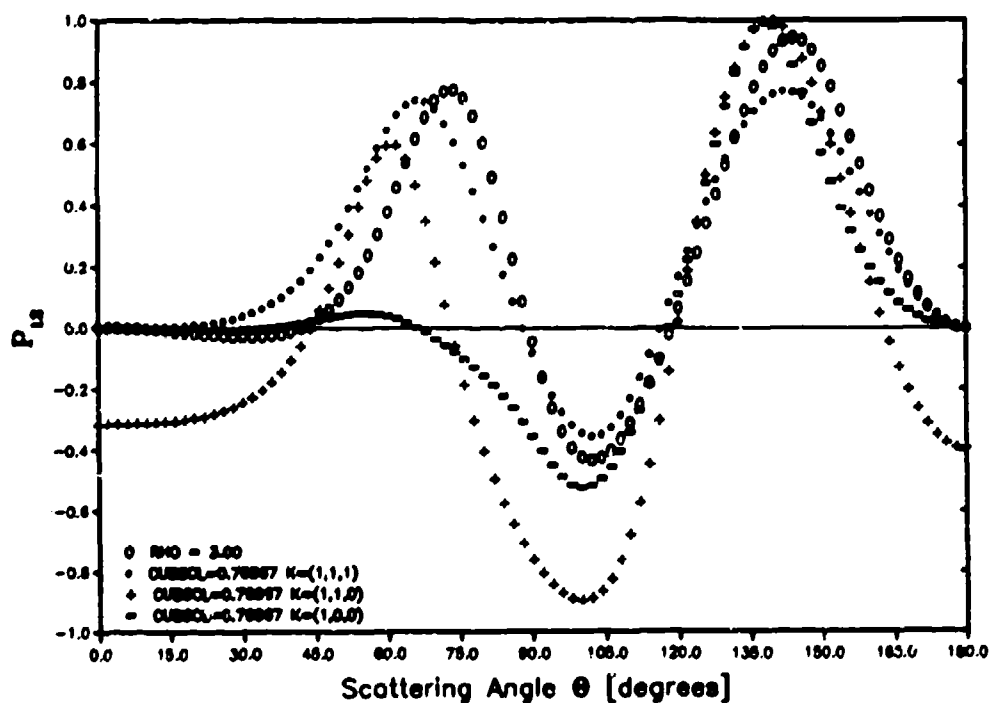


Fig. 1b
Same as Fig. 1a except for reduced
Mueller matrix element P_{12} .

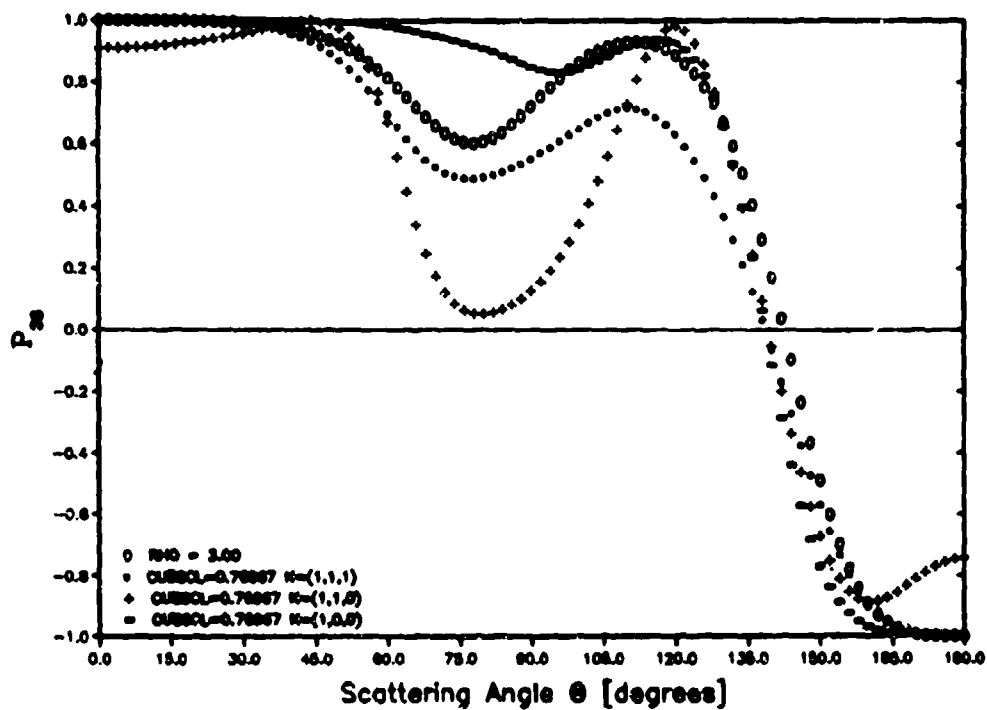


Fig. 2a
Same as Fig. 1a except for reduced
Mueller matrix element P_{33} .

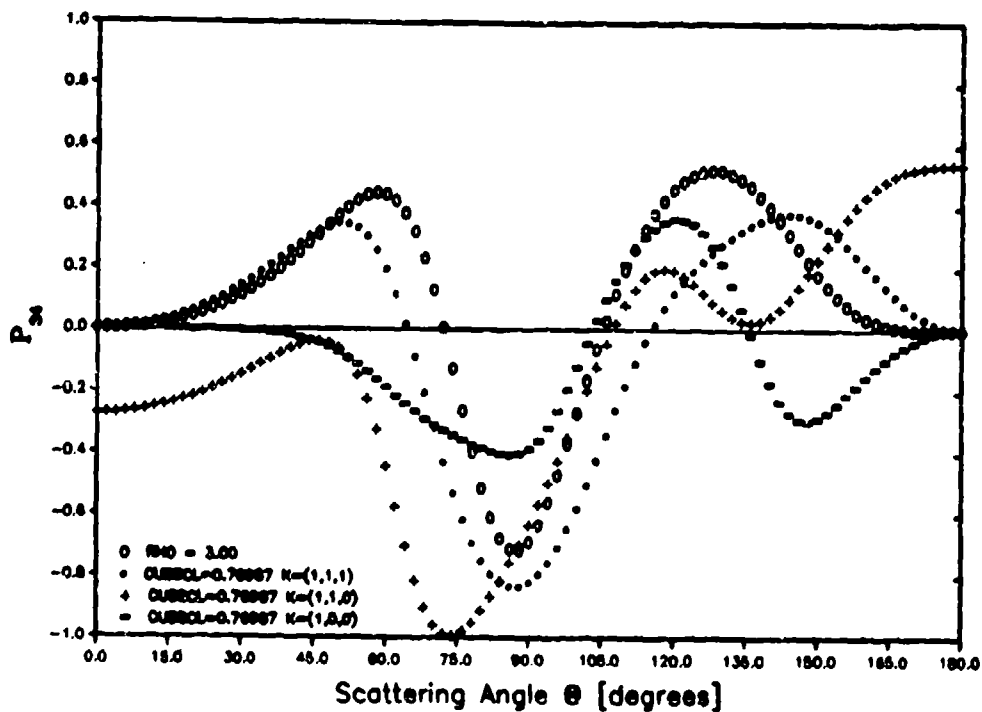


Fig. 2b
Same as Fig. 1a except for reduced
Mueller matrix element P_{34} .

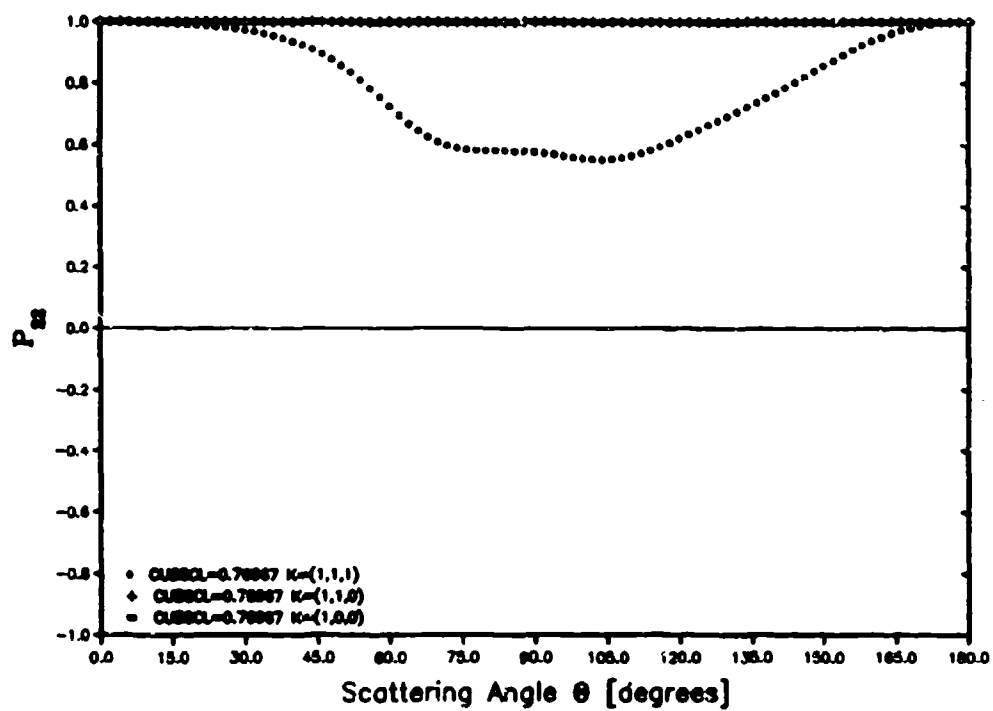


Fig. 3
 Same as Fig. 1a except for reduced
 Mueller matrix element P_{22} .

EXTINCTION BY ROUGH PARTICLES

R.T. WANG

Space Astronomy Laboratory, Univ. of Florida,
Gainesville, FL 32609

ABSTRACT

This paper presents microwave extinction measurement results of 1983-1984 for 10 analog rough particles, their analysis and comparison with Mie theory predictions for equal-volume smooth spheres. Of these 10 particles, 3 have existed in our inventory for 14 years, their extinction measurements by an earlier technique having been reported as part of a larger body of data:

J.M. Greenberg, R.T. Wang and L. Bangs, "Extinction by Rough Particles and the Use of Mie Theory," *Nature, Phys. Sci.*, 230, 110 (1971).

R.T. Wang and J.M. Greenberg, "Scattering by Spheroidal and Rough Particles," NASA NSG 7353 Final Report (Aug. 1978).

R.T. Wang, "Extinction Signatures of Non-spherical/Non-isotropic Particles," in "Proc., 1979 CSL Scientific Conference on Obscuration and Aerosol Research," R. Kohl, ed., ARCSL-CR-81023, Army CSL, Aberdeen, MD. p.111 (1980).

R.T. Wang, "Extinction Signatures of Non/spherical/Non-isotropic Particles," in "Light Scattering by Irregularly Shaped Particles," D.W. Schuerman, ed., Plenum, N.Y. p.255 (1980).

This paper is also an integral part in our long series of systematically investigating the effects of particle shape, size, refractive index and orientation on obscuration of incident light. In addition to the above papers, more detailed accounts of the measurement procedures are referred to in the papers cited at the end of this article, and an extended analysis will also be submitted to *Applied Optics* for publication.

INTRODUCTION

Analytical solutions to the problem of light scattering by particulates whose size and surface roughness are comparable to the wavelength λ of incident radiation are exceedingly complex, and most analytical research treats the case where λ is small compared to a characteristic particle dimension [see Refs. 1, 2, 3, 5, 6]. On the other hand, such particles are abundant in nature and are indeed responsible for the bulk of observed light obscuration/scattering phenomena. This is the principle reason for our undertaking systematic studies using the microwave analog technique [11, 15]. In this paper we report only the most recent extinction measurement results and their analysis and, where applicable, comparison with our earlier results. Although extinction and angular distribution are mutually inseparable light scattering phenomena, quite different measurement procedures and interpretations of raw data are required at present by microwave techniques. We describe the results of angular data in a separate article in these proceedings. Despite our effort to write this paper in a self-contained form, frequent references to our earlier papers were found to be necessary.

We investigated 10 rough particles consisting of 2 refractive index groups $m = 1.61 - i0.004$ and $m = 1.36 - i0.005$, resembling silicate and ice at optical wavelengths, respectively. Only two simple geometric shapes were considered in this investigation; i.e., particles with either a complete rotational symmetry or a mirror symmetry with a 6-fold rotational axis (in the crystallographic sense), so as to reduce the measurement time. In Sec. 3 data for each particle is presented in the uniform format of a P,Q plot, which is a cartesian representation of the particle-orientation dependence of the complex

$\theta=0$ scattering amplitude $S(0)$ and which also shows the comprehensive, detailed light-obscuration process as the particle rotates. In the same section, the volume-equivalent extinction efficiency averaged over random particle orientations, $\overline{Q_{\text{ext},v}} = \overline{C_{\text{ext}}} / \pi a_v^2$, is plotted versus the volume-equivalent phase-shift parameter $\rho_v = 4\pi a_v (m'-1)/\lambda$ and is compared to extinction curves for smooth spheres. a_v is the radius of a smooth sphere equal in volume to the rough particle. Analysis and discussion of the observed extinction data are also included in this section, and a summary is given in Sec. 4.

EXPERIMENTAL AND THEORETICAL CONSIDERATIONS

On Target Preparation

A total of 10 rough particles with 2 shapes and 2 refractive index groups were prepared, with the following considerations: (1) The overall shape would resemble a roughened sphere whose surface roughness would be comparable to the microwave wavelength $\lambda = 3.1835$ cm (2) The shape would have some symmetry, preferably axisymmetric. (3) Particle size would span the first major resonance and the maximum linear dimension would be less than the acceptable portion of the beam wavefront; i.e., ≤ 18 cm. (4) The volume-equivalent ($x_v = 2\pi a_v / \lambda$) and surface-area-equivalent ($x_s = 2\pi a_s / \lambda$) size parameters of a particle must be easily defineable. a_v and a_s are the radii of smooth spheres equal in volume and equal in surface-area to the rough particle, respectively. This gives the nonsphericity parameter $p_n = (x_s/x_v)^2$; a parameter which not only gives the measure of deviation of particle from a smooth spherical shape, but is also useful in converting the volume-equivalent efficiencies to the surface-area-equivalent efficiencies (especially for any convex particles), and vice versa. Examples are: $Q_{\text{ext},v} = p_n Q_{\text{ext},s}$; $Q_{\text{sca},v} = p_n Q_{\text{sca},s}$; and so on.

The actual target parameters are shown in Table I with corresponding coded particle identification numbers. Each particle of the first shape is prepared by machining a 1:1 circular cylinder block so that an annular section having depth and length equal to 1/4 of the cylinder diameter is removed from each end. A particle of the second shape is a stack of 7 equal-diameter cylinders, 6 of which have a common length/diameter ratio of 2:1 and symmetrically surround a longer central cylinder which has the ratio 3:1. The first target shape is perfectly axisymmetric so that we can considerably reduce the number of required measurements to assess the scattering quantities averaged over random particle orientations [8, 12]. Although the second target shape lacks complete axisymmetry, it nevertheless possesses such symmetries as: (1) every 60° rotation about the center axis brings the particle to an equivalent position, (2) there exist 7 planes of mirror symmetry, one of which is perpendicular while the rest are parallel to the cylinder axes. Analysis of the extinction as well as angular scattering data suggest that it also closely approximates the desired complete axisymmetry. Two plastic materials

were employed for the target medium. One is the plexiglass material used in our former investigation [11], with a refractive index $n=1.61-i0.004$ which is characteristic of silicate at visible wavelengths. The other is a molded plastic from expandable polystyrene [8], whose refractive index $n=1.36-i0.005$ resembles that of ice at visible wavelengths. Seven out of these 10 rough particles are newly fabricated, while the remaining 3 are from older target inventories (CIRCA 1970).

P,Q Plots, Symmetry Relations and Averaging Scattering Quantities

Presently, we standardize the presentation of our extinction data in uniform formats. A P,Q plot is a cartesian representation of the complex $\Theta=0$ scattering amplitude $S(\chi, \psi)$ of a particle as a function of its orientation angles (χ, ψ) . χ is the angle between the beam direction \vec{k} and the particle axis. ψ is the azimuth angle of the particle axis around \vec{k} as measured from the \vec{k} direction in the plane containing the incident electric and magnetic fields \vec{E} and \vec{H} , i.e., the E-H plane. Due to the mathematical symmetry, the totality of scattering quantities of an arbitrarily oriented axisymmetric particle can be evaluated in a very simple manner. The particle axis needs only to be swept through 90° from the k -direction in two mutually orthogonal planes, the k -E plane (where $\psi=0$) and the k -H plane (where $\psi=\frac{1}{2}\pi$) of the incident wave. We have shown that the 2×2 $\Theta=0$ complex scattering amplitude matrix elements [7] for such an arbitrarily oriented axisymmetric particle can be represented as [8, 12]:

$$\begin{aligned} S_1(\chi, \psi) &= S_1(\chi, 0) \cos^2 \psi + S_1(\chi, \frac{1}{2}\pi) \sin^2 \psi \\ S_2(\chi, \psi) &= S_1(\chi, 0) \sin^2 \psi + S_1(\chi, \frac{1}{2}\pi) \cos^2 \psi \\ S_3(\chi, \psi) &= S_4(\chi, \psi) = (S_1(\chi, \frac{1}{2}\pi) - S_1(\chi, 0)) \cos \psi \sin \psi \end{aligned} \quad (1)$$

From Eq. (1) the expressions for the perpendicular (i_{11}), parallel (i_{22}) and cross-polarized (i_{12}) scattering intensity components, and their values averaged over random particle orientations (I_{11} , I_{22} and I_{12}) are found to be:

$$\begin{aligned} i_{11} &= |S_1|^2 = |S_1(\chi, 0)|^2 \cos^4 \psi + |S_1(\chi, \frac{1}{2}\pi)|^2 \sin^4 \psi \\ &\quad + 2 [\operatorname{Re}(S_1(\chi, 0)) \operatorname{Re}(S_1(\chi, \frac{1}{2}\pi)) + \operatorname{Im}(S_1(\chi, 0)) \operatorname{Im}(S_1(\chi, \frac{1}{2}\pi))] \cos^2 \psi \sin^2 \psi \\ i_{22} &= |S_2|^2 = |S_1(\chi, \frac{1}{2}\pi)|^2 \cos^4 \psi + |S_1(\chi, 0)|^2 \sin^4 \psi \\ &\quad + 2 [\operatorname{Re}(S_1(\chi, 0)) \operatorname{Re}(S_1(\chi, \frac{1}{2}\pi)) + \operatorname{Im}(S_1(\chi, 0)) \operatorname{Im}(S_1(\chi, \frac{1}{2}\pi))] \cos^2 \psi \sin^2 \psi \\ i_{12} &= |S_3|^2 = |S_4|^2 = |S_1(\chi, \frac{1}{2}\pi) - S_1(\chi, 0)|^2 \cos^2 \psi \sin^2 \psi \end{aligned} \quad (2)$$

and

$$\begin{aligned} I_{11} &= \frac{1}{4\pi} \int_0^{2\pi} d\psi \int_0^\pi i_{11} \sin \chi \, d\chi = \frac{3}{8} \int_0^{\frac{1}{2}\pi} [|S_1(\chi, 0)|^2 + |S_1(\chi, \frac{1}{2}\pi)|^2] \sin \chi \, d\chi \\ &\quad + \frac{1}{4} \int_0^{\frac{1}{2}\pi} [\operatorname{Re}(S_1(\chi, 0)) \operatorname{Re}(S_1(\chi, \frac{1}{2}\pi)) + \operatorname{Im}(S_1(\chi, 0)) \operatorname{Im}(S_1(\chi, \frac{1}{2}\pi))] \sin \chi \, d\chi \end{aligned} \quad (3)$$

$$\begin{aligned} I_{22} &= I_{11} \\ I_{12} &= \frac{1}{4\pi} \int_0^{2\pi} d\psi \int_0^{\pi} i_{12} \sin\chi \, d\chi = \frac{1}{8} \int_0^{2\pi} |S_1(\chi, \frac{1}{2}\pi) - S_1(\chi, 0)|^2 \sin\chi \, d\chi \end{aligned} \quad (3)$$

The extinction cross section $C_{\text{ext}}(\chi, \psi)$ at particle orientation (χ, ψ) is related to the $\Theta=0$ complex scattering amplitude $S_1(\chi, \psi)$ through the well-known Optical Theorem [7]:

$$C_{\text{ext}}(\chi, \psi) = \frac{4\pi}{k} \text{Re} \{S_1(\chi, \psi)\} \quad (4)$$

The P and Q components of all P, Q plots in this paper are defined as

$$P(\chi, \psi) = \frac{4}{x_v} \text{Im} \{S_1(\chi, \psi)\}, \quad Q(\chi, \psi) = \frac{4}{x_v} \text{Re} \{S_1(\chi, \psi)\} \quad (5)$$

i.e., the Q coordinate gives the volume-equivalent extinction efficiency $Q_{\text{ext},v}$ at the particle orientation (χ, ψ) while the similarly calibrated P coordinate gives the phase shift $\phi(\chi, \psi)$ of the $\Theta=0$ scattered wave via the relation

$$\phi(\chi, \psi) = \tan^{-1} [Q(\chi, \psi)/P(\chi, \psi)] \quad (6)$$

The magnitude of the $\Theta=0$ scattering amplitude $S_1(\chi, \psi)$ can also be evaluated as

$$S_1(\chi, \psi) = \frac{x_v^2}{4} [iP + Q], \quad |S_1(\chi, \psi)| = \frac{x_v^2}{4} [P^2 + Q^2]^{1/2} \quad (5')$$

Finally, the averaged volume-equivalent extinction efficiency $\overline{Q_{\text{ext},v}}$ is evaluated from Eqs.(5) & (1) as

$$\overline{Q_{\text{ext},v}} = \frac{1}{4\pi} \int_0^{2\pi} \sin\chi \, d\chi \int_0^{\pi} Q(\chi, \psi) \, d\psi = \frac{1}{2} \int_0^{2\pi} [Q(\chi, 0) + Q(\chi, \frac{1}{2}\pi)] \sin\chi \, d\chi \quad (7)$$

Two numerical examples of such averaged efficiencies are shown in Figs. 1B & 1C.

EXPERIMENTAL RESULTS, ANALYSIS AND DISCUSSIONS

All extinction measurement results are shown in Figs. 1A-1D in uniform P, Q plot formats. Figs. 1A and 1D contain data for 4 particles, while Figs. 1B and 1C contain one for each figure to avoid overlapping of plotted curves. For each particle the Mie theory result for the smooth sphere possessing the same volume and identical refractive index is also tabulated in Table II, along with the numerical results for the averaged scattering intensity I_{11} and the volume-equivalent extinction efficiency $\overline{Q_{\text{ext},v}}$ averaged over random particle orientations (See Eqs.(3) & (7)). The range of variation of the phase shift $\phi(\chi, \psi)$ of the $\Theta=0$ scattered wave as observed during the entire particle rotation is also tabulated in Table II as $\Delta\phi$, measured from its median value ϕ . We have reported earlier that for randomly oriented particles of moderately low refractive indices the volume-equivalent phase-shift parameter $\rho_v = 2x_v(m'-1)$ was one of the most dominant parameters in the extinction process [12,13,14]. This is again clearly seen in Fig. 2 for the 10 rough particles in this investigation. We mention several remarkable features as noted from the analysis of these experimental P, Q plots (Figs. 1A-1D) and the comparison with Mie theory predictions for smooth spheres of equal volume (Fig. 2 and Table II): (1) Compared to the P, Q plots for nonspherical particles of simpler geometrical shapes such as spheroids, cylinders and disks [8, 11, 13]

rough particles are much more complex in their particle-orientation dependence, and very few predictable trends are apparent. Yet a closer examination shows that for a given refractive index the extent of variation and the complexity of curves in P,Q space increase with increasing particle size. Also, the median point in P,Q space, representing the mean of P,Q coordinates over all possible orientations of a given rough particle, traces a clockwise spiral as the size or the parameter ρ_v increases, converging toward a limiting point $P=0, Q=2p_n$ at $\rho_v=\infty$. This is analogous to a trend exhibited by smooth spheres [Ref. 7, p.264] and by oriented infinite cylinders [8]. (2) For most of the individual particles the scattering intensity I_{11} and extinction efficiency $\overline{Q_{ext,v}}$ averaged over random orientations are better approximated by Mie theory for the corresponding equal-volume (same x_v) spheres than for the equal-surface-area (same x_s) spheres (See Table II. Results for the same x_s are, however, not shown.). More remarkably, Mie theory phase-shift using x_v falls within the limits of the observed phase-shift $\phi \pm \Delta\phi$. These facts clearly indicate that *particle volume is one of the dominant controlling parameters in the extinction process, and surface roughness enters as a second order perturbation parameter.* (3) The effect of surface roughness on extinction appears primarily in the particle-orientation dependence. The larger the particle size and hence the more pronounced the surface roughness for the particle shapes in this paper, the larger are the variations in $|S_1(\chi, \psi)|$ and $\phi(\chi, \psi)$ during a particle's rotation - which in turn lead to a larger variation in extinction efficiency. This suggests that in evaluating extinction averages over particle orientations, a larger number of orientations are needed for larger rough particles than for smaller ones. For this reason the estimated $\overline{Q_{ext,v}}$ values for the larger rough particles ($\rho_v \gtrsim 4.5$) in our earlier publications [4, 9, 10] could have been seriously overestimated due to the rather small total number of orientations then available (~ 10 orientations compared to our present 37 orientations). (4) The extinction averaged over all random orientations for such a roughened sphere-like particle is not very different from that for an equal volume smooth sphere with the same refractive index. The extinction curve for such rough particles (Fig. 2) will nevertheless show a slight damping in its resonance profile, resembling that for smooth spheres with a slightly increased absorption part of the complex refractive index. Notice that both of the particle shapes are roughly 1:1 in aspect ratio; i.e., that of a sphere. Combined with our earlier findings [8, 9, 10, 12, 13, 14] it is reasonable to conclude that ρ_v and the aspect ratio are the two major controlling factors in an extinction process for *randomly oriented nonspherical particles.*

SUMMARY

(1) The two most dominant parameters which control the extinction for *randomly oriented* nonspherical particles are the volume-equivalent phase-shift parameter ρ_v and the aspect ratio of the particle shape. For the rough particles of this investigation whose overall aspect ratio does not differ significantly

from that of spheres, the extinction averaged over random orientations is therefore closely approximated by equal volume spheres with identical refractive index. (2) The effect of surface roughness on extinction shows up mainly in the particle-orientation dependence. The larger the particle size and surface roughness, the greater is the variation in extinction as the particle rotates. (3) Such orientation-dependent variation can be considered as a perturbation caused by surface roughness on extinction by a smooth sphere of equal volume, although no simple quantitative formulation is presently available. (4) At least up to the 2nd major extinction peak in particle size, the extinction by randomly oriented roughened spheres is closely approximated by that of equal volume spheres of the same refractive index.

ACKNOWLEDGMENT

The author is indebted to Dr. J. L. Weinberg and other Space Astronomy Laboratory colleagues for critical review of this article. Special thanks are due to Yu-Lin Xu for extensive measurement assistance. This work was jointly supported by the Army Research Office and the Air Force Office of Scientific Research.

REFERENCES

1. Abdelazez, M.K., IEEE Trans. Ant. Prop. AP-31, 375 (1983).
2. Bahar, E. and Barrick, D.E., Radio Science 18, 129 (1983).
3. Bahar, E. and Chakrabarti, S., and "Proc., 1983 CSL Scientific Conference on Obscuration and Aerosol Research", J. Farmer and R. Kohl, eds., RHK & A., Tullahoma, TN. p. 215 (Draft for speaker's use only. Formal Proc. in press).
4. Greenberg, J.M., Wang, R.T. and Bangs, L., Nature, Phys. Sci. 230, 110 (1971).
5. Mukai, S., Mukai, T. and Giese, R.H., in "Light Scattering by Irregularly Shaped Particles", D.W. Schuerman, ed., Plenum, N.Y. p. 219 (1980).
6. Pollack, J.B. and Cuzzi, J.N., J. Atmos. Sci. 37, 868 (1980).
7. van de Hulst, H.C., Light Scattering by Small Particles, Wiley, N.Y. (1957).
8. Wang, R.T. and Greenberg, J.M., NASA NSG 7353 Final Rept., (Aug. 1978).
9. Wang, R.T., in "Proc., 1979 CSL Scientific Conference on Obscuration and Aerosol Research, R. Kohl, ed., ARCSL-81023, Army CSL, Aberdeen, MD. p.111 (1980).
10. Wang, R.T., in 'Light Scattering by Irregularly Shaped Particles', D.W. Schuerman, ed., Plenum, NY. p.255 (1980).
11. Schuerman, D.W., Wang, R.T., Gustafson, B.A.S. and Schaefer, R.W., Appl. Opt., 20, 4039 (1981).
12. Wang, R.T. and Schuerman, D.W., in 'Proc., 1981 CSL Scientific Conference on Obscuration and

Aerosol Research,' R. Kohl, ed., ARCSL-SP-82022, Army CSL, Aberdeen, MD (1982).

13. Wang, R.T., in 'Proc., 1982 CSL Scientific Conference on Obscuration and Aerosol Research,'
R. Kohl, ed., ARCSL-SP-83011, Army CSL, Aberdeen, MD p223 (1983).
14. Wang, R.T., in 'Proc., 1983 CSL Scientific Conference on Obscuration and Aerosol Research,'
J. Farmer and R. Kohl, eds., RHK & A, Tullahoma, TN p.223 (Draft for speaker's use only. Formal
Proc. in press).
15. Zerull, R.H., Giese, R.H. and Weiss, K., SPIE 112, Optical Polarimetry 191 (1977).

TABLE I. MICROWAVE TARGET PARAMETERS

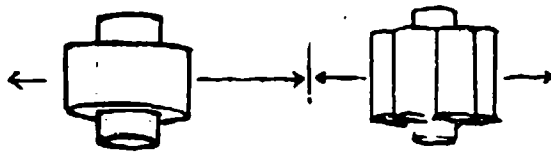
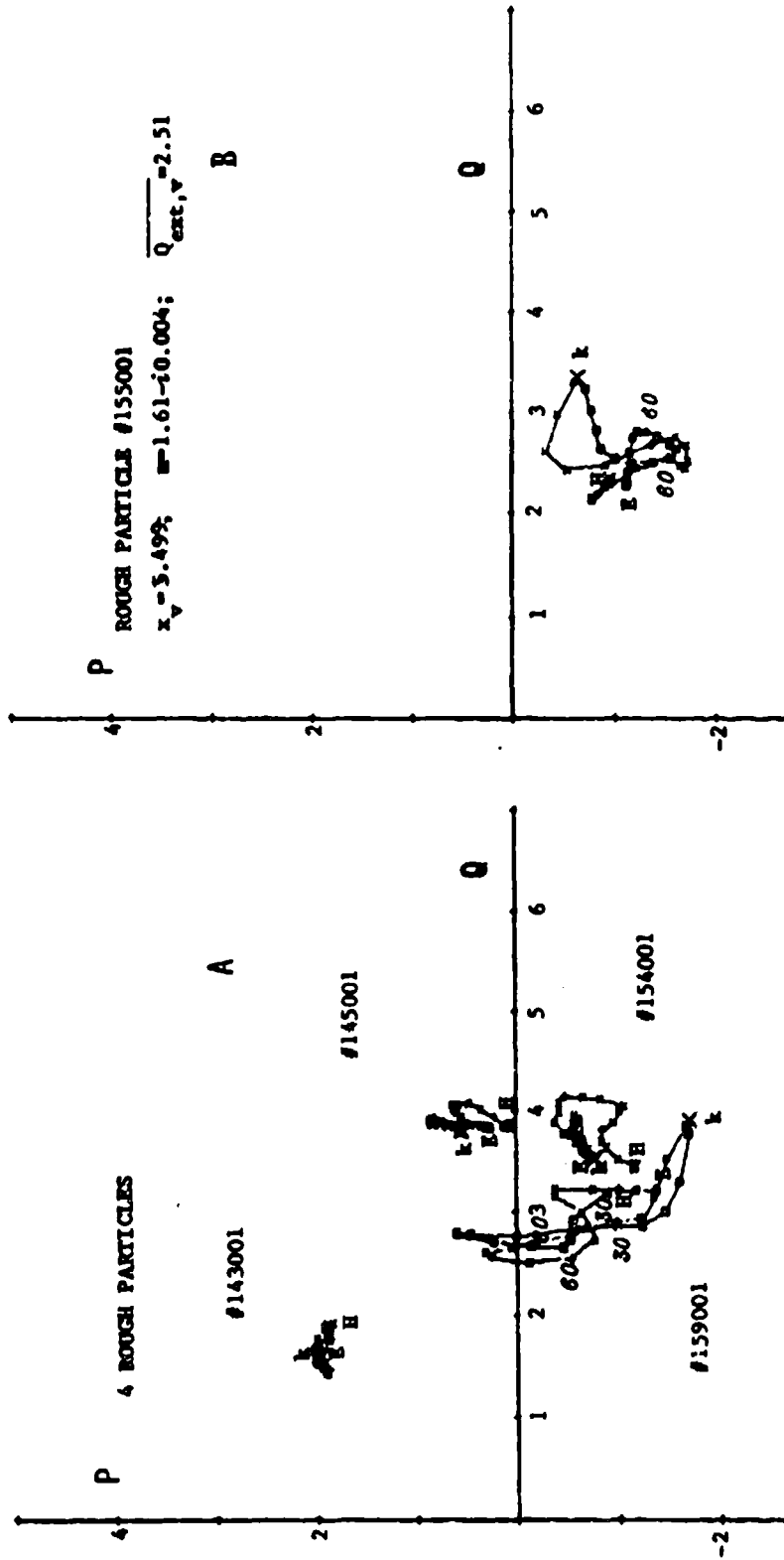
Target ID #	Target Shape	Target Material	Complex Refractive Index	Surface-Equivalent Size Parameter	Volume-Equivalent Size Parameter	Volume-Equivalent Phase-Shift Parameter	Non-Sphericity Parameter
			$n - i\kappa$	x_s	x_v	ρ_v	$(x_s/x_v)^2$
154001		plexiglass	1.61-i0.004	4.171	3.650	4.453	1.3056
155001		plexiglass	1.61-i0.004	6.282	5.499	6.709	1.3094
157001		plexiglass	1.61-i0.004	8.395	7.346	8.962	1.3058
159001		plexiglass	1.61-i0.004	9.849	8.626	10.524	1.3037
143001		expanded polystyrene	1.256-i0.003	3.982	3.592	1.839	1.2289
145001		expanded polystyrene	1.388-i0.005	5.920	5.184	4.023	1.3040
020003		expanded polystyrene	1.366-i0.005	4.921	4.257	3.116	1.3364
020002		expanded polystyrene	1.367-i0.005	7.014	6.069	4.454	1.3356
020001		expanded polystyrene	1.360-i0.005	8.890	7.694	5.540	1.3349
020000		expanded polystyrene	1.353-i0.005	14.893	12.882	9.095	1.3367

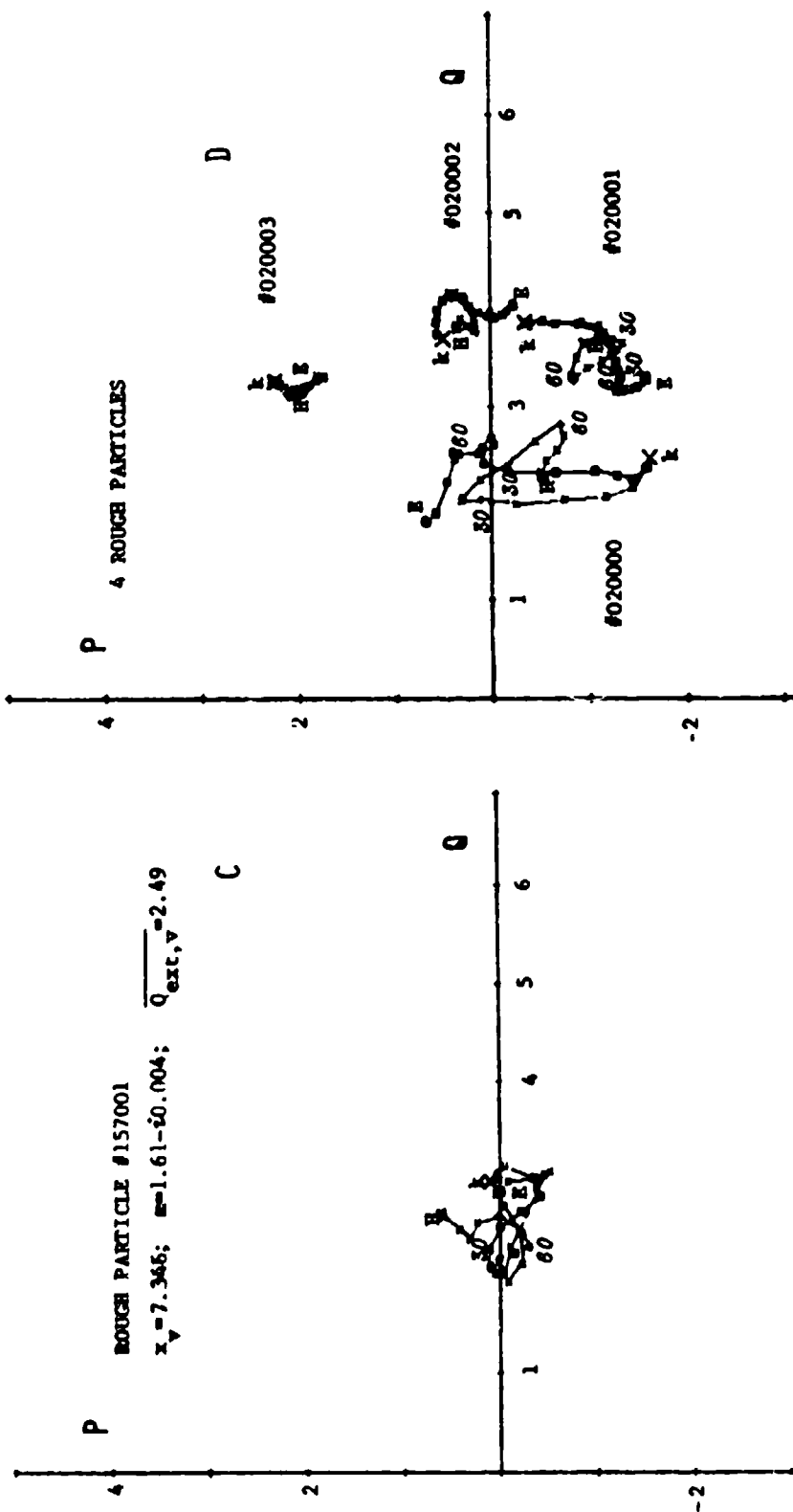
TABLE II COMPARISON BETWEEN $\theta = 0$ MICROWAVE DATA FOR RANDOMLY ORIENTED ROUGH PARTICLES AND MIE THEORY RESULTS FOR EQUAL-VOLUME SPHERES.

Target ID #	Vol.-Equiv. Size Parameter x_v	Vol.-Equiv. Phase-shift Parameter ρ_v	Complex Refractive Index $m = m' - im''$	Data Source	Averaged Scatt. Intensity I_{11}	Phase Shift/Range (Deg.) $\phi \pm \Delta\phi$	Averaged Vol.-Equiv. Extinction Efficiency $\overline{Q_{ext,v}}$
154001	3.650	4.453	1.61- i0.004	EXPT.	153.4	102.4 \pm 6.6	3.68
				MIE	187.09	91.2	4.106
155001	5.499	6.709	1.61- i0.004	EXPT.	456.4	110.8 \pm 13.8	2.51
				MIE	382.99	110.0	2.433
157001	7.346	8.962	1.61- i0.004	EXPT.	1155.6	88.2 \pm 11.2	2.49
				MIE	974.31	83.7	2.300
159001	8.626	10.524	1.61- i0.004	EXPT.	3104.0	97.0 \pm 19.0	2.89
				MIE	3332.4	86.8	3.098
143001	3.592	1.839	1.256- i0.003	EXPT.	70.10	42.0 \pm 4.5	1.78
				MIE	69.305	36.3	1.5461
145001	5.184	4.023	1.388- i0.005	EXPT.	697.9	83.5 \pm 6.0	3.90
				MIE	713.36	80.9	3.925
020003	4.257	3.116	1.366- i0.005	EXPT.	295.5	59.0 \pm 3.5	3.25
				MIE	290.68	63.6	3.370
020002	6.069	4.454	1.367 i0.005	EXPT.	1339.4	87.5 \pm 6.0	3.96
				MIE	1236.1	89.0	3.818
020001	7.694	5.540	1.360- i0.005	EXPT.	2925.5	105.5 \pm 10.5	3.43
				MIE	2146.6	105.7	3.014
020000	12.882	9.095	1.353- i0.005	EXPT.	10129.2	96.4 \pm 27.2	2.34
				MIE	9385.1	79.4	2.295



FIGURES 1A & 1B P, Q PLOTS FOR 5 ROUGH PARTICLES

The particle orientation dependence of extinction for each of the 5 rough particles in Table I is shown. Orientation marks \vec{k} , \vec{E} and \vec{H} respectively denote when the particle axis is parallel to the incident-wave \vec{k} , \vec{E} and \vec{H} vectors, while the italic numbers show the tilt angle of the axis from the \vec{k} vector. Target parameters can be found from Table I via the coded ID number. See also Sec. 2 for more detailed explanations. Square denote $\psi = 0$; crosses denote $\psi = \pi/2$.



FIGURES 1C & 1D P, Q PLOTS FOR 5 ROUGH PARTICLES
 Same as in Figures 1A & 1B except for the particles displayed. In particular, Fig. 1D shows four P, Q plots for the 4 rough particles of type 2 shape. Target parameters can be found from Table 1 via the coded ID number. See also Sec. 2 for more detailed explanations. Square denote $\psi = 0$; crosses denote $\psi = \pi/2$.

EXTINCTION BY RANDOMLY ORIENTED ROUGH PARTICLES

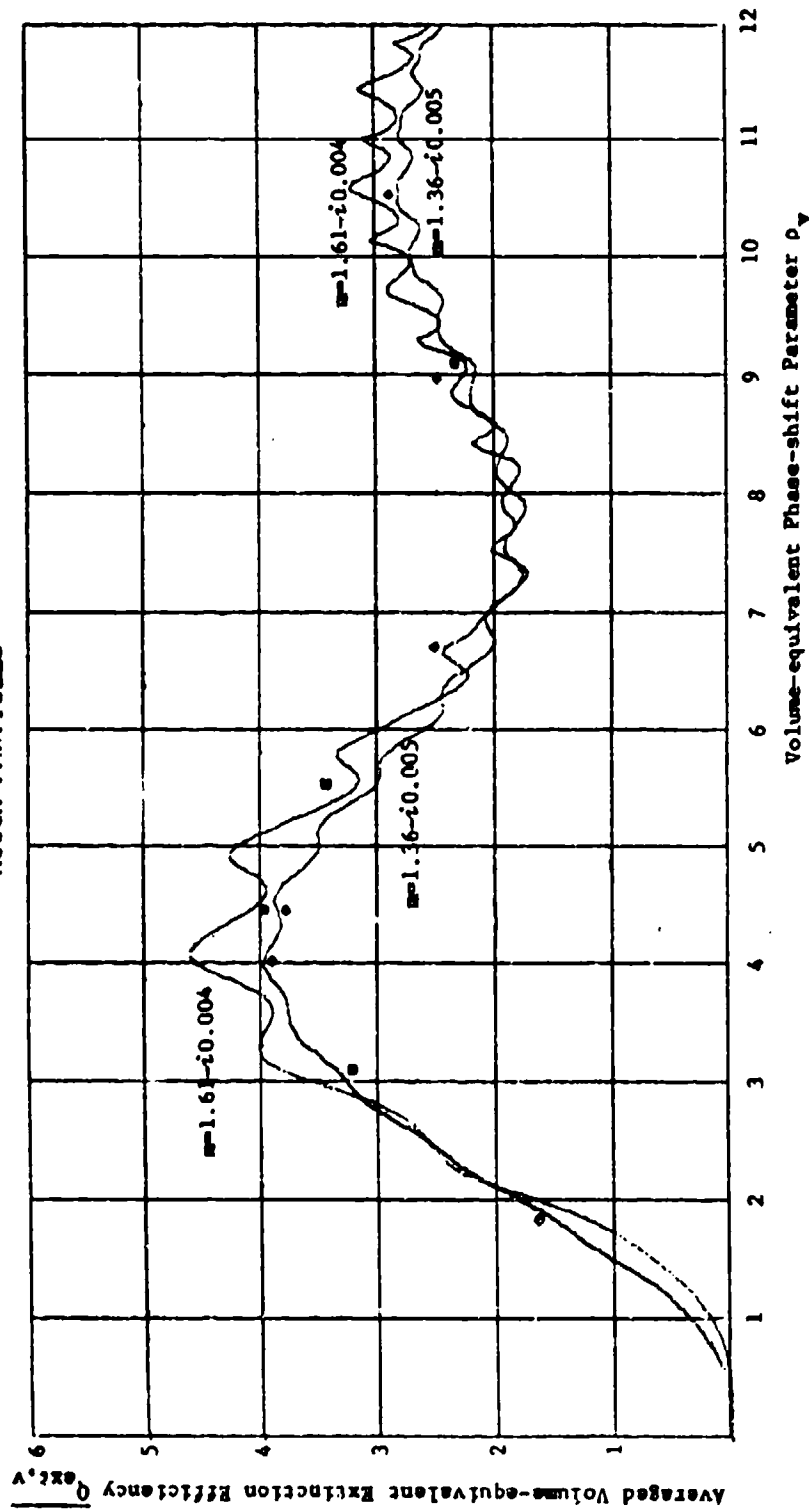


FIGURE 2. $Q_{ext,v}$ Versus ρ_v Plot For 10 Rough Particles

Continuous curves are the Mie theory results for smooth spheres.

Symbols: \diamond Type 1 plexiglass particles; \circ Type 1 dyelite particles;

\bullet Type 2 dyelite particles.

See also Table I for the target parameters.

ANGULAR SCATTERING BY ROUGH PARTICLES

R. T. Wang
Space Astronomy Laboratory, Univ. of Florida,
Gainesville, FL 32609

ABSTRACT

This paper presents the microwave angular scattering measurement results of 1983-1984 for the 10 rough particles whose extinction-measurement results and analysis have been reported in

R. T. Wang, Extinction by Rough Particles, in 'Proc., 1984 CRDC Scientific Conference on Obscuration and Aerosol Research,' R. Kohl, ed., Army CRDC, Aberdeen, MD (this volume).

Data for both randomly and preferentially oriented particles are shown in extensive but uniform form. Comparisons are also made with Mie theory results for smooth spheres possessing the same volume and refractive index as the individual particles, and with Mie-theory results for spheres whose sizes are distributed according to a narrow gamma distribution [See Refs. 1, 2] around individual particle size. We followed closely the procedures and formats employed in our previous investigations for other particle shapes:

D. W. Schuerman, R. T. Wang, B. Å. S. Gustafson and R. W. Schaefer, Systematic Studies of Light Scattering. 1: Particle Shape, Appl. Opt. 20, 4039 (1981).

R. T. Wang and B. Å. S. Gustafson, Angular Scattering and Polarization by Randomly Oriented Dumbbells and Chains of Spheres, in 'Proc., 1983 CSL Scientific Conference on Obscuration and Aerosol Research,' J. Farmer and R. Kohl, eds., RHK & A, Tullahoma, TN. pp 237-247 (Draft for speaker's use only. Formal Proc. in press).

Mie-theory analysis for size-distributed spheres is an extension of the author's previous similar work in extinction:

R. T. Wang, Similarities and Differences between Light-wave and Scalar-wave Extinctions by Spheres, in 'Proc., 1982 CSL Scientific Conference on Obscuration and Aerosol Research,' R. Kohl, ed., ARCSL-SP-83011 pp. 187-200, Army CSL, Aberdeen, MD (1983).

Strikingly similar angular scattering patterns between a randomly oriented cube [Refs. 11, 12] and a similarly sized, randomly oriented rough particle are also presented. This paper is another step in our continuing endeavour to systematically understand and characterize the scattering by irregular particles; the summarized findings or the extended analysis will also be submitted to Applied Optics for publication.

INTRODUCTION

This article reports our first microwave measurements on the detailed angular distribution of light scattered by single *rough* particles of precisely known *size, surface roughness, refractive index* and *orientation* in the beam. This type of measurement is presently possible only through the use of the microwave analog technique [4, 10] because of its exceptional capability for accurately controlling the above important scattering parameters. In addition, the employment of the microwave-unique compensation technique allows us to discriminate the true scattered wave against the unwanted, yet large coherent background, even in the beam direction. As was described in a separate article of this volume [9], we focus our investigation here only on those particles which can be considered as roughened spheres; i.e., whose overall aspect ratio is not significantly different from 1:1, thereby allowing us to compare the results with those for smooth spheres of equal volume.

The following section, Sec. 2, briefly describes the definitions, symbols and notation for the scattering quantities displayed in this article; it also gives short accounts on experimental procedures and on averaging scattering quantities over random particle orientations or over size-distributed spheres. This is followed by Sec. 3 where the scattering data are displayed, comparisons are made with Mie theory for the equal-volume spheres and with size-distributed spheres and/or a cube [11], and where the related analysis and discussions are included. This article then concludes with the summary of findings.

EXPERIMENTAL AND THEORETICAL CONSIDERATIONS

Particle Shape and Measurement Procedures

Preparation of targets in this investigation has been explained in the preceding article [9] and we duplicate here its Table I showing the detailed parameters for each particle. Of these 10 rough particles, 6 are axisymmetric in shape. To assess the scattering from these particles averaged over random orientation, one needs by virtue of mathematical symmetry, at each scattering angle θ , only to measure the scattering at those particle orientations (33 in total) where the particle-axis directions are uniformly distributed in an octant of space bounded by the bisectrix plane. Although the remaining 4 particles lack such complete axisymmetry, they do closely approximate this partly due to the fact that there exist 7 planes of mirror symmetry in their shape, and we employed the same procedures in orienting the particles in the beam for both particle shapes.

The measurement procedures are the same as in our previous investigations [4, 8]. We measure 3 polarization components of the scattered intensity at each scattering angle θ . These components are: t_{11} , where both the beam and the reception antennas are polarized vertically (i.e., perpendicular to the scattering plane); t_{22} , where both are horizontal; and t_{12} , where the beam polarization is vertical and the reception polarization horizontal. At each of these polarization settings, the target is varied through 44 preselected orientations with respect to the beam, of which 35 are used in computing the mean intensity averaged over random orientations while the remaining 9 are the preferential orientations for convenience in theoretical/calibrational purposes. Immediately after attaining each of these 44 orientations, the target-orientation mechanism is halted to record the detected signal onto a computer discette before proceeding to the next orientation. The random orientation averages of t_{11} , t_{22} and t_{12} over the 35 orientations, denoted in this paper by I_{11} , I_{22} and I_{12} respectively, are also computed during the actual run along with their standard deviations. At $\theta=0$, the averaged intensities I_{11} , I_{22} ($=I_{11}$) and I_{12} are derived from the extinction measurements [Eqs. (3), Ref. 9].

The absolute magnitudes of I_{11} , I_{22} and I_{12} (also t_{11} and t_{22}), in which all the results are plotted, are calibrated by standard targets of known scattering intensity. For example, I_{11} , I_{22} , t_{11} and t_{22} are calibrated by a standard sphere of $x=5.001$, $m=1.629-10.0125i$, $t_{11}(50^\circ)_{\text{Mie}}=31.27$ and

$i_{22}(50^\circ)_{\text{Me}} = 24.36$, run shortly before and after a series of runs in $10^\circ \leq \theta (5^\circ) \leq 170^\circ$ for each rough particle with fixed beam/receiver polarizations. Similarly, the cross-polarized component I_{12} is calibrated by a standard spheroid of $x_v = 5.807$, $m = 1.61 - i0.004$, $I_{12}(120^\circ)_{\text{theoretical}} = 3.0897$. For the measurement of I_{12} a coarser angular interval $20^\circ \leq \theta (20^\circ) \leq 170^\circ$ was employed, due to the generally lower-level signals of I_{12} compared to I_{11} and I_{22} (1-3 orders of magnitude lower, even near their peaks at $100^\circ \leq \theta \leq 140^\circ$). Moderately small, rough particles have rather smooth variations of I_{11} and I_{22} over the entire angular range. In such cases a coarser interval of 10° was taken for the measurements, especially when $\theta \geq 70^\circ$. The missing I_{11} , I_{22} and I_{12} data at the omitted angles, such as $\theta = 5^\circ, 75^\circ$, etc., were filled in by a 3rd order Aitken-Lagrange polynomial interpolation technique [5]. In all cases, I_{11} , I_{22} and I_{12} are the simple arithmetic means of i_{11} , i_{22} and i_{12} , respectively, over the 35 particle orientations.

Scattering by Size-Distributed Spheres

In most situations, the scattering particles are distributed in size. The resulting scattering pattern by such a *polydisperse* system of particulates is simply an integrated pattern of all single-particle contributions from individual particulates, as long as they are mutually well separated and hence scatter independently of each other. The evaluation of such a cumulative pattern is further based on a number of simplifying assumptions such as: (1) All scatterers are spherical in shape. (2) The refractive indexes of all particles are the same. (3) The particle size follows a certain law of distribution; e.g., the power law, the log-normal, the bimodal, the gamma distribution, etc [1, 2, 3]. In a previous paper [7] we reported that the use of a gamma distribution [1, 2] of sphere sizes to replace a single-size sphere resulted in the smoothing out of ripples in extinction curves for smooth spheres. The observed smoothing out of phase functions for rough particles has motivated us to extend the same size-distribution analysis for the present work.

In terms of the size parameter $x = 2\pi a/\lambda$ of each constituent sphere the standard size distribution (or simply the gamma distribution) of Hansen and Travis [2] is

$$n(x) = \text{const } x^{(1-3b)/b} \exp \left[-x/(x_v b) \right] \quad (1)$$

where b is the *effective variance* of the distribution, a measure of spread of the particle number density $n(x)$ around the *effective size parameter* $x_v = 2\pi a_v/\lambda$, the volume-equivalent size parameter of the rough particle. a_v is the radius of the sphere equal in volume to the rough particle. For this investigation the observed phase functions of rough particles were found rather well approximated by those for size-distributed spheres with a very narrow spread in size; i.e., with $b = 0.005$. The explicit expressions for I_{11} and I_{22} , averaged over the distribution are

$$\begin{aligned}
I_{11}(x, m, \theta) &= \frac{\int_{x_1}^{x_2} i_{11}(x, m, \theta) n(x) dx}{\int_{x_1}^{x_2} n(x) dx} \\
I_{22}(x, m, \theta) &= \frac{\int_{x_1}^{x_2} i_{22}(x, m, \theta) n(x) dx}{\int_{x_1}^{x_2} n(x) dx}
\end{aligned} \tag{2}$$

To avoid exponential overflows/underflows of integrands in Eqs. (2) during numerical evaluation, a constant multiplication factor was incorporated into both numerators and denominators, i.e.,

$$\begin{aligned}
I_{11} &= \frac{\int_{x_1}^{x_2} i_{11} \exp \left[(1/b-3) \ln x - x/(x_v b) - \{ (1/b-3) \ln x_v - 1/b \} \right] dx}{\int_{x_1}^{x_2} \exp \left[(1/b-3) \ln x - x/(x_v b) - \{ (1/b-3) \ln x_v - 1/b \} \right] dx} \\
I_{22} &= \frac{\int_{x_1}^{x_2} i_{22} \exp \left[(1/b-3) \ln x - x/(x_v b) - \{ (1/b-3) \ln x_v - 1/b \} \right] dx}{\int_{x_1}^{x_2} \exp \left[(1/b-3) \ln x - x/(x_v b) - \{ (1/b-3) \ln x_v - 1/b \} \right] dx}
\end{aligned} \tag{2}'$$

From Eqs. (2)' the total brightness I_N (the S_{11} element of the Mueller scattering matrix) and the degree of linear polarization P ($= -S_{12}/S_{11}$), averaged over the size distribution, are derived as

$$\begin{aligned}
I_N &= (I_{11} + I_{22}) / 2 \\
P &= (I_{11} - I_{22}) / (I_{11} + I_{22})
\end{aligned} \tag{3}$$

Sphere angular functions $i_{11}(x, m, \theta)$ and $i_{22}(x, m, \theta)$ were computed by Mie theory. The numerical integrations in Eqs. (2)' were then performed over 60 equally spaced x intervals by Simpson's rule, taking $x_1 = 0.6x_v$ and $x_2 = 1.5x_v$ for the integration limits. At these limits the number densities $n(x_1)$ and $n(x_2)$ are both 4 orders of magnitude smaller than $n(x_v)$, the number density at the effective size $x = x_v$.

EXPERIMENTAL RESULTS, ANALYSIS AND DISCUSSIONS

Extensive graphical displays of the measured angular distribution data are presented in this section, employing the same formats as in our previous investigation for sphere chains [8]. Except for a set of data for a randomly oriented cube [from Refs. 11, 12], all data are shown in the sequence given in Table I for each of the 10 rough particles investigated. A total of 40 figures, Figs. 1A-10D inclusive, show the angular data for *randomly oriented* rough particles, four figures for each particle. For example, Figs. 1A to 1C respectively show in semilog form the scattering intensities I_{11} , I_{22} , I_{12} and $I_N = (I_{11} + I_{22} + 2I_{12})/2$, versus scattering angle θ . All θ 's are in the common range $0^\circ \leq \theta \leq 170^\circ$,

with the $\theta = 0^\circ$ data being derived from the extinction measurements [9]. Each of these 40 figures contains a continuous theoretical curve representing the Mie theory result for the sphere equal in volume and refractive index to the rough particle. These 40 figures are followed by similarly sequenced additional 40 figures, Figs. 11A-20D, which are identical to the corresponding figures in Figs. 1A-10D except that the theoretical curve in each figure is for the size-distributed spheres explained in the preceding section. These 80 figures are then followed by 20 more figures, Figs. 21A-30B, for *preferentially oriented* particles, again in the same sequence as in Table I. Only two figures are shown for each particle — i_{11} versus θ and i_{22} versus θ — in each of which 3 scattering intensities recorded at each of the 3 special orientations are plotted. These 3 special orientations were selected out of 9 recorded preferential orientations so that the particle axis is either parallel to \vec{k} or \vec{E} or \vec{H} vectors of the incident wave. The figure presentation concludes with angular data for a randomly oriented cube provided by R. Zerull [12]. His results are presented here in Figs. 31A-31D and Figs. 32A-32D in the same format. This particular cube has nearly the same x_v and refractive index as one of our rough particles (#154001) and was found to have remarkably similar scattering signatures to the latter (Cf. Figs. 1A-1D against Figs. 31A-31D; and Figs. 11A-11D against Figs. 32A-32D).

On Angular Distribution of Scattering from Randomly Oriented Particles

Examinations of these phase functions by *randomly oriented* particles and comparisons with those by single equal-volume spheres (Figs. 1A-10D, Figs. 31A-31D) and with those by gamma-size-distributed spheres (Figs. 11A-20D, Figs. 32A-32D) lead to the following interesting features: (1) Angular distribution of scattered light appears to be best discussed separately in 3 angular regions of scattering angle θ : the forward scattering region which contains the first and second scattering lobes; the back-scattering region which is roughly $\theta \geq 140^\circ$; and the middle scattering region where θ lies between the above two regions. The boundary between the forward and middle scattering regions is primarily dependent on the particle size. (2) In the forward scattering region the absolute magnitudes of all phase function components, I_{11} and I_{22} and hence I_N , are surprisingly well predicted by Mie theory for the smooth sphere possessing the same volume and refractive index as the individual particle. The smaller the particle size, the better is this agreement (Figs. 1A-1D; Figs. 5A-5D; Figs. 7A-7D). (3) The first forward scattering lobe is of particular interest for all rough particles. In general it peaks at $\theta = 0$ and troughs rather steeply at an angle which depends on the particle size. Mie theory for the single equivalent-volume sphere predicts a deeper trough and the size-distributed theory a shallower one than the observed data; but for larger rough particles (#159001 & #020000) the widths of the lobes are noticeably narrower than the Mie curves (Figs. 4A-4C; Figs. 10A-10C; also Figs. 14A-14C; Figs. 20A-20C). This suggests that the apparent size of such a large particle may appear larger than the equal-volume-sphere size if one judges the particle size from the forward-scatter lobe alone. (4) Passing on to the middle

scattering angle region, we observe that as long as the particle size is moderately small so that $\rho_v \leq 5.5$, Mie theory results continue to agree well with the observed angular scattering, especially when the size-distributed-spheres theory with small variance $b=0.005$ was employed. Large oscillations in angular distribution characteristic of smooth spheres are, however, markedly damped for these rough particles and the Mie theory for single volume-equivalent spheres fails to account for the smearing out of the profile — especially near the troughs. We note, however, that the choice of other values for the effective variance, $b=0.01$ and $b=0.05$ for example, resulted in over-smearing of the angular distribution profiles. (5) When the particle size becomes larger ($\rho_v \geq 5.5$), marked differences between observation and theory are obvious by inspection of these figures. In addition to the absence of large oscillations in angular profile which is characteristic for smooth spheres, the angular positions and magnitudes of peaks/troughs of scattering lobes are not well correlated to the theoretical predictions. Nevertheless, there exist a number of peaks/troughs, which are indicative of the particle size and whose amplitudes of oscillation are less prominent than spheres but are more pronounced than many of those we have investigated so far [4]. In general, more oscillations in scattering lobes are observable in I_{11} component than in I_{22} component (Figs. 2A-2C; Figs. 3A-3C; Figs. 4A-4C; Figs. 5A-5C; Figs. 10A-10C). (6) Also in the middle scattering angles, all intensity components I_{11} , I_{22} and I_N are in general larger than those corresponding Mie theory results for the larger particles; the I_{11} intensity components being the most significantly different (Figs. 3A-3C; Figs. 4A-4C; Figs. 9A-9C; Figs. 10A-10C; Also Figs. 13A-13C; Figs. 14A-14C; Figs. 19A-19C; Figs. 20A-20C). (7) Significant departures of the observed scattering from the theoretical results occur mainly in backscattering angles, large and small rough particles alike. Except for a few exceptional cases (Figs. 15A-15C), sphere-theoretical results increasingly overestimate the backscatter intensities as one goes toward $\theta=180^\circ$. The onset backscatter angle of the above departure is not clearly definable, however. It appears to be easiest to estimate this onset angle by inspecting the I_N (the 1,1 element of the Mueller scattering matrix) versus θ plot and comparing with the *size-distributed-spheres Mie theory results*. For example, inspection of Fig. 11C for the particle #154001 gives the onset angle $\theta \approx 135^\circ$ with backscatter intensity reduction of about a factor 2 at $\theta=170^\circ$; while a similar examination of Fig. 14C for the particle #159001 gives $\theta \approx 150^\circ$ with the reduction factor ≈ 5 at $\theta=170^\circ$. These two particles are the smallest and the largest of the first shape rough particles (See Table I) which possess the silicate-like refractive index $m=1.61-i0.004$. On the other hand, studies of Figs. 17C and 20C for the smallest and largest of the second shape rough particles (ice-like refractive index $m=1.36-i0.005$) show that the onset angles and the backscatter reduction factors are respectively (120° , 1.5) and (120° , 2). Thus, it suggests that the backscatter profiles are considerably affected by both the shape and the refractive index of a particle. (8) Agreement between the Mie theory prediction and the observed *degree of linear polarisation* is good

only for the 4 smallest rough particles where $\rho_v \leq 4.45$ (#143001, #145001, #020003 and #154001; see Figs. 5D & 15D; Figs. 6D & 16D; Figs. 7D & 17D; Figs. 1D & 11D). For the larger-sized particles the polarization is unpredictable but it appears the polarization is much more reduced in magnitude than the Mie theory results, and is in general within $\pm 50\%$. (9) The *cross-polarised component* of scattering intensity averaged over random-particle orientations, I_{12} , is in general 1-3 orders of magnitude smaller than the corresponding I_{11} and I_{22} at all scattering angles. For example, the absolute magnitude of I_{12} itself was found in many cases so small that it was comparable to that of the uncompensated background signal. Unless I_{12} is greater than -0.2 , it can thus be neglected in comparison to I_{11} and I_{22} in computing the total brightness I_N and the degree of linear polarization. Nevertheless, we kept all I_{12} terms in our actual evaluation. (10) Figs. 31A-31D show the angular distribution data for a randomly oriented cube whose target parameters are very close to those of our rough particle #154001 (See also Table I and Figs. 1A-1D). The same cube data as compared to the Mie theory results for gamma-size-distributed spheres are shown in Figs. 32A-32D, to be compared to the similar set of figures, Figs. 11A-11D, for the above rough particle. The cube data were obtained using an 8 mm microwave analog facility in Ruhr Univ., Bochum, FRG by R. Zerull who also provided the numerical results in his publication [11, 12], from which we could present them in our format. Aside from several differences from ours (such as their data for $\theta < 15^\circ$ were absent and the scattering intensities at $\theta \approx 30^\circ$ were markedly smaller than those of the equal-volume sphere) the rough particle and cube data are remarkably similar in angular signatures. These similarities suggest that for *small randomly oriented irregular particles whose overall aspect ratio is close to that of a sphere*, the angular distribution can be fairly accurately predicted by Mie theory for the equal-volume sphere with the same index of refraction.

On Angular Distribution of Scattering for Preferentially Oriented Particles

Figs. 21A-30B, a total of 20 figures, are the angular data for preferentially oriented rough particles, in which A is for the i_{11} intensity component where both the beam and receiver polarizations are perpendicular to the horizontal scattering plane, and B is for the i_{22} component where both polarizations are parallel to the horizontal scattering plane. Only 3 special particle orientations are selected in this paper to avoid overcrowding. These 3 are distinguished by symbols \oplus , $+$ and \times to denote respectively the rough-particle orientations when the particle axis is parallel to the incident beam direction \vec{k} , parallel to the incident electric field \vec{E} , and parallel to the incident magnetic field \vec{H} (for the latter two the particle axis is perpendicular to \vec{k}). Unlike the previous cases where the scatterings are averaged over the random orientations, far less outstanding features are obvious by examination of these figures for oriented particles. Nevertheless, there are several notable signatures characteristic of the particle shape: (1) Fixing our attention only on one special orientation, say \vec{E} , the angular distribution profile consists of distinct lobes with respect to the variation in scattering

angle θ ; and the larger the particle size the greater the number of lobes along with larger variations in the amplitudes of the lobes. (2) The angular positions of the peaks and troughs of these lobes can be roughly estimated from Mie theory for the equal-volume sphere at forward scattering angles ($\theta < 50^\circ$), but this correlation becomes progressively poorer at higher scattering angles. (3) The difference in absolute magnitude of scattering between any 2 of the 3 special orientations is smaller at small scattering angles but is more pronounced at higher θ 's. Similar features were also observed for spheres with suspected non-homogeneous target material [6]. Up to ~ 2 orders of magnitude difference between 2 different orientations were noticeable from these figures. Although not shown, variations of up to ~ 3 orders of magnitude were frequently observed during many series of orientation changes for these rough particles, especially when the particle size was large and when observed at high scattering angles. This leads us to believe the angular scattering by a rough particle is *very orientation sensitive*, particularly at large scattering angles. Thus, in a scattering chamber using visible wavelengths, a rotating irregular particulate would manifest itself by the "twinkling" of scattered light.

SUMMARY

- (1) Particle volume is one of the most dominant parameters which characterizes the angular scattering by *randomly* oriented, roughened-sphere-like particles.
- (2) For such a small rough particle whose volume-equivalent phase-shift parameter ρ_v is less than about 5.5, a rather good approximation to the observed angular distribution and polarization of scattered light can be made by use of Mie theory for spheres whose sizes follow the gamma distribution around the effective size x_v (the volume-equivalent size parameter of the rough particle) and with an effective variance $b=0.005$ for the distribution, all spheres having the same refractive index as that of the rough particle. The approximation is, however, not applicable to the backscatter region where no theory is presently available to explain the reduced backscatter intensity in comparison to the smooth-sphere models.
- (3) For a larger randomly oriented rough particle ($\rho_v \geq 5.5$) the effects of surface roughness appear primarily in the middle and backscattering angles, in that a rough particle scatters more light in the middle-scattering-angle region, and less in the backscatter region, compared to the equivalent sphere or to the equivalent ensemble of gamma-size-distributed spheres. In the forward scatter region up to the second major scattering lobe, the afore-mentioned size-distributed-spheres Mie theory continues to be a good approximation, but it tends to underestimate the depth of the first trough and slightly overestimate the angular width of the first major lobe.
- (4) Scattering by a rough particle is extremely particle-orientation sensitive in the middle and back-scattering angles. For each of the 3 selected principal orientations in this report, however, the angular scattering profile consists of distinct lobes, the angular positions of the peaks/troughs

in the forward and middle scattering region can be fairly well predicted by Mie theory for the smooth sphere having the same volume and refractive index as the rough particle.

- (5) Analysis of the data is still in progress. When combined with the extinction data also reported in this volume, it may render additional crucial information concerning the scattering, absorption and radiation pressure efficiencies, the single-scattering albedo and the asymmetry factor for each of these rough particles.

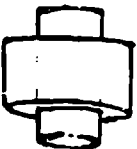
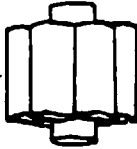
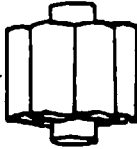
ACKNOWLEDGMENT

The author again thanks Dr. J. L. Weinberg for critical review of this article and other Space Astronomy Laboratory colleagues for helpful discussions and engineering assistance. Without the extensive assistance of Yu-Lin Xu in measurement and data reduction, this work could not have been completed in time. This work was jointly supported by the Army Research Office and the Air Force Office of Scientific Research and their continued interest is highly appreciated.

REFERENCES

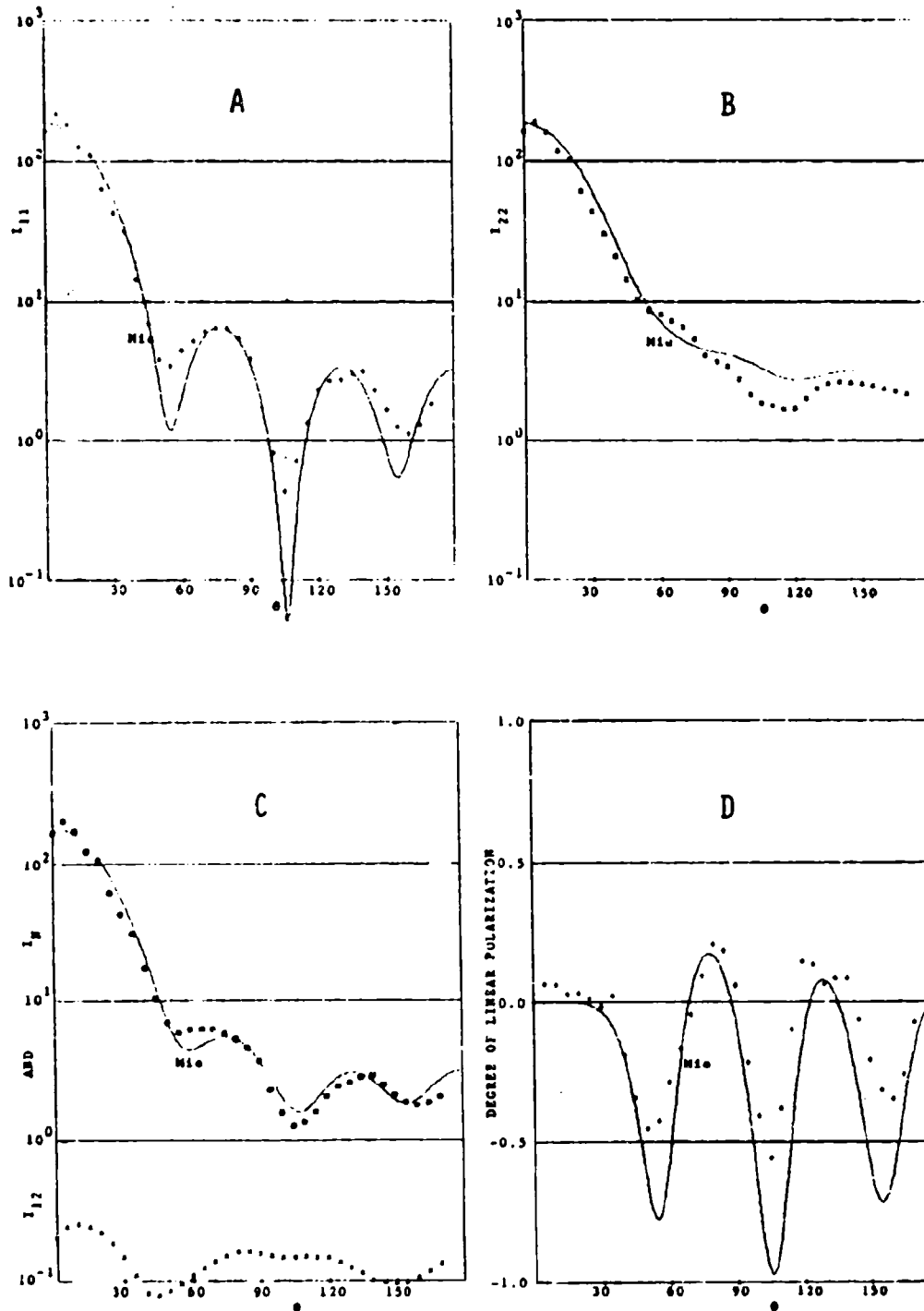
1. Deirmendjian, D., Electromagnetic Scattering on Spherical Polydispersions, Elsevier, N.Y. (1969).
2. Hansen, J. E. and Travis, L. D., Space Sci. Rev., 16, 527 (1974).
3. Kerker, M., The Scattering of Light and Other Electromagnetic Radiation, Academic Press, N.Y. (1969).
4. Schuerman, D. W., Wang, R. T., Gustafson, B. Å. S. and Schaefer, R. W., Appl. Opt. 20, 4039 (1981).
5. Todd, J., in 'Handbook of Physics,' E. U. Condon & H. Odishaw, eds., McGraw-Hill, N.Y. p. 1-94, (1967).
6. Wang, R. T., Ph.D. Thesis, Rensselaer Polytechnic Institute, Troy, N.Y. pp. 109-111 (1968).
7. Wang, R. T., in 'Proc., 1982 CSL Scientific Conference on Obscuration and Aerosol Research,' R. Kohl, ed., ARCSL-SP-83011, pp. 187-200, Army CSL, Aberdeen, MD (1983).
8. Wang, R. T. and Gustafson, B. Å. S., in 'Proc., 1983 CSL Scientific Conference on Obscuration and Aerosol Research,' J. Farmer & R. Kohl, eds., RHK & A, Tullahoma, TN pp. 237-247 (Draft for speaker's use only. Formal Proc. in press).
9. Wang, R. T. in 'Proc., 1984 CRDC Scientific Conference on Obscuration and Aerosol Research,' R. Kohl, ed., Army CRDC, Aberdeen, MD (this volume).
10. Zerull, R. H. and Giese, R. H., in 'Planets, Stars, and Nebulae Studied with Photopolarimetry,' T. Gehrels, ed., Univ. of Arizona Press, p.901 (1974).
11. Zerull, R. H., Beitr. Phys. d. Atmos. 49, 168 (1976).
12. Zerull, R. H., Private Communication (1984).

TABLE I. MICROWAVE TARGET PARAMETERS

Target ID #	Target Shape	Target Material	Complex Refractive Index	Surface-Equivalent Size Parameter	Volume-Equivalent Size Parameter	Volume-Equivalent Phase-Shift Parameter	Non-Sphericity Parameter
			$m-m'-im''$	x_s	x_v	ρ_v	$(x_s/x_v)^2$
154001		plexiglass	1.61-i0.004	4.171	3.650	4.453	1.3056
155001		plexiglass	1.61-i0.004	6.282	5.499	6.709	1.3094
157001		plexiglass	1.61-i0.004	8.395	7.346	8.962	1.3058
159001		plexiglass	1.61-i0.004	9.849	8.626	10.524	1.3037
143001		expanded polystyrene	1.256-i0.003	3.982	3.592	1.839	1.2289
145001		expanded polystyrene	1.388-i0.005	5.920	5.184	4.023	1.3040
020003		expanded polystyrene	1.366-i0.005	4.921	4.257	3.116	1.3364
020002		expanded polystyrene	1.367-i0.005	7.014	6.069	4.454	1.3356
020001		expanded polystyrene	1.360-i0.005	8.890	7.694	5.540	1.3349
020000		expanded polystyrene	1.353-i0.005	14.893	12.882	9.095	1.3367

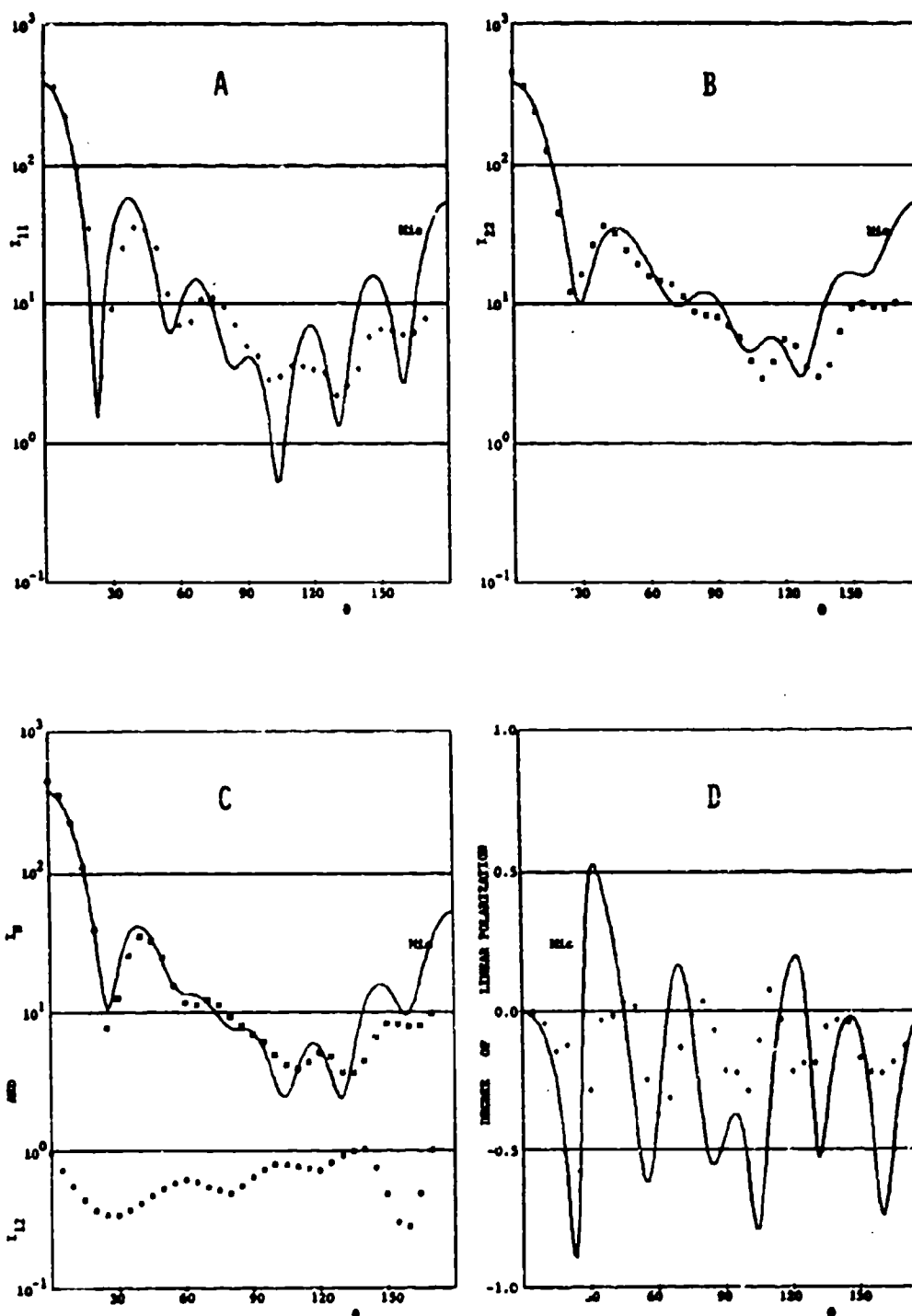
FIGURES

RANDOMLY ORIENTED ROUGH PARTICLE #154001
Volume-Equivalent Size Parameter $x_v = 3.650$
Complex Refractive Index $m = 1.61 - 0.004i$

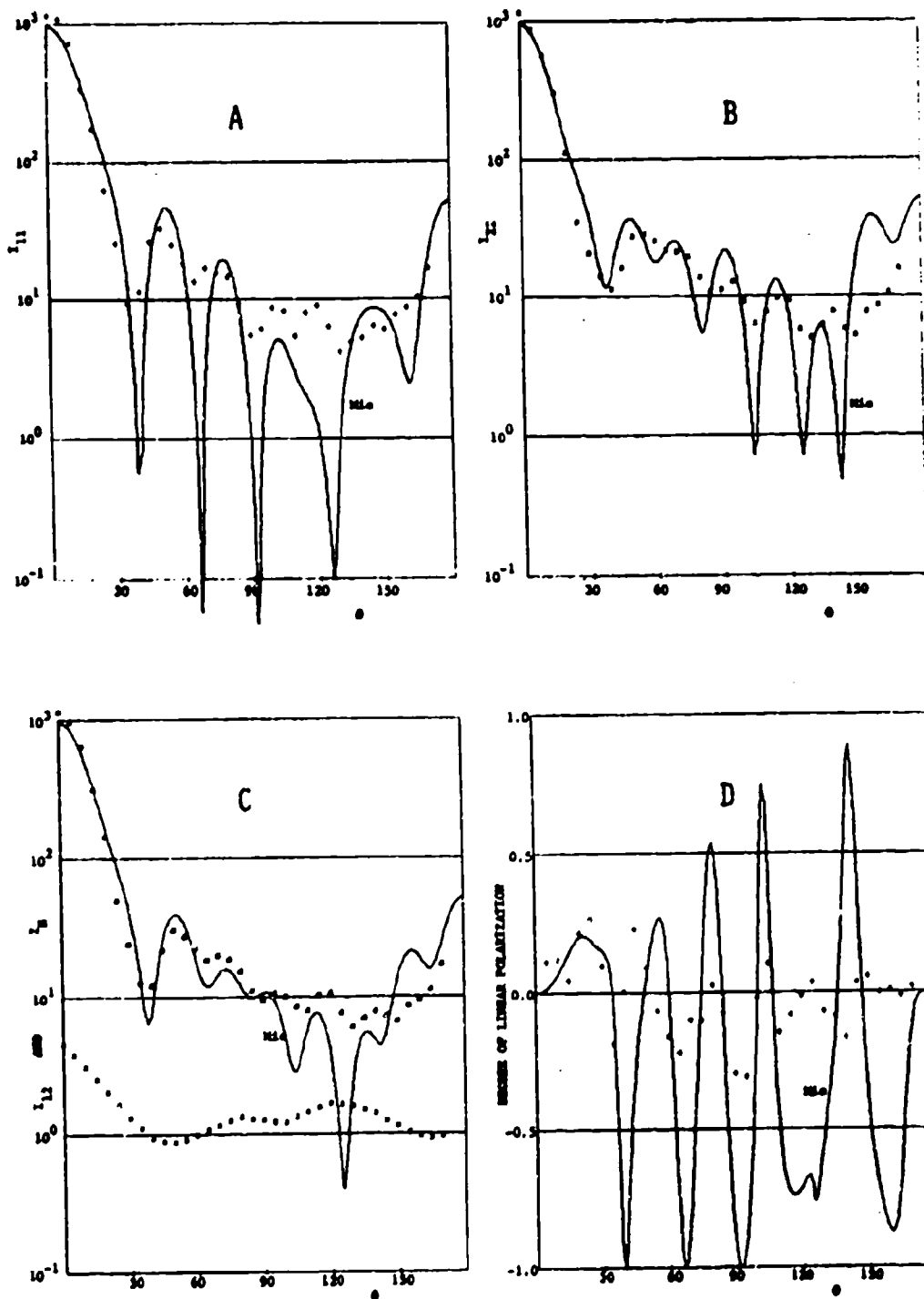


FIGURES 1A-1D ANGULAR DISTRIBUTION DATA FOR A RANDOMLY ORIENTED ROUGH PARTICLE (#154001)

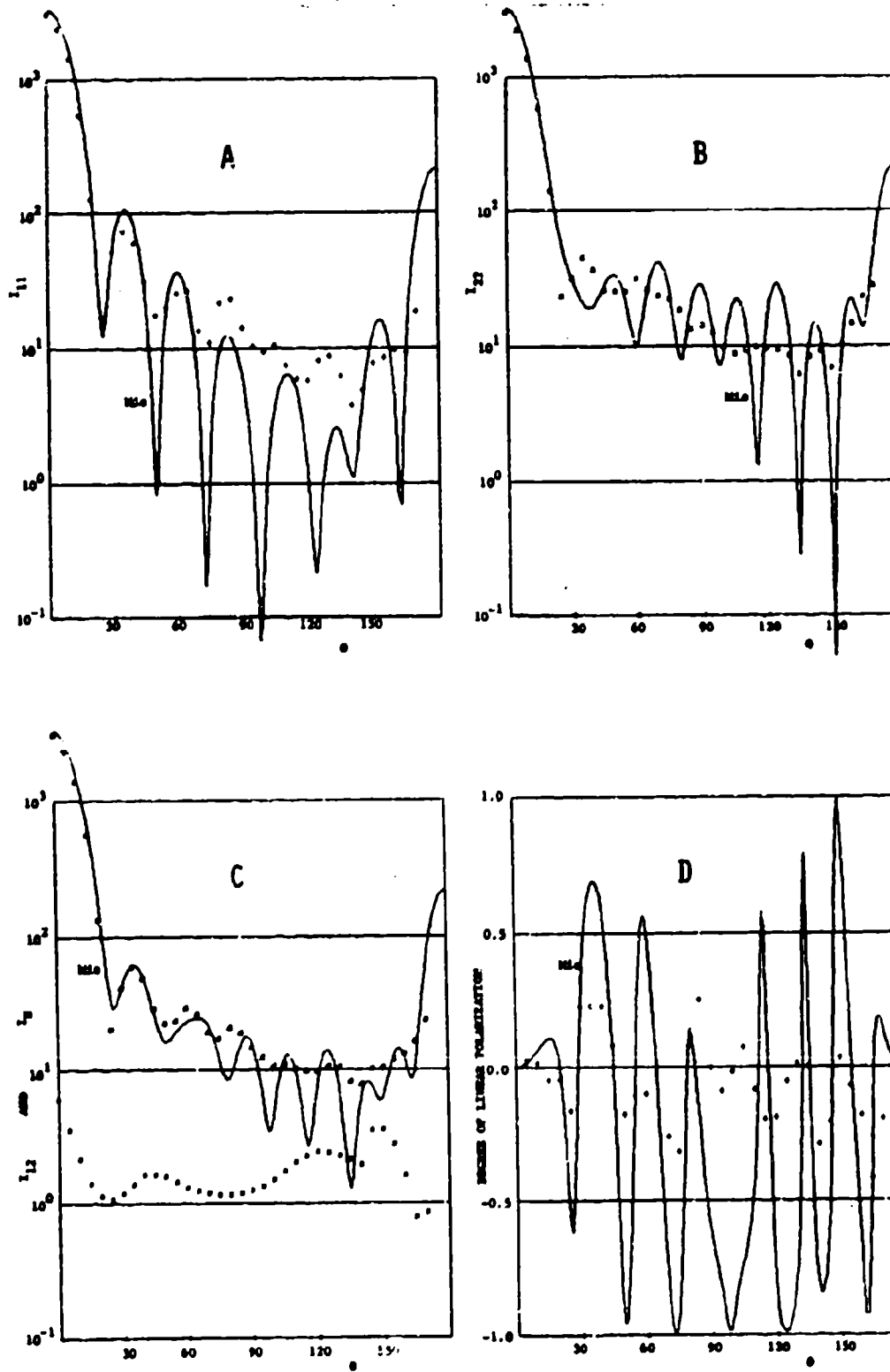
Continuous curves are the Mie theory results for the equal-volume smooth sphere.



FIGURES 2A-2D ANGULAR DISTRIBUTION DATA FOR A RANDOMLY ORIENTED ROUGH PARTICLE (#153001)
 Continuous curves are the Mie theory results for the equal-volume smooth sphere.

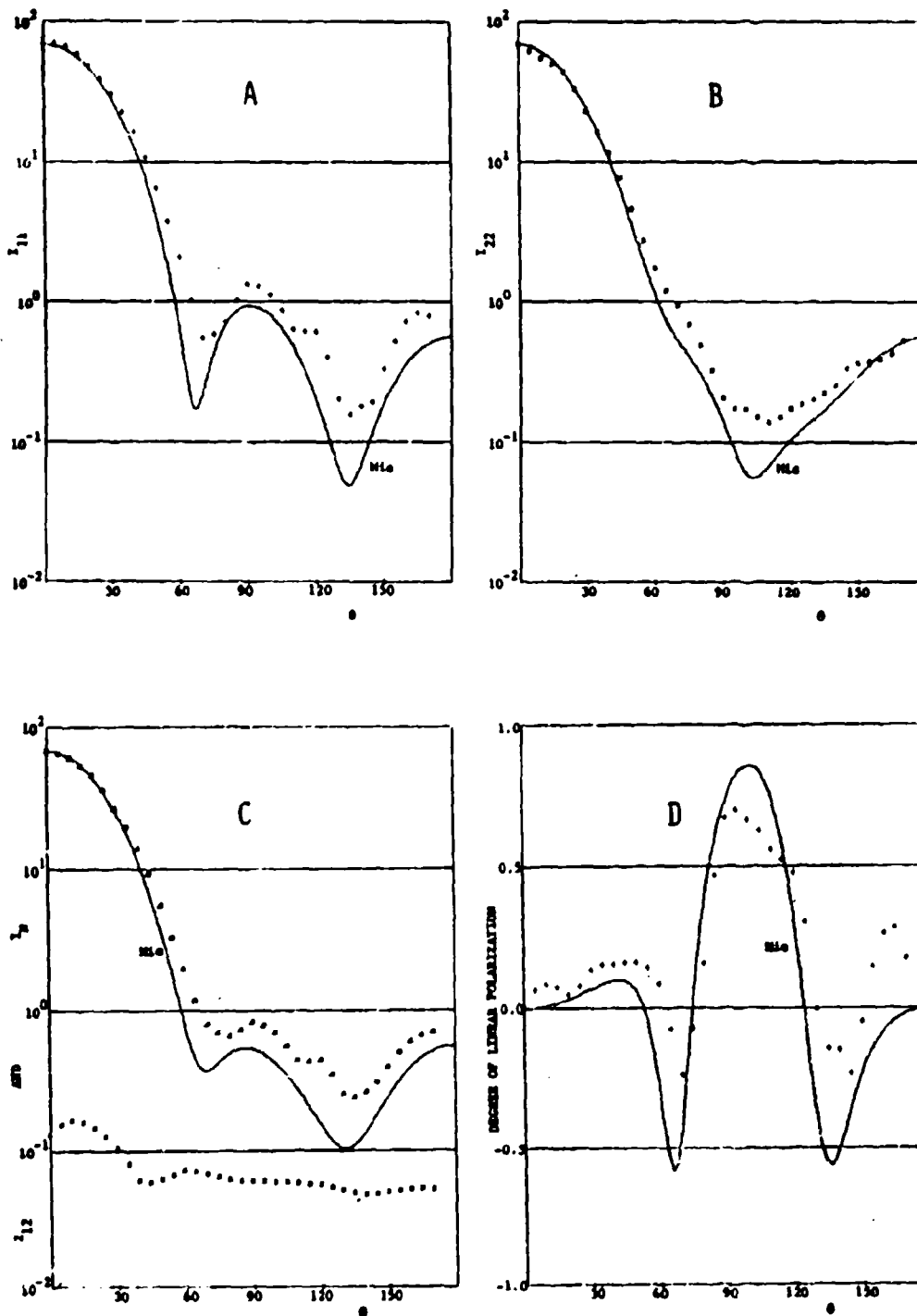


FIGURES 3A-3D ANGULAR DISTRIBUTION DATA FOR A RANDOMLY ORIENTED ROUGH PARTICLE (#157001)
 Continuous curves are the Mie theory results for the equal-volume smooth sphere.



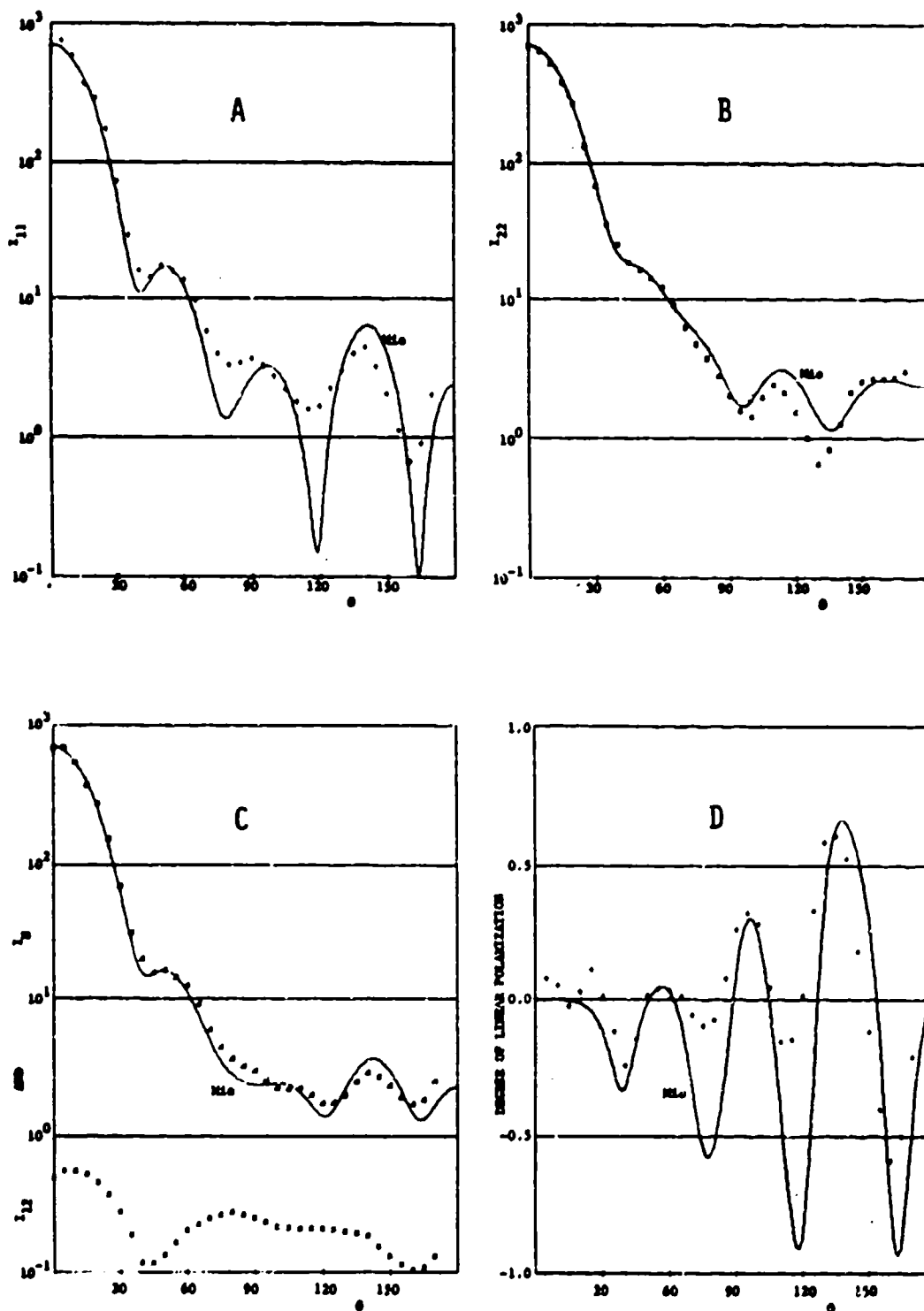
FIGURES 4A-4D ANGULAR DISTRIBUTION DATA FOR A RANDOMLY ORIENTED ROUGH PARTICLE (#159001)

Continuous curves are the Mie theory results for the equal-volume smooth sphere.



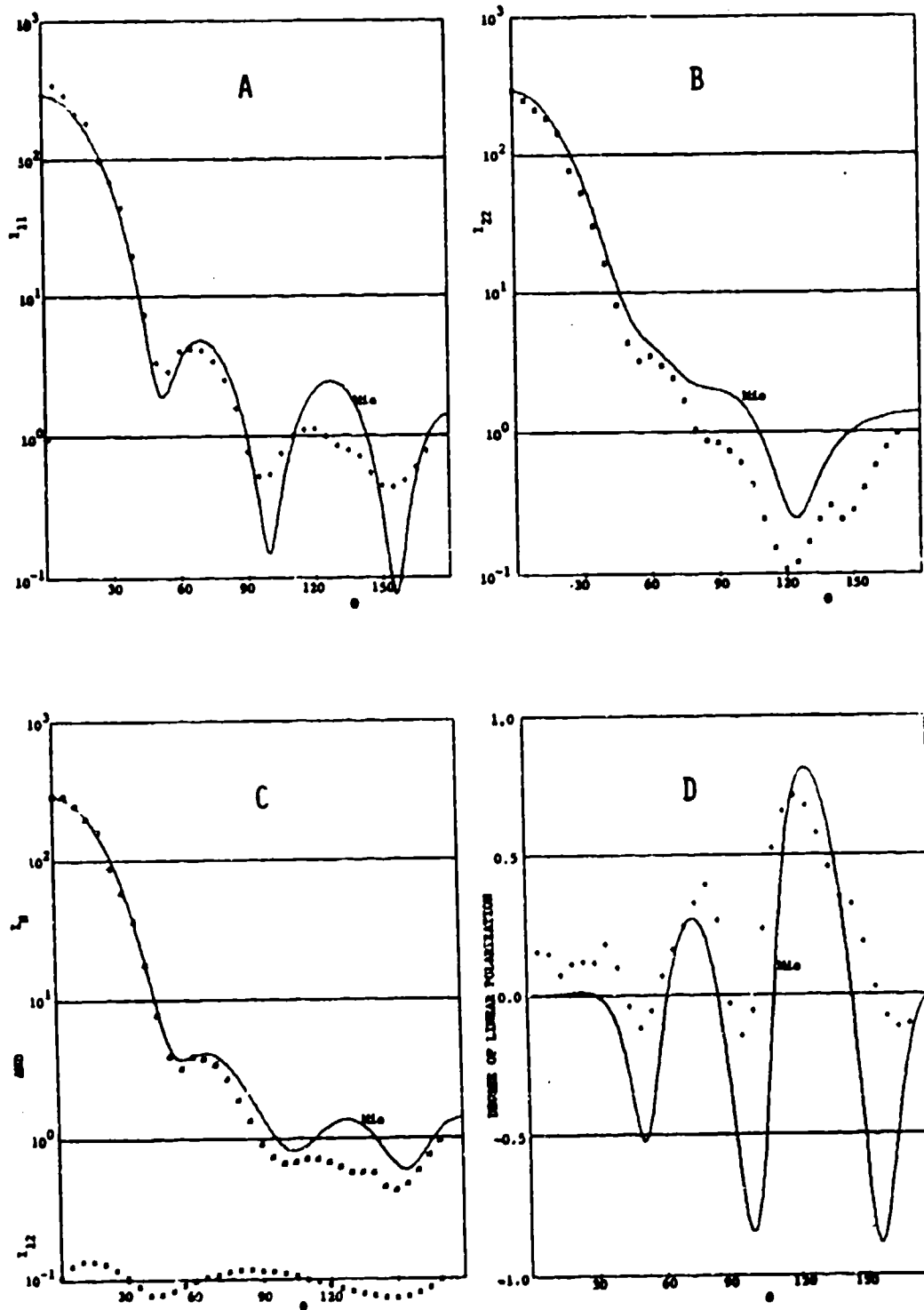
FIGURES 5A-5D ANGULAR DISTRIBUTION DATA FOR A RANDOMLY ORIENTED ROUGH PARTICLE (#143001)

Continuous curves are the Mie theory results for the equal-volume smooth sphere.



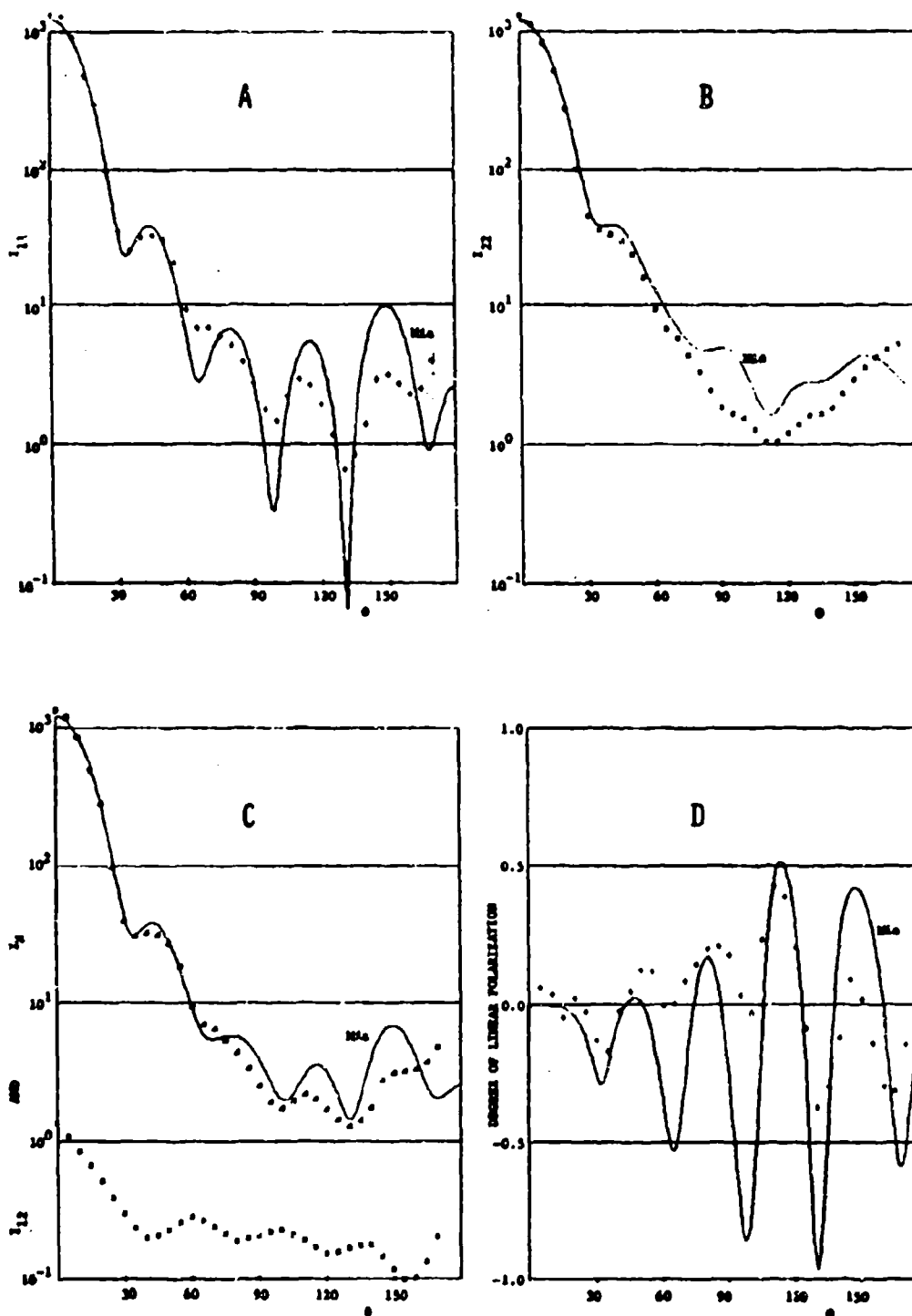
FIGURES 6A-6D ANGULAR DISTRIBUTION DATA FOR A RANDOMLY ORIENTED ROUGH PARTICLE (#145001)

Continuous curves are the Mie theory results for the equal-volume smooth sphere.



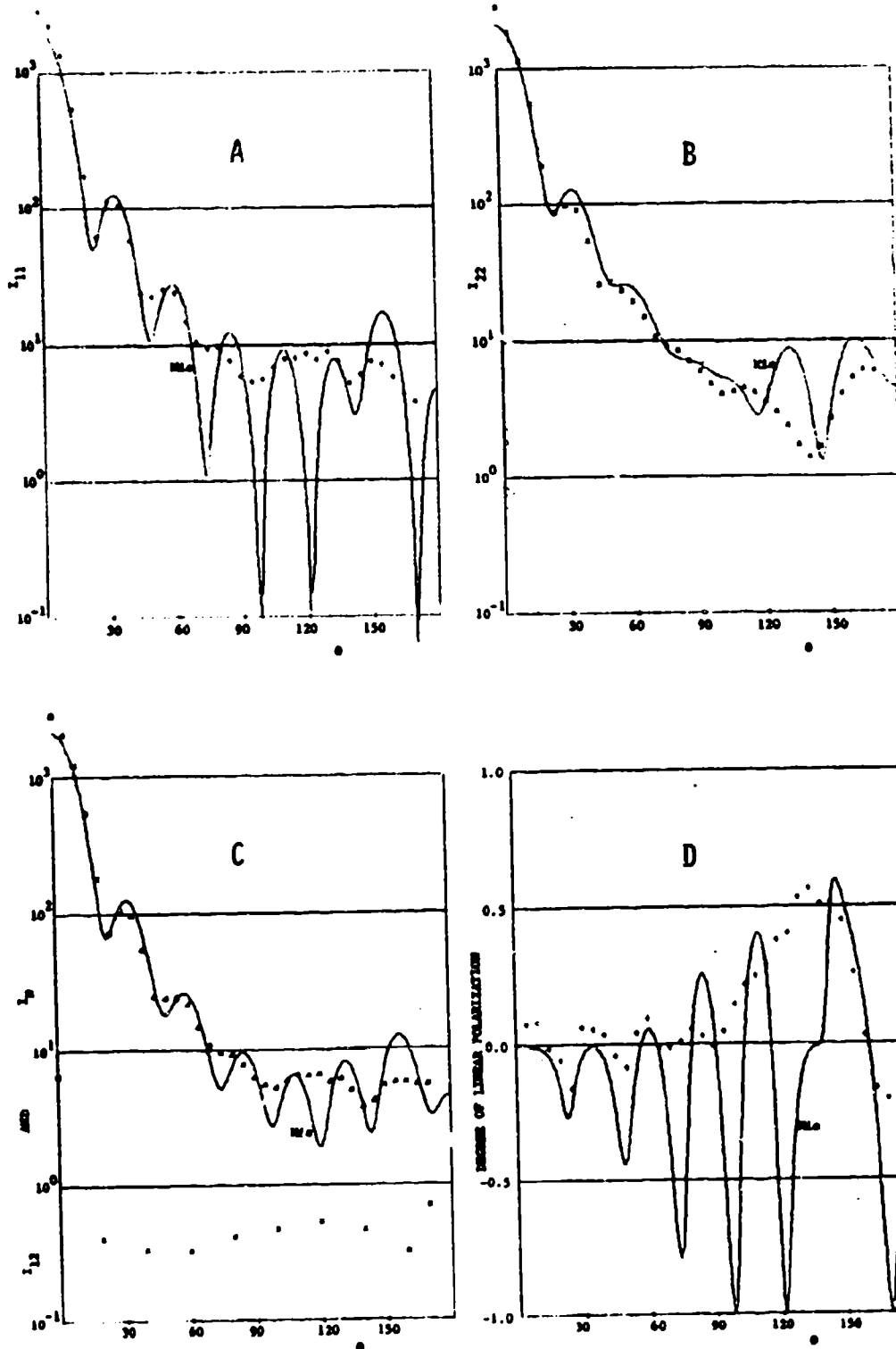
FIGURES 7A-7D ANGULAR DISTRIBUTION DATA FOR A RANDOMLY ORIENTED ROUGH PARTICLE (#020003)

Continuous curves are the Mie theory results for the equal-volume smooth sphere.



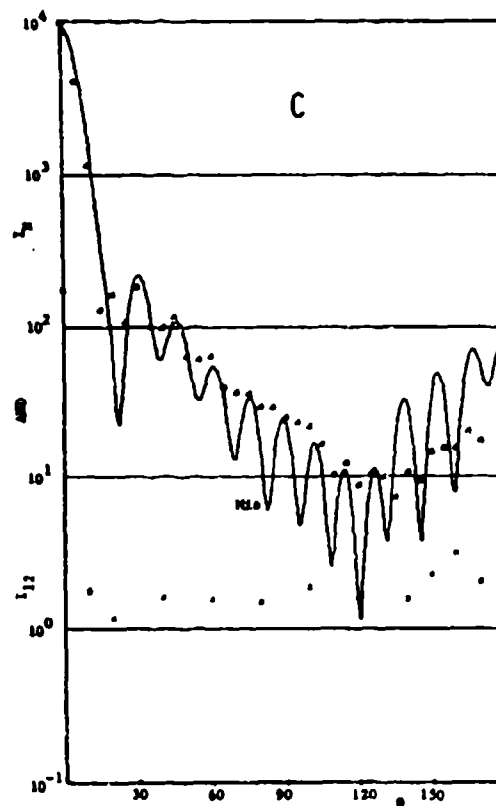
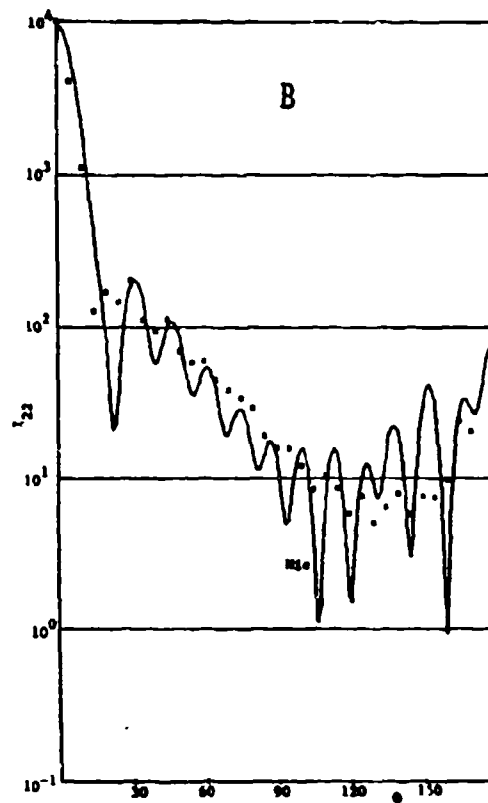
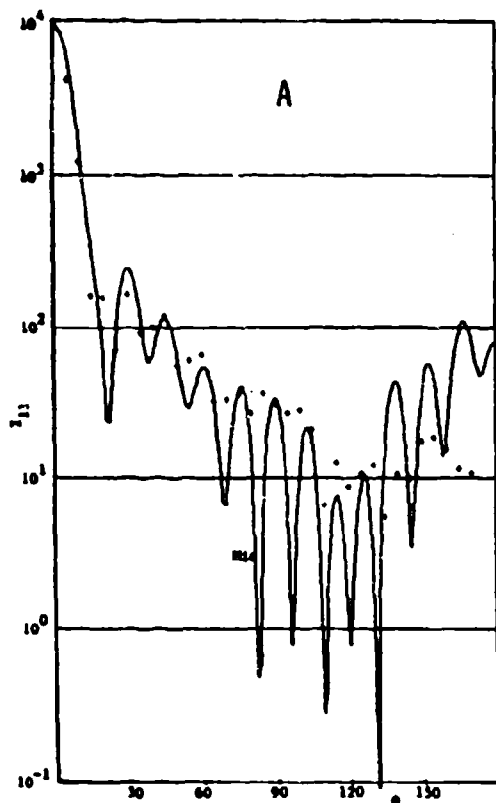
FIGURES 8A-8D ANGULAR DISTRIBUTION DATA FOR A RANDOMLY ORIENTED ROUGH PARTICLE (#020002)

Continuous curves are the Mie theory results for the equal-volume smooth sphere.

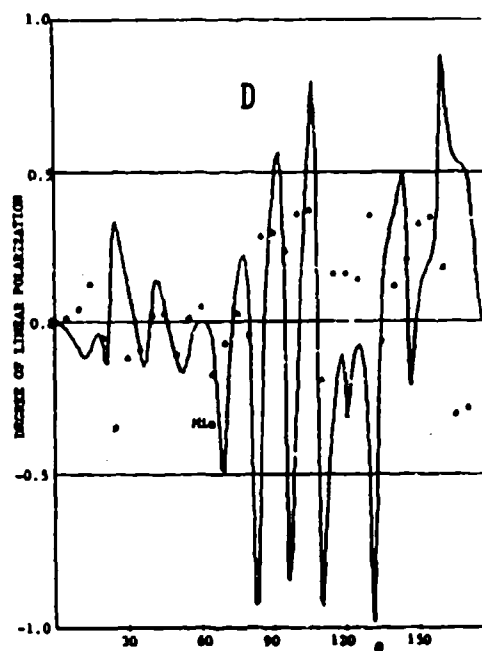


FIGURES 9A-9D ANGULAR DISTRIBUTION DATA FOR A RANDOMLY ORIENTED ROUGH PARTICLE (#020001)

Continuous curves are the Mie theory results for the equal-volume smooth sphere.



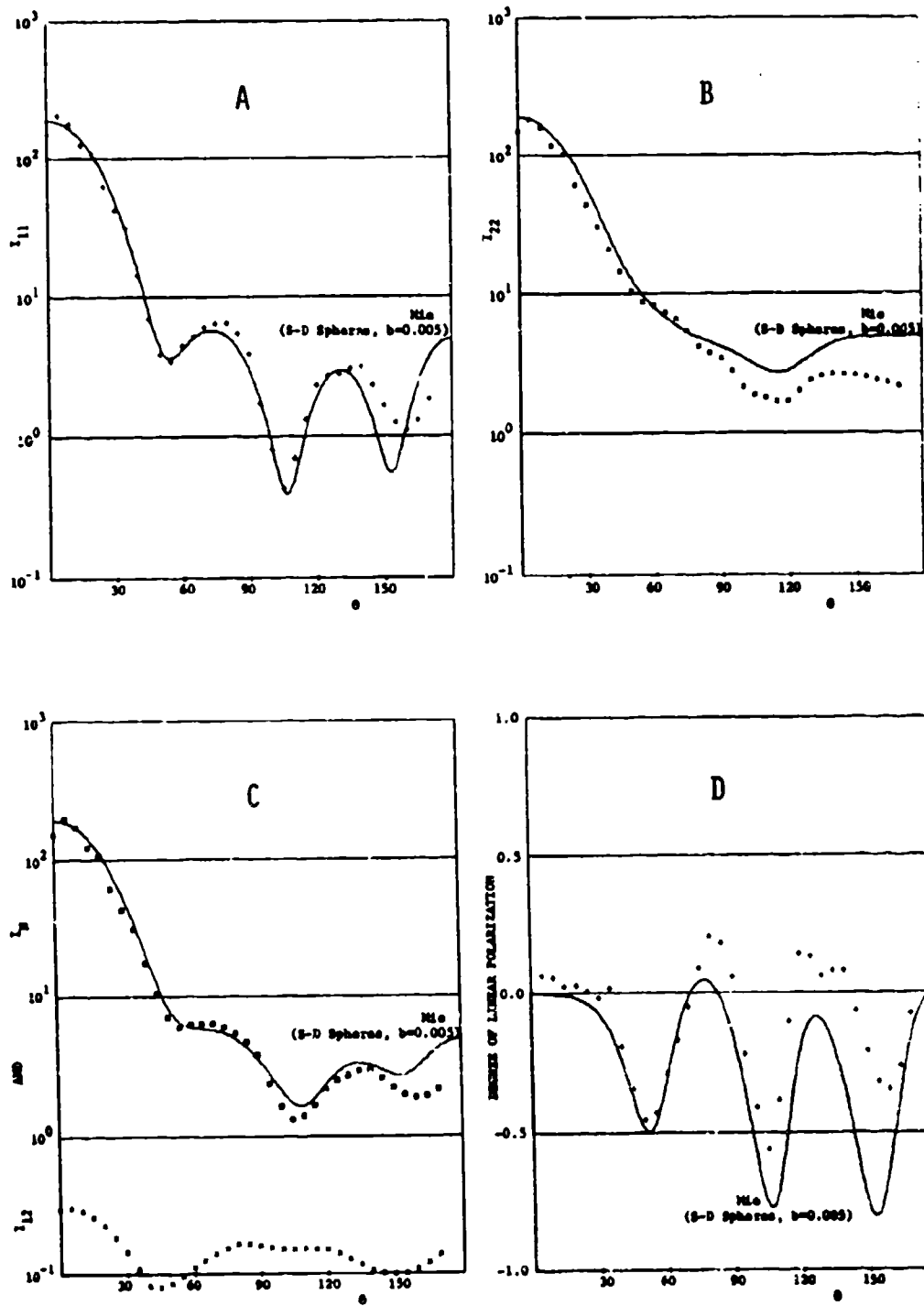
RANDOMLY ORIENTED ROUGH PARTICLE ADDRESS
Volume-Equivalent Size Parameter $x_v = 12.082$
Complex Refractive Index $m = 1.353 - i0.083$



FIGURES 10A-10D ANGULAR DISTRIBUTION DATA FOR A RANDOMLY ORIENTED ROUGH PARTICLE (#020000)

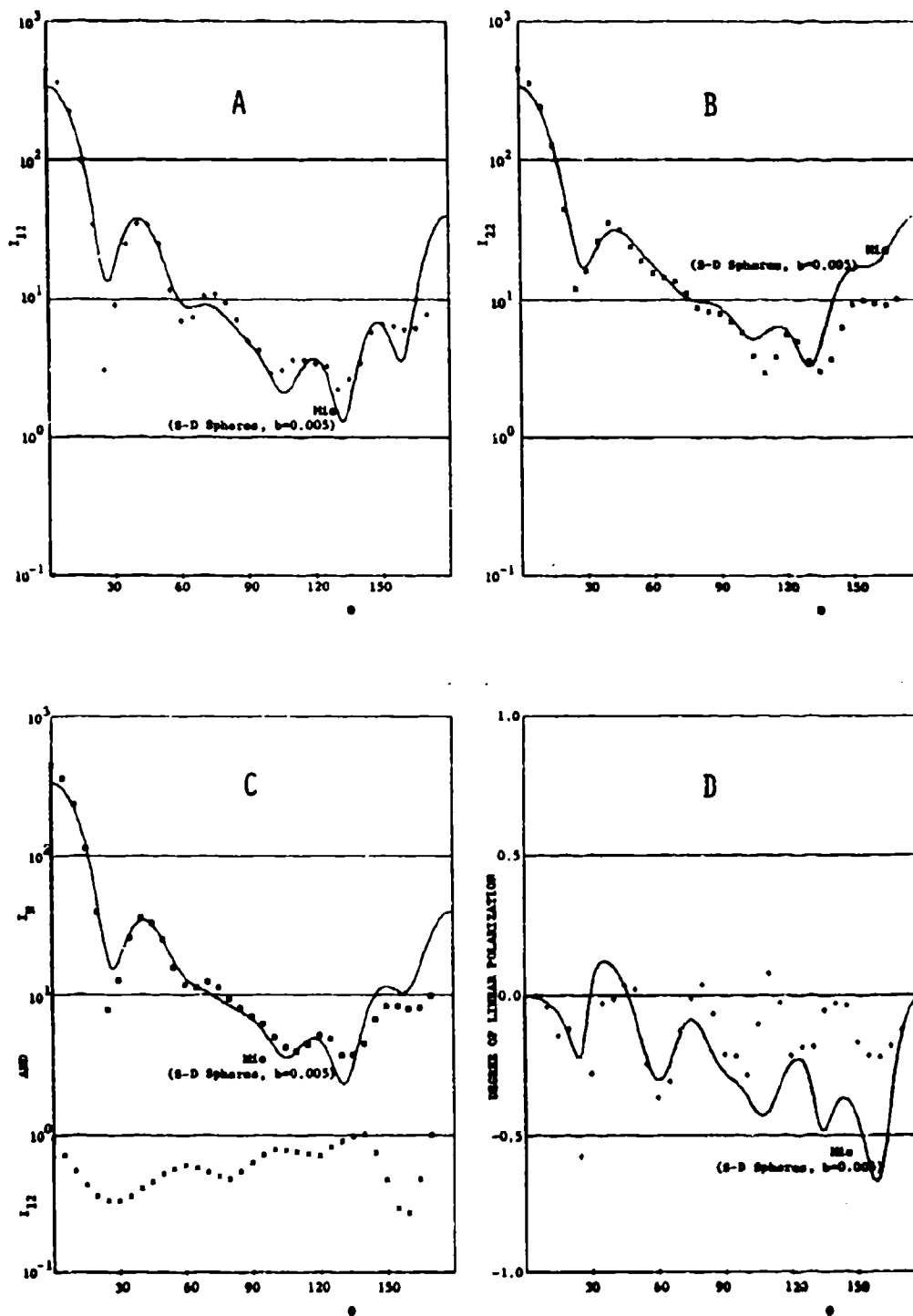
Continuous curves are the Mie theory results for the equal-volume smooth sphere.

RANDOMLY ORIENTED ROUGH PARTICLE #154001
 Volume-Equivalent Size Parameter $x_v = 3.630$
 Complex Refractive Index $m = 1.61 - i0.004$



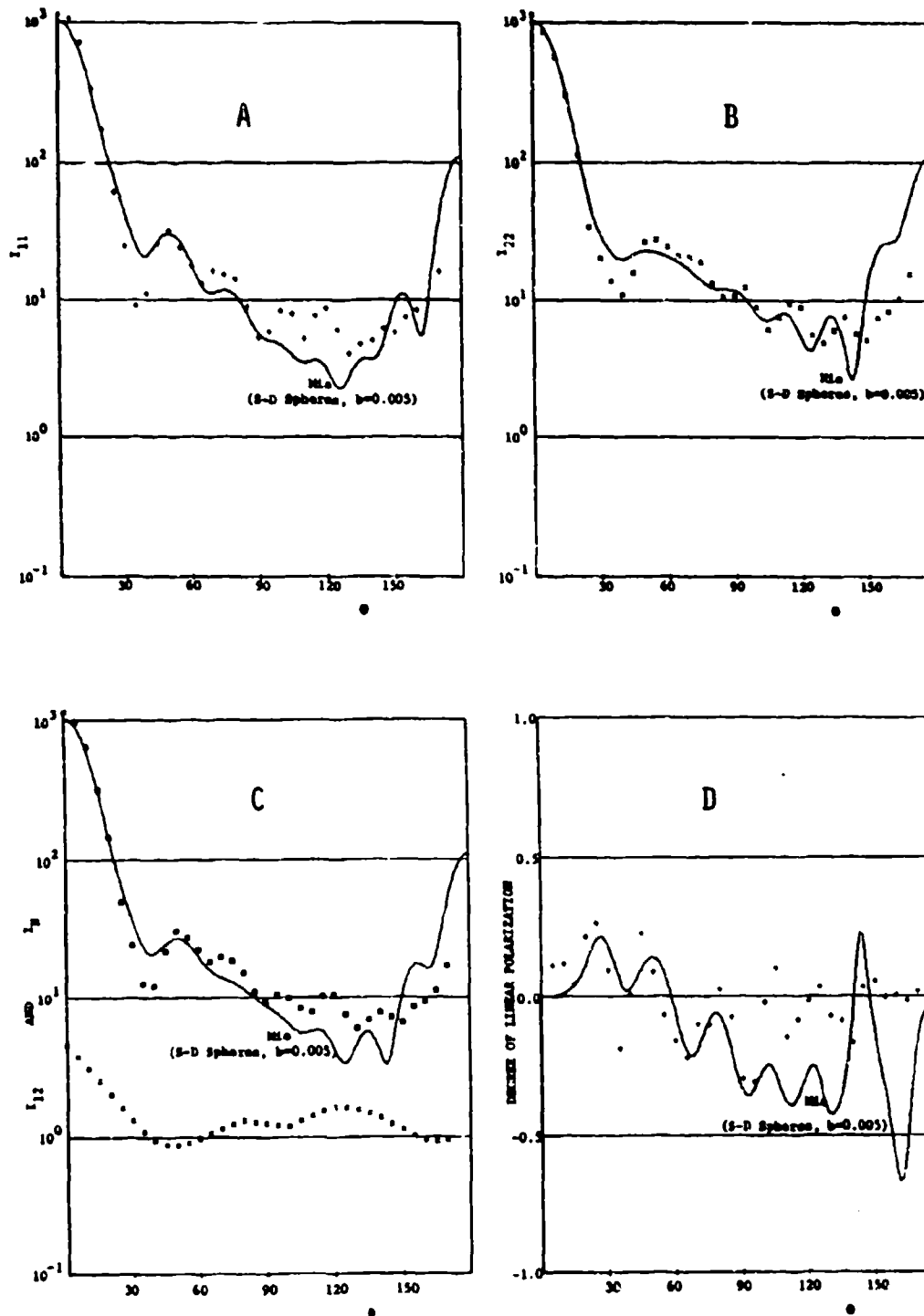
FIGURES 11A-11D ANGULAR DISTRIBUTION DATA FOR A RANDOMLY ORIENTED ROUGH PARTICLE (#154001)
 Continuous curves are the Mie theory results for the gamma-size-distributed polydisperse spheres
 with effective mean size x_v and effective variance b .

RANDOMLY ORIENTED ROUGH PARTICLE #153001
 Volume-Equivalent Size Parameter $x_v = 3.499$
 Complex Refractive Index $m = 1.61 - i0.004$



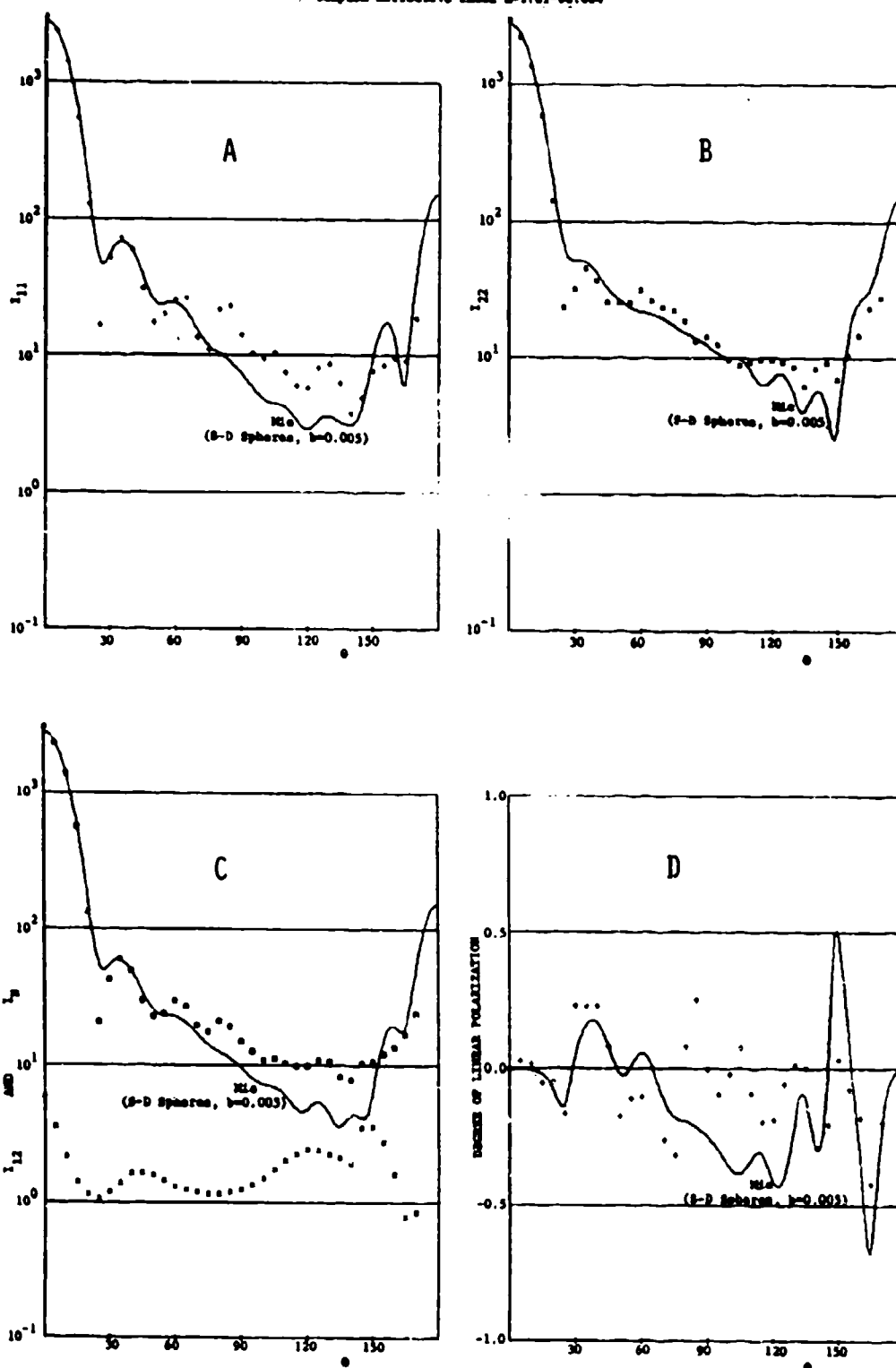
FIGURES 12A-12D ANGULAR DISTRIBUTION DATA FOR A RANDOMLY ORIENTED ROUGH PARTICLE (#153001)
 Continuous curves are the Mie theory results for the gamma-size-distributed polydisperse spheres
 with effective mean size x_v and effective variance b .

RANDOMLY ORIENTED ROUGH PARTICLE #157001
 Volume-Equivalent Size Parameter $x_v = 7.346$
 Complex Refractive Index $m = 1.61 - 0.004i$

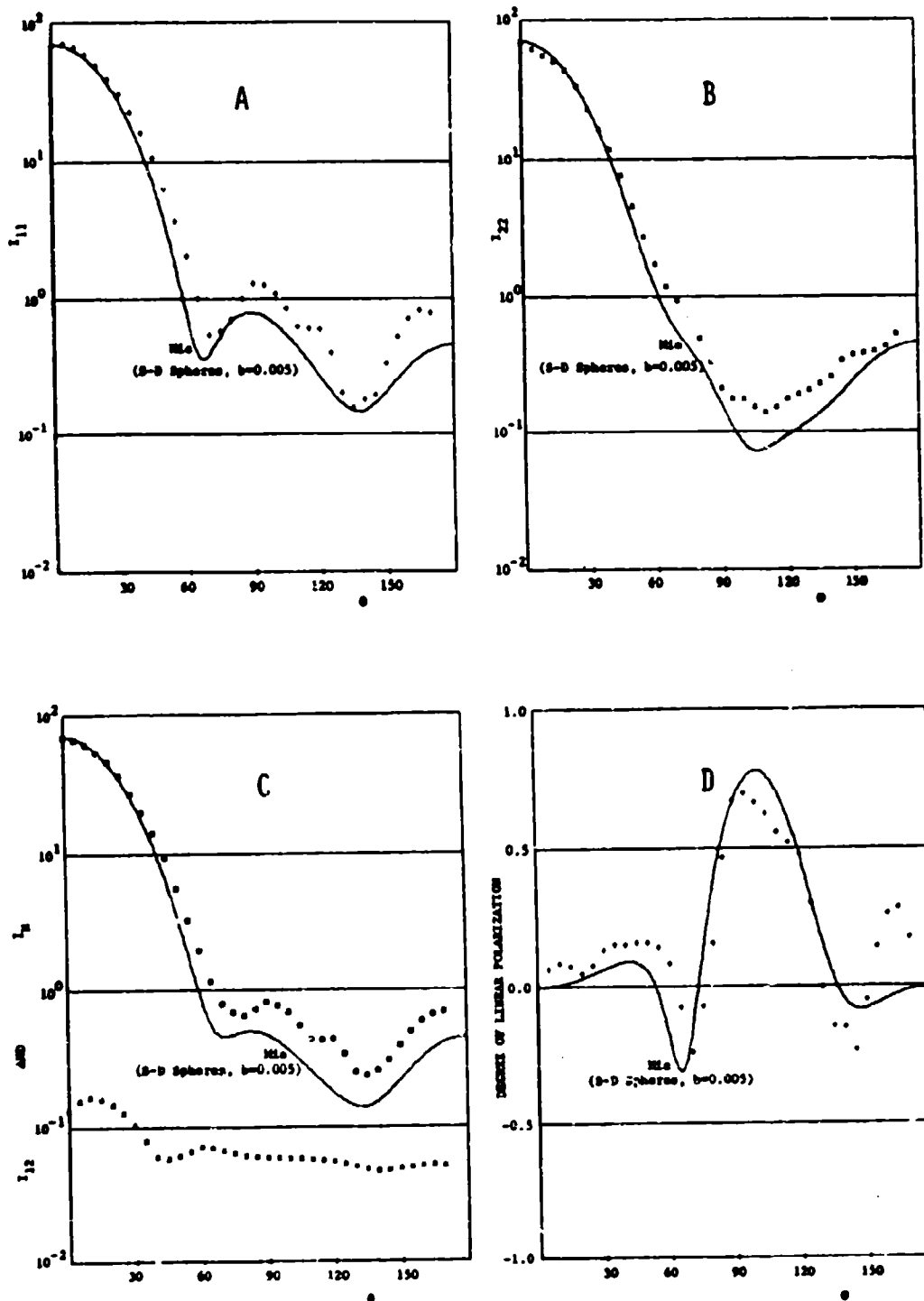


FIGURES 13A-13D ANGULAR DISTRIBUTION DATA FOR A RANDOMLY ORIENTED ROUGH PARTICLE (#157001)
 Continuous curves are the Mie theory results for the gamma-size-distributed polydisperse spheres
 with effective mean size x_v and effective variance b .

RANDOMLY ORIENTED ROUGH PARTICLE #159001
 Volume-Equivalent Size Parameter $x_v = 8.636$
 Complex Refractive Index $m = 1.61 - 0.004i$

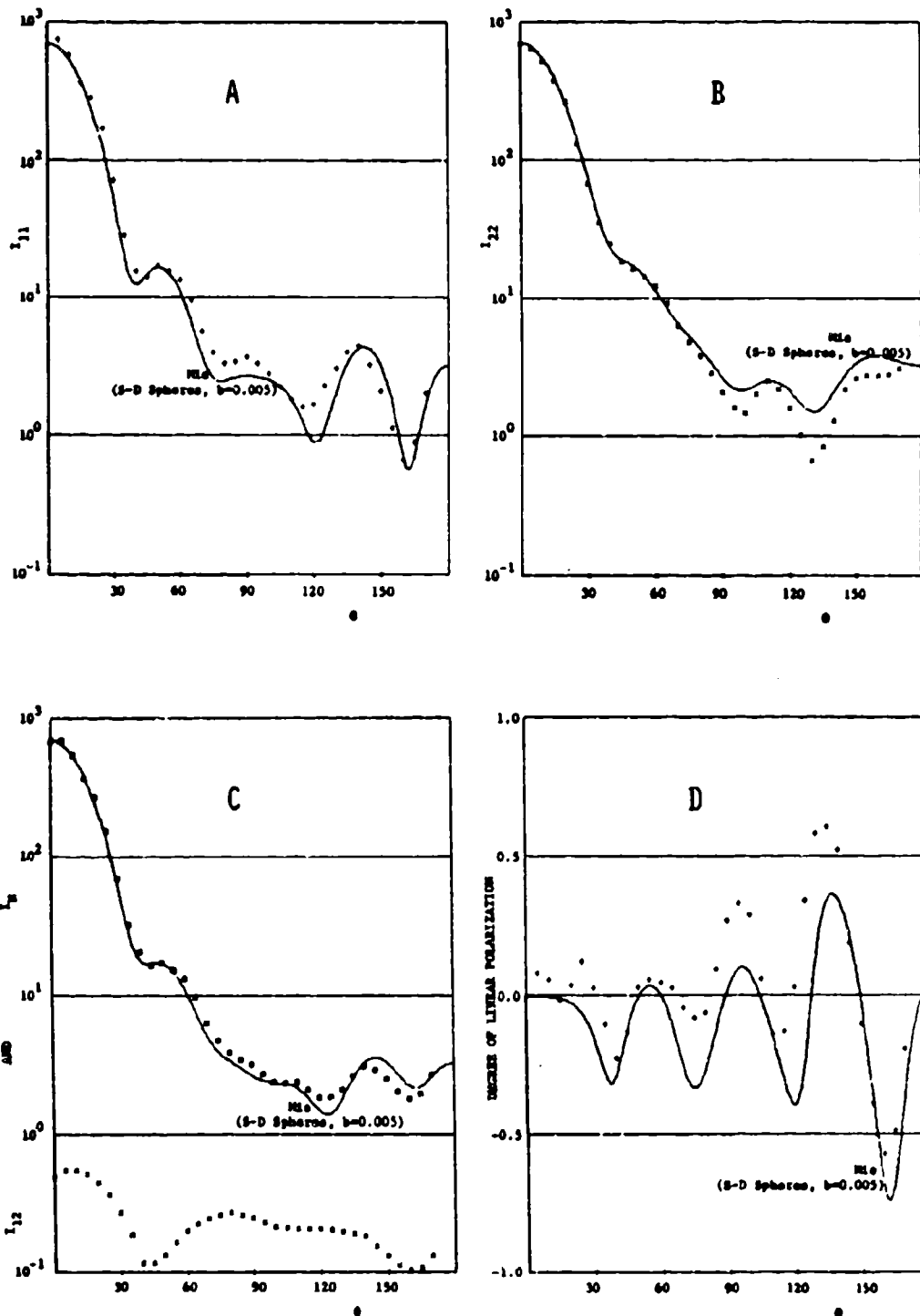


FIGURES 14A-14D ANGULAR DISTRIBUTION DATA FOR A RANDOMLY ORIENTED ROUGH PARTICLE (#159001)
 Continuous curves are the Mie theory results for the gamma-size-distributed polydisperse spheres
 with effective mean size x_v and effective variance b .



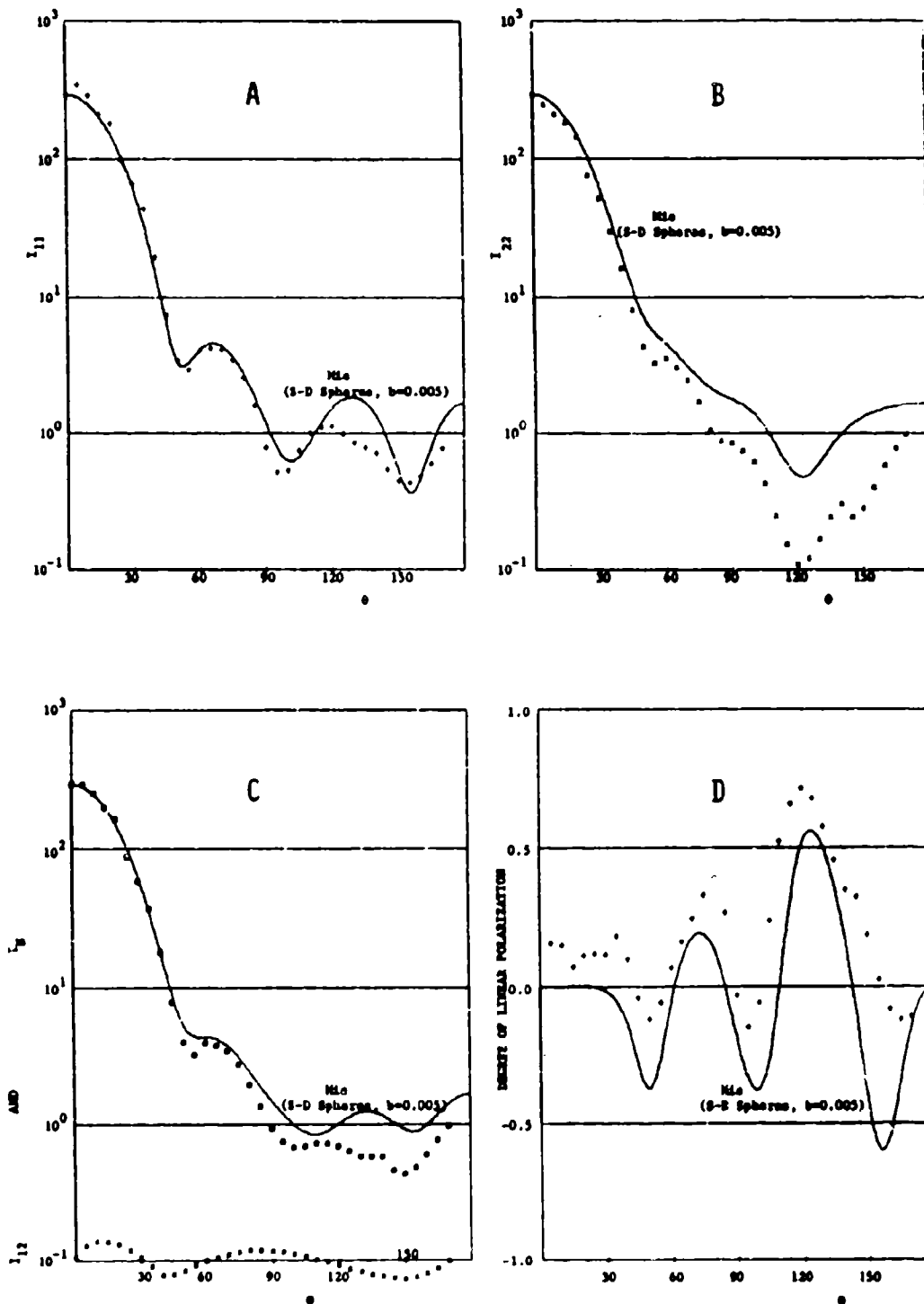
FIGURES 15A-15D ANGULAR DISTRIBUTION DATA FOR A RANDOMLY ORIENTED ROUGH PARTICLE (#143001)
 Continuous curves are the Mie theory results for the gamma-size-distributed polydisperse spheres
 with effective mean size x_v and effective variance b .

RANDOMLY ORIENTED ROUGH PARTICLE #145001
 Volume-Equivalent Size Parameter $x_v = 5.184$
 Complex Refractive Index $m = 1.388 - 0.005i$



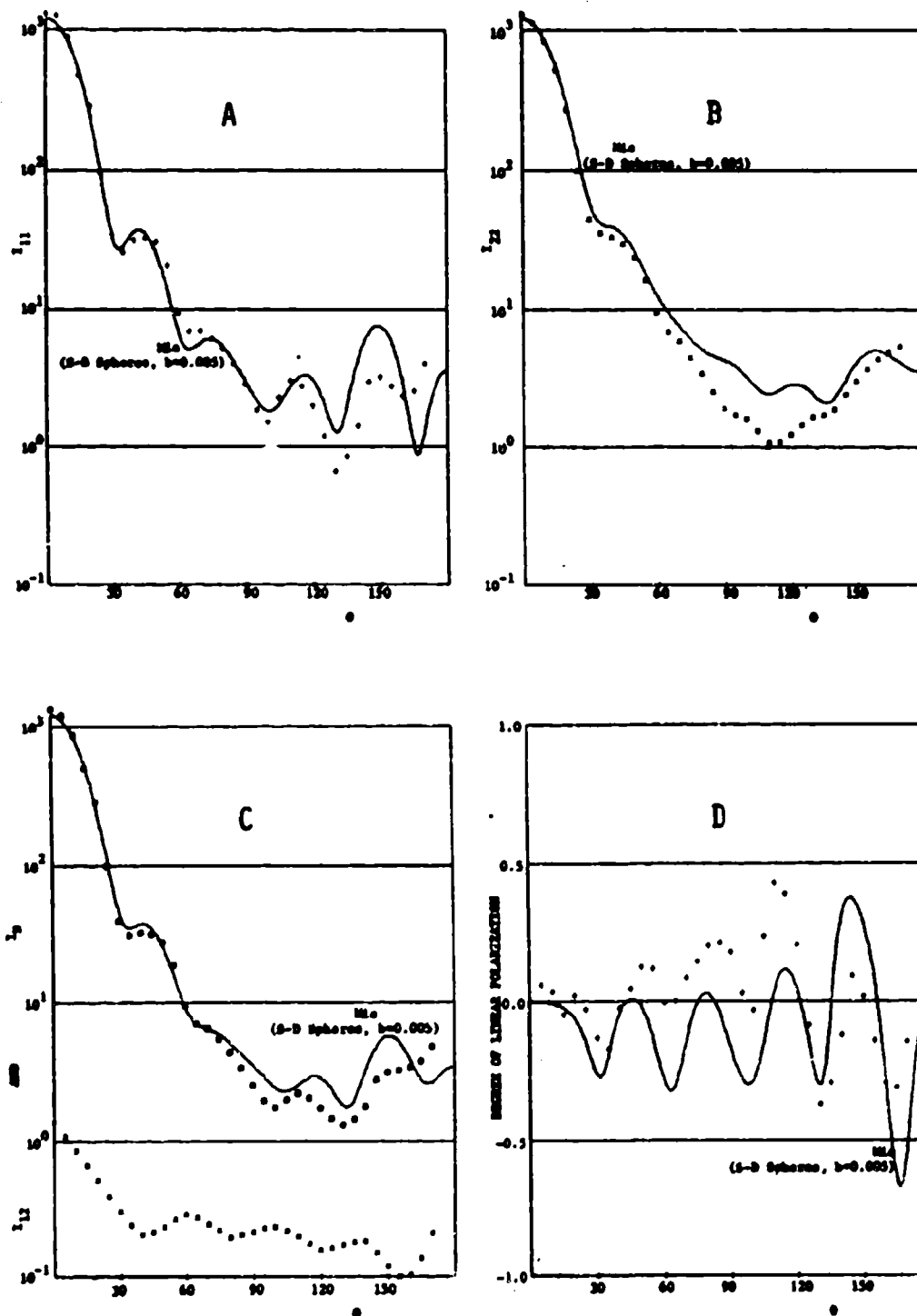
FIGURES 16A-16D ANGULAR DISTRIBUTION DATA FOR A RANDOMLY ORIENTED ROUGH PARTICLE (#145001)
 Continuous curves are the Mie theory results for the gamma-size-distributed polydisperse spheres
 with effective mean size x_v and effective variance b .

RANDOMLY ORIENTED ROUGH PARTICLE (#020003)
 Volume-Equivalent Size Parameter $x_v = 4.257$
 Complex Refractive Index $m = 1.364 - i0.005$



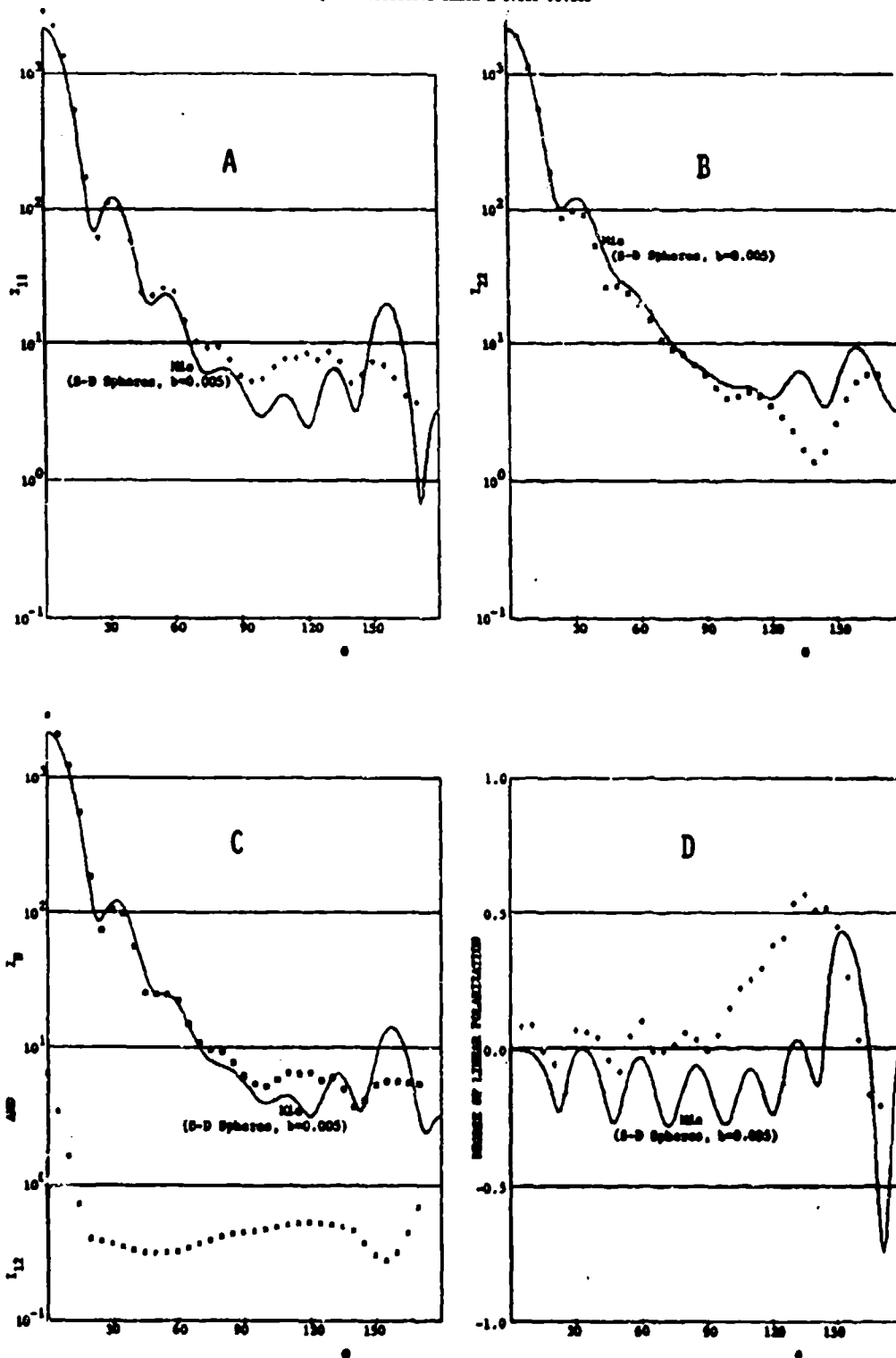
FIGURES 17A-17D ANGULAR DISTRIBUTION DATA FOR A RANDOMLY ORIENTED ROUGH PARTICLE (#020003)
 Continuous curves are the Mie theory results for the gamma-size-distributed polydisperse spheres
 with effective mean size x_v and effective variance b .

RANDOMLY ORIENTED ROUGH PARTICLE 0020002
 Volume-Equivalent Size Parameter $x_v = 6.059$
 Complex Refractive Index $m = 1.367 - 0.093i$

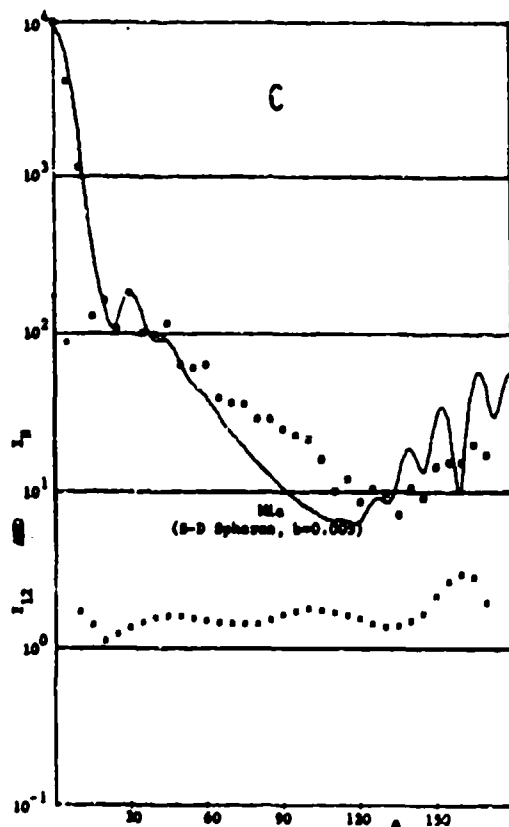
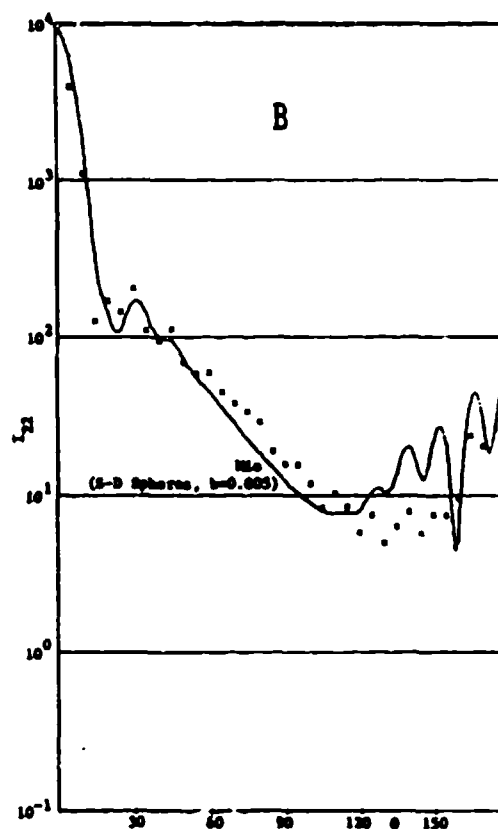
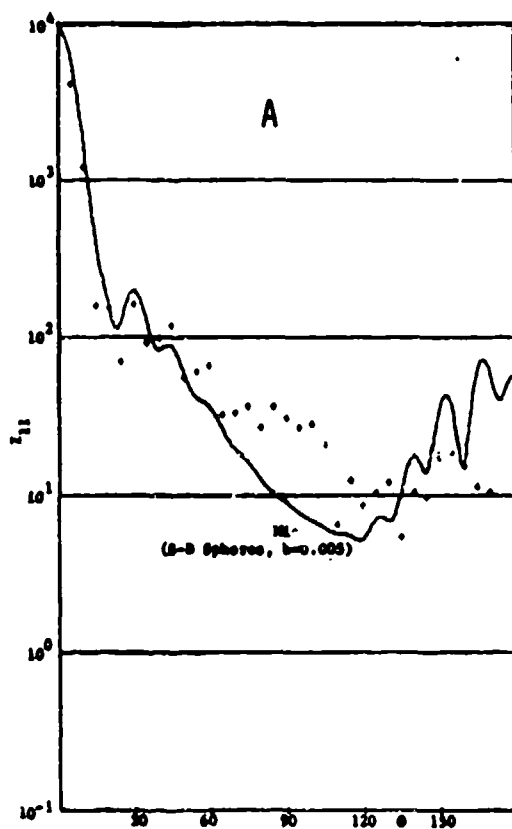


FIGURES 18A-18D ANGULAR DISTRIBUTION DATA FOR A RANDOMLY ORIENTED ROUGH PARTICLE (0020002)
 Continuous curves are the Mie theory results for the gamma-size-distributed polydisperse spheres
 with effective mean size x_v and effective variance b .

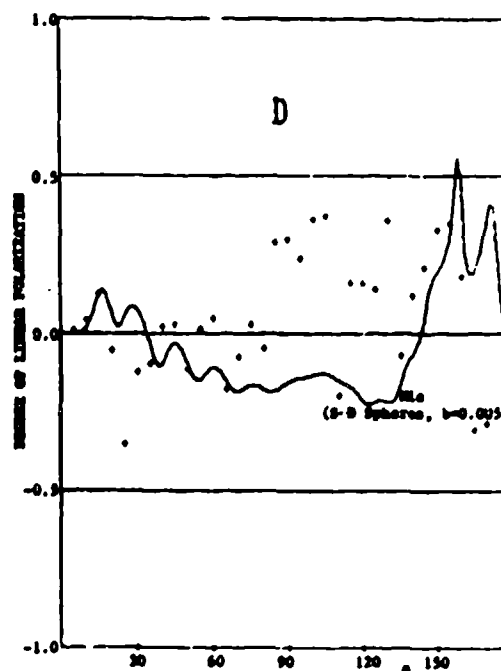
RANDOMLY ORIENTED ROUGH PARTICLES (#020001)
 Volume-Equivalent Size Parameter $x_v = 7.694$
 Complex Refractive Index $m = 1.368 - i0.005$



FIGURES 19A-19D ANGULAR DISTRIBUTION DATA FOR A RANDOMLY ORIENTED ROUGH PARTICLE (#020001)
 Continuous curves are the Mie theory results for the gamma-size-distributed polydisperse spheres
 with effective mean size x_v and effective variance b .

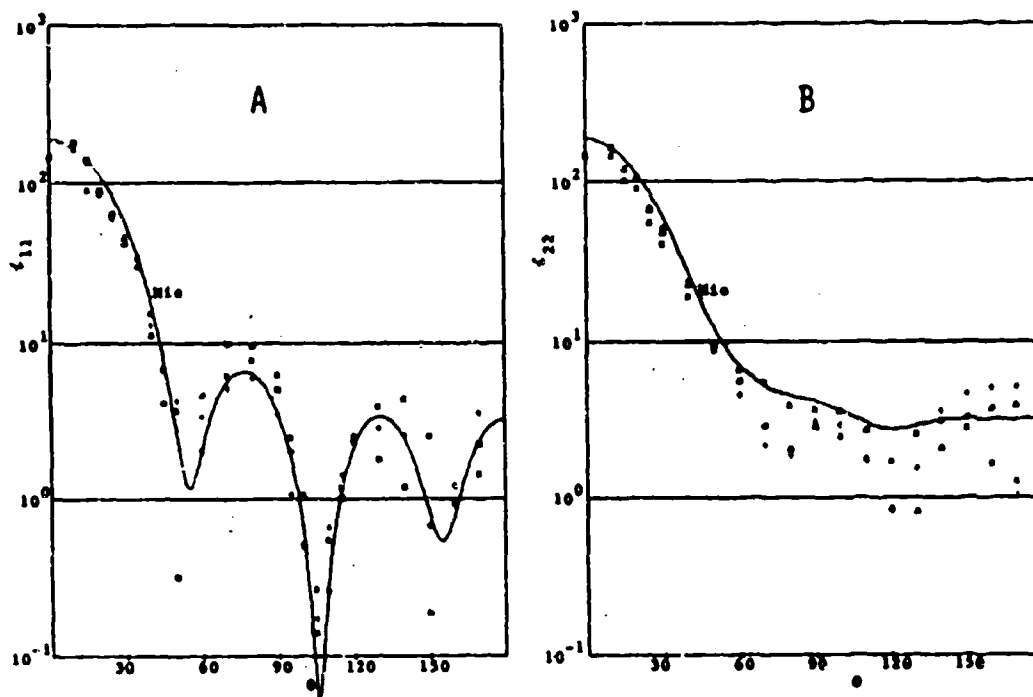


RANDOMLY ORIENTED ROUGH PARTICLE (0020000)
Volume-Weighted Size Parameter $x_v = 12.082$
Complex Refractive Index $m = 1.353 - 0.005i$



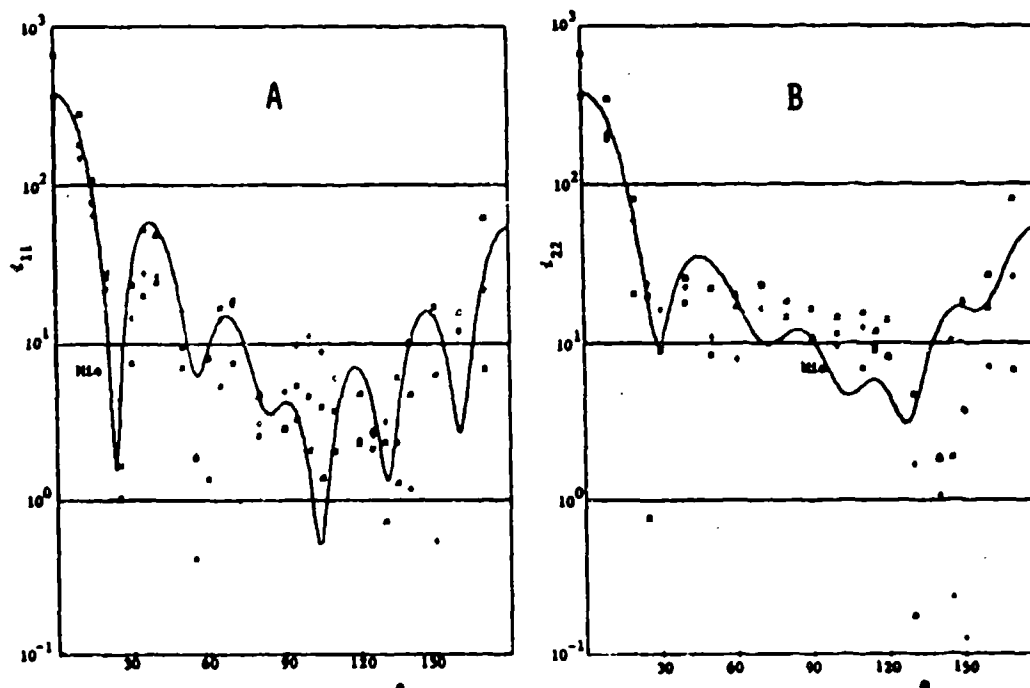
FIGURES 20A-20D ANGULAR DISTRIBUTION DATA FOR A RANDOMLY ORIENTED ROUGH PARTICLE (0020000)
Continuous curves are the Mie theory results for the gamma-size-distributed polydisperse spheres
with effective mean size x_v and effective variance b .

ORIENTED ROUGH PARTICLE
#154001

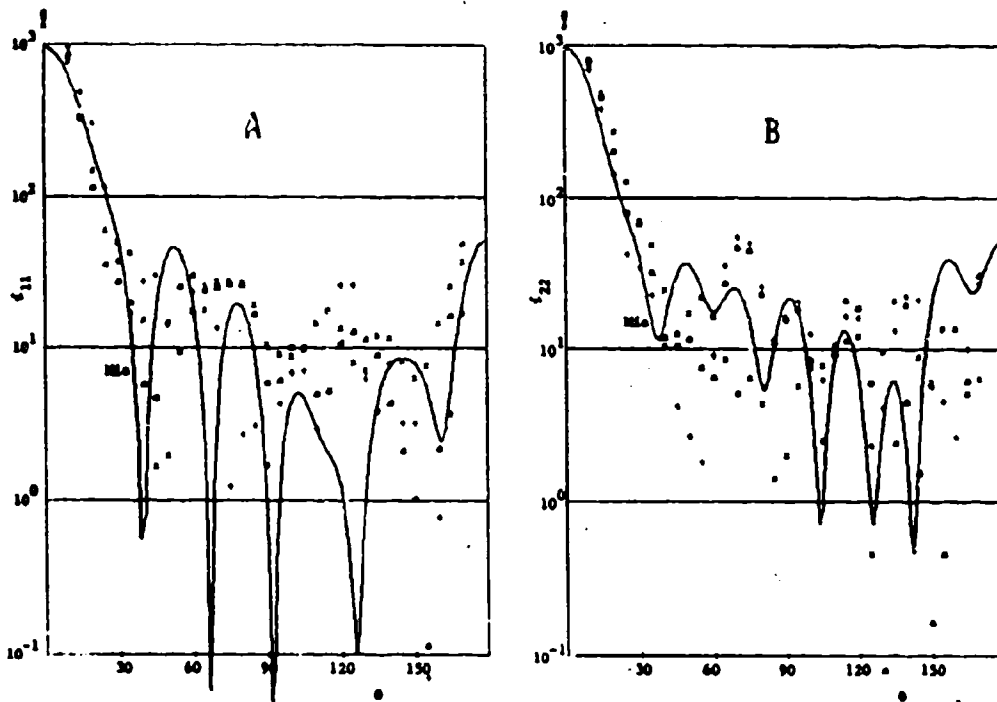


FIGURES 21A&21B ANGULAR DISTRIBUTION DATA FOR A PREFERENTIALLY ORIENTED ROUGH PARTICLE (#154001). 3 orientation symbols respectively denote when the particle axis is: parallel to the incident k vector (\odot); parallel to the E vector (+); and parallel to the H vector (\times). Continuous curves are the Mie theory results for the smooth sphere of the same volume and refractive index.

ORIENTED ROUGH PARTICLE
#155001

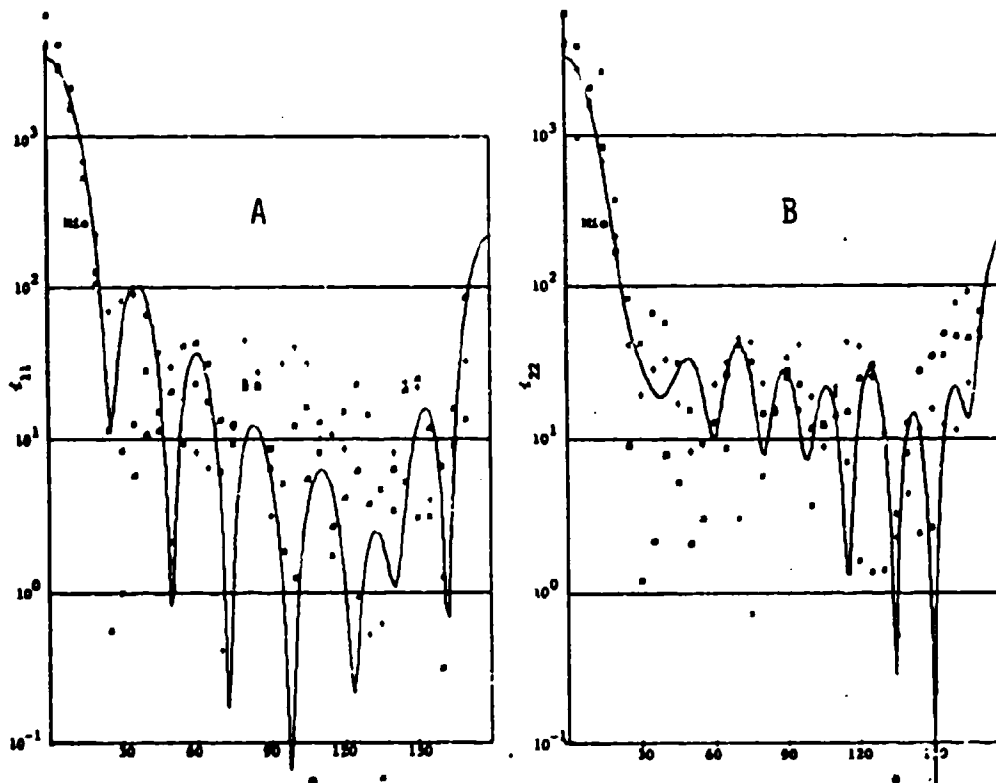


FIGURES 22A&22B ANGULAR DISTRIBUTION DATA FOR A PREFERENTIALLY ORIENTED ROUGH PARTICLE (#155001). 3 orientation symbols respectively denote when the particle axis is: parallel to the incident k vector (\odot); parallel to the E vector (+); and parallel to the H vector (\times). Continuous curves are the Mie theory results for the smooth sphere of the same volume and refractive index.



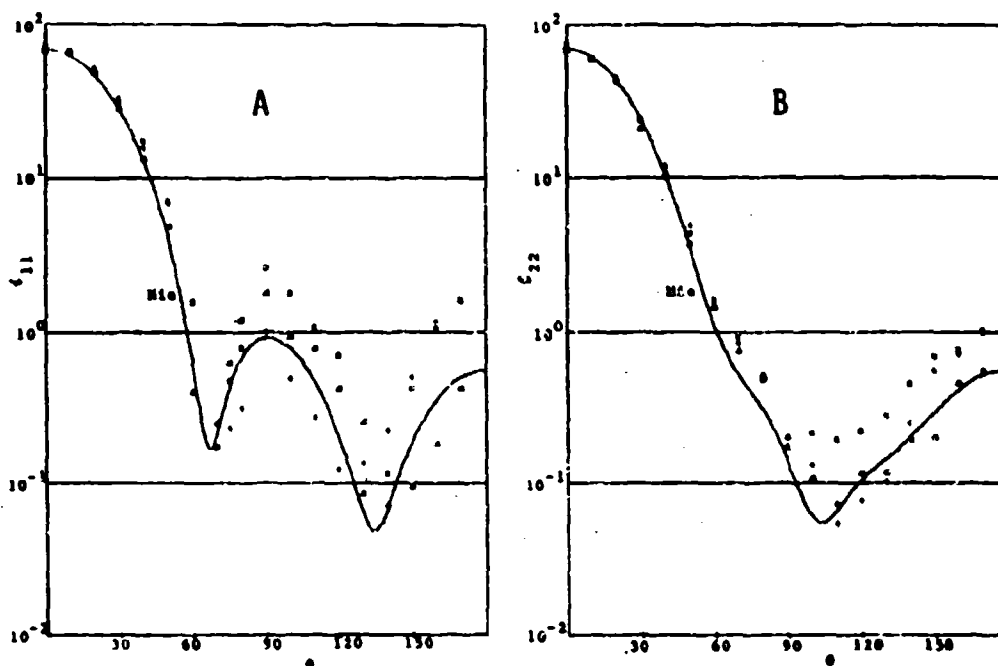
FIGURES 23A&23B ANGULAR DISTRIBUTION DATA FOR A PREFERENTIALLY ORIENTED ROUGH PARTICLE (#157001)
3 orientation symbols respectively denote when the particle axis is: parallel to the incident
k vector (O); parallel to the E vector (+); and parallel to the H vector (x). Continuous
curves are the Mie theory results for the smooth sphere of the same volume and refractive index.

#159001



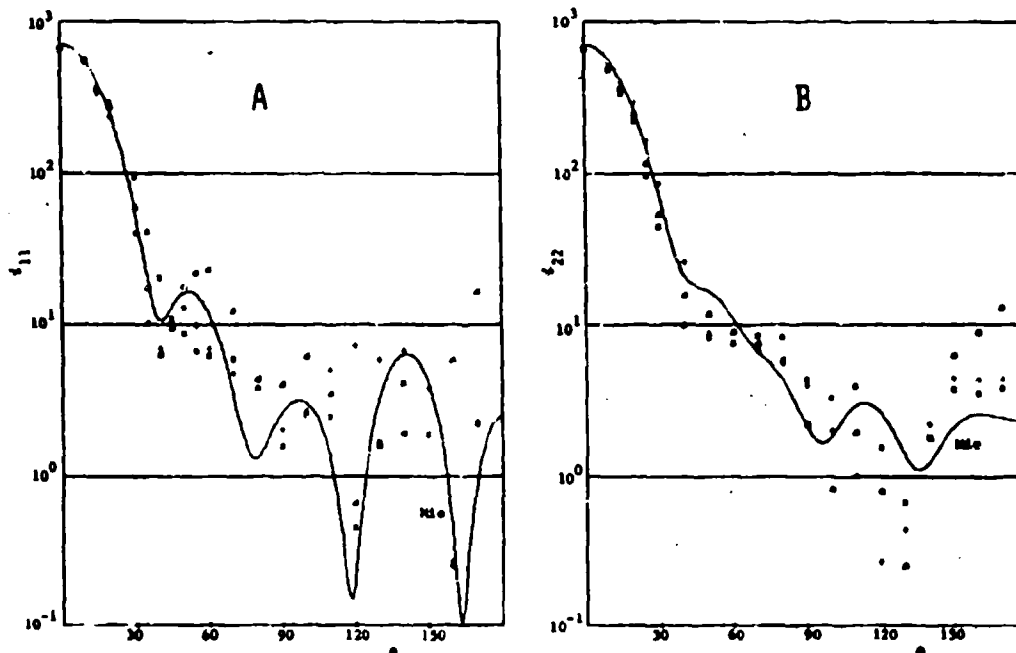
FIGURES 24A&24B ANGULAR DISTRIBUTION DATA FOR A PREFERENTIALLY ORIENTED ROUGH PARTICLE (#159001)
3 orientation symbols respectively denote when the particle axis is: parallel to the incident
k vector (O); parallel to the E vector (+); and parallel to the H vector (x). Continuous
curves are the Mie theory results for the smooth sphere of the same volume and refractive index.

ORIENTED ROUGH PARTICLE
#143001



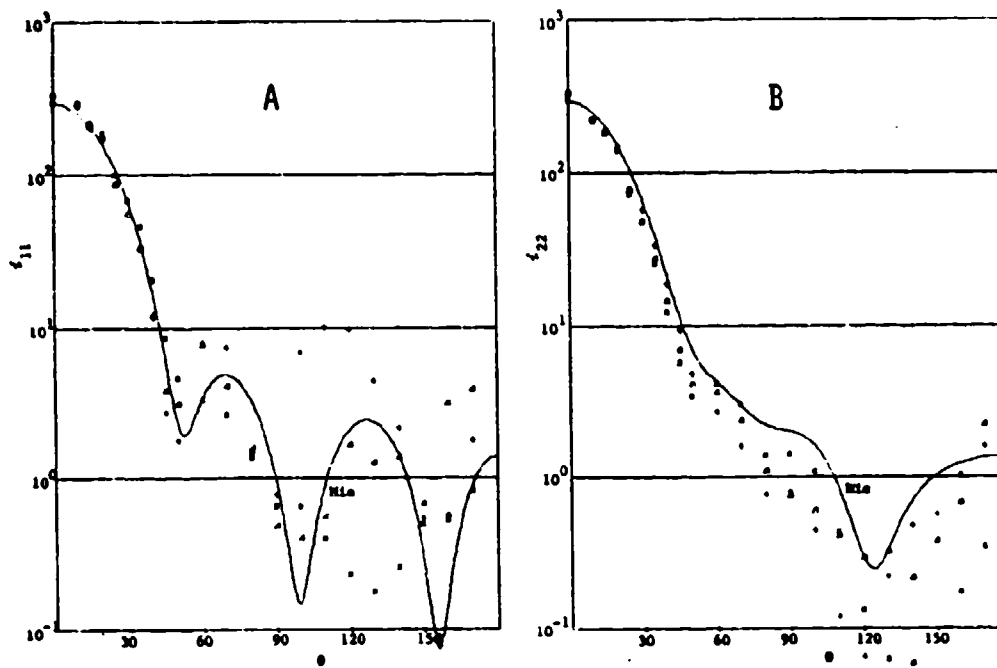
FIGURES 25A&25B ANGULAR DISTRIBUTION DATA FOR A PREFERENTIALLY ORIENTED ROUGH PARTICLE (#143001)
3 orientation symbols respectively denote when the particle axis is: parallel to the incident
k vector (\odot); parallel to the E vector (+); and parallel to the H vector (\times). Continuous
curves are the Mie theory results for the smooth sphere of the same volume and refractive index.

ORIENTED ROUGH PARTICLE
#145001



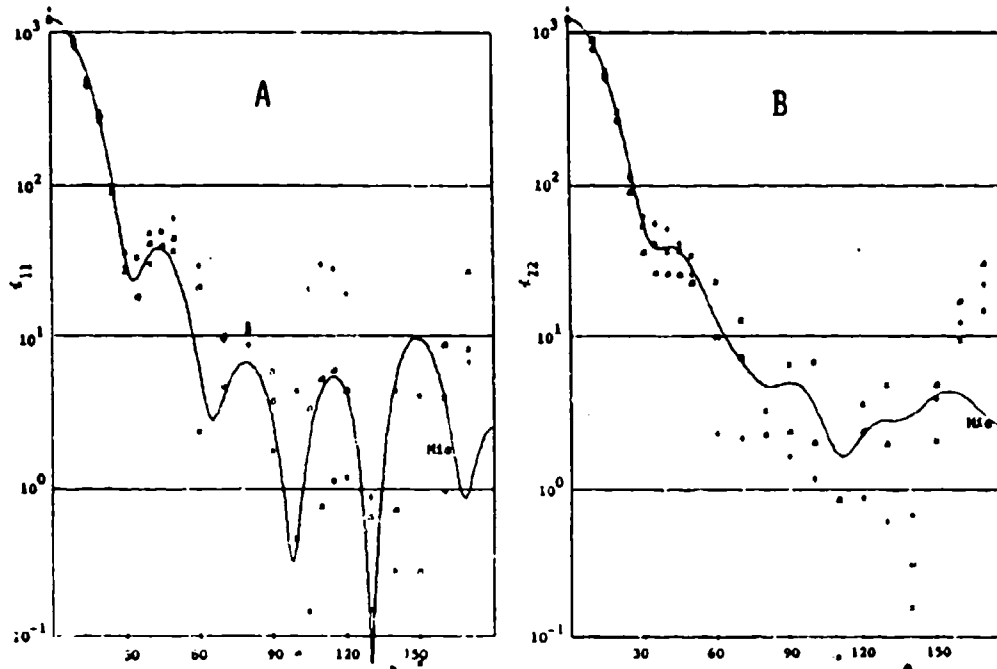
FIGURES 26A&26B ANGULAR DISTRIBUTION DATA FOR A PREFERENTIALLY ORIENTED ROUGH PARTICLE (#145001)
3 orientation symbols respectively denote when the particle axis is: parallel to the incident
k vector (\odot); parallel to the E vector (+); and parallel to the H vector (\times). Continuous
curves are the Mie theory results for the smooth sphere of the same volume and refractive index.

ORIENTED ROUGH PARTICLE
#020003

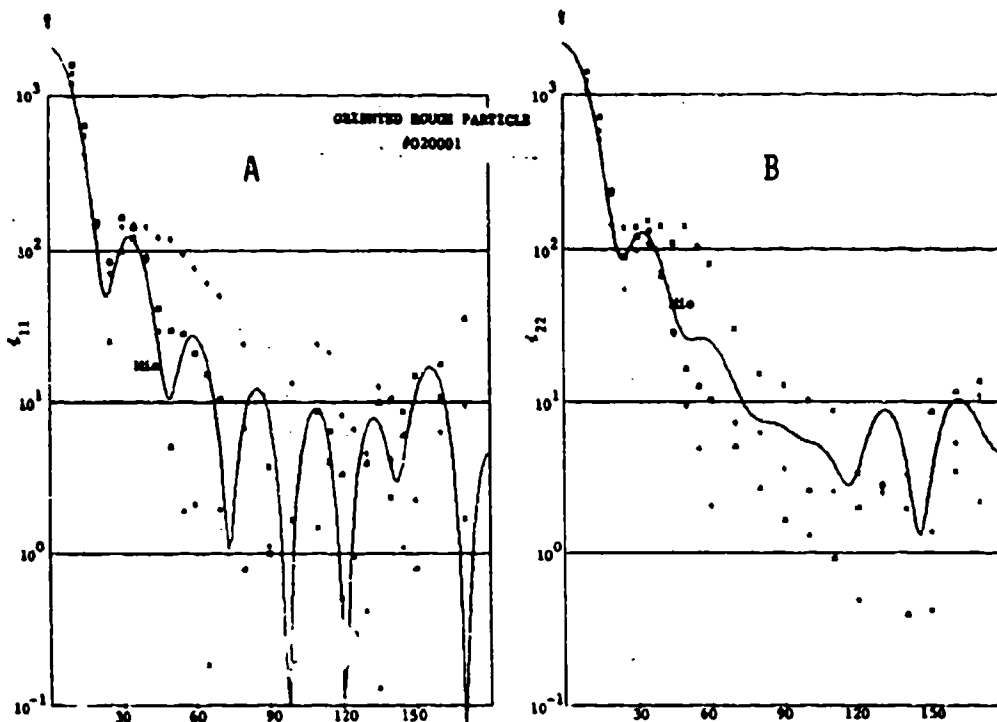


FIGURES 27A&27B ANGULAR DISTRIBUTION DATA FOR A PREFERENTIALLY ORIENTED ROUGH PARTICLE (#020003)
3 orientation symbols respectively denote when the particle axis is: parallel to the incident
k vector (\odot); parallel to the E vector (+); and parallel to the H vector (\times). Continuous
curves are the Mie theory results for the smooth sphere of the same volume and refractive index.

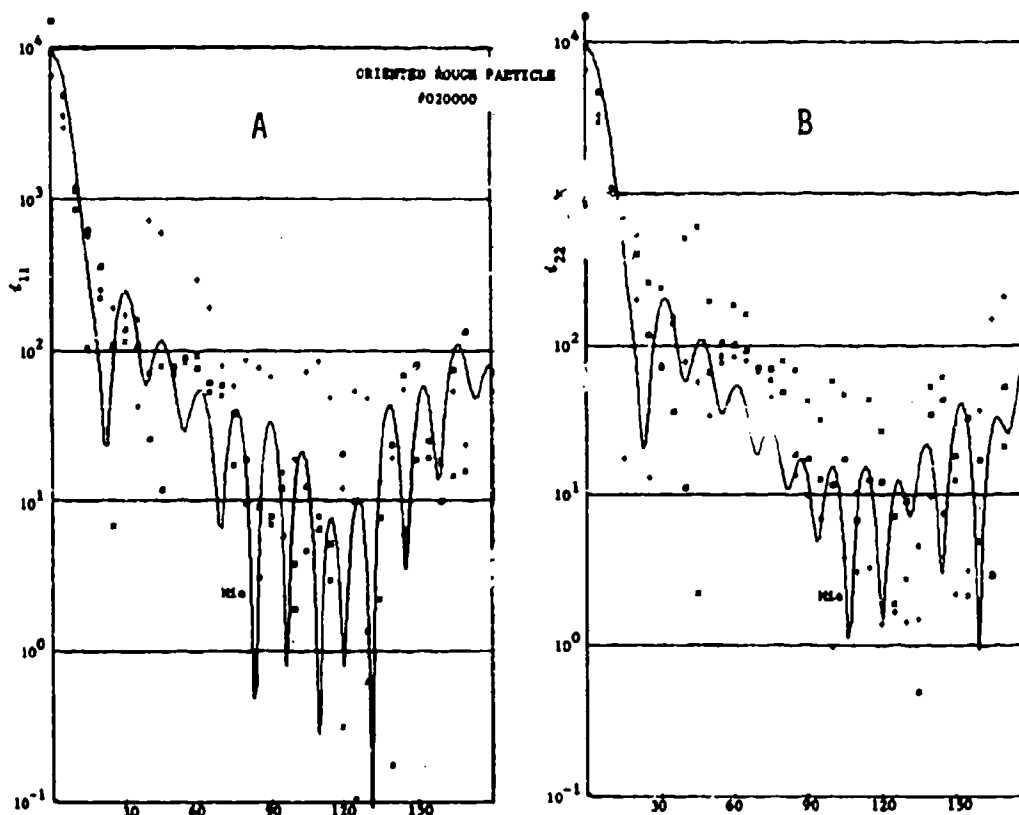
ORIENTED ROUGH PARTICLE
#020002



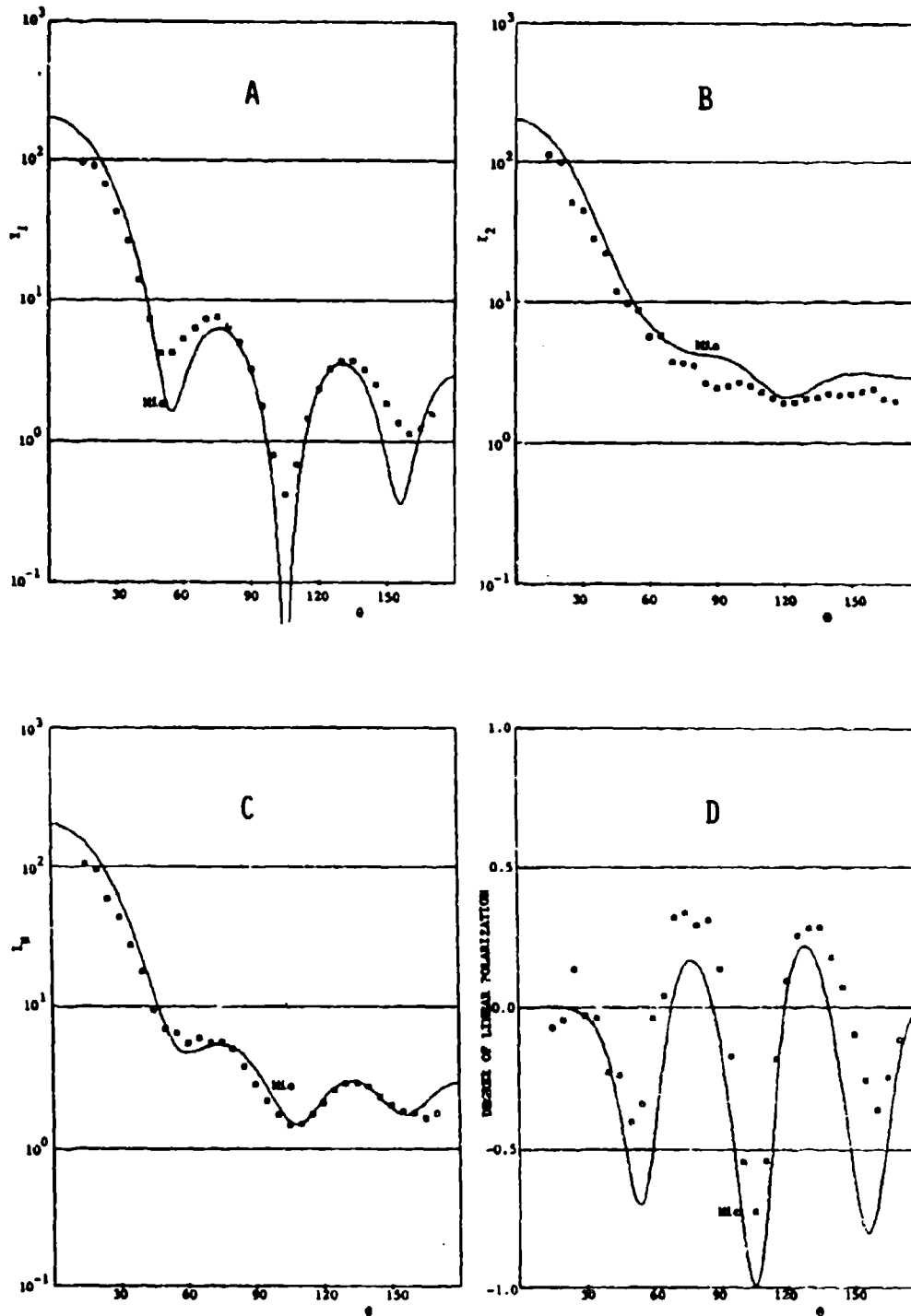
FIGURES 28A&28B ANGULAR DISTRIBUTION DATA FOR A PREFERENTIALLY ORIENTED ROUGH PARTICLE (#020002)
3 orientation symbols respectively denote when the particle axis is: parallel to the incident
k vector (\odot); parallel to the E vector (+); and parallel to the H vector (\times). Continuous
curves are the Mie theory results for the smooth sphere of the same volume and refractive index.



FIGURES 29A&29B ANGULAR DISTRIBUTION DATA FOR A PREFERENTIALLY ORIENTED ROUGH PARTICLE (#020001) 3 orientation symbols respectively denote when the particle axis is: parallel to the incident k vector (O); parallel to the E vector (+); and parallel to the H vector (x). Continuous curves are the Mie theory results for the smooth sphere of the same volume and refractive index.

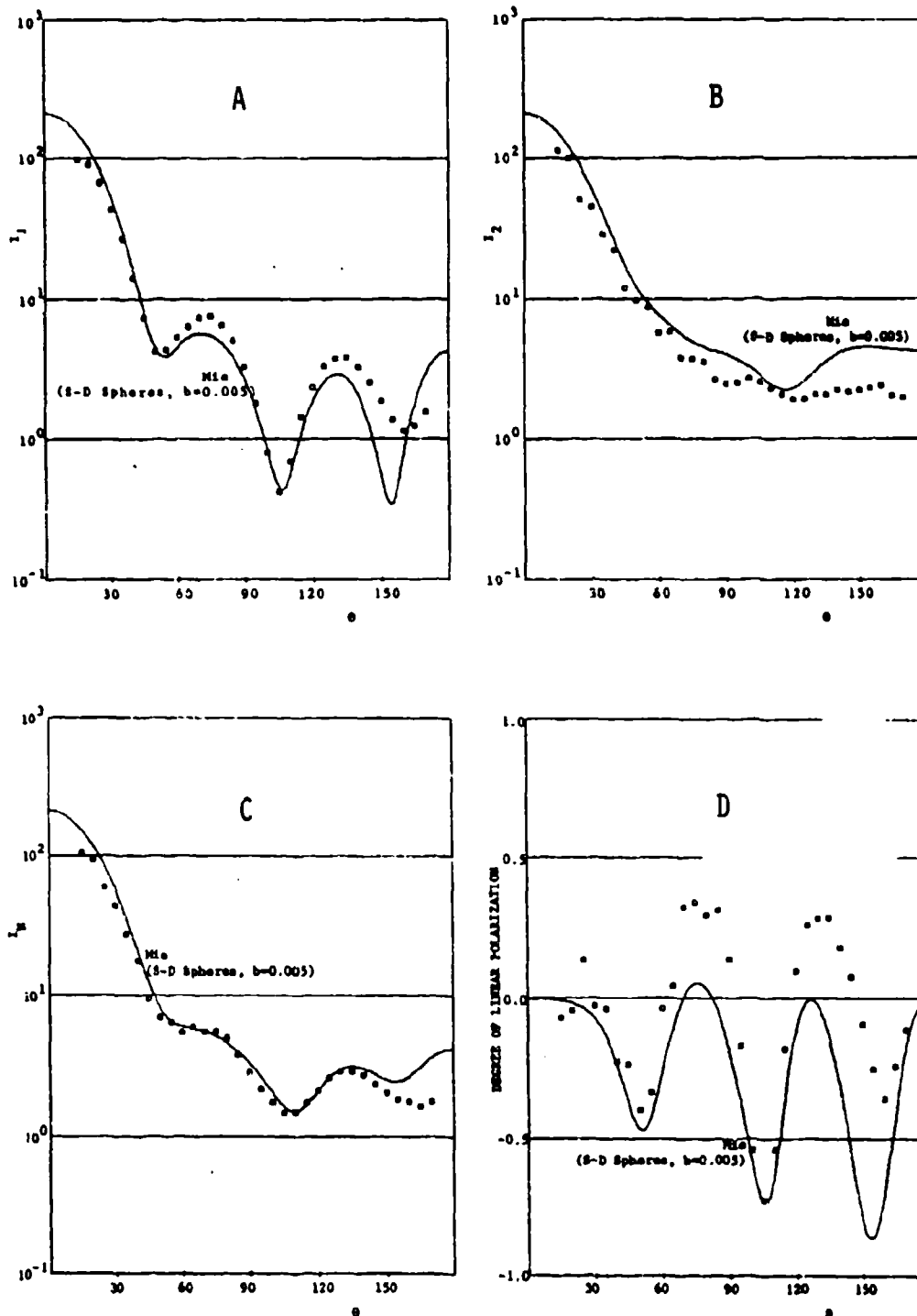


FIGURES 30A&30B ANGULAR DISTRIBUTION DATA FOR A PREFERENTIALLY ORIENTED ROUGH PARTICLE (#020000) 3 orientation symbols respectively denote when the particle axis is: parallel to the incident k vector (O); parallel to the E vector (+); and parallel to the H vector (x). Continuous curves are the Mie theory results for the smooth sphere of the same volume and refractive index.



FIGURES 31A-31D ANGULAR DISTRIBUTION DATA FOR A RANDOMLY ORIENTED CUBE
 Continuous curves are the Mie theory results for the smooth sphere of the same volume
 and refractive index.

RANDOMLY ORIENTED CUBE
 $\mu_v = 3.75$; $\sigma = 1.374 - 10.006$
 From Microwave Data of E. Zerull
 Beitr. Phys. d. Atmos. **49**, 168 (1976).



FIGURES 32A-32D ANGULAR DISTRIBUTION DATA FOR A RANDOMLY ORIENTED CUBE
 Continuous curves are the Mie theory results for the gamma-size-distributed polydisperse
 spheres with effective mean size x_v and effective variance b .

BLANK

SCATTERING AND DEPOLARIZATION BY CONDUCTING CYLINDERS
WITH VERY ROUGH SURFACES

Ezekiel Bahar
and
Mary Ann Fitzwater
Electrical Engineering Department
University of Nebraska--Lincoln
Lincoln, NE 68588-0511

ABSTRACT

Like- and cross-polarized scattering cross sections are determined at optical frequencies for conducting cylinders with very rough surfaces. Both normal and oblique incidence with respect to the cylinder axis are considered. The full-wave approach is used to account for both the specular point scattering and the diffuse scattering. For the roughness scales considered, the scattering cross sections differ significantly from those derived for smooth conducting cylinders. Several illustrative examples are presented.

1. Introduction

The problem of electromagnetic scattering by finitely conducting circular cylinders or spheres has been dealt with extensively in the technical literature. Perturbation theory has been used to extend these results to scattering by slightly rough circular cylinders or spheres (Barrick 1970). However, perturbation theory is limited to surfaces for which the roughness parameter $\beta = 4k_0^2 \langle h_g^2 \rangle < 0.1$ (k_0 is the electromagnetic wavenumber and $\langle h_g^2 \rangle$ is the mean square height of the rough surface, Brown 1978). For $\beta < 0.1$ the scattering cross sections are not significantly different from those for smooth conducting circular cylinders.

In this work the full-wave approach is used to determine the like- and cross-polarized scattering cross sections at optical frequency for finitely conducting cylinders with roughness scales that significantly modify the scattering cross sections. The radii of curvature of the unperturbed cylinders considered are large compared to wavelength λ . (However, the cross section of the unperturbed cylinder need not be circular). Both specular point scattering and diffuse scattering are accounted for in the analysis in a self consistent manner and the cross sections are expressed as a weighted sum of two cross sections.

In Section 2 the special forms of full-wave solutions are presented for long cylinders with mean circular cross sections and both the specular point and diffuse contributions are identified. In Section 3 several illustrative examples are considered for cylinders with roughness parameter $\beta = 1$. The rough surface is characterized by its surface-height spectral-density function. The results are compared with solutions based on the perturbation approach.

2. Formulation of the Problem

The scattered radiation fields for two dimensionally rough surfaces can be expressed in matrix form as follows (Bahar 1981)

$$\begin{pmatrix} G^{Vf} \\ G^{Hf} \end{pmatrix} = G_o \begin{pmatrix} D^{VV} & D^{VH} \\ D^{HV} & D^{HH} \end{pmatrix} \begin{pmatrix} G^{Vi} \\ G^{Hi} \end{pmatrix} \exp[i\vec{v} \cdot \vec{r}_s] dS \quad (2.1)$$

in which G^{Vf} and G^{Hf} are the vertically and horizontally polarized (electric or magnetic) fields scattered at a distance r in the direction of the unit vector \vec{n}^f . Similarly G^{Vi} and G^{Hi} are the vertically and horizontally polarized fields incident (at the origin) in the direction of the unit vector \vec{n}^i . The scattering matrix D is given by

$$D = C_o^{in} T^f \mathcal{T} T^i \quad (2.2)$$

in which the transformation matrices T^f and T^i relate the scattered and incident waves in the local planes of scatter and incidence to reference planes of scatter and incidence while \mathcal{T} is the scattering matrix defined in the local planes of incidence and scatter. The coefficient G_o is

$$G_o = -ik_o \exp(-ik_o r) / 2\pi r \quad (2.3)$$

the vector \vec{v} is

$$\vec{v} = k_o (\vec{n}^f - \vec{n}^i) = v_x \vec{a}_x + v_y \vec{a}_y + v_z \vec{a}_z \quad (2.4)$$

and

$$C_o^{in} = -\vec{n}^i \cdot \vec{n} \quad (2.5)$$

where \vec{n} is the unit vector normal to the rough surface S . The position vector to a point on the rough surface is \vec{r}_s and for a reference cross sectional area in the x, z plane

$$dS = dx dz / (\vec{n} \cdot \vec{a}_y) \quad (2.6)$$

The expression (2.1) is invariant to coordinate transformations. For very (infinitely) long cylinders the surface integral (2.1) can be reduced to a line integral by noting that

$$\int_{-\infty}^{\infty} \exp(iv_z z) dz = 2\pi \delta(v_z) \quad (2.7)$$

On evaluating the expressions for the radiation (far) fields from the expressions for their transforms (using the steepest descent method, Bahar and Rajan (1979) it can be shown that

$$G^f = G_o^1 \int DG^1 \exp[i\vec{v} \cdot (x \vec{a}_x + y \vec{a}_y)] dx / (\vec{n} \cdot \vec{a}_y) \quad (2.8)$$

in which

$$G_o^1 = - \left(\frac{k_o}{2\pi \rho \cos \theta_o^1} \right)^{1/2} \exp(i\pi/4) \exp[-ik_o (\rho \cos \theta_o^1 + z \sin \theta_o^1)] \quad (2.9)$$

and for oblique incidence (with respect to the z axis) the direction of the incident plane wave is

$$\vec{n}^i = -\cos \theta_o^1 \vec{a}_y + \sin \theta_o^1 \vec{a}_z \quad (2.10)$$

The direction of the scattered wave is (Bahar 1981)

$$\vec{n}^f = \sin\theta_0^f \cos\phi^f \vec{a}_x + \cos\theta_0^f \vec{a}_y + \sin\theta_0^f \sin\phi^f \vec{a}_z \quad (2.11)$$

(where the polar angle is measured with respect to the y axis, see Figs. 1 and 2). In view of (2.7)

$$\sin\theta_0^f \sin\phi^f = \sin\theta_0^i \quad (2.12)$$

Thus (2.11) can also be expressed as

$$\vec{n}^f = \cos\theta_0^i (\sin\phi' \vec{a}_x + \cos\phi' \vec{a}_y) + \sin\theta_0^i \vec{a}_z \quad (2.13)$$

where the azimuth angle ϕ' is measured in the xy plane with $\phi' = 0$ on the y axis (see Figs. 1 and 2).

The explicit expression for the scattering coefficients D (2.2) have been presented earlier when the reference incident plane is normal to $\vec{n}^i \times \vec{a}_y$ and the reference scatter plane is normal to $\vec{n}^f \times \vec{a}_y$.

However, if the plane of incidence (and scatter) is taken to be the plane normal to \vec{n}^i and \vec{n}_s (the normal to the cylinder at the specular point) (Barrick 1970), in these expressions for T^f and T^i the unit vector \vec{a}_y must be replaced by the unit vector

$$\begin{aligned} \vec{n}_s &= \vec{v}/v = \sin(\phi'/2) \vec{a}_x + \cos(\phi'/2) \vec{a}_y = \vec{a}_r \\ &= \frac{\sin\theta_0^f \cos\phi^f \vec{a}_x + (\cos\theta_0^f + \cos\theta_0^i) \vec{a}_y}{[2 \cos\theta_0^i (\cos\theta_0^i + \cos\theta_0^f)]^{1/2}} \end{aligned} \quad (2.14)$$

The normalized scattering cross sections (or scattering width) are for P,Q = V,H

$$\begin{aligned} \langle \sigma^{PQ} \rangle &= \frac{\langle |G^{Pf}|^2 \rangle}{|G^{Qi}|^2} \frac{2\pi\rho}{\pi a} \\ &= \langle \chi_2 \frac{k_0}{\pi a \cos\theta_0^i} \int \frac{D^{PQ} D^{PQ*} \exp[i v_x (x-x') + i v_y (y-y')]}{(\vec{n} \cdot \vec{a}_y)(\vec{n}' \cdot \vec{a}_y)} dx dx' \rangle \end{aligned} \quad (2.15)$$

where the radius vector to the surface of the cylinder is

$$\vec{r}_s = (a+h_s) \vec{a}_r = (a+h_s) \frac{(x \vec{a}_x + y \vec{a}_y)}{a} \quad (2.16)$$

and $a = (x^2 + y^2)^{1/2}$ is the radius of the unperturbed cylinder. The characteristic function χ and the joint characteristic function χ_2 for the random rough-surface height h_s are

$$\chi = \langle \exp(i v h_s) \rangle \quad (2.17)$$

where

$$v = 2k_0 \cos(\phi'/2) \quad (2.18)$$

and

$$\chi_2 = \langle \exp[i v (h_s - h'_s)] \rangle \quad (2.19)$$

For Gaussian distributions

$$|\chi|^2 = \exp[-\beta \cos^2(\phi'/2)] \quad (2.20)$$

and

$$\chi_2 = |\chi|^2 \exp(v^2 \langle h_s h'_s \rangle) \quad (2.21)$$

where

$$\beta = 4k_0^2 \langle h_s^2 \rangle \quad (2.22)$$

and the surface-height autocorrelation function $\langle hh' \rangle$ is the Fourier transform of the surface height spectral density function W

$$\frac{W(k)}{4} = \frac{1}{2\pi} \int_{-\infty}^{\infty} \langle h_s h_s' \rangle \exp(ik\tau) d\tau. \quad (2.23)$$

In (2.23) $\langle h_s h_s' \rangle$ is assumed to be a function of the distance measured along the cylinder's circumference. The normalized scattering cross section (2.15) is expressed as a weighted sum of two cross sections (Bahar 1981, Bahar and Barrick 1982)

$$\langle \sigma^{PQ} \rangle = |\chi|^2 \langle \sigma_{\infty}^{PQ} \rangle + \langle \sigma^{PQ} \rangle_R. \quad (2.24)$$

The first term in (2.24) is the physical optics contribution $\langle \sigma_{\infty}^{PQ} \rangle$ modified by the coefficient $|\chi|^2$.

It can be shown (using the steepest descent method) that for a conducting circular cylinder

$$\langle \sigma_{\infty}^{PQ} \rangle = \frac{k_0}{\pi a \cos \theta_o^i} \left| \int_{-a}^a \frac{D^{PQ}}{(\bar{n} \cdot \bar{a}_y)} \exp(iv_x x + iv_y y) dx \right|^2 = \frac{\cos(\phi'/2)}{\cos^2 \theta_o^i} \left| \frac{D^{PQ}}{\bar{n} \cdot \bar{a}_y} \right|_{\bar{n}=\bar{n}_s}^2. \quad (2.25)$$

When the plane of incidence is taken to the normal to $\bar{n}^i \times \bar{n}_s$,

$$\langle \sigma_{\infty}^{PQ} \rangle = \cos(\phi'/2) |R_p|^2 \delta_{PQ} \quad (2.26)$$

in which R_p is the Fresnel reflection coefficient and δ_{PQ} is the Kronicker delta.

Due to the surface roughness the contribution due to specular scattering is decreased by the factor $|\chi|^2$ (2.20). The surface roughness also gives rise to the diffuse scattering term

$$\langle \sigma^{PQ} \rangle_R = \sum_{m=1}^{\infty} \langle \sigma^{PQ} \rangle_{Rm}$$

$$= \sum_{m=1}^{\infty} \frac{2k_0}{\cos \theta_o^i} \int_{-\pi/2}^{\pi/2} \left| D^{PQ} \right|^2 P_2(\bar{n}^f, \bar{n}^i | \bar{n}) \cdot \exp(-v_n^2 \langle h_s^2 \rangle) \left(\frac{v_n}{2} \right)^{2m} \frac{W_m(v_T)}{m!} dy \quad (2.27)$$

where

$$\frac{W_m(v_T)}{2^{2m}} = \frac{1}{2\pi} \int_{-\infty}^{\infty} \langle h h' \rangle^m \exp(ik\tau) d\tau \quad (2.28)$$

in which v_n and v_T are the components of \bar{v} (2.7) normal and tangential to the surface of the unperturbed circular cylinder and $P_2(\bar{n}^f, \bar{n}^i | \bar{n})$ is the shadow function (Bahar and Barrick 1982).

3. Illustrative Examples

Assuming that the random rough (homogeneous and isotropic) surface height autocorrelation function $\langle hh' \rangle$ is a function of distance measured around the circumference of the unperturbed cylinder, we consider in the following examples the surface-height spectral density function $W(k)$ (2.23) given by (Rice 1951)

$$W(k) = \frac{2B(k-k_d)^4}{\pi[(k-k_d)^2 + \kappa^2]^4} \cdot k_d < k < k_c \quad (3.1)$$

where

$$k_d = 2/a \quad k_c = 4 k_0 \quad (3.2)$$

and $W(k)$ peaks for $k - k_d = \kappa = 0.3k_d$. The electromagnetic wavelength is

$$\lambda_0 = 10 \mu m \quad (3.3)$$

and the corresponding relative (complex) dielectric coefficient for aluminum is

$$\epsilon_r = -6000(1 + i) \quad (3.4)$$

(where an $\exp(i\omega t)$ time dependence for the fields is assumed). The radius of the unperturbed cylinder is

$$a = 2.5 \lambda_0 \quad (3.5)$$

The shadow function is a product of the unit step functions u

$$P_2(\vec{n}^f, \vec{n}^i | \vec{n}) = u(\vec{n}^f \cdot \vec{n}) u(-\vec{n}^i \cdot \vec{n}) \quad (3.6)$$

The constant B in (3.1) is determined by the surface roughness parameter

$$\beta = 4k_0^2 \langle h_s^2 \rangle = 1 \quad .$$

In Figs 3, 4 and 5 $\langle \sigma^{VV} \rangle$, $\langle \sigma^{HH} \rangle$ and $\langle \sigma^{HV} \rangle = \langle \sigma^{VH} \rangle$ are plotted for $\theta_0^i = 30^\circ$ as functions of ϕ' for cylinders with smooth (unperturbed) surfaces, (+) and random rough surfaces, (\square). The incident and scatter planes are normal to $-\vec{n}^i \cdot \vec{a}_y$ and $\vec{n}^f \cdot \vec{a}_y$ respectively. Note that for finitely conducting smooth cylinders $\langle \sigma^{VV} \rangle$ and $\langle \sigma^{HH} \rangle$ are very small for $\phi' = \pi/2$, and for $\phi' = 0$ these normalized cross sections are near unity. For the corresponding rough cylinder, the cross sections do not display the sharp minima and near normal incidence they are significantly less than unity. The cross-polarized cross sections $\langle \sigma^{VH} \rangle = \langle \sigma^{HV} \rangle$ are significantly different near normal incidence. For the smooth cylinder $\langle \sigma^{VH} \rangle$ vanishes for $\phi' = 0$, while it is about -5db for the rough cylinder. Thus as the surface roughness increases all three plots of the cross sections tend to flatten out (as functions of ϕ') except near grazing angles $\phi' \rightarrow \pi$ where the cross sections for the smooth and rough surfaces merge.

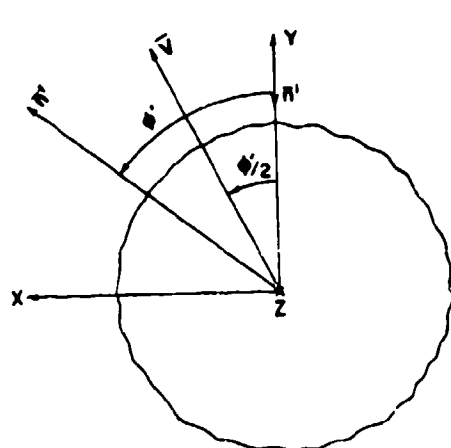
In conclusion, therefore, even a surface roughness corresponding to $\beta = 4k_0^2 \langle h_s^2 \rangle = 1$ cannot be ignored since it has the effect of making the scattered fields more isotropic and unpolarized. Using a perturbation approach to solve the problem one is restricted to values of $\beta < 0.1$ (Brown 1978). In this case the perturbation diffuse scattering term can be shown to correspond to the first term $\langle \sigma^{PQ} \rangle_{R1}$ in the expression for $\langle \sigma^{PQ} \rangle_R$. In this case, however, the effects of surface roughness are practically insignificant.

Acknowledgments

This investigation was sponsored by the U. S. Army Research Office, Contract No. DAAG-29-82-K-0123.

References

1. Bahar, E. (1981), "Scattering Cross Sections for Composite Random Surfaces--Full Wave Analysis," Radio Science, 16 (6), pp. 1327-1335.
2. Bahar, E., D. E. Barrick (1982), "Scattering Cross Sections for Composite Surfaces that Cannot be Treated as Perturbed Physical Optics Problems," Radio Science, Vol. 18, No. 2, pp. 129-137.
3. Bahar, E., G. G. Rajan (1979), "Depolarization and Scattering of Electromagnetic Waves by Irregular Boundaries for Arbitrary Incident and Scatter Angles Full Wave Solutions," IEEE Transactions on Antennas and Propagation, AP-27 (2), pp. 214-225.
4. Barrick, D. E. (1970), "Rough Surfaces in Radar Cross Section Handbook," Chapter 8, Plenum Press, New York.
5. Brown, G. S. (1978), "Backscattering From Gaussian-Distributed Perfectly Conducting Rough Surfaces," IEEE Transactions on Antennas and Propagation, AP-26 (3), pp. 472-482.
6. Rice, S. O. (1951), "Reflection of Electromagnetic Waves From a Slightly Rough Surface," Communication of Pure and Applied Math, Vol. 4, pp. 351-378.



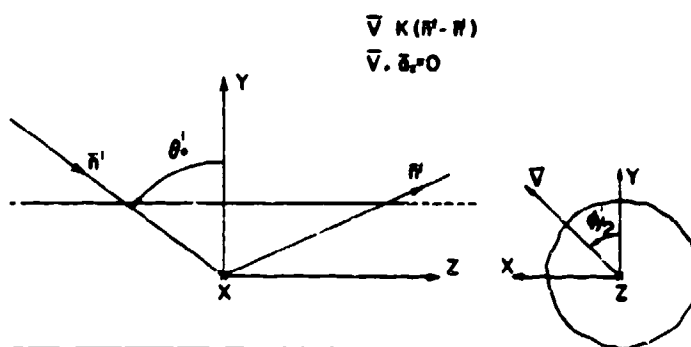
INCIDENT AND SCATTERED WAVES IN THE X-Y PLANE

Fig. 1

$$\theta^i = 0^\circ$$

$$\nabla = k (n^i - n^s)$$

$$\nabla \cdot \vec{E}_i = 0$$



PLANE WAVE INCIDENT IN THE Y-Z PLANE

Fig. 2

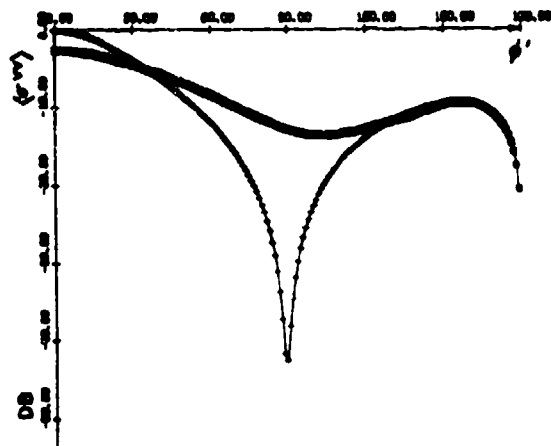


Fig. 3. $\langle \sigma^{VV} \rangle$, (2.24) smooth cylinder (+), rough cylinder (x)

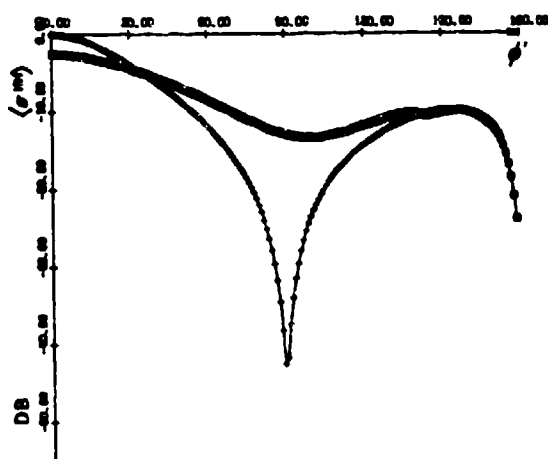


Fig. 4. $\langle \sigma^{HH} \rangle$, (2.24) smooth cylinder (+), rough cylinder (x)

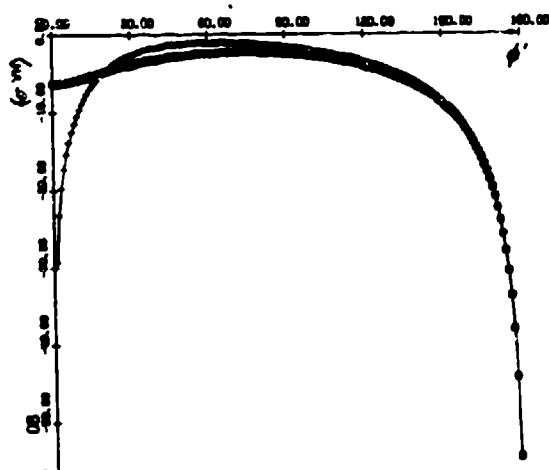


Fig. 5. $\langle \sigma^{VH} \rangle$, (2.24) smooth cylinder (+), rough cylinder (x)

BLANK

ANGULAR SCATTERING DISTRIBUTIONS
BY LONG COPPER AND BRASS CYLINDERS - EXPERIMENT AND THEORY

A. COHEN*, L.D. COHEN, AND R. HARACZ
Drexel University
Department of Physics and Atmospheric Science
Philadelphia, PA 19104

and

V. TOMASELLI, J. COLOSI AND K.D. MOELLER
Fairleigh Dickinson University
Teaneck, N.J. 07666

ABSTRACT

Experimental measurements of electromagnetic radiation scattered by long copper and brass cylinders were performed in the IR spectral range ($\lambda = 10.6 \mu\text{m}$). The cylinders were oriented essentially normal to the scattering plane. The results of the measurements were compared with the theory for infinite cylinders modified for relatively large refractive indices. The good agreement is presented and discussed.

INTRODUCTION

The scattering by infinitely long cylinders is characterized by its two dimensional angular scattering surface forming an envelope of a cone. The opening angle of the cone ϕ^* is related to the tilting angle $\phi^+ = \frac{\pi}{2} - \phi^*$, and the scattering surface reduces to a plane when the incident light is perpendicular to the cylinder axis. Experimental scattering measurements involving long cylinders thus become very sensitive to the orientation angle of the cylinder axis relative to a measuring plane, the last being determined by the rotation axis of the detector.

In the visible range angular scattering measurements for long dielectric fibers have been reported^{2,3} which show good agreement between the polarization ratio and the theory. The polarization ratio measurements permit inaccuracies in the alignment of the fibers since the same reduction in the light intensity is expected in both polarizations (I_1 and I_2).

On the other hand long tilted cylinders have different scattering patterns for each tilting angle and, therefore, comparisons between experiments and theoretical predictions should take the tilting angle into account. For such measurements, an accurate experimental setup is required to allow the comparison between relative scattering intensities and the theory.

* On leave from the Hebrew University, Department of Atmospheric Sciences, Jerusalem, Israel

Below we present the experimental curves of CO₂ laser radiation scattered by a carefully oriented copper cylinder, and a brass cylinder the orientation of which was slightly different.

Since the materials discussed have very large real and imaginary parts of refractive indices, the scattering theory has been modified to include large refractive indices.

The agreement between the theory for infinite cylinders and real metallic particles suggest that in the IR the theory can serve as an accurate predictor to the scattering properties of materials with long cylindrical shape. In particular, this result is shown to be applicable for materials of large refractive indices for which the basic assumptions of the approximated the ^{4,5} for finite cylinders are not satisfied.

THEORETICAL CALCULATIONS OF EM SCATTERING BY LONG CYLINDERS OF LARGE INDICES OF REFRACTION

The far-field scattering of infinite tilted cylinders is given by^{5,1,6}

$$I_{11} = [2/(k_0 \pi r)] |b_{0I} + 2 \sum_{n=3} b_{nI} \cos(n\theta)|^2 \quad (1)$$

$$I_{12} = I_{21} = [2/(k_0 \pi r)] |2 \sum_{n=1} a_{nI} \sin(n\theta)|^2 \quad (2)$$

and

$$I_{22} = [2/(k_0 \pi r)] |a_{0II} + 2 \sum_{n=1} a_{nII} \cos(n\theta)|^2 \quad (3)$$

The first index in I_{ij} refers to the polarization of the incidence light relative to the incident plane, and the second - the polarization of the scattered light relative to the scattering plane. For detailed definitions of the incident and the scattering planes, and the expressions for an arbitrary incident polarization, see ref.6. The angle θ is the scattering angle, and b_{nI} can be reduced to:

$$b_{nI} = \frac{A J_n(\alpha) + [B J'_n(\alpha) - m^2 C J_n(\alpha)] [-B H'_n(\alpha) - C H_n(\alpha)]}{A H_n(\alpha) + [B H'_n(\alpha) - m^2 C H_n(\alpha)] [-B H'_n(\alpha) - C H_n(\alpha)]} \quad (4)$$

where

$$A = (n\ell/\alpha)^2 h^2 (m^2 - 1)^2 H_n(\alpha) J_n^2(\beta); \quad B = \ell j^2 J_n(\beta); \quad C = \ell^2 j J'_n(\beta).$$

$J_n(\alpha)$ and $H_n(\alpha)$ are the Bessel and Hankel functions of order n ; $\alpha = \frac{2\pi a \cos\phi}{\lambda}$ is the "tilted" size parameter (a is the cylinder radius, λ the incident wavelength and ϕ is the tilting angle); m is the complex refractive index; $h = \sin\phi$; $\ell = \cos\phi$; $j = (m^2 - \sin^2\phi)^{1/2}$, and $\beta = \frac{1}{\ell}\alpha$.

The infinite sums in eqs.(1) - (3) can be truncated a few terms after the order exceeds the "tilted" size parameter, since $J_n(\alpha) \rightarrow 0$ for $n > \alpha$ (n, α large). For example, it is generally agreed that for $\alpha \gtrsim 1$ the number of terms in (1) - (3) is of the order of $N = 1.2\alpha + 5$. Therefore, when m is large (i.e., $m > 10$), the argument in $J_n(\beta)$ satisfies $\beta \gg n$ for all b_{nI} in (1), or⁷

$$J_n(\beta) \sim (2/\pi\beta)^{1/2} [\cos(\beta - \frac{1}{2}n\pi - \frac{1}{4}\pi)] + (|\beta|^{-1}) \quad (5)$$

For copper and brass cylinders $m = 12-50i$ and $5.8-29i$ respectively (see below). It follows that for any size parameter $\alpha = \frac{2\pi a \cos\phi}{\lambda}$ larger than 1, $\text{Im}(\beta)$ becomes so large that $J_n(\beta)$ cannot be calculated since it contains the term $\exp\{+\text{Im}(\beta)\}$. Hence, in order to calculate the scattering function for those materials, the expression for b_{nI} has to be modified:

Dividing equation (4) by B^2/B^2 we get

$$b_{nI} = \frac{\frac{A}{B^2} J_n(\alpha) + [J'_n(\alpha) - m^2 \frac{C}{B} J_n(\alpha)] [-H'_n(\alpha) - \frac{C}{B} H_n(\alpha)]}{\frac{A}{B^2} H_n(\alpha) + [H'_n(\alpha) - m^2 \frac{C}{B} H_n(\alpha)] [-H'_n(\alpha) - \frac{C}{B} H_n(\alpha)]} \quad (6)$$

The ratio $\frac{C}{B}$ is the only term containing $J_n(\beta)$ and $J'_n(\beta)$

$$\frac{C}{B} = \frac{l J'_n(\beta)}{J J_n(\beta)} \quad (7)$$

For the large values of β , $J'_n(\beta)$ can be approximated to⁷

$$J'_n(\beta) \sim - (2/\pi\beta)^{1/2} \sin(\beta - \frac{1}{2}n\pi - \frac{1}{4}\pi) \quad (8)$$

or

$$\frac{C}{B} \sim \pm \frac{l}{J} \quad (I_m(\beta) < 0) \quad (9)$$

We note that for $m \rightarrow \alpha$, b_{nI} reduces to the known ratio¹ $b_{nI} \rightarrow J_n(\alpha)/H_n(\alpha)$. Similar expressions can be derived for a_{nII} .

When the cylinder axis is not perpendicular to the measurement plane (see Discussion), the scattering intensities calculated by eqs.(1) - (3) will have their maximal intensities within the envelope of a cone formed around the cylinder axis. In the event that the tilt angle between such a cylinder and

the normal plane to the incident direction is $\phi^\dagger = 0$, the scattering plane will form an angle ϕ relative to the measurement plane.

The comparison between theory and experiment for $\phi \neq 0$ becomes then dependent on the opening angle of the light source and its cross sectional variation of intensity (usually Gaussian). Here, we discuss quantitatively the case of $\phi_1 = 0$ (copper), and qualitatively the scattering from the brass cylinder for which $\phi \neq 0$ but $\lesssim 3^\circ$.

EXPERIMENTAL DETAILS

Figure 1 is a schematic diagram of the apparatus used to obtain the scattering data. The source of radiation is a Spectra Physics Model 950 CO_2 laser ($10.6 \mu\text{m}$ output) operated with temperature controlled cooling water. The incident beam is chopped (220 Hz) for phase sensitive detection. Scattered radiation is detected by a liquid nitrogen cooled PbSnTe (Barnes Engineering Co., Model 503) photovoltaic detector. The detector chamber is mounted on a rotating support platform having an arm radius $a = 48 \text{ cm}$. Because of structural limitations of the platform frame, the range of scattering angle values is $\sim 15^\circ$ to 50° . A synchronous motor drives the detector arm of the apparatus at a scan rate of $2^\circ/\text{min}$. The detector signal is amplified using a Princeton Applied Research Model 128 amplifier and displayed on a Leeds & Northrup strip chart recorder.

The targets used in this experiment were a copper wire ($242 \mu\text{m}$) and a brass wire ($150 \mu\text{m}$), whose composition was 70% copper, 30% zinc. The corresponding size parameters ($\alpha = \pi d/\lambda$) were 71.7 and 44.5 respectively. Wire targets were cemented in angular rings which were compressed slightly during the drying of the cement. Upon relaxation of the compressed ring, the wire is subject to a slight tension so that its cylindrical shape is insured. The mounted wire target is then clamped in a holder so that its axis is colinear with that of the rotation axis of the detector chamber. The laser beam diameter is 4.5 mm at the a^{-2} field points and the beam divergence is less than 3.5 m rad .

All measurements were made with the laser beam incident perpendicular to the axis of the target cylinder. Since the laser is vertically polarized, the electric field of the incident radiation is parallel to the cylinder axis. Scattered radiation was also detected in a plane perpendicular to the target axis.

There are several sources of experimental error inherent in this apparatus and type of measurement. The diameters of the wires were measured using a traveling microscope to $\pm 1\%$. Uncertainty in measuring the scattering angle is estimated to be $2^\circ - 3^\circ$. A collimator with variable aperture iris is mounted at the entrance to the detector chamber and serves to limit the spread in angles, $\Delta\theta$, that the detector can receive. With the iris at maximum aperture, $\Delta\theta = 4.8^\circ$. Measurements were usually made with the aperture closed down from its maximum diameter although no significant differences were observed in

doing so.

Alignment of the wire axis relative to the polarization direction of the electric field is estimated to be within $\sim 3^\circ$. This assumes that the laser output is vertically polarized. Because of the type of wire mounts used, deviation from the zero tilt angle is probably 2° .

Other sources of error which affect the level of the output signal are of somewhat less significance for this experiment. Figures 2a and 3a show that the noise level is quite low. This was accomplished by using a low-noise transformer inserted between the detector output and the amplifier. The traces shown represent data recorded with the instrument settings chosen to optimize the signal-to-noise level. Repeated tracings were reproducible with respect to curve contour and maxima/minima points. However, the relative intensity of the overall trace was subject to vertical drifting on the chart. Part of this uncertainty was attributed to drift of the laser output. Even with the temperature controlled coolant ($18.0 \pm 1^\circ\text{C}$) circulating around the laser tube at the recommended flow rate, some output signal drift was observed after a one hour warm-up period. Consequently, the procedure adopted was to allow all components to warm up for two hours before data were recorded.

OPTICAL CONSTANTS OF TARGET MATERIALS

The optical constants of several metals from infrared to far-infrared wavelengths have recently been tabulated by M.A. Ordal, et al.⁸ Both n and k are rapidly increasing functions of wavelength in the infrared region. For pure copper at $10.6 \mu\text{m}$, representative values are $n \approx 12$ and $k \approx 60$. The brass target wire used has a Cu/Zn ratio of 70/30. For metals at low frequencies, the optical constants can be approximated by⁹

$$n \approx k \approx \sqrt{\lambda / 2\omega\epsilon_0\rho} \quad (9)$$

where ρ is the static resistivity, ω is the angular frequency, and ϵ_0 is the permittivity of free space. Since the resistivities of metals and alloys are easily found, we used the above approximation together with the tabulated data¹⁰ for ρ to obtain the optical constants. The results for brass at $10.6 \mu\text{m}$ are $n \approx 5.8$ and $k \approx 29$.

The experimental data were taken for wires of various sizes. Figures 2a and 3a represent the angular scattering results from copper of diameter $242 \mu\text{m}$ and brass of diameter $150 \mu\text{m}$, respectively.

RESULTS AND DISCUSSION

The theoretical calculations for the copper wire ($a = 121 \mu\text{m}$) show that the general angular scattering as well as the accurate angular values of the maxima and minima are predictable by means of the

infinite theory. This is clearly shown in comparing the experimental with the theoretical results in Fig.2. The accurate match shows that the experiment was performed in such a way that the scattering plane and the measurement plane coincided to permit the angular measurements in the same relative units. It is important to note that the general behavior is very sensitive to the size parameter and, therefore, provides an accurate method for the determination of the size of the scatterer. However, the scattering intensities of the different metallic cylinders are relatively insensitive to changes in the refractive index. This suggests that many properties can be approximately derived by inserting $m \gg 1$ in the scattering equations.

In the case of the brass cylinder (the experimental results are given in Fig. 3a and the theoretical in Fig.3b) the scattering angles for which maxima and minima occur can be predicted, but the general behavior of the experiment (a decreasing envelope) is different than the theoretically predicted increasing envelope. However, the theoretical prediction was calculated for a scattering plane that is perpendicular to the cylinder axis. In the event that the wire is not perpendicular to the measurement plane, having an orientation angle of $(\frac{\pi}{2} - \phi)$, the scattering directions will be tilted relative to the measurement plane with a varying tilt angle against the scattering angle.

As can be seen in Fig.4, this varying angle reaches its maximum at $\theta = \frac{\pi}{2}$ where it equals ϕ . More specifically, denoting the measured scattering angle by θ and the varying tilt angle by ϕ' , we get

$$\tan \phi' = \sin \theta \tan \phi \quad (10)$$

The larger the angle ϕ' is, the less is the overlap between the scattering plane F.O.V. and the measurement plane F.O.V. resulting qualitatively in a general decrease of the scattering intensity with increasing θ in the interval $0 \leq \theta \leq \frac{\pi}{2}$.

When $\phi \neq 0$, the scattering angle must also be modified. Denoting the scattering angle in a plane perpendicular to the cylinder by θ' , the following relations hold (see Fig.4):

$$\sin \phi' = \sin \theta' \sin \phi, \quad \sin \theta' = \frac{\cos \phi'}{\cos \phi} \sin \theta \quad (11)$$

As stated in the section describing the experiment, the orientation of the wire is uncertain to within 3° . Thus, $\phi \leq 3^\circ$, and as $\phi' \leq \phi$, the deviation between θ' and θ is less than the accuracy in the measurement of the scattering angle ($\Delta\theta = 4.8^\circ$). Therefore, this effect was not included in the calculation.

As already mentioned, the theoretical intensity pattern for scattering from an infinite cylinder is mainly restricted to the plane perpendicular to the cylinder axis, and the intensity falls off sharply

at even small angular deviations from this plane. This is true even for finite cylinders of aspect ratios larger than 20 as shown in Ref.4. Thus, the varying values of ϕ' allowed by this experiment are sufficient to gradually lower the theoretical intensity pattern as a function of the scattering angles. This explains the apparent discrepancy between the results given in Figures 3a and 3b.

REFERENCES

1. M. Kerker, The Scattering of Light, (Academic Press, N.Y., 1969).
2. W.A. Farone and M. Kerker, J.O.S.A 56, 481 (1966).
3. D. Cooke and M. Kerker, Rev. Sci. Instr. 39, 1111 (1968).
4. L.D. Cohen, R.D. Haracz, A. Cohen, and C. Acquafredda, Appl. Opt. 21, 742 (1983).
5. J.R. Wait, Electromagnetic Radiation from Cylindrical Structures, (Pergamon Press, Oxford, 1959).
6. A. Cohen, Opt. Lett. 5, 150 (1980).
7. M. Abramowitz and A. Stegun, Eds, Handbook of Mathematical Functions (Dover Publications, N.Y., 1972); 9.2., and 9.2.11.
8. M.A. Ordal, et al., Appl. Opt. 22, 1099 (1983).
9. G.R. Fowles, Introduction to Modern Optics, (Holt, Rinehart, and Winston, N.Y., 1975); chapter y.
10. Metals Reference Handbook, 5th ed, C.J. Smithells, ed. (Butterworth, London, 1976); p.1035.

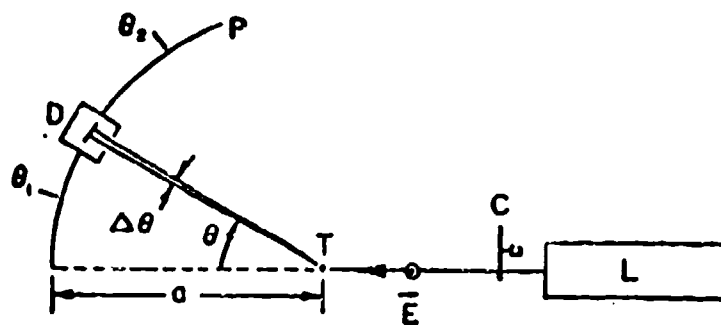


Fig 1.

Fig.1. Schematic diagram of the apparatus; top view: L - laser, C - chopper, T - target, $a (= 48 \text{ cm})$ - radius of path (P), of detector (D), θ - scattering angle in the measurement plane, $\Delta\theta$ - range of scattering angles accepted by the detector chamber. The electric field of the incident beam, \vec{E} , is shown perpendicular to the plane of the diagram and parallel to the axis of the target. The angles θ_1 and θ_2 indicate minimum and maximum angles of the scan of the detector.

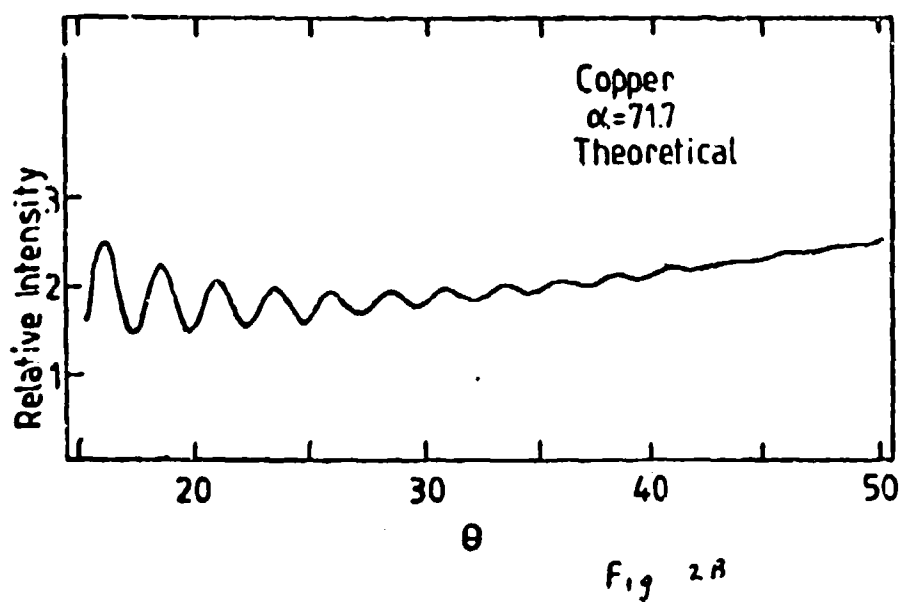
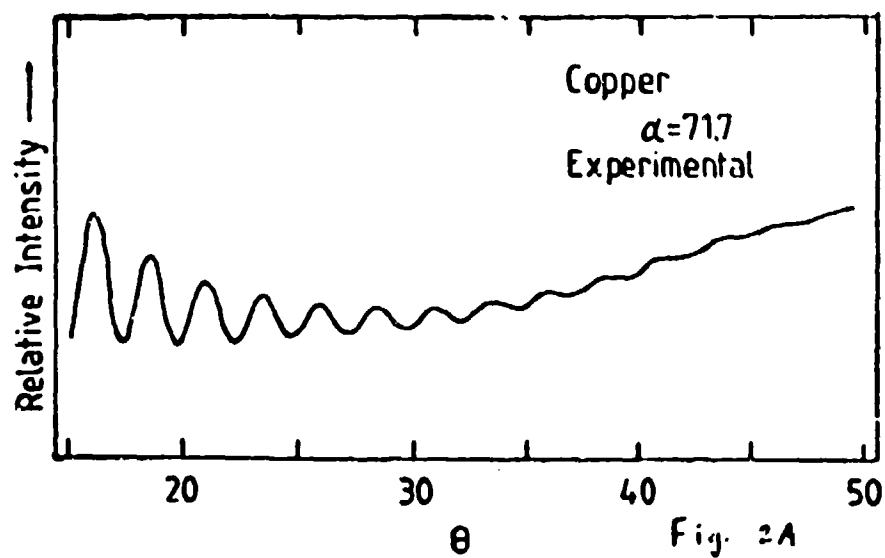


Fig. 2. Distribution of the scattered laser radiation as a function of the scattering angle for the copper wire target. The size parameter is $\alpha = 71.7$, $m = (12, -60i)$, and $\phi = 0^\circ$. The incident light is polarized with E parallel to the cylinder axis. a) experiment; b) theory.

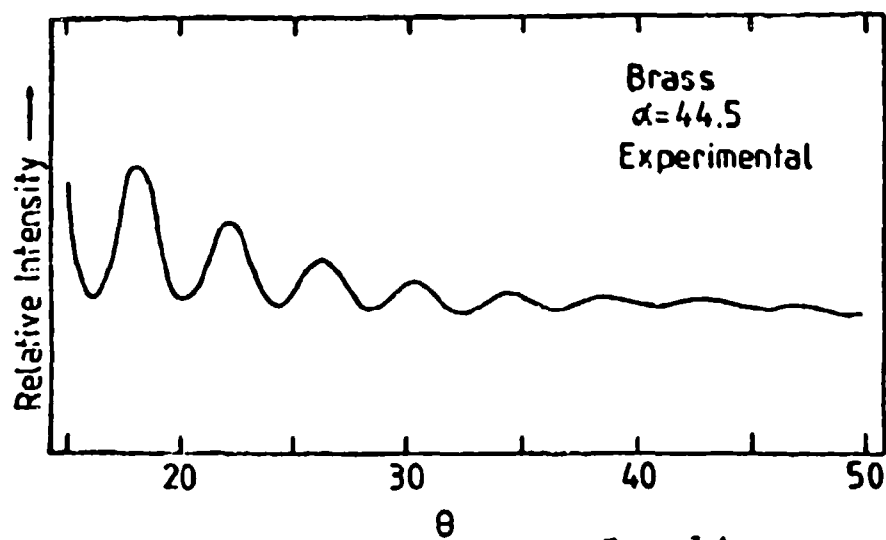


Fig. 3 A

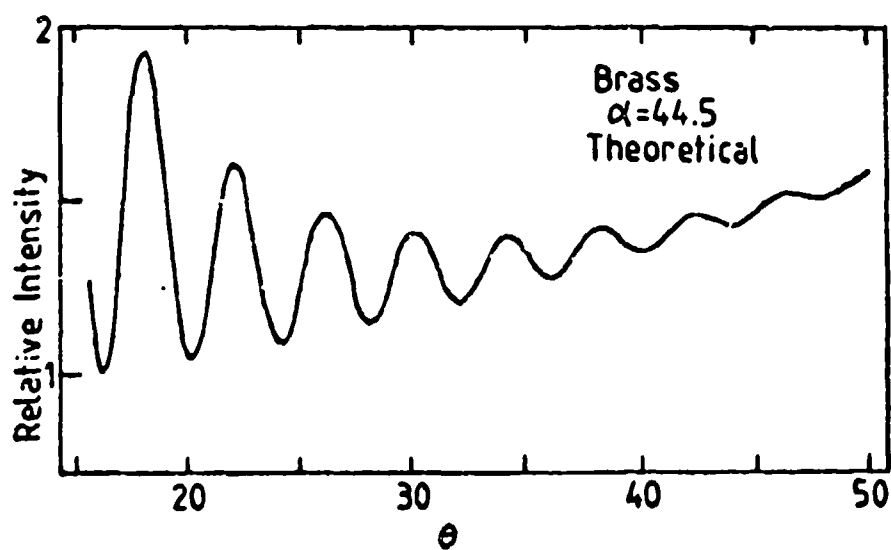


Fig. 3 B

Fig.3. Distribution of scattered laser radiation as a function of the scattering angle for the brass wire target. The size parameter is $\alpha = 44.5$, $m = (5.8, -291)$, and the orientation angle $\phi \approx 3^\circ$ (see text). a) experiment; b) theory.

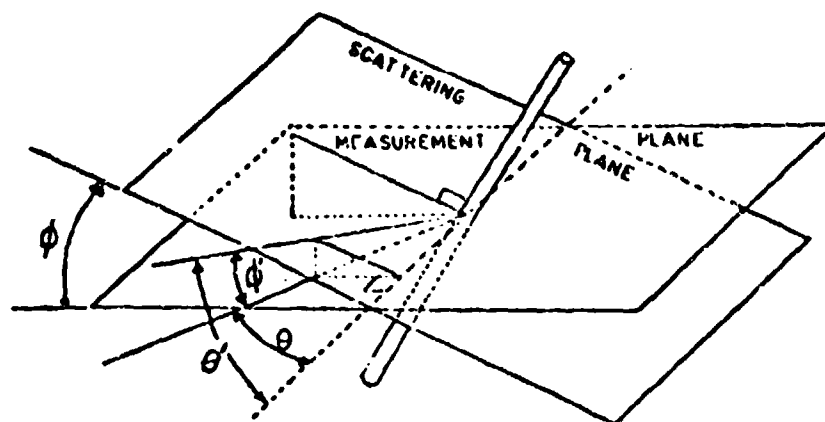


Fig. 4

Fig.4. Geometry of the orientation angle ϕ . ϕ is the angle between the measurement plane (containing the incident direction and the detector direction) and the scattering plane (containing the incident direction and perpendicular to the cylinder). θ is the angle of the detector arm, and θ' is the angle in the scattering plane marking the direction of maximal intensity. ϕ' is the angle between the detector arm and the corresponding direction of the maximal intensity.

BLANK

Recent Results in the Scattering and Absorption
by Elongated Conductive Fibers

By

M. E. Pedersen
J. C. Pedersen
P. C. Waterman

Panametrics, Inc.
221 Crescent Street
Waltham, MA 02254

Abstract

This paper deals with electromagnetic scattering and absorption by thin fibers having arbitrary length, orientation, and electrical conductivity. This and related work have been published and presented as follows:

M. E. Pedersen, J. C. Pedersen and P. C. Waterman, Final Report on Theoretical Investigation of Absorptive Processes, Prepared by Panametrics, Inc. for U.S. Army Chemical Systems Laboratory (Dec. 21, 1982).

J. C. Pedersen, M. E. Pedersen and P. C. Waterman, "Electromagnetic Theory of Scattering and Absorption from Finite Elongated Objects," Proceedings of the 1983 CSL Conference on Obscuration and Aerosol Research (submitted Sept. 1983).

M. E. Pedersen, J. C. Pedersen and P. C. Waterman, "Recent Results in the Scattering and Absorption by Elongated Conductive Fibers," presented at the 1984 CRDC Conference on Obscuration and Aerosol Research (June 1984).

M. E. Pedersen, J. C. Pedersen and P. C. Waterman, Final Report on Theoretical Study of Single and Multiple Scattering by Cylinders, prepared by Panametrics, Inc. for U.S. Army Chemical Systems Laboratory (Sept. 27, 1984).

Although further development is planned, the associated computer programs are now developed to the point where various specific fiber parameters, such as tabulated optical constants, can be utilized.

1.0 INTRODUCTION AND SUMMARY

In this paper we present theoretical results obtained in the areas of single scattering and absorption of electromagnetic radiation by arbitrarily oriented conductive fibers, and in radiative transfer by large aggregates of such fibers.

It has been determined that, in the case of single scattering and absorption, the theory in its present form is capable of producing reliable results over a very wide range of length-to-wavelength ratio. An asymptotic expression is given for the backscatter cross section in the large length-to-wavelength ratio limit. In the small (Rayleigh) limit, it is shown that a previous theory by two of the authors is in agreement with the more complex present theory. Two classes of cases have been identified in which the present theory is in error. In practical computations, these cases can be easily avoided without substantial loss of information.

The detailed differential scattering cross sections have been appropriately averaged for input to a Radiative Transfer computer program, which we have developed concurrently and which is presented elsewhere in these Proceedings.

2.0 ELECTROMAGNETIC PROPERTIES OF CONDUCTIVE FIBERS

2.1 Basic Theory

This theory is based upon a variational procedure first set forth by Tai for perfectly conducting wires,¹ and later extended to the case of finite conductivity by Cassedy and Fainberg, who, however, considered only broadside incidence.² In the present theory, scattering, absorption, extinction, and radar cross sections are calculated for arbitrary angles of incidence. The results can then be averaged over all angles of incidence to obtain results for a cloud of randomly oriented particles.

Consider a plane electromagnetic wave incident upon a cylindrical wire of finite conductivity at arbitrary angle of incidence, θ_i , and arbitrary polarization angle, ψ , as shown in Fig. 1. Assuming the wire is sufficiently thin for the current to be radially symmetric, one may consider the current as a current filament $I(z)$ along the axis. Since the wire is assumed to be thin, only the component of the electric field parallel to the axis will stimulate a response, and the integral equation for the boundary condition at the cylinder surface may be written

$$E_0 \sin \theta_i \cos \psi e^{jkz \cos \theta_i} = I(z)Z + \frac{1}{2\pi} \int_0^{2\pi} d\phi' \int_{-h}^h I(z') \left(1 + \frac{\partial^2}{k^2 \partial z'^2} \right) \frac{e^{-jkR}}{R} dz' d\phi' \quad (1)$$

Here, Z is the skin impedance per unit length of the cylinder, relating E_θ to E_z , and is given by³

$$Z = \frac{g}{2\pi a(\sigma + j\omega\epsilon)} \left(\frac{I_0(ga)}{I_1(ga)} \right) \quad (2)$$

where

$$g^2 = \omega^2 [(\mu_0 \epsilon_0 \cos^2 \theta_i - \mu\epsilon) + \frac{j\mu\sigma}{\omega}] \quad (3)$$

$I_0(ga)$ and $I_1(ga)$ are modified Bessel functions. It may be noted that the real part of g^2 may become important in the visible region. In Eq. (1)

$n = \mu_0/\epsilon_0$ is the characteristic impedance of free space, and

$$R = \sqrt{(z-z')^2 + 4a^2 \sin^2 \left(\frac{\phi - \phi'}{2} \right)}$$

A stationary homogeneous functional expression can now be constructed for the current in terms of the backscattered amplitude S , giving

$$\frac{1}{S} = \frac{\frac{k}{2\pi} \int_0^{2\pi} d\phi \int_{-h}^h \int_{-h}^h I(z)I(z') \left(1 + \frac{\partial^2}{k^2 \partial z'^2} \right) \frac{e^{-jkR}}{R} dz' dz - \frac{4\pi jZ}{\eta} \int_{-h}^h I^2(z) dz}{\left[k \sin \theta_i \int_{-h}^h I(z) e^{jkz \cos \theta_i} dz \right]^2} \quad (4)$$

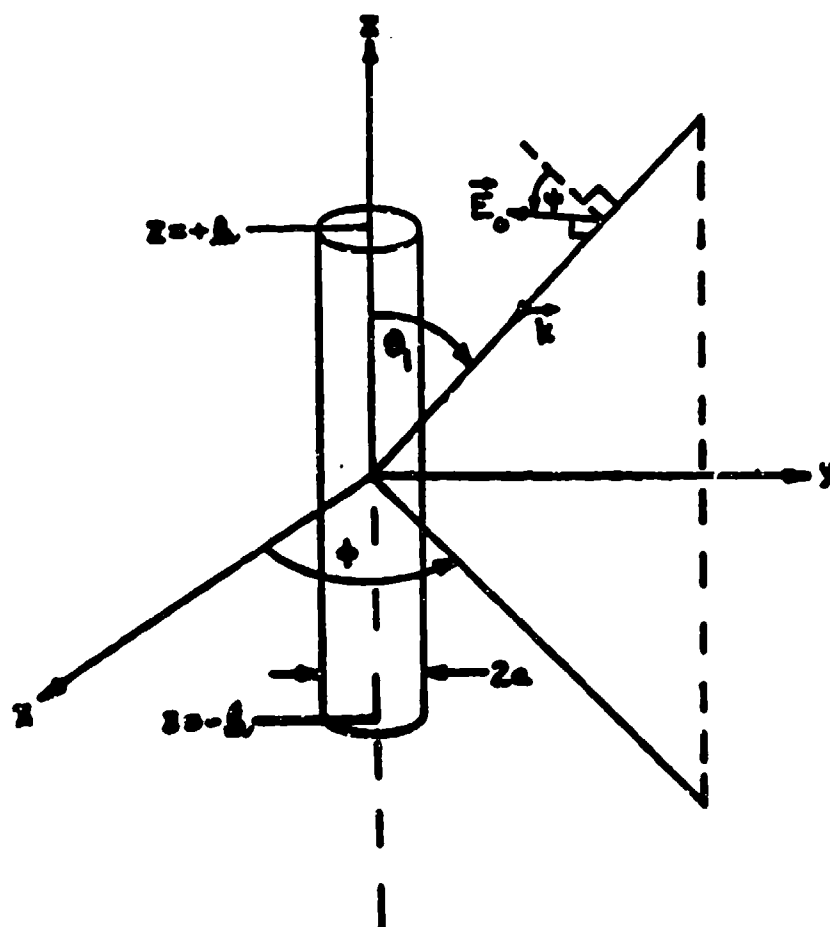


Fig. 1 Geometry of the cylindrical wire with respect to the propagation vector k , and the electric field vector, E . θ_1 is the angle between k and the z axis; φ is the angle E makes with the k - z plane.

For the current function, we choose that given by Tai¹

$$I = I_0 [f_0(z) + A f_s(z)] \quad (5)$$

where

$$f_0(z) = \cos kz \cos qz - \cos z \cos qkz \quad (6)$$

and

$$f_s(z) = \sin kz \sin qz - \sin z \sin qkz. \quad (7)$$

where $q = \cos \theta_1$ and $\pi = kh$. Note that both $f_0(z)$ and $f_s(z)$ vanish at $z = \pm h$, which is appropriate if the current is to be zero at the end of the fiber.

Using the variational technique, we set

$$\frac{\partial \left(\frac{1}{A} \right)}{\partial A} = 0$$

and obtain for A

$$A = \frac{g_s (\gamma_c - \lambda_c)}{g_c (\gamma_s - \lambda_s)} \quad (8)$$

where

$$g_c = k \sin \theta_1 \int_{-h}^h f_c(z) e^{jkz \cos \theta_1} dz \quad (9)$$

$$g_s = k \sin \theta_1 \int_{-h}^h f_s(z) e^{jkz \cos \theta_1} dz \quad (10)$$

$$\lambda_c = \frac{4\pi jZ}{\eta} \int_{-h}^h f_c^2(z) dz \quad (11)$$

$$\lambda_s = \frac{4\pi jZ}{\eta} \int_{-h}^h f_s^2(z) dz \quad (12)$$

$$\gamma_c = \frac{k}{2\pi} \int_0^{2\pi} d\phi \int_{-h}^h \int_{-h}^h f_c(z) f_c(z') \left(1 + \frac{1}{k^2} \frac{\partial^2}{\partial z'^2} \right) \frac{e^{-jkR}}{R} dz dz' \quad (13)$$

$$\gamma_s = \frac{k}{2\pi} \int_0^{2\pi} d\phi \int_{-h}^h \int_{-h}^h f_s(z) f_s(z') \left(1 + \frac{1}{k^2} \frac{\partial^2}{\partial z'^2} \right) \frac{e^{-jkR}}{R} dz dz' \quad (14)$$

Equations (9) through (14) have been evaluated analytically. Having determined A, the general, far-field scattered amplitude can be written as

$$\begin{aligned}
S(\theta, \theta_1) = & 2\sqrt{1-p^2} \left\{ \frac{B_c}{(\gamma_c - \lambda_c)} \left[\frac{\cos qx}{(1-p^2)} (\sin x \cos px - p \cos x \sin px) \right. \right. \\
& - \frac{\cos x}{(q^2 - p^2)} (q \sin qx \cos px - p \cos x \sin px) \Big\} \\
& + j \frac{B_s}{(\gamma_s - \lambda_s)} \left\{ \frac{\sin qx}{(1-p^2)} (p \sin x \cos px - \cos x \sin px) \right. \\
& - \frac{\sin x}{(q^2 - p^2)} (p \sin qx \cos px - q \cos qx \sin px) \Big\}
\end{aligned} \quad (15)$$

where $p = \cos \theta$, θ being the scattering angle.

By definition, the differential scattering cross section is then given by

$$\begin{aligned}
\sigma(\theta, \theta_1) &= R_0^2 \left| \frac{E_{S\theta}}{E_0} \right|^2 \\
&= \frac{1}{k^2} \left| S(\theta, \theta_1) \right|^2
\end{aligned} \quad (16)$$

The total scattering cross section is

$$\sigma_s = \frac{2\pi}{k^2} \int_0^\pi \left| S(\theta, \theta_1) \right|^2 \sin \theta d\theta. \quad (17)$$

The extinction cross section is defined by the well-known forward amplitude theorem as

$$\sigma_e = \left(\frac{4\pi}{k^2} \right) \text{Im} \{ S(\pi - \theta_1, \theta_1) \} \quad (18)$$

The absorption cross section is just the rms power absorbed in the scatterer divided by the rms intensity of the incident beam. The rms power absorbed in the wire is given by

$$P_A = P_0(Z) \int_{-h}^h \left| I(z) \right|^2 dz$$

and the rms intensity of the θ component of the incident beam is

$$I_{\theta} = \frac{E_o^2}{2\eta}$$

so that the absorption cross section is given by

$$\sigma_a = \frac{2\eta \operatorname{Re}(Z)}{E_o^2} \int_{-h}^h |I(z)|^2 dz. \quad (19)$$

Finally, the radar cross section is defined to be

$$\begin{aligned} \sigma_{\text{RCS}} &= 4\pi \sigma(\theta_i, \theta_i) \\ &= \frac{4\pi}{k^2} |S(\theta_i, \theta_i)|^2 \end{aligned} \quad (20)$$

Equations (16-20) are for polarization in the k - z plane, i.e., $\phi = 0^\circ$.

The results achieved by using the above equations will be discussed in the following section. It appears at this time that this theory may be valid for kh values much larger than 30.

3.0 RESULTS

In the following pages, we present the results of a detailed investigation to determine the validity of the present theory in various parametric regimes. Although this investigation is still in progress, we believe that the results presented below demonstrate that, with certain specified restrictions, the present theory is capable of providing good results over very wide ranges of parameters. Specific questions to be addressed in the foregoing pages are:

- (a) Over what range of kh is the theory useful?
- (b) In the limit of very large kh , do the differential scattering patterns give reasonable results?
- (c) Assuming that the theory is well behaved in the $kh \gg 1$ limit, can one obtain simplified asymptotic expressions for the various cross sections?
- (d) How do these asymptotic expressions compare with those which can be obtained from infinite length cylinder calculations?
- (e) Do the results agree with Rayleigh theory in the appropriate limit?

In the remainder of this Section, we present results which demonstrate good asymptotic behavior in the large kh limit, as well as good quantitative agreement with published experimental data and with Rayleigh theory.

3.1 Differential Scattering Cross Section

In this sub-section we present computed curves of differential scattering cross section per square wavelength (σ_{diff}/λ^2) as a function of scattering angle θ . It is important to note (see Fig. 1) that the scattering angle is measured with respect to the cylinder axis, as is the angle of incidence θ_i . In all cases, the electric field is in the plane of the incident k vector and the cylinder axis.

In Figs. 2 through 9, the incident wavelength is 3.14 mm and the cylinder radius is 3.0 micron ($ka = 6 \times 10^{-3}$). The electrical conductivity is 3×10^4 mho/m. These parameters are representative of graphite fibers illuminated by a 3 mm plane wave.

3.1.1 Behavior as a Function of kh

Figures 2, 3, 4 and 5 show the behavior of the scattering pattern for three values of kh , where h = half length. In Fig. 2, $kh = 1$. This particle should, therefore, scatter like a simple dipole and we see from the figure that this is indeed

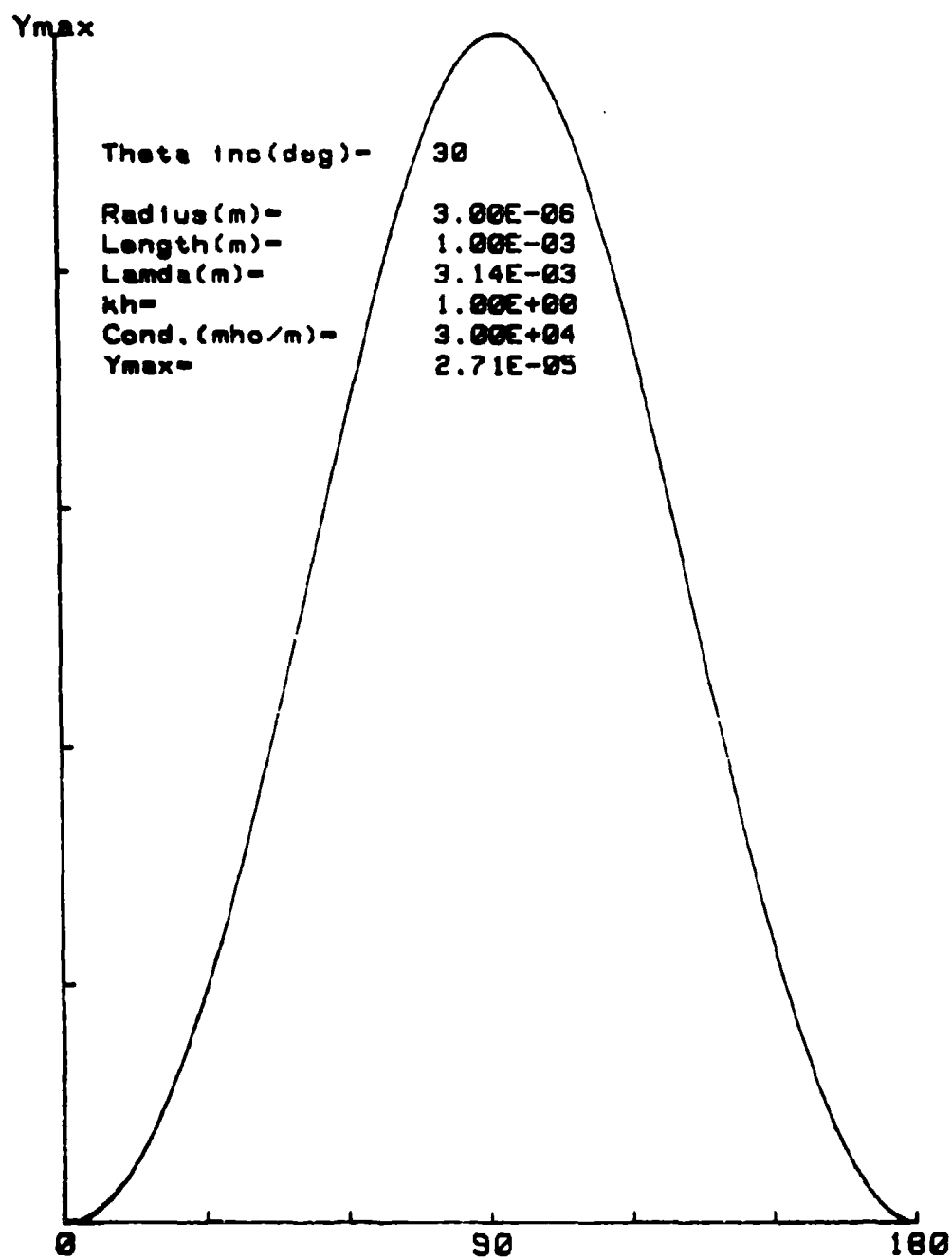


Fig. 2 Differential cross section/ λ^2 for $\theta_i = 30^\circ$; $kh = 1$.

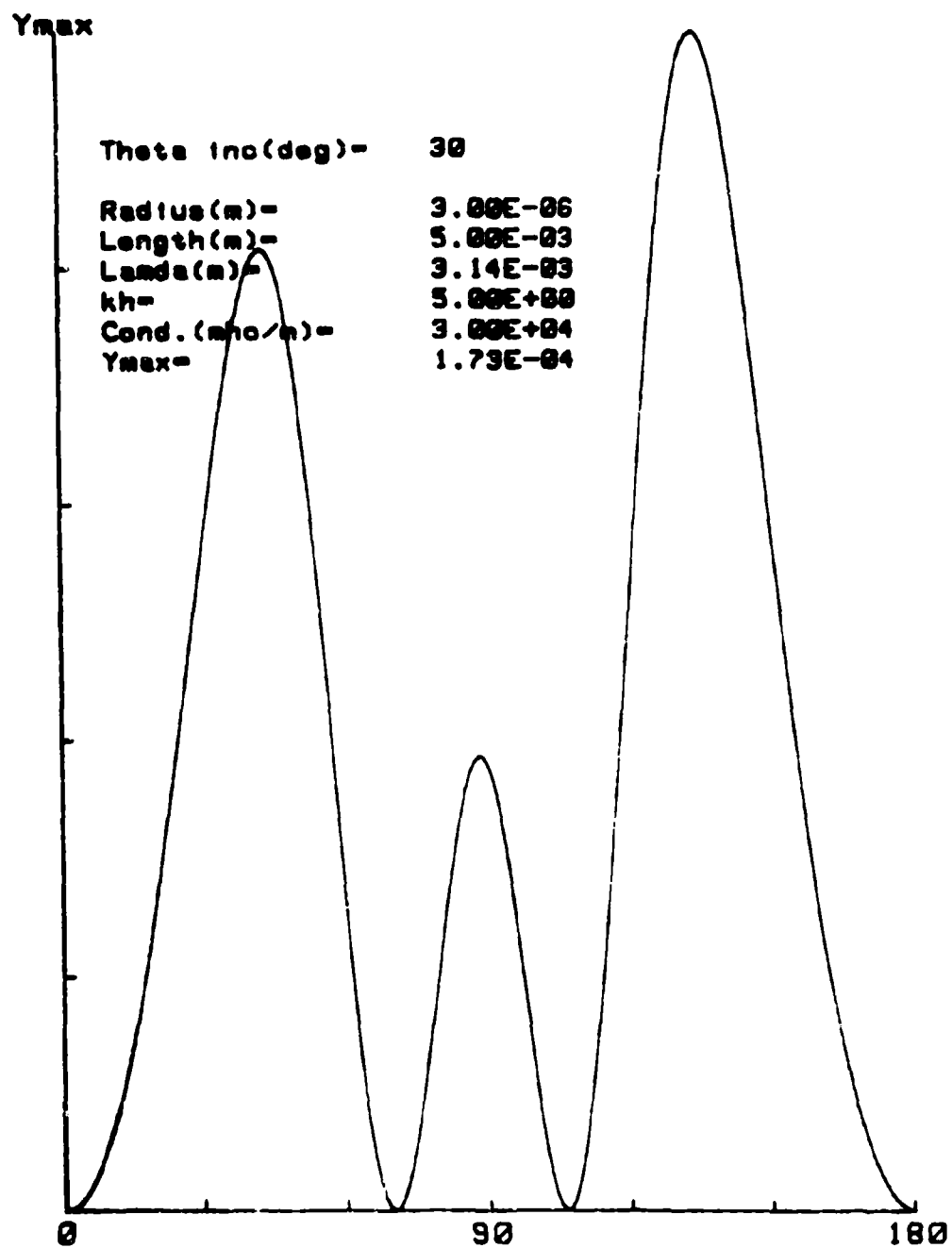


Fig. 3 Differential cross section/ λ^2 for $\theta_1 = 30^\circ$; $kh = 5$.

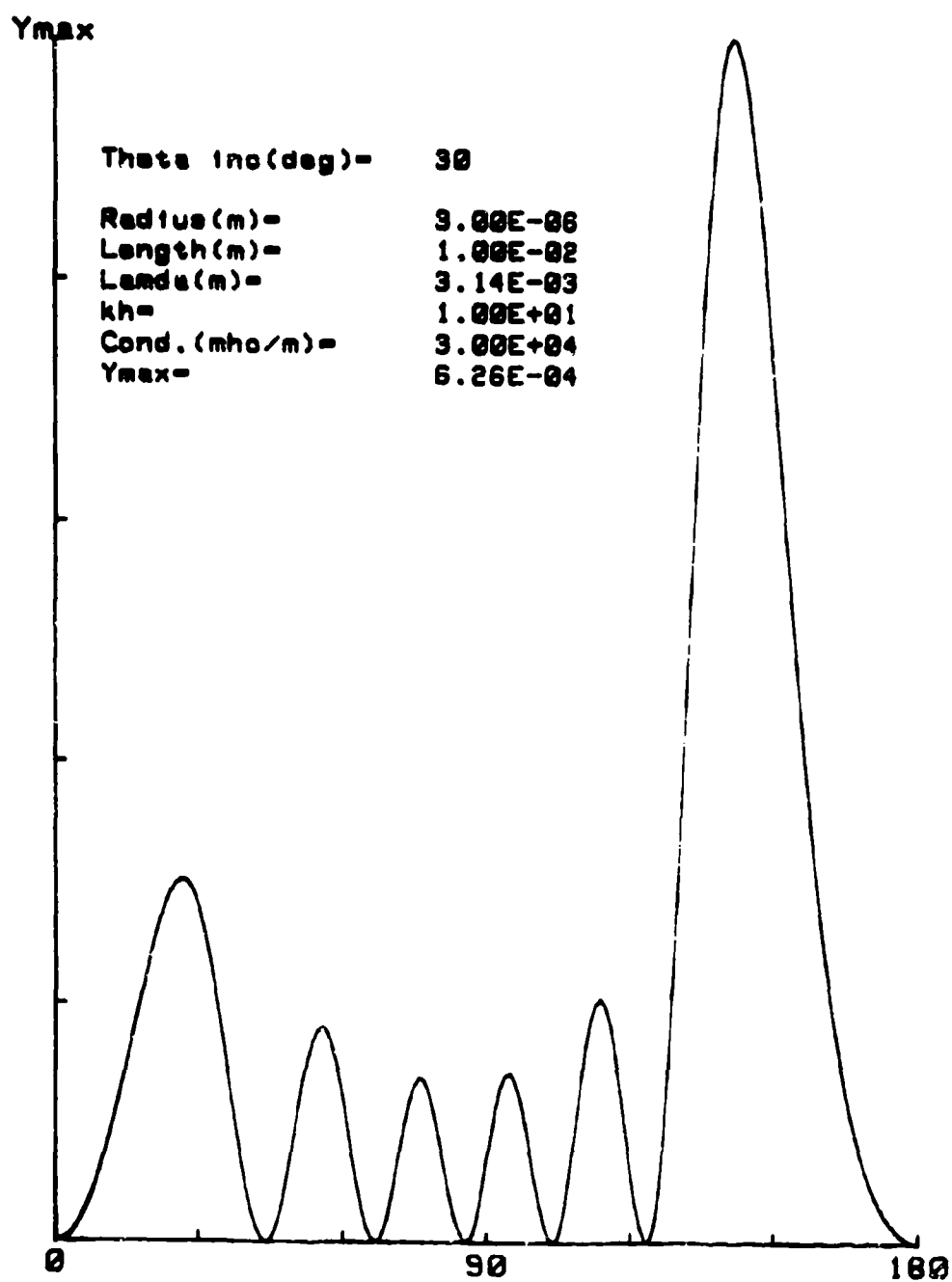


Fig. 4 Differential cross section/ λ^2 for $\theta_1 = 30^\circ$; $kh = 10$.

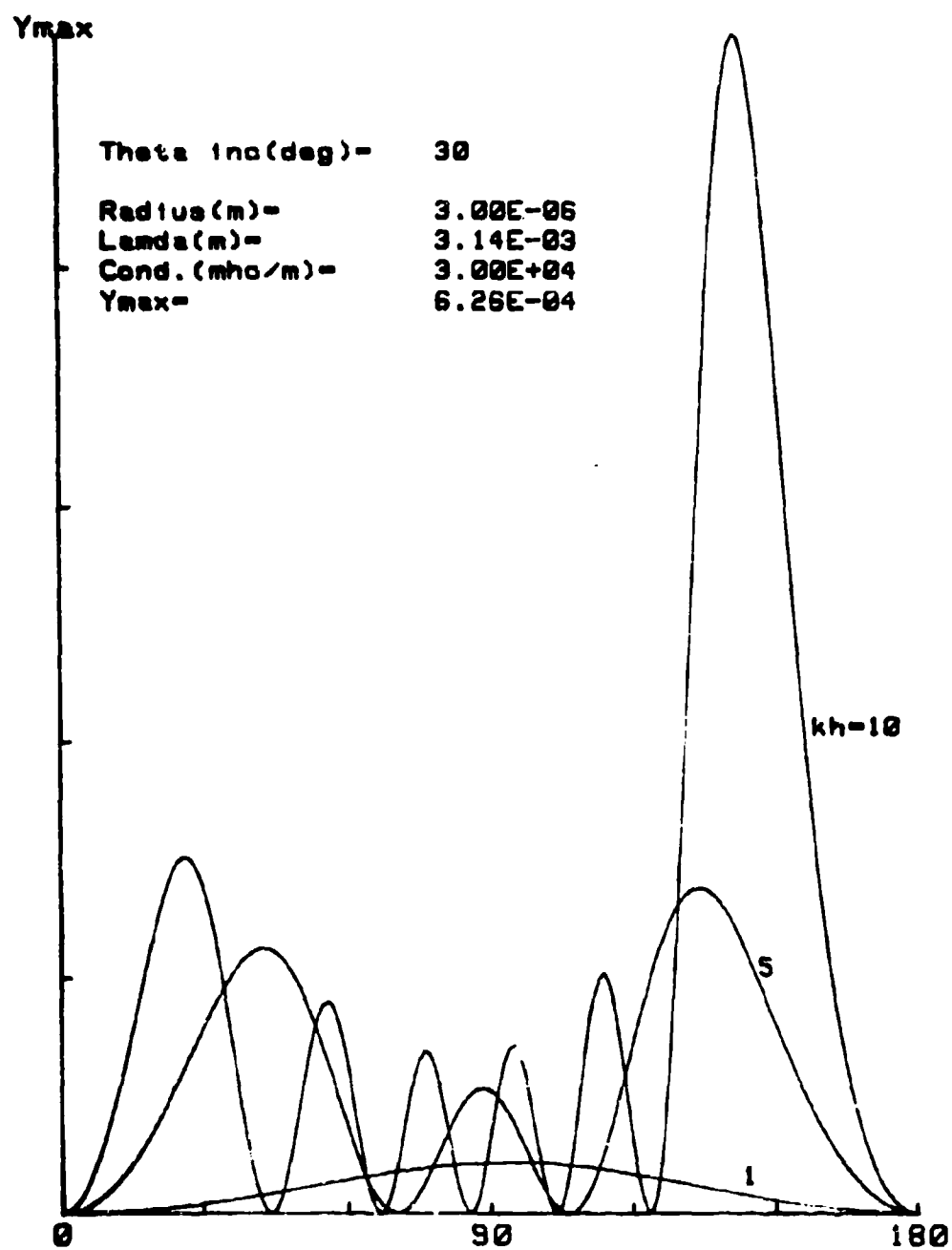


Fig. 5 Composite differential cross section/ λ^2 for $kh = 1, 5, 10$ and $\theta_1 = 30^\circ$.

so. Note that, even though $\Theta_1 = 30^\circ$, the scattering displays a single broad lobe which is symmetric and has a maximum at 90° , which is perpendicular to the axis.

In Fig. 3, the length has been increased from 1 mm to 5 mm, corresponding to $kh = 5$. We see that, in this case, the scattering pattern is more complicated. We still see a little bit of the symmetric (dipole-like) scattering at 90° . This is in the intermediate range of kh . The pattern is largely symmetric, with the major lobe appearing in the vicinity of $180^\circ - \Theta_1 = 150^\circ$.

Note that, in the case of $kh \gg 1$, the scattering amplitude is constant in the axisymmetric cones whose included half angle is Θ , the differential scattering angle of the figures. Therefore, the differential scattering cross section at $\Theta = 180^\circ - \Theta_1$ is the same as that at $\Theta = 180^\circ + \Theta_1$. But, this latter scattering angle is the direction of the incident k vector, and therefore, is the forward scattering direction. It is well known that, for large kh , we should expect to find a major lobe in the forward direction. Therefore, the lobe at $\Theta \approx 150^\circ$ qualitatively agrees with what we would intuitively expect for a moderately large value of kh and small ka .

If we next increase the length so that $kh = 10$ (a value well into the $kh \gg 1$ region), we see in Fig. 4 that the major lobe of Fig. 3 develops into a much more pronounced peak in the vicinity of $\Theta \approx 150^\circ$. This shows that the forward ($\Theta = 180^\circ + \Theta_1$) and specular ($\Theta = 180^\circ - \Theta_1$) scattering patterns are fairly well developed.

Figure 5 is a composite of Figures 2, 3, and 4, with all data shown in correct numerical scale. It is interesting to note that the peak for $kh = 10$ is closer to 150° than that for $kh = 5$, which is in agreement with our expectations.

3.1.2 Behavior as a Function of Θ_1

In the next set of Figs. (6 through 9), we fix kh at a value of $kh = 5$ and choose three angles of incidence: $\Theta_1 = 30^\circ$, 60° , and 90° .

The scattering pattern of Fig. 6, for which $\Theta_1 = 30^\circ$, is that of Fig. 3 and is repeated for continuity. We see in Fig. 7 that, when Θ_1 is increased to 60° , the major lobe shifts to $\Theta \approx 180^\circ - 60^\circ = 120^\circ$, which is just what we should expect.

At $\Theta_1 = 90^\circ$ (Fig. 8), we have broadside incidence and the major lobe has shifted to 90° as expected. The pattern is symmetrical about 90° as it should be.

A composite of the preceding three curves is shown in Fig. 9, which demonstrates how significantly the magnitudes of the scattering cross sections differ as a function of angle of incidence.

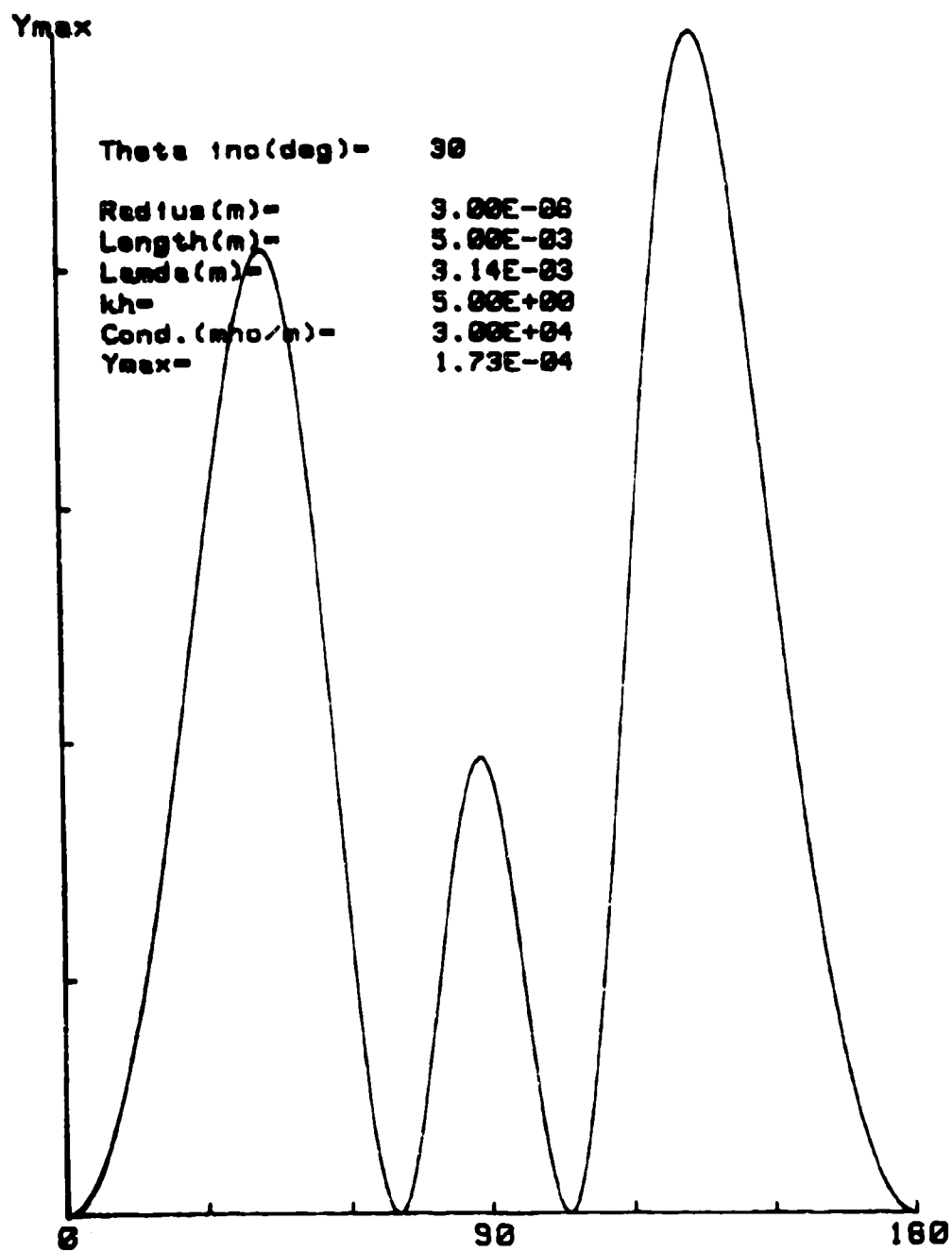


Fig. 6 Differential cross section/ λ^2 for $kh = 5$; $\theta_1 = 30^\circ$.

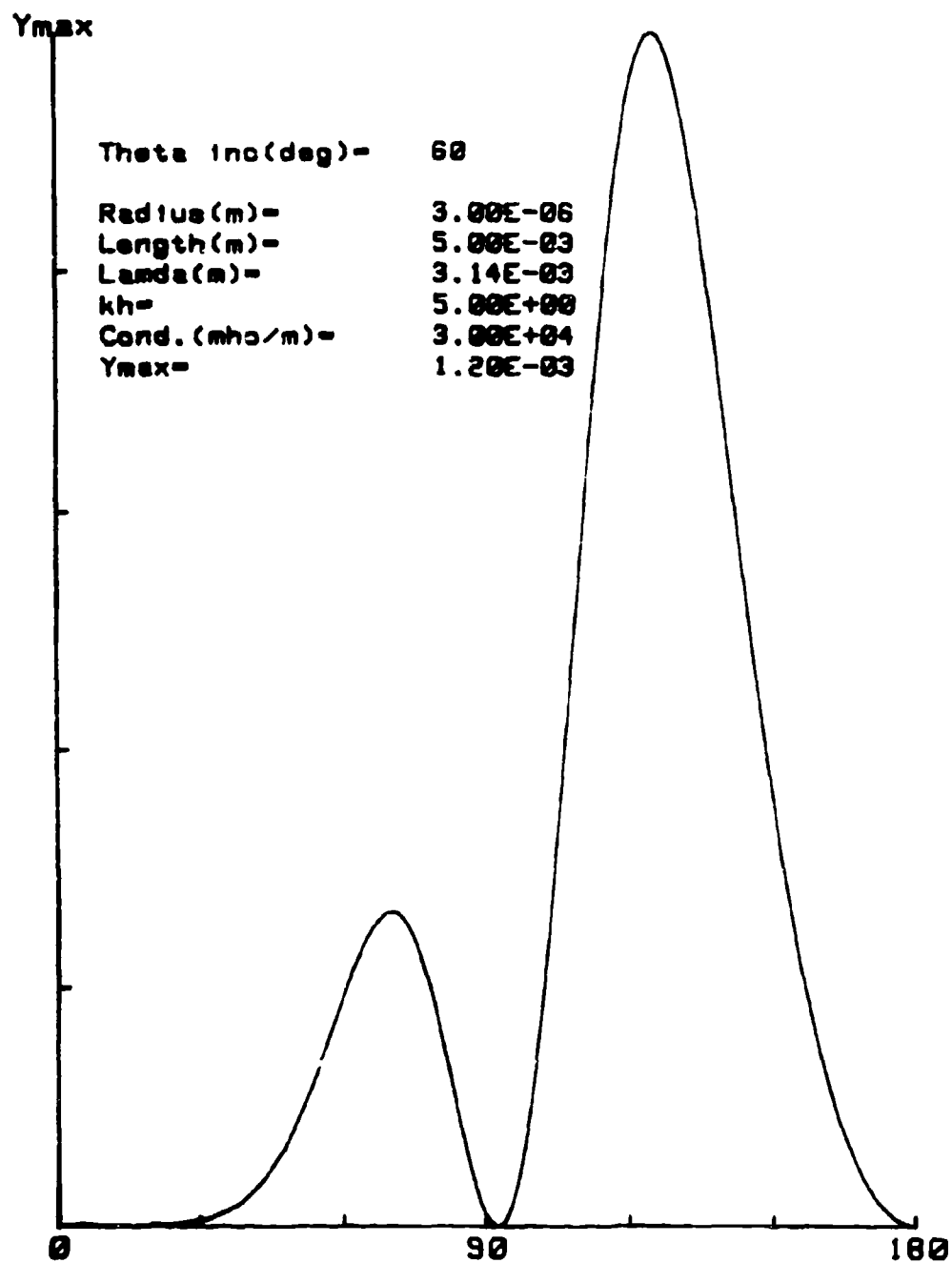


Fig. 7 Differential cross section/ λ^2 for $kh = 5$; $\theta_1 = 60^\circ$.

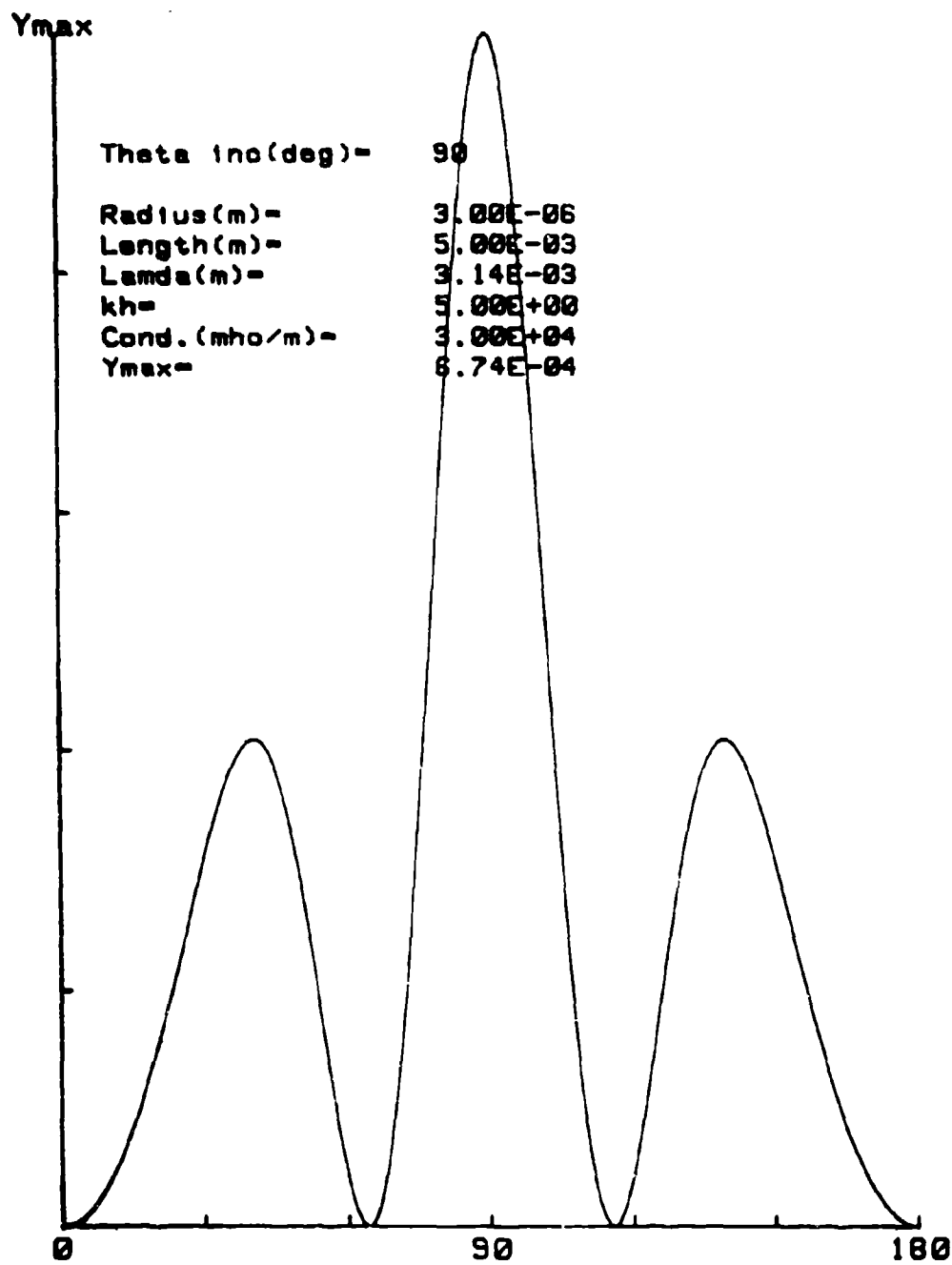


Fig. 8 Differential cross section/ λ^2 for $kh = 5$; $\theta_1 = 90^\circ$.

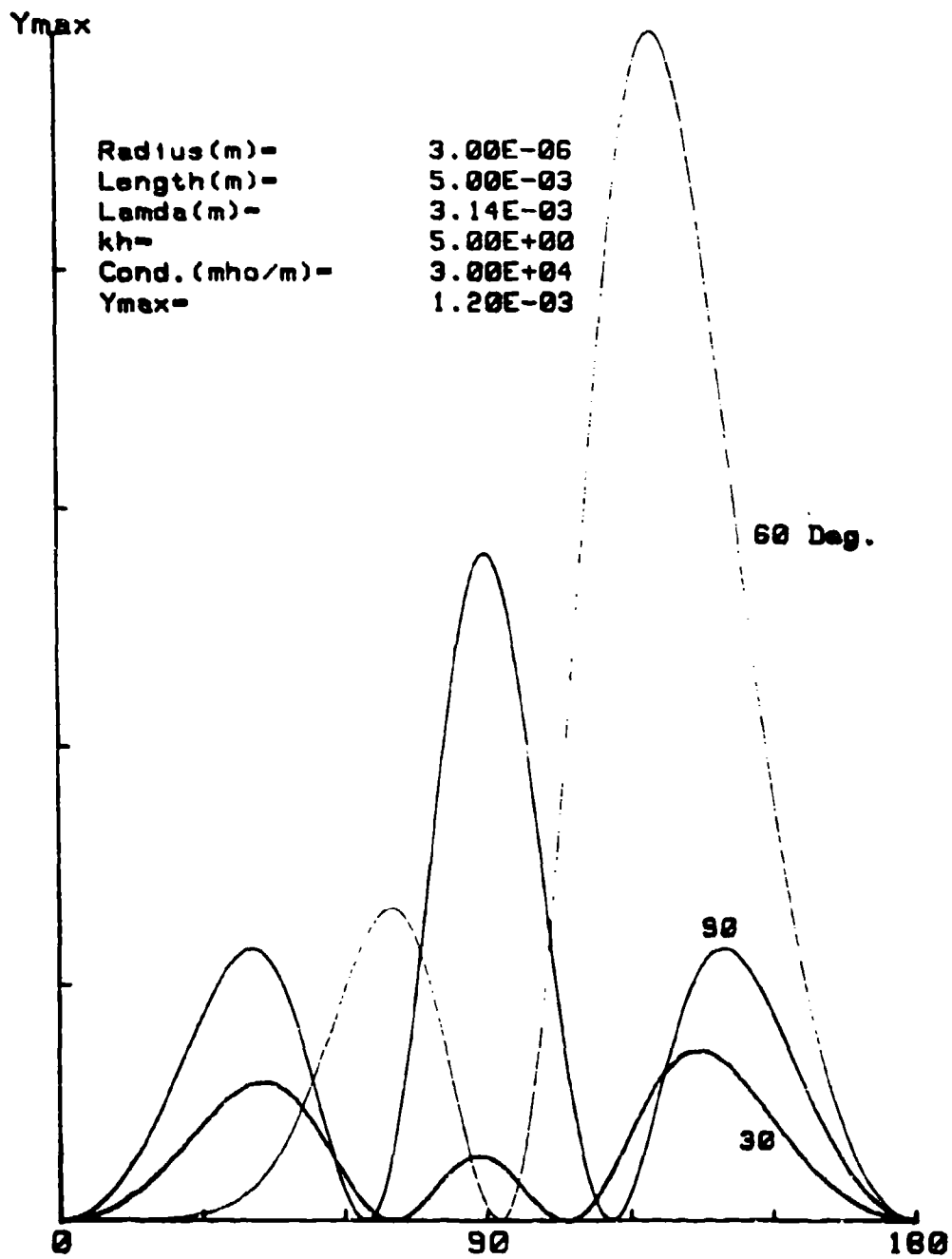


Fig. 9 Composite differential cross section/ λ^2 for $\theta_i = 30^\circ, 60^\circ$, and 90° and $kh = 5$.

3.2 Backscatter Cross Sections

We have made a number of comparisons between the results of the present theory and available measurements. The data presented in this section are limited to moderate values of $kh \leq 10$. It is unfortunate that more experimental data are not available. In particular, we have found no experimental data for lossy cylinders. Available experimental data with which we can compare appears to be limited to the backscatter cross sections of perfectly conducting, but thin ($ka < 1$) wires. Notwithstanding, considerable insight can be gained in the foregoing comparisons.

3.2.1 Radar Cross Section vs. Aspect Angle

In this sub-section we compare the results of the present theory with experimental data taken at Lockheed Georgia⁵ for tungsten wires in the resonance region. The measurement frequency was 9.375 GHz. Wire diameters ranged from 1 to 3 mils. The skin depth of tungsten is 0.04 mils at this frequency and we can, therefore, consider the conductivity to be infinite for Figs. 10 through 16. In these Figures, the solid curves are our theoretical results and the dotted curves are experimental data. These Figures are plots of backscatter cross section per square wavelength vs. aspect angle with the E vector and the cylinder axis in the rotational plane. Note that 90° and 270° represent broadside incidence, while 0° and 180° represent end-on incidence.

Figure 10 corresponds to the onset of the first (\sim half wavelength) resonance. Note that the angular symmetry of the data is off by 10 to 15 degrees. If this were corrected, reasonably good quantitative agreement would be observed.

Figure 11 corresponds to the first resonance ($l/\lambda = 0.480$) and we find excellent agreement between theory and experiment. Figure 12 ($l/\lambda = 0.496$) shows good experimental symmetry and agrees with it within 10%. In Fig. 13, in which $l/\lambda = 0.523$, the agreement is better than 10% when corrections are made for experimental asymmetry.

Note in Fig. 14, for which $l/\lambda = 0.854$ the broadside (90°) peak observed in Figs. 11 through 13, has split and the RCS is reduced. Although the features of the theory vs. experiment agree, the quantitative agreement is only within $\sim 25\%$ to 30% in Fig. 14.

Figures 15 and 16 correspond to $l/\lambda = 0.929$ and $l/\lambda = 1.051$, respectively. In Fig. 15, the experimental amplitude asymmetry is about 12%, while the agreement between theory and experiment are within about 18%. In Fig. 16, a new maximum has formed at 90° and 270° . The entire pattern is reduced and only moderate (20 to 25%) theoretical experimental agreement is observed.

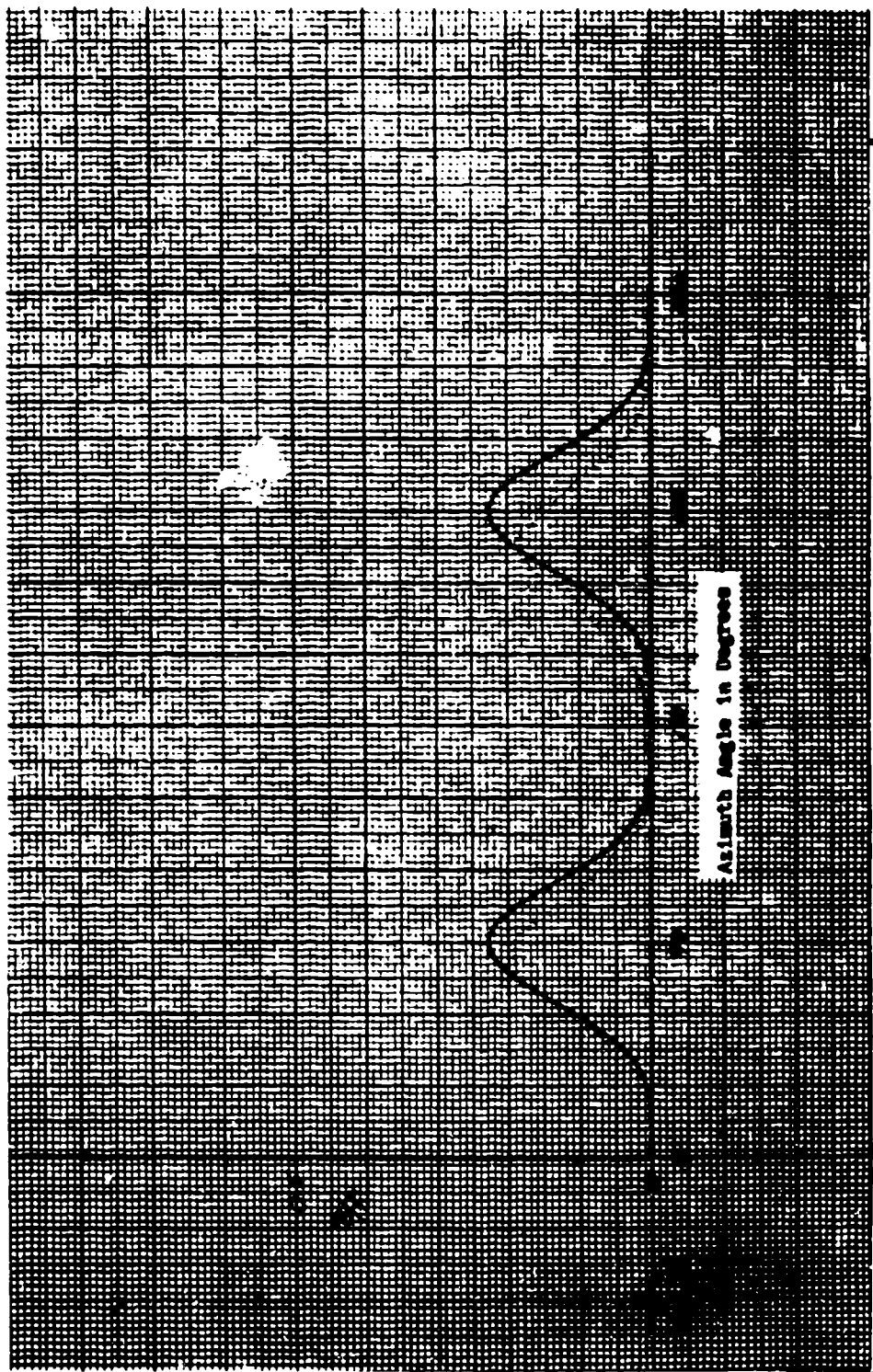


Fig. 10 Radar cross section/lambda² of a tungsten wire as a function of angle of incidence, θ_i , for $k/\lambda = 0.437$ and $k/d = 500$.

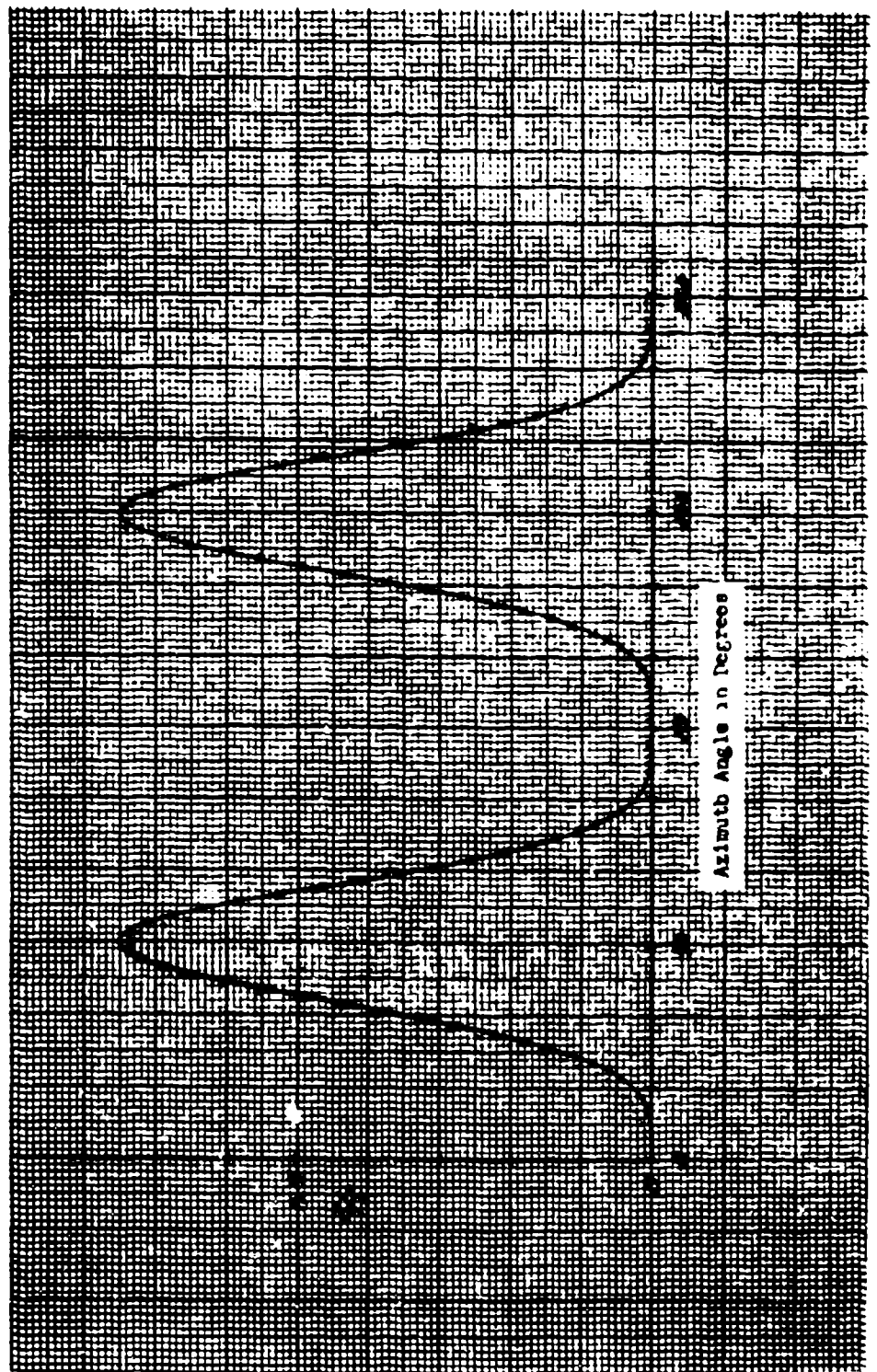


Fig. 11 Radar cross section/ $\lambda d b^2$ of a tungsten wire as a function of angle of incidence, θ_i , for $\ell/\lambda = 0.480$ and $\ell/d = 605$.

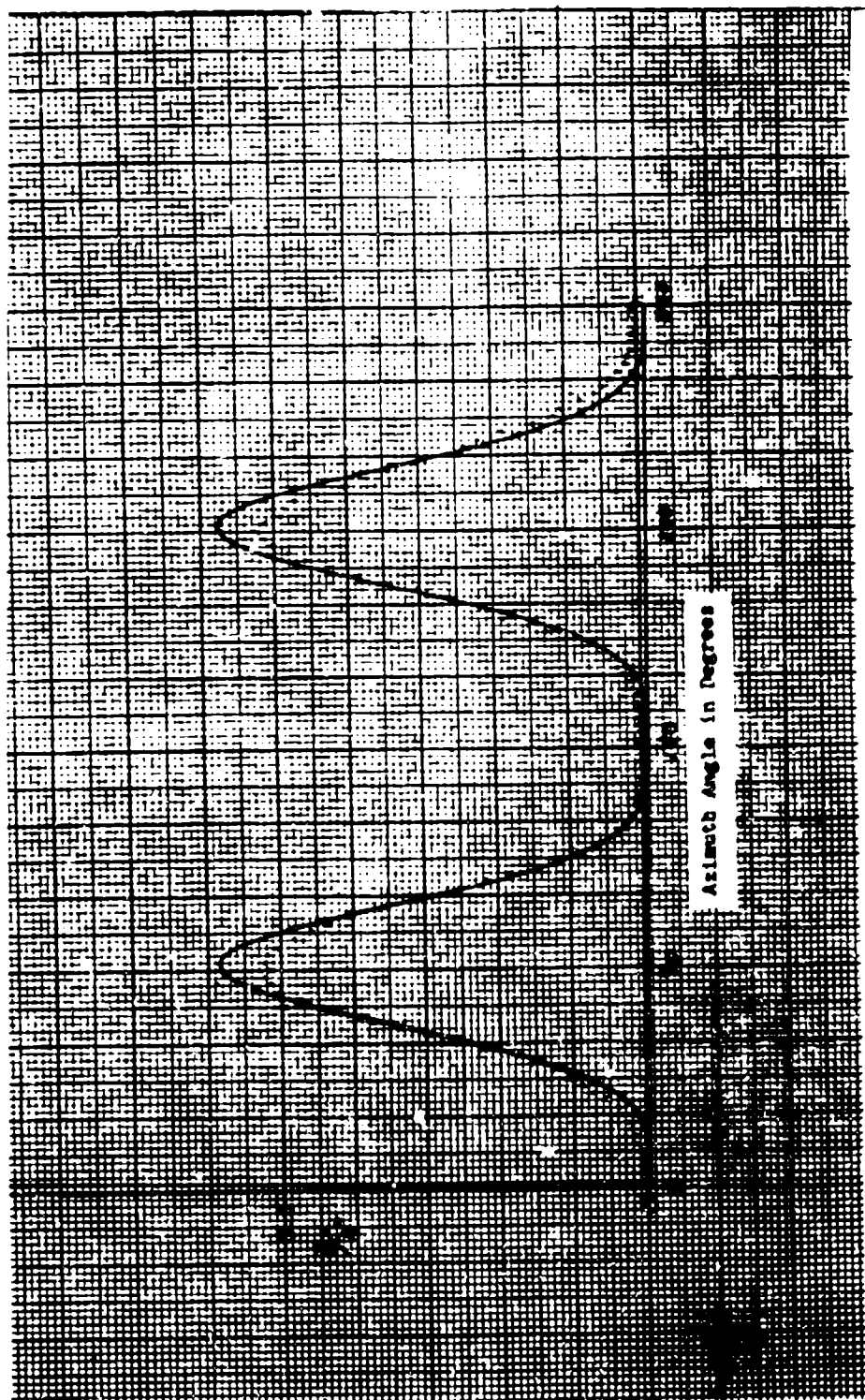


Fig. 12 Radar cross section/ λ^2 of a tungsten wire as a function of angle of incidence, θ_i , for $\ell/\lambda = 0.480$ and $\ell/d = 500$.

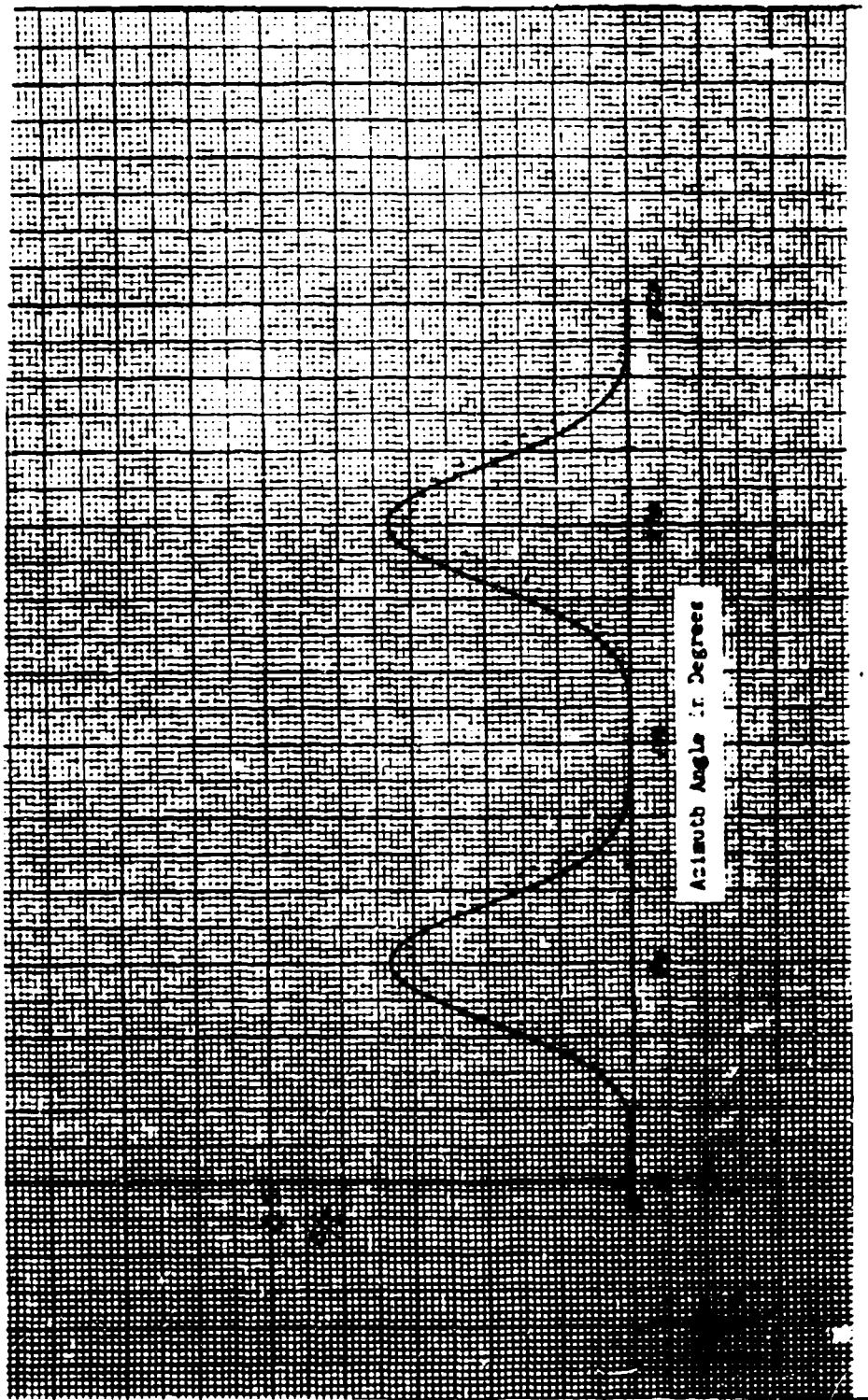


Fig. 13 Radar cross section/ λ^2 of a tungsten wire as a function of angle of incidence, θ_i , for $l/\lambda = 0.525$ and $l/d = 660$.

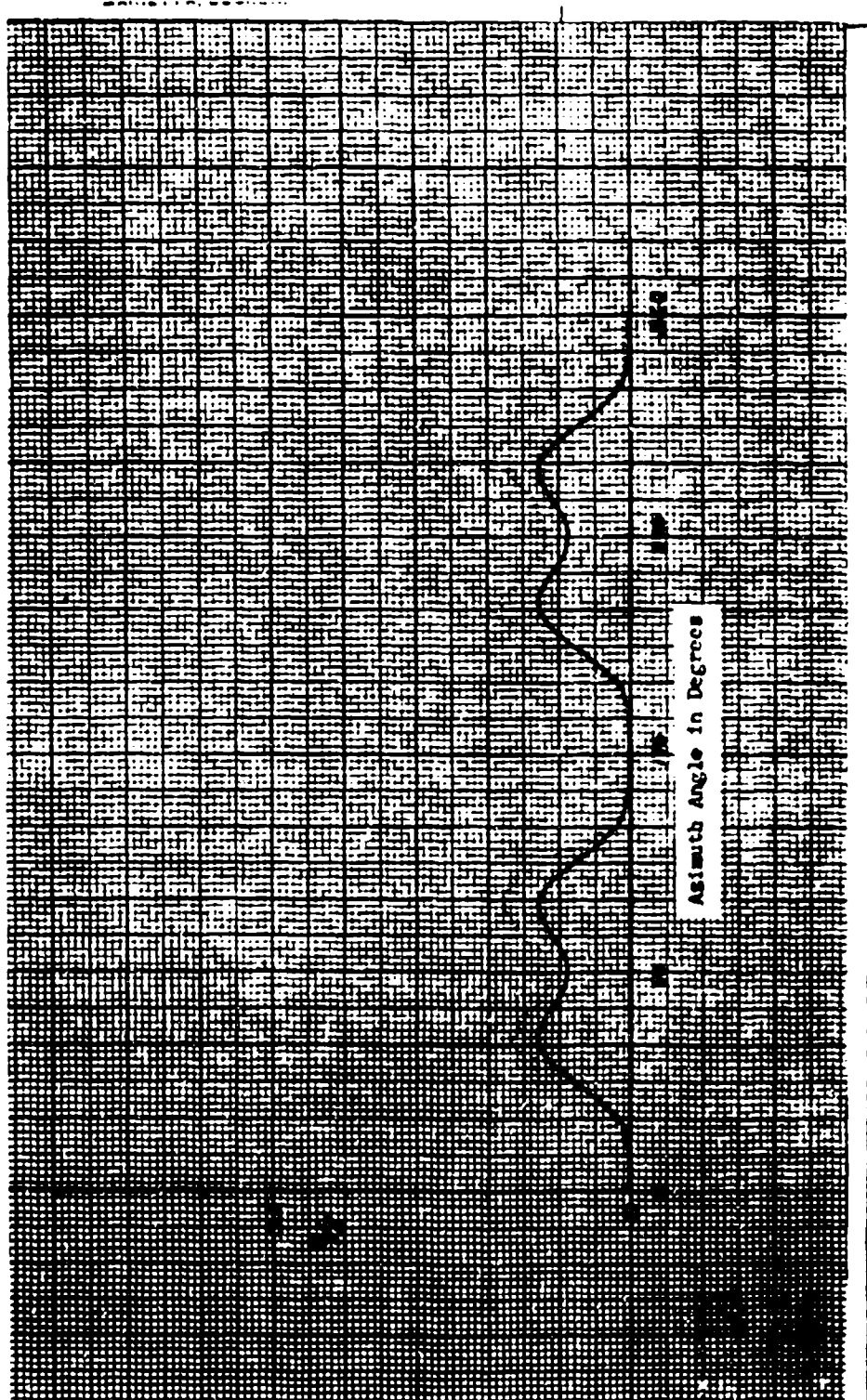


Fig. 14 Radar cross section/ λ^2 of a tungsten wire as a function of angle of incidence, θ_i , for $\lambda/\lambda = 0.854$ and $\lambda/d = 717$.

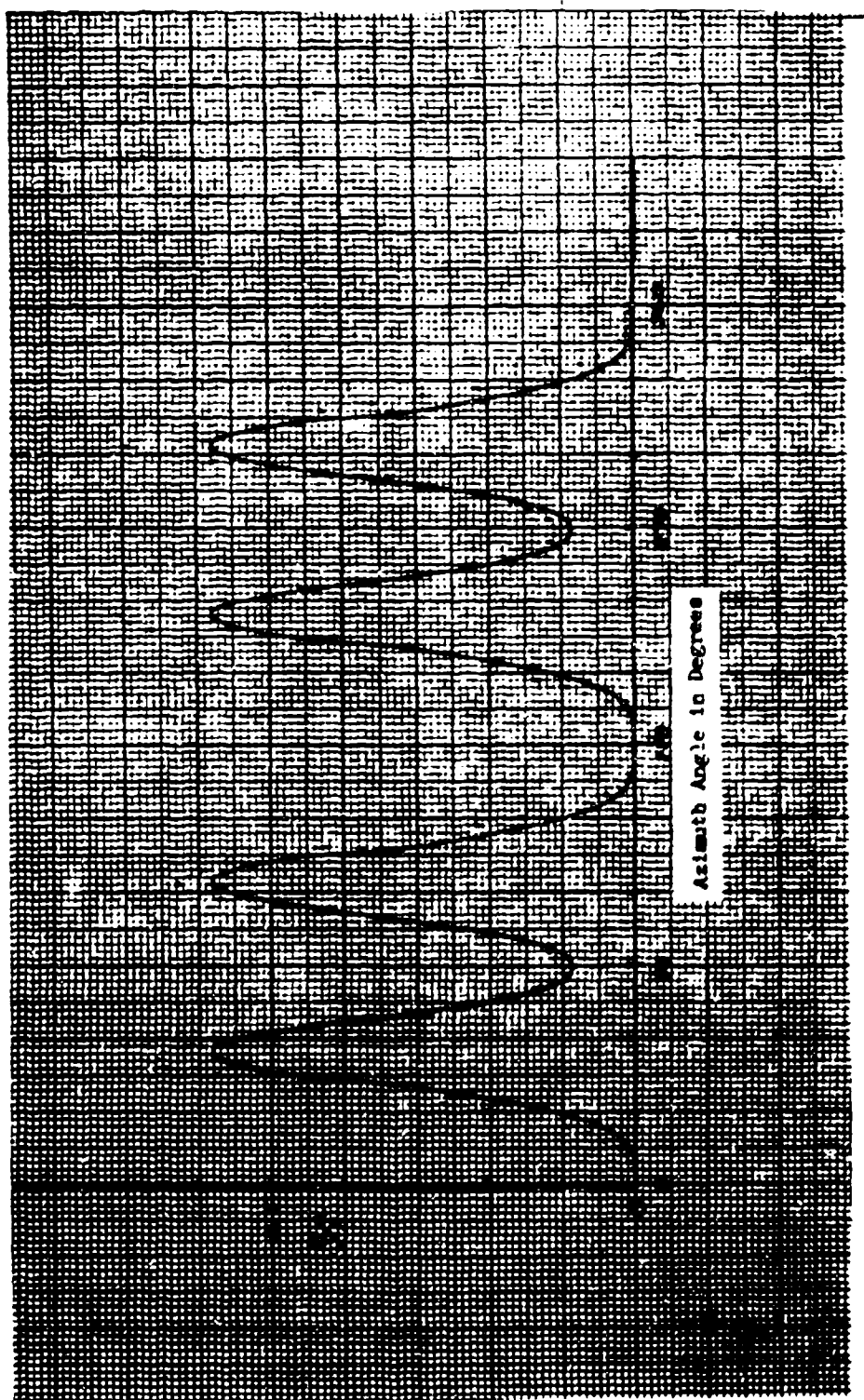


Fig. 15 Radar cross section/ λ^2 of a tungsten wire as a function of angle of incidence, θ_i , for $l/\lambda = 0.929$ and $l/d = 780$.

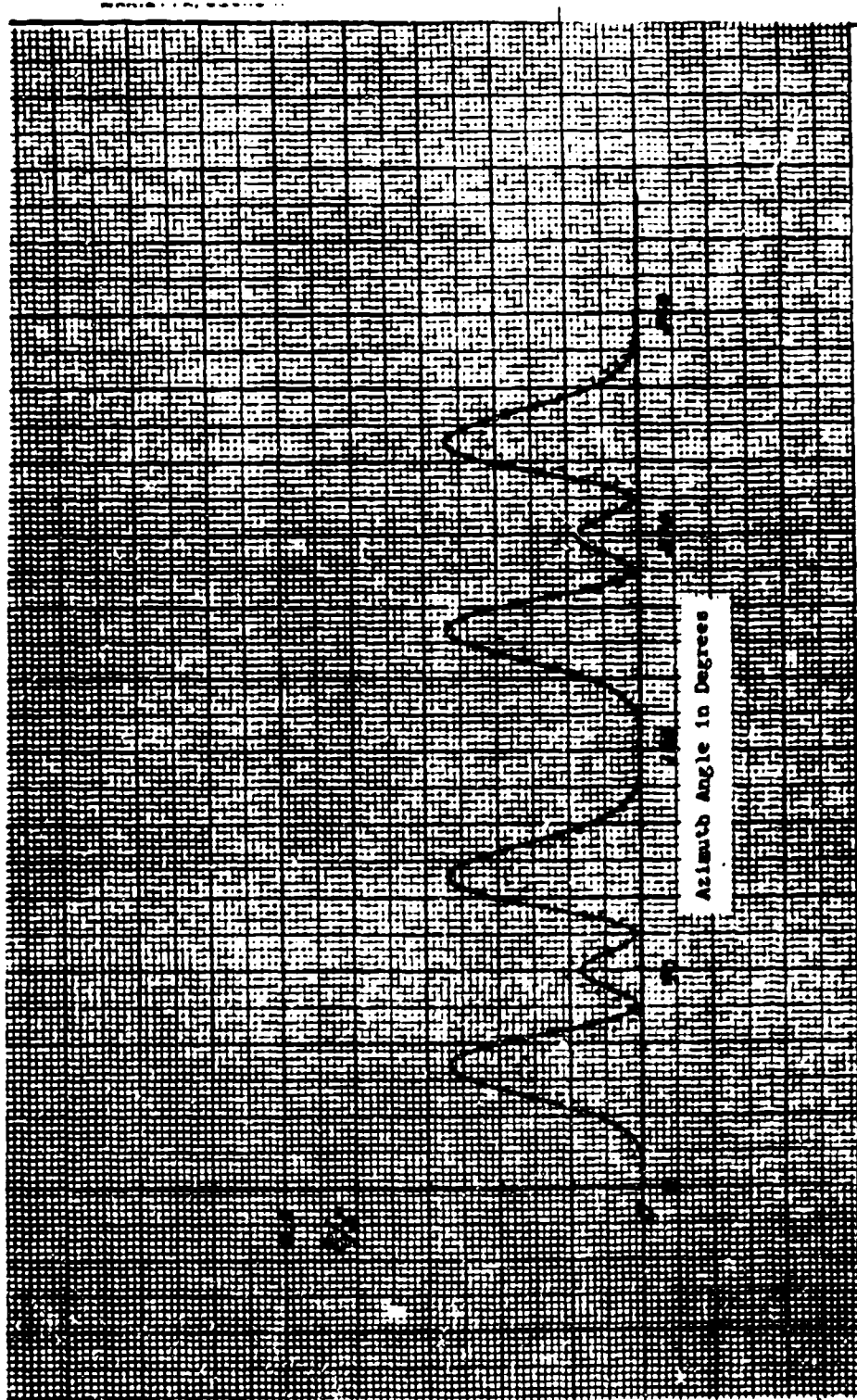


Fig. 16 Radar cross section/ λd^2 of a tungsten wire as a function of angle of incidence, θ_i , for $l/\lambda = 1.051$ and $l/d = 884$.

3.2.2 Backscatter Cross Section vs. kh

In this sub-section, we first compare the results of the present theory with some early experimental measurements on highly conducting wires by As and Schmitt^{6,7} with the results of the present theory. Figure 17, the experimentally observed backscatter cross section per square wavelength is plotted as a function of kh for three values of ka . Note that an error exists in this Figure. The solid line ($ka = 0.132$) and the dotted line ($ka = 0.026$) were obviously inadvertently interchanged in the original paper by As and Schmitt and the error was reproduced in King and Vu.

Figure 18 shows the results of the present theory for the same parameters as those of Fig. 17. Note that, except for the deep minima of Fig. 18, excellent quantitative agreement is demonstrated. The existence of these minima will be discussed in Section 3.5.

Figure 19 shows the behavior of the backscatter cross section vs. kh for four electrical conductivity values ranging from 100 mho/m to infinity. Note that (a) as we would expect, the backscatter cross sections decrease with decreasing conductivity, (b) the plateaus degenerate to simple maxima, and (c) the three very deep minima persist even for small values of electrical conductivity.

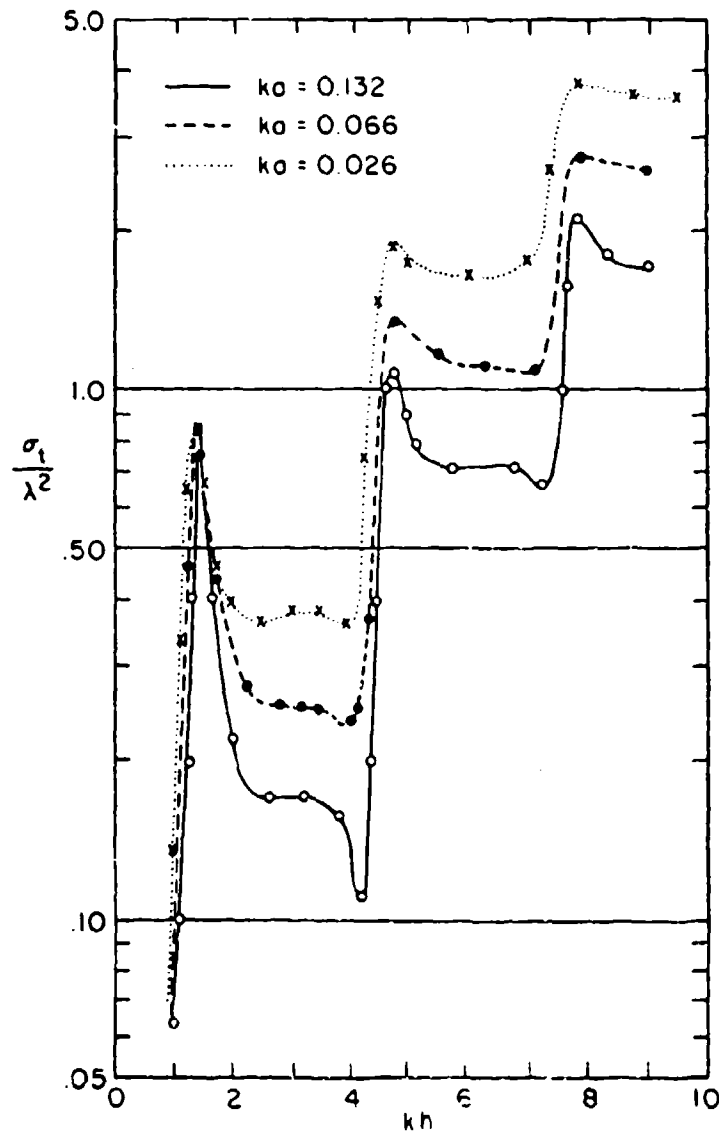


Fig. 17 Experimentally measured backscatter cross section/ λ^2 for infinitely conducting cylinders at broadside incidence as a function of kh .^{7,8}

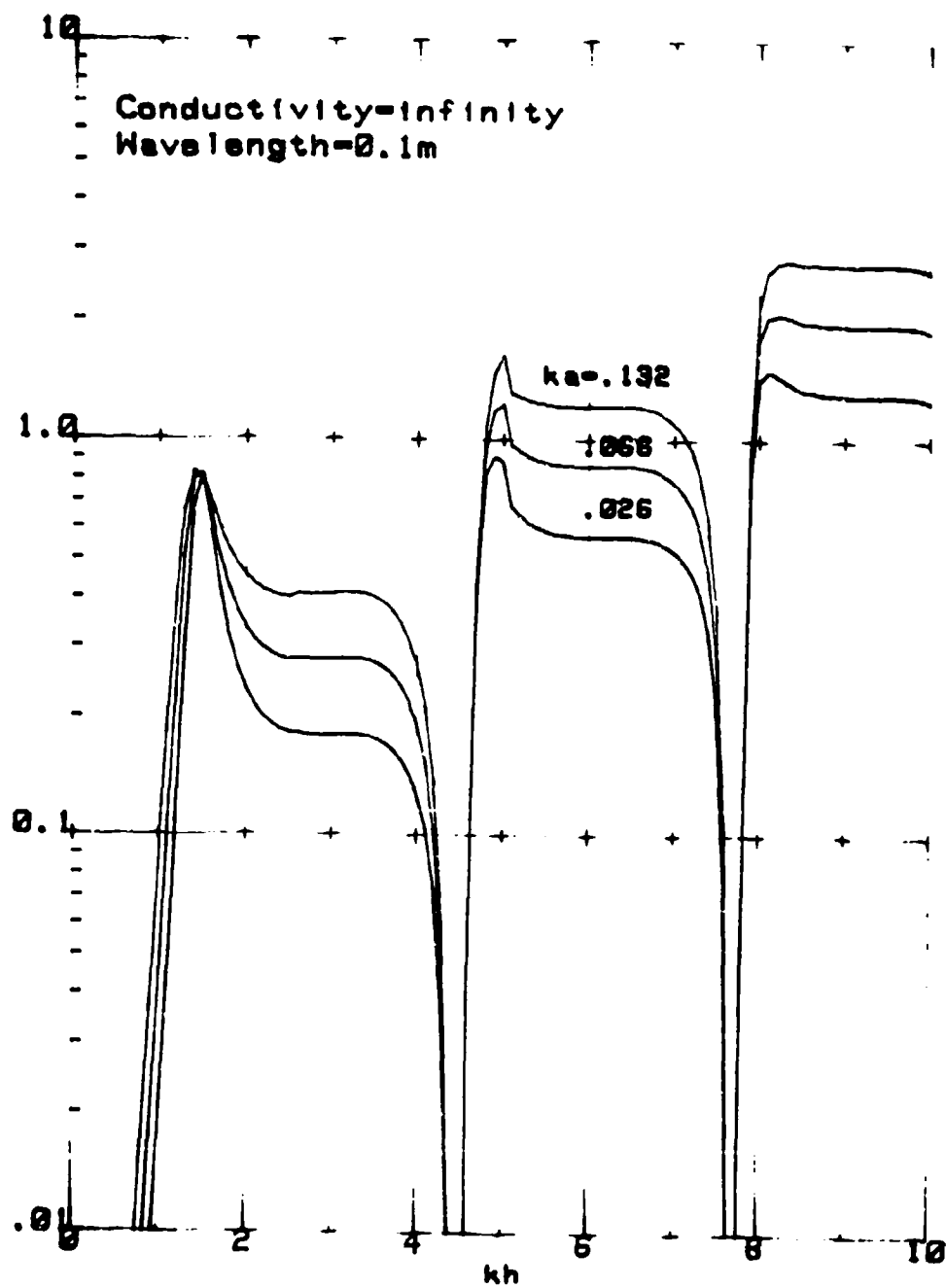


Fig. 18 Calculated backscatter cross section/ λ^2 for infinitely conducting cylinders at broadside incidence as a function of kh , $kh \leq 10$.

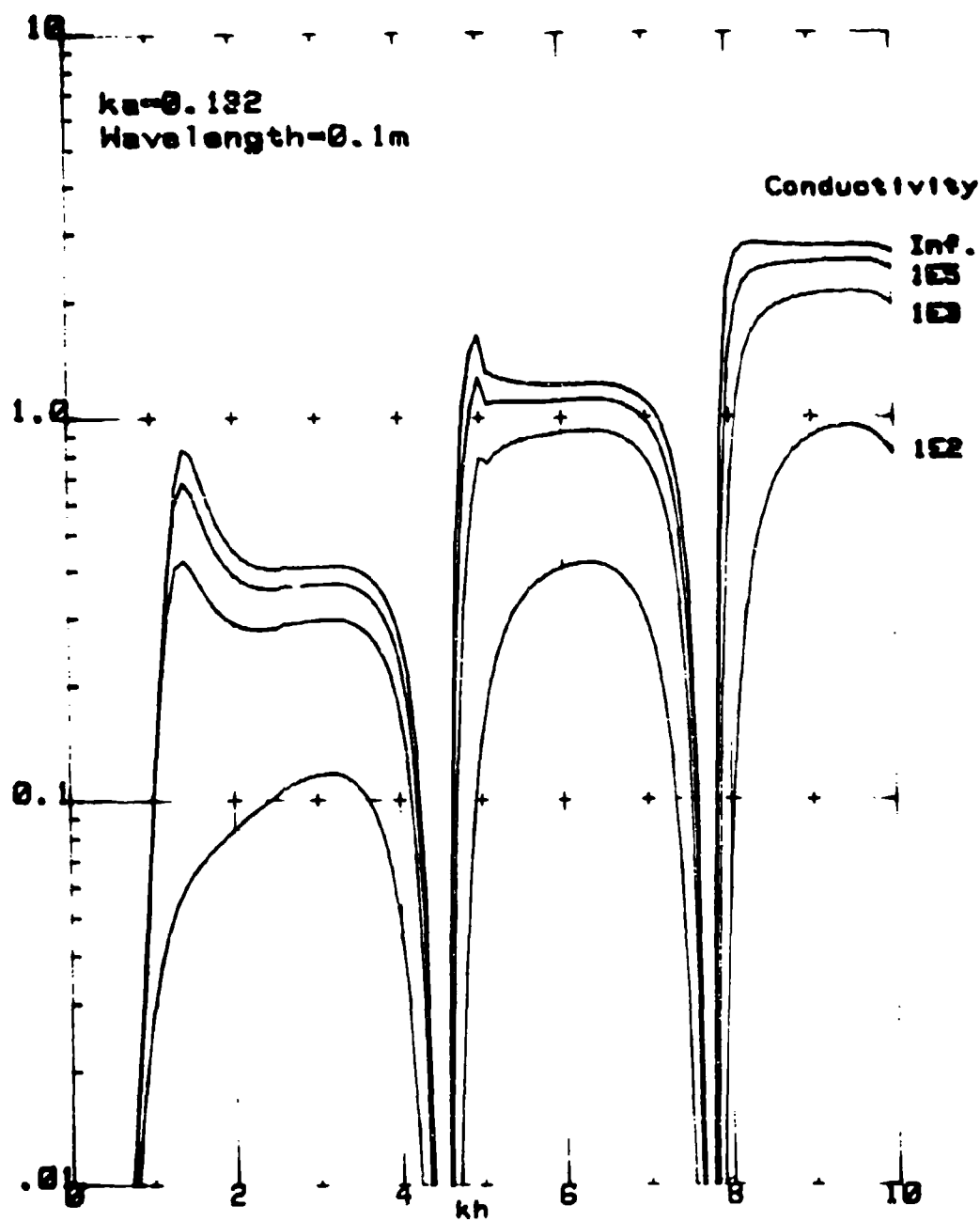


Fig. 19 Calculated backscatter cross section/ λ^2 for resistive cylinders at broadside incidence as a function of kh , $kh \leq 10$.

3.3 Very Large Values of kh

We next investigate the behavior of the theory when kh becomes very large. The purposes of this are (a) to test the stability of our solutions in the very large kh range, (b) to determine, if possible, asymptotic expressions for the cross sections, and (c) to see if the solutions appear to be reasonable on physical grounds.

In Figures 20 and 21, which are analogous to Fig. 17, we have plotted (linear plot) backscatter cross section per square wavelength vs. kh over the range $0.25 \leq kh \leq 100$. In Fig. 20, $ka = 10^{-4}$ and in Fig. 21, $ka = 10^{-3}$. We find that

(a) the backscatter cross section appears to be well behaved in the very large kh regime

(b) The minima of Fig. 17 persist to at least $kh = 100$.

An analysis of Figs. 20 and 21 gives the following asymptotic relationship:

$$\frac{\sigma_{RCS}}{\lambda^2} = \frac{1}{4} \left(\frac{kh}{\ln(ka)} \right)^2 \quad (21)$$

The above equation is plotted, along with the theoretical results, in Figs. 20 and 21.

Another test of the theory is to observe the behavior of the differential scattering cross section in the very large kh limit. The results of these computations are given below.

Figures 22, 23, 24 and 25 show the behavior of the differential scattering cross section per square wavelength for various values of kh. The cylinder orientation is broadside, with E parallel to the cylinder axis. The values are $kh = 10, 15, 25$ and 100 . Note that, as kh is increased, (a) the width of the central maximum decreases, (b) the lobe structure becomes compressed, and (c) unexpected minor lobes appear near 0° and 180° . The relative amplitude of these minor lobes appears to diminish as (ka) is decreased. We do not presently have a conclusion as to whether or not these are real or are the result of the use of the simple current function given in Section 2.

Except for (c) above, the curves of Figs. 22 through 25 appear very normal and well behaved. Also, we have shown that the main lobe structure agrees exactly with the usual $(\sin 2khs \sin \theta / 2khs \sin \theta)^2$ representation.

Figures 26 and 27 represent an interesting and unanticipated result. First, note that the angle of incidence is 40° (50° off broadside). In Fig. 26 the total length (2h) of the cylinder is an odd multiple of a quarter wavelength. Specifically, the

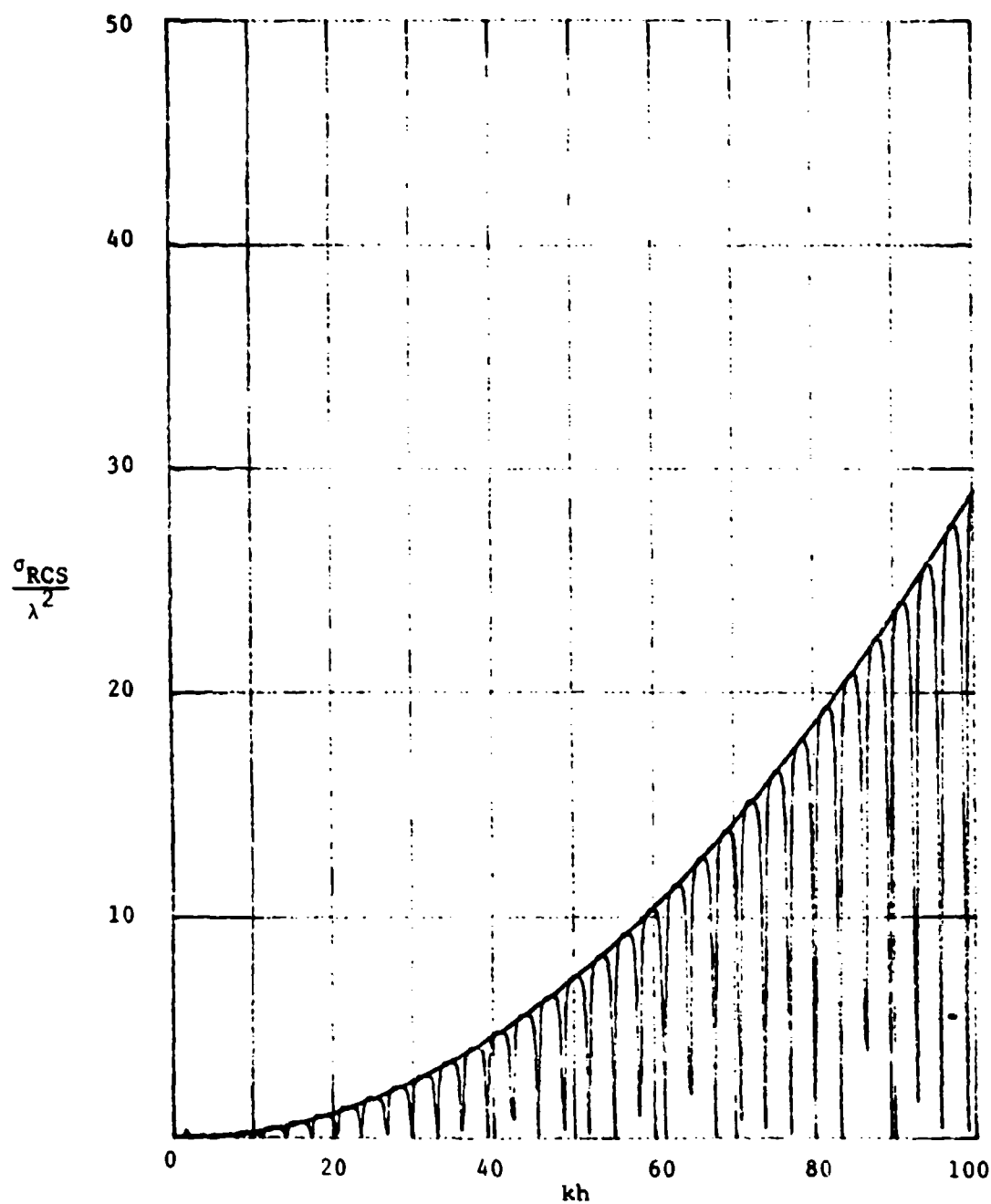


Fig. 20 Calculated backscatter cross section/ λ^2 for infinitely conducting cylinders at broadside incidence as a function of kh . $kh \leq 100$ and $ka = 10^{-4}$. The solid curve is a plot of Eq. (21).

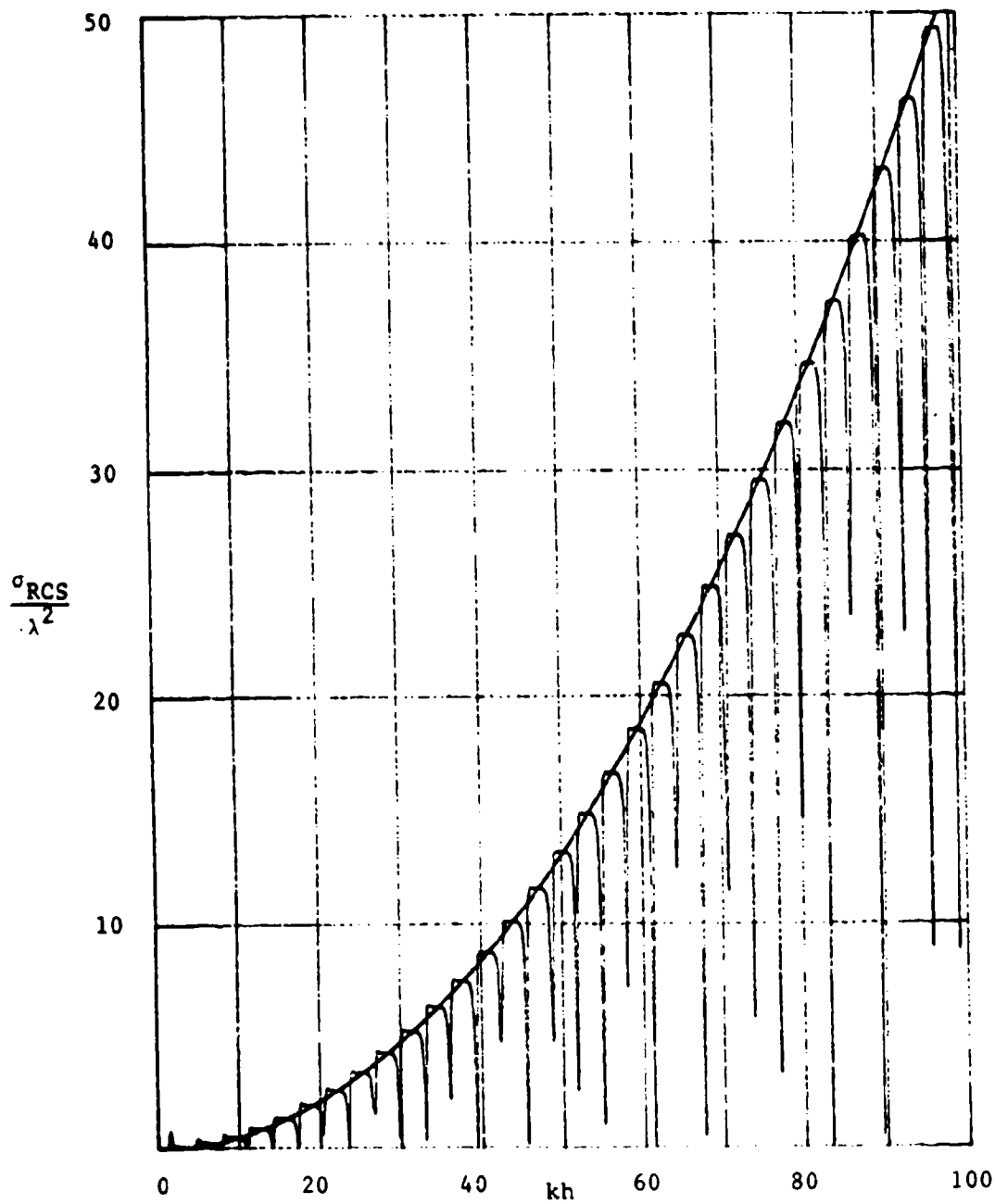


Fig. 21 Calculated backscatter cross section/ λ^2 for infinitely conducting cylinders at broadside incidence as a function of kh , $kh \leq 100$ and $ka = 10^{-3}$. The solid curve is a plot of Eq. (21).

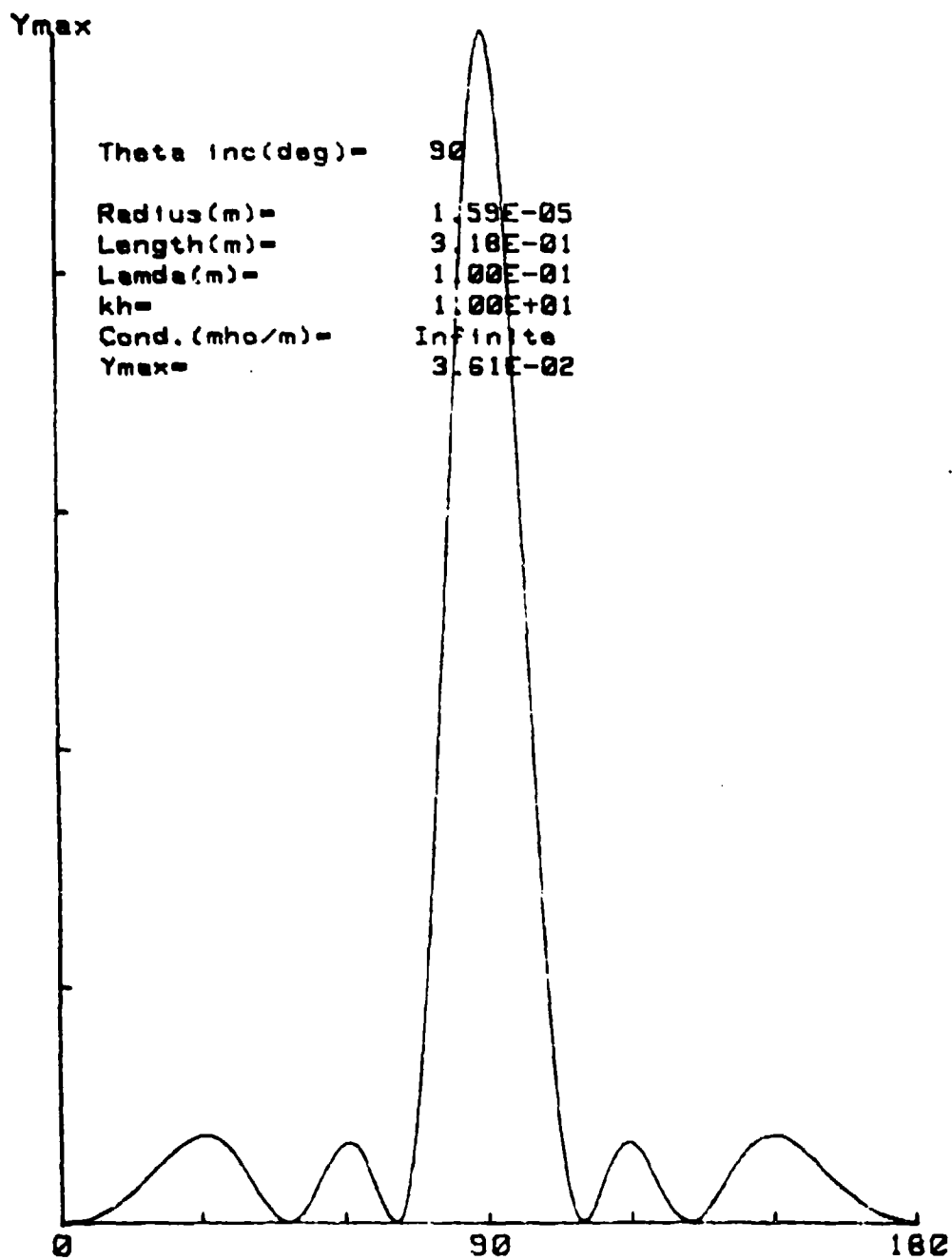


Fig. 22 Differential cross section/ λ^2 for an infinitely conducting cylinder, broadside incidence and $kh = 10$.

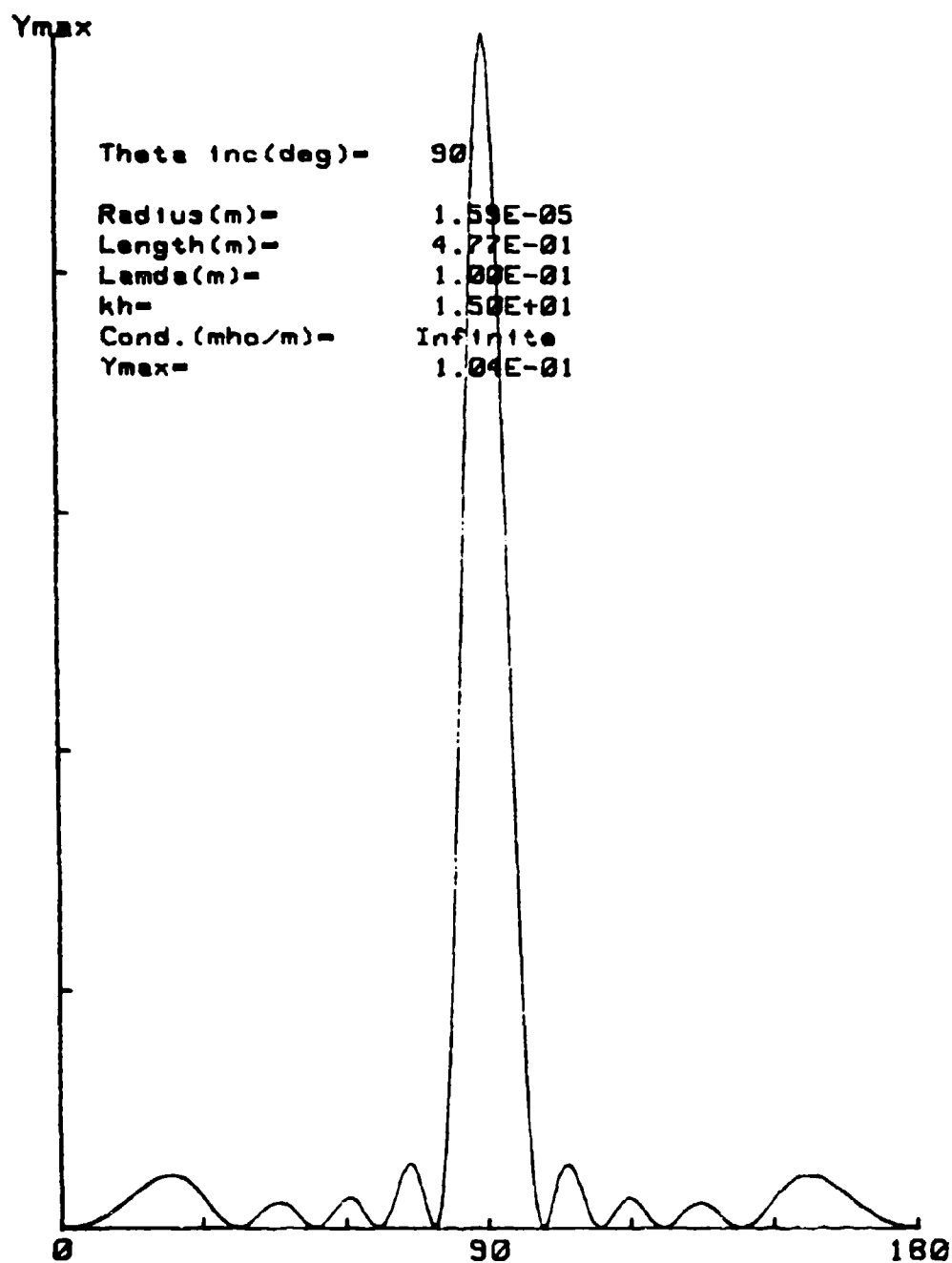


Fig. 23 Differential cross section/ λ^2 for an infinitely conducting cylinder, broadside incidence and $kh = 15$.

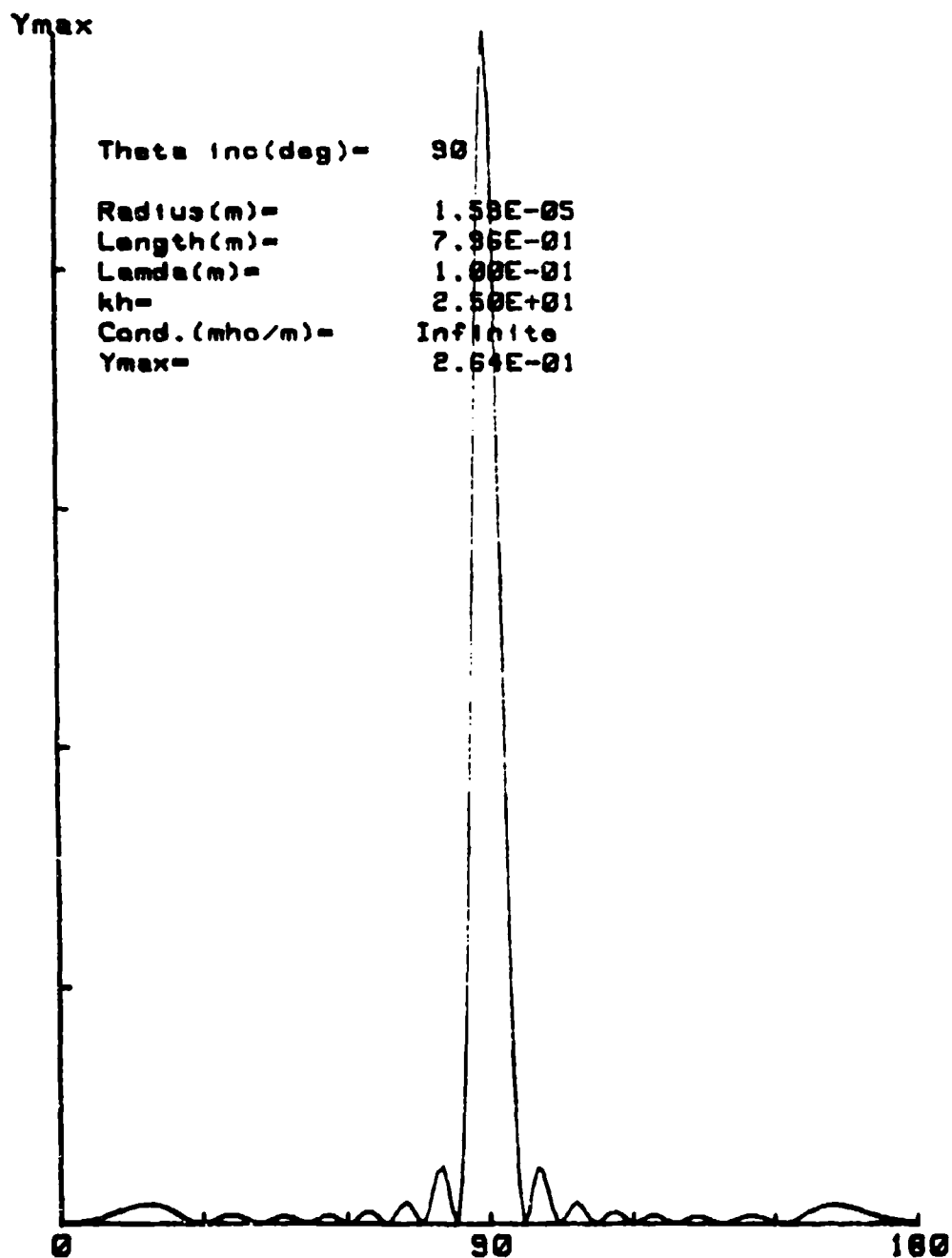


Fig. 24 Differential cross section/ λ^2 for an infinitely conducting cylinder, broadside incidence and $kh = 25$.

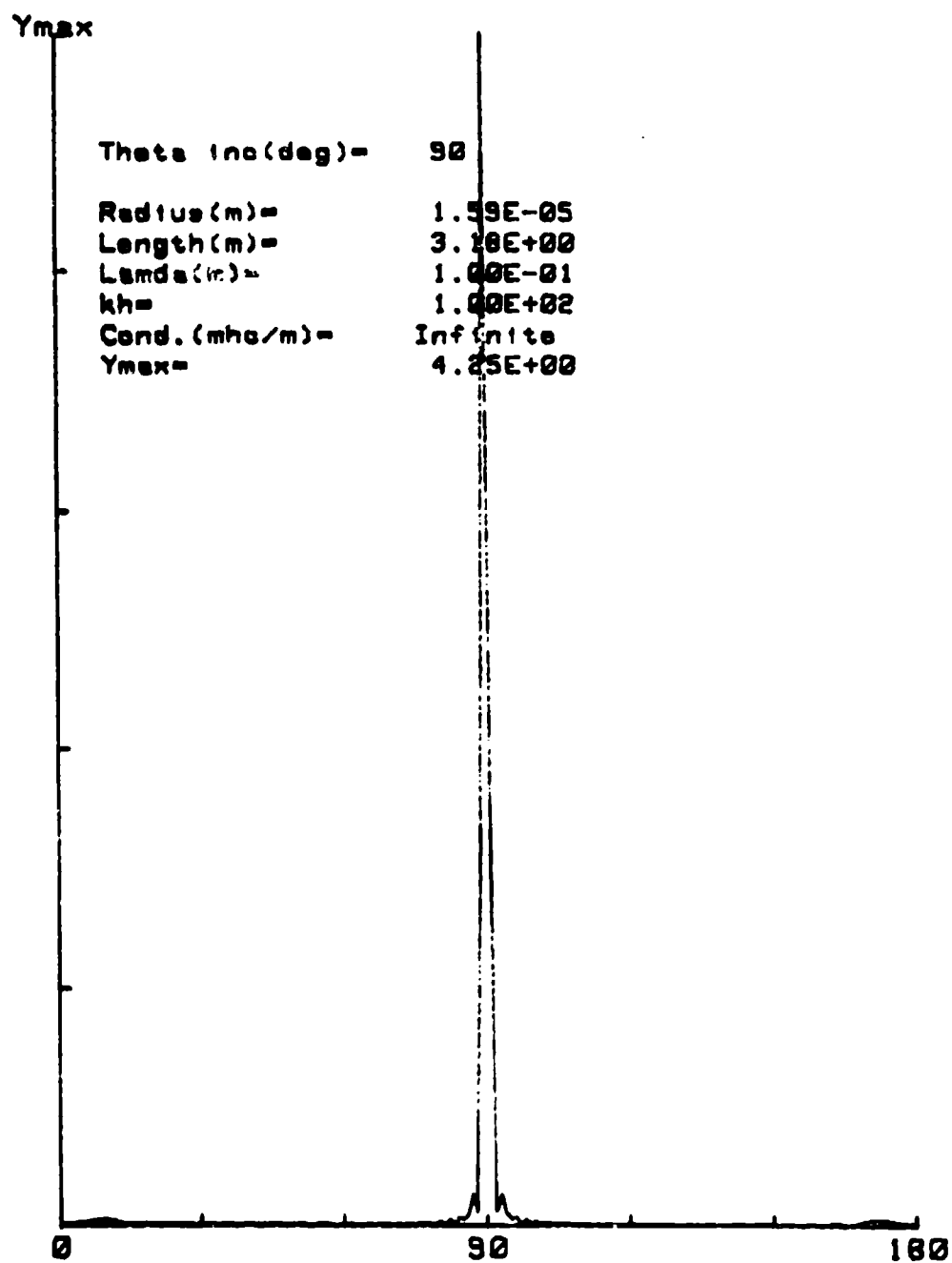


Fig. 25 Differential cross section/ λ^2 for an infinitely conducting cylinder, broadside incidence and $kh = 100$.

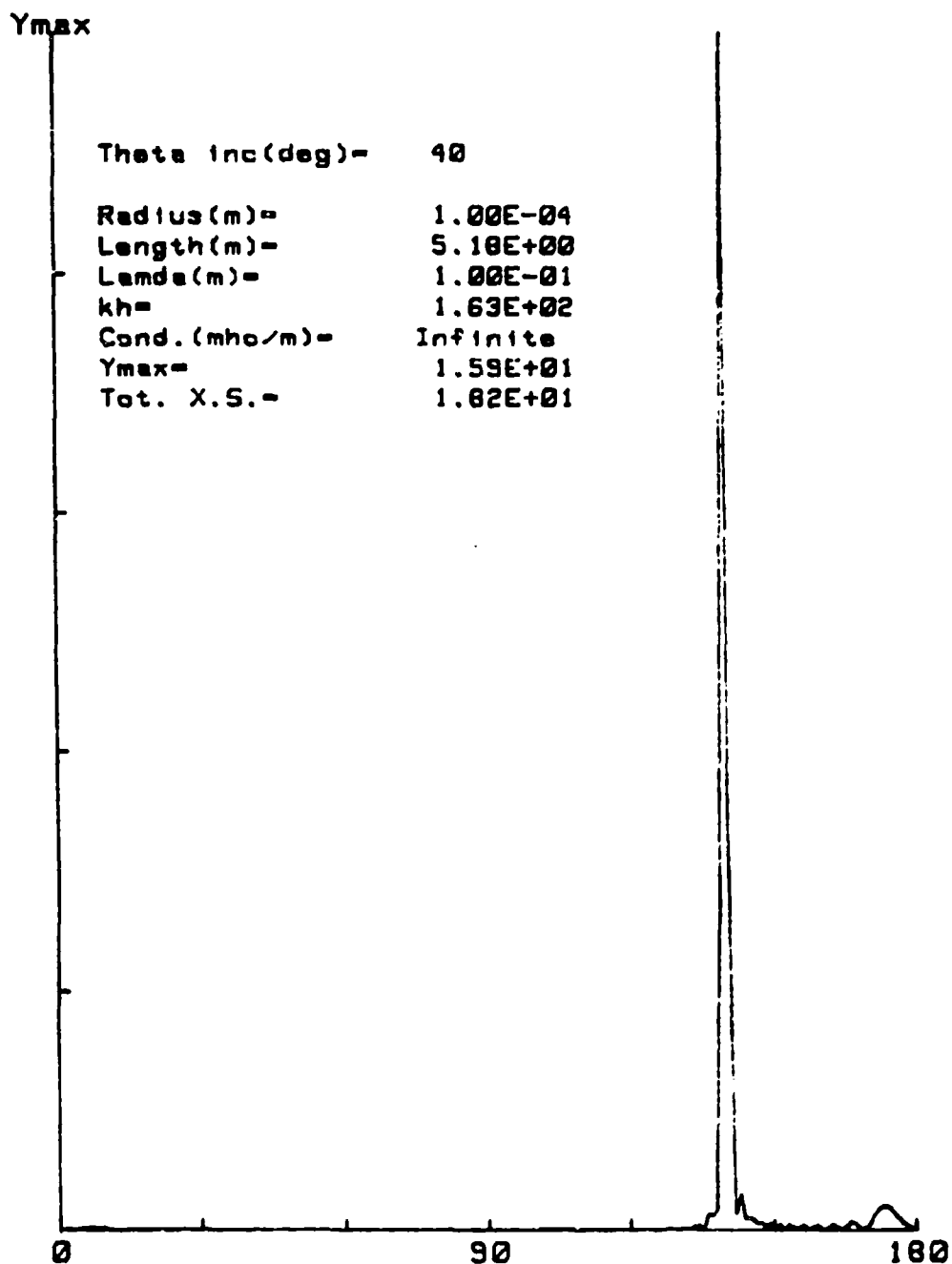


Fig. 26 Differential cross section/ λ^2 for an infinitely conducting cylinder with $\theta_1 = 40^\circ$ and $kh = 163$.

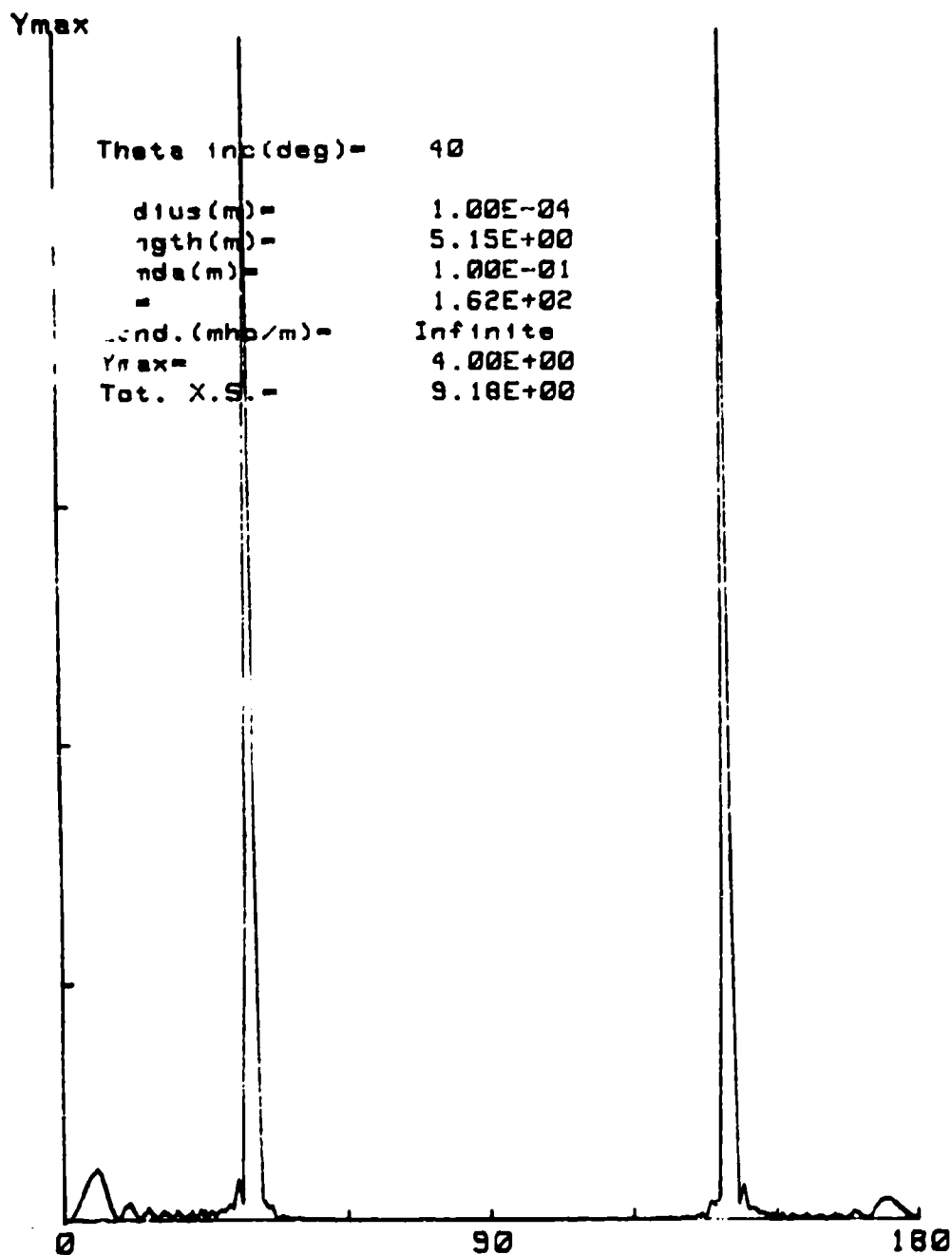


Fig. 27 Differential cross section/ λ^2 for an infinitely conducting cylinder with $\theta_i = 40^\circ$ and $kh = 162$.

total length, $l = 2h$, is given by $l = 103.3 (\lambda/2)$. Although points are computed only for every degree of scattering angle, it can be seen that the scattering pattern is well behaved, with a large peak in the forward direction*.

This expected behavior of the scattering pattern is typical of nearly all of the $kh \gg 1$ scattering patterns which we have plotted. We have, however, found an exception to this behavior. It occurs within a very narrow range of kh when the total length is approximately equal to any (even or odd) multiple of a half wavelength. When such multiples occur, i.e., $l = 2h = N\lambda/2$ when $N \gg 1$, we find a large peak (equal to the forward scattering peak) in precisely the backscattering direction $\theta = \theta_1$. This backscatter peak occurs for all angles of incidence for which we have made computations. An example of this is shown in Fig. 28. This anomalous behavior occurs for less than 5% of the cylinder lengths if we continuously vary cylinder length ($\theta_1 \neq 90^\circ$ and $kh \gg 1$) and observe the scattering in the backscattering ($\theta = \theta_1$) direction. A further discussion of this anomaly will be given in Section 3.5

3.4 Averaged Extinction, Absorption, and Scattering Cross Sections vs. Wavelength

In the case of transmission of electromagnetic radiation into clouds of randomly oriented conductive fibers, one is interested in the orientation averaged values of the extinction, absorption, and scattering cross sections. In particular, the cross section per unit volume of the particle is of importance. We have developed a computer program for the calculation of the above cross sections as a function of the wavelength of the incident radiation. The fixed parameters in the calculation are fiber radius, length, and conductivity.

As examples of the above mentioned plots, Figs. 28, 29, and 30 predict the spectral characteristics of thin graphite fibers in the spectral range $0.1 \text{ micron} \leq \lambda \leq 100 \text{ microns}$. The fixed parameters are radius = 0.1μ , conductivity = $3.3 \times 10^4 \text{ mho/m}$, and total length = 1μ , 3.3μ , and 10μ for Figs. 28, 29, and 30, respectively. The dashed lines correspond to scattering and absorption in the Rayleigh limit. Note that the various electromagnetic cross sections are averaged over particle orientation. It should also be noted that the orientation averaged scattering and absorption cross sections are computed by averaging these over all aspect angles and (in the case of scattering) all scattering angles, as shown by Eqs. (17) and (19). However, the extinction cross sections are computed using the Forward Amplitude theorem Eq. (18). At any wavelength, the sum of the scattering and absorption cross sections should, of

*As was pointed out earlier in this paper, the scattering is the same at the angle $180^\circ + \theta_1$ as at $180^\circ - \theta_1$. Therefore, the large peak at $180^\circ - \theta_1$ can be interpreted as forward scattering as well as scattering at $180^\circ - \theta_1$.

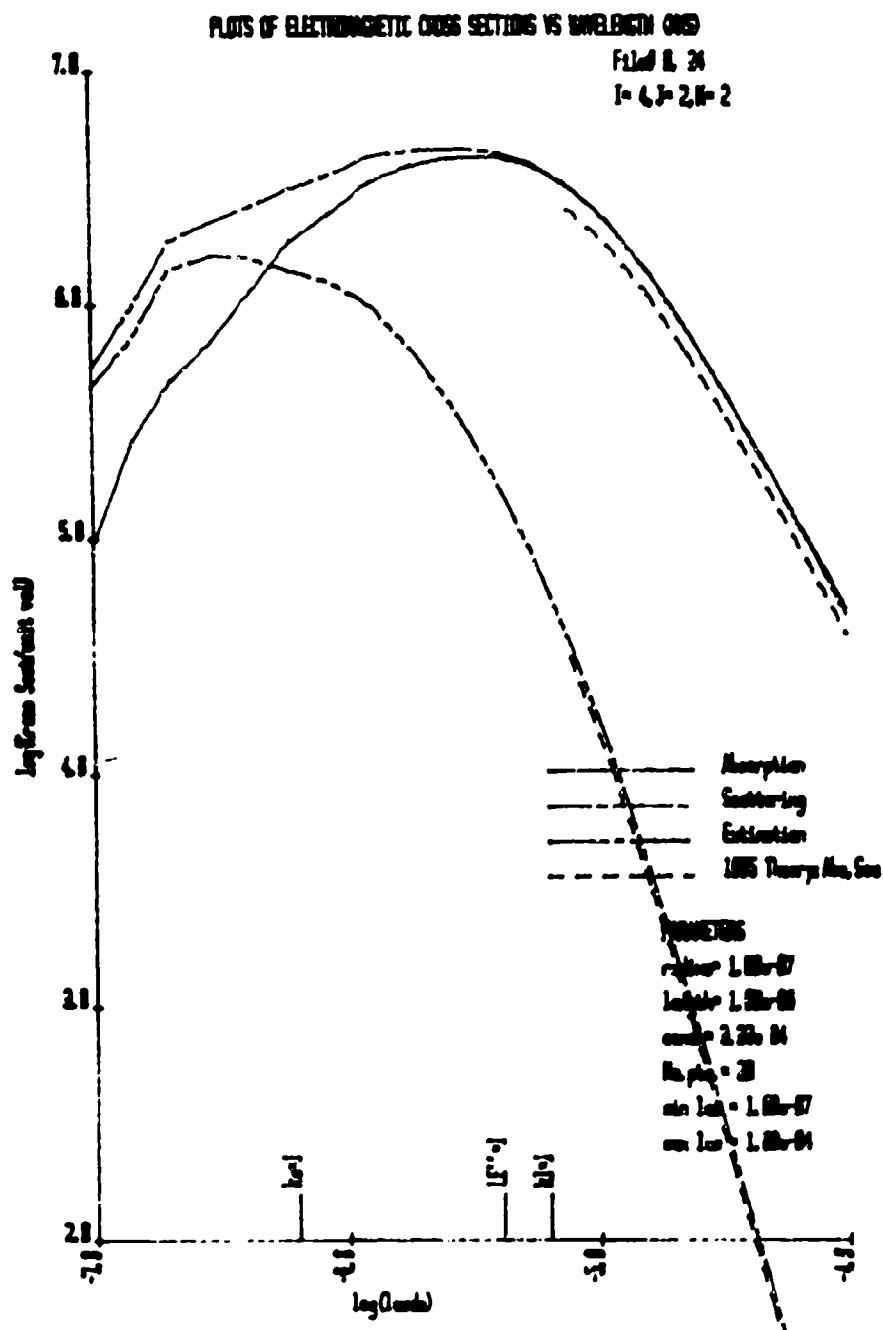


Fig. 28 Orientation averaged electromagnetic cross section/particle volume versus wavelength for a cylinder 1×10^{-6} meters in length.

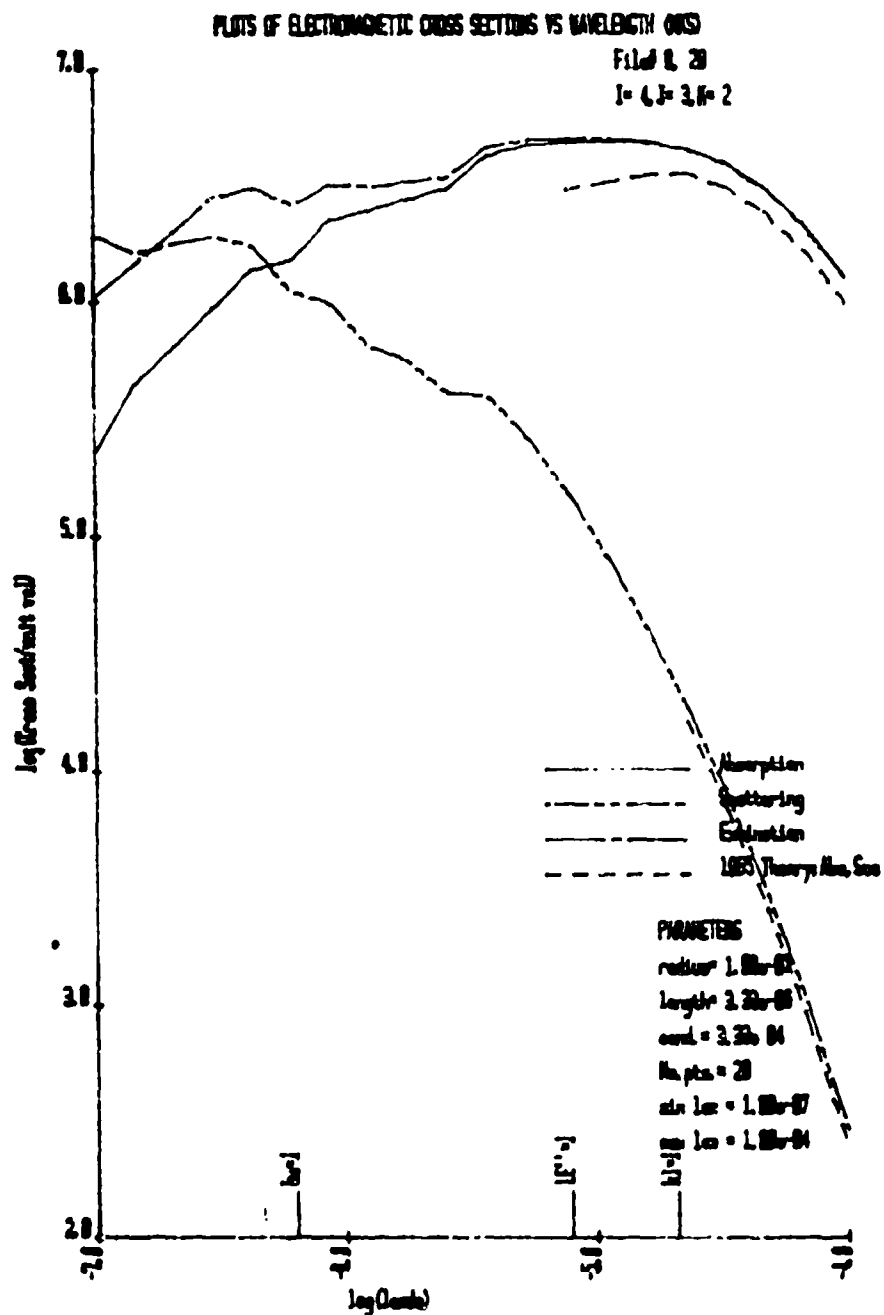


Fig. 29 Orientation averaged electromagnetic cross sections/ particle volume versus wavelength for a cylinder 3.33×10^{-6} meters in length.

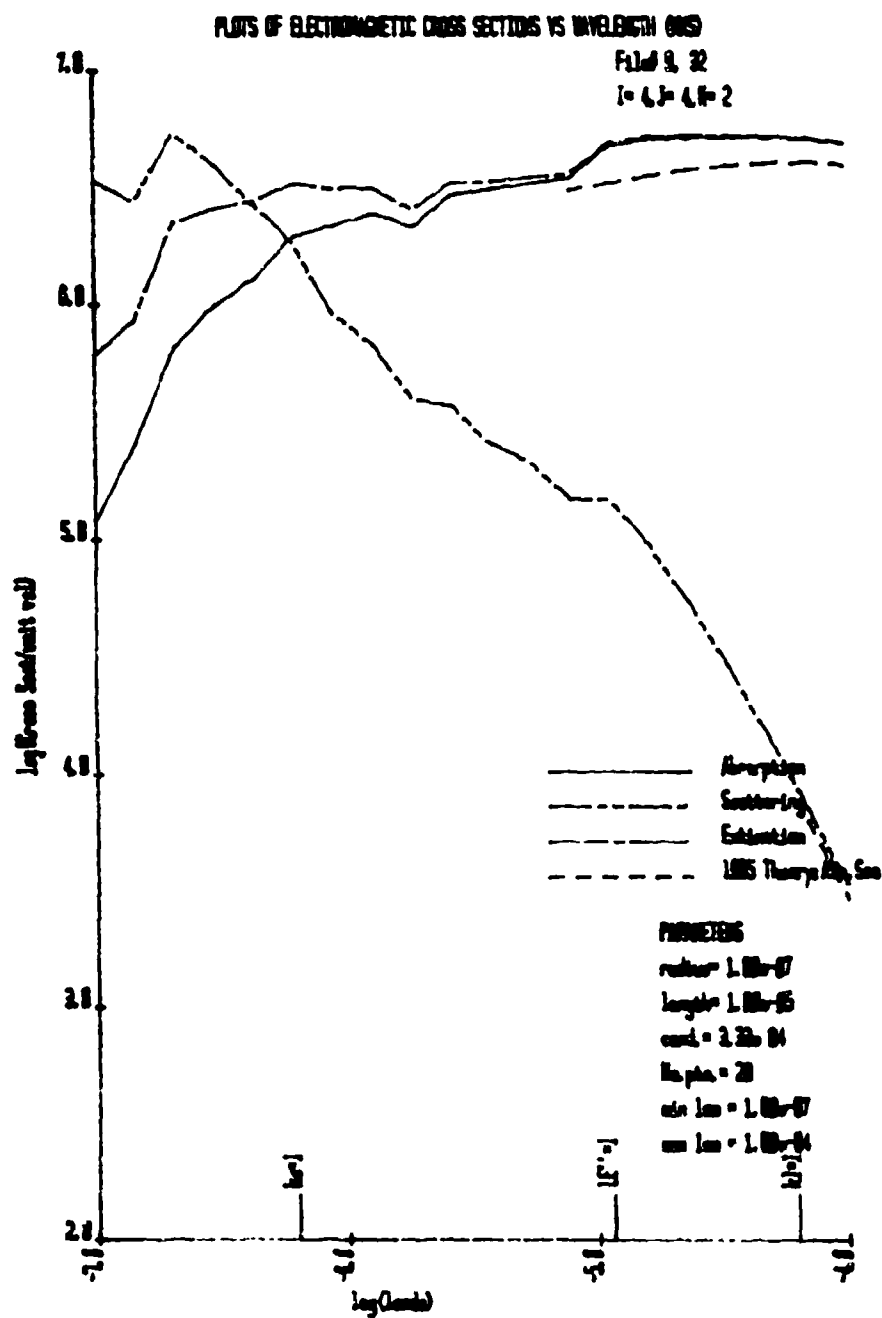


Fig. 30 Orientation averaged electromagnetic cross sections/ particle volume versus wavelength for a cylinder 1×10^{-5} meters in length.

course, be equal to the extinction cross section. Since the extinction cross section is computed by independent means, a good check on the theory is to determine whether or not the equality $\bar{\sigma}_{abs} + \bar{\sigma}_{scat} = \bar{\sigma}_{ext}$ prevails. Indeed, it can be seen by inspection of the three figures that the equality does exist throughout all but the shortest wavelength range of these.

The main purpose of including three figures is to demonstrate the behavior of the cross sections as the fiber length is increased from one micron to ten microns. In Fig. 28, we see that the absorption cross section becomes maximum at about $\lambda = 10 \mu$ and is more than two orders of magnitude higher than the scattering cross section for wavelengths longer than 10μ .

In Fig. 29, the length has been increased from 1μ to 3.3μ and we see that the absorption reaches its maximum at $\lambda = 20$ to 30 microns and the scattering cross section is greater than that of Fig. 28.

Figure 30 shows the behavior when the total length is increased to 10 microns. Here, we see that the absorption (and extinction) are fairly constant over the range $1 \mu \leq \lambda \leq 100 \mu$.

The above Figures show that, when the fiber/length is increased from 1μ to 10μ , one obtains improved absorptive (and extinction) properties of the fiber at the longer infrared wavelengths. It is also seen that, as fiber length is increased, the ratio of scattering to absorption cross sections increases (as we should expect).

It is important to note that the numerical integrations for $\bar{\sigma}_{scat}$ and $\bar{\sigma}_{abs}$ were carried out in 5° increments in both θ and θ_1 . This rather coarse increment was necessary because of computer memory limitations. As kh becomes larger, the scattering patterns become more peaked, and the finer the angular integration increment should be. The use of a 5° increment is probably the reason for the inequality of $\bar{\sigma}_{scat} + \bar{\sigma}_{abs} = \bar{\sigma}_{ext}$. This tentative conclusion is reinforced by noting that the exact specular peak at $\theta = \pi - \theta_1$ is always one of the points included in the angular integration of the differential scattering cross sections, and it is therefore weighted more strongly as the width of the peak approaches the angular integration increment. We plan to compute a limited number of plots similar to those of Figs. (28), (29), and (30) using 1° increments, and to compare the short wavelength behavior with that of Figures 28, 29, and 30.

Finally, it is interesting to note that, in the long wavelength limit, previous results^{8,9} based on Rayleigh scattering and absorption (dashed line) are in close agreement with those of the present theory.

3.3 Discussion

The primary purpose of our theoretical work on scattering and absorption by cylinders has been to include ohmic losses in the historic formalism developed by Tai¹, Cassey and Fainberg², and others. The reason for this has been to provide a useful procedure for the computation of scattering, absorption, and extinction cross sections for lossy fibers. It turns out that essentially all of the available experimental data with which we can compare the theoretical results involves wires having a conductivity so high that, for all practical purposes, it is infinite. This is why a large portion of the data presented in this report involve infinitely conducting fibers.

The details of the various scattering patterns which we have investigated obviously depend to a very high degree upon the current function. The absorptive properties, of course, also depend upon the current function. We believe that good behavior of the scattering patterns in a given regime justifies the use of the present current function in that regime for the calculation of absorption as well as scattering. To say this in another way, a careful analysis of the scattering predictions of the theory is a powerful tool in determining where the use of the present theory is acceptable and where it is not. In addition, as mentioned in Section 3.2.3, the conservation of energy criterion ($\sigma_{\text{scat}} + \sigma_{\text{abs}} = \sigma_{\text{ext}}$) also serves as an important validation tool.

With regard to the data which we have included in the preceding pages, we have the following specific comments:

- (1) The features of the differential scattering data of Sections 3.1.1 and 3.1.2 (Figs. 2 through 9) appear to be as one would expect, with the forward scattering lobe becoming more pronounced as $kh \rightarrow 10$. A somewhat disturbing feature of these data is the presence of rather larger lobes near 0° and 180° (end-on) than we expected to find.
- (2) The data on backscatter cross sections is very instructive. Our predictions agree very well with the Lockheed measurements over the (rather small) range of $0.480 \leq 2/\lambda \leq 1.051$ in Section 3.2.1 (Figs. 10 through 16). The quantitative and qualitative details of the theory vs. these measurements are in good agreement.

In Section 3.2.1 very good agreement is demonstrated between theory and experiment for the three ka values of Figs. 17 and 18. However, note that the deep minima appearing in Fig. 18 are definitely incorrect. These zeroes in the backscatter cross section occur for arbitrarily small ka values, and therefore, signify zero values of $S(0)$, the forward scattering amplitude. This, in turn, forces the conclusion that the total cross section is zero at these values of kh , which cannot be.

The above problem can be directly traced to the current function of Eqs. (5), (6), and (7). If we integrate the current function over the length of the wire and set the integral equal to zero (e.g. net current = 0), we find that the relation $\tan(kh) = kh$ obtains. We have done parametric plots of this equation and find that the zeros of Fig. 18 occur precisely at the values of kh which satisfy the above transcendental equation. We should note that, in re-reading Tai's paper,¹ we found that he had discovered the same problem and produced the same transcendental equation. This is a definite limitation of the theory. Aside from this, we seem to be in good agreement with experiment. Therefore, taking this reservation into account, the theoretical backscatter data for various finite values of conductivity (Fig. 19) have high credibility.

- (3) In the case of very large values of kh , we see that the minima mentioned above persist out to at least $kh = 100$ (Section 3.3, Figs. 20 and 21), and predictions in the near vicinity of $\tan(kh) = kh$ should be disregarded. Aside from this, we find that the theory is well behaved for extremely large values of kh for broadside scattering. An asymptotic expression for the broadside backscatter cross section vs kh was derived and is given by Eq. (35).

The calculations of differential scattering cross section vs scattering angle plotted in Figs. 26 and 27 are very well behaved and produce exactly the narrow forward scattering lobe which we expected. However, we have determined (as discussed in Section 3.3) that, within a very narrow range of l/λ , a large backscatter peak occurs at all values of $l/\lambda = N$, where N is any large integer. Since this behavior is essentially independent of the angle of incidence, we conclude that it is incorrect and reflects a limitation of the simple current function which we are using.

- (4) The computations plotted in Figs. 28, 29, and 30 (Section 3.4) provide an example of the use of the theory which we have developed. In order to obtain accurate results in the larger kh range, we must obviously use finer angular increments in the integrations to obtain the total scattering cross sections. We have realized this for some time and are taking steps to obtain higher computational speed and more needed computer memory. It is particularly interesting to note the good agreement in the Rayleigh region between the early calculations of Pedersen and the present theory.

It is recognized that realistic calculations in the infrared and visible portions of the spectrum require the use of established optical constants (complex refractive index) and appropriate modification thereof in the very thin limit of particle radius.

In conclusion, we have found surprisingly good agreement between the theoretical predictions and available experimental data. The calculations are well behaved out to very large values of kh where we find no onset of instability. Two limitations of the theory were identified. These occupy only a very small fraction of the kh values in any given kh range and such kh values can be avoided in future computations without serious limitations of the overall information which one can obtain. We believe that theory as it now stands is, with these specific restrictions, applicable to many problems of more than passive interest to DoD.

References

1. C. T. Tai, Electromagnetic Backscattering from Cylindrical Wires, J. Appl. Phys., Vol. 23, pp. 909-916 (August, 1952).
2. E. S. Cassedy and J. Fainberg, Electromagnetic Cross Sections of Finite Conductivity, The Johns Hopkins Laboratory Technical Report No. AF-81, August 1960.
3. J. R. Wait, Exact Surface Impedance for a Cylindrical Conductor, Electr. Lett. 15, 659-660 (1979).
4. N. E. Pedersen, J. C. Pedersen and P. C. Waterman, "Theoretical Investigation of Absorptive Processes," Final Report for Period 1 April 1979 - 1 April 1981, Prepared for Army Research Office and U.S. Army Research and Development Command (May, 1981).
5. J. R. Webb, "Radar Backscatter Measurements for Tungsten and Copper Dipoles," Report No. ER-6984, (June 1, 1964).
6. B. O. As and H. J. Schmitt, "Back-Scattering Cross Section of Reactively Loaded Cylindrical Antennas," Scientific Report No. 18, Cruft Laboratory, Harvard University (August, 1957).
7. R. W. King and T. T. Wu, "The Scattering and Diffraction of Waves," p. 161, Harvard University Press (1959).
8. N. E. Pedersen and J. C. Pedersen, Theoretical, Experimental and Systems Studies on a New Technique for Radar Cross Section Reduction, (Secret), AVCO RADTN-65-67, 8 December 1965.
9. N. E. Pedersen, J. C. Pedersen and H. A. Bethe, "A New Method of Radar Target Concealment," Proc. Tri-Service Radar Symposium, San Diego, 1969 (Secret).

DIPOLE-DIPOLE SCATTERING INTERACTION AND ITS RELATION TO PARTICLE SEPARATION IN COATINGS AND CLOUDS*

D. L. Dye, D. C. Capps, C. Gulacsik, and D. H. Holze
Boeing Aerospace Company, P.O. Box 3999, Seattle, WA 98124
and

John W. Bond
Belvoir Research and Development Center, Ft. Belvoir, VA 22060

ABSTRACT

Eleven dipole interaction calculations were carried out. It was found that absorption is reduced if dipoles interact, that use of short dipoles can provide more absorption per unit volume, and that scattering and absorption characteristics can be optimized through choice of dipole conductivity.

INTRODUCTION

Dipoles are used to scatter and absorb EM radiation in many practical applications. Often it is assumed that the dipoles act independently, so the effect of N dipoles is N times that of one dipole. If, instead, the dipoles interact, they generally tend to shield one another, reducing the net effect to less than N times that of one dipole.

We report on calculations made to assess the distances between dipoles, in various configurations, at which one may assume they act independently. First we examine two extreme cases that are tractable theoretically: a Rayleigh-sized sphere and an infinitely long cylinder. Then we discuss several cases that are best handled by numerical analysis, specifically by a moments method computation. These are cases where the dipole length is near its resonance range.

In all cases the approach is to determine the ratio of scattered to incident field, $|E_s/E_i|$, as a function of distance from the dipole or group of dipoles. One expects little effect of the illuminated dipole upon another dipole placed at a distance where the ratio is small.

THEORETICAL CASES

CASE I - CONDUCTING RAYLEIGH SPHERE

The scattered field, E_s , at distance r along the direction of incidence and in the plane perpendicular to the dipole moment due to an incident field, E_i , polarized parallel to the dipole is given by (ref. 1):

$$\left| \frac{E_s}{E_i} \right| = \frac{k^2 R^3}{r} \left[1 - \frac{1}{(kr)^2} + \frac{1}{(kr)^4} \right]^{1/2}$$

or

$$\left| \frac{E_s}{E_i} \right| = \frac{\beta^3}{z} \left[1 - \frac{1}{z^2} + \frac{1}{z^4} \right]^{1/2}$$

*This work was supported by contract DAAK70-83-C-0066.

for $r > R$, where R = sphere radius

$$k = 2\pi/\lambda$$

$$\lambda = \text{wavelength}$$

$$\beta = kR$$

$$Z = kr$$

For a particular case with $R = 0.265$ mm and $\lambda = 0.5$ cm, this ratio is plotted in figure 1 as a function of distance from the sphere center. As expected, the scattered field decreases rapidly as one proceeds away from the sphere, and is less than 10% of the incident field for distances greater than about one sphere radius.

CASE II - INFINITELY LONG CONDUCTING CYLINDER

Reference 2 gives for the scattered field about an infinitely long conducting cylinder of radius R :

$$\left| \frac{E_s}{E_i} \right| = \frac{\{[J_0(kr)]^2 + [Y_0(kr)]^2\}^{1/2}}{\{1 + [(2/\pi) \ln(kR/2) + 0.5772]^2\}^{1/2}}$$

for $r > R$ and $kR \ll 1$ (Rayleigh condition on diameter).

For a particular case with $R = 4$ microns and $\lambda = 0.5$ cm, figure 2 plots this ratio as a function of distance, r . As expected, the scattered field decreases slowly with distance from the very long fiber, becoming less than 10% only at about one wavelength distance.

NUMERICALLY ANALYZED CASES

For cases III et seq., more realistic dipole configurations were investigated, cases not generally tractable except by use of numerical analysis methods. The Numerical Electromagnetics Code (NEC), a moments method code developed at Lawrence Livermore Laboratory, was used for this study (ref. 3). NEC allows one to solve for currents and fields around wires and other structures in free space and over ground planes. The analysis proceeds by solving integral equations for induced currents, then computing resultant fields. The output for this study consisted of both currents and fields.

As with any numerical solution, care must be exercised in setting up the problems and choosing enough elements, i.e., segments of conductors to provide for adequate accuracy and convergence. Convergence of solutions is checked by running the code for the same problem with variations in segmentation. In the cases reported below, no attempt was made to compute fields very close to the wire surfaces since these values are not of interest and they add complexity in setting up and obtaining convergence.

CASE III - SHORT DIPOLES

Case III approximated the Rayleigh dipole calculated theoretically above. The scattered field about a stainless steel dipole 8 microns in diameter and $\lambda/100$ long was calculated and is plotted in figure 3. Microwave band stainless steel conductivity was taken from reference 4. As expected, the scattered field falls off rapidly with distance, being about 2% at one dipole length.

CASE IV - HALF-WAVELENGTH DIPOLES

Figure 4 plots the scattered field versus radial distance from a resonant fiber. The field decreases quite slowly with distance, being nearly 20% at $\lambda/2$ and still 10% at a distance of two dipole lengths. As a variation of this case, figure 5 plots the same quantities when the conductivity of the fiber is taken to be that of graphite, 1.33×10^5 mhos/m, an order of magnitude smaller than that of stainless steel. This value is also from reference 4. Figure 6 shows the scattering field when the dipole material is a highly conductive metal such as silver, 6.17×10^7 mhos/m. The effect of conductivity is seen to be an increase in scattering for more conductive materials, as one would expect. Interaction between low-conductivity dipoles is smaller, allowing the dipoles to be spaced more closely and still act independently as absorbers.

CASES V, VI, AND VII - TWO PARALLEL DIPOLES, SPACED VARIOUSLY

Applications may involve a number of these dipoles spaced apart variously. Case V studied the scattered field around two parallel half-wavelength dipoles a tenth wavelength apart; case VI, the same dipoles spaced one-third of a wavelength apart; and case VII, two-thirds of a wavelength apart. These three cases are plotted in figures 7, 8, and 9, respectively. They show that at close spacing, the scattered field away from the dipole pair falls off with distance somewhat more slowly than at wider spacing. At very close spacing, the two dipoles appear to behave as one and the falloff is similar to that of a single dipole.

CASE VIII - CURRENTS IN DIPOLES

To assess the effect of dipole-dipole interactions on both absorption and scattering, NEC runs were made of two different half-wave configurations, spaced far apart and closely ($\lambda/10$). Figure 10 shows these bounding cases. The curves reinforce the point made earlier about fields: the current in each dipole becomes smaller as the dipoles get closer, and the sum of the currents generates a single dipole-like field pattern. However, if the resistivity of the wire material is the same in both dipoles, then the power absorbed in two dipoles carrying half the current is less than that of one dipole carrying the total current.

CASES IX, X, AND XI - PERPENDICULAR DIPOLES

A dipole perpendicular to the incident E-field will not respond to it; hence, dipoles centrally crossed at right angles behave as a single aligned dipole, whether the dipoles are in contact or not. A similar situation exists for

perpendicular dipoles formed in the shape of the letter "T" when they are not in contact. The NEC calculation for both of these cases shows a scattered/incident field ratio virtually identical to that of a single dipole of the same length.

However, if in the T-shaped dipole arrangement the two dipoles are in electrical contact, then there is current flow into the top of the T from the stem and some effect upon the radiation field from this altered current distribution. The NEC result for this case (XI) is plotted as figure 11. It is seen that the scattered field drops off much more rapidly from these T-shaped dipoles than from a single aligned dipole. One expects this behavior to occur for any case where contacting dipoles are asymmetrically arranged.

DISCUSSION AND CONCLUSIONS

We have shown by a moments method calculation that:

1. Interactions between dipoles reduce the current per dipole, and thus reduce the energy absorption in the dipoles.
2. Short dipoles have a shorter range of interaction, and thus can provide space for more scattering and absorbing elements in a given volume.
3. A perpendicular dipole in proximity to the illuminated dipole (aligned with the incident field), but not in contact with it, has no effect on the scattered field. However, perpendicular dipoles touching away from their centers have reduced interaction range.

These results imply that small (e.g., Rayleigh) and randomly oriented dipoles in coatings and/or clouds will be more effective than resonant or long aligned dipoles. Also, there is a tradeoff to be made between high and low conductivity of the dipoles depending upon whether one is optimizing scattering or absorption.

REFERENCES

1. Principles of Optics, M. Born and E. Wolf, Pergamon Press, Sixth Edition, 1980, p. 650.
2. J. R. Wait, Canadian Journal of Physics, vol. 33, p. 189.
3. Numerical Electromagnetics Code (NEC) - Method of Moments, NOSC technical document 116, vol. 1, 1980, Naval Ocean Systems Center, San Diego, CA.
4. Multispectral Techniques for Radar, Infrared and Visual Camouflage, Volume IV, R. L. Moore, J. P. Montgomery, and T. B. Wells, Georgia Tech Research Institute, 1983 (Secret).

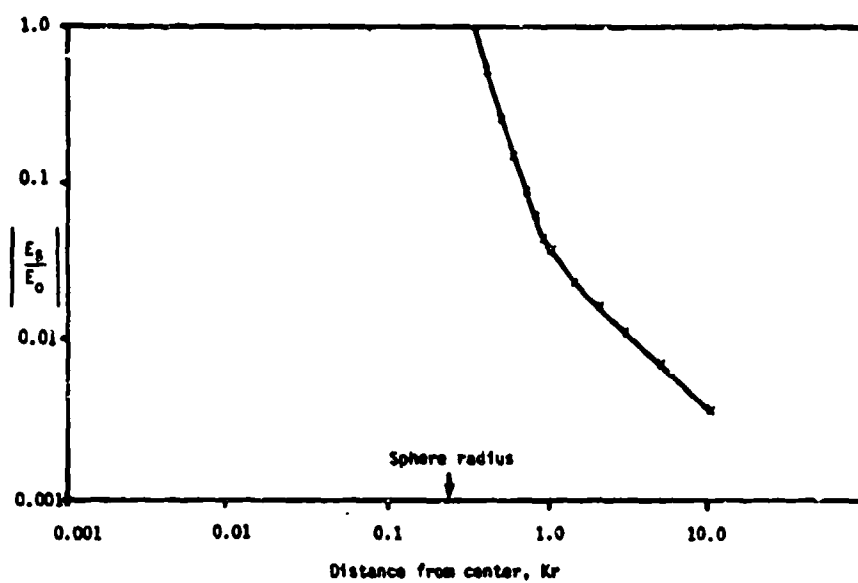


FIGURE 1. SCATTERED FIELD OF A RAYLEIGH SPHERE VERSUS RADIAL DISTANCE (THEORETICAL).

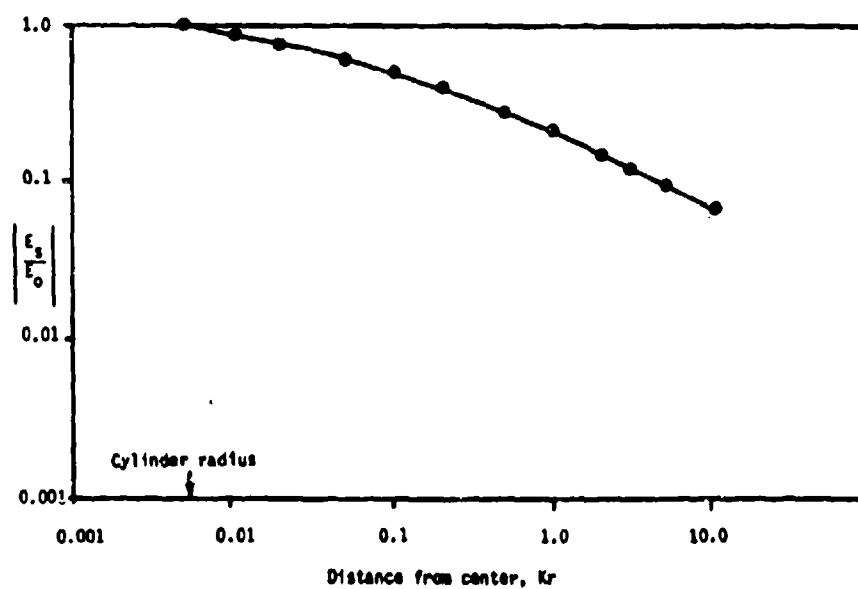


FIGURE 2. SCATTERED FIELD OF AN INFINITE THIN CYLINDER VERSUS RADIAL DISTANCE (THEORETICAL).

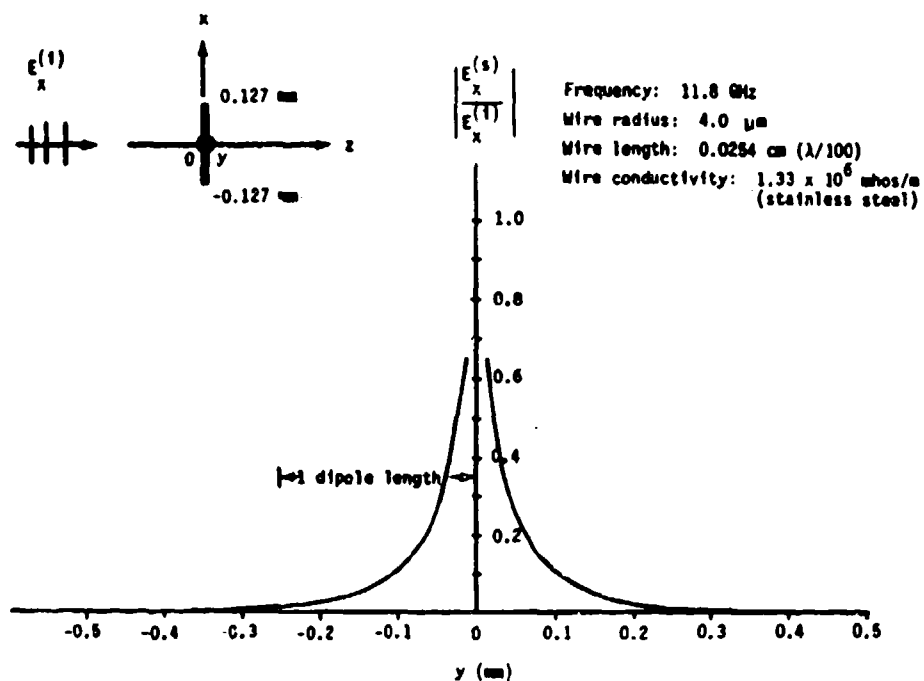


FIGURE 3. SCATTERED FIELD OF A $\lambda/100$ LENGTH DIPOLE (NEC CALCULATION).

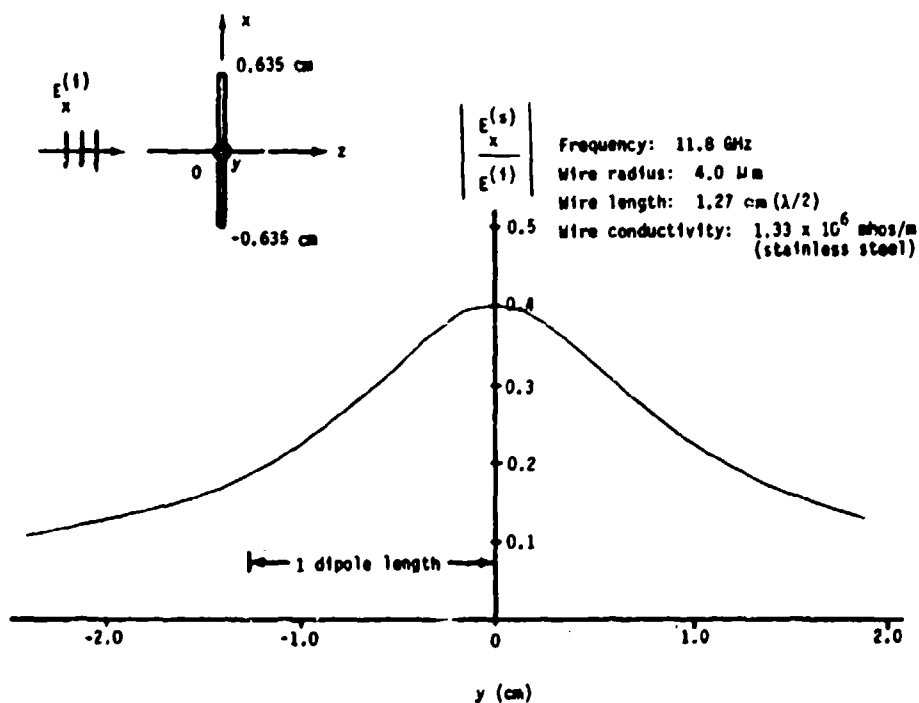


FIGURE 4. SCATTERED FIELD OF A $\lambda/2$ LENGTH DIPOLE WITH CONDUCTIVITY 1.33×10^6 MHOS/M (NEC CALCULATION).

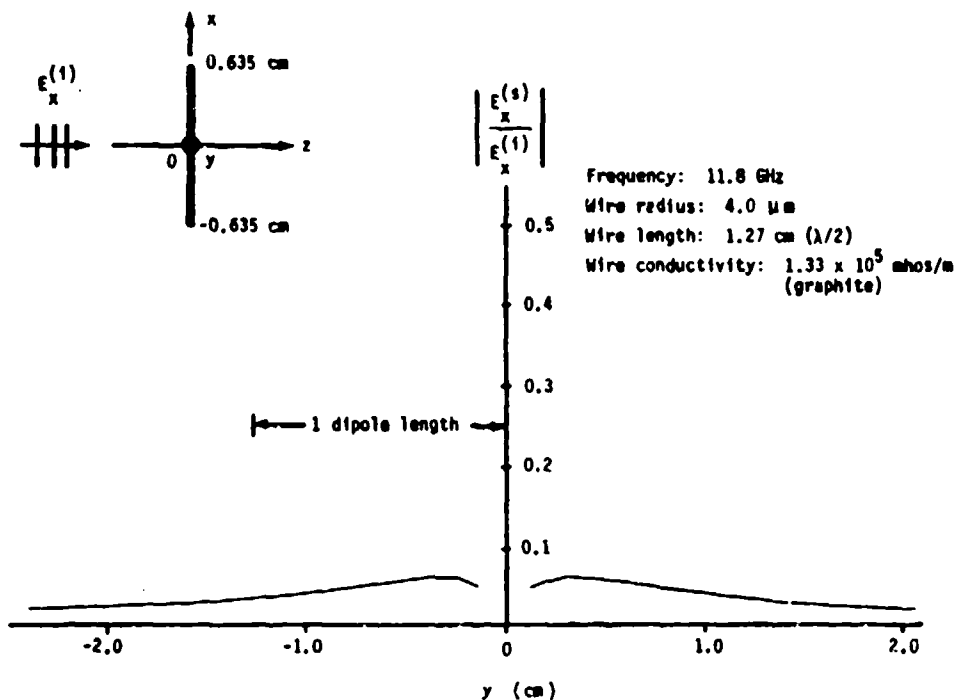


FIGURE 5. SCATTERED FIELD OF A $\lambda/2$ LENGTH DIPOLE WITH CONDUCTIVITY 1.33×10^5 MHOS/M (NEC CALCULATION).

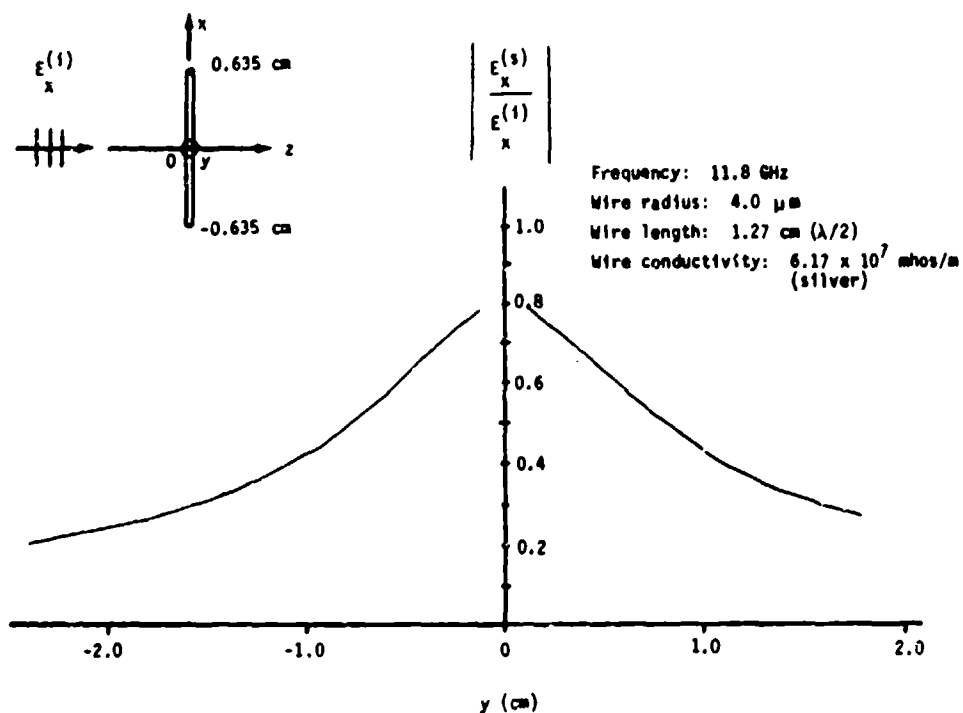


FIGURE 6. SCATTERED FIELD OF A $\lambda/2$ LENGTH DIPOLE WITH CONDUCTIVITY 6.17×10^7 MHOS/M (NEC CALCULATION).

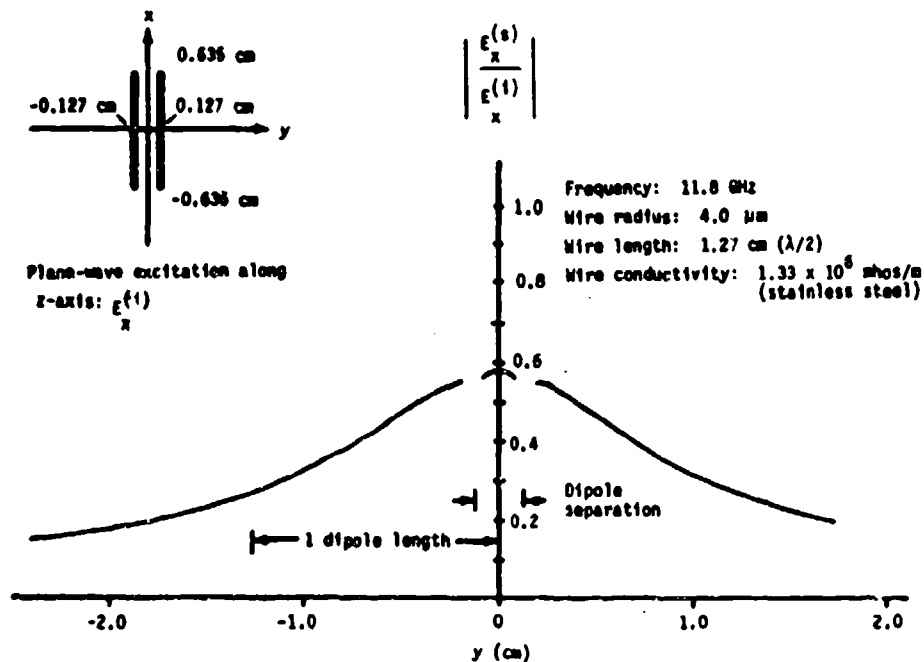


FIGURE 7. SCATTERED FIELD OF A PAIR OF $\lambda/2$ LENGTH DIPOLES SPACED $\lambda/10$ APART (NEC CALCULATION).

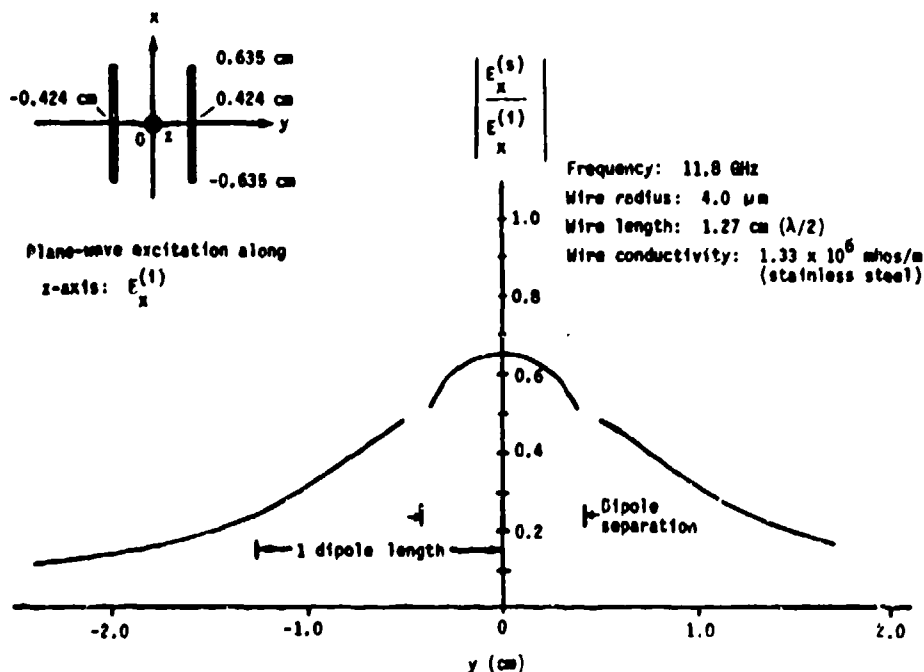


FIGURE 8. SCATTERED FIELD OF A PAIR OF $\lambda/2$ LENGTH DIPOLES SPACED $\lambda/3$ APART (NEC CALCULATION).

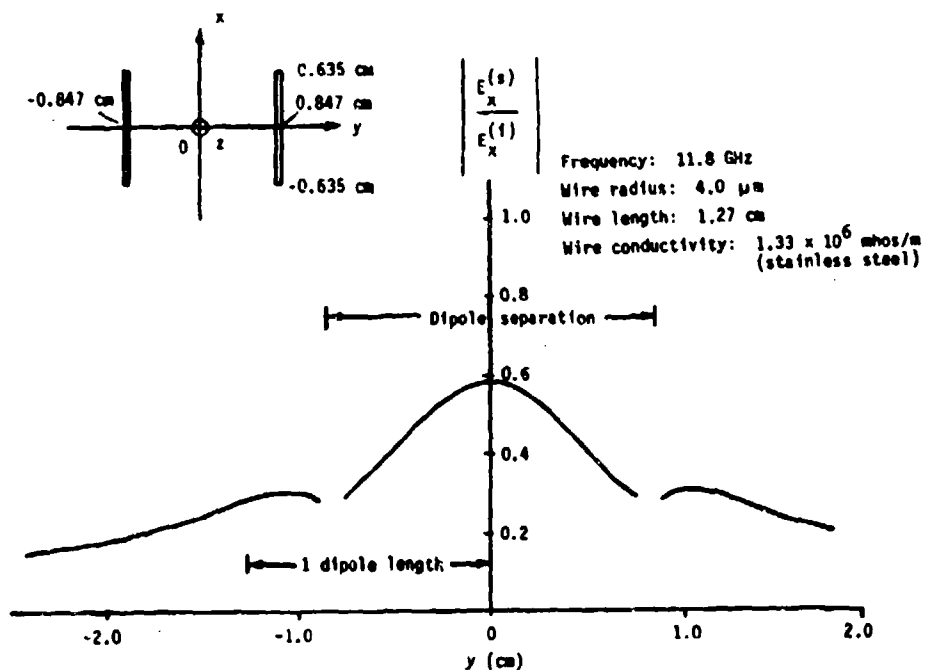


FIGURE 9. SCATTERED FIELD OF A PAIR OF $\lambda/2$ LENGTH DIPOLES SPACED $2\lambda/3$ APART (NEC CALCULATION).

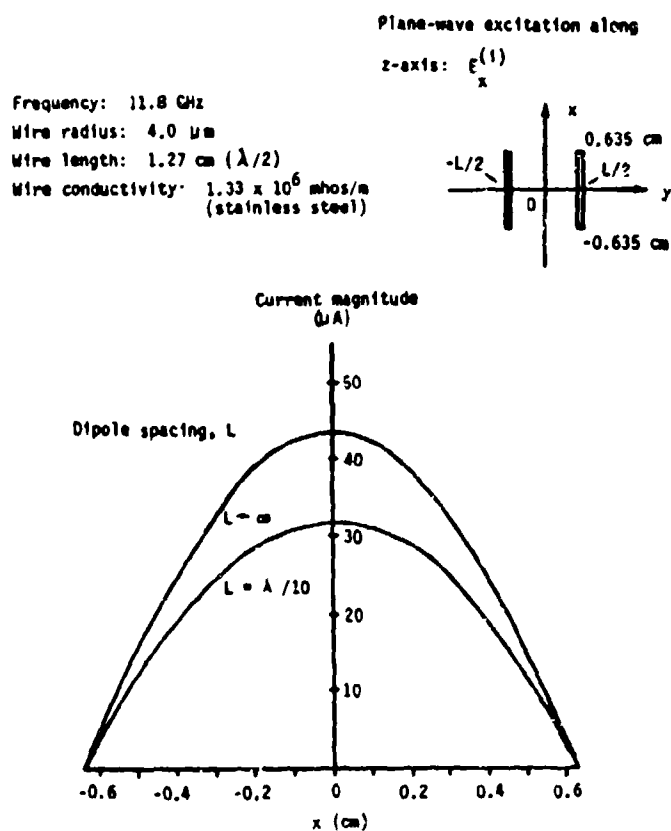


FIGURE 10. MAGNITUDE OF CURRENT ALONG EACH DIPOLE OF A PAIR SPACED FAR APART AND AT $\lambda/10$.

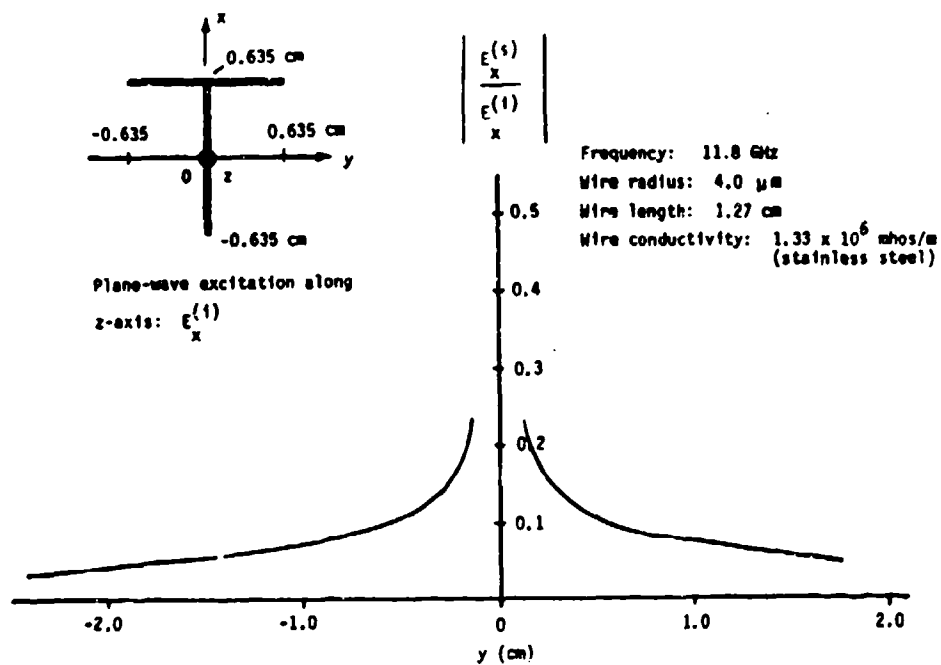


FIGURE 11. SCATTERED FIELD OF A PAIR OF PERPENDICULAR LENGTH DIPOLES, CONTACTING AT THE END OF ONE AND THE CENTER OF THE OTHER ("T" SHAPE).

DOUBLE SCATTERING FROM CYLINDERS AND SPHEROIDS

RICHARD D. HARACZ, LEONARD D. COHEN AND ARIEL COHEN
Department of Physics and Atmospheric Science
Drexel University
Philadelphia, Pennsylvania 19104

ABSTRACT

The perturbation theory for the double scattering of light from finite cylinders and spheroids is described for the range of wavelengths satisfying $ka(m-1) \leq 1$. Significant differences are noted at large scattering angles. The special geometry for double scattering is also described, and it requires the ability to describe single scattering with all directions randomly oriented.

INTRODUCTION

Finite cylinders and spheroids are compared to test the possible effect of edge effects on the scattering amplitudes. The theory for this application follows the Shiffrin method¹ modified by Acquista² and applied to cylinders and spheroids as described in Haracz, L. Cohen, and A. Cohen.³ The perturbation theory is used for ease of calculation, but necessitates the restriction $ka(m-1) \leq 1$, where m is the index of refraction, k the wave number and a the radius of the target.

We will also discuss the particular geometry for double scattering for finite targets with a symmetry axis and indicate the constraint imposed by infinite cylindrical targets. The ability to do double scattering implies the ability to describe the scattering processes with all directions (light directions and polarization) perfectly random. Thus, not only can multiple scattering be handled, but also scattering from clouds of randomly oriented particles.

We will also discuss the constraints imposed on the double scattering geometry by infinite cylinders. This latter application has the advantage of being described by an exact theory that holds for all sizes and indices of refraction. In addition, the results for infinite cylinders have recently been shown to agree well with scattering from long cylindrical metallic wires.⁴

COMPARISON OF FINITE CYLINDERS AND SPHEROIDS FOR SINGLE SCATTERING

As described in Ref.3, finite cylinders are compared for aspect ratios from 1/2 to 5, for equal volumes of about $2 (\mu m)^3$, and index of refraction $m = 1.33$ (to compare the spheroid results with the results of an exact theory), and $k = 1$.

a) Finite Cylinder

The target frame of reference is defined by the incident direction of light (\vec{x}_0), the target axis (\vec{z}_A), and the direction perpendicular to this plane (\vec{x}_0). The y_0 axis is in the \vec{x}_0 - \vec{z}_A plane.

The first-order contribution to the scattered wave in the target frame of reference is then given by

$$(\vec{E}_{SA})_A = (\vec{E}_A \cdot \hat{k}_{AB} \hat{k}_{AB} - \vec{E}_A)_A$$

where the quantity in parenthesis is a projection of the scattered wave that is transverse to the scattered direction \hat{k}_{AB} . The vector \vec{E}_A is

$$\vec{E}_A = \frac{e^{ik_0 r}}{r} A^2 \kappa(k_0 \hat{k}_{AB} - \vec{k}_0)(P) \vec{E}_0,$$

where

$$\kappa(\vec{x}) = \frac{2\pi a^2 h \sin(x_n h/2) J_1(x_\perp a)}{(x_n h/2)(x_\perp a)},$$

with

a = radius, h = height of cylinder,

x_n = component of \vec{x} parallel to \vec{z}_A ,

x_\perp = component of \vec{x} perpendicular to \vec{z}_A ,

and the polarization matrix is derived in the electrostatic limit as

$$(P) = \begin{pmatrix} a_{TE} & 0 & 0 \\ 0 & a_{TM} & 0 \\ 0 & 0 & a_{TM} \end{pmatrix}$$

described in Ref.3. The second-order term in the perturbation theory is also described in this reference.

b) The spheroid.

The first-order scattered wave from a spheroidal target has a similar form, but in this case the pupil function has the form

$$\begin{aligned} \kappa(\vec{x}) &= V f[a(x^2 - \epsilon^2 x_\perp^2)] , \text{ prolate } , \\ &= V f[a(x^2 - \epsilon^2 x_n^2)] , \text{ oblate } , \end{aligned}$$

$$f(y) = 3 [\sin(y) - y \cos(y)] / y^3$$

with V the volume of the spheroid and ϵ the eccentricity. The polarization matrix has the terms (prolate)

$$a_{rm} = \{ n^2 - \delta(n^2 - 1) [(1 - \delta^2) \coth^2 \delta + \delta] \}^{-1},$$

$$a_{re} = 2 \{ 2 + \delta(n^2 - 1) [(1 - \delta^2) \coth^2 \delta + \delta] \}^{-1},$$

with

$$\delta = 1/\epsilon.$$

c) Conclusions.

Typical results of this comparison is shown in Fig.2 (normal incidence, polarization parallel to axis of symmetry). A study of results such as these indicates the following:

- (1) The perturbation theory through the second order agrees well with the theory of Asano and Yamamoto.⁵ The second-order correction is no larger than about 20% for the cases chosen in Ref.3.
- (2) The results for the cylinder and spheroid, though similar, differ at large scattering angles.
- (3) The differences noted could be significant for double scattering where one must include all orientations of the symmetry axes.

DESCRIPTION OF THE GEOMETRY FOR DOUBLE SCATTERING

The double scattering events are shown in Fig.1. The incident wave \vec{E}_0 is linearly polarized. The direction of the incident light is z_0 and the direction of the scattered light is z_{AB} . The plane formed by these two directions is called the reference plane. The direction perpendicular to the reference plane is called x_0 , and the reference frame is x_0, y_0, z_0 . The incident wavefront is in the $(xy)_0$ plane and its polarization makes an angle of α with x_0 .

a) The first scattering.

In our discussion of scattering from finite targets, we presented the scattered wave in the "target frame". The orientation of the first target A is given in terms of the reference frame by the angles ϕ_A and γ_A shown in Fig.1. The same scene is shown in Fig.3 concentrating on target A. The target-A frame of reference is denoted x_A, y_A, z_A with z_A the axis of symmetry. As the plane $(sx)_A$ contains z_0 , the y_A axis is perpendicular to z_0 , and it is related to the y_0 axis by a rotation about z_0 through the angle γ_A . It follows that the target-A frame and the reference frame are related as

$$(x_0, y_0, z_0) \xrightarrow{R_{0A}(\phi_A, \gamma_A)} (x_A, y_A, z_A),$$

where

$$R_{0A}(\phi_A, \gamma_A) = R_{\gamma_A}(\phi_A) R_{\phi_A}(\gamma_A) \\ = \begin{pmatrix} \cos \phi_A \cos \gamma_A & \cos \phi_A \sin \gamma_A & -\sin \phi_A \\ -\sin \gamma_A & \cos \gamma_A & 0 \\ \sin \phi_A \cos \gamma_A & \sin \phi_A \sin \gamma_A & \cos \phi_A \end{pmatrix}.$$

The treatment of the first scattering then proceeds by specifying the incident field in the reference frame, transforming it to the target-A frame, applying the scattering operator to get the scattered wave in the target-A frame, and finally transforming this scattered wave back to the reference frame:

$$\vec{E}_0 = \begin{bmatrix} E_0 \cos \alpha \\ E_0 \sin \alpha \end{bmatrix}, \\ (\vec{E})_A = R_{0A} \vec{E}_0, \\ (\vec{E}_{SA})_A = S_A (\vec{E})_A, \quad S_A = \text{scattering matrix}, \\ (\vec{E}_{SA})_0 = R_{0A}^{-1} (\vec{E}_{SA})_A$$

b) The second scattering.

The second scattering is depicted in Fig.4. Again, the reference frame is defined as above. The target-B frame is defined as for target A with z_B the symmetry axis. The reference frame and the target-B frame are related as

$$(x_0, y_0, z_0) \xrightarrow{R_{0B}(\phi_B, \gamma_B)} (x_B, y_B, z_B)$$

where

$$R_{0B}(\phi_B, \gamma_B) = \begin{pmatrix} \cos \phi_B \cos \gamma_B & \cos \phi_B \sin \gamma_B & -\sin \phi_B \\ -\sin \gamma_B & \cos \gamma_B & 0 \\ \sin \phi_B \cos \gamma_B & \sin \phi_B \sin \gamma_B & \cos \phi_B \end{pmatrix}.$$

Thus, given the scattered wave from the target A in the reference frame, as treated in section a), one must transform it to the target-B frame. The scattering matrix for target B can then be applied and the result is a second-scattered wave in the target-B frame. Finally, one transforms this scattered wave back to the reference frame. It is noted that the final direction is back towards the lidar (the source of light), or the final direction is $-z_0$.

c) Case of the infinite cylinder.

For an infinite cylinder, the scattering is well known to be restricted to a cone. This situation has been analyzed by us for double scattering⁶, shown in this reference that the angular parameters introduced in the above discussions are related as

$$\cot \phi_A = \cos \chi_A \cot \phi_0 ,$$
$$\sin(\theta_A/2) = \sin \phi_0 / \sin \phi_A ,$$

where θ_A is the scattering angle. Thus the number of orientational degrees of freedom are reduced in the case of the infinite cylinder. The details for the double scattering of light from infinite cylinders is given in Ref.6.

CONCLUSIONS

The various theories for the scattering of light from targets with a symmetry axis requires that a frame of reference containing the incident direction and the direction of symmetry be used. In double scattering, the directions of incidence and polarization are random, and a different coordinate system is needed to take this randomness into account. We call this the reference frame. The description of double scattering thus involves relating the two target frames (in which the scattering matrices are applied) to the reference frame. Triple scattering would be handled in a similar way with a second reference frame defined (between the second and third target).

REFERENCES

1. K.S. Shifrin, Scattering of Light in a Turbid Medium (Moscow, 1951; NASA TTF-477, Washington D.C., 1968).
2. C. Acquista, Appl. Opt. 15, 2932 (1976).
3. R. Haracz, L. Cohen, A. Cohen, Appl. Physics 23, 436 (1984).
4. A. Cohen, L. Cohen, R. Haracz, V. Tomaselli, J. Colosi and K. Moeller, J. Appl. Phys., (to be published).
5. S. Asano and G. Yamamoto, Appl. Opt. 14, 29 (1975).
6. A. Cohen, L. Cohen, R. Haracz, Appl. Physics, (to be published).

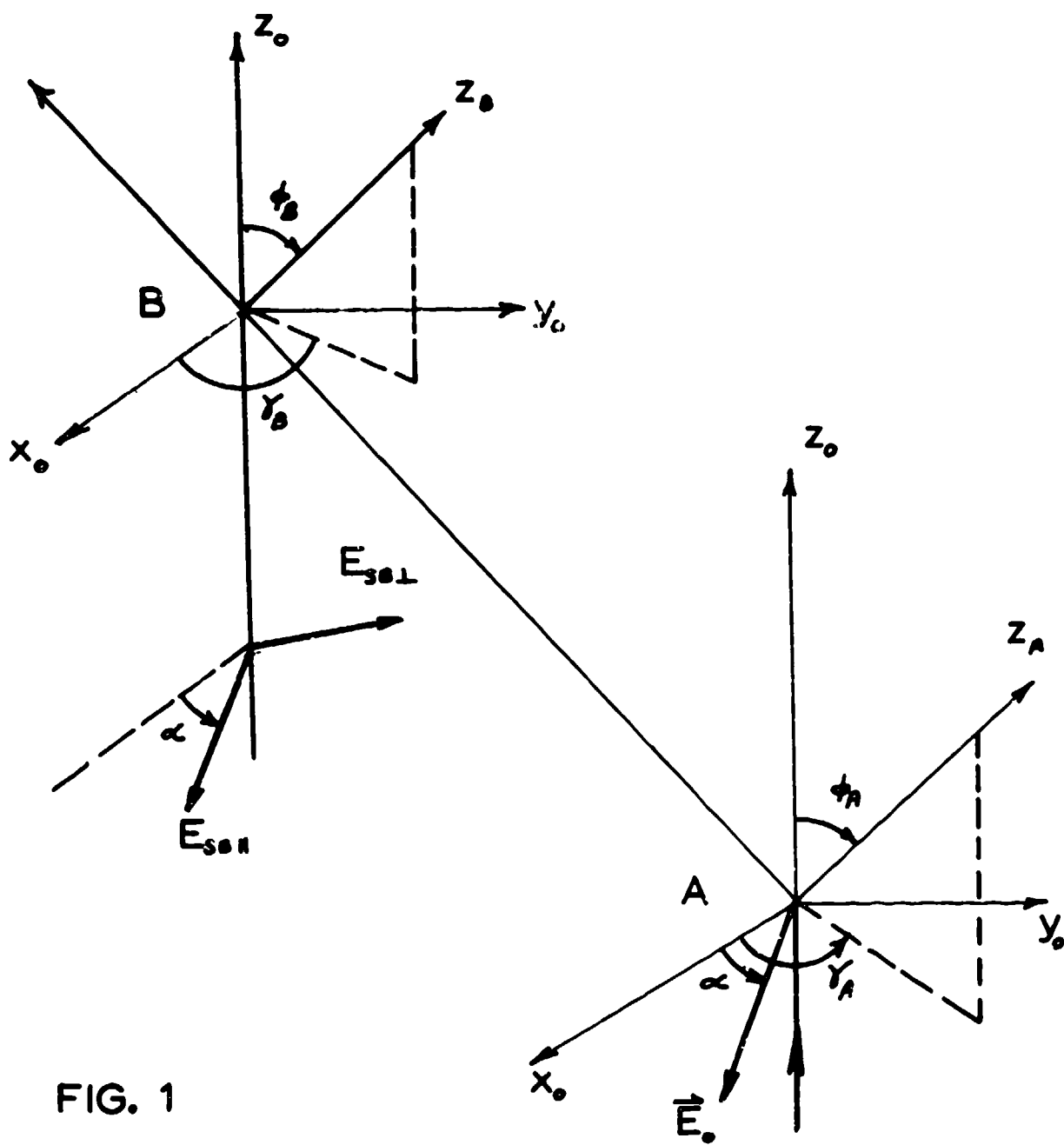


FIG. 1

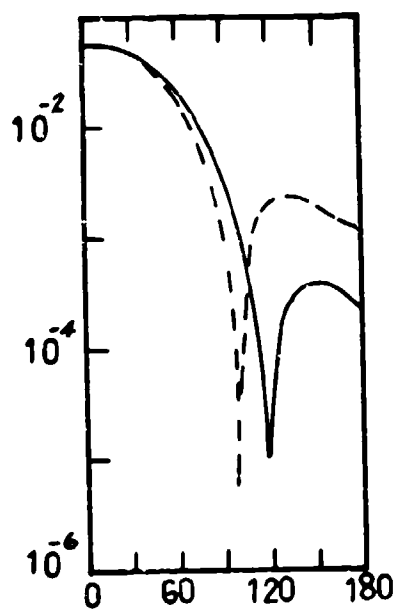


FIG. 2

I_1 VERSUS θ_s

$$V = 4.81 \mu\text{m}^3$$

$$h/2a = 5$$

—— SPHEROID
 ---- CYLINDER

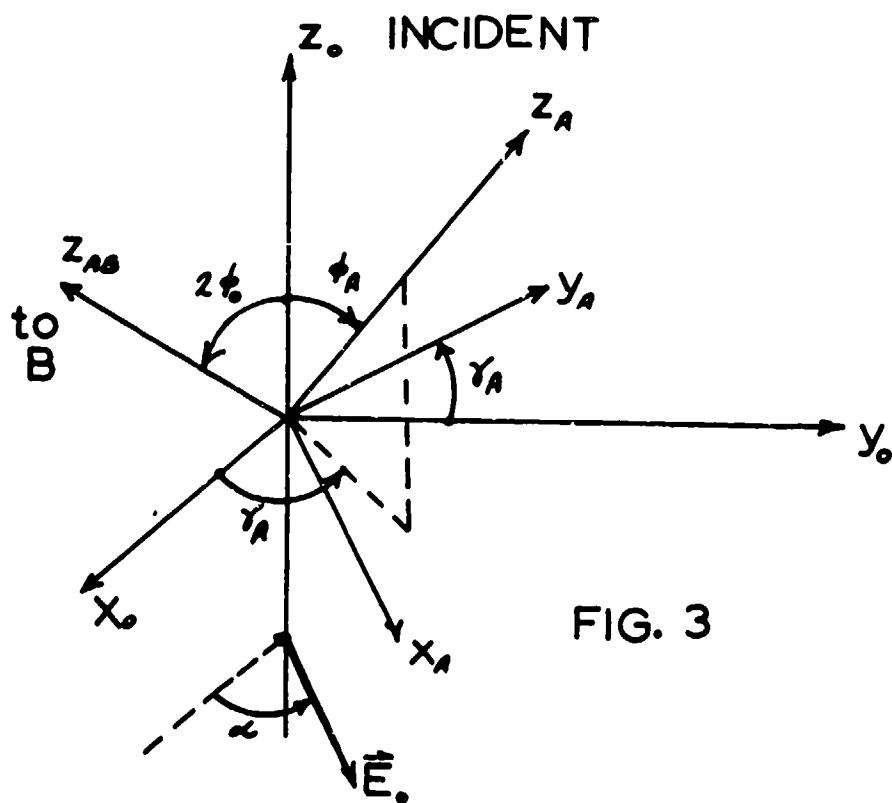


FIG. 3

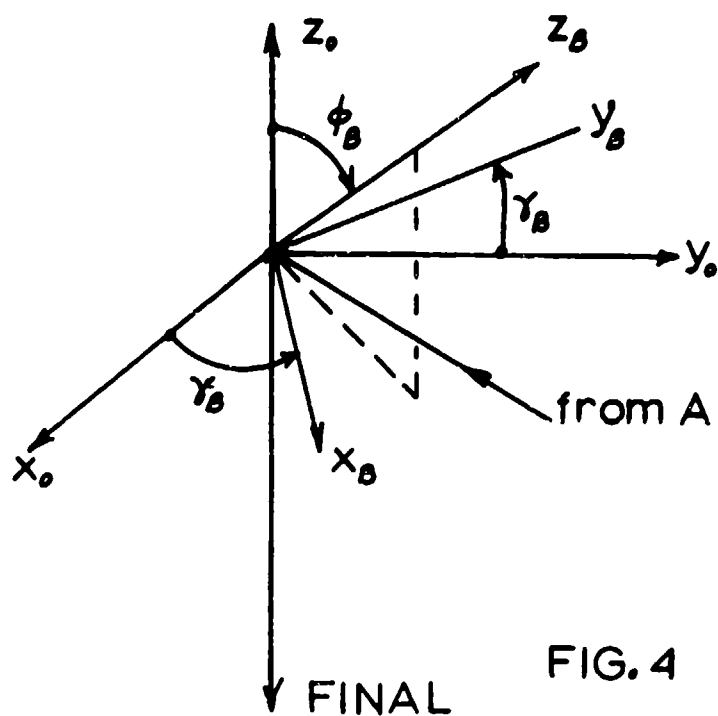


FIG. 4

ELASTIC AND INELASTIC SCATTERING OF COLLOIDAL PARTICLES

Milton Kerker
Clarkson University
Potsdam, New York 13676

ABSTRACT

This paper concerns experimental and theoretical studies of both elastic and inelastic light scattering by colloidal particles. The work has been published or accepted for publication as follows:

ITEM

173. M. Kerker, D.-S. Wang and C.L. Giles, Electromagnetic Scattering by Magnetic Spheres, *J. Opt. Soc.* 73, 765-767 (1983).
175. C.G. Blatchford, O. Siiman and M. Kerker, Potential Dependence of Surface-enhanced Raman Scattering (SERS) from Citrate on Colloidal Silver, *J. of Phys. Chem.* 87, 2503-2508 (1983).
176. O. Siiman, A. Lepp and M. Kerker, Combined Surface-enhanced and Resonance-Raman Scattering from the Aspartic Acid Derivative of Methyl Orange on Colloidal Silver, *J. of Phys. Chem.* 87, 5319-5325 (1983).
177. M. Kerker, Elastic and Inelastic Light Scattering in Flow Cytometry, *Cytometry* 4, 1-10 (1983).
179. C.G. Blatchford, M. Kerker and D.-S. Wang, Surface-enhanced Raman Spectroscopy of Water: Implications of the Electromagnetic Model, *Chem. Phys. Lett.* 100, 230-235 (1983).
180. O. Siiman, A. Lepp and M. Kerker, Absorption and Surface-enhanced Raman Spectra of Silver Organosols in Ethanol, *Chem. Phys. Lett.* 100, 163-168 (1983).
181. H. Chew, D.-S. Wang and M. Kerker, Effect of Surface Coverage in Surface-enhanced Raman Scattering. Interaction of Two Dipoles, *Phys. Rev. B.* 28, 4169-4178 (1983).
184. M. Kerker and D.-S. Wang, Comments on Intense Electrochemical SERS Signal Following Hydrogen Evolution, *Chem. Phys. Lett.* 104, 516-519 (1984).
185. H. Chew, D.-S. Wang and M. Kerker, Surface Enhancement of Coherent Anti-Stokes Raman Scattering by Colloidal Spheres, *J. of the Opt. Soc. of Am.* 1, 56-66 (1984).
186. M. Kerker, An Electromagnetic Model for Surface Enhanced Raman Scattering (SERS) Accounts of Chemical Research, Accepted.
188. M. Kerker, O. Siiman and D.-S. Wang, Effect of Aggregates on Extinction and Surface-Enhanced Raman Scattering Spectra of Colloidal Silver, *J. of Phys. Chem.*, Accepted.
189. O. Siiman, R. Smith, C. Blatchford and M. Kerker, Combined Surface-enhanced and Surface Resonance Raman Spectra of Dabsyl Aspartate Adsorbed on a Silver Electrode, *Langmuir*, Submitted.

The papers listed in the abstract indicate that our main effort has been to study both experimental and theoretical aspects of surface-enhanced Raman scattering. We will review only one of these aspects in this report (#188), leaving it to the reader to pursue the others in the published literature.

The preponderant current view is that the major contribution to SERS is due to the local electromagnetic field enhancement associated with resonant excitation of

electron oscillations, otherwise termed surface plasmons. Although the vast majority of experimental studies have utilized other substrates, colloidal particles are uniquely advantageous for theoretical analysis and it has been possible to expand upon classical light scattering theory in order to articulate an electromagnetic field theory of SERS. Not only has it been possible to predict the magnitude of the enhancement in agreement with measurements but this electromagnetic field analysis also depicts the remarkable dependence of SERS on the optical properties and morphology of the colloidal particles and in turn upon the excitation wavelength. The colloidal model may be considered prototypic of other substrates for none of which has it been possible to derive a definitive theory. Yet we had noted in an earlier paper a discordant aspect which suggested the possibility of a discrepancy between the experimentally obtained and theoretically calculated SERS excitation spectra and also between the former quantities and the measured extinction spectra. The silver hydrosols studied contained small, approximately spherical particles with average diameters as estimated by electron microscopy ranging from 10 to 40 nm, varying degrees of polydispersity and a small fraction of aggregates, depending upon method of preparation. Theoretical analysis indicated that these systems should exhibit a pronounced extinction peak at about 400 nm, which indeed was observed, and that the SERS excitation spectrum should also peak at about this wavelength, even for systems having a rather broad distribution of spherical particle sizes. However, we were unable in our laboratory to extend the SERS measurements to wavelengths as low as 400 nm, where the extinction peaked, but in every case a large enhancement ($>10^5$) was observed which peaked at 500 nm or higher. Although the magnitude of the peak agreed with theory its position at longer wavelengths required an explanation.

Measured extinction spectra and the corresponding SERS excitation spectra are plotted in Fig. 1 for four representative samples. The extinction spectra each have a major peak near 400 nm and in addition there is the development of an increasingly pronounced shoulder and then a second maximum as one proceeds from curve 1 to 4. This secondary feature moves from about 475 to 520 nm, and it is characteristic of particle aggregation, particularly chain-like aggregation as noted by Blatchford, Campbell and Creighton. Indeed, the preparation depicted by Curve 4 was obtained by coagulation of a more narrowly dispersed sol by bringing it to pH 3.5 upon addition of H_2SO_4 .

The accompanying SERS excitation spectra on Fig. 1 are plotted using an arbitrary scale since the absolute enhancement was determined only for Curve 1 (peak value 4×10^5).

In each case the peak in the SERS spectrum occurs at a wavelength similar to that for the shoulder or secondary peak in the corresponding extinction spectrum. As already noted, we were unable to extend the Raman measurements to the 400 nm wavelength region where the major extinction peak occurs.

These results in themselves create no dilemma in the cases of Curves 3 and 4 in which the pronounced shoulder and secondary maximum indicate a significant number of aggregates, perhaps sufficient to give rise to the corresponding Raman enhancements. Linear aggregates would be expected to display a similar red shift in both extinction and SERS.

However, the problem which appeared to present itself was that the absence of a pronounced shoulder at 500 nm in extinction curves 1 and 2 did not seem consistent with the measured SERS excitation profile. We surmised, based on these extinctions, that there could hardly have been a sufficient number of aggregates to give the large ($\sim 10^5$) corresponding enhancements. That surmise appears to have been erroneous as calculations, which we now present, indicate.

These calculations utilize the formalism for SERS by spheroids described earlier and a standard calculation of the extinction cross section. Mixtures of three classes of silver particles dispersed in aqueous medium have been assumed: (1) 5 nm radius spheres, (2) 2 to 1 axial ratio prolate spheroids having double the volume of the spheres and 3 to 1 axial ratio prolate spheroids having triple the volume. The Raman shift was taken to be 1400 cm^{-1} . These spheroids were presumed to simulate singlets, doublets and triplets (linearly aggregated). The computed extinction and SERS excitation spectra are shown in Figs. 2 and 3 for four mixtures shown in Table 1. The results suggest that the measured SERS excitation spectra and extinction spectra are consistent with each other and with the theoretical model.

Consider in any real system, that there will be a distribution of singlet particle sizes which upon coagulation would give rise to a still more complicated distribution of doublets and triplets, that the coagulation kinetics for such solid particles in an electrolyte media is not well understood, that the orientation distribution of the multiplet particles must be considered and that the spheroid configuration is only an approximation to the coagula. Thus it seems reasonable that the trimodel curves shown in Figs. 2 and 3 can only be considered approximations to more smoothed relations for real systems. Yet these curves offer insights.

For the curves B, C and D shown in Fig. 2 the ratios of major peaks to the first secondary peak are 45, 14 and 4.5 bracketting the corresponding ratios at these wavelengths of 17 and 12 for the experimental curves 1 and 2 in Fig. 1. Within the crudeness of this model, as has just been noted, these experimental extinction curves are reasonably consistent with a very small number of aggregates, comparable to row C in Table 1, e.g. 5% doublets and 0.5% triplets. Yet such a small fraction of aggregates still gives rise to enhancements in the range 10^5 to 10^6 shown in curve C of Fig. 3. And these are the values that have been observed experimentally. Indeed, so effective are such aggregates in promoting SERS that even with only 0.5% doublets and 0.02% triplets, calculated enhancements greater than 10^4 are obtained (see curve A of Fig. 3).

The conclusion from this calculation is clear. Strong red-shifted SERS signals may occur in the presence of a very small fraction of aggregates even when this number of aggregates is insufficient to give a significant shoulder on the extinction spectrum at the corresponding wavelength.

TABLE I

FRACTIONAL COMPOSITION FOR SYSTEMS
SHOWN IN FIGS. 2 AND 3

<u>CURVE</u>	<u>SINGLET</u>	<u>DOUBLETS</u>	<u>TRIPLETS</u>
A	0.989	0.005	0.0002
B	0.942	0.026	0.0021
C	0.882	0.051	0.0054
D	0.755	0.101	0.0144

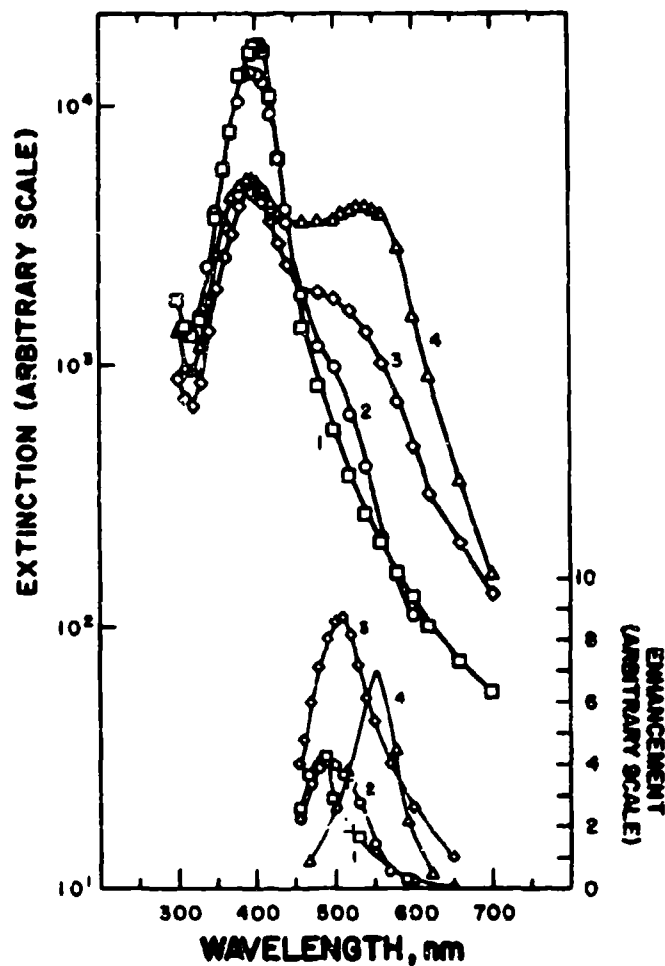


FIGURE 1. Measured extinction spectra and corresponding measured SERS excitation spectra for four Ag hydrosols (arbitrary units).

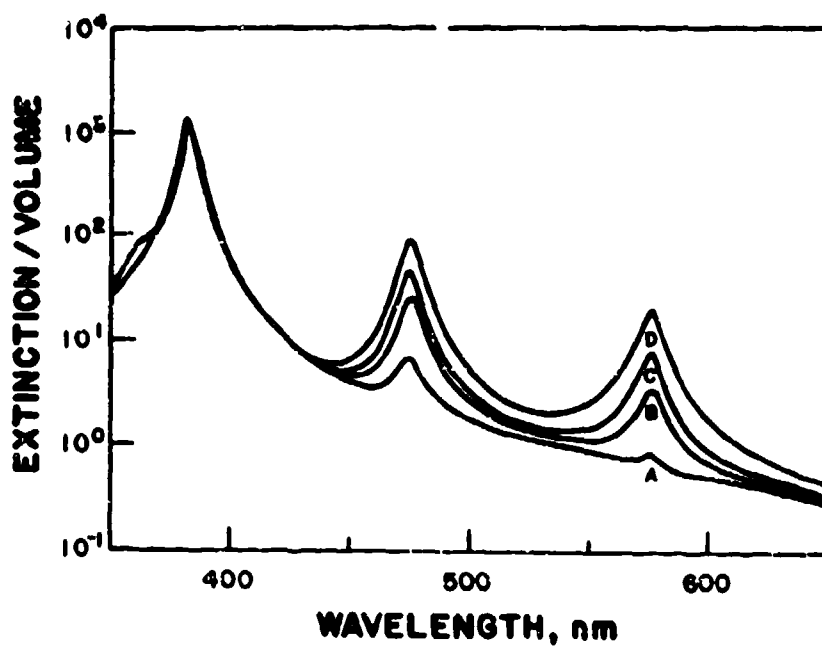


FIGURE 2. Computed extinction spectra per unit volume of Ag in water for mixtures in Table I (arbitrary units).

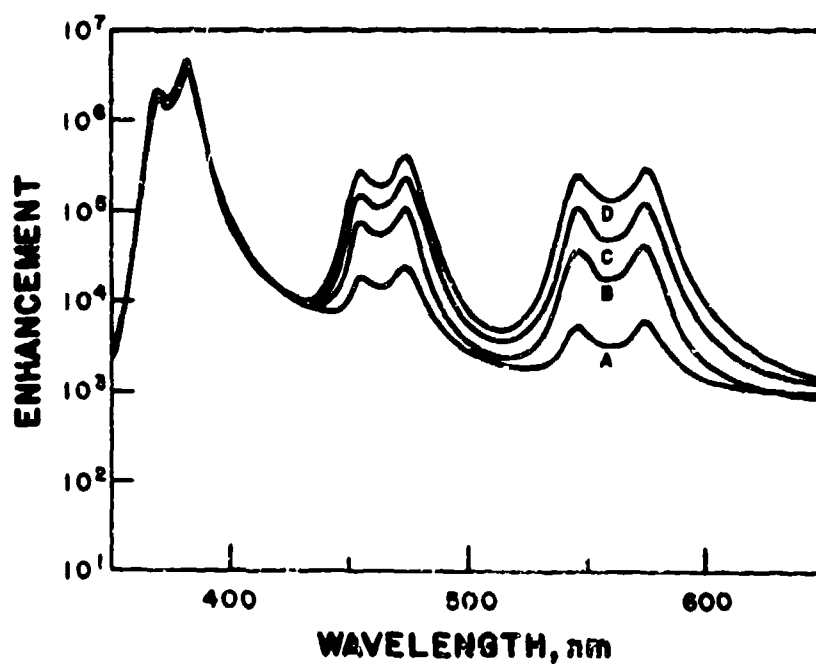


FIGURE 3. Computed SERS excitation spectra of Ag in water for mixtures in Table I and for 1400 cm^{-1} Raman shift (arbitrary units).

Absorption and Scattering by Aggregated Aerosol Particles

by

J. R. Aronson, A. G. Emslie, I. Simon and E. M. Smith
Arthur D. Little, Inc.
Cambridge, Massachusetts 02140

ABSTRACT

This paper concerns the extension of a theory of particulate scattering to the difficult case of aggregated aerosols. Photoacoustic measurements of absorption and scattering in the infrared and visible spectral regions have been made for SiO_2 and C smokes to test the validity of the theory. This work was presented as:

J. R. Aronson, A. G. Emslie, I. Simon and E. M. Smith,
"Scattering and Absorption by Aggregated Aerosol Particles,"
1984 CRDC Conference on Obscuration and Aerosol Research, June 1984.

This is a progress report. Further measurements and refinements are continuing.

1. INTRODUCTION

The problem of scattering and absorption by particles is presently well understood in terms of Mie theory for spheres and similarly for cylinders¹ and spheroids². There is presently considerable work going on utilizing more approximate methods for irregularly shaped particles³. Roessler and Faxvog have investigated the absorption and scattering of carbon smokes^{4,5} and found that the Mie theory could adequately explain scattering and absorption by smoke particles (which are believed to be largely chained aggregates) by treating them as spheres if one worked only at visible wavelengths. However, attempts at treating infrared measurements by the same method failed.

We concluded that a viable approach to the problem of scattering by aggregated aerosols might be made by treating the aggregate as an individual particle having effective-medium optical constants⁶ established by the optical constants of the material and its volume fraction within the aggregate. A similar approach had been previously used by us for fine particle soils with some success⁷. We then proposed that the gross characteristics of the aggregate could be handled by our previously developed theory^{8,9} in much the same way as we had handled irregularly shaped particles in the past. In order to guide and validate the theoretical treatment we proposed to use photoacoustic spectroscopy with

He-Ne and CO₂ laser sources operating in the visible, near-infrared and mid-infrared spectral regions. The reason for the choice of the photoacoustic method was principally that it permits one to obtain a scattering coefficient without the use of an integrating sphere, as would be necessary with standard infrared methods.

II. THEORETICAL APPROACH

Our previous theoretical treatment has been described in the literature quite fully^{8,9}. We needed to modify our theory in several minor ways, however. As most of the particles are small compared to the wavelengths in question (infrared) we only modified our fine particle theory, which for globular aggregates consists of a Raleigh scattering calculation using the effective optical constants of the medium. For fibers we used our treatment described previously¹⁰ if the length of the fiber was not small compared to the wavelength and our usual treatment^{8,9} if all dimensions of the fiber were small. As we rarely have fibers larger than the wavelength we only needed to implement this portion of the computer program for those fibers which fell within the region to be bridged by the two theories. As shown in our previous work, bridging is useful in the intermediate region; therefore, a bridging formula such as the one previously used¹¹ was also implemented.

III. GENERATION OF AEROSOLS AND ESTIMATION OF THEIR PARAMETERS

The two types of aerosols we studied in this work were acetylene-flame smoke and pyrolytic-silica smoke. Both consist of small primary, nearly spherical particles of the pure substance (carbon, silicon dioxide) coagulated into larger aggregates of various configurations.

A. Acetylene Smoke Generator

The apparatus used to generate the carbon aerosol is similar to that described by Roessler⁵. Acetylene is mixed with air in a closely controlled proportion in a burner with a 1.0 mm dia. orifice mounted in a vertical chamber of ~15 cm diameter and ~90 cm height. The laminar flame is approximately 15 to 20 cm high and under proper conditions (around ~0.5 air-to-gas ratio by volume) produces dense carbon aerosol throughout the chamber. Some of it is lead from the chamber into the photoacoustic cell and to the sampling filter (Nucleopore, 0.1 μ m pore size) for subsequent electron microscope examination. The aerosol could be diluted, if necessary, by air added to the stream.

B. Silica Smoke Generator

The apparatus used to generate silica aerosol is similar to that described by Kanapilly¹². Tetraethoxysilane is carried by nitrogen gas from a glass bubbler, mixed with humidified air, and reacted in a quartz tube at 670°C. A dry-ice trap removes condensable reaction products. The aerosol could be diluted with air and a downstream pump causes the aerosol to flow to the photoacoustical cell at a constant rate of about 1 l/min.

C. Smoke Parameter Estimation

In order to carry out our theoretical simulations it is necessary to obtain estimates of the aggregate dimensions and porosity, and number of aggregates per unit volume in the sample space. The former are accomplished by electron microscopy and the latter by weighing collected samples on Nucleopore filters. The latter required about 15 to 20 minutes at a flow rate of 1 l/min. An opacity monitor measuring the optical density of the smoke (in visible light) was used to monitor the rate of carbon aerosol generation. Having calibrated the opacity vs. the gravimetric mass concentration, we were able to use the former in the later runs for estimating the mass concentration without having to collect samples for long time intervals.

We categorize the particles as spheres, ellipsoids and cylinders and measure appropriate dimensions for each. In order to estimate the porosity of the soot particles, we examine the TEM grids from the filter at magnifications of 40 to 120,000. Areas of photographs of these are then selected where we can estimate a volume, count the number of subparticles in it, and thence calculate the porosity. For silica smokes we used the SEM photographs at 5000 magnification both to determine the dimensions of the particles and the dimensions of individual spheres that make up the filamentary particles. We determined that for this we needed to make the measurements using stereo pairs of photographs since the filaments tend to project at various angles from the filter surface.

As a consequence of the well known uncertainty of optical constants for soot¹³ we chose to make our experiments with an acetylene-based smoke known to be principally pure carbon, and to use the dispersion theory formulation of Lee and Tien¹⁴ as the best values we could obtain. Clearly, any errors which result from having inappropriate optical constants will be difficult to track down. For silica smokes the problem is less severe, but it does occur, and we chose to try values obtained by Zolotarev¹⁵ and those obtained by Huffman¹⁶. Somewhat better simulations were obtained using the latter, principally at 10.6 μ m.

IV. PHOTOACOUSTIC MEASUREMENTS

The photoacoustic method is particularly suited for the determination of absorption and scattering because the photoacoustic effect arises only from the radiation absorbed by the aerosol particles and converted to heat; the radiation scattered by the particle does not contribute to the acoustic signal. This circumstance makes it possible to separate the two components making up the extinction of the radiation propagating through the aerosol.

The photoacoustic effect¹⁷ is a thermal phenomenon in which periodic heating of a gas manifests itself by corresponding periodic pressure variations detectable by a microphone coupled to the absorption cell. In an aerosol we assume that the heat is generated by absorption of the radiation in the particles only, but is transferred rapidly to the gas, which in itself is perfectly transparent. The condition for rapid heat transfer between the particles and the gas is that the time constant τ for the heat transfer be shorter than the period τ_a of the acoustic frequency used in the experiment. For spherical particles the heat-transfer time constant was obtained by Chan¹⁸ as

$$\tau = a^2 C_p \rho_p / 3 K_a, \quad (1)$$

where a is the radius of the particle, C_p is its specific heat, ρ_p its density and K_a is the thermal conductivity of the air. For carbon particles of radius $1 \mu\text{m}$ in air we find $\tau = 2 \times 10^{-5}$ sec while the acoustic period at our operating frequency (150 Hz) is $\tau_a = 6.7 \cdot 10^{-3}$ sec. Thus the condition for rapid heat transfer is satisfied and the determination of the absorption from the corresponding photoacoustic signal is undoubtedly valid.

The determination of scattering is somewhat less certain, depending on the assumptions made about the scattering parameters of the particles constituting the aerosol. Basically, it is necessary to determine the total extinction ϵ and then obtain the scattering by subtracting the absorption from it

$$S = \epsilon - \alpha. \quad (2)$$

If we assume isotropic scattering we may determine ϵ either by measuring the optical extinction of a collimated beam of radiation passing through the photoacoustic cell of length L (single path method)

$$\epsilon_1 = \frac{1}{L} \ln (I_0/I), \quad (3)$$

or by passing the beam through the cell twice (forward and back again) and measuring the two acoustic signals S_1 and S_2

$$\epsilon_2 = \frac{1}{t} \ln [t^2 r S_1 / (S_2 - S_1)] \quad (4)$$

where t is the transmittance of the cell windows and r is the reflectance of the retroreflecting mirror (double pass method).

The experimental apparatus used in our measurements can be described following the diagram in Figure 1. The photoacoustic cell is a copper tube 1.10 cm I.D., 51.7 cm long, provided with barium fluoride windows (W) inclined at the Brewster angle. The tube is blackened inside to minimize the reflection of scattered radiation. The valves on the cell provide for filling it with the aerosol and for subsequent flushing with dry nitrogen. They are closed during the measurement in order to minimize the acoustic noise. The microphone M picks up the acoustic pressure variations and delivers the signal, via preamplifier PA to the lock-in amplifier LA where it is filtered and synchronously demodulated. The phase reference is derived from the optical chopper which modulates the laser beam at 150 Hz. The photoacoustic cell is operated well below its fundamental resonance frequency (~ 320 Hz).

Two lasers can be used alternatively; a Jodon He-Ne laser for operation at three wavelengths: 0.633, 1.15 and 3.39 μm , and a Laakman CO_2 laser, at about 28 wavelengths between 9.27 and 10.63 μm . The waveguide type, rf-excited CO_2 laser is grating tunable and has a beam output up to ~ 2 watt (cw). It is stabilized by a cavity servo control system which makes it possible to lock in on any selected line in the 9 to 11 μm vibrational-rotational bands of CO_2 spectrum. The He-Ne laser is of the dc-plasma discharge type and produces the visible radiation at 0.633 μm with a ~ 20 mW (cw) power output. With other sets of cavity mirrors optimized for the infrared emissions it delivers ~ 6 mW at 1.15 μm and ~ 8 mW at 3.39 μm .

The CO_2 laser beam has an angular divergence of 3 to 5 millirad (the He-Ne is much less) and is sufficiently narrow to pass through the cell without grazing the walls. However, for the double-pass operation, it is necessary to narrow down the beam which is accomplished by use of a long focal length concave mirror M2. A spurious acoustic signal generated by the laser beam passing through the cell windows was occasionally troublesome, in particular, when the signal from the aerosol was very weak. Therefore, we subtracted the "empty cell" signal from that received from the aerosol.

The laser beam power is measured by a thermopile power meter P, normally placed behind the cell, as shown in Figure 1. For the double-pass measurement the power meter is removed from the beam path. The photoacoustic responsivity of the cell is determined by filling it with an IR absorbing gas

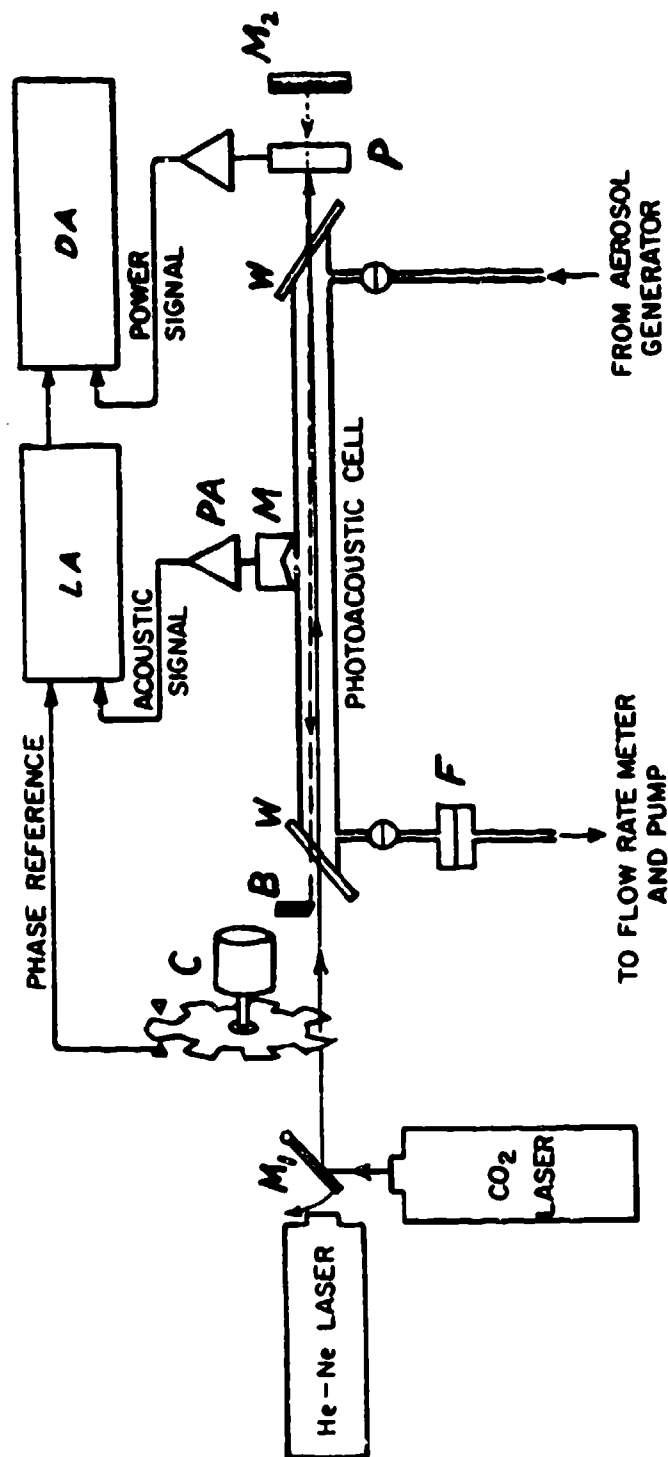


FIGURE 1. SCHEMATIC DIAGRAM OF THE PHOTOACOUSTIC APPARATUS

(ethylene-nitrogen mixture) and measuring the acoustic signal corresponding to a given beam power. The responsivity was, typically ~ 100 mV/W.

In the course of this work we routinely used both the single and double pass methods for the determination of absorption and scattering coefficients. However, the data presented here were obtained by the conventional single pass method since we found the double pass method to be more susceptible to experimental errors associated with the reverse beam operation.

V. RESULTS

Tables 1 and 2 give a summary of our experimental results together with the measured parameters and theoretical simulations. Simulations have been made for those cases (infrared) in which the theory is believed to be applicable. We did not attempt to model ellipsoids large compared to the wavelength as our objective was to deal with infrared measurements of aerosols, and such large particles are unlikely to remain airborne. The mixtures of shapes that were found in our experiments were modeled by calculating individual absorption coefficients and scattering coefficients (K's and S's) and adding them to get the K's and S's for the mixture. The ratios (K/S) are useful in that errors in estimation of the number of particles cancel out.

The results obtained with carbon aerosols (acetylene smoke) are presented in Table 1. At the $10.5 \mu\text{m}$ wavelength the theoretical values of the absorption coefficient K are reasonably close to the measured values and their mean value is also close to that obtained from the data of Roessler and Faxvog⁴ at $10.6 \mu\text{m}$. The calculated values of the scattering coefficients appear to be systematically smaller than the experimental values, but the latter seem to be very close to those obtained from Ref. 4. The experimental K/S ratios are seen to be always smaller (~ 2 to 3 times) than the theoretical ones. At the $3.39 \mu\text{m}$ wavelength the only case theoretically modeled is in good agreement with the experiment. The results of measurements in the visible at ($0.633 \mu\text{m}$) are shown only for general interest and for comparison with literature values. No comparison was made with the theory as that was deemed unwarranted. ($\lambda < D$).

We are uncertain as to the principal causes of the disagreement between the theory and the experiment, but we note that the poorest known parameter is the porosity of the aggregate as this is very difficult to estimate from the TEM and SEM photographs. Figure 2 shows that this parameter can have a very significant effect. For the given specific case K/S can be either greater or less than unity

TABLE 1

CARBON AEROSOL

AEROSOL PARAMETERS					THEORY			EXPERIMENT		
λ	Shape	% Vol.	N	D	ρ	K	S	K/S	K	S
μm			$cm^{-3} \times 10^{-5}$	μm	$= 1-fv$	$cm^{-1} \times 10^{-4}$	10^{-4}	cm^{-1}	cm^{-1}	$\times 10^{-4}$
0.63		0.3							27.0	13.3
0.63		1.46							79.2	32.1
0.63		1.39							37.7	31.2
							blue			1.9
										5.5
1.15		1.6							35.8	18.8
1.15		2.9							88.1	47.1
3.39	ellip.	14	0.37	1.3		5.93	11.5	0.52		
	sph.	9	1.9	0.64		3.63	0.84	4.31		
	cyl.	77	2.7	0.71	2.1	10.0	4.16	2.40		
					0.50	19.6	16.5	1.19	26.7	24.8
3.39		1.3							10.1	14.8
3.39		2.0							16.1	16.6
3.39		3.0							36.9	26.1

Roessler & Faxvog, mean (at $\lambda = 0.514$)

TABLE 1 (Continued)

CARBON AEROSOL

λ	AEROSOL PARAMETERS					THEORY			EXPERIMENT				
	M	Shape	% Vol.	N	D	ℓ	ρ	K	S	K/S	K	S	K/S
μm	$\text{g cm}^{-3} \times 10^{-7}$			$\text{cm}^{-3} \times 10^5$	μm	μm	g cm^{-3}	$\text{cm}^{-1} \times 10^{-4}$	$\text{cm}^{-1} \times 10^{-4}$	cm^{-1}	cm^{-1}	$\times 10^{-4}$	$\times 10^{-4}$
10.5	3.3	ellip.	74	4.2	1.5		0.17	4.79	0.394	12.2			
		sph.	17	2.7	1.1			1.21	0.039	30.7			
		cyl.	9	3.6	0.36	2.4		0.16	0.0015	112.4			
10.5	2.6	ellip.	50	0.93	1.3		0.59	6.16	0.435	14.2	13.0	2.66	4.9
		sph.	42	1.2	1.1			3.86	0.728	5.3			
		cyl.	8	0.64	0.37	2.4		3.01	0.345	8.7			
								0.23	0.008	28.7			
10.5	1.4	ellip.	66	1.4	1.45		0.32	7.10	1.081	6.6	8.07	2.53	3.2
		sph.	26	3.5	1.06			2.68	0.338	7.9			
		cyl.	8	8.1	0.38	2.4		3.26	0.199	16.4			
								0.88	0.017	52.6			
								6.82	0.554	12.3	6.08	1.29	4.7

mean value 4.27

Roessler & Faxvog, mean 4.22

Optical Constants: $n = 2.64$, $k = 1.68$ at $\lambda = 3.39 \mu\text{m}$ (Lee & Tien, 1981)
 $n = 3.78$, $k = 3.15$ at $\lambda = 10.5 \mu\text{m}$

TABLE 2

SILICA AEROSOL

λ	AEROSOL		PARAMETERS			THEORY			EXPERIMENT		
	Shape	% Vol.	N	D	ρ	K	S	K/S	K	S	K/S
μm			$\text{cm}^{-3} \times 10^5$	μm	μm	$\text{cm}^{-1} \times 10^{-4}$	10^{-4}		$\text{cm}^{-1} \times 10^{-4}$		
0.633	4.2*	100*	11.4*	0.35*	3.1*	0.017	20	8.4×10^{-4}	0.28	49.7	56×10^{-4}
	*) assumed the same as in run indicated below										
9.3	4.8	92	13.4	0.34	2.5	10.2	0.185	55	37	2.3	16.1
10.5	4.2*	100	11.4	0.35	3.1	0.33	0.014	24	11.9	1.2	9.9
10.5	5.4	98	19.0	0.36	2.9	0.45	0.022	20	14.4	2.3	6.3

464

Optical $n = 1.46, k = 1.16 \times 10^{-4}$ at $\lambda = 0.633 \mu\text{m}$ (Dupont Pifax S-220)Constants $n = 1.9, k = 0.05$ at $\lambda = 10.6 \mu\text{m}$ } Steger, et al. 1974 $n = 2.59, k = 2.06$ at $\lambda = 9.3 \mu\text{m}$ }

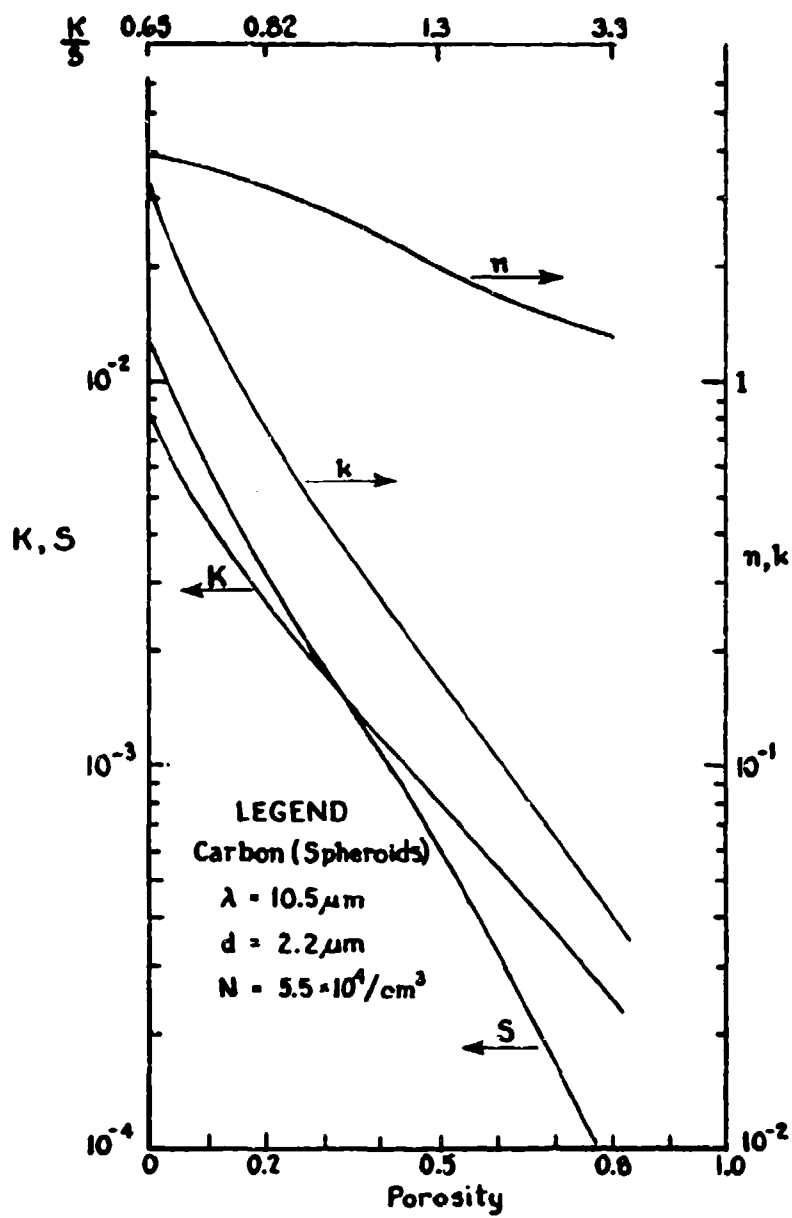


FIGURE 2. EFFECTS OF AGGREGATE POROSITY

depending on whether the porosity of the aggregate is estimated to be greater or less than ~ 0.3 . While our work and most of the literature shows $K > S$ it should be noted that Dugin, et al¹⁹ found the reverse for carbon smoke.

Table 2 summarizes the results obtained with the silica aerosols. The measurements in the infrared were made at 9.3 and 10.5 μm and in both instances the agreement with the theory is reasonably close only for the K/S ratio. The absolute values of K and S seem to be greatly underestimated by the calculation as compared with the experiment (possibly with the exception of the case at $\lambda = 9.3 \mu\text{m}$). In the visible ($\lambda = 0.633 \mu\text{m}$) the theoretical values of both K and K/S are smaller than the experimental ones, contrary to all other cases. It is to be noted that in this case we find $(K/S) \ll 1$ both by the theory and the experiment in agreement with expectation.

ACKNOWLEDGEMENT

We thank Clark Grain and Fred Johnston for producing the SiO_2 aerosol, Ray Cornish for electron microscopy and Madeline Goode for typing the manuscript. This work was supported by the U.S. Army Research Office.

VI. REFERENCES

1. K. N. Liou, Appl. Opt. 11, 667 (1972).
2. S. Asano and G. Yamamoto, Appl. Opt. 14, 29 (1975)
3. "Light Scattering by Irregularly Shaped Particles," ed by D. W. Schuerman, Plenum Publishing Corp., 1980.
4. D. M. Roessler and F. R. Faxvog, J. Opt. Soc. Am. 69, 1699 (1979).
5. D. M. Roessler and F. R. Faxvog, J. Opt. Soc. Am. 70, 230 (1980).
6. C. G. Granqvist and O. Hunderi, Phys. Rev. B 18, 2897 (1978).
7. J. R. Aronson, A. G. Emslie and H. G. McLinden, Science 152, 345 (1966).
8. A. G. Emslie and J. R. Aronson, Appl. Opt. 12, 2563 (1973).
9. J. R. Aronson and A. G. Emslie in "Infrared and Raman Spectroscopy of Lunar and Terrestrial Minerals," Ed. by C. Karr, Jr., Academic Press (1975).
10. J. R. Aronson, A. G. Emslie, F. E. Ruccia, C. R. Smaliman, E. M. Smith, and P. F. Strong, Appl. Opt. 18, 2622 (1979).
11. J. R. Aronson and A. G. Emslie, J. Geophys. Res. 80, 4925 (1975).
12. G. M. Kanapilly, K. W. Tu, T. B. Larsen, G. R. Fogel and R. J. Luna, J. Colloid and Interface Sci. 65, 533 (1978).
13. J. T. Twitty and J. A. Weinman, J. Appl. Meteor. 10, 725 (1971).
14. S. C. Lee and C. L. Tien, 18th Symp. on Combustion, The Combustion Institute, 1150-1166 (1981).
15. V. M. Zolotarev, Opt. and Spectrosc. 29, 34 (1970).
16. T. R. Steger, K. L. Day and D. R. Huffman, Appl. Opt. 13, 1586 (1974).
17. "Optoacoustic Spectroscopy and Detection," Ed. by Y. M. Pao, Academic Press (1977).
18. C. H. Chan, App. Phys. Letters 26, 628, (1975).
19. V. P. Dugin, Yu. G. Toporkov and N. V. Zadovina, Izvestiya, Atm. and Oceanic Phys. 17, 728 (1981).

BLANK

PROGRESS IN RESEARCH ON WAVE PROPAGATION AND SCATTERING
IN DISCRETE RANDOM MEDIA USING MULTIPLE SCATTERING THEORY

V.K. Varadan and V.V. Varadan
Department of Engineering Science and Mechanics
Wave Propagation Laboratory
The Pennsylvania State University
University Park, PA 16802

ABSTRACT

This paper is concerned with a propagator model for multiple scattering and wave propagation in discrete random media. The coherent and incoherent intensity of a time harmonic electromagnetic field in such a medium are calculated and compared with available experimental results showing good agreement. This work has been published and submitted for publication as follows:

V.V. Varadan and V.K. Varadan, "The Quasi-Crystalline Approximation and Multiple Scattering of Waves in Random Media", IEEE Trans. A and P., submitted for publication.

V.K. Varadan and V.V. Varadan, "A Propagator Model for Multiple Scattering and Wave Propagation in Discrete Random Media", Radio Science, submitted for publication.

V.K. Varadan, Y. Ma and V.V. Varadan, "Coherent Electromagnetic Wave Propagation Through Randomly Distributed and Oriented Pair-correlated Scatterers", Radio Science, in press.

V.V. Varadan, Y. Ma and V.K. Varadan, "Frequency Dependence of the Attenuation of Electromagnetic Waves in Media with Anisotropy Induced by Microstructure", IEEE Trans. A and P., submitted.

INTRODUCTION

We consider the propagation of plane coherent electromagnetic waves in an infinite medium containing identical, loss-less, randomly distributed particles. Our aim here is to characterize the random medium by an effective complex wave number K (which would be a function of particle concentration, the electrical size, and the statistical description of the random positions of the scatterers), and to study both coherent and incoherent intensities as a function of frequency for various values of concentration c (the fractional volume occupied by the scatterers). Although the formulation is generally valid for non-spherical, aligned or randomly oriented scatterers, initial calculations are confined to spherical scatterers which generally gives a better picture of the order of magnitude of the different contributions to the intensity without the additional complications of non-spherical geometry and orientation.

Extensive work by Tversky¹⁻² has laid the foundation for multiple scattering theory in discrete random media. A related approach using the T-matrix of a single scatterer together with configurational averaging procedures, has been used by the authors to develop a computational method for electromagnetic wave propagation problems in inhomogeneous media³⁻⁴. Lax's quasi-crystalline approximation (QCA) is used in conjunction with suitable models for the pair-correlation function to obtain an effective wave number $K = K_1 + iK_2$ which is complex and frequency dependent. The real part K_1 is related to the phase velocity while the imaginary part K_2 is related to coherent attenuation. In this paper, we present a propagator model which is shown to present the same dispersion equation as the one obtained in our previous papers³⁻⁴. In addition, this model enables us to compute both coherent and incoherent intensities for more realistic

FORMULATION

Consider wave propagation in an infinite medium of volume $V \rightarrow \infty$ containing a random distribution of N scatterers, $N \rightarrow \infty$, such that $n_0 = N/V$, the number density of scatterers, is finite. Plane harmonic waves of frequency ω propagate in the medium and undergo multiple scattering. Let \vec{E} , \vec{E}^0 , \vec{E}_1^a , and \vec{E}_1^s denote respectively the total field, the incident field, the field exciting the i -th scatterer and the field scattered by the i -th scatterer. Then self consistency requires the following relationships between the fields^{3,4}.

$$\vec{E} = \vec{E}^0 + \sum_{i=1}^N \vec{E}_i^s \quad (1)$$

and


$$\vec{E}_i^a = \vec{E}^0 + \sum_{j \neq i}^N \vec{E}_j^s \quad (2)$$

The configurational average of the total field results in

$$\begin{aligned} \langle \vec{E}(\vec{r}) \rangle = & \vec{E}^0(\vec{r}) + \sum_i T_{nn'} \int d\vec{r}_1 \psi_n(\vec{r}-\vec{r}_1) a_n^i p(\vec{r}_1) d\vec{r}_1 \\ & + \sum_i \sum_j T_{nn'} T_{n'n''} \int d\vec{r}_1 \psi_n(\vec{r}-\vec{r}_1) \sigma_{n'n''}(\vec{r}_{1j}) a_n^i p(\vec{r}_1) p(\vec{r}_j | \vec{r}_1) d\vec{r}_j d\vec{r}_1 + \dots \end{aligned} \quad (3)$$

In Eq. (3), $T_{nn'}$, is the T-matrix of an isolated scatterer, a_n^i are the known coefficients of expansion of the incident field at the site of the i -th scatterer, $\sigma_{nn'}(\vec{r}_y)$ is the translation matrix for vector spherical functions and describes the propagation of waves from \vec{r}_1 to \vec{r}_j . The functions $p(\vec{r}_j)$, $p(\vec{r}_j | \vec{r}_1)$... etc. are the single particle, two particle conditional probabilities distribution functions. We have shown⁵ that invoking the QCA implies that the coherent field and the resulting dispersion equation were limited to terms of the form

$$\langle \vec{E} \rangle_{\text{QCA}} = \text{---} \circ \text{---} + \text{---} \circ \text{---} \text{---} \circ \text{---} + \text{---} \circ \text{---} \text{---} \circ \text{---} \text{---} \circ \text{---} + \dots \quad (4)$$

where  denotes positional correlation between two scatterers. It is clear from the diagrams that each scatterer participates only once in a given term; there is no back and forth scattering, all scattering is sequential, and only sequential positional correlations are allowed.

Introducing spatial Fourier transforms of the translation matrix σ and the radial distribution

functions g (given by $p(\vec{r}_j | \vec{r}_1) = \frac{1}{V} g(\vec{r}_{1j})$) which are denoted by $\bar{g}(K)$ and $\bar{g}(K)$, respectively, and using the convolution theorem, we obtain

$$\langle E(\vec{r}) \rangle = E^0(\vec{r}) + 0u \psi_n(\vec{r}-\vec{r}_1) T_{nn}, n_o \int [1-n_o \bar{g}(K) T]^{-1} e^{iK \cdot (\vec{r}_1-\vec{r}_2)} a_n^{(2)} d\vec{K} d\vec{r}_1 d\vec{r}_2 \quad (5)$$

This new form of the average field can be interpreted as an incident plane wave propagating through an effective medium of propagation constant K and propagator $[1-n_o \bar{g}(K)T]^{-1}$ undergoing scattering from a particle at \vec{r}_1 and then propagating to the observation point \vec{r} with the wave number of the host medium. The dispersion equation in the model medium can be obtained by setting the determinant of the propagator equal to zero:

$$|1-n_o \bar{g}(K) T| = 0 \quad (6)$$

This equation is identical to the one obtained by us earlier using the self-consistent multiple scattering approach, see Ref. 4.

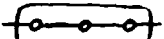
The field fluctuations $\Delta \vec{E}$ may now be given by

$$\Delta \vec{E} = \vec{E} - \langle \vec{E} \rangle \quad (7)$$

and can be represented as a multiple scattering series which may be represented by the following diagrams



where — denotes propagation of the field from one point to the other and 0 denotes a scatterer.

If two or more scatterers are enclosed in an area, such as , arbitrary multiple scattering any number of times and in any order can go on between scatterers 1, 2 and 3.

Along these lines, we define the incoherent intensity or the spectral density $G_\alpha(\vec{R}, \omega)$ at position \vec{R} , for field polarization in the direction α :

$$\begin{aligned} G_\alpha(\vec{R}, \omega) &= \frac{1}{4} \langle |\alpha \cdot \Delta \vec{E}|^2 \rangle \\ &= \text{Diagram 1} + \text{Diagram 2} + \text{Diagram 3} + \dots \\ &+ \text{Diagram 4} + \text{Diagram 5} + \text{Diagram 6} + \dots \\ &\approx \text{Diagram 7} + \text{Diagram 8} + \text{Diagram 9} + \dots \\ &+ \text{Diagram 10} + \text{Diagram 11} + \text{Diagram 12} + \dots \end{aligned} \quad (8)$$

The first set of the above diagrams represents a partial summation of QCA type terms incorporating two body correlations while the second set represents the conventional ladder diagrams. In both sets of diagrams, we can use so called "dressed propagators" obtained from Eq. (6) between scatterers instead of "bare propagators". This means that K from (6) can be used as the wave number characterizing the medium between scatterers involved in calculation of the spectral density, i.e., the other scatterers that participate in only one or other of the field lines are averaged over separately and replaced by K .

NUMERICAL RESULTS

The numerical procedure is described in detail in Refs. 3-4, and will not be repeated here. The effective wave number $K(=K_1+K_2)$ is computed for Revacryl spheres in distilled water for a range of frequencies and concentrations of scatterers. The real part K_1 is related to the phase velocity while the imaginary part K_2 is related to coherent attenuation. We have also calculated the coherent and incoherent intensity for electromagnetic wave propagation through ice particles ($\epsilon_r = 3.168$) in free space using the first term of the two series of diagrams given in Eq. (8).

In Figs. 1 and 2, the real and imaginary parts of the wave number are compared with the experimental measurements of Killey and Meeten⁶. In Fig. 3, calculations of the coherent intensity for a suspension of Revacryl spheres in distilled water show excellent comparison with measurements of Killey and Meeren⁶.

In Fig. 4, the incoherent intensity is plotted as a function of ka for $c = 0.0524$ and for various angles θ . It is interesting to note that as ka increases, the leading term of the incoherent intensity approaches a constant value for all values of θ . Figure 5 displays the incoherent intensity as a function of the observation angle θ , and the intensity reduces to zero at $\theta = 90^\circ$ as expected.

ACKNOWLEDGEMENTS

This work was supported by the U.S. Army Research Office under contract DAAG29-83-K-0097. Many helpful discussions with Dr. W.A. Flood are gratefully acknowledged.

REFERENCES

1. V. Twersky, Coherent scalar field in pair-correlated random distributions of aligned scatterers, J. Math. Phys., **18**, 2468-2486, 1977.
2. V. Twersky, Coherent electromagnetic waves in pair-correlated random distributions of aligned scatterers, J. Math. Phys., **19**, 215-230, 1978.
3. V.N. Bringi, V.K. Varadan and V.V. Varadan, Coherent wave attenuation by a random distribution of particles, Radio Sci., **17**, 946-952, 1982.
4. V.K. Varadan, V.N. Bringi, V.V. Varadan and A. Ishimaru, Multiple scattering theory for waves in discrete random media and comparison with experiments, Radio Sci., **18**, 321-327, 1983.

5. V.V. Varadan and V.K. Varadan, The quasi-crystalline approximation and multiple scattering of waves in random media, submitted to IEEE Trans. Antennas and Propagation.
6. A. Killey and G.H. Meeten, Optical extinction and refraction of concentrated latex dispersions, J. Chem. Soc., Faraday Trans. 2, 587-599, 1981.

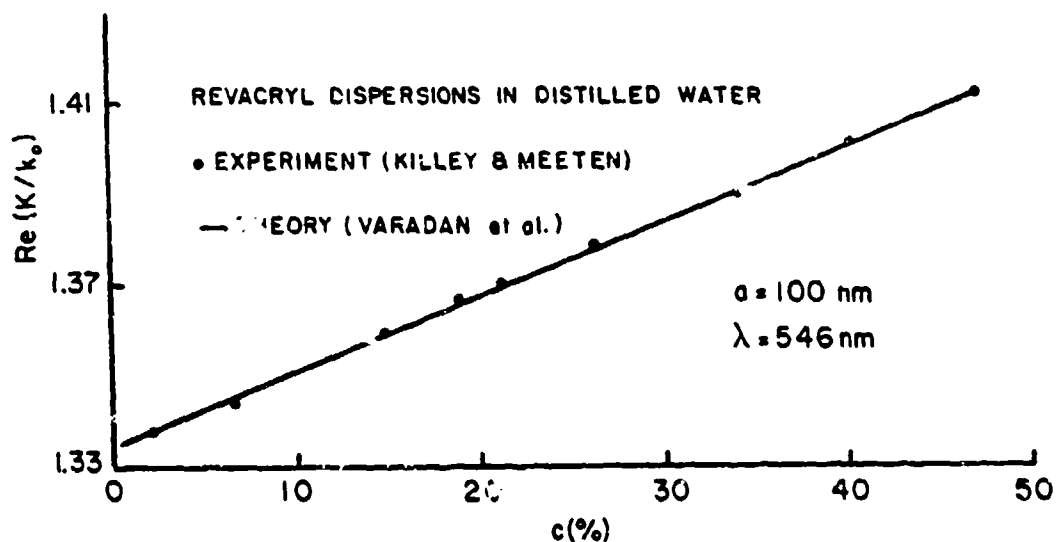


Figure 1. Phase velocity vs. concentration c for $\lambda = 546 \text{ nm}$.

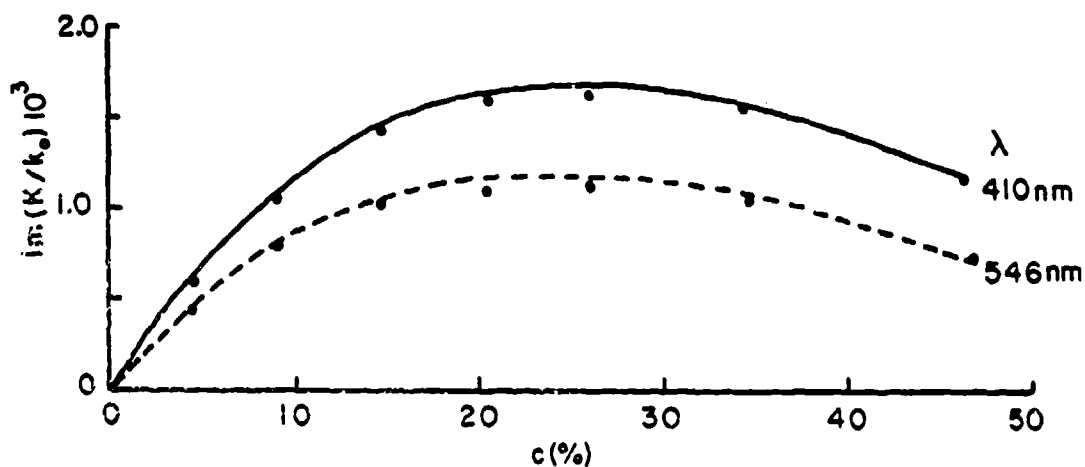


Figure 2. Coherent attenuation vs. concentration c for $\lambda = 410 \text{ nm}$, 546 nm .

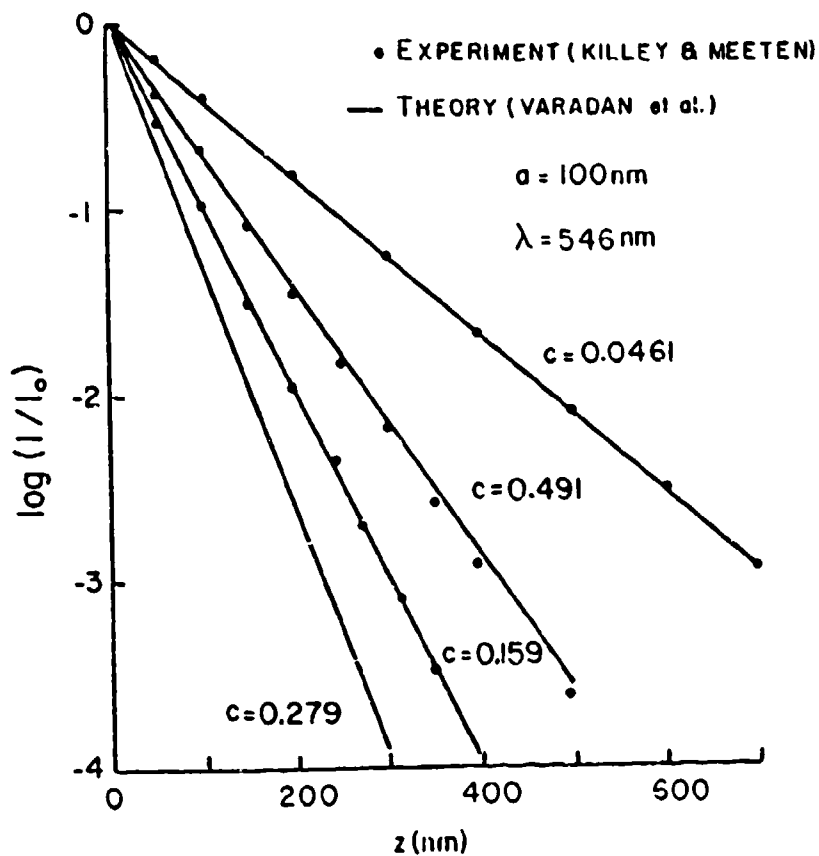


Figure 3. Coherent intensity as a function of depth z for various values of concentration c and for $\lambda = 546 \text{ nm}$.

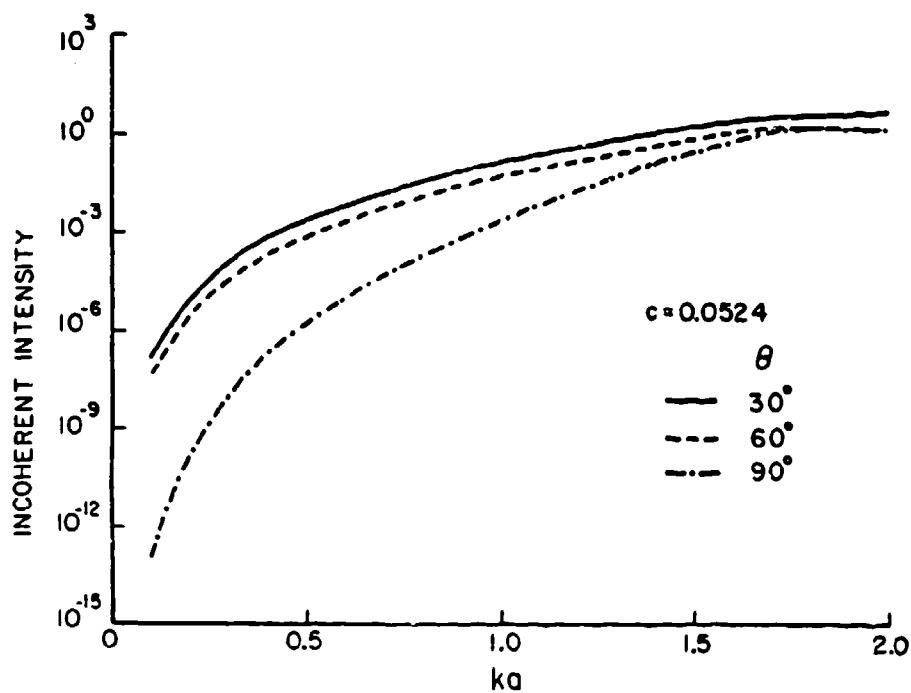


Figure 4a. Normalized incoherent intensity vs. ka for $c = 0.0524$ and for various angles θ .

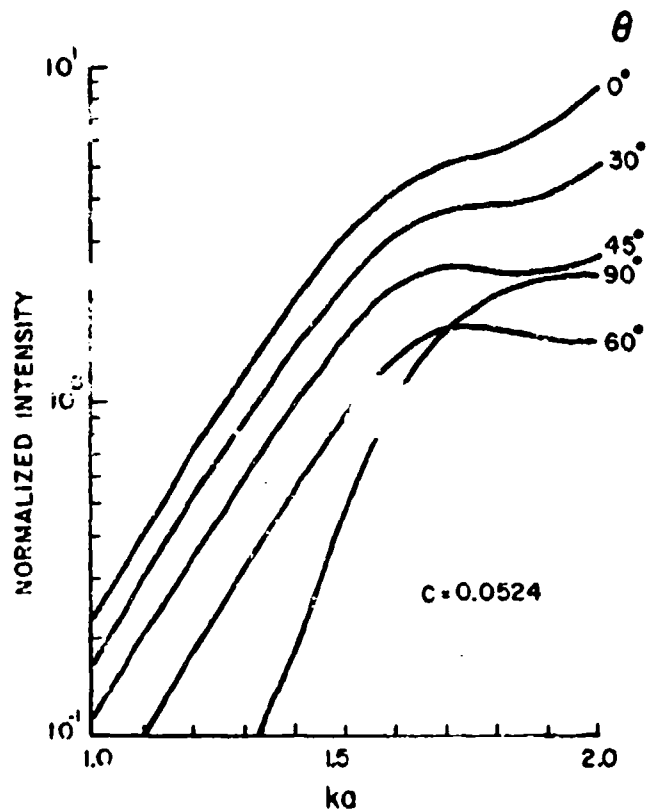


Figure 4b. Expanded version of figure 4a for the range of k_0 from 1.0 to 2.0.

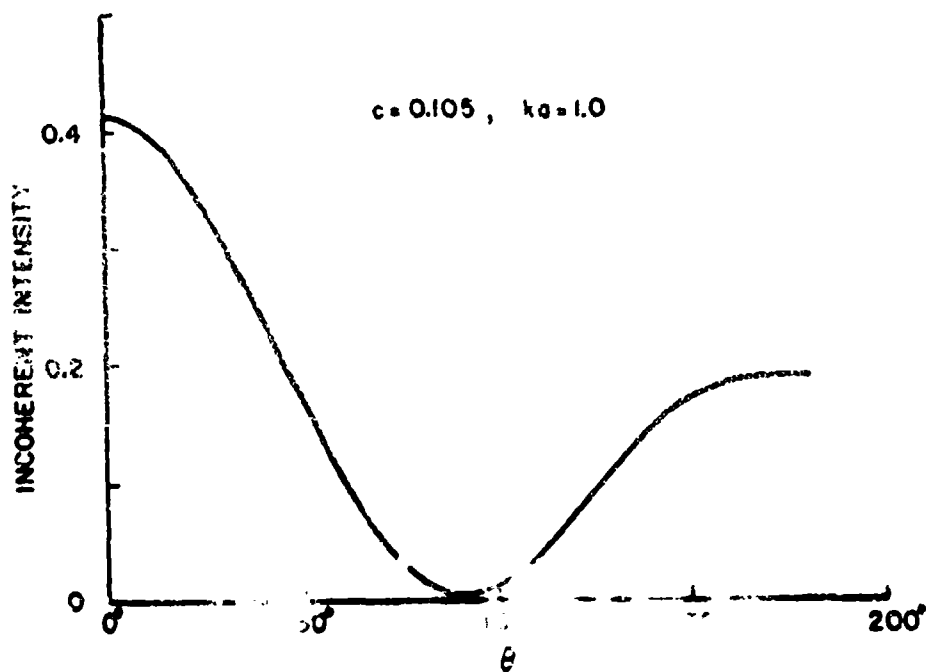


Figure 5. Normalized incoherent intensity as a function of observation angle θ for $c = 0.105$ and $k_0 = 1.0$.

BLANK

RADIATIVE TRANSFER BY CLOUDS OF CONDUCTIVE FIBERS

By

Peter C. Waterman
Jeanne C. Pedersen
Norman E. Pedersen

Panametrics, Inc.
221 Crescent Street
Waltham, MA 02254

ABSTRACT

This paper is concerned with radiative transfer computations for a cloud of randomly oriented conductive fibers. This and related work has been presented, published, and submitted for publication as follows:

Peter C. Waterman, "Matrix-exponential Description of Radiative Transfer," J. Opt. Soc. Am. 71, 410-422 (1981).

Peter C. Waterman, Jeanne C. Pedersen and Norman E. Pedersen, "Computation of Radiative Transfer," Proceedings of the 1983 CSL Conference on Obscuration and Aerosol Research, submitted September 1983.

Peter C. Waterman, Jeanne C. Pedersen and Norman E. Pedersen, "Radiative Transfer by Clouds of Conductive Fibers," 1984 CRDC Conference on Obscuration and Aerosol Research, June 1984.

Norman E. Pedersen, Jeanne C. Pedersen and Peter C. Waterman, "Final Report on Theoretical Study of Single and Multiple Scattering by Cylinders," Panametrics, Inc. (September, 1984).

Although some further development is planned, the associated computer programs are now developed to the point where specific applications involving fiber clouds can be investigated.

1. Introduction

For the past several years, under contract to CRDC, Panametrics has been engaged in a program to compute the electromagnetic scattering and absorption behavior of small lossy conductive fibers, and subsequently to compute the radiative transfer (RT), properties of a cloud of such fibers. The present report describes recent theoretical results, and shows some typical numerical results for transmitted and reflected angular intensity patterns associated with fiber clouds.

Recent results associated with the single fiber scattering problem are presented elsewhere in these Proceedings. A more detailed and comprehensive description of both aspects of the problem is given in the final report.¹

2. Orientation Averages

We are interested in the radiative transfer properties of a cloud of randomly oriented fibers. Thus, the first step in the analysis involves orientation averaging of the single-fiber differential scattering patterns. If $\hat{p}(\alpha, \beta)$ is a unit vector along the fiber axis, with spherical angles α, β relative to a fixed cartesian coordinate system, for a linearly polarized incident wave \hat{e}_{in} along the positive z direction we have $\sigma_{diff} = \sigma_{diff}(\alpha, \beta, \theta, \phi)$, and the orientation-averaged differential scattering pattern is given by

$$\bar{\sigma}_{diff}(\theta) = \left(\frac{1}{4\pi}\right) \int_0^{2\pi} d\alpha \int_0^\pi d\beta \sin\beta \sigma_{diff}(\alpha, \beta, \theta, \phi) \quad (1)$$

Note that strictly speaking it is also necessary to average over the polarization angles of the incident - & scattered waves. Because we are only interested in scalar intensities, however, it suffices to choose the incident polarization in the plane of incidence (plane formed by the fiber and the direction of incidence). The scattered intensity is then taken without regard to its polarization. It is not difficult to verify that this simplification does not affect the angular dependence of the result.

The scattering patterns are actually computed in fiber coordinates, i.e., in terms of the angle $\cos \theta_f = \hat{p} \cdot \hat{k}_{out}$ formed by the fiber and the observation direction $\hat{k}_{out}(\theta, \phi)$. The angle θ_f can be expressed in terms of the orientation angles by noting that

$$\cos \theta_f = \sin \theta \sin \beta \cos(\phi - \alpha) + \cos \theta \cos \beta. \quad (2)$$

We see that the ϕ -dependence drops out during the integration, so that the resulting pattern, Eq. (1), is rotationally symmetric.

The short-fiber limit $kh \ll 1$ (h = half-length of fiber) provides a useful check on the computation. In this limit we can assume that the axial current induced in the fiber is proportional to $\hat{e}_{in} \cdot \hat{p} = \sin \beta$ and that the corresponding scattered amplitude is given by $\hat{e}_{in} \cdot \hat{p} \sin \theta_f$, so that

$$\sigma_{diff} = \sigma_0 (\hat{e}_{in} \cdot \hat{p} \sin \theta_f)^2, \quad (3)$$

where σ_0 is the maximum cross section obtained at broadside incidence and observation. Putting this expression in Eq. (1), and dividing by a factor of 4 to correct for not averaging over incident and received polarization, gives finally

$$\bar{\sigma}_{diff}/\sigma_0 = (1/30) (3 + \cos^2 \theta). \quad (4)$$

This $3 + \cos^2 \theta$ angular dependence constitutes a new elementary scatterer for radiative transfer, which might be called the Rayleigh fiber. Note that it falls intermediate relative to the isotropic and Rayleigh sphere ($1 + \cos^2 \theta$) cases.

Numerical computations of orientation-averaged scattering from perfectly conducting fibers are shown in Fig. 1 for several values of kh (for clarity normalized to 4 in the forward direction $\mu = \cos \theta = 1$). The uppermost curve is the Rayleigh fiber pattern of Eq. (4), and one notes that the numerical results converge smoothly to this limit for $kh \ll 1$ (the $kh = 0.1$ curve, not shown, is indistinguishable). As kh becomes greater than unity a significant peak is seen to develop in the forward direction, typical behavior for scatterers when dimensions are not small compared to wavelength.

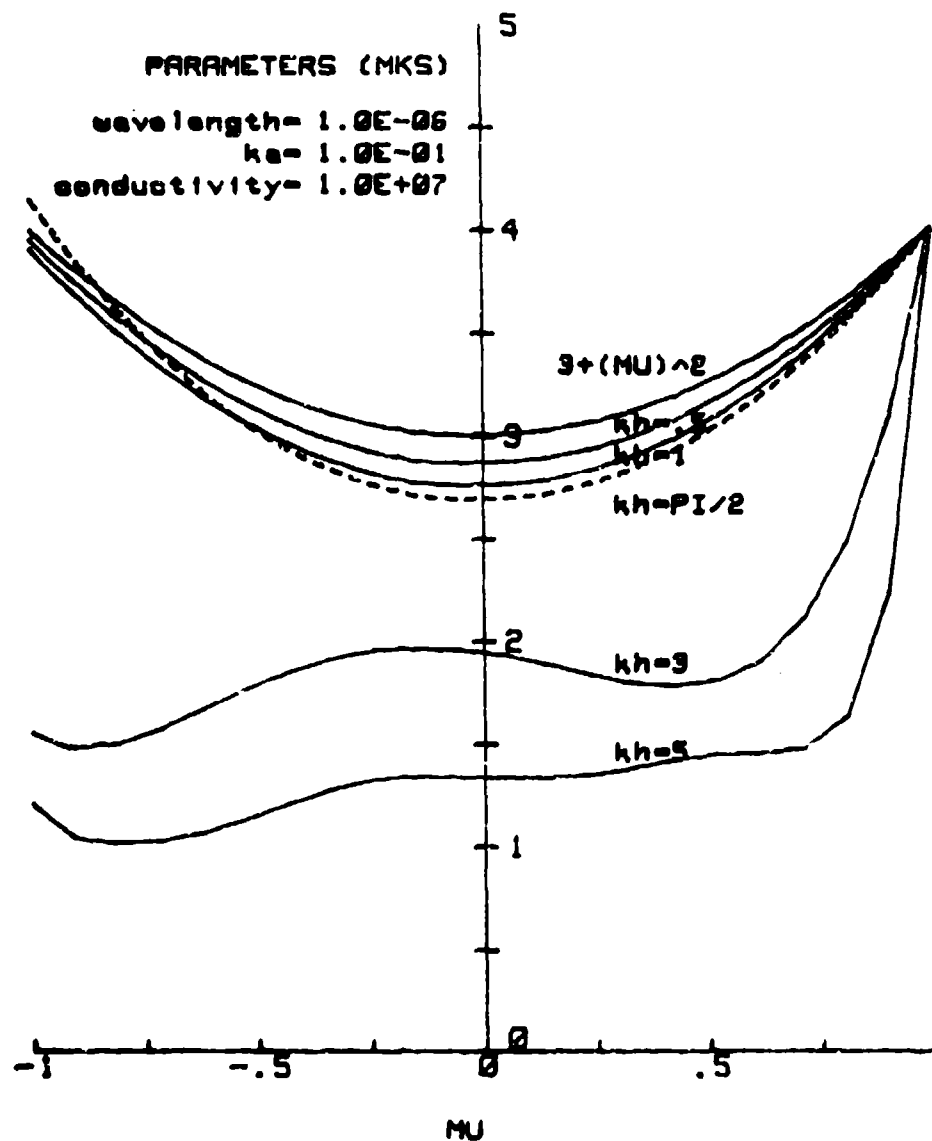


Fig. 1. Orientation-averaged cross sections.

It is interesting to note that the orientation-average has been computed by Borison, but for half-wave dipoles ($kh = \pi/2$).² Upon averaging his results over incident and received polarizations one obtains precisely Eq. (4). This does not agree with the curve of Fig. 1; we believe that Borison's assumption of simple cosine behavior of the surface current for all fiber orientations is no longer adequate at $kh = \pi/2$.

3. The Thin-Layer Limit

We consider the slab geometry for a cloud of randomly oriented fibers, as shown in Fig. 2. The cloud has optical depth x , and one desires to compute the angular intensities transmitted and reflected, $T(\theta)$ and $R(\theta)$, respectively, as shown in the figure. We employ the doubling method, with a fourth-order starting formula based on the matrix-exponential description, as described elsewhere.³

A simple check is available on numerical computations in the thin-layer limit $x \ll 1$. As shown in Fig. 3, the transmitted intensity per steradian in the direction $\mu = \cos \theta$ must originate in the differential cone of fibers indicated. But, in the thin-layer limit, the contribution from an element of the cone will be proportional to albedo κ , the phase function $p(\mu)$, and exponential factors accounting for attenuation of radiation over the travel path within the slab. Thus, with $x' = x - \mu x$,

$$I(\mu) = \kappa \alpha p(\mu) \int_0^{x/\mu} ds e^{-x'} e^{-s}, \quad \mu \geq 0. \quad (5)$$

A similar equation can be written down for the reflected intensity, and carrying out the integrations gives

$$I(\mu) = \kappa \alpha p(\mu) \begin{cases} e^{-x} (1 - e^{-(1-\mu)x/\mu}) / (1-\mu), & \mu \geq 0 \\ (1 - e^{(1-\mu)x/\mu}) / (1-\mu), & \mu \leq 0 \end{cases} \quad (6)$$

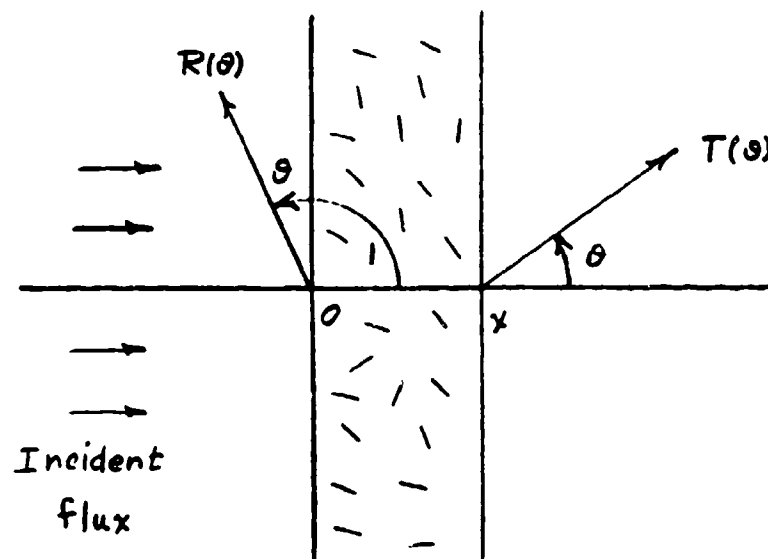


Fig. 2 Slab geometry of fiber cloud.

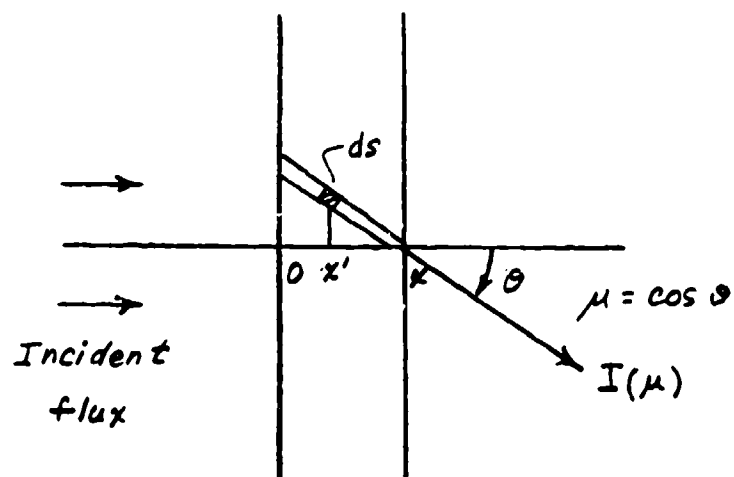


Fig. 3. Geometry for thin-layer approximation.

These last formulas are given by van de Hulst¹⁵ for the isotropic case $p(\mu) = 1$; clearly, from our derivation they must continue to hold for arbitrary $p(\mu)$.

Intensity patterns have been computed numerically for an optical depth $\tau = 0.1$ and the three elementary scatterers, isotropic, Rayleigh sphere (dipole), and Rayleigh fiber. Results are shown by the points in Fig. 4. The corresponding analytical approximations of Eq. (6) are given by the solid curves in the figure, and excellent agreement is seen throughout. Incidentally, van de Hulst gives the theoretical value $\kappa = 1/4$ for the proportionality constant of Eqs. (6) and (9). We find that much better results are obtained using a somewhat larger value obtained by matching Eq. (6) to the computed point for normal reflection for transmission ($\mu = \pm 1$). For example, for isotropic scatterers the two computations then agree to four significant figures, excepting only the point $\mu = -.04762$, where agreement is slightly poorer.

4. Numerical Results

Having made the above preliminary checks, we now survey a few typical results obtained using the fiber scattering computer program in conjunction with the radiative transfer program.

In Fig. 5 plots of the transmitted and reflected intensities are given for an optical depth of unity, where the single scatterer is 1) isotropic, 2) Rayleigh sphere, 3) the Rayleigh fiber of Eq. (4), and 4) the short fiber (parameters as noted in the figure). Note that, just as was true for the phase functions, the radiative transfer intensities for the Rayleigh fiber fall intermediate between the isotropic and sphere case. It is also interesting that the Rayleigh fiber and short dipole ($kh = 0.3$) results are now indistinguishable, even though their phase functions are measurably different (see Fig. 1).

The sharp peaks seen in the transmitted intensity in the forward direction $\mu = 1$, of course, represent the coherent portion of the flux (for clarity these peaks are truncated at 1).

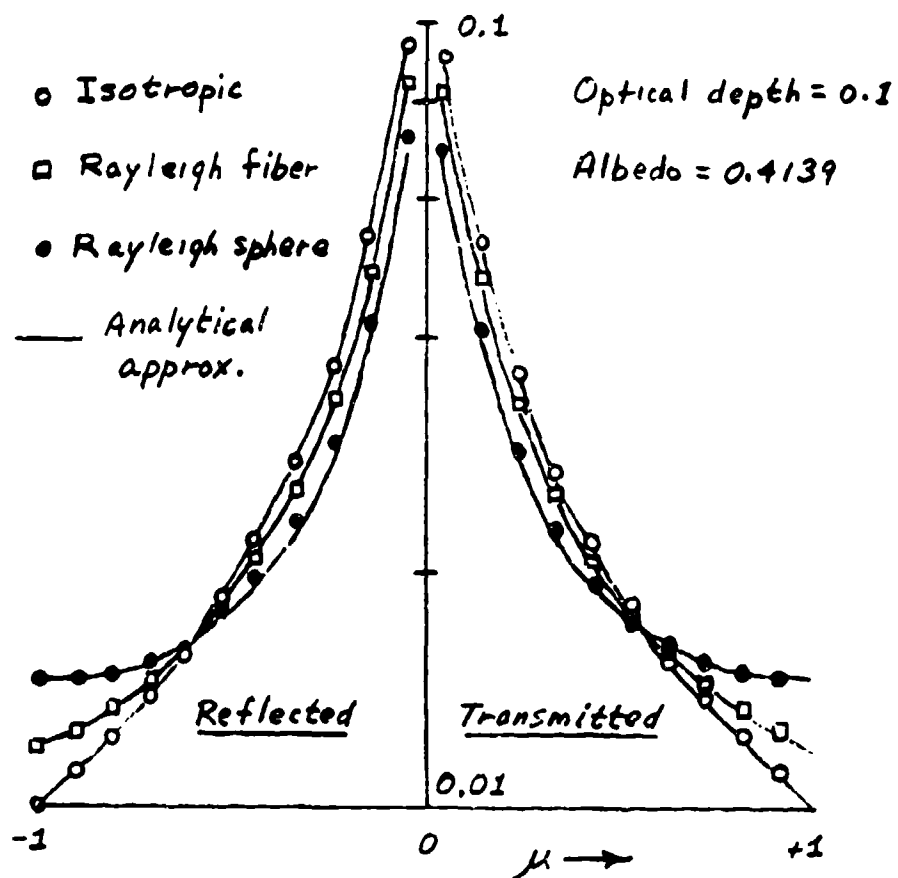


Fig. 4. Thin-layer flux distributions.

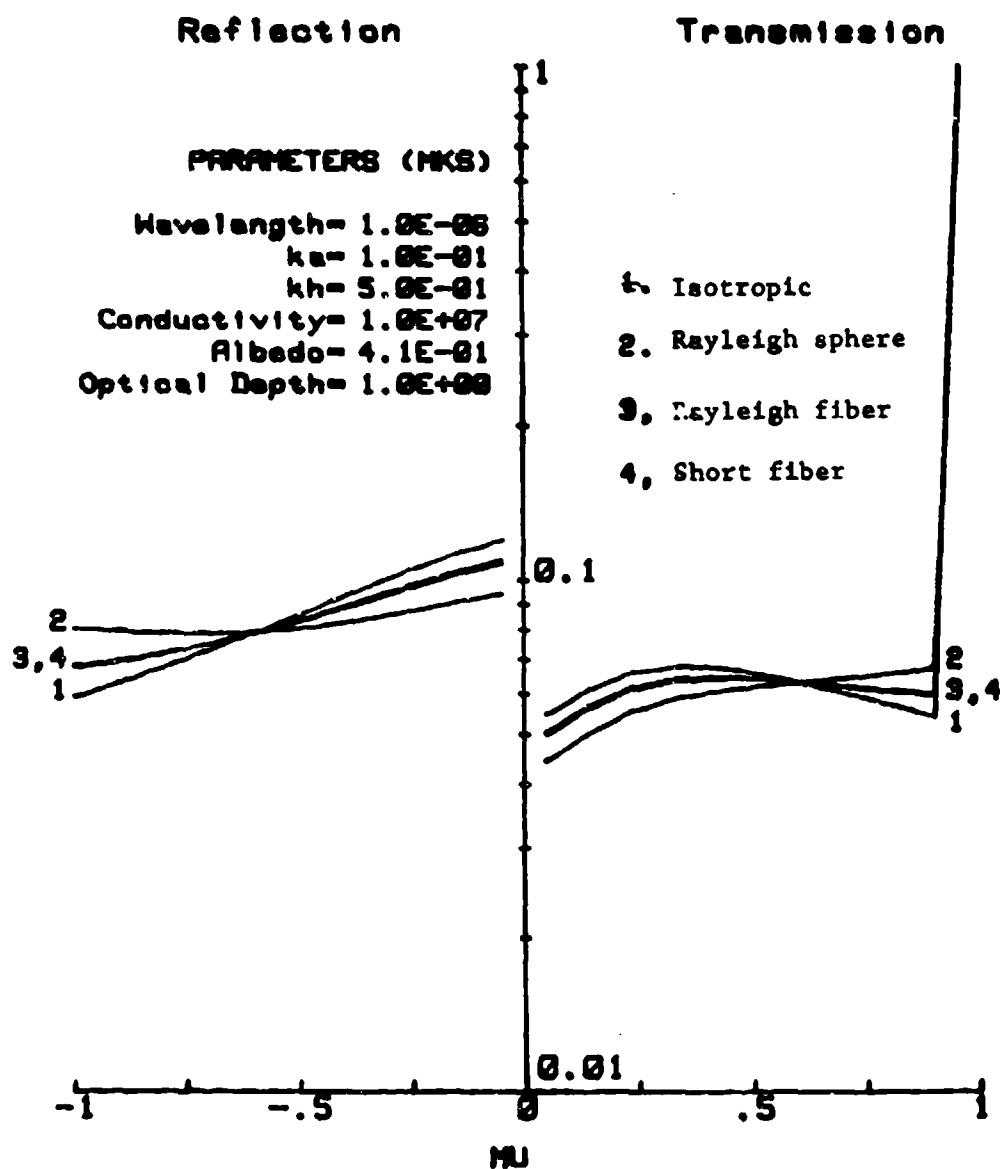


Fig. 5. Transmitted and reflected intensities for different scatterers.

Dependence of the RT intensities on fiber length is indicated in Fig. 6, for fairly highly conducting fibers. From the figure one can see that both the total transmitted and total reflected intensity show a mild peak at about $kh = 3$, although the reason for this is not clear.

For fixed fiber length $kh = 3$, dependence of the RT intensities on optical depth z is shown in Fig. 7. As one would expect, the reflected patterns increase monotonically with z , at the same time becoming more nearly isotropic. The transmitted patterns show the same behavior in the diffusely transmitted flux up to about $z = 1$, with corresponding reductions in the coherent flux (because of truncation the latter effect is not obvious from the figure). With further increases in optical depth the transmitted flux begins to decrease, presumably because scattering and absorption mechanisms now dominate.

Finally, Fig. 8 illustrates the effect of varying the fiber conductivity, maintaining a fixed fiber length $kh = 1$ and optical depth $z = 1$. Both reflected and transmitted patterns are seen to increase monotonically with conductivity, both also showing signs of saturation for the uppermost curves, which are effectively approaching the perfectly conducting limit. Again, the curves behave qualitatively as would be expected, in view of the fact that the albedo is increasing toward unity with increasing conductivity.

The above examples illustrate the usefulness and versatility of the computer programs. These programs are now sufficiently well developed to begin running specific problems of practical interest to CRDC involving both single-fiber scattering and absorption, and the radiative transfer properties of the corresponding fiber clouds.

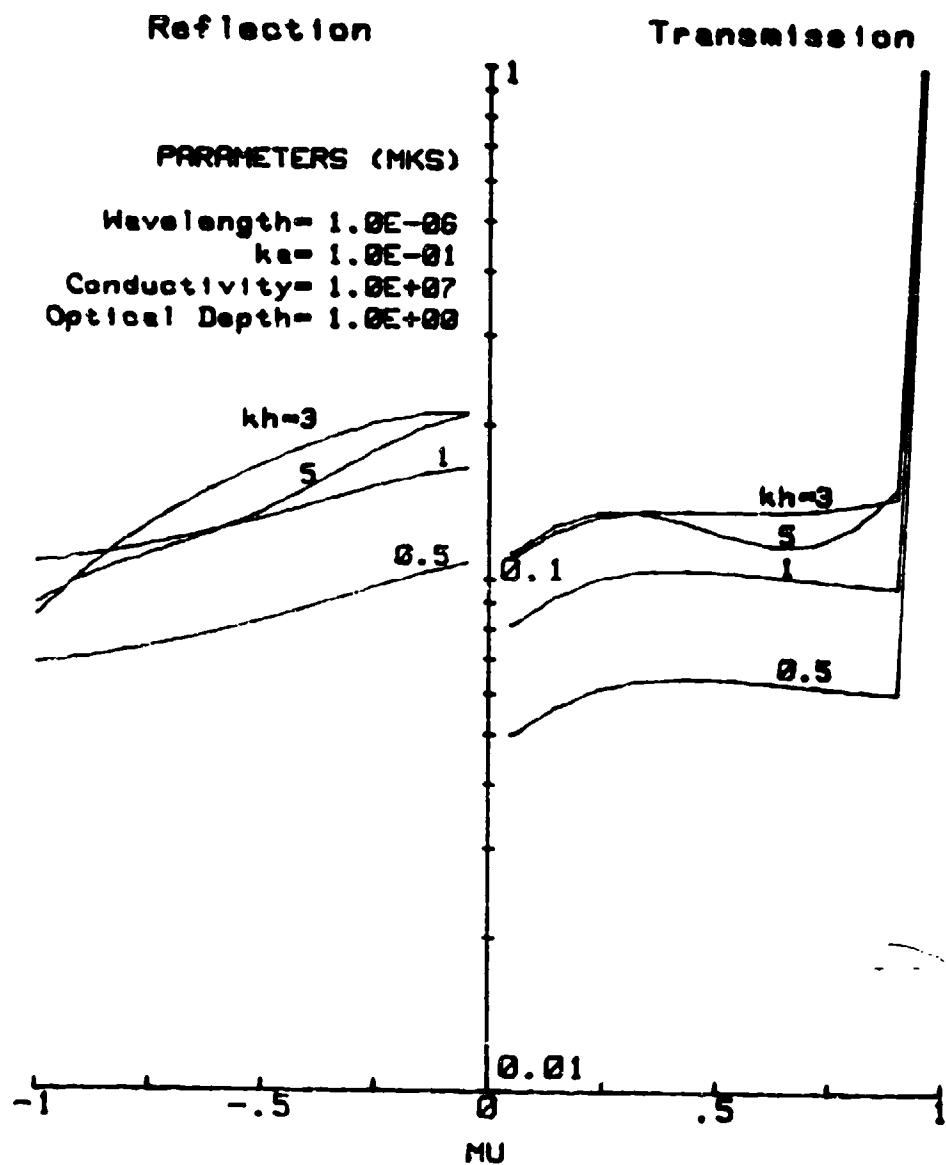


Fig. 6. Transmitted and reflected intensities for different fiber lengths.

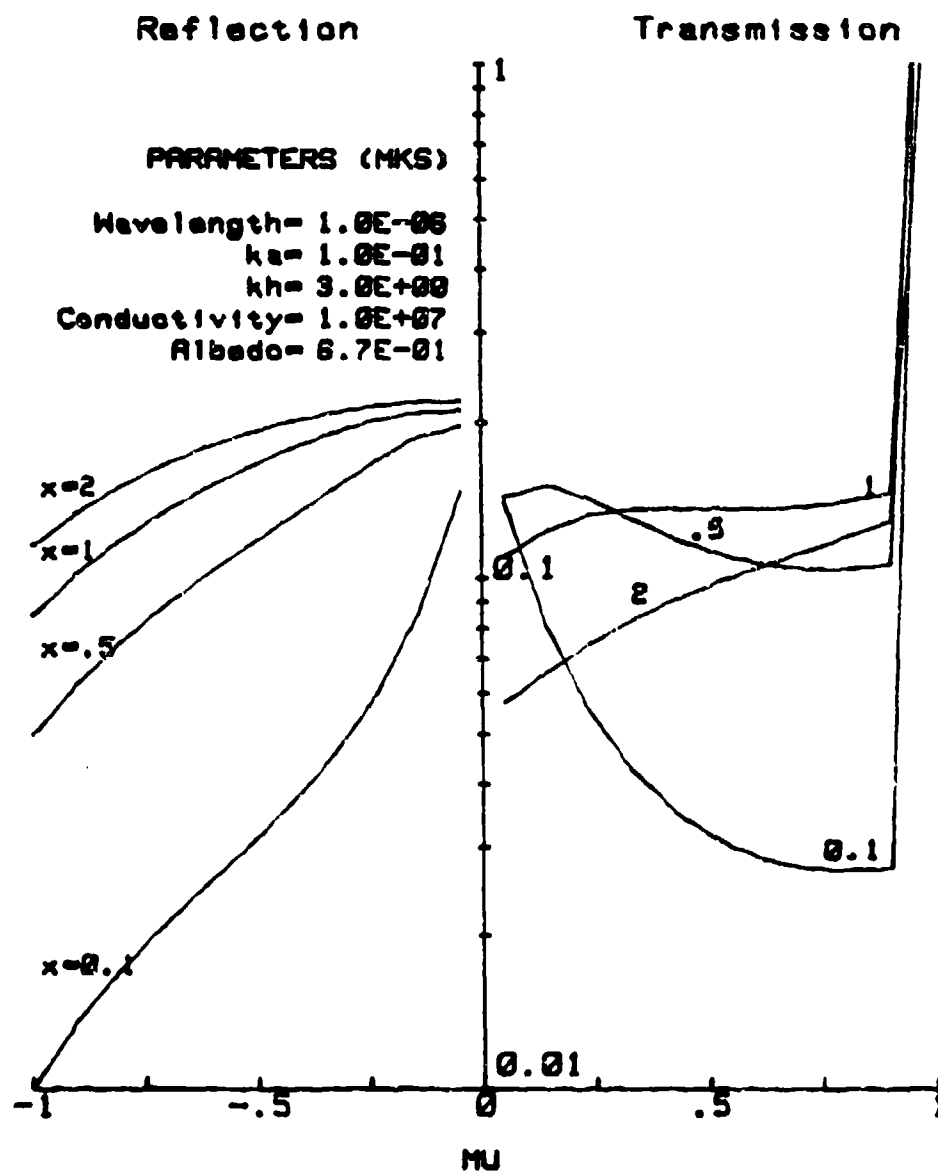
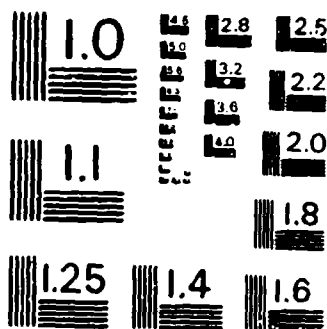


Fig. 7. Transmitted and reflected intensities for different optical depths.



MICROCOPY RESOLUTION TEST CHART
NATIONAL BUREAU OF STANDARDS-1963-A

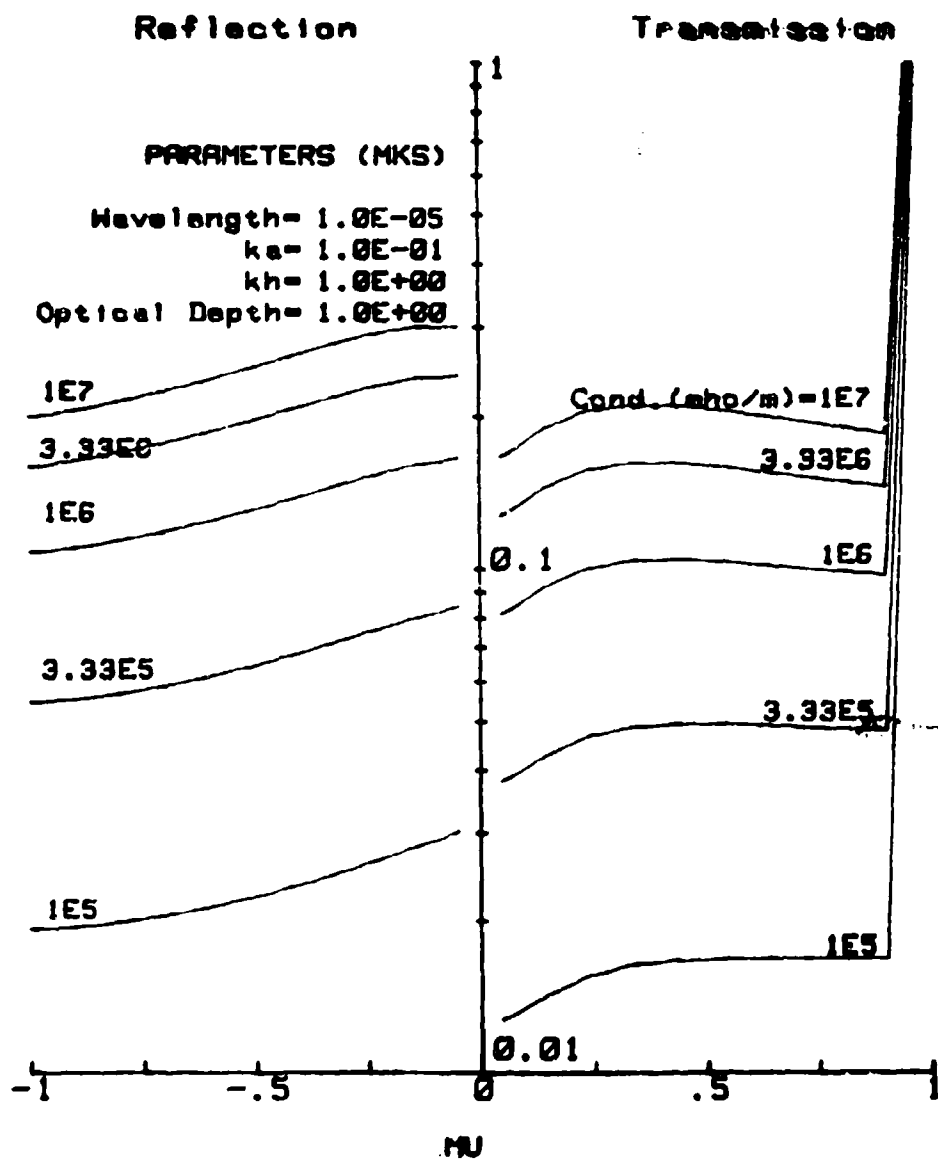


Fig. 8. Transmitted and reflected intensities for different conductivities.

References

1. M. E. Pedersen, J. C. Pedersen and P. C. Waterman, "Final Report on Theoretical Study of Single and Multiple Scattering by Cylinders," Panametrics, Inc. (September, 1984).
2. S. L. Morison, *IEEE Trans. AP-15*, 320 (1967).
3. P. C. Waterman, *J. Opt. Soc. Am.* 71, 410 (1981).
4. H. C. van de Hulst, Multiple Light Scattering (Academic Press, NY, 1980) p. 194.

IMAGING THROUGH A MULTIPLE SCATTERING MEDIUM

A. Sardecki and S. A. W. Gerstl
Theoretical Division, MS P371
Los Alamos National Laboratory
Los Alamos, New Mexico 87545

and

J. P. Embury
Chemical Research and Development Center
Aberdeen Proving Ground, Maryland 21010

ABSTRACT

The existing theory of imaging through an aerosol medium, based on the small-angle approximation to radiative transfer, is extended to the general case of multiple scattering with an arbitrary degree of anisotropy. By applying the discrete-ordinates, finite-element radiation transport code TWOTRAN, we compute the modulation transfer function for a medium characterized by optical depth, single scattering albedo, and a symmetry parameter. An extended version of this investigation will appear in a 1984 issue of Applied Optics.

Experimental evidence^{1,2} strongly supports the concept of spatial-coherence degradation through forward scattering from aerosols. The spatial frequency dependence of the measured Modulation Transfer Function (MTF) indicates that, aside from turbulence, multiple scattering processes can seriously limit image resolution. The theoretical model developed by Kopeika^{1,2} is based on the small-angle approximation to radiative transfer, which is valid for particles larger than or comparable in size to the wavelength of the radiation. Within the context of this theory, a detailed investigation of the image degradation problem is contained in the work of Ishimaru.³

We extend this existing theory to the general case of multiple scattering with an arbitrary degree of anisotropy (particle size not necessary to be larger than wavelength), by applying the discrete-ordinates, finite-element radiation transport code TWOTRAN⁴ to compute the MTF for a medium characterized by optical depth τ , single scattering albedo ω , and asymmetry parameter g . To partially suppress the ray effect in the discrete-ordinates solution to the transfer equation, we separate the radiance distribution function into unscattered (reduced) $I^{(0)}$, and scattered (diffuse), $I^{(s)}$ parts:

$$I(\underline{r}, \underline{\Omega}) = I^{(0)}(\underline{r}, \underline{\Omega}) + I^{(s)}(\underline{r}, \underline{\Omega}) \quad (1)$$

We consider an isotropically emitting line source along the z -axis at the entrance plane of an x - y slab with optical thickness τ . If S_L denotes the power radiated per unit length of the source, the spatial distribution of the unscattered radiation component within the slab is

$$I^{(0)}(\underline{r}, \underline{\Omega}) = \frac{S_L}{2\pi r} F\left(\frac{\pi}{2}, \sigma r\right) \delta(\underline{\Omega} - \underline{\Omega}_0) \quad (2)$$

Here r and $\underline{\Omega}_0$ are the distance and direction vector from the line source to the point \underline{r} , σ denotes the volume extinction coefficient, and F is the Sievert integral, defined as

$$P(\theta, \rho) = \int_0^\theta \exp(-\rho/\cos \theta) d\theta. \quad (3)$$

The scattered radiance is then obtained by solving numerically the transfer equation with a volumetric first-collision source, Q , given as

$$Q(\underline{r}, \underline{\Omega}) = \sigma_s \int p(\underline{\Omega} \cdot \underline{\Omega}') I^{(0)}(\underline{r}, \underline{\Omega}') d\Omega'. \quad (4)$$

In Eq. (4), σ_s is the volume scattering coefficient and $p(\underline{\Omega} \cdot \underline{\Omega}')$ is the scattering phase function. For mathematical convenience we model $p(\underline{\Omega} \cdot \underline{\Omega}')$ as the Henyey-Greenstein phase function characterized by a single asymmetry parameter g .

The line spread function $L(x)$, at the exit plane of the slab, is given as the monochromatic irradiance:

$$L(x) = \int_0^{2\pi} \int_0^\pi I(x, y=0, \theta, \phi) \cos \theta \sin \theta d\theta d\phi, \quad (5)$$

where θ is the angle between an outgoing ray and the y -axis. In Figs. 1 and 2 we show the line spread function for two extreme values of the albedo ω : $\omega = 0.1$ strongly absorbing, and $\omega = 1.0$ purely scattering. It is seen that the dominance of the unscattered radiation is overpowered by the scattered contribution as ω changes from 0.1 to 1.0.

Figure 3 shows the modulation transfer functions that result when a Fast-Fourier Transform algorithm is applied to $L(x)$. The MTF is not sensitive to the value of ω . In addition, the remnants of the ray effect displayed in Figs. 1 and 2 are smoothed out when the Fourier transform is taken. The MTFs roll off at a frequency of the order of 1.0 cycles/rad, which is consistent with formula (36) of Ref. 3, derived for strongly peaked forward scattering. This low value, as stressed by Ishimaru, still allows one to obtain a good Airy pattern, provided $I^{(0)}$ is larger than $I^{(s)}$.

By applying numerical solutions to the two-dimensional radiative transfer equation, we thus extended the present theory of image degradation by random media to the general case where multiple scattering with arbitrary phase functions can be treated. A parametric study of the MTF will delineate the range of validity of the small-angle approximation in imaging problems.

References

1. N. S. Kopeika, "Spatial-frequency dependence of scattered background light: The atmospheric modulation transfer function resulting from aerosols," *J. Opt. Soc. Am.* **72**, 548 (1982).
2. N. S. Kopeika, "Spatial-frequency and wavelength-dependent effects of aerosols on the atmospheric modulation transfer function," *J. Opt. Soc. Am.* **72**, 1092 (1982).

3. A. Ishimaru, "Limitation on image resolution imposed by a random medium," Appl. Opt. 17, 348 (1978).
4. A. Zardecki, S. A. W. Gerstl, and J. P. Embury, "Application of the 2-D discrete-ordinates method to multiple scattering of laser radiation," Appl. Opt. 22, 1346 (1983).

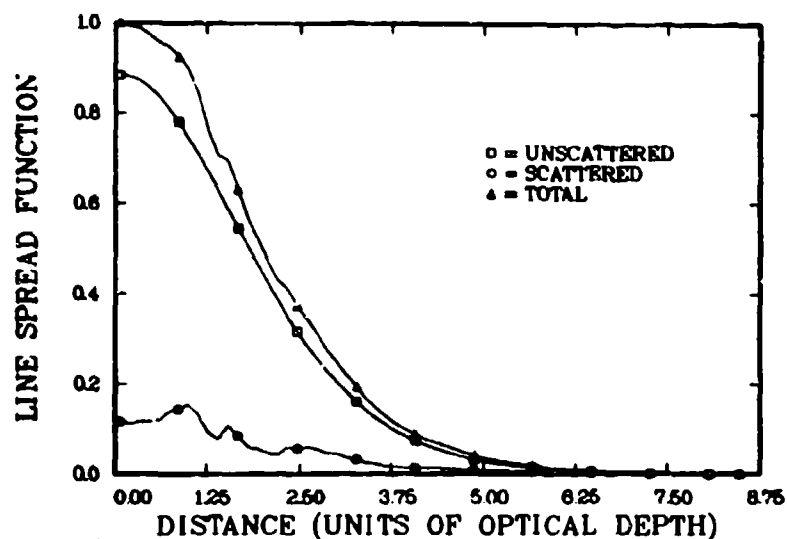


FIGURE 1. Line spread function for a model aerosol cloud with $\tau = 4$, $\omega = 0.1$, and $g = 0.1$.

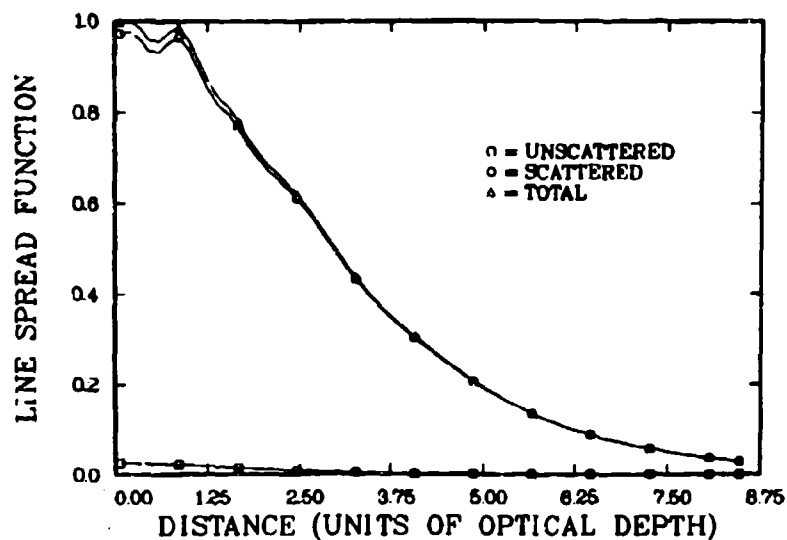


FIGURE 2. Line spread function for a model aerosol cloud with $\tau = 4$, $\omega = 1.0$, and $g = 0.1$.

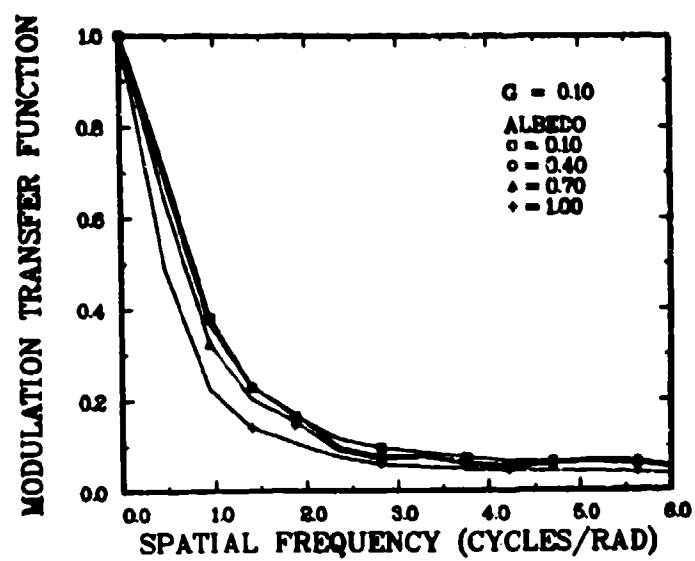


FIGURE 3. Modulation transfer function for four different values of ω . Optical depth $\tau = 4$.

**TRANSPORT METHODS FOR ESTIMATING SINGLE-SCATTERING
COEFFICIENTS FROM REMOTE OR IN SITU
MULTIPLY-SCATTERED RADIANCE MEASUREMENTS**

N.J. McCormick

Department of Nuclear Engineering
University of Washington
Seattle, Washington 98195

ABSTRACT

Different methods are summarized for estimating the albedo of single scattering and the coefficients of a Legendre polynomial expansion of the phase function from the multiply-scattered radiance measured at two locations exterior to a homogeneous plane turbid medium. A simpler method is given for applications in which the radiance is measured within such a medium at two locations far from the surfaces. This paper covers the following work published and submitted for publication:

R. Sanchez and N.J. McCormick, 'Numerical evaluation of optical single-scattering properties using multiple-scattering transport methods', *J. Quant. Spectrosc. Rad. Transfer* **28**, 169 (1982).

N.J. McCormick and R. Sanchez, 'Solutions to an inverse problem in radiative transfer with polarization II,' *J. Quant. Spectrosc. Rad. Transfer* **30**, 527 (1983).

N.J. McCormick, 'Methods for estimating the similarity parameter of clouds from internal measurements of the scattered radiation field', *J. Quant. Spectrosc. Rad. Transfer* (to be published).

Preliminary results from tests just beginning are also reported; these results are based on numerically simulated radiance data to illustrate the potential inaccuracy of some of the methods arising from random statistical fluctuations in the measurements.

I. INTRODUCTION

The focus of much of the research on obscuration by aerosols is on determining the scattering properties of particulates (both smooth and irregular-shape). There are two general classes of problems: direct and inverse. For the first, knowledge of the relative index of refraction of a particle and its shape and size is needed to calculate the scattering matrix; a projection of these results onto the basis functions consisting of the generalized spherical functions (Chu and Churchill, 1955; Kušner and Ribarič, 1959; Hovenier and van der Mee, 1983; de Rooij and van der Stap, 1984) then enables the expansion coefficients to be determined. For example, scattering of the intensity of radiation can be described by the single scattering phase function

$$f(\hat{\Omega}' \cdot \hat{\Omega}) = (4\pi)^{-1} \sum_{n=0}^N (2n+1) f_n P_n(\hat{\Omega}' \cdot \hat{\Omega}), \quad f_0 = 1,$$

where $\hat{\Omega}' \cdot \hat{\Omega}$ is the cosine of the angle between the incoming and outgoing wavefronts and the P_n are Legendre functions. The parameters f_n , $n = 1$ to N , and the albedo of single scattering ω together serve to characterize the interaction of the radiation (of an implicit wavelength) with the particle. The

coefficient f_1 , for example, is the asymmetry factor customarily denoted by g .

The expansion coefficients f_n can be calculated from

$$f_n = \int_{4\pi} d\Omega f(\Omega' \cdot \Omega) P_n(\Omega' \cdot \Omega)$$

provided careful single-scattering experiments of the phase function can be done. Such an estimation of the coefficients f_n from phase function information is the most straight-forward form of inverse problem. The work here, however, deals with inverse problems in which the phase function is not known and must be estimated from radiation that has survived many scattering events.

The methods used to solve inverse multiple scattering problems necessarily must depend upon the geometry of the target. In this paper, we will restrict ourselves to the case of a homogeneous slab or semi-infinitely thick target that is externally illuminated uniformly over one (or both) of the surfaces, with only a brief discussion of the extensions to the methods that have been developed for other geometries. Likewise, for the most part we will assume the incident radiation is of a single frequency and that polarization effects are not of interest. The target is assumed to re-radiate a negligible amount of energy at the frequency of interest, so that there is no spatially-distributed source in the interior of the target. Finally, the particles in the target are assumed to be randomly oriented and in the far field of one another.

So much for the restrictions. The good news is that the target optical thickness can be as large as we like, and the particles can be of arbitrary unknown shape and size. This means that, at least in principle, the methods are valid for an arbitrary degree of angular anisotropy of scattering.

The inverse multiple scattering methods have all been derived by starting with the radiation transport equation

$$\mu \partial_\tau I(\tau, \mu, \xi) + I(\tau, \mu, \xi) = (\omega/4\pi) \int_0^{2\pi} d\xi' \int_{-1}^1 d\mu' f(\Omega' \cdot \Omega) I(\tau, \mu', \xi'),$$

where τ is the optical distance in the plane layer of interest, $\tau_- \leq \tau \leq \tau_+$, while μ is the cosine of the angle with respect to the positive τ axis and ξ is the azimuthal angle. The specific intensity $I(\tau, \mu, \xi)$ is the radiant energy crossing a unit surface area normal to the direction of travel per unit solid angle and per unit time. (The time dependence of the intensity will be briefly discussed later.) The boundary conditions can be arbitrary, i.e.,

$$I(\tau_-, \mu, \xi) = g_1(\mu, \xi), \quad 0 \leq \mu \leq 1, \quad 0 \leq \xi \leq 2\pi,$$

$$I(\tau_+, \mu, \xi) = g_2(\mu, \xi), \quad -1 \leq \mu \leq 0, \quad 0 \leq \xi \leq 2\pi.$$

The basic idea in deriving the methods is to take angular moments of the transport equation. This introduces a set of projections

$$I_{1,n}^m(\tau) = \alpha_n^m \int_{-1}^1 P_n^m(\mu) I_1^m(\tau, \mu) d\mu,$$

$$I_{2,n}^m(\tau) = \alpha_n^m \int_{-1}^1 P_n^m(\mu) I_2^m(\tau, \mu) d\mu, \quad (1)$$

where the Fourier projections are defined as

$$I_1^m(\tau, \mu) = [\pi(1 + \delta_{m0})]^{-1} \int_0^{2\pi} I(\tau, \mu, \xi) \cos m(\xi - \xi_r) d\xi,$$

$$I_2^m(\tau, \mu) = \pi^{-1} \int_0^{2\pi} I(\tau, \mu, \xi) \sin m(\xi - \xi_r) d\xi \quad (2)$$

and α_n^m are the constants

$$\alpha_n^m = [(2n+1)(n-m)/(n+m)!]^{1/2}.$$

The arbitrary azimuthal reference angle is ξ_r .

There are then at least two ways to proceed: if one integrates the transport equation over the spatial variable to counteract the δ_τ operator in the equation, then after manipulations one is left with a set of coupled inverse scattering equations for the f_n coefficients that are quadratic in $I_{1,n}^m(\tau)$ or $I_{2,n}^m(\tau)$ evaluated on the boundaries; such equations thus require that $I(\tau_-, \mu, \xi)$ and $I(\tau_+, \mu, \xi)$ be known for $-1 \leq \mu \leq 1$ and $0 \leq \xi \leq 2\pi$. In the event the plane layer of interest is imbedded within a larger homogeneous layer such that τ_- and τ_+ are far from the outermost boundaries, then azimuthal symmetry may prevail, in which case $I_{1,n}^m(\tau) = 0$, $m \geq 1$, and $I_{2,n}^m(\tau) = 0$, $m \geq 0$. Even with this loss of information, however, it is still possible to obtain some information about a parameter that links m and f_1 , by using only the total intensity $I_{1,0}^0(\tau)$ and the net flux (divided by 2π) $I_{1,1}^1(\tau)$. The different sets of quadratic equations will be discussed in Section II, and some preliminary results on the application of the equations with analytically-simulated radiation intensity that has random statistical fluctuations will be given in Section III.

The second way to proceed to develop inverse equations is to first solve the direct problem and to then find a simple enough functional dependence so that the equations can be inverted to infer the f_n coefficients from the intensity. A set of uncoupled inverse scattering equations for the f_n coefficients

has been developed for the case that a semi-infinite layer is illuminated with a burst of radiation, and the equations require that the time-dependent backscattered radiation be measured at times asymptotically long after the burst. The equations for this method require only moments from Eq. (2), and not the more involved set from Eq. (1), so only the ξ -dependence of the intensity would need be measured at a fixed value of μ . The equations are documented elsewhere (McCormick, 1982; McCormick, 1983) and the extent of their applicability is to be tested in a combined experimental-analytical program, funded by the Department of the Army, that is just now beginning. The experimental program is under the direction of R.A. Elliott (Oregon Graduate Center) while the analytical portion is to be done at the University of Washington.

II. COUPLED-EQUATION METHODS

There are a number of independent sets of equations that can be used to infer the $(2N + 1)$ coefficients w and f_n , $n = 1$ to N , depending upon the type of external illumination and the location of the detectors. In the most general case where the external illumination exhibits an azimuthal dependence and cannot be made symmetric with respect to some azimuth reference angle and the detectors are not deeply imbedded in the medium, there are six independent sets of equations (McCormick and Sanchez, 1983). The first three can be expressed in terms of differences of values at τ_+ and τ_- as

$$w \sum_{n=m}^N (-1)^{n-m} f_n (I_{j,n}^m(\tau) I_{k,n}^m(\tau)) \Big|_{\tau_-}^{\tau_+} = S_{jk}^m \quad (3)$$

for $j = 1, 2$ and $k = 1, 2$ and $m = 0$ to N , where

$$S_{jk}^m = 2 \int_{-1}^1 I_j^m(\tau, \mu) I_k^m(\tau, -\mu) d\mu \Big|_{\tau_-}^{\tau_+}.$$

In these equations, the three sets correspond to $\{j, k\} = \{1, 1\}$, $\{2, 2\}$, or $\{1, 2\} \equiv \{2, 1\}$, but there are actually only $(3N + 2)$ distinct inverse equations because the equation for $m = 0$ in the $\{1, 2\}$ set vanishes identically. The second three sets of equations are obtained from the preceding three by replacing $I_k^m(\tau, \mu)$ by $\mu I_k^m(\tau, \mu)$ and f_n by $f_n / (1 - w f_n)$.

The number of equations is dramatically reduced if the incident radiation can be made symmetric to some azimuthal reference angle ξ_r for then only the two $\{1, 1\}$ sets survive; such a situation arises, for example, in the passive illumination of the earth's atmosphere by plane-parallel rays from the sun. An even more severe reduction in equations occurs if the incident illumination is azimuthally symmetric (as in the case of the sun's normal illumination, for example); then only the $m = 0$ equations from the two $\{1, 1\}$ sets are useful, and these are insufficient to determine the unknowns unless $N \leq 1$.

Another instance for which the radiation field is azimuthally symmetric occurs deep in the interior of an optically-thick medium, such as a large cloud. Then, if the radiation detectors are placed deep enough insidewhere it is known the radiation is in the diffusion domain, then it is possible to use that fact to obtain a single equation with which to estimate the similarity parameter

$$s = [(1 - \omega)/(1 - \omega f_1)]^{1/2} .$$

The form of the equation is (McCormick, 1985)

$$s^2 = F(s) \left[\frac{I_{1,1}^0(\tau)}{I_{1,0}^0(\tau)} \right]^2 \bigg|_{\tau_-}^{\tau_+} \quad (4)$$

where different forms of $F(s)$ are available. For example, for terrestrial clouds

$$F(s) = 3 \left[1 - \frac{(0.568 - 0.146s)s^2}{6.464 - 5.464s} \right]^2 .$$

Another possibility is to use only measurements in the zenith and nadir directions in the equation (McCormick, 1985)

$$s^2 K(s) = \frac{1}{3} \frac{[I_1^0(\tau, -1) - I_1^0(\tau, 1)]^2}{[I_1^0(\tau, -1) + I_1^0(\tau, 1)]^2} \bigg|_{\tau_-}^{\tau_+} \quad (5)$$

where for terrestrial clouds,

$$K(s) = 1.010(1 - 0.281s)^2 / (1 - 0.238s + 0.490s^2)^2 .$$

We now briefly discuss some of the extensions of Eq. (3) that have been developed. The incorporation of a time-dependent incident illumination can be accommodated by Laplace transforming the time dependent intensity $I(\tau, \mu, \xi, t)$ with

$$I(\tau, \mu, \xi, s) = \int_0^\infty e^{-st} I(\tau, \mu, \xi, t) dt .$$

The set of equations (3) then is of the same form, and now an additional degree of independence is achieved because each different value of s gives another set of inverse equations that, at least in principle, might be used to help infer the unknown coefficients ω and f_n , $n = 1$ to N , and also the unknown speed of light in the medium (Sanchez and McCormick, 1982). This additional flexibility was not shown in test calculations to be particularly helpful, however (ibid).

Another generalization involves a non-uniform external illumination (i.e., the 'search light problem'). Sievert and Dunn (1982) have shown that a Fourier transform of the intensities on the

boundaries leads to an equation similar to Eq. (3) which has real and imaginary parts. Such an inverse method would be difficult to use in practice, however, because angular intensity measurements would be required for every point on the plane boundaries.

For a homogeneous three-dimensional target that does not have a slab shape, Larsen (1984) has derived a very general vector inverse equation that, at least in principle, could be used to determine some information about ω and f_n by varying the boundary conditions. Practical applications of the method are probably limited, however, since a very large number of measurements would have to be performed over the surface.

Because of the complications arising from a non-uniform illumination or a non-slab geometry medium, it is worth mentioning that Eq. (3) should be valid in many cases even if the illumination over the surface is not perfectly uniform or the boundaries are not perfectly plane. What is required is that the external illumination be uniform over a distance of perhaps 25 times the inverse of the extinction coefficient, and that the radius of curvature point-wise over the surface be perhaps 25 times the inverse of the extinction coefficient.

As a final extension of Eq. (3), we note that the generalization to incorporate the effects of polarization has been developed (McCormick and Sanchez, 1983). For this case, the transport equation is replaced by a matrix equation in terms of the intensity vector $\underline{I} = (I, Q, U, V)$ consisting of the four Stokes parameters. The single-scattering phase function, in turn, is replaced by the Mueller scattering matrix. Then in the general case there are a total of $(6N-2)$ unknowns for N 'th degree anisotropic scattering, provided $N \geq 2$, instead of the $(N+1)$ unknowns in the unpolarized case. Determination of ω and the $(6N-3)$ unknown expansion coefficients of the Mueller matrix requires measurement of $\underline{I}(\tau, \mu, \xi)$ at $\tau = \tau_+$ and τ_- for all values of μ and ξ . To date there has been no effort to test the equations with simulated or experimental data.

III. NUMERICAL TESTS

An inherent disadvantage of the methods is that the coefficients most useful for identification of an obscurant or natural fog are ω , f_1 and perhaps a few more of the lower-index f_n coefficients, and yet the equations are coupled so that one must first start with the equation with $m = N^*$, where N^* is the assumed degree of anisotropic scattering, and work through the remaining equations for $m < N^*$ to get to those that contain the key unknowns. Hence, errors can be propagated and enhanced from the higher-index coefficients to the lower-index coefficients.

Early numerical tests (Sanchez and McCormick, 1982) of Eq. (3) and its counterpart method with I replaced by μI , etc., showed that as N^* was increased to N the two upper triangular systems of equations

would reproduce the coefficients to any desired accuracy provided the intensity measurements had no random statistical fluctuations and that values of I were known at a sufficiently large enough number of directions (typically at least N polar directions and N azimuthal directions, or more). The real tests of the methods begin when one tries to reduce the number of measurement directions needed for a numerical quadrature approximation to the integrals in Eqs. (1) and (2).

The solution methods were tested with an angular redistribution function that is a combination of two binomial distributions,

$$w(\hat{q}' \cdot \hat{q}) = 0.949(17)2^{-16}(1 + \hat{q}' \cdot \hat{q})^{16} + 0.001(5)2^{-4}(1 - \hat{q}' \cdot \hat{q})^4. \quad (6)$$

This function has an albedo of single scattering of 0.95 and is a smooth angular distribution whose forward peak is a factor of 4×10^4 larger than its minimum, and a backward ('glory') peak a factor of 10 larger than its minimum; as such, it might model an idealized distribution of different size particles. The test for convergence of w and wf_n , $n = 1, 5$, and 10, as N^* was increased to N is shown in Figure 1 for the case of $p = 18$ and 117 nodes in the quadrature set.

In a second test, random errors were introduced into the values of the intensities at the nodes by means of a Monte Carlo sampling from a cosine-squared distribution. A series of calculations were done with Eq. (3) and the averaged results are shown in Figure 2, as normalized to the fractional error in the intensities.

IV. GENERAL COMMENTS

As the assumed degree of scattering anisotropy N^* tends to the actual value N , convergence of the w and f_n -coefficients to their exact values will occur if the number of data points p is large enough and there are small enough random errors. Figure 1 for noise-free intensities shows, however, that $p = 18$ is insufficiently high to accurately reproduce the value of wf_1 for the scattering function of Eq. (6), and yet 18 measurement directions is not such a small number.

Difficulty with the accuracy of the coefficients increases dramatically as the random error becomes sizeable. Figure 2 shows that with random errors the standard deviations in the coefficients increase logarithmically with increasing N^* , so that unless the random fractional errors are significantly lower than 0.1%, the resulting coefficients can be severely in error.

The results reported here confirm that the inverse multiple scattering problem is ill-conditioned, as is characteristic of inverse problems, but several improvements in the inverse methods are underway and will be reported in the future as they are completed.

ACKNOWLEDGMENTS

I am indebted to John C. Oelund for performing the numerical tests in Section III. This work was supported by National Science Foundation Grant CPE-8209908 and by the U.S. Army Research Office.

REFERENCES

- C.-M. Chu and S.W. Churchill, *J. Opt. Soc. Am.* 41, 958 (1955).
- J.W. Moenier and C.V.M. van der Meer, *Astros. Astrophys.* 122, 1 (1983).
- I. Kufner and M. Ribarič, *Optica Acta* 6, 42 (1959).
- E.W. Larsen, *J. Math. Phys.* 25, 131 (1984).
- M.J. McCormick, *J. Opt. Soc. Am.* 72, 756 (1982).
- M.J. McCormick, *Appl. Optics* 22, 2556 (1983).
- M.J. McCormick, *J. Quant. Spectrosc. Rad. Transfer* (to be published, 1985).
- M.J. McCormick and R. Sanchez, *J. Quant Spectrosc. Rad. Transfer* 20, 527 (1983).
- V.A. de Rooij and C.C.A.M. van der Stap, *Astros. Astrophys.* 121, 237 (1984).
- R. Sanchez and M.J. McCormick, *J. Quant. Spectrosc. Rad. Transfer* 22, 169 (1983).
- C.E. Siewert and W.L. Dunn, *J. Math Phys.* 21, 1376 (1982).

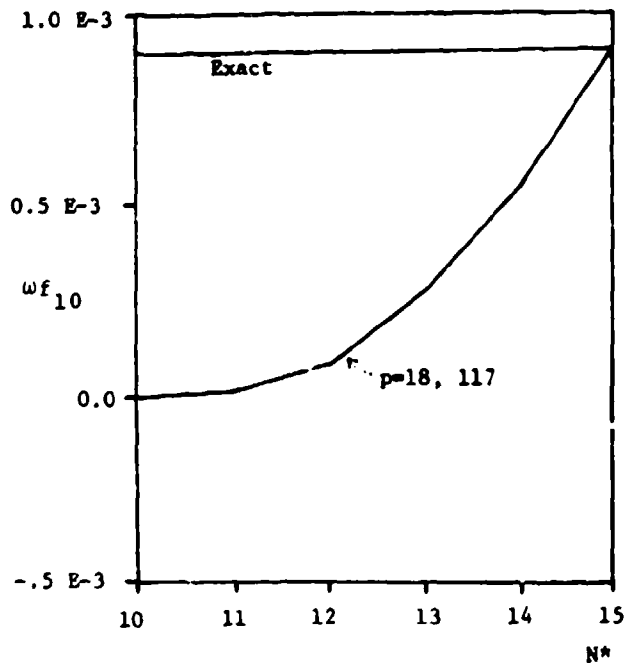
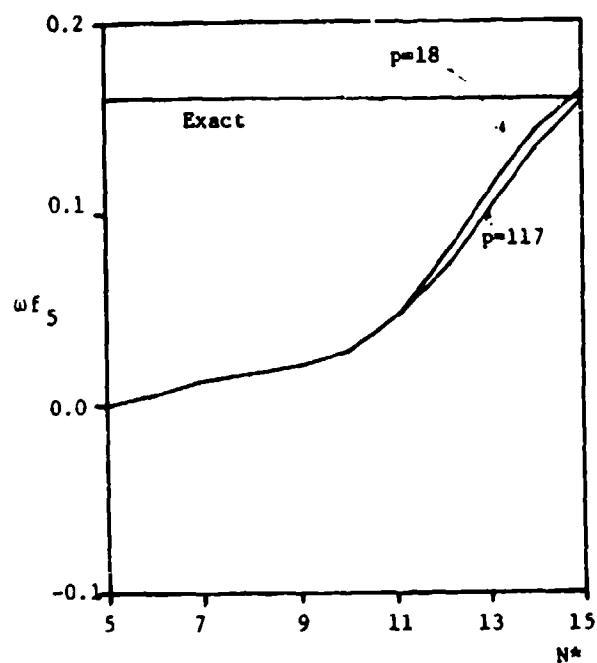
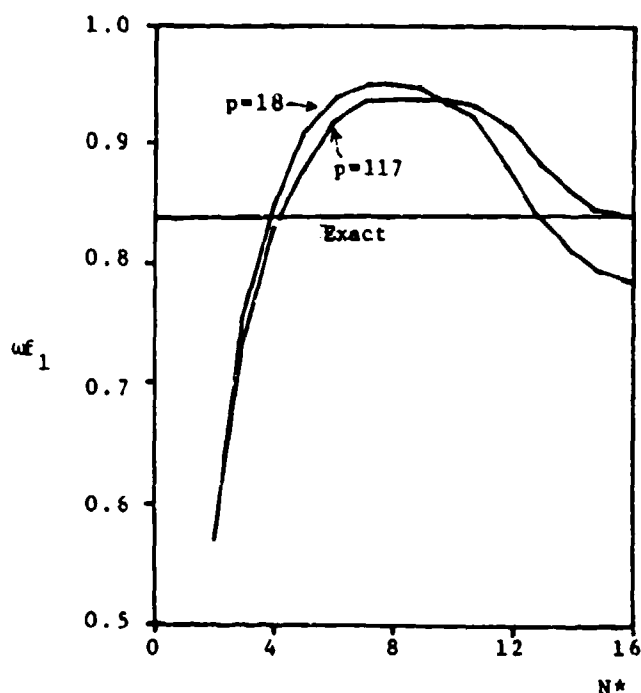
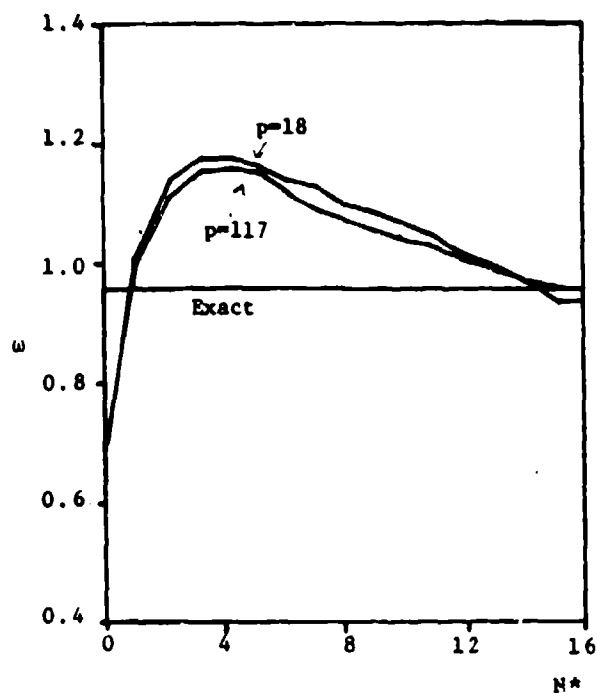


FIGURE 1. COEFFICIENTS ω , ωf_1 , ωf_{10} , AND ωf_{15} FOR THE SCATTERING LAW OF EQ. (6) CALCULATED FROM THE INVERSE METHOD OF EQ. (3). Calculations were done with a quadrature approximation to the combined integrals of Eqs. (1) and (2) consisting of a total of either 18 or 117 nodes using noise-free intensities from a monodirectional beam incident at a direction of $\mu = 0.0$ on a slab optical thickness of 5.

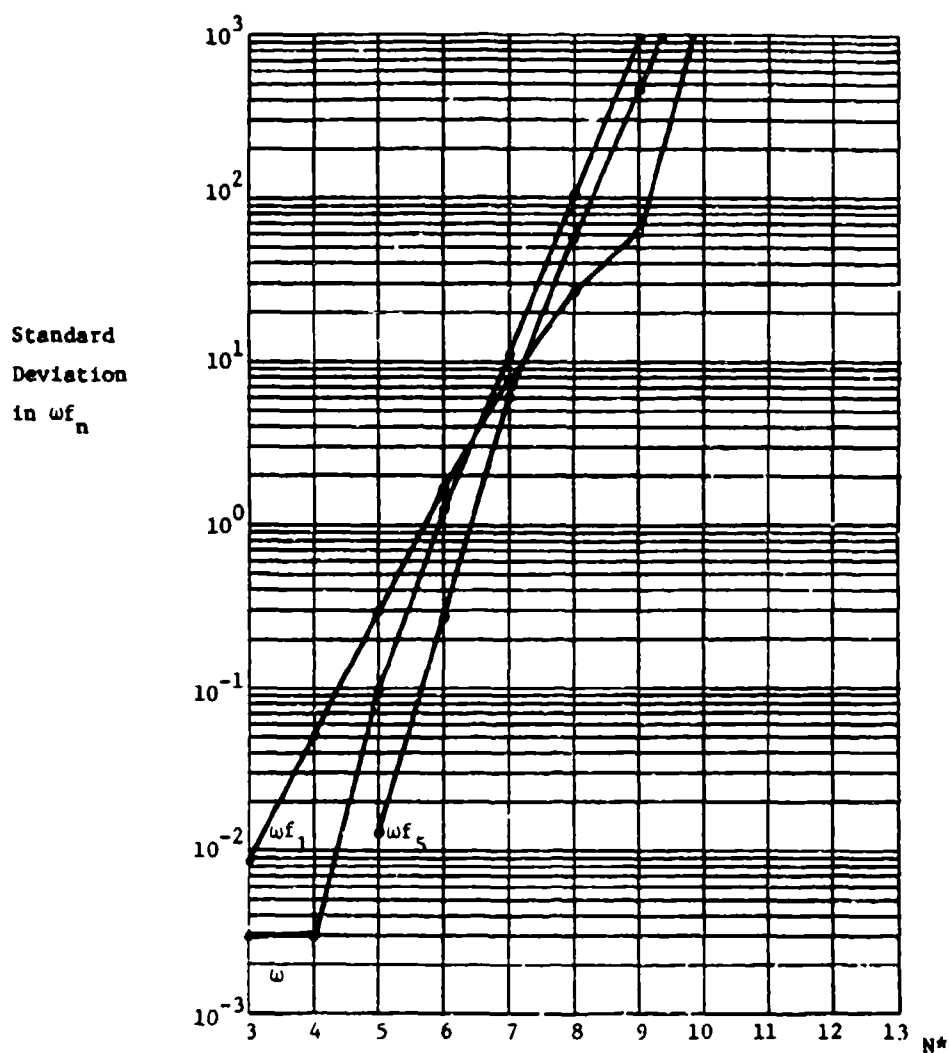


FIGURE 2. STANDARD DEVIATION IN THE COEFFICIENTS ω , ωf_1 , AND ωf_3 VERSUS N^* FOR A RANDOM fractional error of 0.1% in the intensities. The calculations were done using the inverse method of Eq. (3) with an 18-node quadrature approximation to the combined integrals of Eqs. (1) and (2) for an incident direction of $\mu = 0.8$ on a slab optical thickness of 5.

ASSESSMENT OF AEROSOL EXTINCTION TO BACKSCATTER
RATIO MEASUREMENTS MADE AT 694.3nm IN
TUCSON, ARIZONA

J. A. Reagan, M. V. Apte, A. Ben-David and B. M. Herman
The University of Arizona
Tucson, Arizona 85721

ABSTRACT

The aerosol extinction-to-backscatter ratio, S_a , is a key parameter in interpreting scattering measurements made with lidar. While solution techniques for solving the lidar equation generally assume some constraining relation for S_a (i.e., such as S_a is constant with range), few measurements of S_a have been made to establish the statistics and properties of this parameter. Measurements of S_a , for a wavelength 694.3nm, obtained from slant-path lidar observations made in Tucson, AZ from May, 1979 to May, 1982 yielded values of S_a between about 5 to 100 with the majority concentrated between about 10 to 45. The weighted mean (weighted by inverse variances of S_a) of all S_a values and the arithmetic mean of the main grouping of S_a values ($10 < S_a < 45$) both equaled approximately 25. Interpretation of the S_a measurements in terms of various size distributions and refractive index values representative of atmospheric aerosols indicated the following: 1) S_a values in the 10 to 20 range are indicative of coarse mode dominated size distributions, larger real refractive index values (greater than ~ 1.50), and zero or nearly zero imaginary refractive index values, 2) S_a values in the 20 to 35 range appear to correspond to size distributions with less dominant but still significant coarse mode particle concentrations, somewhat lower real refractive index values, and still fairly low imaginary refractive index values (less than ~ 0.005), and 3) S_a values greater than about 40 indicate even lower real refractive index values (values of 1.45 and lower) and/or even larger refractive index values (values in the 0.005 to 0.01 range).

I. INTRODUCTION

The aerosol extinction-to-backscatter ratio, S_a , is a key parameter in interpreting scattering measurements made with basic, incoherent mode lidar systems. Solution techniques for solving the lidar equation to extract profiles of aerosol backscatter and/or extinction from such lidar measurements generally assume some constraint for S_a . The most common assumption is that S_a is constant over a specified range interval.

Few measurements of S_a have been made to establish the statistics of this parameter for various atmospheric conditions, locales, etc. The purpose of this paper is twofold. Firstly, to present the results of S_a measurements, for a wavelength of 694.3nm, obtained from about 75 days of lidar slant-path observations made in Tucson, AZ between May, 1979 and May, 1982. Secondly, to assess the S_a measurements in terms of representative aerosol size distributions and refractive index values which appear to characterize certain ranges of S_a values.

II. EXPERIMENTAL RESULTS

Measurements of S_a were made with the University of Arizona monostatic ruby lidar system (e.g., Reagan et al., 1977; Spinhirne et al., 1980) located at the outskirts of Tucson. To acquire the necessary data set to extract an estimate of S_a , the lidar was fired along a fixed azimuth at several slant or elevation angles ranging from vertically pointing down to an elevation angle about 15° above the horizon. A complete slant-path run consisted of measurements made at 9 different slant angles. About 10 laser shots were taken at each slant angle to average out the noise in individual lidar returns, and a total of 20 to 30 minutes was typically required to complete a slant-path run. To further reduce noise problems, lidar operation was generally restricted to nighttime (typically just after sunset) because the skylight background added too much noise to lidar returns obtained during daylight hours.

Reduction of the lidar measurements to extract S_a values was accomplished using the slant-path lidar reduction technique previously described by Spinhirne et al. (1980). In this approach, slant-path lidar measurements are processed by a multi-angle integral solution of the lidar equation to extract S_a and vertical profiles of aerosol extinction and backscatter. The solution technique employs the constraint that S_a is assumed constant with height through layers of aerosol optical thickness (i.e., integrated extinction) of about 0.05 or greater. This typically corresponds to the entire atmospheric mixing layer (height of a few kilometers) for the relatively clear conditions that generally prevail in Tucson. Horizontal homogeneity is also required, but horizontal variations in aerosol backscatter of 10%-20% at a given height can readily be tolerated without greatly effecting the retrieval. These requirements should be reasonably well met in regions of the atmosphere that are fairly well mixed and removed from strong localized aerosol sources. The solution procedure produces standard deviation estimates for S_a as well as the aerosol extinction and backscatter profiles. These error estimates provide an indication of how well the constraints of the solution procedure are actually met.

Attempts were made to collect lidar slant-path data on approximately 125 days during the period May, 1979 through May, 1982. Of these attempts, complete sets of slant-path data were acquired for about 105 days. Data for 74 days proved eventually to be successful in that they were reducible by the slant-path lidar technique.

Values of S_a obtained from these 74 days of slant-path lidar observations made between May, 1979 and May, 1982 are plotted in Fig. 1 over a 12 month *generic* year interval. The S_a values for the 20 days of preliminary lidar observations reported by Spinhirne et al. (1980) are included in the figure for comparison. A histogram of the S_a values with class intervals of 5 is also given in Fig. 2, and various averages of S_a are given in Table 1.

Table 1. Statistical Properties of S_a Values

Arithmetic mean and standard deviation		
a) For all 74 cases		31.1 ± 18.6
b) For $10 < S_a < 45$ (53 cases)		25.2 ± 7.7
c) For $S_a > 45$ (15 cases)		61.6 ± 13.6
Weighted mean (inverse variance weighting)		25.4

From the figures, it can be seen that the S_a values range between about 5 to 100 with the majority of values concentrated between about 10 to 45. A secondary grouping of values is apparent between about 45 to 65, and there is a significant occurrence of values less than about 20. The weighted mean (weighted by inverse variances of S_a) of all S_a values and the arithmetic mean of the main grouping of S_a values ($10 < S_a < 45$) both are approximately equal to 25. This is slightly higher but not significantly different than the weighted mean of about 20 obtained by Spinhirne et al. (1980). Thus, $S_a = 25$ appears to be a representative value for the majority of observations.

III. ASSESSMENT OF S_a MEASUREMENTS

The aerosol extinction-to-backscatter ratio, S_a , depends on the shape or form of the aerosol size distribution and on the aerosol particle refractive index (i.e., on particle composition). Particle shape also has some influence, apparently causing S_a to increase as particles become more nonspherical

X SPINIRNE □ 79 - 82

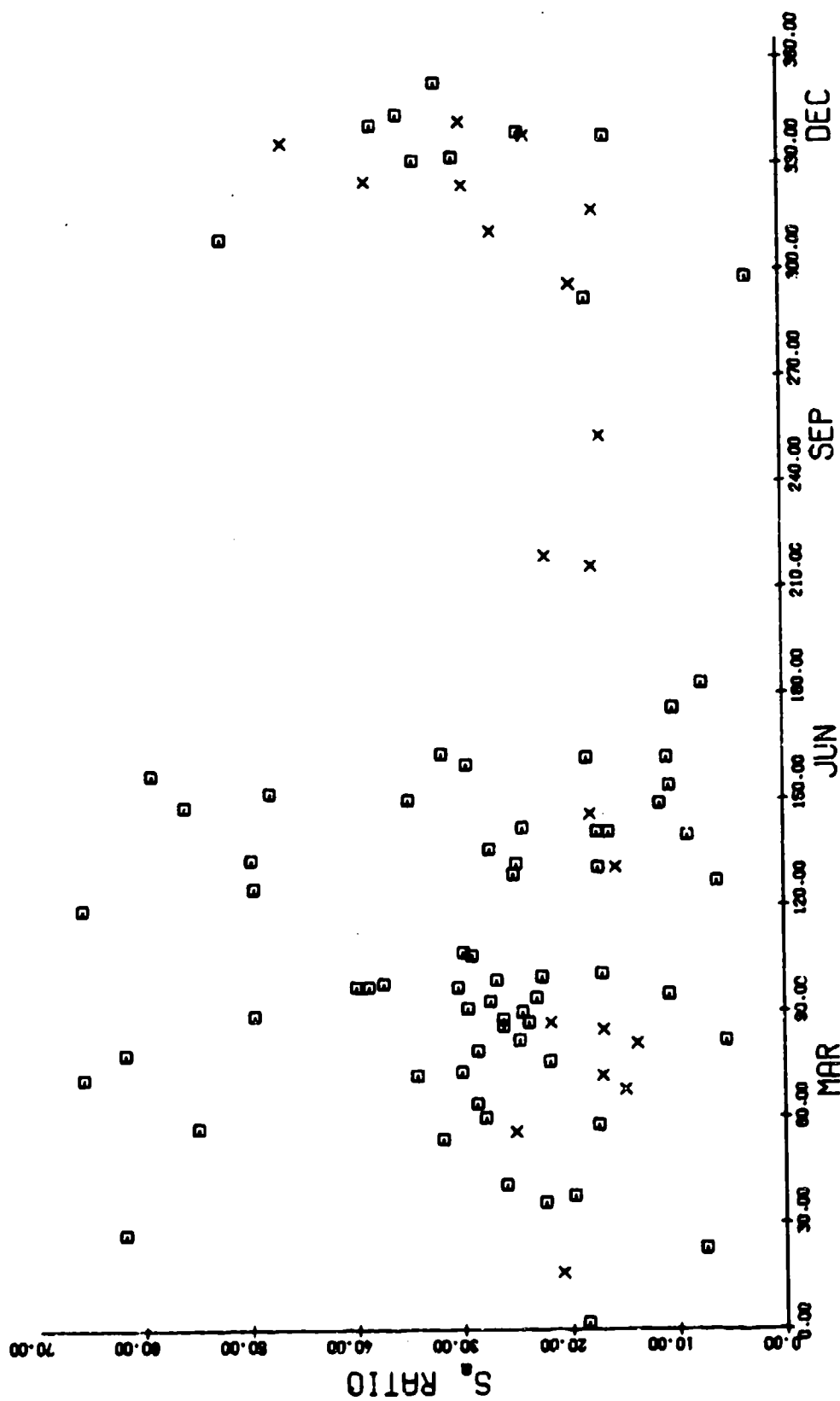


Figure 1. Lidar derived S_a values presented on a generic year basis.

S_a RATIO HISTOGRAM

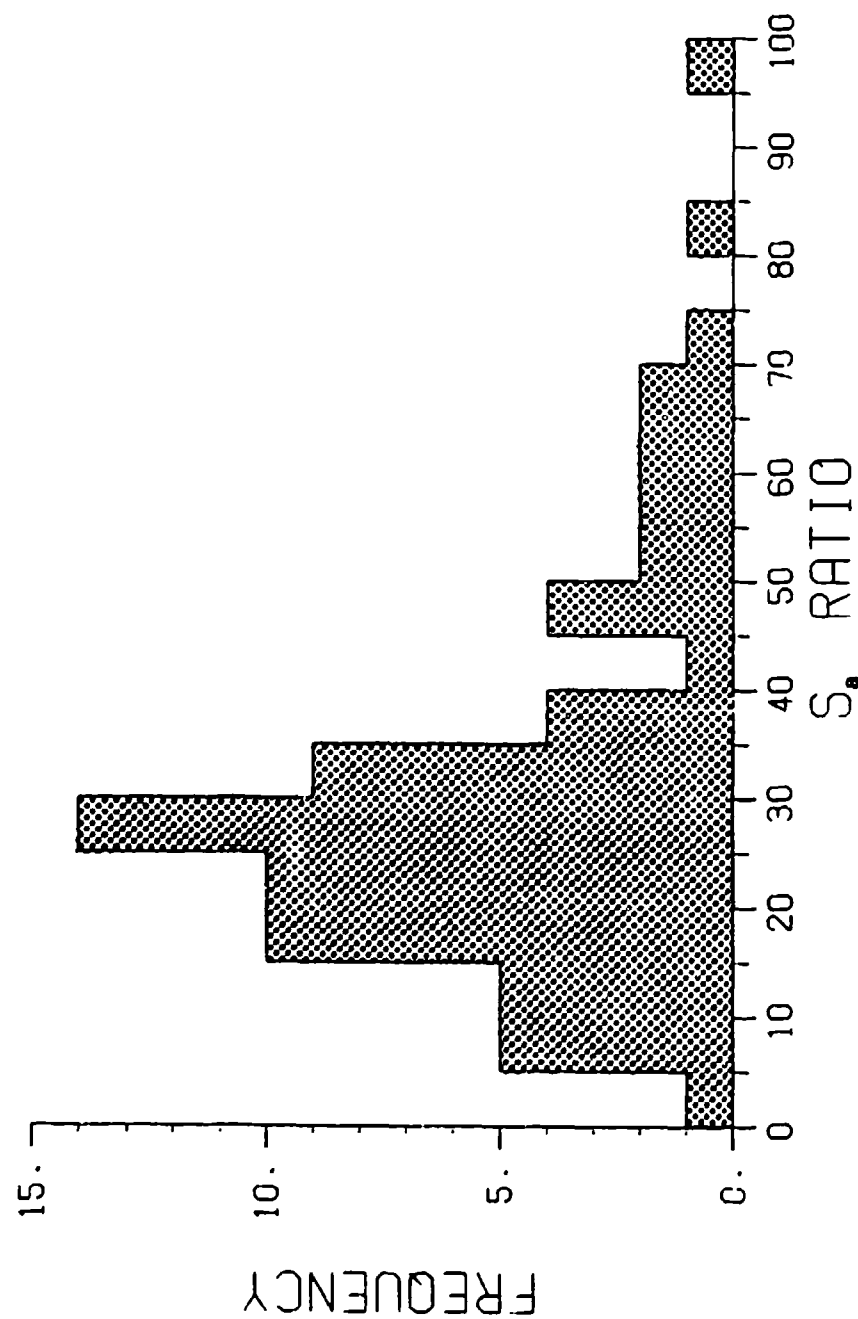


Figure 2. Histogram of the 74 S_a values derived from Tucson lidar measurements between May, 1979 to May, 1982.

(Reagan and Herman, 1980). However, within the limitations of spherical particle or Mie scattering theory, only the effects of size distribution form and particle refractive index can be readily assessed. Additional problems still arise even with the spherical particle restriction because particle composition may be inhomogeneous both within a single particle and as a function of particle radius. Scattering computations for polydispersions of spherical, inhomogeneous particles can produce significantly different values for various optical parameters depending on how the different constituents of which the particles are comprised are assumed to be mixed or averaged (e.g., Gillespie et al., 1978; Ackerman and Toon, 1981; Sloan, 1983). The approach taken here in assessing the S_a observations will be to assume that the individual particles are spherical and homogeneous. Most of the calculations will assume a single, average refractive index over all particle sizes, but some results will also be presented for mixtures of different, homogeneous particles within certain size ranges.

As S_a depends on both the particle size distribution and refractive index, it is clearly impossible to uniquely infer these two particle properties from a given value of S_a . However, by assuming a size distribution that is representative of the aerosols in question, it is possible to infer something about the particle refractive index range that best characterizes a given S_a value.

The size distributions selected as being representative of the various particle distributions that may actually have occurred during the lidar observations are given in Fig. 3 in both volume and number density distribution forms. They have been scaled to make them all similar in magnitude. Only the distribution shape, not the absolute magnitude, is important in computing S_a because S_a is a ratio quantity. The distributions for 13 August and 20 November of 1975 were obtained by inverting spectral optical depth data from solar radiometer measurements made in Tucson as reported by King et al. (1978). They are similar in shape to distributions frequently obtained from inversions of Tucson spectral optical depth data. The distribution for 15 May, 1977 is a composite distribution obtained from airborne Whitby electrical particle analyzer measurements and the inversion of solar aureole and spectral optical depth data acquired from groundbased measurements (Reagan et al., 1978). This distribution has the approximate straight-line form of a Junge distribution with slope or shape factor ν of $\nu \approx 2$. A Junge distribution of slope $\nu = 3$ is also included because Junge type distributions with slopes bounded between $\sim 2 < \nu < 3$ are also frequently obtained from inversions of Tucson spectral optical depth data (King et al., 1978). The final distribution included in Fig. 3, referred to as the mean balloon impactor distribution, is the average of several balloon-borne cascade impactor measurements made in Tucson during April, 1980 as previously reported by Reagan et al. (1984). With the exception of the $\nu = 3$ Junge distribution, the distributions all have significant large or coarse particle mode contributions. A pronounced peaking in the fine particle or accumulation mode is also apparent for the 13 August and 20 November distributions and to a lesser extent for the mean balloon impactor distribution. It should also be noted that the distributions are all height averaged in some sense (i.e., either columnar determinations or the average of measurements at several heights) and are thus representative of a height interval similar to that for which the S_a values were determined, namely, the first few kilometers of the troposphere.

Theoretical Mie scattering computations were made to determine S_a for each of the distributions given in Fig. 3. The calculations were made for a wavelength of 694.3nm and particle refractive index, m , values with real components, m_r , of 1.40, 1.45, 1.50 and 1.54 and imaginary components, m_i , of 0.000, 0.005 and 0.01. The results of these computations are shown in the plots of Fig. 4 where the computed S_a values are plotted versus the real refractive index component and each plot is for a different imaginary refractive index value. With regard to the S_a values obtained from the lidar observations, it is apparent that the low S_a values in the 10 to 20 range are characterized by 1) size distributions with dominant coarse mode particle concentrations, 2) larger real refractive index values of $m_r > \sim 1.5$, and 3) zero or nearly zero imaginary refractive index values of $m_i < \sim 0.005$. This is consistent with the

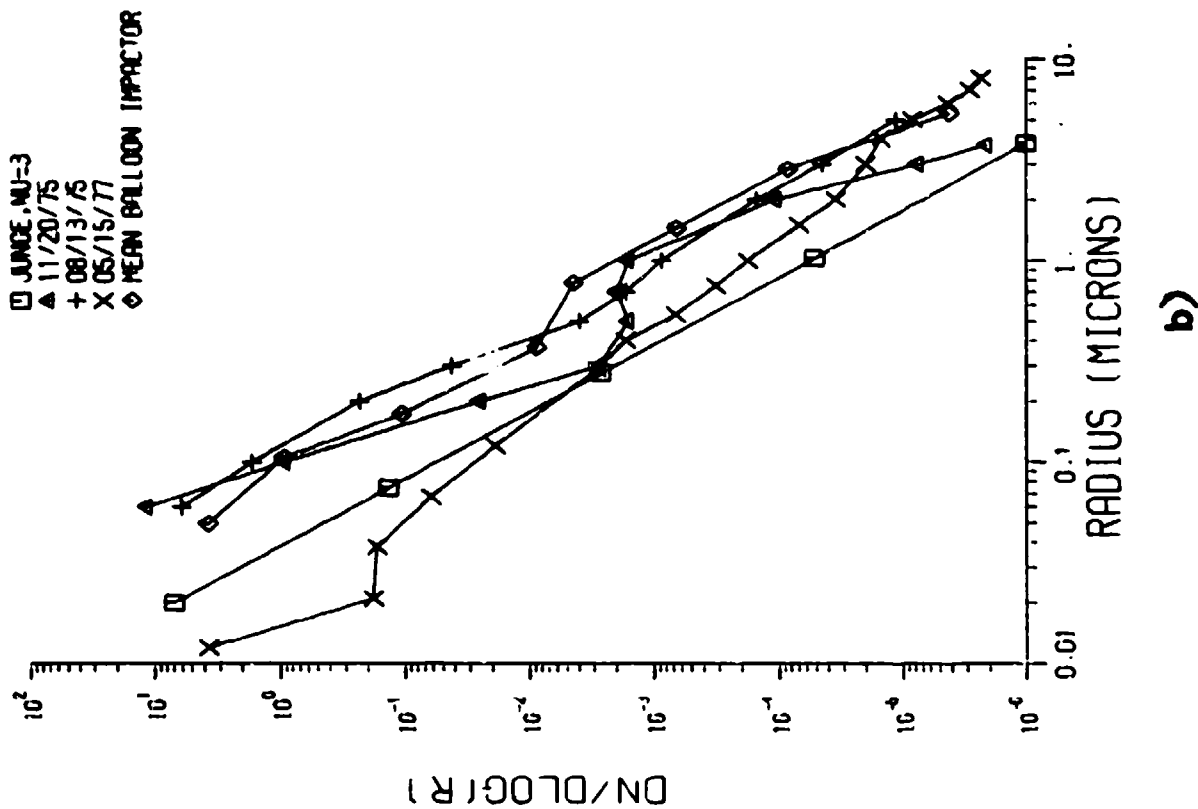
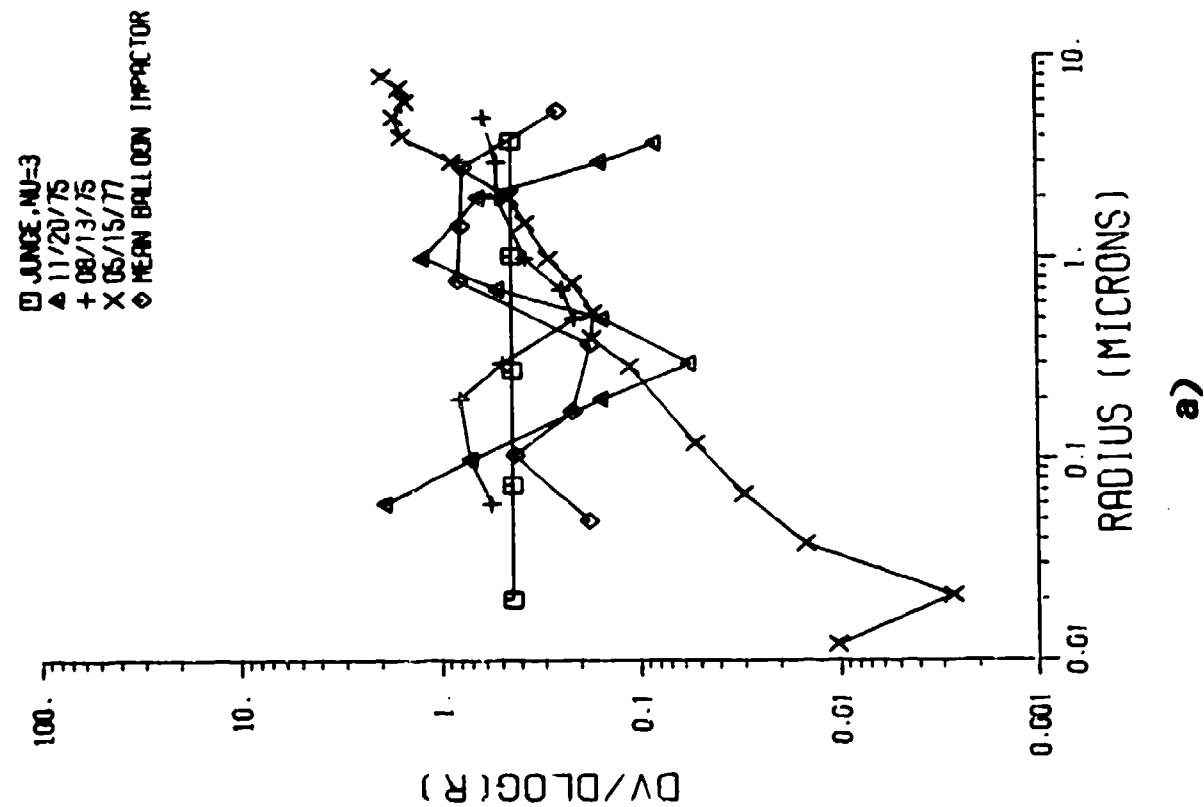
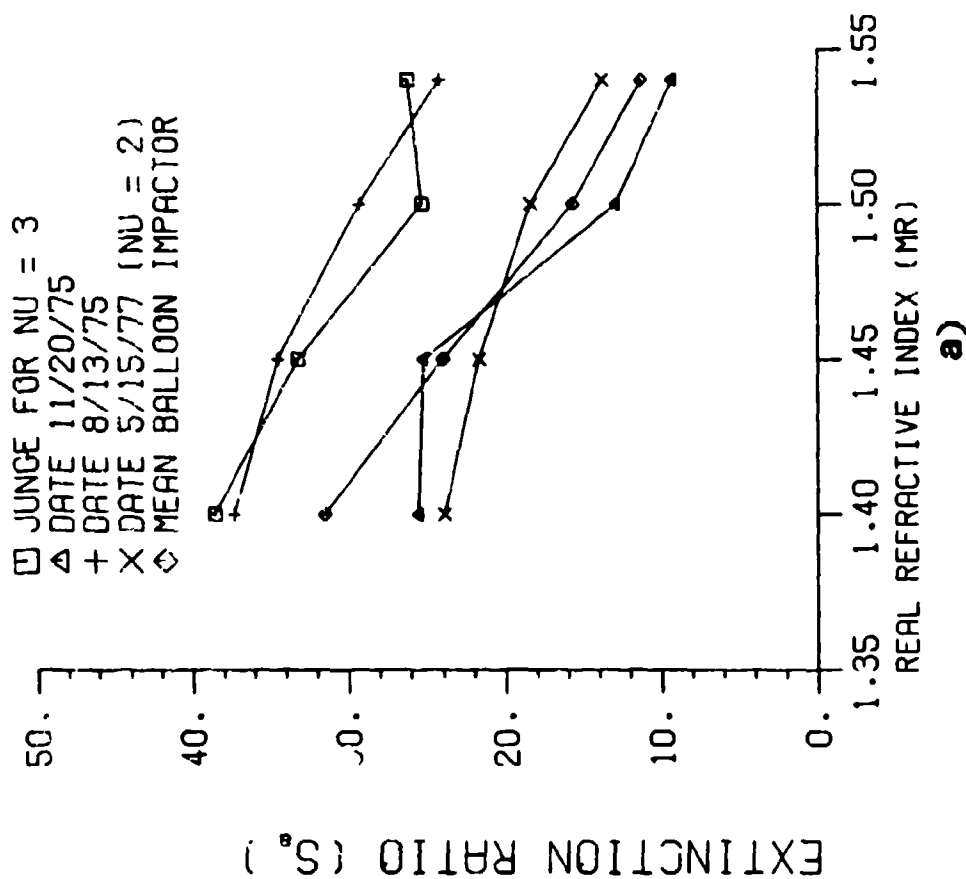


Figure 3. Aerosol size distributions representative of Tucson; a) volume size distribution (particle volume - cm^3/cm^3) and b) number density size distribution (particles/ cm^3).

S_a VERSUS MR, WITH $MI = 0.000$



S_a VERSUS MR, WITH $MI = 0.005$

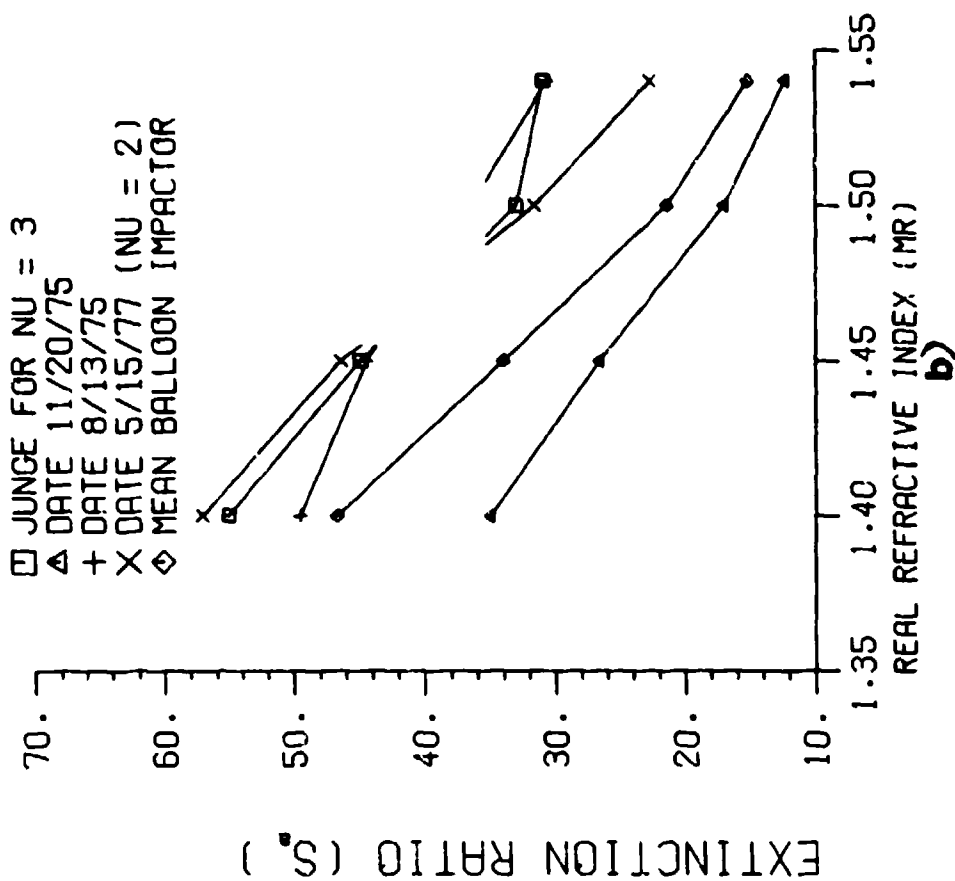
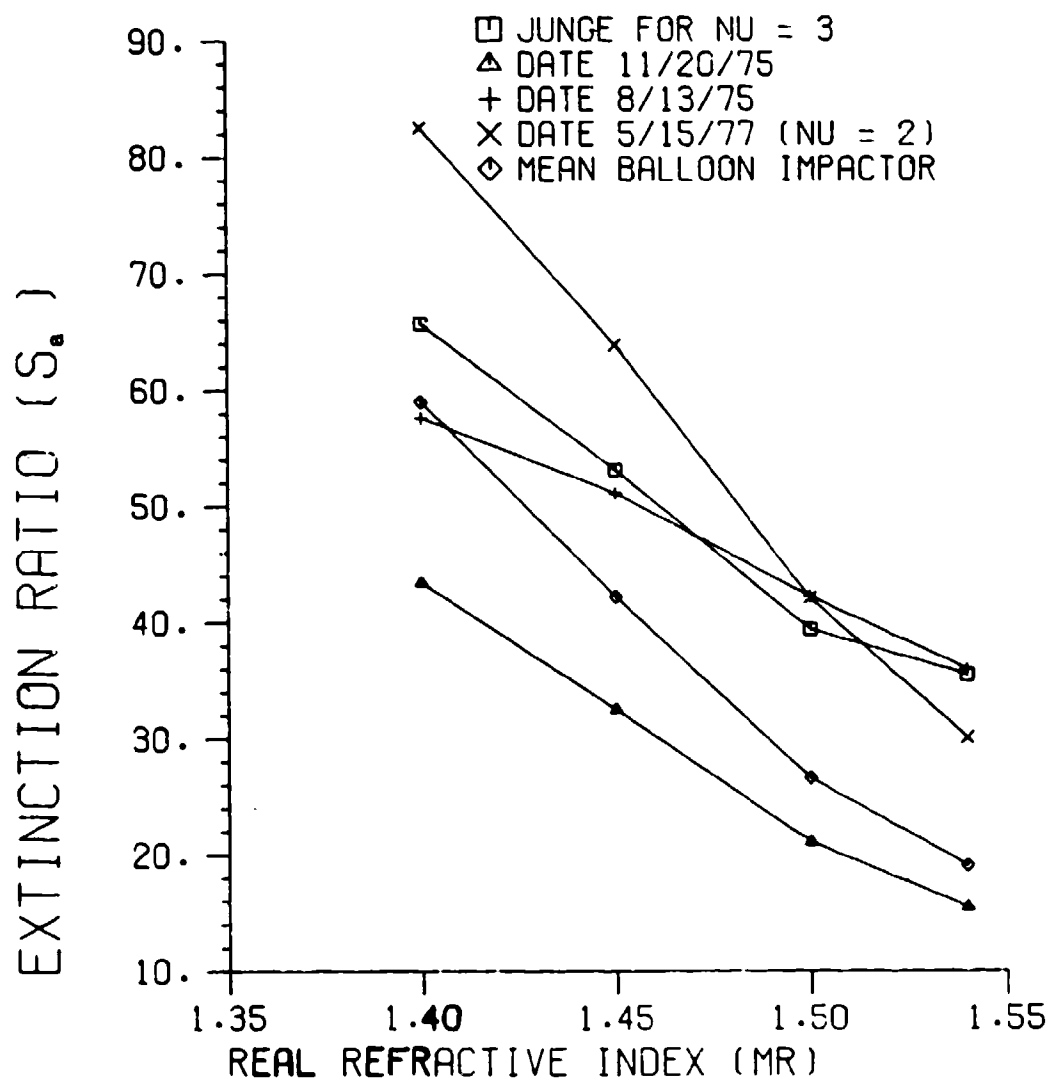


Figure 4. Computed S_a values versus real refractive index for different size distributions and imaginary refractive index values (for wavelength of 694.3nm); a) for $m_i = 0.000$, b) for $m_i = 0.005$, and c) for $m_i = 0.01$.

S_e VERSUS MR , WITH $MI = 0.010$



c)

Figure 4. Continued.

situation one might expect for windy and/or strong convectively mixed conditions in an arid region such as Tucson (i.e., enhanced coarse mode particle concentrations and refractive index values characteristic of soil particles).

Concerning the higher S_a values obtained from the lidar observations, say $S_a > 45$ with an arithmetic mean of ~ 62 , the plots of Fig. 3 indicate that this range of S_a values is principally characterized by 1) lower real refractive index values of $m_r < \sim 1.45$ and 2) larger imaginary refractive index values of $m_i > \sim 0.005$. The low real refractive index component is consistent with the index of acid-sulfate type particles. Analyses of particle samples collected near Tucson by both aircraft (Reagan et al., 1977) and the balloon-borne cascade impactor (Reagan et al., 1984) have revealed an abundance of sulfur for particles with radii as large as $\sim 1.0 \mu\text{m}$. Larger imaginary refractive index values in the 0.005 to 0.01 range do not correspond to any specific substance commonly associated with atmospheric aerosols, but such values may possibly result from small amounts of absorptive material such as carbon mixing with otherwise very weakly absorbing particles (e.g., Lindberg and Gillespie, 1977; Ackerman and Toon, 1981).

It is not possible to be quite as definitive concerning the majority of the lidar derived S_a values which span the range $\sim 15 < S_a < \sim 45$. The plots in Fig. 3 indicate many possible combinations that satisfy this span of S_a values, although the conditions that appear to offer the maximum likelihood for occurrence of S_a over this range are for $\sim 1.45 < m_r < \sim 1.5$ and $m_i = 0.005$. This is basically the refractive index range that remains after excluding the index regions that appear to best characterize the high and low values of S_a . This resulting range also includes the average refractive index value of $1.47 - 0.004i$ determined by Reagan et al. (1984) from the combined lidar and balloon-borne cascade impactor measurements made near Tucson in April 1980.

The S_a calculations presented thus far have assumed that all particles have the same refractive index. As the physical mechanisms which govern the production of particles in the accumulation mode and coarse particle mode are quite different, it is reasonable to consider the possibility of different compositions, hence different refractive index values, for the particles in the two modes. The mean balloon impactor distribution was employed to investigate the effect of mixed particle refractive index values. The radius break between the accumulation and coarse particle modes was taken as about $0.325 \mu\text{m}$ based on the shape of this distribution. Calculations of S_a were made for various combinations of refractive index values for the particles in the two modes. The results were somewhat surprising in that they demonstrated that altering the refractive index of the accumulation mode particles had little effect on the overall S_a value. This is shown in Table 2 which gives the ranges of variation in the computed S_a values due to varying the accumulation mode refractive index over a real value span of $1.4 \leq m_r \leq 1.54$ and an imaginary value span of $0.000 \leq m_i \leq 0.01$. The results show that it is the refractive index of the coarse mode particles that really controls the value of S_a . The reason for this is simply that the small particles don't contribute very much to extinction or backscatter, particularly backscatter which is the controlling factor in determining the change in S_a due to refractive index variations. This is shown in Fig. 5 where the cumulative fraction of backscatter for the mean balloon impactor distribution is plotted versus particle radius for two refractive index values. The curves show that the accumulation mode particles (i.e., particles of radius less than $\sim 0.3 \mu\text{m}$) contribute only a rather small amount to backscatter and, hence, to S_a . The results are not significantly different for the other refractive index values that have been considered here. Furthermore, similar calculations for the other size distributions given in Fig. 3 do not yield greatly different results. While distributions with relatively greater particle concentrations in the accumulation mode, such as the Junge distribution for $v = 3$, do have an increased backscatter contribution from small particles, the increase is not enough to greatly effect S_a , for the wavelength considered here (694.3 nm).

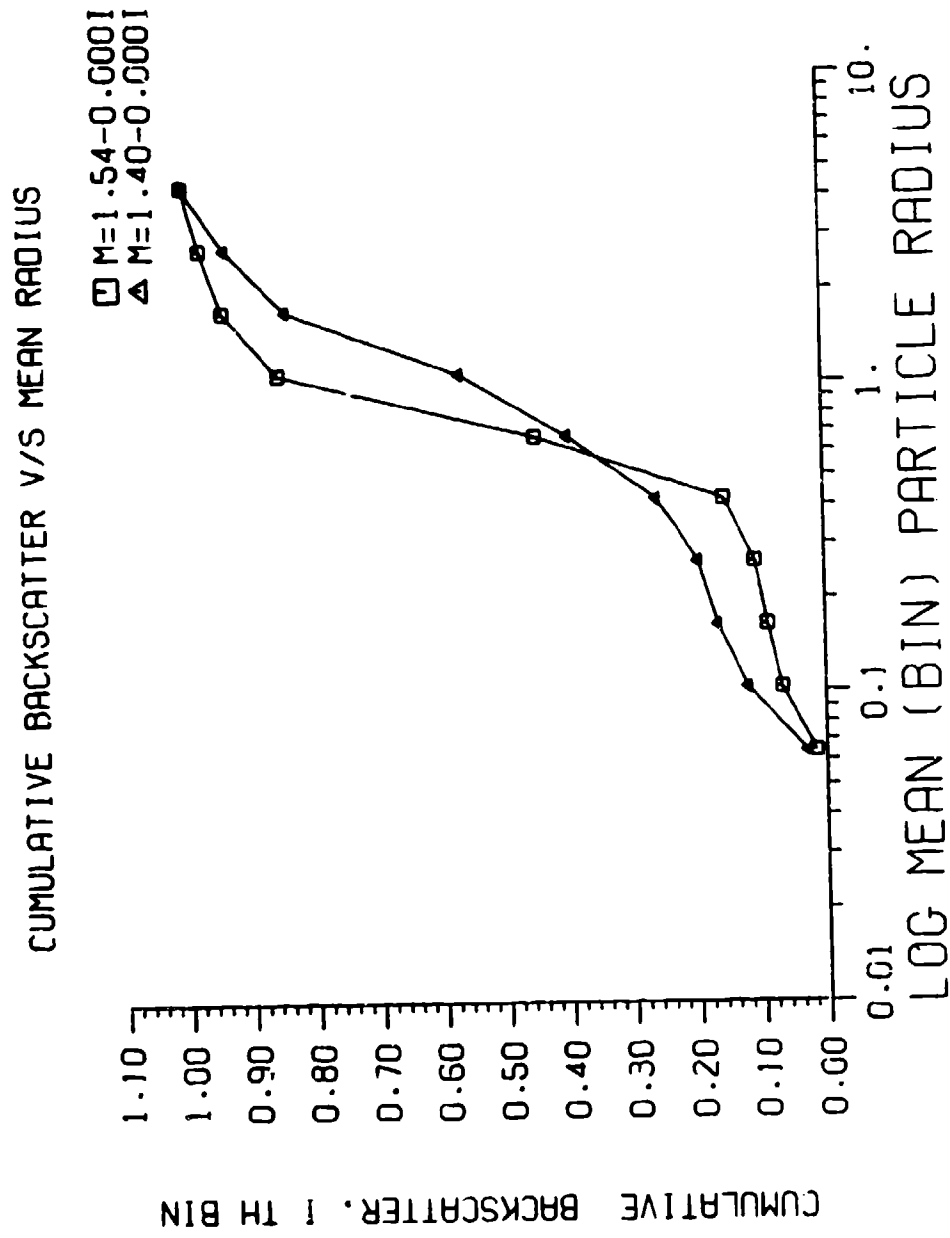


Figure 5. Cumulative fractional backscatter contribution versus particle radius for the mean balloon impactor distribution and the refractive index values as shown (for wavelength of 694.3 nm).

Table 2. Range of S_a Values for Mean Balloon Impactor Distribution and Various Refractive Index Values

Range of m for Accumulation Mode	m for Coarse Mode					
	1.54-0.000i	1.54-0.01i	1.50-0.000i	1.50-0.01i	1.40-0.000i	1.40-0.001i
m_r	10.2	17.4	14.9	25.3	31.5	52.4
1.40 ↔ 1.54	↑	↑	↑	↑	↑	↑
Δ						
m_i						
0.000 ↔ 0.01	↓	↓	↓	↓	↓	↓
	11.5	19.1	16.5	26.9	32.7	59.0

Accumulation mode - coarse mode break at $\sim 0.3\mu\text{m}$ particle radius; S values for wavelength at 694.3 nm.

One other mixed particle, mixed refractive index situation which was also investigated was that of including various percentage amounts of carbon particles, an external type mixture as defined by Ackerman and Toon (1981), in the accumulation mode. As noted earlier, small amounts of an absorptive material such as carbon mixed with otherwise very weakly absorbing particles may be the cause of average or effective imaginary refractive index values in the 0.001-0.01 range sometimes inferred for aerosol particles in that such values are not representative of any specific substance commonly associated with atmospheric aerosols. The carbon is assumed to be restricted to the accumulation mode because it is typically only detected in the very small particle range (Lindberg and Gillespie, 1977; Sloane, 1983). Table 3 lists S_a values computed for the mean balloon impactor distribution with different amounts carbon particles ($m = 1.8 - 0.5i$) in the accumulation mode and all remaining particles with refractive index

Table 3. S_a Values for Mean Balloon Impactor Distribution and Various Refractive Index Values

Percent Carbon Particles in Accumulation Mode	m for Coarse Mode and Remainder of Particles in Accumulation Mode	
	1.4 - 0.005i	1.5 - 0.001i
0%	46.7	15.7
10	49.5	17.1
20	52.1	18.4
40	56.8	21.0
60	60.6	23.5
80	64.0	25.9
100	66.8	28.2

Carbon particles assumed to have $m = 1.8 - 0.5i$. Accumulation mode-coarse mode break at $\sim 0.3\mu\text{m}$ particles radius; S_a values for a wavelength of 649.3 nm.

values of $m = 1.4 - 0.0005i$ or $1.5 - 0.000i$. The two values of m chosen for the non-carbon particles are index values which, when assumed for all the particles present, yielded relatively high and low values of S_a as given earlier in Fig. 3. The results given in Table 3 show that S_a is not greatly altered for relatively small amounts of carbon in the accumulation mode, say $\sim 20\%$ or less which is about as much as might be expected unless conditions were very polluted. Even changing the carbon amount from 0 to 100% causes less than a doubling of S_a , and this is still insufficient to change a low S_a value into a high S_a .

value. Thus, it does not appear that the addition of reasonable amounts of carbon to the accumulation mode has any significant effect on S_g for the particular size distribution considered here, nor is it likely to have much effect for the other size distributions given earlier in Fig. 3. This means that the S_g values are mainly controlled by the coarse mode particle refractive index for the wavelength (694.3nm) and size distributions considered in this paper.

ACKNOWLEDGEMENTS

The authors wish to thank Ian Scott-Fleming for his assistance in preparing some of the graphics included in this paper. The work reported here has been supported by ARO under grant DAAG-29-78-G-0195 and NSF Grant ATM-8012908.

REFERENCES

- Ackerman, T.P., and Toon, O.B. (1981). Absorption of visible radiation in atmosphere containing mixtures of absorbing and nonabsorbing particles, *Appl. Opt.* 20:3661-3667.
- Gillespie, J.B., Jennings, S.G., and Lindberg, J.D. (1978). Use of an average complex refractive index in atmospheric propagation calculations, *Appl. Opt.* 17:989-991.
- King, M.D., Byrne, D.M., Herman, B.M., and Reagan, J.A. (1978). Aerosol size distributions obtained by inversion of spectral optical depth measurements, *J. Atmos. Sci.* 35:2153-2167.
- Lindberg, J.D., and Gillespie, J.B. (1977). Relationship between particle size and imaginary refractive index in atmospheric dust, *Appl. Opt.* 16:2628-2630.
- Reagan, J.A., and Herman, B.M. (1980). Light scattering by irregularly shaped particles versus spheres: What are some of the problems presented in remote sensing of atmospheric aerosols?, in *Light Scattering by Irregularly Shaped Particles* (D. W. Schuerman, Ed.). Plenum Press, New York, p. 319.
- Reagan, J.A., Apte, M.V., and Bruhns, T.V. (1984). Lidar and balloon-borne cascade impactor measurements of aerosols: A case study, *Aerosol Technol.* 3:259-275.
- Reagan, J.A., Herman, B.M., Byrne, D.M., and King, M.D. (1978). Some Results of the UA-ARE Program. Third Conference on Atmospheric Radiation, Amer. Meteor. Soc., *Conf. Preprints*, pp. 241-243.
- Reagan, J.A., Spinhirne, J.D., Byrne, D.M., Thomson, D.W., de Pena, R.G., and Mamane, Y. (1977): Atmospheric particulate properties inferred from lidar and solar radiometer observations compared with simultaneous in situ aircraft measurements: A case study, *J. Appl. Meteor.* 16:911-928.
- Sloane, C.S. (1983). Optical properties of aerosols-comparisons of measurements with model calculations, *Atmos. Environ.* 17:409-416.
- Spinhirne, J.D., Reagan, J.A., and Herman, B.M. (1980). Vertical distribution of aerosol extinction cross section and inference of aerosol imaginary index in the troposphere by lidar technique, *J. Appl. Meteor.* 19:426-438.

INDEXES FOR PAPERS IN THESE PROCEEDINGS

Index		Page
A	Index of Authors	519
B	Index of Authors' Organizations	521

INDEX A

INDEX OF AUTHORS OF PAPERS IN THESE PROCEEDINGS

Alexander, Ralph W., Jr. 167, 179
Apte, M. V. 505
Armstrong, R. L. 259
Arnold, S. 241
Aronson, J. R. 455
Ase, P. 223

Bahar, Ezekiel 365
Barber, Peter W. 89
Beck, S. R. 119
Bell, M. I. 255
Bell, Robert J. 167, 179
Ben-David, A. 505
Benner, R. E. 113
Bond, John W. 431
Bottiger, J. R. 129
Brock, J. R. 23

Capps, C. D. 119, 431
Carroll, M. E. 119
Castleman, A. W., Jr. 13
Cermak, J. E. 49, 53
Cohen, A. 373, 441
Cohen, L. D. 373, 441
Coletti, A. 225
Colosi, J. 373
Conwell, P. R. 113
Crichton, J. H. 233

Davison, S. W. 69
Dye, D. L. 431

Embury, J. F. 491
Emslie, A. G. 455

Farzanah, F. F. 109
Fitzwater, Mary Ann 365

Gallily, Isaiah 57
Geller, Pamela E. 89
Gentry, J. W. 69, 109, 217
Gerstl, S. A. W. 491
Gulacsik, C. 431

Hanna, Steven 43
Haracz, R. D. 373, 441
Herman, B. M. 505
Hess, G. M. 119
Hill, S. C. 113
Holze, D. H. 431
Hong, J. 109
Hu, Chia-Ren 307
Huffman, Donald R. 291
Hwang, S. 69

Iskander, Magdy F. 297

Kaplan, C. R. 109
Kattawar, George W. 307
Keese, R. G. 13
Kerker, Milton 449
Kim, S. G. 23
Krushkal, E. M. 57

Langley, D. S. 239
Latham, J. 37
Lax, Melvin 273
Leong, K. H. 11, 85
Lettieri, T. R. 255
Long, Larry L. 167, 179

Majoch, T. R. 119
Marston, P. L. 233, 239
Martin, J. 73
Mazumder, M. K. 281
McCormick, N. J. 495
Moeller, K. D. 207, 373

Ordal, Mark A. 167, 179

Parkin, Mark E. 307
Paul, R. A. 179
Pearce, W. A. 141
Pedersen, J. C. 385, 477
Pedersen, M. E. 385, 477
Pleim, Jonathan 43
Pluchino, A. B. 241
Podzimek, J. 73
Poreh, M. 49, 53
Preston, R. E. 255

Reagan, J. A. 505
Rubel, Glenn O. 217
Rushforth, C. K. 113

Scheunemann, W. 101
Senior, T. B. A. 295
Simon, I. 455
Smith, E. M. 455
Snelson, A. 223
Stuebing E. W. (Presenter) 89

Tennal, K. 281
Tokuda, A. R. 119
Tomaselli, V. P. 207, 373
Tsang, T. H. 23

Varadan, V. K. 469
Varadan, V. V. 469

Wang, J. 69
Wang, R. T. 315, 327
Waterman, P. C. 385, 477
Weil, H. 295
Wilson, J. D. 281

Yu, P. Y. 109

Zardecki, A. 491

PREVIOUS PAGE
IS BLANK

BLANK

INDEX B

INDEX OF AUTHORS' ORGANIZATIONS AND COUNTRIES (IF NOT U.S.A.) FOR PAPERS IN THESE PROCEEDINGS

- Aberdeen Proving Ground (US Army) 129, 217, 491
- Aerospace Corporation
 - Chemistry and Physics Laboratory
 - Infrared Space Optics Section 241
- AMCCOM (US Army Munitions & Chemical Command)
 - Chemical Research and Development Center 129, 217, 491
- Arizona (see University of)
- Arkansas (see University of)
- Army, US 129, 217, 431, 491
- Arthur D. Little, Inc. 455
- Belvoir Research and Development Center 431
- BICT (West Germany) 101
- Boeing Aerospace Company 119, 431
- Britain 37
- Chemical Research and Development Center (CRDC) (US Army) 129, 217, 491
- City University of New York
 - City College
 - Physics Department 273
 - Graduate Center 273
- Clarkson University 89, 449
- Colorado State University 49, 53
- Drexel University
 - Department of Physics and Atmospheric Science 373, 441
- EG&G Washington Analytical Services Center, Inc. 141
- England 37
- Environmental Research and Technology, Inc. 43
- Fairleigh Dickinson University
 - Physics Research Laboratory 207, 373
- Georgia Institute of Technology
 - School of Geophysical Sciences 225
- Germany, West 101
- Graduate Center for Cloud Physics Research (University of Missouri-Rolla) 73
- Hebrew University of Jerusalem (Israel)
 - Department of Atmospheric Sciences 57
- Illinois Institute of Technology (IIT)
 - Research Institute 223
- Illinois (see University of)
- Israel 57
- Los Alamos National Laboratory 491
- Maryland (see University of)
- Missouri (see University of)
- Michigan (see University of)
- National Bureau of Standards 255
- Nebraska (see University of)
- New Mexico State University
 - Physics Department
 - Applied Optics Group 259
- Panametrics, Inc. 385, 477
- Pennsylvania State University
 - Department of Chemistry 13
 - Department of Engineering Science and Mechanics 469
- Polytechnic Institute of New York
 - Department of Physics 241
- Seattle Pacific University
 - School of Natural and Mathematical Sciences 233
- Space Astronomy Laboratory (University of Florida) 315, 327
- Texas A&M University
 - Department of Physics 307
- Texas (see University of)
- University of Arizona 505
 - Department of Physics 291
- University of Arkansas
 - Graduate Institute of Technology 281
- University of Florida
 - Space Astronomy Laboratory 315, 327
- University of Illinois at U-C 11, 85
- University of Manchester (England)
 - Institute of Science and Technology
 - Physics Department 37
- University of Maryland
 - Baltimore County
 - Engineering Department 69
 - College Park
 - Department of Chemical and Nuclear Engineering 69, 109, 217
- University of Michigan
 - Department of Electrical Engineering and Computer Science
 - Radiation Laboratory 295
- University of Missouri-
 - Kansas City
 - Department of Physics 145
 - Rolla
 - Department of Physics 167, 179
 - Graduate Center for Cloud Physics Research 73
- University of Nebraska
 - Lincoln
 - Department of Electrical Engineering 365
- University of Texas
 - at Austin
 - Department of Chemical Engineering 23
- University of Utah 89
 - Department of Electrical Engineering 113, 297
 - Department of Physics 113
- University of Washington
 - Department of Nuclear Engineering 495
- Washington State University
 - Department of Physics 233, 239
- West Germany, 101

BLANK

APPENDIXES

Appendix		Page
A	Photographs of Conference Attendees	525
B	List of Conference Attendees	531
C	Conference Agenda	545

BLANK

APPENDIX A

PHOTOGRAPHS OF CONFERENCE ATTENDEES
(Taken MidWeek)



LEFT HALF (left to right)

Third &

Fourth Rows:

Philip Marston, Hsu-Chi Yeh, Fred Gebhardt, Ru Wang, Bob Hofland (hidden), Blair Evans, Alan Evans,
Rolf Klucher, Alan Snelson, Ron Pinnick, Jim Hudson, John Cipolla, Robert Sutherland, David Dye,
Dennis Garvey, Glenn Rubel, James Newhouse

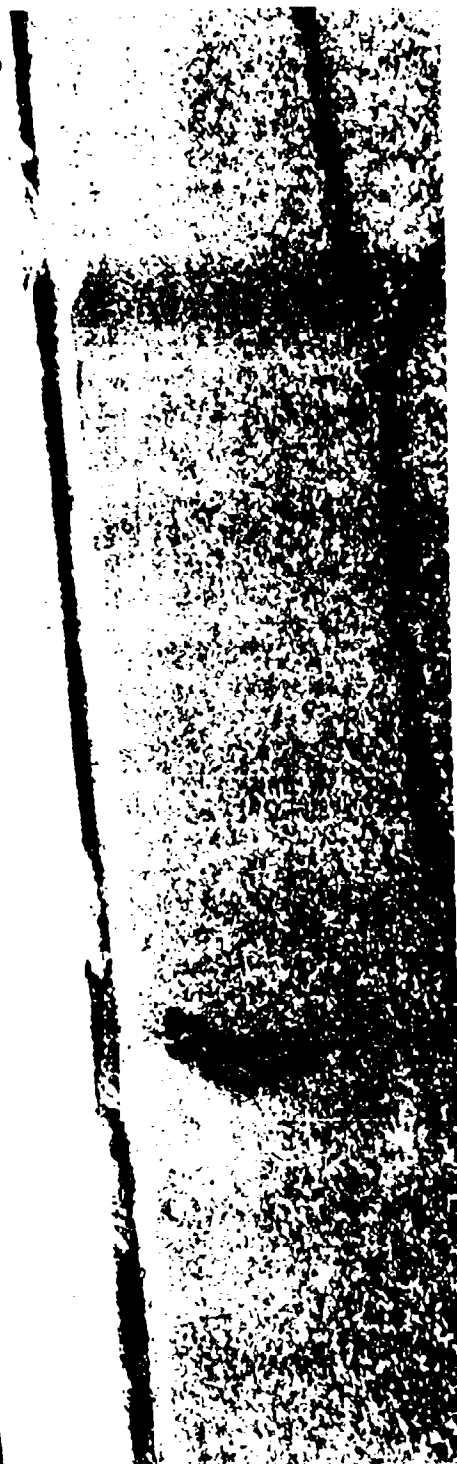
Second Row:

Merrill Milham, Frederick Smith, Ralph Alexander, Jr., George Ruck, Robert J. Bell, George Kattawar,
Chia-Ren Hu, James T. Hanley, Carolyn Kaplan

First Row:

Jerold Bottiger, William Bickel, Paul Ase, D. A. de Wolf, Robert E. Benner, Dennis Alexander

1984 CRDC SCIENTIFIC CONFERENCE ON OBSCURATION AND AEROSOL RESEARCH



RIGHT HALF (left to right)

Third &
Fourth Rows:

Bill Curry (hidden), Claude Phipps, Jr. (partly hidden), Norman McCormick, Tom Lettler (in doorway),
Don Huffman (partly hidden), Wilhelmina Jenkins, N. Erickson (partly hidden), Robert Frickel (partly hidden),
Ed Nielsen (partly hidden), David Capps, Bob Keese, Leon Radziemski (almost hidden), Richard Preston,
Richard Reitz, Shirish Chitanvis, James Brock (almost hidden), Herschel Weff, Peter W. Barber, Howard Smalley,

M. Lax, R. Armstrong, R. K. Chang, O. I. Sindoni, Fred Luther (Row 2), Phil Lawless (Row 2),
W. Scheunemann, B. Guillaume, K. F. Wall, , W. Michael Farmer, John Green

Second Row:

M. K. Mazumder, R. Kohl, R. A. Elliott, A. Zardecki, S. Arnold, A. Pluchino, A. Delfour, J. Podzimek
H. E. Wilhelm, P. Nolan, J. Embury, Ed Stuebing

First Row:

BLANK

APPENDIX B

ATTENDEES

1984 CRDC Scientific Conference On Obscuration and Aerosol Research

ADAMS, GREGG W. DR.
Chemical Research Development Center
DRSMC-CLB-CR(A)
Aberdeen Proving Ground, MD 21010
(301) 671-3753

ASE, PAUL K. MR.
IIT Research Institute
10 W. 35th Street
Chicago, IL 60616
(312) 567-4287

ALEXANDER, DENNIS R. DR.
Mechanical Engineering Laboratory
NEC 255
University of Nebraska-Lincoln
Lincoln, NE 68588
(402) 472-3091

BACH, WALTER
U.S. Army Research Office
P.O. Box 12211
Research Triangle Park, NC 27709
(919) 549-0641

ALEXANDER, RALPH W., JR. PROF.
Physics Department
University of Missouri-Rolla
Rolla, MO 65401
(314) 341-4781

BAHAR, EZEKIEL DR.
Department of Electrical Engineering
W194 Nebraska Hall
University of Nebraska-Lincoln
Lincoln, NE 68588
(402) 488-4074

ARMSTRONG, ROBERT L., DR.
Physics Department, Box 30
New Mexico State University
Las Cruces, NM 88003
(505) 646-4308

BAKER, RICHARD L. DR.
Aerospace Corporation
El Segundo, CA 90274
(213) 416-8916

ARNOLD, STEPHEN DR.
Department of Physics
Polytechnic Institute of New York
333 Jay Street
Brooklyn, NY 11201
(212) 643-4371

BALOG, PAUL P.
Battelle Columbus Labs
505 King Avenue
Columbus, OH 43201
(614) 424-4260

ARONSON, JAMES R. DR.
Arthur D. Little, Inc.
15 Acorn Park
Cambridge, MA 02140
(617) 864-5770, ext. 2369

BARBER, PETER W. DR.
Department of Electrical Engineering
Clarkson University
Potsdam, NY 13676
(315) 268-6511

BELL, ROBERT J. DR.
Physics Department
University of Missouri-Rolla
Rolla, MO 65401
(314) 341-4796

BENNER, ROBERT E. PROF.
Department of Electrical Engineering
3053 Merrill Engineering Building
University of Utah
Salt Lake City, UT 84112
(801) 581-6684

FICKEL, WILLIAM S. DR.
Department of Physics
University of Arizona
Tucson, AZ 85721
(602) 621-6820

BIRD, JOSEPH F.
Applied Physics Laboratory
Johns Hopkins University
Johns Hopkins Road
Laurel, MD 20707
(301) 953-7100, ext. 2582

BIRENZVIGE, AMNON
Chemical Research and Development Center
DRSMC-CLB-PO(A)
Aberdeen Proving Ground, MD 21010
(301) 671-4252

BOTTIGER, JEROLD
Chemical Research and Development Center
DRSMC-CLB-PS(A)
Aberdeen Proving Ground, MD 21010
(301) 671-2395

BROCK, JAMES R. DR.
Department of Chemical Engineering
University of Texas
Austin, TX 78712
(512) 471-3348

BUCKLEY, TOM DR.
Building 222 - Room A. 51
National Bureau of Standards
Gaithersburg, MD 20899
(301) 921-2783

CANNON, WILLIAM C.
Battelle, Pacific Northwest Laboratory
Box 999
Richland, WA 99352
(509) 376-1516

CAPPS, C. DAVID DR.
Boeing Aerospace Company
P.O. Box 3999, MS 8C-23
Seattle, WA 98124
(206) 773-1425

CERMAK, JACK E. DR.
Department of Civil Engineering
Room 8109
Colorado State University
Fort Collins, CO 80523
(303) 491-6696

CHANG, RICHARD K. DR.
Applied Physics Department
Yale University
P.O. Box 2157, Yale Station
New Haven, CT 06520
(203) 432-4470

CHEW, HERMAN DR.
Clarkson University
Potsdam, NY 13676
(315) 268-2390 or 268-2363

CHITANVIS, SHIRISH DR.
Physics Department
City College of New York
New York, NY 10031
(212) 690-6865

CIPOLLA, JOHN DR.
Mechanical Engineering Department
435 LA
Northeastern University
Boston, MA 02115
(617) 437-3805

COHEN, ARIEL DR.
Department of Physics & Atmospheric
Sciences
Drexel University
Philadelphia, PA 19104
(215) 895-2707

COHEN, LEN DR.
Department of Physics & Atmospheric
Sciences
Drexel University
Philadelphia, PA 19104
(215) 895-2710

COHOON, DAVID
USAMRCD and Department of
Mathematics 038-16
Temple University
Philadelphia, PA 19122

COLETTI, ALESSANDRO DR.
Georgia Institute of Technology
School of Geophysical Sciences
Atlanta, GA 30332
(404) 894-3891

CURRY, WILLIAM MR.
VKF/SP Calspan, Inc.
MS 650
Arnold Air Force Station, TN 37389
(615) 455-2611, ext. 7200

DAVISON, STOWELL DR.
Department of Chemical Engineering
University of Maryland-Baltimore County
Catonsville, MD 21228
(301) 455-2659

DEEPAK, ADARSH DR.
Science & Technology Corporation
P.O. Box 7390
Hampton, VA 23666
(804) 865-1894

DELFOUR, ANDRE MR.
O.N.E.R.A.-C.E.R.T.
2, Avenue Edouard Belin
B.P. 4025
31055 Toulouse, Cedex
FRANCE
(33) 61. 55.71.04

de Wolf, DAVID A. DR.
Department of Electrical Engineering
VPI&SU
Blacksburg, VA 24061
(703) 961-6646

DITMARS, DAVID A. MR.
National Bureau of Standards
Building 221, Room A324
Washington, DC 20234

DOHERTY, ROBERT
Chemical Research & Development Center
DRSMC-CLB-PS
Aberdeen Proving Ground, MD 21010
(301) 671-2760

DUFF, JAMES W. DR.
Spectral Sciences, Inc.
Burlington, MA 01803

DYE, DAVID L.
Boeing Aerospace Company
P.O. Box 3999, 8C-23
Seattle, WA 98124
(206) 773-0368

EATON, L. R.
TRM
One Space Park
Redondo Beach, CA 90278
(213) 535-2500

ELLIOTT, R. A. PROF.
Oregon Graduate Center
19600 N.W. Walker Road
Beaverton, OR 97006
(503) 645-1121

EMBURY, JANON (JAY) DR.
Chemical Research & Development Center
DRSMC-CLB-PS(A)
Aberdeen Proving Ground, MD 21010
(301) 671-4256

ENSOR, DAVID S.
Research Triangle Institute
P.O. Box 12194
Research Triangle Park, NC 27709
(919) 541-6000

ERICKSON, NILS
Chem B-24N
National Bureau of Standards
Gaithersburg, MD 20899
(301) 921-2789

EVANS, ALAN J. DR.
Chemical Defense Establishment
Porton Down
Salisbury, Wiltshire
ENGLAND

EVANS, BLAIR DR.
Defense Research Establishment Valcartier
P.O. Box 8800
Courcellette, Quebec
CANADA G0A 1R0
(418) 844-4302

FARMER, MIKE W. DR.
Science and Technology Corporation
Suite 940, First National Tower
Las Cruces, NM 88005
(505) 523-8541

FARRELL, RICHARD A.
Applied Physics Laboratory
Johns Hopkins University
Johns Hopkins Road
Laurel, MD 20707
(301) 792-7800, ext. 571

FLANIGAN, DENNIS MR.
Chemical Research & Development Center
DRSMC-CLC-R
Aberdeen Proving Ground, MD 21010
(301) 671-3484/3884

FLOOD, W. A. DR.
US Army Research Office
P.O. Box 12211
Research Triangle Park, NC 27709
(919) 549-0641

FRASER, ROBERT S.
NASA Goddard Space Flight Center
Code 915
Greenbelt, MD 20771
(301) 344-9008

FREUND, DAVID E.
Applied Physics Laboratory
Johns Hopkins University
Johns Hopkins Road
Laurel, MD 20707

FRICKEL, ROBERT H.
Chemical Research & Development Center
DRSMC-CLB-PS
Aberdeen Proving Ground, MD 21010
(301) 671-3854

FRIEND, JAMES P.
Department of Chemistry
Drexel University
32nd & Chestnut Streets
Philadelphia, PA 19104
(215) 895-2642

FRY, EDWARD S. DR.
Physics Department
Texas A&M University
College Station, TX 77843
(409) 845-19101

GALLILY, ISIAH PROF.
Department of Atmospheric Sciences
Hebrew University
Jerusalem 91904
ISRAEL
(02-639003)

GARVEY, DENNIS M. DR.
US Army Atmospheric Sciences Laboratory
White Sands Missile Range, NM 88002
(505) 678-1526

GAUSS, ARTHUR
Ballistic Research Laboratory
Aberdeen Proving Ground, MD 21005
(301) 278-4884

GEBHARDT, FRED DR.
Science Applications, Inc.
3 Preston Ct.
Bedford, MA 01730
(617) 275-2200

GORDON, MALCOM G.
AAI Corporation
2317 Perry Avenue
Edgewood, MD 21040

GREEN, JOHN J.
Chemical Research & Development Center
DRCPM-SMK-T
Aberdeen Proving Ground, MD 21005
(301) 278-5411

GUILLAME, BERNARD DR.
O.N.E.R.A. - C.E.R.T.
2, Avenue Edouard Belin
B.P. 4025
31055 Toulouse, Cedex
FRANCE
(33) 61557107

HAGER, JOSEPH W. CPT
Air Force Office of Scientific Research
AFOSR/NE
Bolling AFB, DC 20332
(202) 767-4909

HANLEY, JAMES T.
Arvin/Calspan
P.O. Box 400
Buffalo, NY 14225
(716) 632-7500

HANNA, STEVEN, DR.
Environmental Research & Technology
Concord, MA 01742
(617) 369-8910

HARACZ, RICHARD DR.
Department of Physics & Atmospheric
Sciences
Drexel University
Philadelphia, PA 19104
(215) 895-2719

HARRIS, B. I. DR.
Pondsprings
11323 Glen Arm Road
Glen Arm, MD 21957
(301) 668-7352

HEATH, BILL
Battelle, Pacific Northwest Laboratories
300/324/14
P.O. Box 999
Richland, WA 99352
(509) 376-0554

HUFFMAN, DONALD R. PROF.
Physics Department
Building 81
University of Arizona
Tucson, AZ 85721
(602) 626-4804/3634

HERMAN, BENJAMIN M. DR.
Institute of Atmospheric Physics
Building No. 81
University of Arizona
Tucson, AZ 85721
(602) 621-6846

ISKANDER, MAGDY F. DR.
Department of Electrical Engineering
3053 Merrill Engineering Building
University of Utah
Salt Lake City, UT 84112
(801) 581-6944

HOFLAND, ROBERT
The Aerospace Corporation
P.O. Box 92957
Los Angeles, CA 90009
(213) 648-6115

JAGGARD, DWIGHT L. PROF.
Moore School/D2
University of Pennsylvania
Philadelphia, PA 19104
(215) 898-4411

HOLT, E. H.
Atmospheric Sciences Laboratory
USAERADCOM
White Sands Missile Range, NM 88002
(505) 678-2412/1997

JENKINS, WILHELMINA D.
MET A117
National Bureau of Standards
Gaithersburg, MD 20899
(301) 921-2157

HU, CHIA-REN DR.
Physics Department
Texas A&M University
College Park, TX 77843
(409) 845-3531

JORDAN, ARTHUR DR.
Naval Research Laboratory
Code 7942
Washington, DC 20375
(202) 767-6609

HUANG, KAO-HUAH DR.
FWG Associates, Inc.
Rt. 2, Box 271-A
Tullahoma, TN 37388
(615) 455-1982

KAPLAN, CAROLYN MS.
Chemical Engineering Department
University of Maryland
College Park, MD 20742
(301) 454-5098

HUDSON, JIM DR.
Desert Research Institute
University of Nevada
P.O. Box 60220
Reno, NV 89506

KATTAWAR, GEORGE W. DR.
Physics Department
Texas A&M University
College Station, TX 77843
(409) 845-1180

KAUFMAN, YORAM
NASA/Goddard Space Flight Center
Greenbelt, MD 20771
(301) 344-4977

KEESE, ROBERT G. DR.
Department of Chemistry
The Pennsylvania State University
University Park, PA 16802
(814) 863-3574

KERKER, MILTON PROF.
Clarkson University
Potsdam, NY 13676
(315) 268-2390

KIECH, E. L.
VKF/SP Calspan
MS 650
Arnold Air Force Station, TN 37389
(615) 455-2611, ext. 7669

KLEINMAN, RALPH E. DR.
Department of Mathematics
University of Delaware
Newark, DE 19716
(302) 451-2250

KLIMEK, W. G.
Project Manager, Smoke/Obscurants
DRCPM-SMK-T
Aberdeen Proving Ground, MD 21005
(301) 278-5411

KLUCHERT, ROLF E. MR.
Canadian Defence Liaison Staff
2450 Massachusetts Avenue, N.W.
Washington, DC 20008
(202) 483-5505

KOHL, RONALD H. DR.
Ronald H. Kohl & Associates
R 2, Box 2838
Tullahoma, TN 37388
(615) 454-9060

LATHAM, JOHN PROF.
Department of Pure & Applied Physics
U.M.I.S.T.
P.O. Box 88
Manchester M60 1QD
ENGLAND
061-236-3311, ext. 2962

LAULAINEN, NELS S. DR.
Battelle Pacific Northwest Laboratory
Battelle Blvd., P.O. Box 999
Richland, WA 99352
(509) 376-8320

LAWLESS, PHIL A. DR.
Research Triangle Institute
Box 12194
Durham, NC 27709
(919) 541-6782

LAX, MELVIN DR.
Physics Department
City College of New York
New York, NY 10031
(212) 690-6864

LEONG, KENG H. DR.
Department of Civil Engineering
3207 Newmark Civil Engineering Lab
University of Illinois
208 N. Komine
Urbana, IL 61801
(217) 333-8064

LETTIERI, THOMAS R.
National Bureau of Standards
MET A117
Washington, DC 20234
(301) 921-2159

LITTMAN, HOWARD PROF.
Department of Chemical Engineering
Rensselaer Polytechnic Institute
123 Ricketts Building
Troy, NY 12181
(518) 266-6039

LUTHER, FRED DR.
Lawrence Livermore National Laboratory
P.O. Box 808 (L-262)
Livermore, CA 94550
(415) 422-1825

MORGAN, MORRIS H. PROF.
Dept. of Chemical Engineering and
Environmental
Troy, NY 12181
(518) 266-6059

MACK, EUGENE MR.
Arvin/Calspan Corporation
P.O. Box 400
Buffalo, NY 14225
(716) 631-6782

NAGPAL, KRISHEN DR.
Chemical Research Development Center
Aberdeen Proving Ground, Md 21010

MARSTON, PHILIP DR.
Physics Department
Washington State University
Pullman, WA 99164-2814
(509) 335-9531

NEWHOUSE, JAMES R.
Atmospheric Sciences Laboratory
White Sands Missile Range, NM 88002
(505) 678-1561

MATTAR, FARRES DR.
Physics Department
City College of New York
New York, NY 10031
and New York University
4 Washington Pl.
New York, NY 10003
(212) 690-6864

NIELSEN, EDMOND J. DR.
3M Company
3M Center
St. Paul, MN 55144
(612) 733-9618

MAZUMDER, M.K. PROF. Dr. Ing.
Department of Electronics & Instrumentation
Graduate Institute of Technology
University of Arkansas
P.O. Box 3017
Little Rock, AR 72203
(501) 373-2720

NOLAN, PAT M. MR.
Department of Chemistry
Drexel University
32nd & Market Streets
Philadelphia, PA 19104
(215) 895-2642

MCCORMICK, NORMAN J. PROF.
Department of Nuclear Engineering
BF-10
University of Washington
Seattle, WA 98195
(206) 543-4355

PARKER, MIKE
Chemical Research & Development Center
DRSMC-CLM-S(A)
Aberdeen Proving Ground, MD 21010
(301) 671-

MOELLER, K. D. PROF.
Department of Physics
Fairleigh Dickinson University
Teaneck, NJ 07666
(201) 692-2287

PATEL, SUSHIL
State University of New York-Buffalo
Buffalo, NY 14214

PEARCE, WILLIAM A. DR.
EG&G/WASC
P.O. Box 398
Riverdale, MD 20840
(301) 779-2800, ext. 247

PEDERSEN, JEANNE DR.
Panametrics
221 Crescent Street
Waltham, MA 02154
(617) 899-2719

PEDERSEN, NORMAN DR.
Panametrics
221 Crescent Street
Waltham, MA 02154
(617) 899-2719

PENDLETON, J. DAVID (DAVE) DR.
Atmospheric Sciences Laboratory
P.O. Box 236
White Sands Missile Range, NM 88002
(505) 678-5634

PHIPPS, CLAUDE R., JR. DR.
Chemistry Division, MS E535
Los Alamos National Laboratory
Los Alamos, NM 87545
(505) 667-6956

PINNICK, RONALD G. DR.
Atmospheric Sciences Laboratory
DELAS-AR
White Sands Missile Range, NM 88002
(505) 678-5634

PLUCHINO, ANTONINO B. MR.
The Aerospace Corporation
Building A 6-1647
P.O. Box 92957
Los Angeles, CA 90009
(213) 648-5000

PODZIMEK, JOSEF PROF.
Graduate Center for Cloud Physics Research
109 Norwood Hall
University of Missouri-Rolla
Rolla, MO 65401
(314) 341-4338

POND, ROBERT B. SR.
Materials Science & Eng.
Johns Hopkins University
Baltimore, MD 21218

POZIOMEK, EDWARD J. DR.
Chemical Research & Development Center
DRSMC-CLB(A)
Aberdeen Proving Ground, MD 21010
(301) 671-3250

QUERRY, MARVIN PROF.
Department of Physics
University of Missouri-KC
Kansas City, MO 64110
(816) 276-1604

RADZIEMSKI, LEON J. DR.
Department of Physics
P.O. Box 3D
New Mexico State University
Las Cruces, NM 88003-0004
(505) 646-3831

RANADE, MADHAR B.
Research Triangle Institute
Research Triangle Park, NC 27709
(919) 541-6925

REAGAN, JOHN A. PROF.
Department of Electrical & Computer Eng.
Engineering Building #20
University of Arizona
Tucson, AZ 85721
(602) 621-6203

REIST, PARKER
Department of Environmental
Science and Engineering
University of North Carolina
Chapel Hill, NC 27514
(919) 966-1023

REITZ, RICHARD G.
Project Manager, Smoke/Obscurants
DRCPM-SMK-E
Aberdeen Proving Ground, MD 21005-5001
(301) 278-3536/3426
AV 283-3536/3426

REUTTER, DENNIS J.
Chemical Research & Development Center
DRSMC-CLB-R(A)
Aberdeen Proving Ground, MD 21010
(301) 671-

RICHARDSON, MARTIN B. DR.
Atmospheric Sciences Laboratory
DELAS-AE-0
White Sands Missile Range, NM 88002
(505) 678-6780

RILEY, ERICA
Chemical Research & Development Center
DRSMC-CLB-PS(A)
Aberdeen Proving Ground, MD 21010
(301) 671-4294

RILEY, MICHAEL DR.
Chemical Research & Development Center
DRSMC-CLB-PS(A)
Aberdeen Proving Ground, MD 21010
(301) 671-4294

RIN, CHUN-HSUN DR.
Chemical Research & Development Center
DRSMC-CLC-R(A)
Aberdeen Proving Ground, MD 21010
(301) 671-3884

ROBINSON, RAYMOND S. DR.
Physics Department
Colorado State University
Fort Collins, CO 80523

ROSENWASSER, H. DR.
Naval Air Systems Command
Code AIR-320R
Washington, DC 20361
(202) 692-3023

RUBEL, GLENN O. DR.
Chemical Research & Development Center
DRSMC-CLB-PS(A)
Aberdeen Proving Ground, MD 21010
(301) 671-2760

RUBIO, ROBERTO
Atmospheric Science Laboratories
DELAS-AR-M
White Sands Missile Range, NM 88002

RUCK, GEORGE DR.
Battelle Columbus Laboratories
505 King Avenue
Columbus, OH 43201
(614) 424-5685

SARVER, EMORY W.
Chemical Research & Development Center
Aberdeen Proving Ground, MD 21010
(301) 671-3957

SAVAGE, J. DR.
Chemical Research & Development Center
DRSMC-CLB-PS(A)
Aberdeen Proving Ground, MD 21010
(301) 671-4294

SCHEUNEMANN, W. DR.
BICT
D5357 Heimerzheim
WEST GERMANY
(49) 2222-60081

SNELSON, ALAN DR.
IIT Research Institute
10 W. 35th Street
Chicago, IL 60616
(312) 567-4260

SIMON, IVAN DR.
Arthur D. Little, Inc.
15 Acorn Park
Cambridge, MA 02140
(617) 864-5770

SPAIN, IAN L. DR.
Department of Physics
Colorado State University
Fort Collins, CO 80523
(303) 491-6076

SINDONI, ORASIO J.
Chemical Research & Development Center
Aberdeen Proving Ground, MD 21010
(301) 671-4256

STALLINGS, EDNA S.
University of Tennessee Space Institute
Tullahoma, TN 37388
(615) 455-0631, ext. 473

SMALLEY, HOWARD M. DR.
Project Manager, Smoke/Obscurants
DRCPM-SMK-T
Aberdeen Proving Ground, MD 21005
(301) 278-5411

STEPHENS, JOHN R. DR.
Los Alamos National Laboratory
MS/C348
Los Alamos, NM 87545
(505) 667-7363

SMITH, DAVID DR.
United Technology Research Center
Silver Lane
MS 73
East Hartford, CT 06108
(203) 727-7281

STUDE, HENRY JR.
Chemical Research & Development Center
Research Division
Aberdeen Proving Ground, MD 21010

SMITH, FREDERICK G.
2000 Hogback Road, Suite 3
Ann Arbor, MI 48105
(313) 973-1177

STUEBING, EDWARD W.
Chemical Research & Development Center
ATTN: DRSNC-CLB-PS(A)
Aberdeen Proving Ground, MD 21010
(301) 671-3089

SMITH, R. BRENT
Optech, Inc.
701 Petrolia Road
Downsview, Ontario
CANADA
(416) 661-5904

SUTHERLAND, ROBERT A.
Atmospheric Sciences Laboratory
DELAS-EO-MO
White Sands Missile Range, NM 88002
(505) 678-3951

SWAN, CHARLES
AAI Corporation
Cockeysville, MD 21030

THOMAS, ROBERT W. L. DR.
.G&G/WASC
6801 Kenilworth Avenue
Riverdale, MD 20737
(301) 779-2800, ext. 202

TOKUDA, ALAN
Boeing Aerospace Company
P.O. Box 3999, MS 8C-23
Seattle, WA 98124
(206) 773-2638

TSANG, T.H. DR.
Department of Chemical Engineering
University of Kentucky
Lexington, KY 40506
(606) 257-5956

TURETSKY, ABE L.
Chemical Research & Development Center
DRDAR-CLB-PS
Aberdeen Proving Ground, MD 21010
(301) 671-2395

VARADAN, VIJAY K. PROF.
Department of Engineering Science
& Mechanics
Hammond Building
Pennsylvania State University
University Park, PA 16802
(814) 865-4523

WALL, KEVIN F. MR.
Applied Physics Department
Yale University
P.O. Box 2157, Yale Station
New Haven, CT 06520
(203) 436-2087

WANG, RU T. DR.
Space Astronomy Laboratory
University of Florida
1810 N.W. 6th Street
Gainesville, FL 32601
(904) 392-5450

WARD, J. RICHARD
Chemical Research & Development Center
Aberdeen Proving Ground, MD 21010
(301) 671-4144

WASEL, W. D.
Chemical Research & Development Center
DRDAR-CLB-PO
Aberdeen Proving Ground, MD 21010
(301) 671-2796

WATERMAN, PETER DR.
Panametrics
8 Baron Park Lane
Burlington, MA 01803
(617) 272-4494

WEIL, HERSCHEL PROF.
Department of Electrical Eng. &
& Computer Sci.
University of Michigan
Ann Arbor, MI 48109
(313) 764-0500

WILHELM, H. E. PROF.
NWC, Code 914
China Lake, CA 93555

WINTER, JOHN M. JR.
Dept. of Materials Science & Engrg.
Johns Hopkins University
Baltimore, MD 21218

WYATT, PHILIP J. DR.
Wyatt Technology Corporation
P.O. Box 3003
Santa Barbara, CA 93130-3003
(805) 963-5904

YEH, CAVOUR PROF.
EMtec Engineering, Inc.
1100 Glendon Avenue
Suite 2032
Los Angeles, CA 90024
(213) 825-2970

YEH, HSU-CHI, DR.
Lovelace Inhal. Toxicol. Res. Inst.
P.O. Box 5890
Albuquerque, NM 87185
(505) 844-2151

ZARDECKI, ANDREW
Los Alamos National Laboratory
MS 8279
Los Alamos, NM 87545
(505) 667-7646

BLANK

AGENDA*1984 CRDC SCIENTIFIC CONFERENCE ON OBSCURATION AND AEROSOL RESEARCH25-29 June, Bldg. E4810 (Post Theater)

All presentations are listed with the appropriate session topic as well as where they appear in the schedule, if different.
[The second listings for scheduling purposes are enclosed in square brackets.]

MONDAY 25 June

9:30 Registration Opens

10:00 Opening of Conference

Welcome - Dr. B. Richardson, Deputy Director, CRDC
Administrative Remarks - R. Kohl

10:15 Overview of Aerosol Research Program - E. Stuebing G. Rubel,
J. Bottiger, and O. I. Sindoni

11:45 LUNCH

I. PHYSICAL AND CHEMICAL PROPERTIES OF AEROSOLS

Moderator: Glen Rubel

A. Particle Formation, Evolution and Composition

Post. Alistair C. D. Leslie and Nels S. Laulainen (Battelle, Northwest), Inertial Particle Sampler for Fine Size Particle Fractionation and Chemical Speciation by PIXE

Post. James Hudson (Desert Research Institute), Interstitial Particles in Fogs

Tu. AM R. G. Pinnick, G. Fernandez and B. D. Hinds (Atmospheric Sciences Laboratory) Volatility of Near-Surface Aerosols in Southern New Mexico

1:00 Keng H. Leung (University of Illinois), Generation of Monodisperse Nonspherical Aerosol Particles (15)

1:20 R. G. Keesee and A. W. Castleman, Jr. (Pennsylvania State University), Gas-to-Particle Conversion: The Role of Pre-Existing Dimers in the Formation of Clusters During Supersonic Expansion (15)

*Presenters are underlined. Where only the presenter's name appears, other authors may be indicated in the presentation.
"Post." indicates a presentation in the all-topic poster session on Wednesday, late afternoon and evening.

MONDAY 25 June (continued)

I. A. (continued)

- 1:40 J. R. Brock (University of Texas/Austin), Ostwald Ripening and Other Particle Growth Processes (15)

B. Plume Mechanics

- 2:00 T. H. Tsang and J. R. Brock (University of Texas/Austin), Atmospheric Models of Aerosol Plume Dispersion (15)
- 2:20 J. Latham (U.M.I.S.T., England), Turbulent Mixing Processes (15)
- 2:40 Steven F. Hanna (ERT), Characteristics of Observed Concentration Fluctuations During Smoke Week 3 and Comparisons with Theoretical Models (15)
- 3:00 BREAK
- 3:30 J. E. Cermak (Colorado State University), Diffusion in Unstable (Convective) Boundary Layers (15)
- 3:50 B. Evans (DREV, Canada), A Comparison of In-Field Data and Theoretically Derived Vertical Concentration in Man-Made Dust Plumes (15)

C. Particle Dynamics: Orientation Effects, Concentration Sampling, and Size/Shape Analysis

- 4:10 Isaiah Gallily and E. M. Krushkal (Hebrew University, Israel), The Orientation Distribution Function of Non-Spherical Aerosol Particles in a General Shear Flow: The Turbulent Case (20)
- 4:35 S. Davison, S. Hwang, J. Wang and J. W. Gentry (University of Maryland), Unipolar Charging for Ultra Fine Aerosols: Theory, Experiment and Significance for Size Distribution (15)

D. Aerosol Elimination

- 4:55 Joseph Podzimek (Graduate Center for Cloud Physics Research - University of Missouri, Rolla), Results of the Past and Current Investigation of Smoke Particle Scavenging by Nonspherical Collectors (15)

MONDAY 25 June (continued)

I. D. (continued)

5:15 Kang H. Leong (University of Illinois), The Collision of Nonspherical Aerosol Particles with Water Drops (15)

Post. Withdrawn

5:35 Adjournment
Cocktails and Dinner at The Red Fox, Bel Air, MD (casual)

TUESDAY 26 June

I. PHYSICAL AND CHEMICAL PROPERTIES OF AEROSOLS (continued)

A. Particle Formation, Evolution and Composition

8:15 R. G. Pinnick, G. Fernandez and B. D. Hicks (Atmospheric Sciences Laboratory), Volatility of Near-Surface Aerosols in Southern New Mexico (15)

II. AEROSOL CHARACTERIZATION METHODS (Other than Aerodynamic Methods - See Session I. C.)

Moderator: Jerold Bottiger

A. Particle Shape Descriptions and the Value of Effective Size Parameters

8:35 David Shaw (SUNY/Buffalo), A Review of Irregular Particle Measuring Techniques (25)

9:05 W. Scheuerman (BICT, Germany), Characterization of Nonspherical Metallic Particles (15)

Post. C. Kaplan, P. Y. Yu, F. Parsanah, J. Hong, and J. W. Gentry (University of Maryland), Application of Condition Numbers in Particle Size Analysis and Linear Regression

B. Optical Inversion Methods for Size Distribution (Including Optical Particle Size Analyzers)

Post. R. E. Benner, S. C. Hill, C. K. Rushforth and P. R. Conwell (University of Utah), Use of Structural Resonances in Fluorescence Emission for Sizing Spheres Resting on Substrates

TUESDAY 26 June (continued)

II. B. (continued)

- 9:25 W. M. Farmer (STC) and J. Y. Son (UTSI), A Comparison of Phase Functions Obtained by Scattering Intensity and by Interferometric Visibility (15)
- 9:45 A. R. Tokuda, T. R. Majoch, S. R. Beck, C. D. Capps and G. M. Hess (Boeing Aerospace Co.), Multichannel Nephelometer Design (15)
- 10:05 BREAK
- 10:35 J. Bottiger (CRDC), Progress of Inversion Technique Evaluation (15)
- 10:55 B. P. Curry and E. L. Kiech (Calspan Field Services, Inc.), Determination of Particle Size Distribution from Blind Inversion of Synthetic Data (15)
- 11:15 B. M. Herman and A. Ben-David (Inst. of Atmos. Physics, Univ. of Arizona) and J. Reagan (Dept. of Elec. Eng., Univ. of Arizona), Particle Size Distributions Obtained from Multi-Wavelength Backscattering Data (15)
- 11:35 William A. Pearce (EG & G/WASC), Aerosol Size Distribution Inversion from Simulated Nephelometric Data (15)
- Post. André Delfour, Antoine Pérus and Daniel Bize (O.N.E.R.A. - C.E.R.T., France), Particle Size Distribution of Each Constituent of an Heterogeneous Aerosol
- 11:55 Robert W. L. Thomas (EG & G/WASC), The Effect of Representation on the Interpretation of the Remote Sensing of Aerosols (15)
- 12:15 LUNCH
- 1:30 William Hooper and A. K. Jordan (Naval Research Laboratory), Generalized Inversion Method for Data Representations in the Complex Plane (15)

C. Optical Constants of Liquids and Powders

- 1:50 Marvin Quarry (Univ. of Missouri - Kansas City), Optical Constants of Selected Materials in the IR-MIR-Vis-UV Spectral Region: Graphites, Copper, Brass, Aluminum, Aluminum Oxide, Conducting Polymers, Iron, Iron Oxides, Zinc Oxide, Intercalated Graphite and Vitreous Carbon (15)
- Post. Bernard Guilleme, André Delfour and Daniel Bize (O.N.E.R.A. - C.E.R.T., France), The 10.6 μ m Refractive Index Measurement of a Single Particle in Optical Levitation
- 2:10 Vincent Tomaselli and K. D. Moeller (Fairleigh Dickinson University), Far-Infrared Extinction Properties of Metal Powders (15)
- 2:30 CONVERSATION/DISCUSSION BREAK (1½ hours)

TUESDAY 26 June (continued)

II. C. (continued)

- 4:00 K. D. Moeller (Fairleigh Dickinson University), Beamsplitter and Detectors for the Submillimeter and Millimeter Region (15)
- 4:20 Robert J. Bell, M. A. Ordal, R. E. Paul, L. L. Long and R. W. Alexander (University of Missouri - Rolla), Prediction of the mm Wavelength and Sub-mm Wavelength Optical Properties of Metal and Some New Data for Iron and Graphite (15)
- 4:40 Larry Long, R. J. Bell and Ralph Alexander (University of Missouri - Rolla), Changes in the Submillimeter Spectra of Minerals with Loss of Water of Hydration (15)

III. OPTICAL PROPERTIES OF AEROSOLS

Moderator: E. Stuebing (Moderator for III. C. is O. I. Sindoni)

A. Infrared Emission from Aerosols

Post. Withdrawn

- 5:00 Glen O. Rubel (CRDC), Investigation of the Reaction Between Acid Droplets and Ammonia Gas (15)
- 5:20 Adjournment
Cocktails and Dinner at Giovanni's, Edgewood, MD (casual) or
Cocktails and Dinner at Hausner's Restaurant, Baltimore, MD

WEDNESDAY 27 June

III. A. (continued)

- 8:15 A. Snelson (ITT Research Institute), Some Further Studies on Emissive Aerosols and a New Broadband IR Aerosol (15)
- B. Interaction of Radiation and Spherical (Including Layered) Particles
- 8:35 A. Coletti (Georgia Institute of Technology), On Possible Experimental Application of Some Properties of the First Expansion Coefficients of the Phase Function and Phase Matrix (15)
- Post. Philip L. Marston and Dean S. Langley (Wash. State Univ.), Transmitted-Wave and Rainbow-Enhanced Glories of Dielectric Spheres

WEDNESDAY 27 June (continued)

III. B. (continued)

- 8:55 S. Arnold (Polytechnic Institute of N.Y.) and A. B. Pluchino (The Aerospace Corp.), Infrared Spectroscopy of Single Micron-Sized Particles (15)
- Post. Thomas R. Lettieri, Richard E. Preston and Michael Bell (National Bureau of Standards), Raman Spectroscopy of Single Liquid Droplets
- 9:15 K. F. Wall, H. M. Tzeng and R. K. Chang (Yale University), Droplet Lasing and Evaporation/Condensation Studies in a Highly Monodisperse ($1:10^5$) Linear Droplet Stream (15)
- 9:35 John Cipolla (Northeastern University) and T. F. Morse (Brown University), Some Recent Results in Laser-Aerosol Interactions in Horizontal and Vertical Tubes (15)
- Th.AM Philip L. Marston (Washington State Univ.) and James H. Crichton (Seattle Pacific University), Radiation Torque on a Sphere Illuminated with Circularly Polarized Light
- 9:55 BREAK

C. Workshop: Nonlinear Phenomena

Moderator: O. I. Sindoni

- 10:25 Janon Embury (CRDC), Aerosol Countermeasures to Directed Energy Weapons (15)
- 10:45 David Smith (United Technology Research Center), Aerosol-Induced Gas Breakdown and Aerosol-Induced Thermal Blooming: A Review (30)
- 11:20 Leon J. Radziemski (New Mexico State University), Time-Resolved Spectroscopy of Laser-Induced Air Plasmas (15)
- 11:40 LUNCH
- 12:55 R. Armstrong (New Mexico State University), Interactions of Absorbing Aerosols with High Energy Lasers (15)
- 1:15 Withdrawn
- Post. S. T. Amimoto (Aerospace Corp), G. L. Trusty and D. H. Leslie (Naval Research Lab.) and R. Hofland (Aerospace Corp.), DF-Laser-Pulse Breakdown Induced by Land and Maritime Aerosols
- 1:35 J. D. Pendleton and R. G. Pinnick (Atmospheric Sciences Laboratory), Explosive Vaporization of Spherical Aerosol Droplets by Pulsed Lasers (15)
- 1:55 R. K. Chang, J. B. Snow, S.-X. Qian, K. F. Wall and H.-M. Tzeng (Yale University), Nonlinear Optical Effects from a Liquid Droplet Irradiated by High Energy Lasers (15)
- 2:15 Mel Lax (City College of New York), Problems in HEL-Aerosol Interactions (15)
- 2:35 BREAK

WEDNESDAY 27 June (continued)

III. (continued)

D. Interaction of Radiation and Nonspherical Particles (Including Aggregates) with or without Cooperative Effects

- 3:05 Donald R. Huffman (University of Arizona), Low Temperature Matrix Isolation Spectroscopy of Carbon and Metal Alloys - Bridging the Gap Between Molecular and Microcrystal Spectroscopies (15)
- 3:25 M. P. Iskander (University of Utah), New Iterative Extended Boundary Condition Method for Calculating Scattering and Absorption by Elongated and Composite Objects (15) [Given at the end of Thursday]

(III. D. listing continued under Thursday 28 June)

PREVIEWS OF PRESENTATIONS in the ALL-TOPIC POSTER SESSION

I. PHYSICAL AND CHEMICAL PROPERTIES OF AEROSOLS

A. Particle Formation, Evolution and Composition

- 3:45 James Hudson (Desert Research Institute), Interstitial Particles in Fogs (2)

Add Alistair C. D. Leslie and Nelu S. Iaulainen (Battelle, Northwest), Inertial Particle Sampler for Fine Size Particle Fractionation and Chemical Speciation by PIXE (2)

D. Aerosol Elimination

3:48 Withdrawn

II. AEROSOL CHARACTERIZATION METHODS (Other than Aerodynamic Methods - See Session I. C.)

A. Particle Shape Descriptions and the Value of Effective Size Parameters

- 3:51 C. Kaplan, P. Y. Yu, F. Farzanah, J. Hong and J. W. Gentry (University of Maryland), Application of Condition Numbers in Particle Size Analysis and Linear Regression (2)

B. Optical Inversion Methods for Size Distribution (Including Optical Particle Size Analyzers)

- 3:54 R. E. Benner, S. C. Hill, C. K. Rushforth, and P. R. Conwell (University of Utah), Use of Structural Resonances in Fluorescence Emission for Sizing Spheres Resting on Substrates (2)

- 3:57 André Delfour, Antoine Pérus and Daniel Bize (O.N.E.R.A. - C.E.R.T., France), Particle Size Distribution of Each Constituent of an Heterogeneous Aerosol (2)

PREVIEWS (continued)

II. AEROSOL CHARACTERIZATION METHODS (continued)

C. Optical Constants of Liquids and Powders

- 4:00 Bernard Guillame, André Delfour and Daniel Bize (O.N.E.R.A. - C.E.R.T., France), The 10.6 μ m Refractive Index Measurement of a Single Particle in Optical Levitation (2)

III. OPTICAL PROPERTIES OF AEROSOLS

A. Infrared Emission from Aerosols

- 4:03 Withdrawn

B. Interaction of Radiation and Spherical (Including Layered) Particles

- 4:06 Philip L. Marston and Dean S. Langley (Washington State University), Transmitted-Wave and Rainbow-Enhanced Glories of Dielectric Spheres (2)

Add Thomas R. Lettieri, Richard E. Preston and Michael Bell (National Bureau of Standards), Raman Spectroscopy of Single Liquid Droplets

C. Workshop: Nonlinear Phenomena

Add S. T. Amimoto (Aerospace Corp), G. L. Trusty and D. H. Leslie (Naval Research Lab) and R. Hofland (Aerospace Corp.), DP-Laser-Pulse Breakdown Induced by Land and Maritime Aerosols

D. Interaction of Radiation and Nonspherical Particles (Including Aggregates) with or without Cooperative Effects

- 4:09 M. F. Iskander and R. E. Banner (University of Utah), Potential Applications of the New Iterative Extended Boundary Condition Method in the Optical Regime (2)

4:12 Withdrawn

- 4:15 Ru Wang (Space Astronomy Laboratory, Univ. of Florida), Extinction and Angular Scattering by Rough Particles (2)

E. Propagation/Multiple Scattering in Aerosol Media and Radiative Transfer

- 4:18 J. A. Reagan, A. Ben-David and B. M. Herman (Univ. of Arizona), Assessment of Aerosol Extinction-to-Backscatter Ratio Measurements Made at 694.3 nm in Tucson, Arizona (2)

- 4:21 A. Coletti (Georgia Institute of Technology), Contours of Isophots in the Stratospheric Cloud of El Chichón (2)

- 4:24 Adjournment to Officers Club for Poster Session during Social Hour, Breaking for Beef and Burgundy Dinner approximately 6:30 (casual), and Resuming Conversation/Poster Session over Coffee and Dessert

THURSDAY 28 June

III. OPTICAL PROPERTIES OF AEROSOLS (resumed)

B. Interaction of Radiation and Spherical (Including Layered) Particles

- 8:15 Philip L. Marston (Washington State University) and James H. Crichton (Seattle Pacific University), Radiation Torque on a Sphere Illuminated with Circularly Polarized Light (15)

D. Interaction of Radiation and Nonspherical Particles (Including Aggregates) with or without Cooperative Effects (resumed)

Post. Withdrawn

- 8:35 Edward S. Fry, William White and Ken Voss (Texas A & M University), Mueller Matrix of a Single Dielectric Cube in a Fixed Orientation: Experiment (15)

- 8:55 [combined presentation] Mueller Matrix of a Single Dielectric Cube in a Fixed Orientation:

Chia-Ren Hu (Texas A & M University), Theory (10)

George W. Kattawar (Texas A & M University), Numerical Results (10)

- 9:20 A. B. Pluchino and M.E. Fahrner (Aerospace Corp.), Measured IR Scattering from Single Irregularly Shaped Ice Crystals (15)

- 9:40 Steven C. Hill and A. Clyde Hill (Univ. of Utah Research Institute) and Peter W. Barber (Clarkson University), Light Scattering by Size/Shape Distributions of Soil Particles and Spheroids (15)

10:00 BREAK

- 10:30 K. Tennal, J. D. Wilson, D. Jackson and M. K. Mazumder (University of Arkansas), Application of the Spectraphone to Measurement of Light Absorption by Multicomponent Aerosols (15)

- 10:50 H. Weil, T. B. A. Senior, T. M. Willis III (Univ. of Michigan), Internal and Near Fields of Small Particles Illuminated in Spectral Absorption Bands (15)

- 11:10 Donald R. Huffman (University of Arizona), Wavelength Dependence of Scattered Light Through Spectral Regions with Strong Absorption Bands, Using Laboratory and Field Measurements (15)

Post. Ru Wang (Space Astronomy Laboratory, Univ. of Florida), Extinction and Angular Scattering by Rough Particles

THURSDAY 28 June (continued)

III. D. (continued)

- 11:30 E. Bahar and M. A. Fitzwater (Univ. of Nebraska - Lincoln), Scattering and Depolarization by Very Long Finitely Conducting Cylinders with Pough Surfaces (15)
- 11:50 LUNCH
- 1:05 Ariel Cohen, Lenard Cohen and Richard Haracz (Drexel University) and V. Tomaselli, J. Colosi and K. D. Moeller (Fairleigh Dickinson University), Angular Scattering Distributions by Long Copper and Brass Cylinders-- Experiment and Theory (15)
- 1:25 Jeanne C. Pedersen, Norman E. Pedersen and Peter C. Waterman (Parax, Inc.), Recent Results in Scattering and Absorption by Conductive Fibers (15)
- 1:45 D. H. Holze, D. L. Dye, C. D. Capps, C. Gulascik (Boeing Aerospace Co.), and J.W. Bond (Belvoir Research and Development Center), Dipole-Dipole Scattering Interaction and Its Relation to Particle Separation in Coatings and Clouds (15)
- 2:05 Ariel Cohen, Lenard Cohen and Richard Haracz (Drexel University), Double Scattering by Finite Dielectric Cylinders (15)
- 2:25 B. Schlicht, K. F. Wall and R. K. Chang (Yale University), Fiber above a Mirror: Mirror-Fiber Distance Dependence of the Angular Scattering Pattern and the Morphology-Dependent Resonances in the Elastic Scattering (15)
- 2:45 Michael Riley (CRDC), An Invitation to Research: Co-operative Scattering Effects of Conductive Filaments (5)
- 2:55 CONVERSATION/DISCUSSION BREAK (1½ hours)
- 4:25 Milton Kerker (Clarkson University), Are Aggregates Necessary in Order to Observe Surface Enhanced Raman Scattering? (15)
- 4:45 J. R. Aronson, A. G. Ensie, Simon and E. M. Smith (Arthur D. Little, Inc.), Scattering and Absorption by Aggregated Aerosol Particles (15)
- 5:05 William S. Bickel (University of Arizona), Masking of Information in Light Scattering Curves from Complex Scatterers (15)
- [M. F. Iskander's paper, scheduled for 3:25 on Wednesday, was given here.]
- 5:25 Adjournment
Crab Feast at Gabler's Shore Restaurant on the Bush River (very casual)
(Chicken & Hamburgers also available)

FRIDAY 29 June

III. OPTICAL PROPERTIES OF AEROSOLS (continued)

B. Propagation/Multiple Scattering in Aerosol Media and Radiative Transfer

- 8:15 Peter C. Waterman, Norman E. Pedersen and Jeanne C. Pedersen (Panametrics), Radiative Transfer by Clouds of Conductive Fibers (15)
- 8:35 V. K. Varadan, V. V. Varadan and Y. Ma (Pennsylvania State University), Multiple Scattering by Aligned and Randomly Oriented Discrete Scatterers (15)
- 8:55 C. Yeh and A. Ishimaru (EMtec Engineering, Inc.), Multiple Scattering Calculations for Nonspherical Particles Based on the Vector Radiative Transfer Theory (15)
- 9:15 David A. de Wolf (VPI & SU), The Renormalized Wave Equation and Applications (15)
- Post. J. A. Reagan, A. Ben-David and B. M. Herman (University of Arizona), Assessment of Aerosol Extinction-to-Backscatter Ratio Measurements Made at 694.3 nm in Tucson, Arizona
- 9:35 R. B. Smith, T. D. Houston, A. Ulitsky, A. I. Carswell, and S. R. Pal (Optech, Inc.), Propagation and Scattering of Infrared Laser Beams in Dense Clouds (15)
- 9:55 BREAK
- 10:25 N. J. McCormick (University of Washington), Transport Methods for Estimating Single-Scattering Coefficients from Remote or In-Situ Multiply-Scattered Radiance Measurements (15)
- 10:45 A. Zardecki and S. Gerstl (Los Alamos National Laboratory) and J. Embury (CRDC), Imaging through a Multiply Scattering Medium (15)
- Post. A. Coletti (Georgia Institute of Technology), Contours of Isophots in the Stratospheric Cloud of El Chichon

IV. DISCUSSION: DIRECTIONS FOR FUTURE RESEARCH IN THE CRDC AEROSOL RESEARCH PROGRAM

Moderator: E. Stuebing

11:05 Discussion (About 75 minutes)

Approximately 12:20 End of Conference